



Novel mouse models of Col-1 related overlap syndrome, with late onset osteoarthritis

A thesis submitted for the degree of Doctor of Philosophy

August 2021

Andrew Blease

Mammalian Genetics Unit, Medical Research Council Harwell Institute, Harwell, UK

The Open University, Milton Keynes, UK

Discipline: Life and Biomolecular Sciences

Abstract

Collagen I is a member of the Collagen superfamily of proteins, the proteins most abundant in mammals, and an essential component of bones, teeth, skin and connective tissues including ligaments and tendons. *COL1A1* and *COL1A2* are the genes that code for the collagen I alpha chains, $\alpha 1$ and $\alpha 2$ respectively. Collagen I is a heterotrimer of these two alpha chains, formed of two $\alpha 1$ and one $\alpha 2$ chains. Diseases resulting from genetic mutations in *COL1A1* and *COL1A2*, include osteogenesis imperfecta (OI) and Ehlers-Danlos syndrome (EDS), however, mutations in these genes have not been implicated in the development of osteoarthritis (OA).

At MRC Harwell Institute, large-scale mutagenesis screens, including the Harwell Ageing Screen, have been used to identify novel models of disease and establish links between genes and diseases. The mutagenised mouse lines MP-107 and TM44 were identified in such screens, exhibiting early-onset mild bone abnormalities at the pelvis and elbow. These animals subsequently developed late-onset phenotypes including abnormal bone growth at the knee and OA.

Genetic mapping and sequencing revealed that MP-107 and TM44, contained mutations in *Col1a2* and *Col1a1* respectively, which correspond to the genes *COL1A2* and *COL1A1* in humans. The MP-107 mutation was a T to A transversion at position 4521226 of Chromosome 6 resulting in alternative splicing at exon 22 of *Col1a2*. The TM44 mutation was a C to T transition at position 94836670 of Chromosome 11 resulting in a premature stop codon in exon 31 of *Col1a1*.

Extensive phenotyping analysis revealed that the bone abnormalities observed in these lines are a result of an OI phenotype. Evidence of an EDS phenotype was also identified in the line MP-107, indicating that MP-107 is likely a model of Col-1 related overlap syndrome, a proposed EDS subtype exhibiting aspects of OI and EDS. Collagen I related changes to the joint tissues is likely the cause of the OA phenotypes. The project has the potential to enhance understanding of both the development of Col-1 related overlap syndrome and OA, and possible targets for therapy.

Acknowledgments

I would like to thank my supervisors Dr Paul Potter and Prof Steve Brown for their support and guidance over the course of my studies. I would also like to thank my external supervisor Prof Tonia Vincent for her insights, and Prof Roger Cox and Dr Nanda Rodrigues for their support throughout my studies.

I owe an immense amount to the members of the Disease Model Discovery (DMD) group, especially Tom Nicol, Sara Falcone, Laura Wisby, Andy Haynes and Heena Lad, and the members of the deafness group who adopted me when the DMD group was disbanded- Hilda Tateossian, Carlos Aguilar, Sheri Newton, Andy Parker, Amy Southern, Gurpreet Bharj, Pratik Vikhe and Tom Purnell.

Over the course of this project I have worked with some fantastic collaborators: Ilaria Bellantuono, Helen Birch, Karl Kadler, Hazel Screen and Sotcheadt Sim who have provided invaluable advice and assistance, in addition to the use of their labs and equipment, without which this project could not have progressed as it has.

Thanks to Prof Raj Thakker and Dr Chris Esapa for the use of the line TM44, and the genome engineering team at MRC Harwell for producing the *Col1a2* knock out line.

The Mary Lyons Centre is a fantastic mouse facility and the hard work of everyone involved has been greatly appreciated, particularly Dr Sara Wells, Dr Shell Stewart and the fantastic staff of Ward 3 past and present. Special thanks to the Staff who managed my lines Marie Hutchison, Gem Atkins, Rosie Hillier, Bex Starbuck, Emily Ireson, Nat Walters and Lee Kent.

Support from many core groups at MRC Harwell including clinical chemistry, histology, genotyping, and imaging teams, has been of huge help throughout this project.

Thank you to Caroline Fry, Jadwiga Zarebska, Bryony Stott, Ida Parisi, Marcia Curtina, Adele Austin, Caroline Barker and Chavaunne Thorpe for your technical training and assistance.

Finally, I would like to thank my family for their encouragement and support, in particular my partner Delphine for her patience and understanding.

Table of Contents

Abstract	ii
Acknowledgments.....	iii
Table of Contents	iv
Table of Figures	xv
Table of Tables	xxv
Abbreviations	xxviii
Chapter 1: Introduction.....	1
1.1. Collagen I	2
1.1.1. The Collagen Family	2
1.1.2. Collagen I Structure and Synthesis.....	4
1.1.3. Collagen I and Connective Tissues	7
1.1.3.1. Tendons	8
1.1.3.2. Bone	10
1.2. Diseases Associated with Collagen I.....	14
1.2.1. Osteogenesis Imperfecta	14
1.2.1.1. Mechanisms Behind the OI Phenotype.....	19
1.2.1.2. Mouse Models of OI	21
1.2.2. Ehlers-Danlos Syndrome	24
1.2.2.1. Classical EDS	26
1.2.2.2. Cardiac-valvular EDS.....	27
1.2.2.3. Vascular EDS	27
1.2.2.4. Arthrochalasia EDS	28
1.2.2.5. Mouse Models of EDS	29
1.2.3. Osteogenesis Imperfecta/Ehlers-Danlos Syndrome Overlap	29

1.2.3.1.	Mouse models OI/EDS Overlap	31
1.2.4.	Other Conditions Related to Collagen I	31
1.2.4.1.	Osteoporosis.....	31
1.2.4.2.	Atypical Marfan Syndrome.....	32
1.2.4.3.	Caffrey's Disease	33
1.3.	Osteoarthritis	33
1.3.1.	The Synovial Joint.....	34
1.3.1.1.	Articular Cartilage.....	35
1.3.1.2.	Subchondral Bone	39
1.3.1.3.	Other Joint Components	39
1.3.2.	The Osteoarthritic Joint	40
1.3.2.1.	Articular Cartilage.....	42
1.3.2.2.	Subchondral Bone	42
1.3.2.3.	Other Joint Components	43
1.3.3.	Genetics of OA	43
1.3.4.	Ageing as a risk factor for OA.....	46
1.3.5.	Mouse Models of OA	46
1.4.	ENU Mutagenesis	48
1.4.1.	The Harwell Ageing Screen	50
1.5.	Thesis Aims and Objectives	51
Chapter 2: Materials and Method		53
2.1.	Materials Lists.....	54
2.2.	Primers.....	58
2.2.1.	Sequencing Primers for Mutation Validation	58
2.2.2.	Primers for Validation of Alternative Splicing by Electrophoresis.....	58
2.2.3.	Lightscanner Genotyping Primers (Col1a2)	58

2.2.4.	Allelic Discrimination Genotyping Primers (Col1a1)	59
2.2.5.	Copy Number Genotyping Primers (Col1a2-KO).....	59
2.2.6.	Gene Expression Primers	60
2.2.7.	sgRNAs for CRISPR/cas9 Deletion	60
2.2.8.	Primers for CRISPR Confirmation.....	60
2.3.	Primary Antibodies	61
2.4.	Secondary Antibodies.....	62
2.5.	Recipes and Buffers	62
2.6.	Animals	65
2.6.1.	Animal husbandry	65
2.6.2.	MUTA-PED-107 (MP-107)	65
2.6.3.	Bone-TM44 (TM44)	66
2.6.4.	Col1a2-KO.....	67
2.7.	Identifying the Causative Mutations	67
2.7.1.	DNA Extraction	67
2.7.2.	Linkage Mapping	67
2.7.3.	Whole Genome Sequencing.....	68
2.8.	Mutation Validation	68
2.8.1.	Primer Design	68
2.8.2.	PCR Amplification.....	68
2.8.3.	PCR Purification.....	69
2.8.4.	Sanger Sequencing	70
2.9.	Genotyping	70
2.9.1.	Lightscanner	70
2.9.2.	Allelic Discrimination.....	71
2.9.3.	Copy Number	72

2.10.	Time course Phenotyping	73
2.10.1.	X-Ray	73
2.10.2.	Dual X-ray Energy Absorption (DEXA)	73
2.10.3.	Clinical Chemistry	73
2.11.	Histology	74
2.11.1.	Histological Processing of Knee Joints.....	74
2.11.2.	Histological Analysis of Embryonic Lungs.....	74
2.11.3.	Immunohistochemistry	74
2.12.	Skeletal Staining.....	75
2.12.1.	Sample Collection	75
2.12.2.	Sample Preparation	75
2.12.3.	Sample Imaging	76
2.13.	Transmission Electron Microscopy	76
2.13.1.	Sample Collection	76
2.13.2.	Sample Imaging	76
2.14.	Differential Scanning Calorimetry (DSC).....	76
2.14.1.	Harvesting Tail Tendons	76
2.14.2.	Testing Samples.....	77
2.14.3.	Analysis of Samples	77
2.15.	Radiolabelling of Tendons	78
2.15.1.	Harvesting Tail Tendons	78
2.15.2.	Labelling Samples	78
2.15.3.	Sequential Extractions.....	79
2.15.4.	Analysis of Extracts.....	79
2.16.	Gene expression analysis.....	80
2.16.1.	Sample Harvest and RNA Extraction	80

2.16.2.	CDNA Synthesis	80
2.16.3.	Real Time qPCR.....	81
2.17.	Mechanical Testing of Ex-Vivo Tissues	81
2.17.1.	Mechanical Testing of Tendons.....	81
2.17.1.1.	Sample Collection	82
2.17.1.2.	Sample Testing.....	82
2.17.1.3.	Analysis	82
2.17.2.	Three Point Bending of the Humerus.....	83
2.17.2.1.	Sample Collection	83
2.17.2.2.	Sample Testing and Analysis.....	83
2.17.3.	Tensile Testing of Skin	83
2.17.3.1.	Sample Collection	83
2.17.3.2.	Sample Testing and Analysis.....	83
2.17.4.	Micro-Indentation of the Articular Surface.....	84
2.17.4.1.	Sample Collection	84
2.17.4.2.	Sample Testing and Analysis.....	84
2.18.	Micro Computed Tomography of Bones	85
2.18.1.	Sample Collection and Preparation.....	85
2.18.2.	Sample Scanning.....	85
2.18.3.	Sample Analysis	85
2.19.	Optical Projection Tomography of Embryos.....	86
2.19.1.	Sample Collection	86
2.19.2.	Sample Scanning and Analysis.....	86
2.20.	Collagen Analysis of Tendons	86
2.20.1.	Harvesting of Tail Tendons	86
2.20.2.	Extraction of Collagen	87

2.20.3.	Analysis of Collagen Content.....	87
2.21.	Mouse Embryonic Fibroblasts	87
2.21.1.	Fibroblast Harvest	87
2.21.2.	Cell Growth and Maintenance	88
2.22.	Destabilisation of the Medial Meniscus (DMM).....	88
2.23.	Western Blotting.....	89
2.24.	Statistical Analysis.....	90
2.25.	ARRIVE Guidelines	90
Chapter 3: Identification and Initial Characterisation of Phenotypes Associated with a Point Mutation in <i>Col1a2</i>		91
3.1.	Introduction.....	92
3.2.	Initial identification of Mutants by X-ray Imaging.....	93
3.3.	Mapping and Identification of the Causative Mutation in MP-107	100
3.3.1.	Mapping the Mutation.....	100
3.3.2.	Whole Genome Sequencing.....	102
3.3.3.	Confirmation of Mutation	104
3.4.	Analysis of Initial Phenotyping by Genotype.....	105
3.4.1.	X-ray Imaging of the MP-107 G ₃ cohort.....	105
3.4.2.	Dual Energy X-ray Analysis (DEXA) of the MP-107 G ₃ cohort	106
3.4.3.	Clinical Chemistry of the MP-107 G ₃ cohort	110
3.4.4.	Histology of the MP-107 G ₃ cohort.....	113
3.5.	Investigating the Effect of the <i>Col1a2</i> Mutation on Coding DNA	114
3.5.1.	Sequencing of Embryo DNA Confirms the Homozygous Lethal Phenotype	114
3.5.2.	Predicting the Impact of the Mutation on the Transcription of the <i>Col1a2</i> Gene	116
3.5.3.	Confirmation of Effect of the <i>Col1a2</i> Mutation on Coding DNA	119

3.5.3.1.	Confirmation of Alternative Splicing Using PCR.....	121
3.5.3.2.	Confirmation of Alternative Splicing Using qPCR.....	121
3.6.	<i>Col1a2</i> ^{107/107} Phenotypes.....	123
3.6.1.	Identification of Perinatal Lethality in MP-107 Homozygotes.....	123
3.6.2.	Embryonic Lung Phenotype in MP-107 Homozygotes.....	125
3.6.3.	Whole Mount Embryonic Skeletal Staining of MP-107 Embryos	127
3.7.	Deep Phenotyping of MP-107 Over a 2-18 Month Time Course	128
3.7.1.	Overview of Animals and Time Points	128
3.7.2.	X-ray Imaging of MP-107 Animals.....	130
3.7.3.	DEXA Analysis of MP-107 Animals	136
3.7.4.	Clinical Chemistry of MP-107 Animals	139
3.8.	Micro Computed Tomography of MP-107 Animals	143
3.8.1.	3D Imaging of Bone Phenotypes in of MP-107 Animals	144
3.8.2.	Metaphyseal Trabecular Analysis of MP-107 Animals.....	154
3.8.3.	Epiphyseal Trabecular Analysis of MP-107 Animals	159
3.8.4.	Subchondral Bone Plate Analysis of MP-107 Animals	162
3.9.	Time Course Histology of MP-107 Animals.....	163
3.9.1.	Histological analysis of MP-107 knee joints at 4 Months	163
3.9.2.	Histological analysis of MP-107 knee joints at 9 Months	164
3.9.3.	Histological analysis of MP-107 knee joints at 12 Months	165
3.9.4.	Histological analysis of MP-107 knee joints at 18 Months	166
3.10.	Discussion	168
Chapter 4: Tissue Specific Effects of the <i>Col1a2</i> ^{107/+} Mutation		172
4.1.	Introduction.....	173
4.2.	Mechanical Testing.....	173
4.2.1.	Mechanical Testing of Tail Tendon Fascicles of MP-107 Animals.....	174

4.2.2.	Three-point Bone Bending of MP-107 Animals	179
4.2.3.	Tensile Skin Testing of MP-107 Animals	180
4.2.4.	Micro-Indentation of the Articular Surface of MP-107 Animals.....	182
4.3.	Differential Scanning Calorimetry of MP-107 Tail Tendons.....	183
4.4.	Collagen Secretion Analysis of MP-107 Tendons	186
4.5.	Transmission Electron Microscopy of MP-107 Embryonic Tail Tendon.....	188
4.6.	Analysis of ER Stress in MP-107 Mouse Embryonic Fibroblasts (MEFs)	190
4.7.	Immunohistochemistry Analysis of ER Stress in MP-107 Articular Cartilage.	191
4.8.	Destabilisation of the Medial Meniscus (DMM) in MP-107 Knees	194
4.9.	Discussion	197
Chapter 5: Identification and Initial Characterisation of Phenotypes Associated with a Point Mutation in <i>Col1a1</i>		202
5.1.	Introduction.....	203
5.2.	Identification of Early Phenotype in the line TM44	203
5.3.	Mapping and Identification of the mutation in the line TM44	205
5.3.1.	Mapping the Mutation in TM44.....	205
5.3.2.	Exome Sequencing of TM44.....	207
5.3.3.	Confirmation of Mutations in the line TM44.....	207
5.3.4.	Segregation of Mutations in the line TM44.....	208
5.4.	Identification of a Lethal Phenotype in TM44 Homozygotes.....	209
5.5.	Optical Projection Tomography of TM44 Embryos.....	212
5.6.	Phenotyping of the TM44 line.....	214
5.6.1.	X-ray Imaging of TM44 Animals	215
5.6.2.	DEXA Analysis of TM44 Animals.....	223
5.6.3.	Histological analysis of TM44 Knee Joints	226
5.7.	Collagen Content of TM44 Tendons.....	227

5.8.	Discussion	229
Chapter 6: Initial Characterisation of Phenotypes Exhibited by <i>Col1a2</i> Null Mice		233
6.1.	Introduction.....	234
6.2.	Creation of the <i>Col1a2</i> -KO Line.....	234
6.3.	Viability analysis of the <i>Col1a2</i> -KO Line	235
6.4.	Phenotyping of the <i>Col1a2</i> -KO Line	236
6.4.1.	X-ray Imaging of the <i>Col1a2</i> -KO line	236
6.4.2.	DEXA Analysis of the <i>Col1a2</i> -KO line	239
6.5.	Welfare Observations of the <i>Col1a2</i> -KO line	240
6.6.	Collagen Content of <i>Col1a2</i> -KO Tendons	241
6.7.	Discussion	243
Chapter 7: Investigating the Genetics and Effects of Mutations in <i>Col1a1</i> and <i>Col1a2</i> Using Compound Crosses.....		245
7.1.	Introduction.....	246
7.2.	TM44 x MP-107 Compound Cross.....	247
7.2.1.	Viability Assessment of the TM44/MP-107 Compound Cross.....	247
7.2.2.	X-ray Imaging of the TM44/MP-107 Compound Cross at 4-months.....	249
7.2.3.	DEXA Analysis of the TM44/MP-107 Compound Cross at 4-months	251
7.2.4.	X-ray Imaging of the TM44/MP-107 Compound Cross at 12-months....	252
7.3.	MP-107 x <i>Col1a2</i> KO Compound Cross	254
7.3.1.	Viability Assessment of the <i>Col1a2</i> -KO/MP-107 Compound Cross	254
7.3.2.	X-Ray Imaging of the <i>Col1a2</i> -KO/MP-107 Compound Cross at 4-Months	256
7.3.3.	DEXA of the <i>Col1a2</i> -KO/MP-107 Compound Cross at 4-Months	258
7.4.	TM44 x <i>Col1a2</i> KO Compound Cross.....	259
7.4.1.	Viability Assessment of the TM44/ <i>Col1a2</i> -KO Compound Cross	259

7.4.2.	X-ray Imaging of the TM44/ <i>Col1a2</i> -KO Compound Cross at 4-Months	260
7.4.3.	DEXA Analysis of the TM44/ <i>Col1a2</i> -KO Compound Cross at 4-Months	263
7.5.	Discussion	263
Chapter 8: General Discussion		266
8.1.	Summary of Results	267
8.1.1.	MP-107	267
8.1.1.1	Causative mutation in MP-107	267
8.1.1.2	Homozygous Lethal Phenotype of MP-107	268
8.1.1.3	OI phenotypes of MP-107	268
8.1.1.4	EDS phenotypes of MP-107	269
8.1.1.5	OA phenotypes of MP-107	270
8.1.1.6	ER stress phenotypes in MP-107	271
8.1.2.	TM44	272
6.1.1.1.	Causative mutation in TM44	272
8.1.2.1	Bone Phenotypes of TM44	272
8.1.2.2	OA Phenotype of TM44	273
8.1.2.3	Homozygous Lethal Phenotype of TM44	273
8.1.2.4	EDS or Col1 Related Overlap Phenotype of TM44	273
8.1.3.	<i>Col1a2</i> -KO	274
8.1.3.1	Bone Phenotypes of <i>Col1a2</i> -KO	274
8.1.3.2	OA Phenotype of <i>Col1a2</i> -KO	274
8.1.3.3	EDS or Col1 Related Overlap Phenotype of <i>Col1a2</i> -KO	274
8.1.4.	Genetics	274
8.2.	Overall Conclusions	275
8.3.	Implications for the Study of Osteoarthritis	276
8.4.	Implications for the Study of OI/ EDS	279

8.5. Future Work	280
8.4.1. Further Study of Bone Phenotypes	280
8.4.2. Further Study of Collagen Phenotypes	280
8.4.3. Further Study of OA Phenotype	281
8.4.4. Further Study of Genetics	282
Bibliography	283
Appendices.....	299
Appendix 1 - Radiolabelling Gels	299
Appendix 2- Full μ CT Results	300
Appendix 3- Time Course Full Body X-rays.....	302
Appendix 4- High Magnification TEM Images	310
Appendix 5- Full Gels for ER Stress of MEFs.....	313
Appendix 6- Immunohistochemistry Analysis of ER Stress in Articular Cartilage	314

Table of Figures

Figure 1.1. Collagen structure and organisation.....	4
Figure 1.2. A diagram showing the Exon structure of Col1a1 and Col1a2, and which elements of the α chains the exons code.....	5
Figure 1.3. A schematic representation of the type I pro-collagen molecule.....	5
Figure 1.4. An overview of the synthesis of a fibril-forming collagen.....	7
Figure 1.5. Schematic diagram of tendon in cross-section showing the hierarchical structure.....	9
Figure 1.6. Typical stress–strain curve of a rat tail tendon.....	10
Figure 1.7. Hierarchical structure of bone.....	11
Figure 1.8. Schematic of the mineralisation of collagen I fibrils.....	13
Figure 1.9. Overview of collagen type I biosynthesis.....	18
Figure 1.10. Mechanisms contributing to osteogenesis imperfecta.....	20
Figure 1.11. A diagram showing mutations in <i>COL1A1</i> and <i>COL1A2</i> reported in patients fitting the diagnostic criteria of Col-1 related overlap disorder.....	30
Figure 1.12. A diagram comparing a normal knee and an osteoarthritic knee.....	35
Figure 1.13. The extracellular matrix (ECM) of cartilage.....	37
Figure 1.14. Cross-sectional diagram of healthy articular cartilage.....	38
Figure 1.15. The vicious cycle of Osteoarthritis.....	41
Figure 1.16. Signalling pathways and structural changes in the development of osteoarthritis.....	41
Figure 1.17. An overview of strategies for genetic studies.....	44
Figure 1.18. A simplistic diagram showing the roles of genes in OA.....	45

Figure 1.19. Pathogenesis map of OA.....	48
Figure 1.20. An overview of the time scale and phenotyping that were undertaken as part of the Harwell Ageing Screen.	50
Figure 2.1. A diagram showing the breeding strategy employed in the Harwell Ageing screen.....	66
Figure 2.2. Normalized melting curves and peaks, showing how the different genotypes can be identified.	71
Figure 3.1. Examples of high-resolution radiographs of affected and unaffected pelvises, with annotation to show how the phenotype was defined.....	93
Figure 3.2. Examples of high-resolution radiographs of affected and unaffected olecranons, with annotation to show how the phenotype was defined.....	94
Figure 3.3. Radiographs showing affected and unaffected animals at 3 months of age.....	95
Figure 3.4. Examples of high-resolution radiographs of affected and unaffected knee joints, with annotation to show how the phenotype was defined.....	96
Figure 3.5. Radiographs showing affected and unaffected animals at 12 months of age	97
Figure 3.6. Radiographs showing affected and unaffected animals at 18 months of age	99
Figure 3.7. SNP mapping panel showing the region of interest on Chromosome 6....	101
Figure 3.8. Sequencing data for affected and unaffected animals.....	104
Figure 3.9. Genotyping data from the original G3 cohort.....	105
Figure 3.10. Graphs showing the DEXA data from female wild types and heterozygotes at 3-, 12- and 18-month time points.....	107

Figure 3.11. Graphs showing the DEXA data from wild types and heterozygotes of both sexes at the 18-month time point.....	109
Figure 3.12. H&E stained sections of knee joints from wild types and heterozygotes at 18 months.....	113
Figure 3.13. Safranin O stained sections of knee joints from wild types and heterozygotes at 18 months.....	114
Figure 3.14. Chromatographs showing the nucleotides present at position 4521226 for wild types, heterozygotes and homozygotes.....	115
Figure 3.15. A diagram showing how the <i>Col1a2</i> mutation affects the exon.....	118
Figure 3.16. A diagram showing the disruption of the repeating glycine motif.....	118
Figure 3.17. Sanger sequencing chromatograms from all three genotypes using both forward (5'->3' primer) and reverse (3'->5' primer).....	120
Figure 3.18. PCR products showing the wild-type and mutant transcripts across all three genotypes.....	121
Figure 3.19. Graphs showing relative expression of wild-type and mutant transcript using custom Taqman probes across all three genotypes.....	122
Figure 3.20. Graphs showing relative expression of <i>Col1a2</i> and <i>Col1a1</i> across all three genotypes.....	123
Figure 3.21. Genotyping data of embryonic and weaned animals indicate a perinatal lethal phenotype.	125
Figure 3.22. Histological sections of 18.5dpc embryonic lung tissue of wild-type and homozygous embryos.....	126
Figure 3.23. Analysis of airway size and airway number in the lungs of the three genotypes.....	126
Figure 3.24. Whole-mount embryonic skeletal staining, of 18.5dpc embryos of all three genotypes using Alizarin red and Alcian blue.....	127

Figure 3.25. Dissected limbs of 18.5dpc embryos of all three genotypes stained using Alizarin red and Alcian blue.....	128
Figure 3.2. A diagram showing the seven different cohorts and the phenotyping pipeline which each underwent.....	130
Figure 3.27. Examples of high-resolution radiographs of wild-type and heterozygous pelvises at each of the time points.....	132
Figure 3.28. Examples of high-resolution radiographs of wild-type and heterozygous elbow joints at each of the time points.....	133
Figure 3.29. Examples of high-resolution radiographs of wild-type and heterozygous knee joints at each of the time points.....	134
Figure 3.30. A diagram displaying how many animals of each genotype displayed each phenotype, or combination of phenotypes at each of the time points.....	135
Figure 3.31. 3D reconstructions of the elbow joints of a wild type and a heterozygote from the 2-month cohort.....	145
Figure 3.32. 3D reconstructions of the elbow joints of a wild type and a heterozygote from the 2-month cohort with cutaway.....	146
Figure 3.33. 3D reconstructions of the pelvis of a wild type and a heterozygote from the 2-month cohort in the dorsal and ventral views.....	147
Figure 3.34. 3D reconstructions of the pelvis of a wild type and a heterozygote from the 2-month cohort in the anterior and posterior views.....	148
Figure 3.35. Cutaways on the transverse plane of 3D reconstructions of the pelvis of a wild type and a heterozygote from the 2-month cohort.....	149
Figure 3.36. 3D reconstructions of the left knees of wild-type and heterozygous animals from the 4-month cohort.....	150
Figure 3.37. 3D reconstructions of the left knees of wild-type and heterozygous animals from the 9-month cohort.....	151

Figure 3.38. 3D reconstructions of the left knees of wild-type and heterozygous animals from the 18-month cohort.....	152
Figure 3.39. μ CT analysis of trabecular bone in male animals.....	156
Figure 3.40. μ CT analysis of trabecular bone in female animals.....	158
Figure 3.41. μ CT analysis of the subchondral trabecular bone in male animals.....	160
Figure 3.42. μ CT analysis of the subchondral trabecular bone in female animals.....	161
Figure 3.43. μ CT analysis of the thickness of the subchondral bone plate of the lateral and medial tibial plateaux.....	162
Figure 3.44. Safranin O stained histological section of knee joints from wild-type and heterozygous animals at 4 months of age.....	164
Figure 3.45. Safranin O stained histological section of knee joints from wild-type and heterozygous animals at 9 months of age.....	165
Figure 3.46. Safranin O stained histological section of knee joints from wild-type and heterozygous animals at 12 months of age.....	166
Figure 3.47. Safranin O stained histological section of knee joints from wild-type and heterozygous animals at 18 months of age.....	167
Figure 3.48. Maximum OARSI scores of Safranin O stained histological section of knee joints across the four time points.....	168
Figure 4.1. Calculated cross sectional area (CSA) of both heterozygous and wild-type fascicles.....	175
Figure 4.2. Representative force-extension graphs from wild-type and heterozygous fascicles	176
Figure 4.3. Percentage hysteresis of wild-type and heterozygous fascicles.....	176
Figure 4.4. Maximum force of wild-type and heterozygous fascicles.....	177

Figure 4.5. Graphs showing parameters from the ‘pull to failure’ phase of wild-type and heterozygous fascicles.....	178
Figure 4.6. Three-point bending analysis of wild-type and heterozygous humeri.....	180
Figure 4.7. Tensile testing analysis of wild-type and heterozygous skin.....	181
Figure 4.8. Structural stiffness analysis of the femoral condyles and tibial plateaux of heterozygotes and wild types.....	182
Figure 4.9. Representative differential scanning calorimetry thermograms from wild type and heterozygote tendons.....	184
Figure 4.10. Differential scanning calorimetry analysis of heterozygous and wild-type tail tendons.....	185
Figure 4.11. Images of radio labelled collagen extracted from wild-type and heterozygous tendons.....	186
Figure 4.12. Sypro Ruby total protein stained gels of tendon extracts.....	187
Figure 4.13. TEM images of embryonic tail tendon from homozygous, heterozygous and wild-type embryos.....	189
Figure 4.14. Quantative analysis of collagen fibrils in TEM images of embryonic tail tendon from homozygous, heterozygous and wild-type embryos.....	190
Figure 4.15. Western blot analysis showing levels of BIP in MP-107 MEF cell lysates	191
Figure 4.16. Immunohistochemical staining of wild-type and heterozygous knee sections using BIP antibody.....	193
Figure 4.17. Safranin O stained histological section of knee joints from DMM operated and sham operated wild-type and heterozygous animals.....	195
Figure 4.18. Histological analysis of Safranin O stained histological section of knee joints from wild-type and heterozygous animals including from DMM operated and sham operated.....	196

Figure 5.1. An X-ray image of the G ₁ founder animal of the line TM44.....	204
Figure 5.2. Representative X-ray images showing affected and unaffected animals	205
Figure 5.3. SNP mapping panel showing the region of interest on Chromosome 11..	206
Figure 5.4. Sanger sequencing traces confirming the presence of a heterozygous mutation in <i>Col1a1</i> in affected animals.....	207
Figure 5.5. Sanger sequencing traces confirming the presence of a heterozygous mutation in <i>Sectm1a</i> in affected animals.....	208
Figure 5.6. Sanger sequencing traces showing the segregation of mutations in affected animals.....	209
Figure 5.7. Proportions of animals of each genotype at weaning.....	210
Figure 5.8. Proportions of embryos of each genotype at 14.5 days post coitum.....	211
Figure 5.9. Proportions of embryos of each genotype at 12.5 days post coitum.....	212
Figure 5.10. A graph showing the measured crown to rump length of wild-type and homozygous embryos.....	213
Figure 5.11. Representative OPT imaging of wild-type and homozygous embryos...	214
Figure 5.12. Diagram showing the number of animals that exhibited each phenotype, or combination of phenotypes for wild-type and heterozygous animals at 2 months of age.....	215
Figure 5.13. Representative X-ray images of wild-type and heterozygous animals at 2 months.....	216
Figure 5.14. X-ray images of wild-type and heterozygous animals at 2 months showing the olecranon phenotypes.....	218
Figure 5.15. Representative X-ray images of wild-type and heterozygous animals at 12 months.....	219

Figure 5.16. Representative X-ray images of wild-type and heterozygous animals at 18 months.....	220
Figure 5.17. Diagram showing the number of animals that exhibited each phenotype, or combination of phenotypes for wild-type and heterozygous animals at 12- and 18-months.....	222
Figure 5.18. DEXA analysis of wild types and heterozygotes of both sexes at 2-months.....	224
Figure 5.19. DEXA analysis of wild types and heterozygotes of both sexes at 18-months.....	225
Figure 5.20. Safranin O stained sections of knee joints from a wild-type and a heterozygote at 18 months.	226
Figure 5.21. Maximum OARSI scores of Safranin O stained histological section of knee joints from wild-type and heterozygous male animals at 18-months of age.....	227
Figure 5.22. Coomassie stained collagen extracts from wild-type and heterozygous tendons for the lines MP-107 and TM44.....	228
Figure 5.23. A figure comparing the observed phenotypes between the lines MP-107 and TM44.....	231
Figure 6.1. Proportions of animals of each genotype at weaning from intercross matings.....	235
Figure 6.2. Representative X-ray images of female animals of all three genotypes at 2-months of age.....	237
Figure 6.3. Representative X-ray images of female animals of all three genotypes at 12-months of age.....	238
Figure 6.4. DEXA analysis of all three genotypes in the 2- and 12-month female cohorts.....	240

Figure 6.5. X-ray images from a male wild type and a male homozygote, showing the calcified Achilles tendon in the homozygote.....	241
Figure 6.6. Coomassie stained collagen extracts from all available genotypes for each of the lines, MP-107, TM44 and Col1a2-KO.....	242
Figure 7.1. Proportions of animals of each genotype produced from intercross matings between TM44 heterozygotes and MP-107 heterozygotes.....	248
Figure 7.2. Radiographs showing the phenotypes exhibited by each of the compound genotypes resulting from intercross matings between TM44 heterozygotes and MP-107 heterozygotes at 4-months.....	250
Figure 7.3. Radiographs comparing the calcaneus of a compound wild type and a compound heterozygote resulting from intercross matings between TM44 heterozygotes and MP-107 heterozygotes at 4-months.....	251
Figure 7.4. DEXA analysis of all four compound genotypes resulting from intercross matings between TM44 heterozygotes and MP-107 heterozygotes at 4-months.....	252
Figure 7.5. Radiographs showing the phenotypes exhibited by each of the compound genotypes resulting from intercross matings between TM44 heterozygotes and MP-107 heterozygotes at 12-months.....	253
Figure 7.6. Proportions of animals of each genotype produced from intercross matings between Col1a2-KO heterozygotes and MP-107 heterozygotes.....	255
Figure 7.7. Radiographs showing the phenotypes exhibited by each of the compound genotypes resulting from intercross matings between Col1a2-KO heterozygotes and MP-107 heterozygotes at 4-months.	257
Figure 7.8. DEXA analysis of all four compound genotypes resulting from intercross matings between TM44 heterozygotes and MP-107 heterozygotes at 4-month.....	258
Figure 7.9. Proportions of animals of each genotype produced from intercross matings between Col1a2-KO heterozygotes and TM44 heterozygotes.....	260

Figure 7.10. Radiographs showing the phenotypes exhibited by each of the compound genotypes resulting from intercross matings between *Col1a2*-KO heterozygotes and MP-107 heterozygotes at 4-months.262

Figure 7.11. DEXA analysis of all four compound genotypes resulting from intercross matings between TM44 heterozygotes and *Col1a2*-KO heterozygotes at 4-months263

Figure 8.1. A representation of an osteoarthritic knee, including the main contributing tissue and their interactions.....277

Table of Tables

Table 1.1. Table showing each group within the collagen family and the members of those groups, and distribution.....	3
Table 1.2. Types of osteogenesis imperfecta, organised by mechanism and gene.....	16
Table 1.3. A table documenting murine models of OI.....	22
Table 1.4. The 2017 international classification of the Ehlers-Danlos syndromes.....	25
Table 1.5. A table showing the Beighton score for assessment of generalized joint hypermobility	27
Table 1.6. Advantages and disadvantages of in vivo models.....	47
Table 3.1. Table showing numbers of animals with each phenotype at 3 months of age.....	94
Table 3.2. Table showing numbers of animals with each phenotype at 12 months of age.....	96
Table 3.3. Table showing numbers of animals with each phenotype at 18 months of age.....	98
Table 3.4. Summary of all mutations identified within the region ~39Mb region on the proximal end of Chromosome 6.....	102
Table 3.5. Summary of the 57 high confidence mutations identified within the ~39 Mb region on Chromosome 6.....	105
Table 3.6. A table showing numbers of affected and unaffected animals at each time point, and the genotypes of those animals.	106
Table 3.7. A table showing mean BMD for female animals of both genotypes across the three time points.....	108

Table 3.8. A table showing the means, standard deviation and n numbers for each clinical chemistry parameter for both wild-type and heterozygous female animals at each time point.....	112
Table 3.9. A table showing the predicted splice acceptor sites from three different predictor tools.	117
Table 3.10. A table showing the percentage of affected animals across all genotypes and time points.....	136
Table 3.11. DEXA data for all tested cohorts presented in the form of means, standard deviations and n numbers for all DEXA parameters.	138
Table 3.12a. Clinical chemistry data for all tested cohorts presented in the form of means, standard deviations and n numbers for all parameters.	141
Table 3.12b. Clinical chemistry data for all tested cohorts presented in the form of means, standard deviations and n numbers for all parameters.	142
Table 3.13. A table displaying the number of animals phenotyped at each time point and the number of animals presenting with each phenotype.....	153
Table 3.14. A table comparing the number of animals identified with the abnormal bone phenotype at the knee, by μ CT at each time point.....	154
Table 5.1. A table displaying the number of animals phenotyped in the 2-month cohort and the number of animals presenting with each phenotype.	217
Table 5.1. A table displaying the number of animals phenotyped in the 12- and 18-month cohorts and the number of animals presenting with each phenotype.	221
Table 6.1. A table displaying the number of animals presenting with each phenotype in the 2- and 12-month female cohorts.	239
Table 7.1. A table displaying the number of animals of each genotype from intercross matings between TM44 heterozygotes and MP-107 heterozygotes.	248

Table 7.2. A table showing the number of animals exhibiting each phenotype, for each genotype in the phenotyping cohort resulting from the TM44 and MP-107 intercross.....	249
Table 7.3. A table displaying the number of animals of each genotype from intercross matings between MP-107 heterozygotes and <i>Col1a2</i> -KO heterozygotes.	254
Table 7.4. A table showing the number of animals exhibiting each phenotype, for each genotype in the phenotyping cohort resulting from the <i>Col1a2</i> -KO and MP-107 intercross	256
Table 7.5. A table displaying the number of animals of each genotype from intercross matings between TM44 heterozygotes and <i>Col1a2</i> -KO heterozygotes.....	259
Table 7.6. A table showing the number of animals exhibiting each phenotype, for each genotype in the phenotyping cohort resulting from the <i>Col1a2</i> -KO and MP-107 intercross.....	261
Table 7.7. A table displaying the incidence of early phenotype in the lines TM44, MP-107 and <i>Col1a2</i> -KO, and the compound lines.....	265

Abbreviations

AC	Articular cartilage
AD	Autosomal dominant
aEDS	Arthrochalasia EDS
AGEs	Advanced glycation end-products
ALP	Alkaline phosphatase
ALT	Alanine aminotransferase
ANOVA	Analysis of variance
AR	Autosomal recessive
AST	Aspartate aminotransferase
AWERB	Animal welfare and ethical review body
BABB	Benzyl alcohol-benzyl benzoate
BC	Backcross
BCS	Brittle cornea syndrome
BMC	Bone mineral content
BMD	Bone mineral density
BMND18	Bone mineral density quantitative trait locus 18
BRKS2	Bruck syndrome-2
BV	Bone volume
BV/TV	Bone volume/trabecular volume (Bone volume fraction)
CAS9	CRISPR associated 9 nuclease

cDNA	Complementary deoxyribonucleic acid
cEDS	Classical EDS
CK	Creatine kinase
clEDS	Classical-like EDS
COPII	Coat protein complex II
CRISPR	Clustered regularly interspaced short palindromic repeats
CSA	Cross sectional area
CSF	Cerebrospinal fluid
CT	Cycles taken
CTX	C-terminal telopeptide
cvEDS	Cardiac-valvular EDS
DAB	3,3'-Diaminobenzidine
ddH ₂ O	Double distilled water
dEDS	Dermatosparaxis EDS
DEXA	Dual energy x-ray absorpiometry
DMEM	Dulbecco's modified eagle medium
DMM	Destabilisation of the medial meniscus
DNA	Deoxyribonucleic acid
dNTPs	Deoxyribonucleotide triphosphates
DPBS	Dulbecco's phosphate buffered saline
dpc	Days post coitum
DSC	Differential scanning calorimetry

DSLRL	Digital single-lens reflex
EB	Elution buffer
ECM	Extracellular matrix
EDS	Ehlers-Danlos syndrome
EDTA	Ethylenediaminetetraacetic acid
ENSMUSE00001247742	Exon 3 of <i>Col1a2</i>
ENSMUSE00001291037	Exon 2 of <i>Col1a2</i>
ENSMUSE00001305705	Exon 4 of <i>Col1a2</i>
ENU	N-ethyl-N-nitrosourea
ER	Endoplasmic reticulum
ERAD	ER-associated degradation
EU	European union
F ₀	F ₀ generation chimeras
FACIT	Fibril associated collagens with interrupted triple helix
FBS	Fetal bovine serum
gDNA	Genomic deoxyribonucleic acid
GJH	Generalised joint hypermobility
GWAS	Genome wide association studies
H&E	Hematoxylin and eosin
H ₂ O	Water
HDL	High-density lipoproteins
hEDS	Hypermobility EDS

HET	Heterozygous
HOM	Homozygous
IC	Intercross
IHC	Immunohistochemistry
IVC	Individually vented cages
K&L	Kellgren-Lawrence classification
kEDS	Kyphoscoliotic EDS
KO	Knock out
LDH	Lactate dehydrogenase
LDL	Low-density lipoproteins
LDS	Lithium dodecyl sulphate
mcEDS	Musculocontractural EDS
MCL	Medial collateral ligament
mEDS	Myopathic EDS
MEF	Mouse embryonic fibroblast
MEM	Minimum essential medium
MFS	Marfan syndrome
MgCl ₂	Magnesium chloride
MLC	Mary Lyon Centre
MMP	Matrix metalloproteinases
MMTL	Meniscotibial ligament
MONO	Monoclonal

MOPS	3-(N-morpholino) propanesulfonic acid
MRC	Medical Research Council
mRNA	Messenger ribonucleic acid
N	NP-40 extraction
NaCl	Sodium chloride
NACWO	Named animal care and welfare officer
NCP	Non collagenous proteins
NMD	Nonsense-mediated mRNA decay
NVS	Named veterinary surgeon
OA	Osteoarthritis
OARSI	Osteoarthritis Research Society International
OI	Osteogenesis imperfecta
OOA	Old Order Amish
OPT	Optical projection tomography
P0	Postnatal day 0
P21	Postnatal day 21
PAM	Protospacer adjacent motif
PBS	Phosphate buffered saline
PCM	Pericellular matrix
PCR	Polymerase chain reaction
pEDS	Periodontal EDS
PFA	Paraformaldehyde

PLA	Polylactic acid
POLY	Polyclonal
PPII	Polyproline-II
qPCR	Quantative polymerase chain reaction
RNA	Ribonucleic acid
RT	Reverse transcriptase
S1	Salt extraction 1
S2	Salt extraction 2
S3	Salt extraction 3
S4	Salt extraction 4
SBP	Subchondral bone plate
SDS	Sodium dodecyl sulfate
sgRNA	Single guide RNA
SNP	Single nucleotide polymorphism
spEDS	Spondylodysplastic EDS
SPF	Specific pathogen free
TBS	Tris buffered saline
TBST	Tris buffered saline with tween
TEM	Transmission electron microscopy
Tris-HCl	Trisaminomethane hydrochloride
TV	Trabecular volume
UTR	Untranslated region

vEDS	Vascular EDS
WB	Western blot
WGS	Whole genome sequencing
WHO	World Health Organisation
WT	Wild type
XLD	X-linked dominant
XLR	X-linked recessive
μCT	Micro computed tomography

Chapter 1: Introduction

1.1. Collagen I

1.1.1. The Collagen Family

Type I collagen is a member of the Collagen superfamily, which are the most abundant family of proteins in mammals, accounting for around 30% of total dry protein weight [1]. There are currently 28 proteins classified as collagens, numbered with Roman numerals (I-XXVIII). In addition to these there are many other proteins, which contain collagen-like domains, but are not regarded as collagens. The defining feature of a collagen is the presence of 3 polypeptide chains (commonly called α chains) each of which forms a left handed Polyproline-II (PPII) type helix, made up of G-X-Y tripeptide repeats, where X is most commonly Proline, and Y is most commonly Hydroxyproline [2]. This open form of helix, devoid of internal hydrogen bonds, enables the 3 helices to twist together to form a right-handed triple helix, with a one residue stagger between adjacent α chains. The number of helical domains varies in each of the members of the collagen family, collagen I contains a single large helical domain, while Collagen XVII contains 15 smaller helical domains [3].

The majority of collagens are homotrimers, with 3 identical α chains making up the triple helix, while the minority are heterotrimers, such as collagen I which is made up of 2 different α chains, and collagen IV which can be made up of different combinations of up to 6 different α chains [1, 4].

The 28 collagens are split into 7 groups: fibril forming collagens, fibril associated collagens with interrupted triple helix (FACIT), beaded filament forming collagens, anchoring fibril collagens, network forming collagens, transmembrane collagens and endostatins (Table 1.1).

Classification	Type	Distribution/remarks
Fibril-forming	I	Non-cartilaginous connective tissues –e.g. tendon, ligament, cornea, bone, annulus fibrosis, skin
	II	Cartilage, vitreous humour and nucleus pulposus
	III	Co-distributes with collagen I, especially in embryonic skin and hollow organs
	V	Co-distributes with collagen I, especially in embryonic tissues and in cornea
	XI	Co-distributes with collagen II
	XXIV	Shares sequence homology with the fibril-forming collagens; has minor interruptions in the triple helix; selective expression in developing cornea and bone
FACIT	XXVII	Shares sequence homology with the fibril-forming collagens; has minor interruptions in the triple helix; found in a number of embryonic tissues but restricted to cartilage in adults
	IX	Co-distributes with collagen II, especially in cartilage and vitreous humour
	XII	Found with collagen I
	XIV	Found with collagen I
	XVI	Integrated into collagen fibrils and fibrillin-1 microfibrils
	XIX	Rare; localised to basement membrane zones; contributes to muscle physiology and differentiation
	XX	Widespread distribution, most prevalent in corneal epithelium
	XXI	Widespread distribution
Beaded-filament forming	XXII	Localised at tissue junctions – e.g. myotendinous junction, cartilage, synovial fluid, hair follicle-dermis
	VI	Widespread, especially muscle
	XXVI	Also known as EMI domain-containing protein 2, protein Emu2, Emilin and multimerin domain-containing protein 2
Anchoring fibrils	XXVIII	A component of the basement membrane around Schwann cells; a von Willebrand factor A domain-containing protein with numerous interruptions in the triple helical domain
	VII	Dermal-epidermal junction
Network-forming	IV	Basement membranes
	VIII	Descemet's membrane
	X	Hypertrophic cartilage
Transmembrane	XIII	Neuromuscular junctions, skin
	XVII	Also known as the bullous pemphigoid antigen 2/BP180; localised to epithelia; an epithelial adhesion molecule; ectodomain cleaved by ADAM proteinases
	XXIII	Limited tissue distribution; exists as a transmembrane and shed form
	XXV	CLAC-P – precursor protein for CLAC (collagenous Alzheimer amyloid plaque component)
Endostatins	XV	Located between collagen fibrils that are close to basement membranes; found in the eye, muscle and microvessels; a close structural homologue of collagen XVIII
	XVIII	Associated with basement membranes; endostatin is proteolytically released from the C-terminus of collagen XVIII; important for retinal vasculogenesis

Table 1.1. Table showing each group within the collagen family and the members of those groups, as well as distribution. Adapted from *Kadler et al., 2007* [5].

1.1.2. Collagen I Structure and Synthesis

Type I collagen is typically a heterotrimer composed of two α_1 chains (encoded by the gene *COL1A1*) and one α_2 chain (encoded by the gene *COL1A2*), however under certain circumstances type I collagen can exist as a homotrimer of three α_1 chains, including in fetal tissues, fibrosis, and cancer [6]. Collagen I exists extracellularly as collagen fibres, made up of collagen micro fibrils, which are composed of collagen molecules (Figure 1.1). Collagen molecules self-assemble into microfibrils in a staggered offset, which gives collagen fibrils a characteristic D-periodicity of 67nm, which consists of a 40nm gap between molecules, and a 27 nm overlap zone [7].

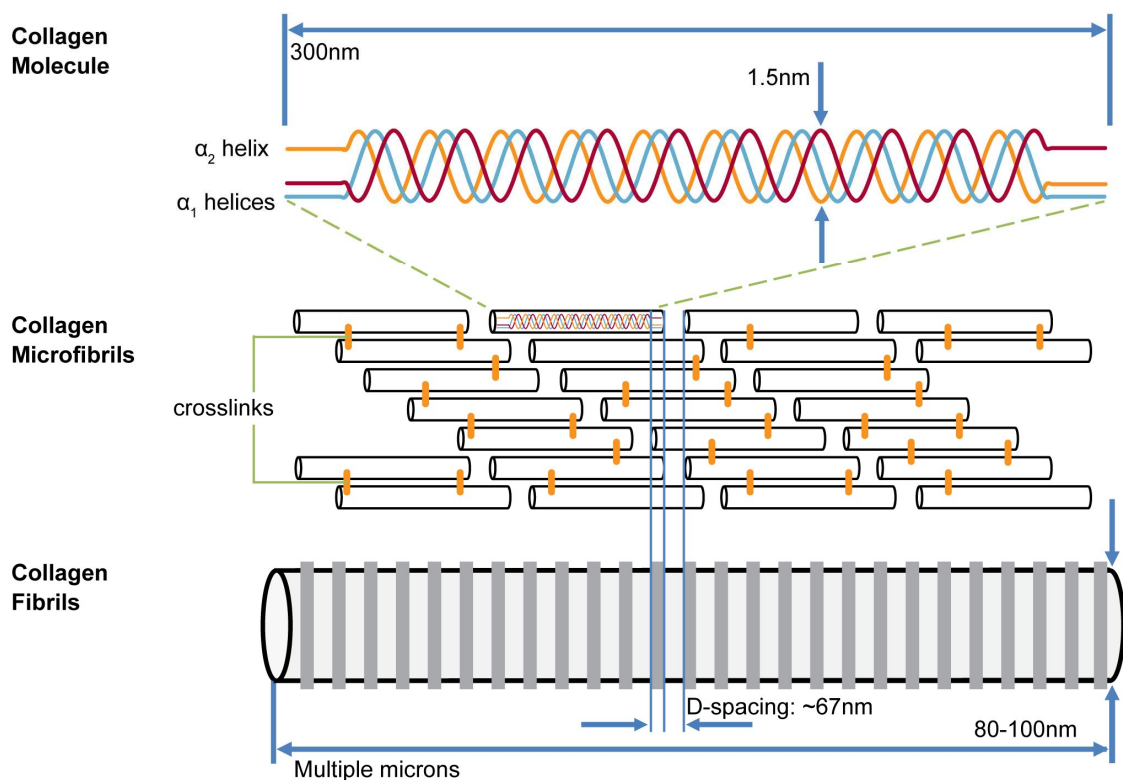


Figure 1.1. Collagen Structure and organisation. Taken from Canelón *et al.*, 2016 [7].

There are a number of essential processes, which occur throughout the production of the collagen molecule, which allow the formation of these microfibrils and fibrils, which will be outlined below, and starts with the genes *COL1A1* and *COL1A2*.

The genes *COL1A1* and *COL1A2* are very similar in terms of their exon structure, resulting in very similar structures in the α_1 and α_2 chains. Both genes contain large triple helical domains flanked by C- and N-propeptides separated from the triple helix by C- and N-

telopeptides respectively. The N-propeptide region also contains a smaller additional triple helical domain (Figure 1.2).

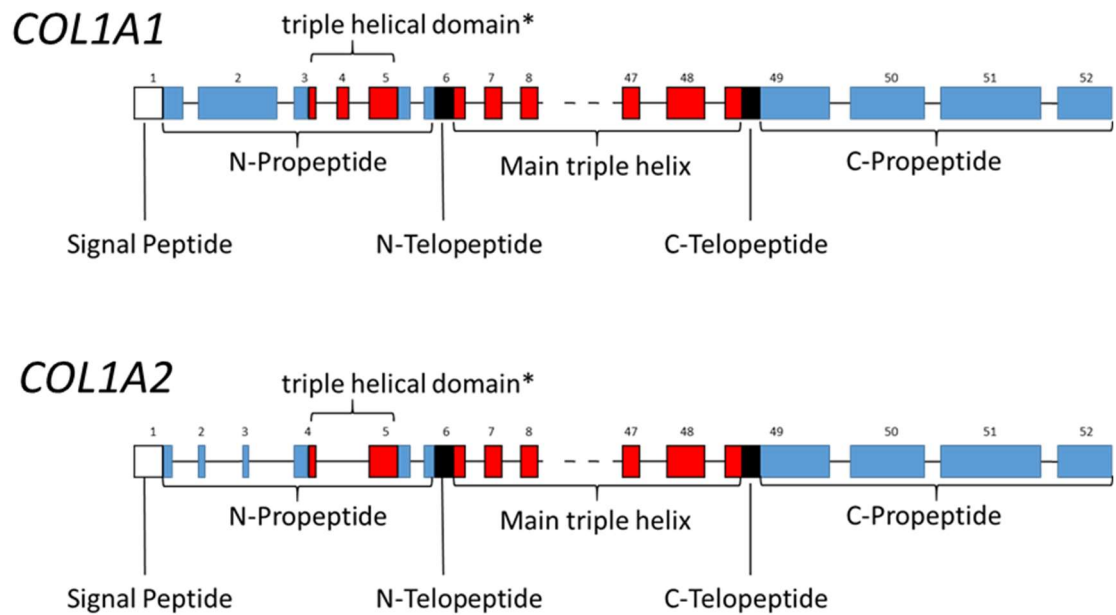


Figure 1.2. A diagram showing the Exon structure of *COL1A1* and *COL1A2*, and the elements of the α chains that they code for. The N-propeptide of both *COL1A1* and *COL1A2* contain a short triple helical domain. Adapted from Rossert and de Crombrugge, 2002 [8]

The similar structure of the collagen I genes, allow the formation of a pro collagen molecule where the 3 left-hand helices (2 pro $\alpha1$ (I) and 1 pro $\alpha2$ (I)) interact and form a right-handed triple helix (Figure 1.3).

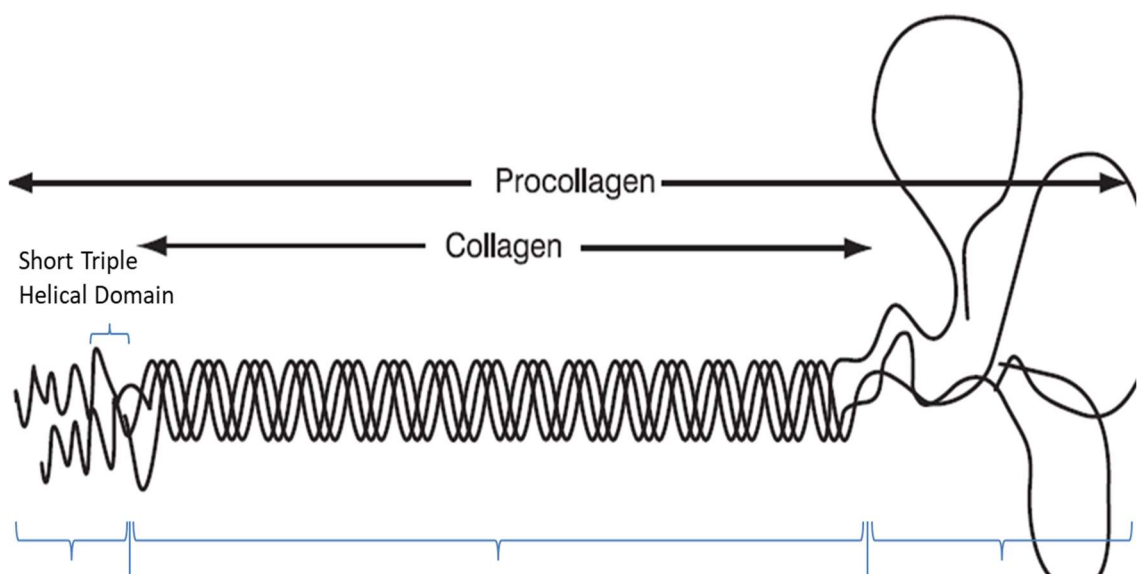


Figure 1.3. A schematic representation of the type I pro-collagen molecule. Adapted from Marcus *et al.*, 2006 [9].

The mechanisms by which collagen I is produced is a complicated process, including synthesis, post-translational modifications, and folding; the processing takes place both intracellularly and extracellularly [10].

Initially the genes for each of the alpha chains are transcribed to mRNA in the nucleus, before the mRNA exits the nucleus and interacts with the membrane-bound ribosomes of the rough endoplasmic reticulum (rER) [11, 12]. The ribosomes translate the mRNA into polypeptide chains, which are secreted into the lumen of the endoplasmic reticulum (ER) [10]. While most proteins fold from the N terminal end before the chain has finished synthesising, procollagens do not start folding until after the entire chain is synthesised, and the folding commences from the C-terminal end [13]. The polypeptide chains undergo a number of post-translational modifications during the folding process, starting with the cleavage of the N-terminal signal peptide. As mentioned previously, the repeating Glycine motif, of Gly-X-Y, where X is most commonly proline and Y is mostly commonly hydroxyproline, is essential to proper folding of the collagen I triple helix. The triple helix of collagens is stabilised by proline in the X position and 4-hydroxyproline and arginine in the Y position [2, 13]. It is therefore also essential that approximately half of proline residues in the Y position are hydroxylated by prolyl 4-hydroxylase, although some specific proline residues are hydroxylated by the prolyl 3-hydroxylation complex, which involves a number of different proteins, including CRTAP, P3H1 and CyPB. The role in the stabilisation of the triple helix of 4-hydroxyproline is by providing hydrogen bonds and water bridges [14]. Additionally, lysine residues are hydroxylated by lysyl hydroxylases to form hydroxylysine residues which can then undergo further modifications such as glycosylation or covalent crosslinking [15]. The folded pro-collagen molecule is then ready for secretion. ER chaperone proteins such as BiP bind to unfolded and partially folded chains and ensure the chains remain in a foldable state. When these chaperones are released it signals that the molecule is ready for transportation [13, 16]. Due to the large, rigid structure of the pro-collagen I molecule, trafficking of the molecule from the endoplasmic reticulum to the Golgi apparatus requires specialised COPII vesicles, which are able to cope with larger molecules. Jin *et al.* showed the actions of ubiquitin ligase CUL3–KLHL12, which catalyses the monoubiquitylation of the COPII-component SEC31, drives the assembly of large COPII coats, although the precise mechanism remains elusive [17, 18]. Golgi to

plasma membrane transport carriers, which are a type of vesicle formed by the detachment of large regions of the trans golgi network, enable the pro-collagen to leave the trans face of the Golgi [19]. C- and N- terminal propeptides are cleaved by their respective proteinases, BMP1 (Bone morphogenetic protein-1) and ADAMTS-2 (A Disintegrin and Metalloproteinase with Thrombospondin Motifs-2) [20]. After the cleavage of the propeptides the ~300nm tropocollagen is then able to self-assemble into microfibrils. It has previously been suggested that interaction of the C-terminal telopeptide with specific binding sites on other triple helical monomers may facilitate the self-assembly [21]. These microfibrils then bind together, forming fibrils which have diameters ranging from 50 to 500nm [22]. Cross-linking between the molecules in the fibril then provides strength and stability [23].

Myllyharju and Kivirikko published a schematic summarising the biosynthesis of fibril forming collagens, which is reproduced in Figure 1.4 [24].

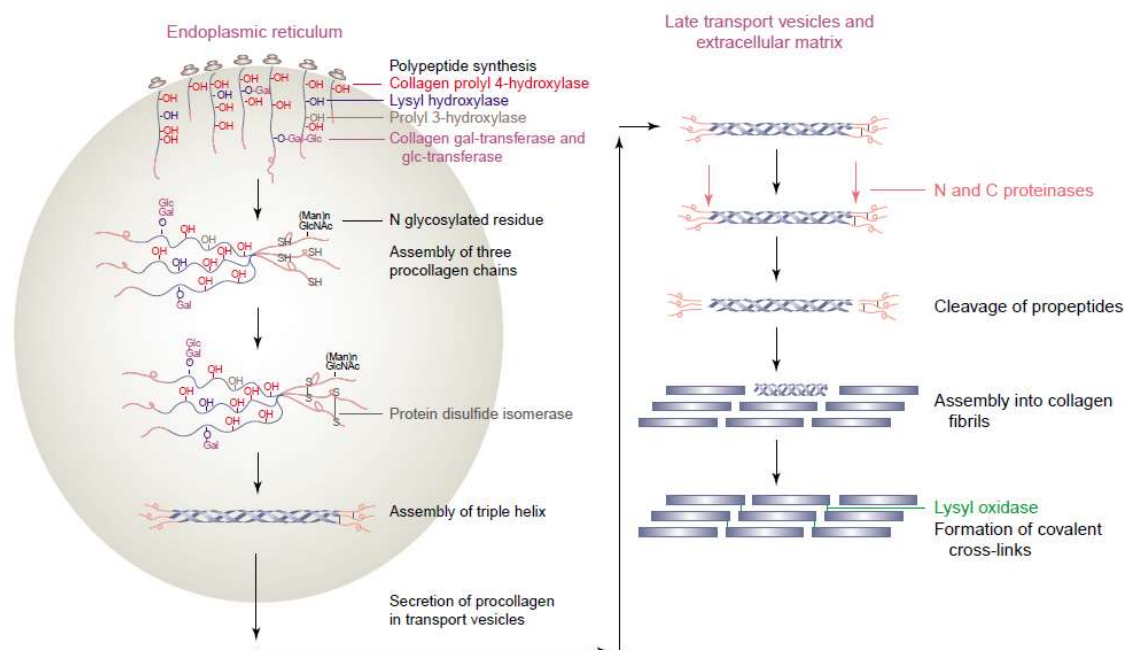


Figure 1.4. An overview of the synthesis of a fibril-forming collagen. Taken from Myllyharju and Kivirikko 2004 [24].

1.1.3. Collagen I and Connective Tissues

Type I collagen is an important protein in tissues with mechanical functions, as it confers mechanical stability, strength and toughness [25].

It is the major constituent of tendons and ligaments, the majority of the organic matrix in bone and dentine, and is also present in a number of other tissues such as skin, arteries, cornea and meniscus [1]. Despite collagen I being major constituents in all these tissues, the tissues all have unique behaviours and functions. In bone, in addition to the collagen I fibrils, the tissue is mineralised, which changes the mechanical properties. In other tissues the collagen fibrils are heterotypic, in that they can contain more than one type of fibrillar collagen. For example, the fibrils in skin are made up of both type I and type III collagen, and those in tendon are predominantly type I and type V [26, 27]. Other differences in tissue behaviours can relate to the orientation of the fibrils or varying ratios of the constituents of the extracellular matrix (ECM) [28].

Additionally, these tissues tend to be anisotropic, meaning the mechanical properties of the tissue varies depending on the direction, much like the grain of wood, the direction of the collagen fibres has an effect on the mechanical properties [29].

Examples of the function of collagen I in connective tissues are outlined in the subsections below.

1.1.3.1. Tendons

Tendon are fibrous tissues that connect muscles to bone and their main function is to transfer force from the muscle to the bone at joints [22]. Tendons are collagen rich tissues, constituting 65-85% of the dry weight of tendons, and approximately 90% of this collagen is collagen I [30]. The collagen fibrils in tendon are heterotypic where collagen V is present in the centre of the collagen I fibrils, likely acting as a template for fibrillogenesis [31]. Other collagens are also present including fibrillar collagens, type III and XI, as well as fibril associated collagens, XII and XIV [30].

Tendons have a hierarchical organisation where collagen molecules and collagen fibrils, which have previously been described, aggregate to form fibres, and fascicles, which are the largest subunit of tendons. The fascicles are surrounded by the interfascicular matrix, or endotendon [22] (Figure 1.5).

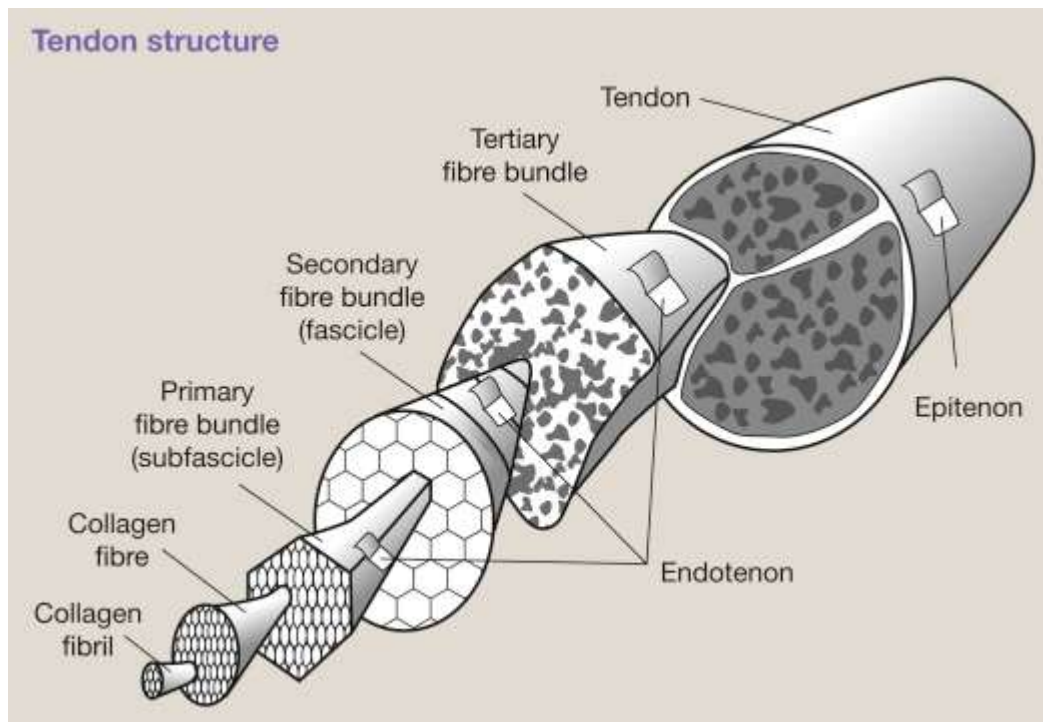


Figure 1.5. Schematic diagram of tendon in cross-section showing the hierarchical structure. Collagen fibrils are bundled into fascicles containing vessels, lymphatics and nerves. The fascicles are grouped together, surrounded by epitenon, and form the gross structure of the tendon, which is further enclosed by paratenon. Taken from Parmar, 2018 [32].

The structure and composition of tendons vary slightly depending on where the tendon is located and whether its primary purpose is as an energy-storing tendon, such as the Achilles tendon or as a positional tendon, such as the anterior tibial tendon. The material and mechanical properties of these tendons vary accordingly. Positional tendons are relatively inextensible under physiological loads, with high stiffness, but low strain, less than 3%, and stresses of 20-30MPa. Energy storing tendons have a high degree of extensibility, high strains and very high stresses up to around 90 MPa, which is close to the failure stress of tendons [33]. The differences between these two tendon types have been attributed to the geometric arrangement of collagen within the fascicles [34]. Another theory is that the presence of trivalent crosslinks within energy storing fibrils appears to limit molecular sliding, which may allow the higher stresses [35]. The multiple hierarchical levels of tendon structure, mean that local extension and sliding mechanics can be altered by small changes at different levels, which can impact the behaviour of the tendon as a whole, enabling tendon behaviour to be tailored to their specific task [22].

Fratzl *et al.* proposed a model attributing the mechanical properties of tendons to the collagen I structure. As the tendon is extended initially, the macroscopic crimp of the fibrils is removed, followed by straightening of molecular kinks in the gaps and finally the linear region to a gliding of molecules [36] (Figure 1.6). This model has been further built upon; Gupta *et al.* found that inter-fibre and inter-fibril shearing are significant mechanisms for dissipation of energy [37]. At the higher hierarchical scale, Thorpe *et al.*, found that inter-fascicular sliding also plays a role in the ability of energy storing tendon to fulfil their role [38].

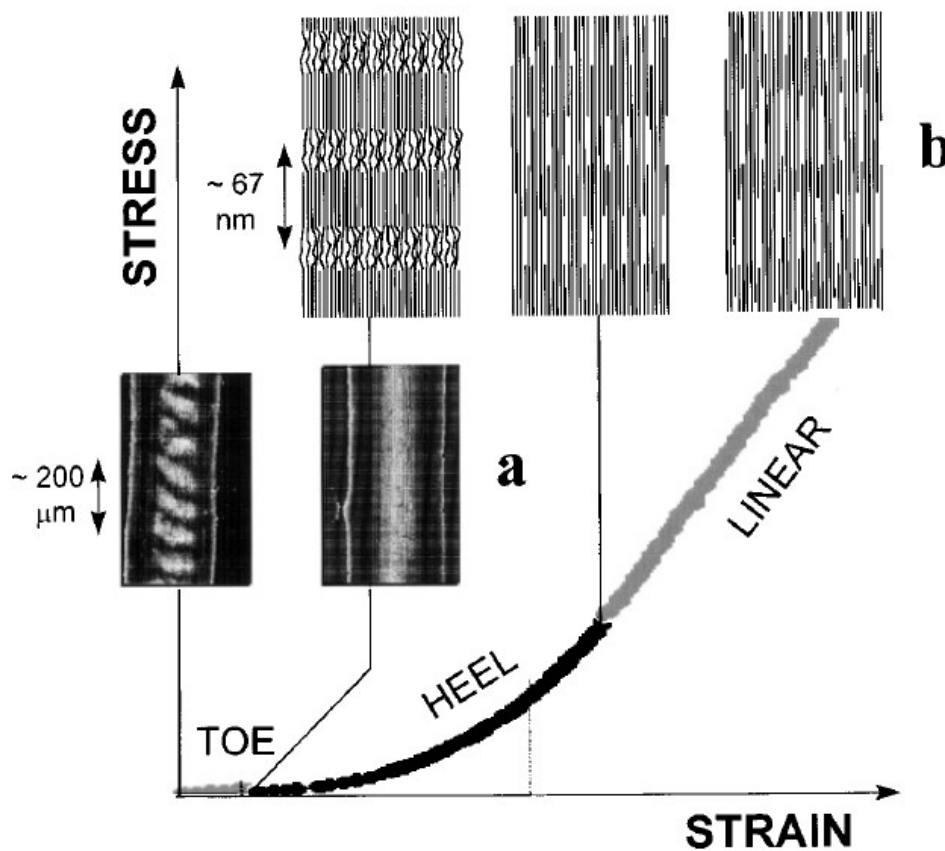


Figure 1.6. Typical stress–strain curve of a rat tail tendon. (A) The removal of the macroscopic crimp visualised with polarized light. (B) Further structural changes occur at the fibrillar level. Taken from Fratzl *et al.*, 1998 [36].

1.1.3.2. Bone

Bone is a hierarchical tissue, which at the macroscale is made up of trabecular or cortical bone and at the nanoscale is composed of mineralised collagen fibrils (Figure 1.7). Mineralised collagen fibrils are linked by an organic phase to form fibril arrays that are

overlaid in layers oriented at different angles to provide the lamellar structure of osteons, which make up the trabecular and cortical bone [39].

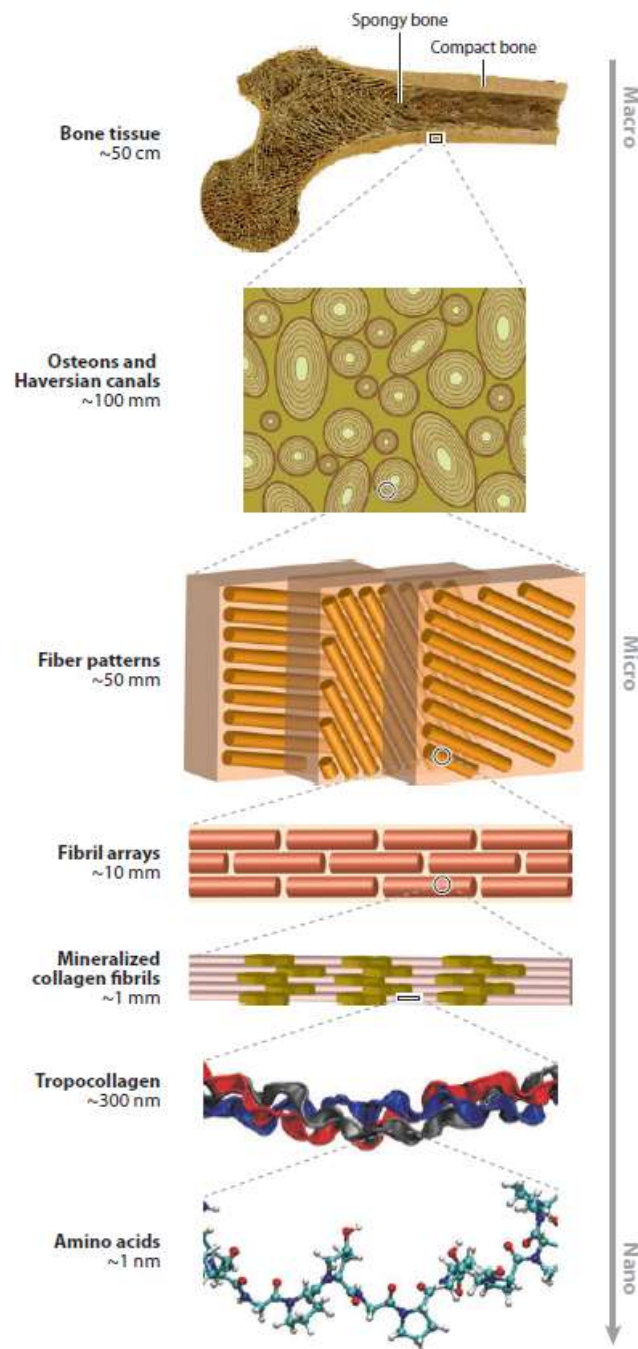


Figure 1.7. Hierarchical structure of bone. The macroscale arrangements of bones are either compact/cortical (dense material found at the surface of all bones) or spongy/cancellous (foam-like material whose struts are some 100 μ m thick). Compact bone is composed of osteons that surround and protect blood vessels. Osteons have a lamellar structure. Each individual lamella is composed of fibres arranged in geometrical patterns. These fibres are the result of several collagen fibrils, each linked by an organic phase to form fibril arrays. Each array makes up a single collagen fibre. The mineralized collagen fibrils are the basic building blocks of bone. They are composed of collagen protein molecules (tropocollagen) formed from three chains of amino acids. Taken from Launcey *et al.*, 2010 [39].

Bones have a variety of functions within the body, and require different structures and make up to fulfil their function. The bones play a major role in structural support, provide leverage to enable movement, and protect vital organs. Approximately 80% of total bone is classified as cortical, with only 20% trabecular, but the ratios in different bones vary according to function. Both cortical and trabecular bone are made up of osteons, but the structure of the bone differs with trabecular bone being a honeycomb of trabeculae with bone marrow compartments and cortical bone being a solid, dense mass [40].

The mineralised collagen fibrils are formed in the extracellular space, where osteoblasts secrete collagen molecules, which self-assemble into fibrils (as previously described in section 1.1.2). The osteoblasts also secrete hydroxyapatite crystals, which form in matrix vesicles before elongation into the extracellular space [41]. They then nucleate in the gaps, provided by the staggered offset between collagen molecules, and grow preferentially in their crystal-axis direction and broaden into nanoplatelets. The hydroxyapatite within bone grows within the collagen fibrils (intrafibrillar) and on the surfaces of the fibrils (extrafibrillar) [42](Figure 1.8). TEM imaging in multiple dimensions has led to the formation of a model that indicates that the mineral lamellae formed by the hydroxyapatite, surrounds the outer surface of the fibril as opposed to mainly being embedded in the fibril. These mineral lamellae improve the stiffness and strength of the tissue, compared to the isolated mineral models [43].

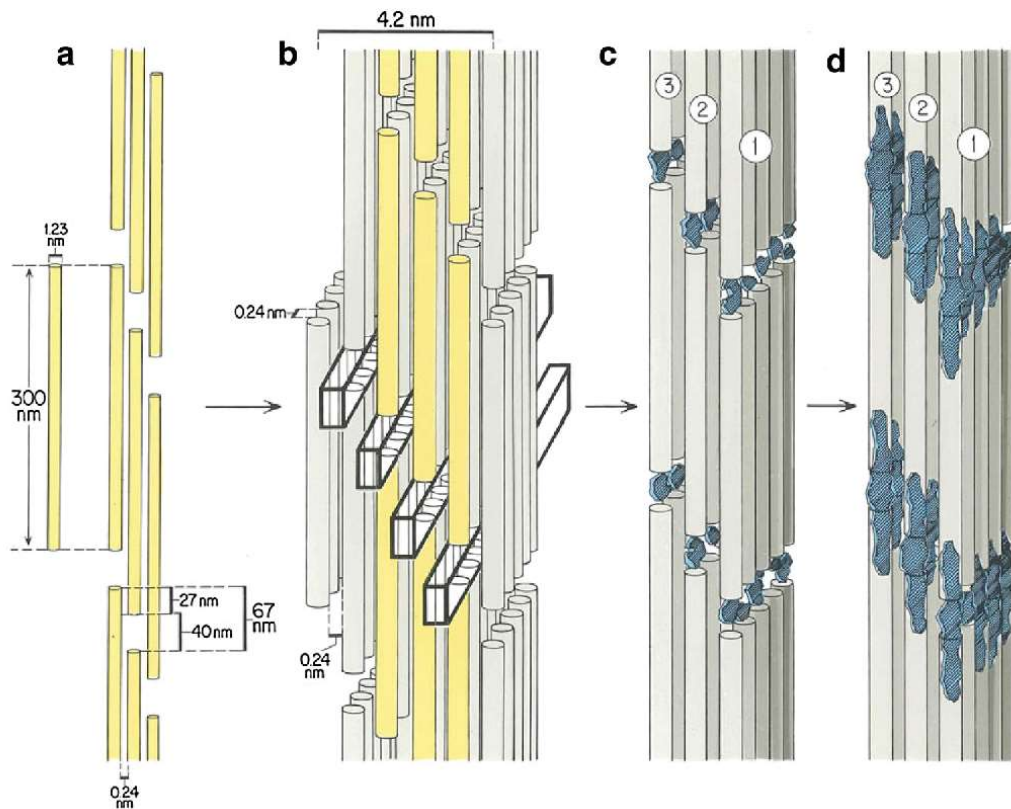


Figure 1.8. Schematic of the mineralisation of collagen I fibrils. (a) A single collagen molecule, 1.23 nm in diameter, 300 nm in length and spaced 0.24 nm apart, is shown as well as a 2D aggregate of collagen molecules, cross-linked into a quarter-staggered array with characteristic gap (40 nm) and overlap (27 nm) zones. (b) Packing of consecutive 2D arrays into 3D assemblages occurs with strict registration of all gap and overlap zones so that channels are created throughout the model. Cuboids indicate these channels. (c) The hydroxyapatite crystals, shown in blue, nucleate principally in the collagen gaps and grow preferentially in their crystal-axis direction. (d) Growth of the hydroxyapatite phase to occupy the entire 40-nm length of the gap. The channels are thought to allow lateral growth of the hydroxyapatite nuclei into nanoplatelets. As pictured, the hydroxyapatite has extended beyond the gap zone, but the narrow pore spaces (0.24 nm) between adjacent collagen molecules have unknown capacity to accommodate mineral. Taken from Stock, 2015 [42].

The hydroxyapatite that mineralises the bone accounts for 50-70 % of the bone mass, with small quantities of other minerals such as carbonate and magnesium and acid phosphate, with 20-40% organic matrix (of which 90% is collagen I), 5-10% water and <3% lipids making up the remained of the tissue [44].

Collagen gives the bone elasticity and the ability to dissipate energy under mechanical deformation through molecular stretching and inter-molecular gliding, which have been mentioned previously. The mineral phase has an elastic modulus, which is more than 10 times higher than collagen, and therefore mineralisation is critical to the stiffness of

bone [44]. Various models have been used to explore the relationships between the mineralised and unmineralised phases of the collagen fibrils. For example, Nair *et al.* developed a model to identify deformation mechanism. They observed that the mineralized fibrils showed a higher modulus compared with the non-mineralised fibril, which increased in samples with higher mineral densities. In addition to the higher modulus, the hydroxyapatite phases of the mineralised fibrils exhibited approximately 4 times higher stress than the collagen phase of the same fibrils. This suggests that the load is predominantly carried by the mineral phase of the mineralised fibril [45].

1.2. Diseases Associated with Collagen I

There are several diseases associated with collagen I, including osteogenesis imperfecta (OI), Ehlers-Danlos syndrome (EDS), osteoporosis and an overlap condition with elements of OI and EDS. Additionally, there are other conditions including atypical Marfan syndrome and Caffrey's disease.

As of November 2020, 2053 individuals were reported with 1065 individual variants in *COL1A1*, and 1069 individuals were reported with 612 individual variants in *COL1A2* [46-48]. These variants result in a number of different conditions, which will be described in this section.

1.2.1. Osteogenesis Imperfecta

Osteogenesis imperfecta (OI) is characterised by an inherent susceptibility to fractures, though the severity ranges from a lethal phenotype to very mild. It was first described in a scientific manner in the thesis 'Congenital osteomalacia' by Olaus Jakob Ekman in 1788. Ekman's observations included the hereditary nature of the bone fragility [49]. The term osteogenesis imperfecta was reportedly first used by the Dutch professor Willem Vrolik, when describing a new-born that was born with numerous fractures and hydrocephalus, and died 3 days after birth [50].

The variability in the phenotypes, and their severity led to a classification system published by Sillence *et al.* in 1979, classifying the patients into four types, each designated a Roman numeral (I-IV). The four types were I- Dominantly inherited OI with blue sclerae, II- Lethal perinatal OI with radiographically crumpled femora and beaded

ribs, III- Progressively deforming OI with normal sclerae and IV- Dominantly inherited OI with normal sclerae [51].

As more cases were studied, and understanding grew, the Sillence classification was modified, expanding the definitions and adding OI types V-VII in 2004 [52]. The vast majority of cases of OI, over 90%, have mutations in one of the collagen I genes, *COL1A1* and *COL1A2*, and are classified as types I-IV [53]. The new classifications (V-VII) were created for cases with unknown aetiology, or clinical classifications that differed from those in type I-IV. As more genetic causes have been identified, the classification system has further changed. It was found that many different genes can cause types I-IV and that the use of VI and VII for cases with unknown aetiology were no longer required, leading to the use of types I-V for clinical diagnosis, and a separate 'molecular type' pertaining to the genetics. Table 1.2. gives a breakdown of the genes involved in OI, the mode of inheritance and the molecular type of OI caused by mutations in these genes, and which of the updated Sillence classification each falls into. The autosomal dominant forms of the disease, making up over 90% of cases of the disease predominantly involve mutations in *COL1A1* and *COL1A2*, the exceptions being *IFITM5* and *PSL3* [53]. The remaining less than 10 % of OI cases are caused by autosomal recessive mutations in a variety of genes.

Pathophysiological mechanism	Gene	Protein	Inheritance	Number of known mutations	Molecular Type	Updated Sillence Type
Defects in collagen type I synthesis, structure, folding, post-translational modification, processing and cross-linking	<i>COL1A1</i>	Collagen alpha-1(I) chain	AD	>1,000	I,II,IV	I,II,IV
	<i>COL1A2</i>	Collagen alpha-2(I) chain	AD AR*	>600	II,IV	I,II,IV
	<i>CRTAP</i>	Cartilage-associated protein	AR	32	VII	II, III, IV
	<i>PPIB</i>	Peptidyl-prolyl cis-trans isomerase B; cyclophilin B	AR	17	IX	II,III, IV
	<i>LEPRE1/P3H1</i>	Prolyl 3-hydroxylase 1	AR	69	VIII	II,III
	<i>FKBP10</i>	Peptidyl-prolyl cis-trans isomerase FKBP10	AR	38	XI	III, IV
	<i>PLOD2</i>	Procollagen-lysine,2-oxoglutarate 5-dioxygenase 2	AR	10	BRKS2	No longer treated as OI
	<i>SERPINH1</i>	Serpin H1	AR	9	X	III
Defects in other proteins leading to abnormal bone mineralization	<i>BMP1</i>	Bone morphogenetic protein 1	AR	11	XIII	III
	<i>SPARC</i>	SPARC; osteonectin	AR	2	XVII	III
	<i>SERPINF1</i>	Pigment epithelium-derived factor (PEDF)	AR	38	VI	III
	<i>IFITM5</i>	Interferon induced transmembrane protein 5	AD	2	V	V
Defects in osteoblast differentiation and function	<i>PLS3</i>	Plastin 3	XLD	17	BMND18	Osteoporosis X-linked form
	<i>TMEM38B</i>	Trimeric intracellular cation channel type B	AR	6	XIV	III
	<i>WNT1</i>	Proto-oncogene Wnt-1	AR AD	35	XV	III,IV, Osteoporosis AD form
	<i>SP7</i>	Transcription factor Sp7; osterix	AR	2	XII	IV
	<i>CREB3L1</i>	Cyclic AMP-responsive element-binding protein 3-like protein 1	AR	3	XVII	III
Unknown	<i>MBTPS2</i>	Membrane-bound transcription factor site-2 protease	XLR	2	XIX	Osteoporosis X-linked form
	<i>TENT5A (FAM46A)</i>	Terminal nucleotidyltransferase 5A	AR	3	XIIX	III

Table 1.2. Types of osteogenesis imperfecta, organised by mechanism and gene. AD, autosomal dominant; AR, autosomal recessive; XLD, X-linked dominant; XLR, X-linked recessive; BRKS1, Bruck syndrome-1; BRKS2 Bruck syndrome-2; BMND18, Bone Mineral Density Quantitative Trait Locus 18. *Seen only in a few consanguineous families. Adapted from Makitie *et al.*, 2019 and Chetty *et al.*, 2020 [54, 55].

In addition to the mutations in genes coding for the collagen I alpha chain, mutations in seven genes known to be involved in the biosynthesis, processing and secretion of collagen I have also been identified as causing OI.

The genes *CRTAP* [56, 57], *LEPRE1* [58] and *PPIB* [59] encode the proteins which form the collagen-3-hydroxylation complex that resides in the endoplasmic reticulum and

modifies the unfolded collagen I $\alpha 1$ and $\alpha 2$ chains [60]. *PLOD2*, encodes Procollagen-lysine, 2-oxoglutarate 5-dioxygenase 2 which catalyses the hydroxylation of lysyl residues in collagens. This enzyme is required for the hydroxylation of lysyl residues of collagens, including those residues that are involved in the formation of glycosylated hydroxylysyl residues and hydroxylysyl-derived collagen cross-links [61]. The specific phenotype caused by mutations in *PLOD2*, lead to Bruck syndrome type 2, which has previously been considered a type of OI, but as of 2020, has been removed from the OI nosology [55]. Mutations in two other genes involved in the biosynthesis of collagen I have also been identified in OI cases, *SERPINH1* and *FKBP10* [62, 63]. *SERPINH1* encodes HSP47, and *FKBP10* encodes FKBP65, which are chaperone proteins that are involved in procollagen transit and folding respectively. *BMP1*, encodes Bone morphogenetic protein 1 (BMP1) which is a procollagen C-endopeptidase, which as the name suggests cleaves the carboxyl propeptides of procollagens (specifically I, II and III) and plays a role in inducing bone and cartilage development. Mutations in *BMP1* can block cleavage of the c-propeptide and lead to impaired assembly of type I collagen, mutation in *COL1A1* and *COL1A2*, that inhibit propeptide cleavage can have similar effects [64]. Figure 1.9 gives an overview of the biosynthesis process and each of the stages where these proteins have their effect.

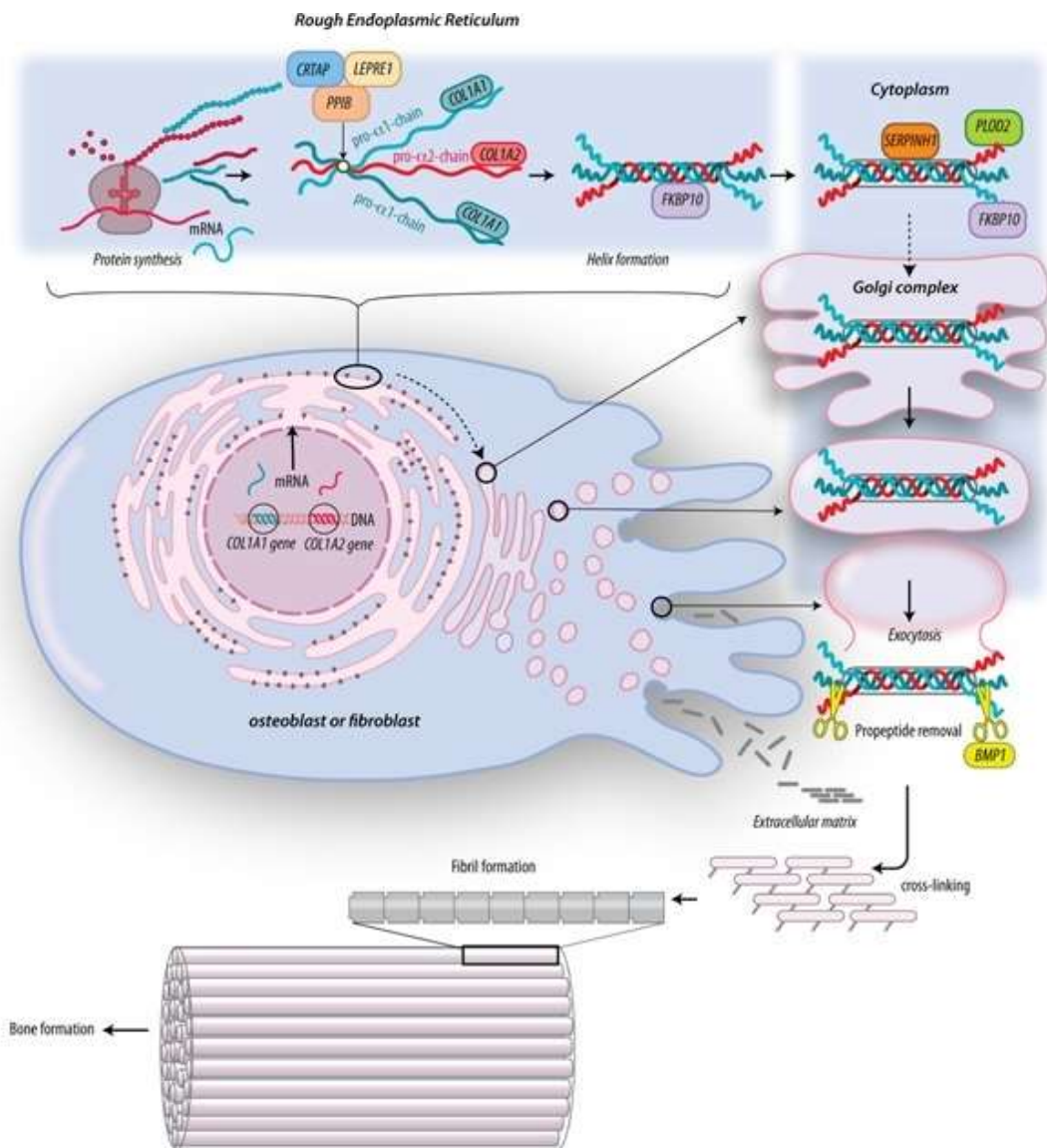


Figure 1.9. Overview of collagen type I biosynthesis. A number of proteins are essential for the biosynthesis of Collagen, mutations in the genes coding for these proteins are known to cause OI. These proteins and their function in the biosynthesis process are marked in the diagram. Taken from Van Dijk and Sillence, 2014 [65].

In addition to abnormal collagen and collagen processing, genes affecting the osteoblast, and mineralisation can also lead to OI, but will not be explored further in this review, however some of the mechanisms will be touched on in the following subchapter.

1.2.1.1. Mechanisms Behind the OI Phenotype

The overwhelming majority of cases of OI are due to mutations in the genes coding for the collagen I alpha chains, but the different types of mutation can manifest in different ways and by different mechanisms. These mechanisms will be discussed here.

Most cases of type I OI, the least severe form, have haploinsufficiency due to a null *COL1A1* allele. Mutations causing a frameshift, premature stop codon, or abnormal splicing leading to a premature stop codon, lead to a quantitative reduction of type I collagen without affecting collagen structure [66]. Mutations in *COL1A2* have been noted to cause similar phenotypes, including splice site mutation reducing levels of *COL1A2* transcript [67]. The other three types of OI caused by mutations in collagen I genes, II-IV are generally caused by structural defects in one of the collagen I chains, which can then lead to a variety of downstream effects. The most common of these is a substitution of glycine, disrupting the repeating motif, and the next most common, causing about 20% of cases, are mutations affecting splicing, which can lead to exon skipping or intronic inclusion [68]. Should the structural changes prevent trimerisation, the protein is degraded by the proteasome in a process known as ER-associated degradation (ERAD) [69]. If the proteins are able to trimerise, but are unable to be retrotranslocated from the ER, due to over modification or defects in folding, then the proteins, or their aggregates, are removed by autophagy. Both of these processes can lead to ER stress, which in turn can lead to apoptosis of osteoblasts, as can delays in the collagen processing. Osteoblasts are essential for bone remodelling and therefore apoptosis impairs bone homeostasis [70, 71]. Structurally abnormal protein often leads to delayed helical folding, leading to over modification. Upon secretion, these modifications can cause a variety of effects downstream including, impairing the ability of non-collagen proteins to bind to the fibrils. This is often the case in the lethal type II form [66, 72, 73]. Forlino *et al.* summarised these mechanisms in a figure, which is replicated in Figure 1.10 [66].

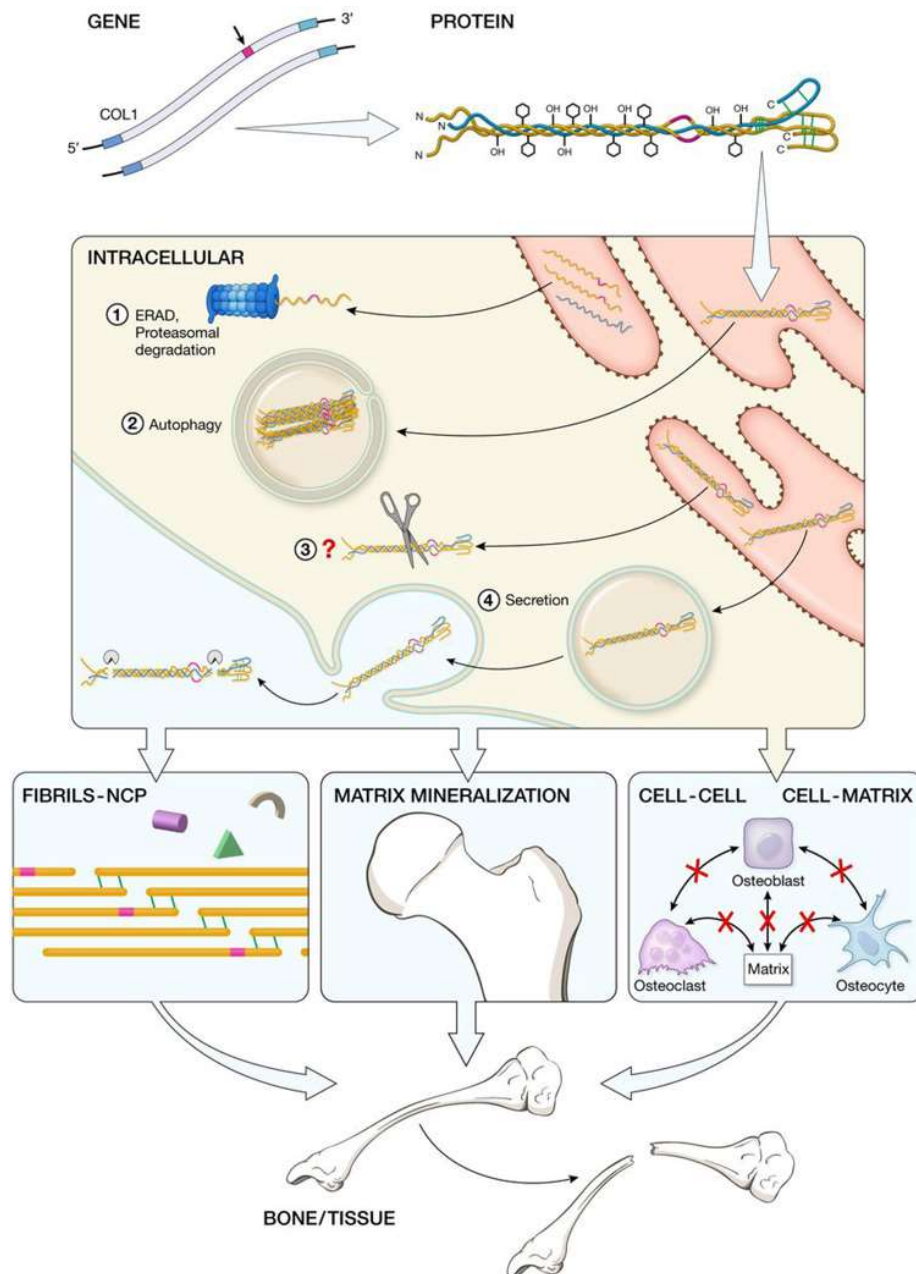


Figure 1.10. Mechanisms contributing to osteogenesis imperfecta. (1) Mutant procollagen chains unable to incorporate into heterotrimer are retrotranslocated into the cytosol and degraded by the ER-Associated Degradation (ERAD) pathway. (2) Fully misfolded heterotrimers with structural defects generate supramolecular aggregates that are eliminated by autophagy. (3) Mutant molecules with triple helical mutations can be degraded through an unidentified pathway. (4) Abnormal procollagen can be secreted, processed and incorporated in the extracellular matrix. The secreted mutant collagen affects fibril structure and interactions of non-collagen proteins (NCPs) with matrix, as well as matrix mineralization and osteoblast development and cell-cell and cell-matrix cross-talk. The overall result is bone deformity and fragility. Taken from Forlino *et al.* [66].

Matrix abnormalities including heterogeneity of collagen forms, abnormal fibril organization and altered modifications may increase stress in osteoblast and altered

cell-cell signalling, which in turn alters bone homeostasis, leading to enhanced bone dissolution and absorption by osteoclasts [66, 74].

1.2.1.2. Mouse Models of OI

The majority of murine models of OI have alterations to the genes *Col1a1* and *Col1a2*, however a number of genes known to be involved in collagen biosynthesis, bone mineralisation, and osteoblast function have been knocked out to create further models. A summary of murine models of OI is shown in Table 1.3.

As with the mechanisms of OI, only the models that involve the genes *Col1a1* and *Col1a2* will be discussed further. Unsurprisingly, due to defects in *Col1a1* generally being more deleterious than mutations in *Col1a2*, there are also more mouse models involving *Col1a1* than *Col1a2*. These murine models of OI replicate phenotypes seen in all four Sillence type that are caused by mutations in *COL1A1* and *COL1A2* in human. However due to the sheer number of different mutations detected in human OI cases, it is not feasible that these models will replicate all the different mechanisms by which mutations lead to OI, however they can help elucidate mechanisms. Examples of models resulting in all 4 OI types involving both *Col1a1* and *Col1a2* will be described briefly below.

The Mov-13 mouse is essentially a *Col1a1* null, as the transcription is blocked by the insertion of Moloney leukaemia virus [75]. The homozygous *Mov-13*^{-/-} exhibits arrested development between day 11 and 12 of gestation [76]. This model is classed as a model of type II OI due to the lethal phenotype; however, it does not replicate the type II OI phenotypes seen in humans. The heterozygous *Mov-13*^{+/-} animals exhibit a 50% reduction in type I collagen production; however, the protein is structurally normal, heterotrimeric, and indistinguishable from wild-type [77]. The heterozygous *Mov-13*^{+/-} animals did not exhibit an overt OI phenotype, such as spontaneous fractures, however the animals were shown to have reduced mechanical properties in bone (around a 25% reduction in bending strength, among other parameters), and hearing loss, together these phenotypes indicate a type I OI phenotype [77, 78].

Common name	Human OI type	Gene	Characteristics
Mov-13 ^{-/- a}	OI II	<i>COL1A1</i>	Perinatal mortality
Mov-13 ^{-/+ a}	OI I	<i>COL1A1</i>	Hearing loss, reduced mechanical properties in bone, and reduced collagen production
<i>oim/oim^b</i>	OI III	<i>COL1A2</i>	Fragile bones, osteopenia, cortical thinning, bone deformities, joint laxity, kyphosis
<i>oim^{+ b}</i>	OI I	<i>COL1A2</i>	Decreased material properties of bone
G610C/G610C ^{Neo+ c}	OI IV	<i>COL1A2</i>	Decreased body weight, bone mineral density, bone volume, and mechanical properties of bone
+/G610C ^{Neo+ c}	OI I/IV	<i>COL1A2</i>	Decreased body weight, bone mineral density, bone volume, and mechanical properties of bone
+/G610C ^{Neo-} (Amish) ^c	OI IV	<i>COL1A2</i>	Decreased body weight, bone mineral density, bone volume, and mechanical properties of bone
G859C ^d	OI II	<i>COL1A1</i>	Short and wavy ribs, poor bone mineralization, underdeveloped skeleton, pliable limbs, perinatal death
Aga2 ^{+ e}	OI II/III	<i>COL1A1</i>	Skeletal deformities, fragile bones, osteopenia, perinatal death (in some cases)
Aga2 ^{-/- e}	OI II	<i>COL1A1</i>	Embryonic mortality
BrtlIII ^f	OI II	<i>COL1A1</i>	Rib fractures, short vertebral bodies, poor skull mineralization, perinatal mortality
BrtlIV ^{+ f}	OI IV	<i>COL1A1</i>	Perinatal death to long-term survival, bone deformity, fragile bones, osteopenia
BrtlIV/BrtlIV ^f	OI IV (mild)	<i>COL1A1</i>	Bone deformity, bone fragility, osteopenia
Human <i>COL1A1</i> minigene ^d	OI II–IV	<i>COL1A1</i>	Fragile bones, low bone mineral density, ~90% perinatal mortality rate (when high levels of minigene expressed)
Ifitm5 transgenic ^a	OI V	<i>IFITM5</i>	Skeletal deformities, fragile bones, poor bone mineralization, perinatal death
Pedf ^{-/- *}	OI VI	<i>SERPINF1</i>	Decreased material properties of bone
Crtap ^{-/- c}	OI VII	<i>CRTAP</i>	High bone mineralization and mineral density in bone (but low bone density), progressive kyphoscoliosis, cartilage dysplasia, decreased material properties in skin
P3h1 ^{-/- a}	OI VIII	<i>LEPRE1</i>	Small body size, low mineral density in calvarial and long bones, decreased material properties of bone, impaired hearing
Ppib ^{-/- *}	OI IX	<i>PPIB</i>	Decreased body size and weight, low bone mineral density and volume, progressive kyphosis, decreased material properties in skin
Hsp47 ^{-/- a}	OI X	<i>SERPINH1</i>	Embryonic mortality
Fkbp10 ^{-/- a}	OI XI	<i>FKBP10</i>	Delayed growth beginning at E13.5, fragile tissue, skeletal deformities, perinatal mortality
Sp7 ^{-/- c}	Possibly OI XII	<i>SP7</i>	Decreased trabecular bone mineralization, osteopenia, cortical bone thinning
Wnt1 ^{Sw/Sw *} (Swaying)	OI XV	<i>WNT1</i>	Poor coordination, osteopenia, fragile bones, cerebellar deficit

Table 1.3. A table documenting murine models of OI. Backgrounds of these models are as follows ^a C57BL/6J, ^b B6C3Fe, ^c 129/SvEv, ^d FVB, ^e C3HeB/FeJ, ^f 129/SvJ x C3H/HeJ, *not specified. Adapted from Enderli *et al.*, 2016 [79].

The *Aga2* mouse model was identified as part of an ENU screen, where a mutation caused a C-terminal frame shift, leading to a poorly secreted protein and ER-stress induced apoptosis [71]. The *Aga2*^{-/-} animals were lethal around day 9 of gestation, and the heterozygous *Aga2*^{+/-} animals showed reduced viability in addition to increased bone fractures, fragility and deformity, and osteopenia [71]. The heterozygous *Aga2*^{+/-} models type II or type III OI, depending on the severity of the phenotype. The homozygous *Aga2*^{-/-} could be viewed as modelling type II OI, however as with *Mov-13*^{-/-}, aside from lethality it does not resemble the phenotype seen in humans.

The *BrtIII* and *BrtIV* mouse models were created in an attempt to induce a G349C substitution using the Cre/Lox system in *Col1a1*. An unexpected allelic expression due to the stop cassette created the *BrtIII* where heterozygous animals died within hours of birth and exhibited rib fractures and poor skeletal mineralisation, modelling type II OI [80]. The stop cassette was subsequently removed to create an F2 generation that possessed the desired G349C substitution, *BrtIV*. The heterozygous animals showed a variable phenotype with a severe lethal phenotype and a moderately severe non-lethal phenotype, both exhibited fragile bone, deformity and osteopenia, the bones appeared more fragile in the lethal animals [80]. The heterozygotes that showed the lethal phenotype showed increased expression of transforming growth factor beta (TGF- β), which the non-lethal heterozygotes did not [81]. *BrtIV* appears to model type II/IV of OI. The homozygous *BrtIV* animals show a similar OI IV phenotype, but milder than the non-lethal heterozygotes [66].

The *OIM* mouse model is the result of a spontaneous mutation in *Col1a2*, resulting the deletion of a guanine at position 3978 causing a frameshift, leading to a deficiency in the pro $\alpha 2(I)$ chains, which in turn leads to the production of $\alpha 2(I)$ homotrimer [82]. The homozygous animals exhibit phenotypes including spontaneous fractures, bone deformity, small body size and reduced material properties under mechanical testing (around a 50% reduction in maximum load, among other parameters), indicating a type III OI phenotype [82, 83]. The heterozygotes did not show spontaneous fractures, but did exhibit reduced material properties under mechanical testing (around a 20% reduction in maximum load) indicating a mild type I OI phenotype.

The G610C (Amish) mouse model is a knock-in replicating the G610C mutation in *COL1A2* first identified in Old Order Amish (OOA) kindred [84]. The initial line retained a neomycin-targeting vector, which caused the secretion of homotrimer in addition to heterotrimer containing the G610C substitution. The neomycin-targeting vector was subsequently removed. The homozygotes retaining the neomycin-targeting vector were viable, and the homozygotes, which did not, were found to die perinatally. The heterozygotes without the vector, which replicates the genetic mutation in the OOA, exhibited decreased body weight, BMD, bone volume, and mechanical properties of bone testing (around a 40% reduction in maximum load) [84].

1.2.2. Ehlers-Danlos Syndrome

Ehlers-Danlos Syndrome (EDS) is a heterogeneous group of connective tissue disorders with phenotypes including joint hypermobility, skin hyperextensibility and fragility [85]. EDS is named for two dermatologist Edvard Ehlers and Alexandre Danlos. Ehlers described some of the most important clinical signs of EDS, including joint hypermobility, skin fragility and haemorrhages in a condition he called *cutis laxa* [86]. Danlos also made a description of *cutis laxa* in which he emphasised excessively stretchable skin [87]. It later transpired that the case described by Danlos was more likely to be *Pseudoxanthoma elasticum* than the syndrome that bears his name [88]. Much like the classification of OI, the nosology of EDS has changed over time with different types, and subtypes being identified or re-classified. The different genetic causes of EDS has further diversified the classification, which started with 3 types described by Barabas in 1967 [89], increasing to 5 types described by Beighton in 1968 [90], and 7 types described by Mckuisick in 1972 [91]. The 2017 international classification of the Ehlers-Danlos syndromes recognises 13 subtypes of EDS which maintains the clinical classification, as opposed to genetic classification, primarily because the names are widely used in the scientific and medical communities [92]. These 13 types are shown in Table 1.4. After the publication of the 2017 international classification of the Ehlers-Danlos syndromes, variants in the gene *AEBP1* have been found to cause an EDS-like phenotype, inherited in an autosomal recessive manner. The phenotypes include joint hypermobility, hyperextensible skin, poor wound healing with atrophic scarring, and osteoporosis [93, 94]. This potential new subtype on EDS has not been included in Table 1.4, as it has not been given a designation yet.

Clinical EDS subtype	Abbreviation	IP	Genetic basis	Protein
Classical EDS	cEDS	AD	Major: <i>COL5A1</i> , <i>COL5A2</i> Rare: <i>COL1A1</i> c.934C>T, p.(Arg312Cys)	Type V collagen Type I collagen
Classical-like EDS	clEDS	AR	<i>TNXB</i>	Tenascin XB
Cardiac-valvular EDS	cvEDS	AR	<i>COL1A2</i> (leading to NMD and absence of pro $\alpha 2$ (I) chains)	Type I collagen
Vascular EDS	vEDS	AD	Major: <i>COL3A1</i> Rare: <i>COL1A1</i> c.934C>T, p.(Arg312Cys) c.1720C>T, p.(Arg574Cys) c.3227C>T, p.(Arg1093Cys)	Type III collagen Type I collagen
Hypermobile EDS	hEDS	AD	Unknown	Unknown
Arthrochalasia EDS	aEDS	AD	<i>COL1A1</i> , <i>COL1A2</i>	Type I collagen
Dermatosparaxis EDS	dEDS	AR	<i>ADAMTS2</i>	ADAMTS-2
Kyphoscoliotic EDS	kEDS	AR	<i>PLOD1</i> <i>FKBP14</i>	LH1 FKBP22
Brittle Cornea syndrome	BCS	AR	<i>ZNF469</i> <i>PRDM5</i>	ZNF469 PRDM5
Spondylodysplastic EDS	spEDS	AR	<i>B4GALT7</i> <i>B3GALT6</i> <i>SLC39A13</i>	$\beta 4$ GalT7 $\beta 3$ GalT6 ZIP13
Musculocontractural EDS	mcEDS	AR	<i>CHST14</i> <i>DSE</i>	D4ST1 DSE
Myopathic EDS	mEDS	AD or AR	<i>COL12A1</i>	Type XII collagen
Periodontal EDS	pEDS	AD	<i>C1R</i> <i>C1S</i>	C1r C1s

Table 1.4. The 2017 international classification of the Ehlers-Danlos syndromes. IP, inheritance pattern; AD, autosomal dominant; AR, autosomal recessive, NMD, nonsense-mediated mRNA decay. Adapted from Malfait et al., 2017 [92].

There is considerable overlap in phenotypes of these different forms of EDS, and many include some of the hallmarks of EDS, joint hypermobility, skin fragility and hyperextensibility. As such the new classification includes major and minor criterion for diagnosis, however, definite diagnosis relies on molecular confirmation of a causative

variant with the exception of hypermobile EDS, where the causative gene is unknown [92].

There are 4 acknowledged types of EDS which can be caused by mutations in *COL1A1* and *COL1A2*: classical EDS, cardiac-valvular, vascular EDS and arthrochalasia EDS. Due to the high degree of overlap of the 13 types of EDS, this brief overview will only specifically cover these 4 forms of EDS.

1.2.2.1. Classical EDS

Classical EDS is inherited in an autosomal dominant manner, and is caused by mutations in *COL5A1* or *COL5A2* in over 90% of cases [95], however a specific amino acid substitution (Arg134Cys) in *COL1A1* has been observed to cause a classical EDS phenotype [96]. Where there was a causal involvement of Collagen V, the majority of mutations affect *COL5A1*, with less than 20% affecting *COL5A2*. The majority of *COL5A1* mutations lead to a *COL5A1* null allele, with the remainder, structural mutations including missense mutation and in-frame splicing or deletions. To date no *COL5A2* mutations have been found to lead to a *COL5A2* null allele, mutations tend to be structural mutations including missense mutations and in-frame splicing or deletions [95]. The arginine to cysteine mutation in *COL1A1* occurs at the X position of the previously mentioned G-X-Y repeating motif. It has been suggested that the cysteine could lead to intermolecular di-sulphide bridges, which could impair efficient secretion [96].

Diagnosis of most forms of EDS is made on the basis of major and minor criteria. The major criteria for classical EDS are skin hyperextensibility and atrophic scarring, and generalised joint hypermobility (GJH). A minimal criteria for diagnosis is either both major criteria, or skin hyperextensibility and atrophic scarring with at least 3 of the minor criteria. Minor criteria include easy bruising, doughy skin, skin fragility, molluscoid pseudotumors, subcutaneous spheroids, hernias, epicanthal folds, complications of joint hypermobility, and a family history of a first degree relative who meets clinical criteria [92].

GJH is defined as having a Beighton score of 5 or more out of a possible total of 9. The Beighton score for assessment of generalized joint hypermobility was first published in 1973 [97] (Table 1.5).

	Right	Left
Passively dorsiflex the fifth finger to 90°	1	1
Bend the thumb to the volar aspect of the forearm	1	1
Hyperextend the elbow to 10°	1	1
Hyperextend the knee to 10°	1	1
Place hands flat on floor without bending the knees		1
Total possible score	9	

Table 1.5. A table showing the Beighton score for assessment of generalized joint hypermobility [97].

1.2.2.2. Cardiac-valvular EDS

Cardiac-valvular EDS is inherited in an autosomal recessive manner and is caused by mutations in *COL1A2*, leading to a complete deficiency of pro $\alpha 2$ (I) collagen. A number of causes have been identified including splice mutations that lead to mRNA instability and nonsense mutations creating premature termination codons. Both the aberrant splicing and nonsense mutations alters mRNA processing, leading to nonsense mediated decay, and an absence of the pro $\alpha 2$ (I) collagen chain [98, 99].

The major criteria for cardiac-valvular EDS are more diverse than classical EDS, in addition to joint hypermobility (which can be generalised as in classical, or restricted to smaller joints) and skin involvement including hyperextensibility and atrophic scarring (as in classical EDS), as well as easily bruised or thin skin, the key major criterion is severe progressive cardiac-valvular problems. The minimal criteria for diagnosis is the cardiac-valvular problems with a family history compatible with recessively inherited disease and one other major criterion, or two minor criteria. Minor criteria include inguinal hernias, pectus deformity, joint dislocations and foot deformities [92].

1.2.2.3. Vascular EDS

Vascular EDS is inherited in an autosomal dominant manner and is caused by mutations in *COL3A1* in the vast majority of cases, although a number of different arginine to cysteine substitution in *COL1A1* have been observed to cause a vascular EDS phenotype. A large number of different mutations in *COL3A1* have been identified, and the majority

are missense or splice mutations, with a few nonsense mutations. The majority of these missense mutations alter the repeating glycine motif, and the splice variants introduce premature termination codons that lead to mRNA instability through nonsense-mediated decay and a null allele [100]. The mechanism by which mutations in *COL1A1* lead to vascular EDS is not known, however delayed procollagen processing by N-proteinases has been noted in some patients [101]. Another possibility that has been suggested is that the introduction of the cysteine residue could lead to intermolecular di-sulphide bridges, which could impair efficient secretion [96].

Vascular EDS is unique among the EDS subtypes, in that the major criteria do not include joint hypermobility or skin involvement, but include ruptures of tissues such as arteries and uterus, colon perforation and the formation of carotid-cavernous sinus fistulas. Minor criteria include easy bruising, thin translucent skin, acrogeria (skin ageing), and characteristic facial appearance, spontaneous pneumothorax, talipes equinovarus (club foot), hypermobility of small joints, congenital hip dislocation, tendon and muscle rupture, keratoconus (corneal defect), gingival recession or fragility, early onset varicose veins. There are not minimal criteria for diagnosis, only criteria suggestive of vascular EDS, and generally, diagnosis is made by molecular testing. The criteria are a family history of the disorder and one other major criteria; however, combinations of major and minor criteria should be tested [92].

1.2.2.4. Arthrochalasia EDS

Arthrochalasia EDS is the type of EDS most commonly associated with collagen I defects. Mutations causing arthrochalasia EDS occur in either *COL1A1* or *COL1A2*, but in either gene, the mutations cause either complete or partial deletion of Exon 6, most commonly due to exon skipping caused by a splice variant. The downstream effect of this is that the N-propeptide is retained due to the loss of the cleavage site [102, 103].

The major criteria for arthrochalasia EDS include congenital bilateral hip dislocation, severe GJH with dislocations and subluxations and skin hyperextensibility. Minor criteria include muscle hypertonia, kyphoscoliosis, radiologically mild osteopenia, tissue fragility and easily bruised skin. A minimal criteria for diagnosis is congenital bilateral hip dislocation and skin hyperextensibility, or congenital bilateral hip dislocation, severe GJH dislocations and subluxations and two of the minor criteria [92].

1.2.2.5. Mouse Models of EDS

There are a number of mouse models of EDS, including classical EDS and vascular EDS, however a literature search revealed no mouse models of arthrochalasia EDS or cardiac-valvular EDS. The models of classical EDS involve *Col5a1*, either *Col5a1* haploinsufficiency, or a tissue specific homozygous *Col5a1* deletion due to the homozygous *Col5a1* null allele being lethal [104, 105]. Models of vascular EDS all involve *Col3a1*, including *Col3a1* haploinsufficiency and glycine substitutions [106-108]. As none of these mouse models involves either *Col1a1* or *Col1a2*, they will not be explored further here.

1.2.3. Osteogenesis Imperfecta/Ehlers-Danlos Syndrome Overlap

A number of publications have reported patients as having mixed features of both EDS and OI [109-112]. These cases were termed osteogenesis imperfecta/Ehlers-Danlos syndrome overlap (OI/EDS overlap).

Cabral *et al.* identified 7 children with type III or IV OI which also showed a joint laxity, and found that each child had a mutation in the first 90 residues of the helical region of *COL1A1*, leading to a delay in, or a prevention of, cleavage of the N-propeptide. In 6 of the 7 cases, the mutation was a glycine substitution and in one case a skipping of Exon 7 [113].

Malfait *et al.* reported 7 cases of OI/EDS overlap, where the patients predominantly presented with an EDS phenotype that resembled, but was distinct from, the acknowledged EDS subtypes, with elements of OI phenotypes. Two patients had mutations in *COL1A1*, both glycine substitutions in exons 7 or 8, however the remaining 5 patients had mutations in *COL1A2*, two with glycine substitutions in exons 8 or 12, and 3 mutations leading to exon skipping of exons 7, 9 and 14. The conclusions were similar to those of Cabal *et al.*, that the phenotypes arise from mutations in the most N-terminal region of the helical domain, causing delayed, or impaired N-propeptide processing, and disturbing collagen fibrillogenesis [114].

More recently, it has been suggested, by Morlino *et al.*, that the OI/EDS overlap should be renamed Col1-related overlap disorder and that it should be included as part of the EDS nosology [115]. To aid with diagnosis, and to prevent confusion with either EDS or OI, new diagnostic criteria were suggested, which included exclusion criteria. Major

criteria include, blue sclera, flat feet with valgus deformity, generalized joint hypermobility according to age and soft, doughy, or hyperextensible skin. Minor criteria include dolichostenomelia, hearing loss, short stature, two or more atrophic scars, two or more fractures in pre-pubertal age, two or more joint dislocations and two or more injuries or ruptures of ligaments/tendons/muscles. The exclusion criteria include, congenital fractures, dentinogenesis imperfecta, molluscoid pseudotumors, papyraceous scars, progressive/severe heart valve disease, platyspondyly, and stable or progressive long bone deformities. The diagnosis criteria for Col-1 related overlap disorder is three major criteria; or two major criteria and two or more minor criteria, or one major criterion and 5 or more minor criteria [115].

Whilst the majority of OI/EDS overlap cases are caused by mutations at the N-terminal end of the helical region, this is not always the case. Nicholls *et al.* reported an OI/EDS case caused by homozygous splice mutation in *COL1A2* yielding a non-functional pro α 2(I) chain [110]. A number of other examples of this are shown in Figure 1.11.

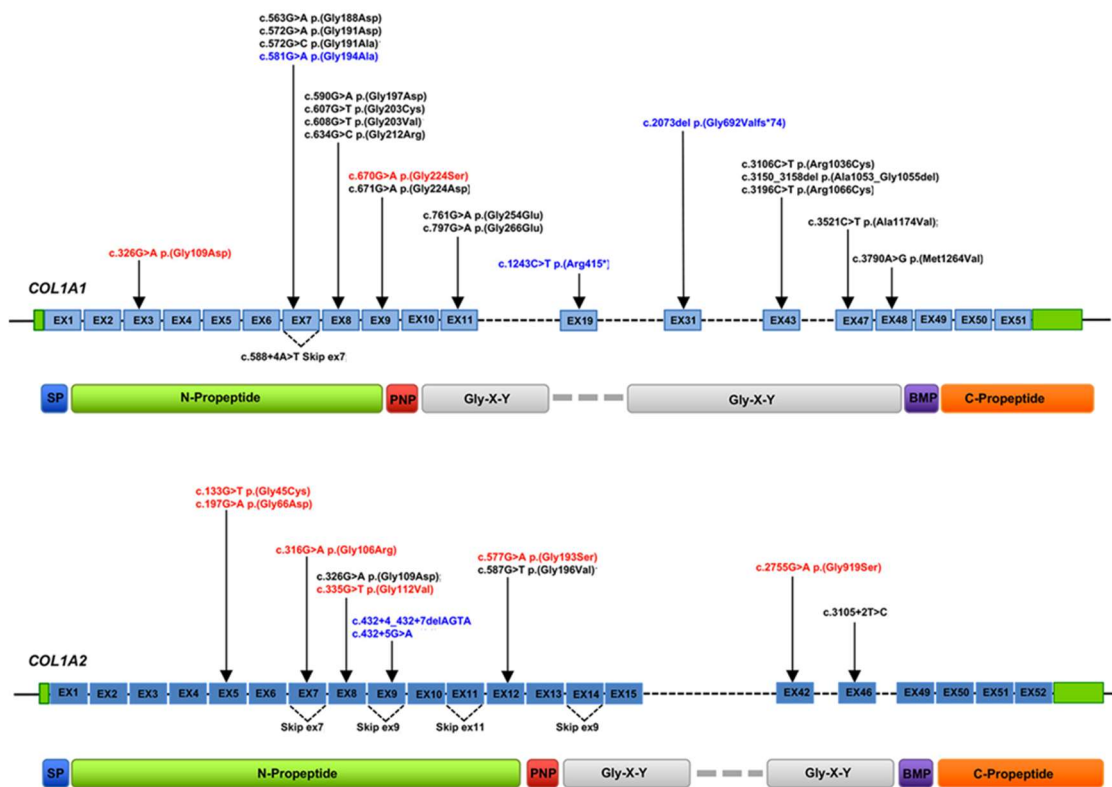


Figure 1.11. A diagram showing mutations in *COL1A1* and *COL1A2* reported in patients fitting the diagnostic criteria of Col-1 related overlap disorder. Notations in red are novel mutations reported in Morlino *et al.*, notations in blue are previously reported mutations but also included the Morlino *et al.* study, notations in black are previously reported mutations, which were not included the Morlino *et al.* study. Figure adapted from Morlino *et al.*, 2019 [115].

The phenotypes of this syndrome are variable and cases with the identical mutations often have different combinations of phenotypes, this is the case in several of the families reported by Morlino *et al.* In one such family, one patient would have been diagnosed with non-deforming OI (type I) if assessed separately from the other family members with identical mutations, due to the lack of generalised joint hypermobility, however the other family members did show generalised joint hypermobility [115].

1.2.3.1. Mouse models OI/EDS Overlap

There is only one acknowledged mouse model of OI/EDS overlap disorder, however it is possible that mouse models with mutations in *Col1a1* or *Col1a2* currently categorised as OI models, could also model this disorder. An example of this is the *oim* mouse (see section 1.2.1.3), where the phenotype includes joint laxity and altered skin and tendon physiology of OI, in addition to the OI phenotype, although it should be noted that skin fragility has not been reported [116]. None of the currently known EDS mouse models are attributed to mutations in *Col1a1* or *Col1a2*, and therefore cannot be models for OI/EDS.

The mouse model of OI/EDS is known as *Jrt*, and was published by Chen *et al.*, an ENU induced splice variant led to skipping of Exon 9 in *Col1a1*. The homozygous animals were not viable, and phenotypes observed in the heterozygotes included small body size, a number of bone related phenotypes including reduced BMD, bone volume/tissue volume ratio, trabecular number, and fragile, fracture prone bones, in addition to fragile skin [117].

1.2.4. Other Conditions Related to Collagen I

1.2.4.1. Osteoporosis

Osteoporosis is a disease characterised by low bone mass and deterioration of the bone microarchitecture, leading to an increase in bone fragility, and an increased susceptibility to fracture [118]. Fractures occurring at the hip and vertebrae are the “classic” osteoporotic fractures [119]. The diagnostic criterion for osteoporosis is having a bone mineral density (BMD) T score of -2.5 or less (2.5 standard deviations below an established baseline calculated from a mean BMD from young adults of the appropriate

sex) at the femoral neck [120]. Incidences of osteoporosis increase with age, and affects women far more frequently than men, affecting 21% and 6% respectively in the 50-84 year age bracket in the EU in 2010 [121].

Osteoporosis has a strong genetic component as shown by both familial studies and twin studies on the heritability of BMD [122-124]. Generally, osteoporosis is viewed as a complex polygenic disease where multiple genes each have a modest individual effect on BMD, and combine with environmental factors to have an effect greater than their individual parts [125]. Several possible monogenic causes of osteoporosis have been identified including WNT1 [126] and PLS3 mutations [127, 128].

There is some overlap in the clinical manifestation of mild OI and osteoporosis, with both diseases having similar bone fragility and low BMD [129]. Patients have been identified with mutations in *COL1A2*, where the clinical criteria for OI were not met, resulting in a diagnosis of osteoporosis [130]. Additionally, a polymorphism in the SP1 binding site of *COL1A1* has been found to predispose patients to osteoporotic fractures in multiple clinical studies [131-133].

1.2.4.2. Atypical Marfan Syndrome

Marfan syndrome (MFS) is typically caused by mutations in the fibrillin-1 gene (*FBN1*). MFS is associated with abnormalities of the skeleton, cardiac and ocular systems [134]. Abnormalities of the skeleton can include disproportionate overgrowth of the long bones, chest deformity (caused by over growth of the ribs), arachnodactyly, scoliosis and joint laxity [135]. Abnormalities of the ocular system can include dislocation of the lens, flat cornea and hypoplastic iris [136]. Cardiac abnormalities can include thickening and/or prolapse of the atrioventricular valves, dilated cardiomyopathy, aortic dissection and aneurysm, and congestive heart failure [137, 138]. The mechanism by which mutations in *FBN1* lead to MFS is not fully realised, however, there is evidence that it may lead to dysregulation of TGF β activity and signalling [139, 140].

A case of atypical Marfan syndrome has been identified by Phillips *et al.*, where the patient presented with skeletal and cardiovascular abnormalities consistent with MFS, including progressive lumbar scoliosis, and aortic dilation, resulting in congestive heart failure, arachnodactyly and a decreased upper to lower segment ratio. A mutation in *COL1A2* causing an arginine to glutamine substitution (R618Q) was detected and found

to cause abnormal migration of the Pro $\alpha 2(I)$ chain in SDS gels. It should be noted that this mutation does not affect the repeating glycine motif as it occurs at the Y position of the G-X-Y repeat, and the mechanism by which this mutation causes the phenotypes is unknown [141].

1.2.4.3. Caffrey's Disease

Caffrey's disease was first described in 1945 by Caffrey and Silverman, but the first case identified as a distinct entity was in 1930 [142, 143]. Caffrey's disease is an autosomal dominant disorder the "classical" disease presents in the first 5 months after birth, with periosteal hyperostosis in bones including mandible, ulna, ribs, clavicle and scapulae, which normally resolves by 2 years of age [144, 145]. Patients also exhibit joint hyperlaxity, soft, hyperextensible skin, similar to Ehlers-Danlos syndrome type III, which does not resolve. Approximately 50 % of cases in the Gensure *et al.* study had experienced peripheral fractures indicating an OI/EDS like phenotype [146]. If the disease presents prior to birth, it is usually lethal, and presents as OI type II, with periosteal hyperostosis [147].

A mutation in *COL1A1* resulting in an arginine to cysteine substitution in exon 41 (R836C) has been identified in both the non-lethal "classical" [146] and the lethal Caffrey's disease [147]. Gensure *et al.* observed some lethal cases did not contain this mutation, and Kamoun-Goldrat *et al.*, also state "it is likely that the mutation of an unknown gene is responsible for some cases of cortical hyperostosis, either classical (infantile) or prenatal forms" [147].

1.3. Osteoarthritis

Osteoarthritis (OA) is a metabolically active, progressive degenerative arthropathy, which affects the synovial joints and is characterized by degradation of the articular cartilage [148]. OA is a complex syndrome, a group of overlapping disorders with similar biological and clinical outcomes [149, 150]. OA has previously been regarded as a disease of the cartilage, a disease of 'wear and tear', however this idea has evolved and OA is now viewed as a disease of the whole joint [151].

There are many risk factors for OA including systemic risk factors such as age, gender and hormones, and genetics; as well as local risk factors such as obesity and injury [152]. Epidemiologically OA can be defined pathologically, radiographically or clinically, and these classifications are not necessarily synonymous [152]. Clinically, OA is characterised by pain and impairment of joint function [153]. Radiographic OA is most commonly defined using the Kellgren-Lawrence classification (K&L) [154, 155] with a 0 grade indicating no OA, 2 or higher indicating definite OA, with 4 indicating severe OA. The radiographic evidence of OA includes osteophytes (new bone growth at the periphery of the joint), joint space narrowing and sclerosis of the sub-chondral bone [156]. There is often a discordance between clinical and radiographic OA, which is likely to be because patients tend not to experience symptoms during the early stages of OA, due to articular cartilage being aneural [157].

1.3.1. The Synovial Joint

There are three main classifications of joint in the body; cartilaginous joints, fibrous joints and synovial joints. Synovial joints are freely movable joints and are identified by articulating bones capped with articular cartilage, enclosed within a flexible articular capsule. Within this joint class there are three main sub-classes, uniaxial (such as the knee), biaxial (such as the metacarpophalangeal joints) and multiaxial (such as the hip) [158]. OA can affect any synovial joint, but is most common in the hips, knees, spine and specific joints in the hands (including first carpometacarpal joints, proximal interphalangeal joints and distal interphalangeal joints) [159]. Interestingly, these examples of the most commonly affected joints include all three sub-classes of synovial joints; uniaxial, biaxial and multiaxial, and are also the joints which are most commonly subjected to excessive and repeated loading [160].

As mentioned previously, OA is a disease of the whole joint, and whilst cartilage degradation is a hallmark, OA phenotypes in other tissues include synovial inflammation, new bone formation (sclerosis and osteophyte formation), degeneration of ligaments and tendons, hypertrophy of the joint capsule and where present, degradation of the meniscus or articular disc [161] (Figure 1.12).

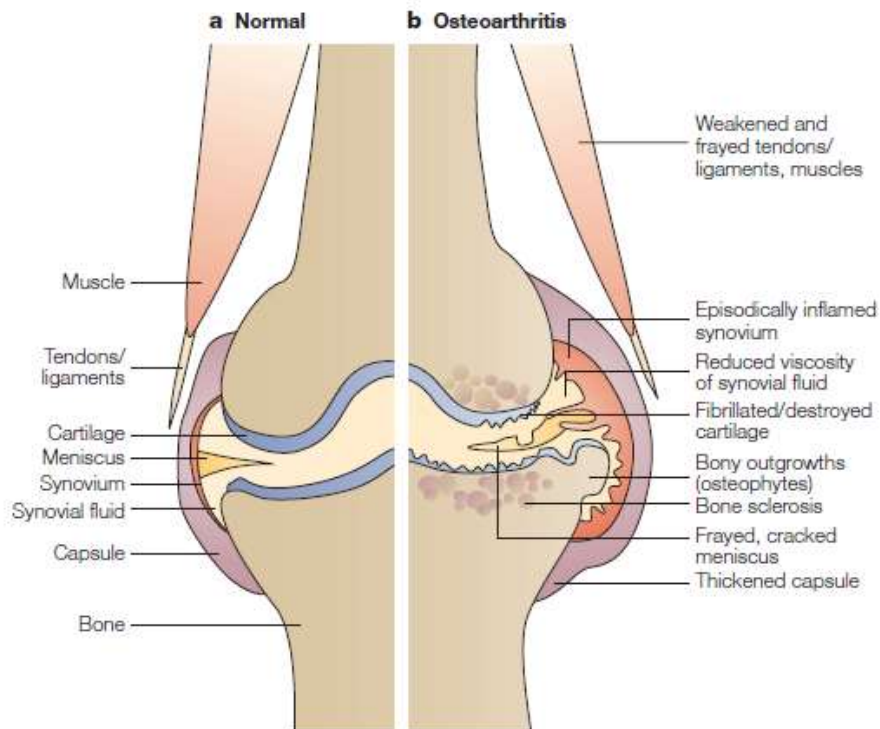


Figure 1.12. A diagram comparing a normal knee and an osteoarthritic knee. Taken from Wieland *et al.*, 2005 [162].

1.3.1.1. Articular Cartilage

Articular cartilage is a low-friction, wear-resistant tissue, which is ideal to bear and distribute loads [163]. The articular cartilage is normally between 2 and 4mm thick, and is avascular, aneural and alymphatic [164]. Cartilage contains a single cell type, chondrocytes, surrounded by an extracellular matrix (ECM), which is primarily composed of water, collagens, proteoglycans, with a smaller fraction of non-collagenous proteins [165].

Water is by far the most abundant component of articular cartilage comprising approximately 65-80% of its 'wet weight', with collagen II then next most abundant component at approximately 10-20%. Chondrocytes, make up less than 5% of the total articular cartilage volume, but are essential for maintenance of the homeostasis of the cartilage [163, 166]. The chondrocytes respond to stimuli such as chemical factors, and mechanical factors such as, hydrostatic pressure and mechanical forces, and modifies the ECM metabolism. The most important of these factors are the growth factors and pro-inflammatory cytokines that have catabolic and anabolic effects, which in turn

modulate the synthesis and degradation of the matrix molecules [167]. Imbalances in the metabolic processes can lead to a 'vicious cycle' of degeneration [162, 166].

The ECM can be viewed as a biphasic structure, of a solid and fluid phase, the solid being collagens and proteoglycans, and the fluid, being water and ions. The biphasic nature is due to the low permeability of the solid phase, creating a high interstitial fluid pressure, which contributes greatly to the load transmission of cartilage [163, 168]. The fluid phase also plays an important role in nutrient transport, as the chondrocytes are avascular and therefore acquire nutrients through osmosis from the synovial fluid via the water in the ECM.

The structure of the ECM is created by a three-dimensional mesh of collagen fibrils, predominantly type II, interacting with proteoglycans (including aggrecan, decorin, biglycan and fibromodulin). The majority of the intrafibrillar space is filled with large proteoglycan aggregates formed by the interaction of aggrecan monomers, and hyaluronan by way of link proteins. Aggrecan monomers themselves are formed when glycosaminoglycan (GAGs) chains, such as keratan sulphate or chondroitin sulphate, are bound to an aggrecan core [169]. These proteoglycan aggregates provide compressive and tensile strength due to the highly negatively charged nature of the GAGs, which makes them hydrophilic, and therefore able draw water into the ECM [170] (Figure 1.13).

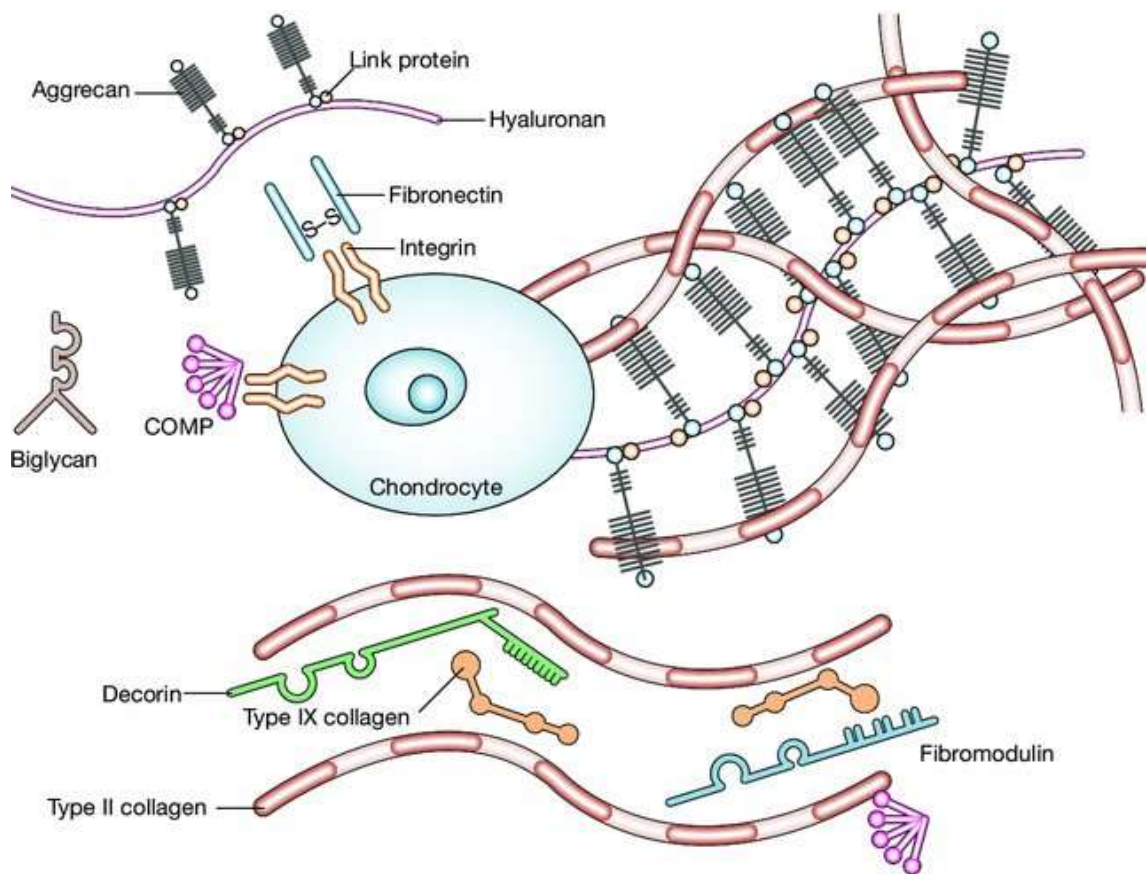


Figure 1.13. The extracellular matrix (ECM) of cartilage. The ECM features a network of proteins including collagens (predominantly type II), proteoglycans (predominantly aggrecan); and other non-collagenous proteins (including link protein, fibronectin, cartilage oligomeric matrix protein (COMP)) and the smaller proteoglycans (biglycan, decorin and fibromodulin). The interaction between highly negatively charged cartilage proteoglycans and type II collagen fibrils is responsible for the compressive and tensile strength of the tissue, which resists load *in vivo*. Taken from Chen *et al.*, 2006 [170].

The articular cartilage is divided into 3 identifiable zones; the superficial zone, the middle zone and the deep zone. The superficial zone, which makes up 10-20% of the ECM, is the zone closest to the articular surface. The chondrocytes in this zone are flattened, and the collagen fibrils, are aligned parallel with the articular surface. The middle zone, which as the name suggests is sandwiched between the other zones, makes up 40-60% of the ECM volume. The chondrocytes are not flattened, and are more spherical in shape, and less densely packed than the superficial zone. The collagen fibrils in this zone are thicker and are arranged more obliquely. Figure 1.14 shows the shape and position of the chondrocytes and the orientation of the collagen fibrils.

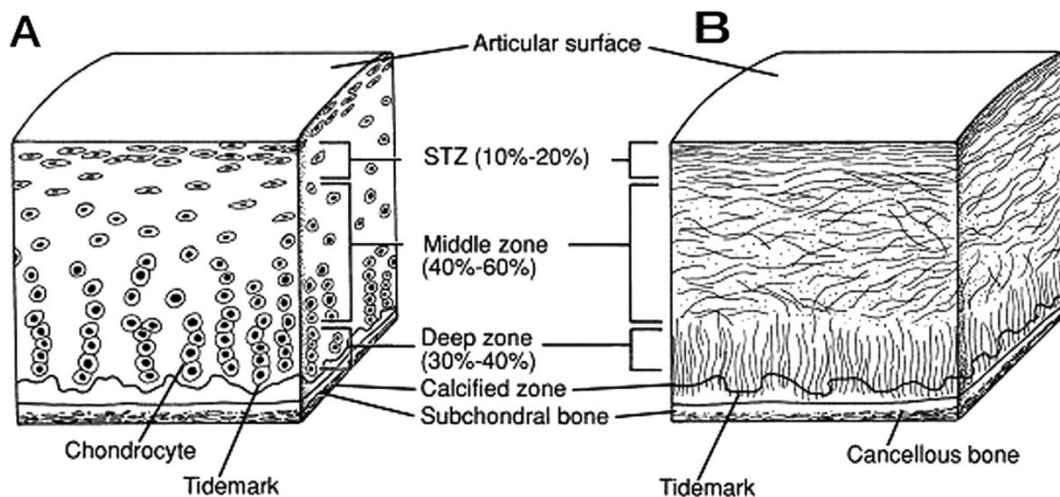


Figure 1.14. Cross-sectional diagram of healthy articular cartilage: A- cellular organization in the zones of articular cartilage; B- collagen fibre architecture. Taken from Buckwater,1994 [171]

In terms of resisting mechanical forces, the deep zone provides the greatest resistance to compressive forces due to the collagen fibrils being positioned at right angles to the subchondral bone and running through the calcified cartilage. The middle zone is responsible for resistance to compressive forces, but to a lesser extent. The superficial zone is responsible for resisting the tensile and shear forces [171].

Aside from the difference in the organisation of chondrocytes and the orientation of collagen fibres within the different zones of the cartilage, the ECM also has a different make up depending on proximity to chondrocytes. The regions with differing constituents are referred to as the pericellular matrix (PCM), the territorial region and the interterritorial region (the latter two regions are sometimes referred to collectively as the further removed matrix). The PCM surrounds the chondrocyte and contains mostly proteoglycans with some loose collagen fibres (Collagen VI and IX, but not II) [172]. It has been suggested that the PCM plays a role in mechanotransduction [173]. The PCM is thought to amplify mechanical signals transmitted through the ECM and release growth factors and other regulatory molecules in response to these signals [174]. The territorial region surrounds the PCM, and contains abundant collagen fibrils (mainly collagen II) arranged in a web-like manner as well as proteoglycans [175]. The interterritorial region is the largest of the three regions, and fills the spaces between the territorial zones, and contains similar components to the territorial regions, but with a far higher concentration of proteoglycan aggregates [176].

Cartilage requires a balance between catabolic and anabolic factors in the ECM, some of which are secreted by the chondrocytes and others that are provided through the synovial fluid. Catabolic factors include cytokines, such as interleukin-1 (IL-1), tumor necrosis factor α (TNF α) and leukemia-inhibitory factor (LIF), and proteinases, such as the metalloproteinases, and factors such as cathepsin K and Dickkopf-related protein. Anabolic factors include cytokine regulators such as interleukin-1 receptor agonist (IL-1RA); growth factors, such as fibroblast growth factor (FGF), epidermal growth factor (EGF) and transforming growth factor- β (TGF β); and proteinase inhibitors [177-179]. Mueller *et al.* provide a good summary of the various catabolic and anabolic factors [177].

1.3.1.2. Subchondral Bone

Below the deep zone of the articular cartilage, the cartilage becomes calcified at a point called the tidemark, and is known as the zone of calcified cartilage (ZCC). The ZCC attaches the cartilage to the subchondral bone and is an important interface for the transmission of force [180]. The subchondral bone is generally defined as the bony tissue that lies distal to the calcified cartilage, separated by the cement line, and comprises the subchondral bone plate and the subchondral trabecular bone [181]. The subchondral bone plate consists of relatively nonporous cortical bone, which is poorly vascularised [182], however channels do provide a direct link between articular cartilage and trabecular bone, with blood vessels and nerves penetrating into the calcified cartilage [183]. The trabeculae of the subchondral trabecular bone connect to the subchondral bone plate and plays an important role in shock absorbing and supportive functions in the normal joint [181, 184]. The subchondral bone and articular cartilage, and the layers between them can be viewed as a single functional unit, the osteochondral junction, where there is intensive biomechanical and biochemical cross talk, and alteration of one tissue in the unit can modify the function of others [185].

1.3.1.3. Other Joint Components

The capsule is a triple layered structure that surrounds the joint, the outer layer is made of fibrous connective tissue and the middle and inner layer, which together are called the synovium or synovial membrane, are the subintima and the intima respectively [186]. The outer capsule is thickened in places by the blending of ligaments and helps to

stabilise the joint [187]. Two types of synoviocytes reside in the intima, Type A, or synovial macrophages and Type B, or synovial fibroblasts. Type A cells remove waste and debris from the joint cavity and Type B cells produce specialized matrix constituents including hyaluronan, collagens and fibronectin for the synovial fluid [188].

The synovial fluid is an ultrafiltrate of blood plasma that lubricates the joint, provides nutrients to the articular cartilage and allows transport of regulatory cytokines. Synovial fluid contains lubricating molecules such as proteoglycan 4, hyaluronan and surface-active phospholipids [189].

The menisci of the knee are crescent-shaped wedges of fibrocartilage located on the medial and lateral aspects of the knee joint. The menisci increase the stability of the joint, and due to their shape, are able to help disperse force through the knee due to hoop stress among other mechanisms [190]. The outer portion of the meniscus connected to the joint capsule is called the red zone, which is thickest part of the meniscus, the inner most zone is the white zone, and the area between is known as the red-white zone. The red zone is vascular and the white zone is avascular. The red zone is predominantly comprised of collagen I (approximately 80% dry weight), the white zone is about 60% collagen II and 40% collagen I by weight [191].

There are various ligaments within the knee, attaching the meniscus to the tibial plateau, joining the tibia and femur, and forming part of the capsule. The structure and content of ligaments are very similar to tendons, which have been described in an earlier subchapter.

1.3.2. The Osteoarthritic Joint

OA has a complex pathogenesis involving mechanical, inflammatory and metabolic factors, which ultimately lead to damage to multiple tissues and failure of the synovial joint [192]. The 'vicious cycle' in Figure 1.15 is regarded as a good overview for the pathophysiological processes that occur during OA. What is unclear is where the 'entry' and 'exit' points to the vicious cycle are.

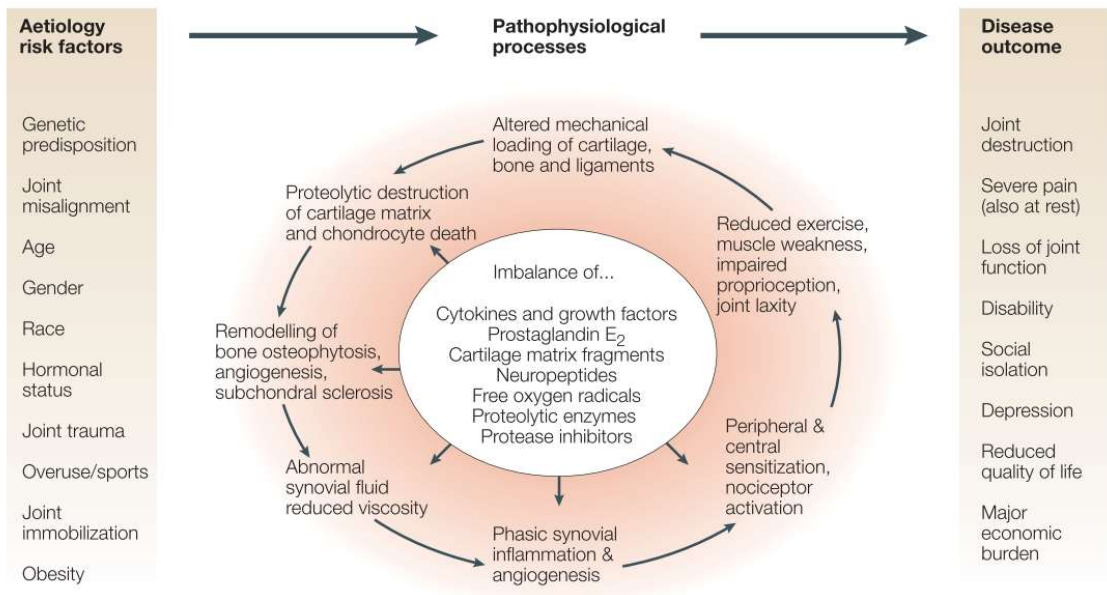


Figure 1.15. The vicious cycle of Osteoarthritis. Taken from Wieland *et al.*, 2005 [162].

The changes in the OA joint are numerous, Glyn- Jones *et al.* summarised these changes in a figure, which is replicated below [193] (Figure 1.16).

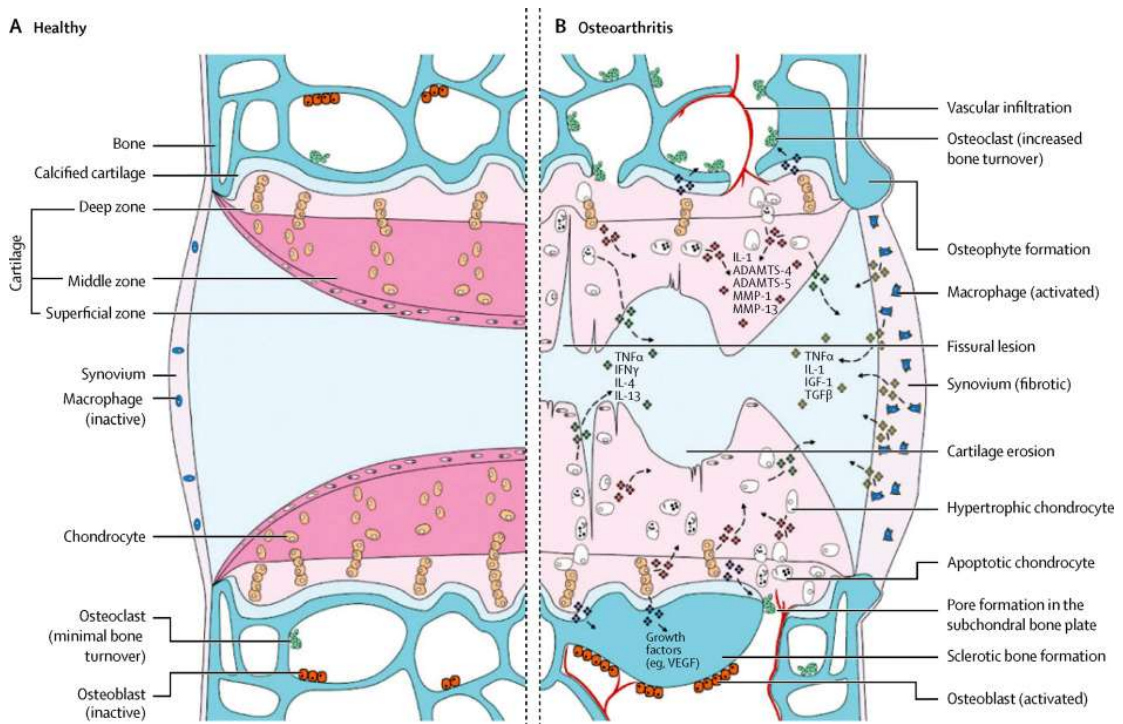


Figure 1.16. Signalling pathways and structural changes in the development of osteoarthritis. ADAMTS=a disintegrin and metalloproteinase with thrombospondin-like motifs. IL=interleukin. MMP=matrix metalloproteinase. TNF=tumour necrosis factor. IFN=interferon. IGF=insulin-like growth factor. TGF=transforming growth factor. VEGF=vascular endothelial growth factor. Taken from Glyn- Jones *et al.* [193].

1.3.2.1. Articular Cartilage

As previously stated, healthy articular cartilage exists in a state of homeostasis with a balance of synthesis and degradation of the components of the ECM. OA results from an imbalance between synthesis and degradation of the components of the ECM [194]. It is not known exactly what initiates the swing toward degeneration, but once it begins the 'vicious cycle' in Figure 1.15 propagates the process, with synovial macrophages taking up the degraded molecules from collagen and proteoglycans from the ECM, which stimulates the production of more catabolic factors, such as TNF α , IL-1 and IL-6, leading to further degradation of the cartilage [195].

1.3.2.2. Subchondral Bone

There is a significant increase in bone remodelling at the bone-cartilage interface below damaged cartilage in OA. This is what leads to the sclerosis of the subchondral bone. This is likely due to the increase mechanical load, due to the loss of the protective cartilage, in addition to the increase of cytokines and growth factors within the joint cavity [196]. A process called eburnation occurs where spikes of granulation and fibrous tissue advance from the calcified cartilage into the articular cartilage [162]. As OA progresses this tissue undergoes endochondral ossification, which is where the cartilage is converted into bone. The chondrocytes undergo hypertrophy, mineralize and are replaced with bone tissue. This ossification alters the subchondral bone architecture and decreases cartilage thickness simultaneously [197]. This process is accompanied by angiogenesis and can occur even below the areas with minimal cartilage damage.

Osteophytes are the bony growth that appear at the margins of the joint [198]. Growth factors such as TGF- β , fibroblast growth factors (FGFs) and bone morphogenetic proteins (BMPs) have all been shown to play a role in osteophyte development [198, 199]. Osteophyte development is thought to be caused by the excessive proliferation of mesenchymal stem cells, stimulated by the previously mentioned growth factors, in the periosteum and synovium, which then undergo chondrogenesis and differentiate into hypertrophic chondrocytes, before being replaced by osteoblasts which form the bone [200]. There is some evidence that absence of osteophytes may be linked to a higher risk of disease progress in some patients with OA, which lends credence to the theory that osteophyte development may be an adaptive process to stabilise the joint

[201]. The development of osteophytes, while thought to be an attempted repair process often leads to negative effects such as pain and loss of movement [167].

1.3.2.3. Other Joint Components

Synovial inflammation in OA is thought to develop secondarily to pathological processes in cartilage and bone, and is rarely as severe as in rheumatoid arthritis. Synovial inflammation tends to occur in areas of the synovial membrane that are close to, or in contact with cartilage. Synovitis could be caused by cartilage debris and catabolic mediators in the synovial cavity [156]. This could accelerate the damage to the cartilage in patients with OA, due to synovial macrophages producing catabolic and pro-inflammatory mediators, which in turn destabilise the balance of cartilage damage and repair [202, 203]. It is thought that the synovium could be the root cause of some of the pain suffered by patients with OA, this is because the synovium is highly innervated with sensory nerve fibres [204].

Pathological changes occurring in the ligaments and in the menisci in OA, include matrix disruption, fibrillation, cell clusters, calcification and cell death [161].

1.3.3. Genetics of OA

It has been long been known that there is a genetic component to OA, in 1944 Stecher noted sisters of affected women were three times more likely to exhibit Heberden's nodes (a hard swelling in the fingers, indicating OA in the distal interphalangeal joints), compared to the population in general [205]. Spector *et al.* used a twin study to show a genetic influence ranging from 39-65% in hand and knee OA, due to the correlation of disease state and status being consistently higher in identical twins compared with non-identical twins [206]. In addition to twin studies and familial aggregation studies, linkage studies and genome wide association studies (GWAS) have been used to investigate the role of genetics in OA, as outlined in (Figure 1. 17).

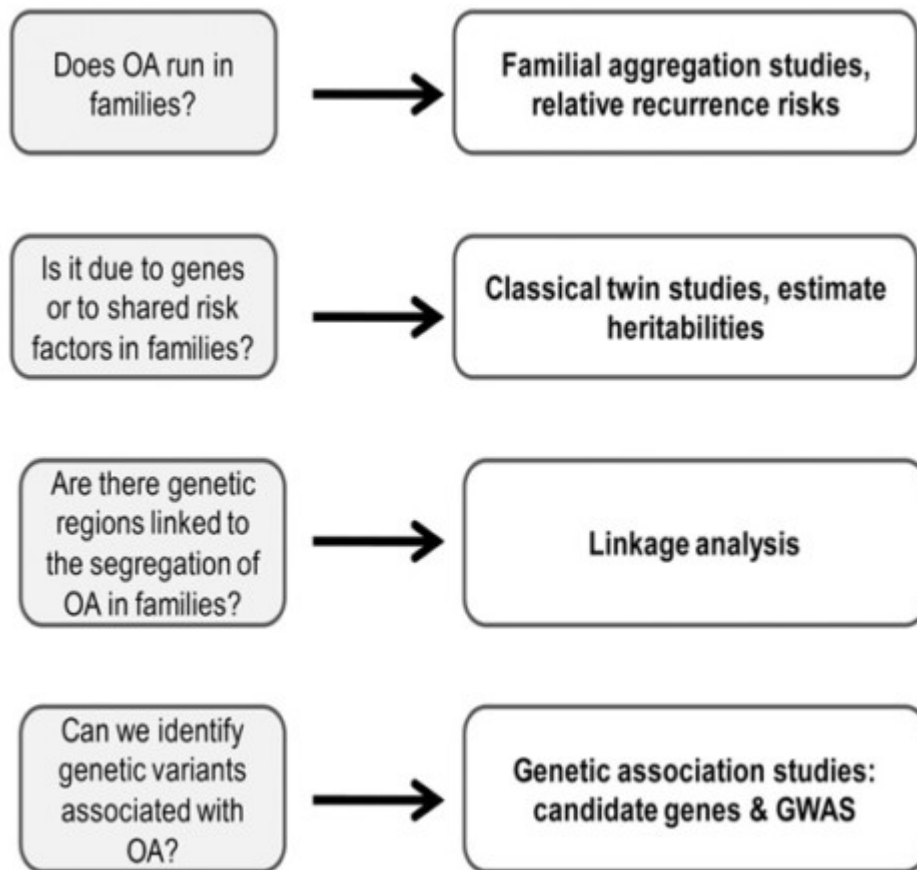


Figure 1.17. An overview of strategies for genetic studies. Taken from Valdes and Spector, 2008 [207].

Due to the multifactorial nature of OA, there are many ways in which genetic factors can affect the development and progression of disease. In addition to the direct effects that the genetic factors may have on the joint, they can also play a role in other risk factors such as obesity, inflammation and bone density [208] (Figure 1.18).

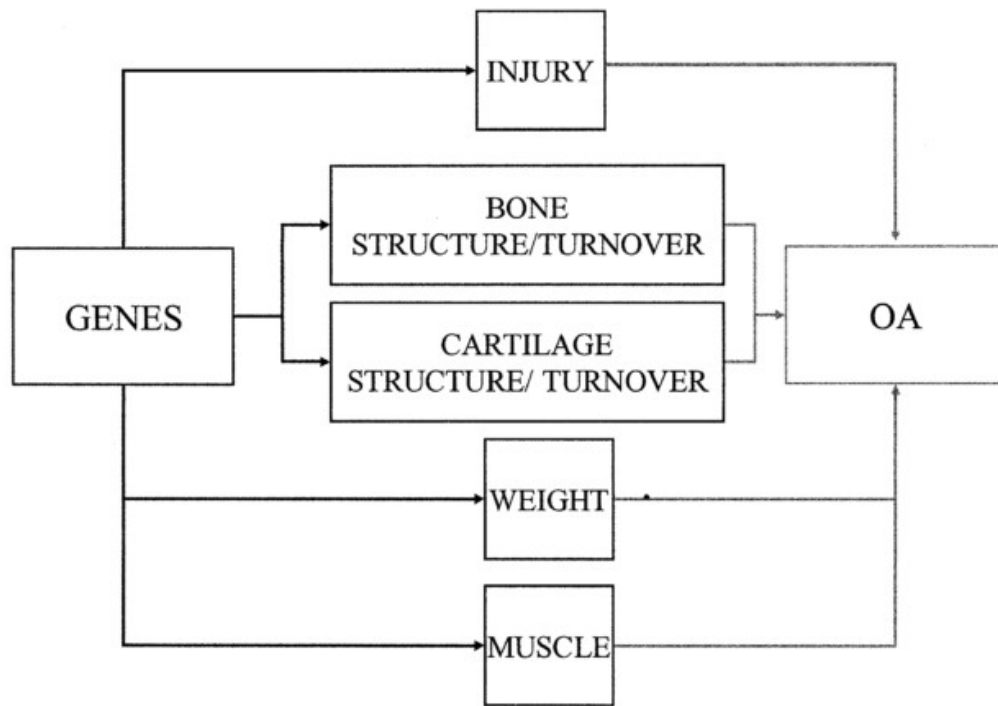


Figure 1.18. A simplistic diagram showing the roles of genes in OA. Taken from Spector and Macgregor, 2004 [209]

The joint can be directly affected by the genetic factors causing skeletal malformations leading to changes in joint shape, alignment, or structure. Some developmental defects can result in congenital misalignment of joints and lead to loss of articular cartilage and damage to other joint structures, due to distinct degrees of biomechanical instability [208]. The form and function of cartilage itself can also be affected by the genetic factors.

Genetic linkage occurs when a locus involved in the trait of interest (specific OA phenotypes) and alleles at nearby markers are inherited jointly. This allows identification of relationships between genetic markers and specific traits or diseases [206, 210]. These linkages then provide a good starting point for identifying candidate genes for further investigation. For example, linkage analyses have identified several regions which are likely to contain OA susceptibility genes one of which, 2q13-32 included IL-1 and frizzled related protein 3 (FRZB). These genes are currently the subject of further research [211].

GWAS studies involve comparing the DNA of two groups of people, normally a control group and a group with a specific trait (in this case OA). The individuals are all genotyped

for a large number of known single nucleotide polymorphisms (SNPs), and if significantly more individuals with a specific allele occurs in the affected group, then the SNP is said to be associated with the trait or disease. These studies have proved very successful in associating genes with monogenic disorders, but somewhat less successful with complex multifactorial diseases such as OA. The variability of the disease including age of onset compounds these issues, as members of the control group, can cease to be controls. However, a number of loci have been identified as being associated with OA, for example 7q22 which has been found to be associated in multiple studies [212, 213].

The number of genetic risk loci associated with OA has been increasing dramatically over the last few years and now number over 100. However, functional studies are required to elucidate the molecular mechanism that cause these variants to increase OA risk [214, 215].

1.3.4. Ageing as a risk factor for OA

Ageing has been known as the greatest risk factor of OA for many years and is perhaps one of the reasons why OA was viewed as a disease of wear and tear, however OA is not an inevitable part of growing old [216]. There are many consequences of ageing which can increase the likelihood of OA, including direct changes to the cartilage and changes to joint function. Age-related cartilage changes include dissipation of the chondrocytes in the superficial region of the ECM, and an increase in chondrocytes in the deep zone, leads to decreased hydration of the cartilage [167] and accumulation of advanced glycation end-products (AGEs), which crosslink with collagen molecules increasing the brittleness of cartilage [216]. Age-related changes to joint function can result from sarcopenia, and increased joint laxity [217]. Chondrocyte senescence has also been implicated in the degradation of cartilage, both through increased oxidative stress and increased secretion of MMPs [218, 219].

1.3.5. Mouse Models of OA

There is currently no consensus model for OA that naturally reflects human disease [220]. *Ex vivo* models are useful for modelling aspects of OA, but are unable to replicate the joint environment properly. There are a number of naturally occurring models of OA including mice, rabbits, guinea pigs, dogs and horses [221]. Each species has its own benefits and drawbacks, for example, mice are easily managed with low cost, which is

advantageous, but the cartilage has different cellular structure and is over 70x thinner compared to human cartilage, horses on the other hand have very similar cartilage thickness and cellular structure, but are expensive and require more management [220], additionally in accordance with the 3Rs principle (reduce, refine, replace) lower order animals are preferable if possible. Genetically modified models have been created, where genes involved in OA pathogenesis are knocked out, to model elements of OA. There are also number of induced models of OA, where disease can be induced surgically, chemically, or through non-invasive procedures such as cyclic AC tibial compression. A summary of these models is shown in Table 1.6 [221].

Model/Example	Advantages	Disadvantages
Naturally occurring models - Dunkin-Hartley Guinea pig	Spontaneous models, no need for intervention, used to study pathogenesis of naturally occurring OA, variable in OA manifestation such as in human OA	Time-consuming due to slow progression of OA, high cost
Genetically modified models -IL-6 Knock-out mouse	Spontaneous models, easy to produce, used to study the contribution of specific genes in OA and develop disease-modifying treatments	High cost, production of additional cartilage abnormalities and potential lethal gene deletions
Surgically induced Models -Destabilisation of the medial meniscus	Rapid progression of OA and therefore short study timeframe, reproducible, induces post-traumatic OA, allows the study of various lesions/stages of disease and assess therapeutic efficacy of agents for OA treatment	Inappropriate for studies of degenerative OA since generated by traumatic invasive intervention
Chemically induced Models -Monoiodoacetate (MIA) injection	Most rapidly progressing OA, easy to implement, relatively less invasive than surgically induced models, reproducible, useful for short-term studies, allows the study of various lesions/stages of disease and assess therapeutic efficacy of pain-alleviating agents for OA treatment	Rapid and widespread changes generated by invasive intervention, poor correlation with the pathogenesis of human OA
Non-invasive models -cyclic AC tibial compression	Non-invasive, severity of the lesions can be adjusted, low risk of infection, reproducible, allows the study of early OA changes after acute or chronic overuse injuries of joints and the effects of early therapeutic intervention	Equipment is not commonly available, several loading cycles and episodes are needed to induce severe OA changes, still in the early stages of understanding its application

Table 1.6. Advantages and disadvantages of in vivo models. Adapted from Samvelyan et al., 2020 [210].

Animal models of OA are a very important tool for investigating the pathogenesis. Due to early OA in humans being difficult to detect, using animal models can help us fill the gaps in our knowledge such as: Why and where in the joint is OA initiated? [222]. It is unlikely that any one model will mirror all facets of human OA. Nevertheless by

combining the knowledge gained from multiple model types, we can have fairly comprehensive coverage [222] (Figure 1.19).

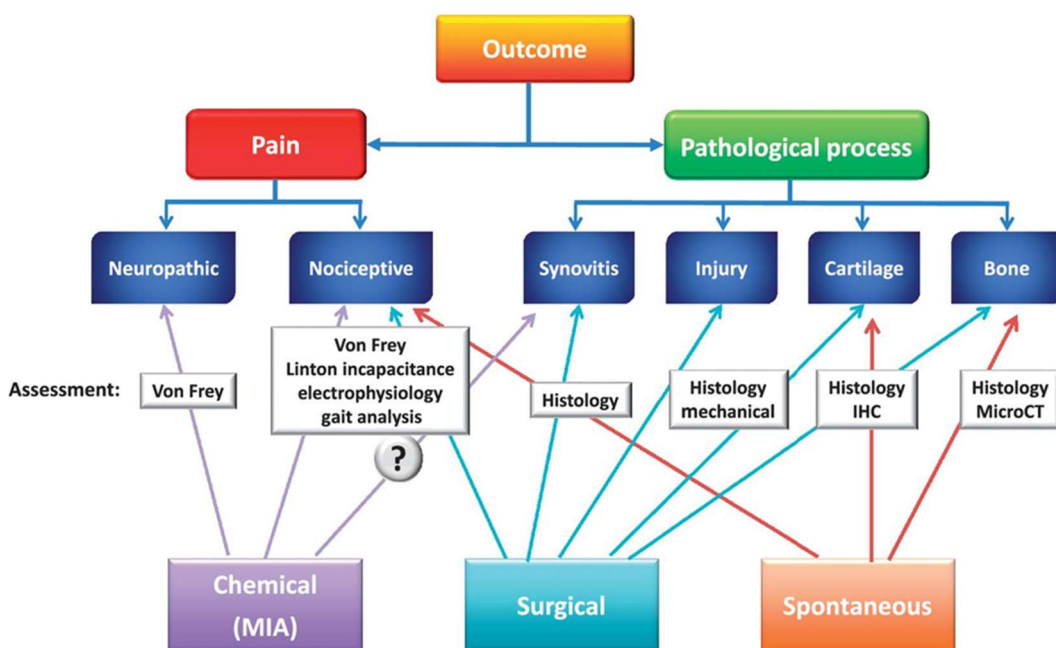


Figure 1.19. Pathogenesis map of OA. The map of OA is divided into pain and the different pathological processes that can be modelled. Taken from Vincent *et al.*, 2012 [222].

Spontaneous models such as the STR/ort mouse, enable the pathogenesis of the disease (in this particular case) to be thoroughly investigated [223, 224]. Spontaneous models of OA are not particularly common, and even when they do occur, do not mirror the chronic late onset disease seen in humans. New spontaneous models, especially late onset/chronic models will likely facilitate the investigation of disease pathogenesis. Another advantage of spontaneous or genetic models is the ability to challenge them with induced OA, as has previously been done with the STR/ort mouse model, which showed that the OA in these animals was unlikely to be due to greater vulnerability to mechanical trauma [225].

1.4. ENU Mutagenesis

The use of *N*-ethyl-*N*-nitrosourea (ENU) as a potent chemical mutagen in the mouse, was first reported by Russell *et al.* in 1979, producing 5 times the mutation rate as the most effective dose of X-ray while retaining fertility [226]. This process was further improved by repeated dosing which increased the maximal mutation frequency induced to 12 times the maximal mutation frequency achievable with a single exposure to x-rays [227].

ENU acts primarily as an alkylating agent, transferring its ethyl group to nucleotides by way of nucleophilic oxygen or nitrogen sites. The transferred ethyl group constitutes a DNA adduct that during cell proliferation and DNA replication results in heritable mutations [228].

At low doses ENU is ineffective as the damage is repaired, and at high doses fertility or health is impaired so a balance is required for optimum results [229, 230]. Optimum dosing as set out in Blease *et al.* leads to mutations at a rate of one mutation every 1.-1.5Mb [231]. Mutation rates for individual genes is size dependent, with larger genes having a higher likelihood of being mutated [232, 233].

ENU predominantly modifies A/T base pairs (87%) compared to C/G pairs (13%). Of the modifications of A/T the most common is A/T to T/A transversions (44%) followed by A/T to G/C transitions (38%), with only a fraction of A/T to C/G transitions (5%). The comparatively infrequent transitions and transversions at the C/G site, are primarily G/C to A/T transitions (8%), followed by G/C to C/G transversions (3%), and G/C to T/A transitions (2%) [228]. Following translation into proteins, these substitutions result most commonly in nonsynonymous changes (72%) of which approximately 65% are missense changes and the remainder are nonsense or splice mutations. The remaining 28% are synonymous mutations that do not alter amino acid sequence [234].

Large-scale phenotype driven ENU mutagenesis screens have been utilised to explore gene function. The premise of these screens was to induce mutations at random, identify a phenotype resulting from the mutagenesis, and then identify the causative mutation [235, 236]. The unbiased and hypothesis-free nature of phenotype-driven ENU screens has proved successful in identifying a large number of novel genes underlying the observed phenotypes often uncovering novel mechanisms across a diversity of biological systems [237].

Different breeding schemes can be used to produce cohorts of mice that are heterozygous or wild-type for the mutations (a dominant screen), or homozygous, heterozygous and wild-type for the mutations (a recessive screen). Recessive screens require larger cohorts of mice but are potentially more informative.

1.4.1. The Harwell Ageing Screen

The Harwell ageing screen was a large-scale phenotype-driven ENU screen, designed to identify mutations resulting in age related disease [238]. C57BL/6J males were injected with a total dose of 320mg/kg of ENU. After a period of sterility caused by the ENU, these C57BL/6J males (now referred to as G₀) are crossed to C3H.pde6b⁺ female animals to produce G₁ animals. A G₁ male animal is selected and again crossed with a C3H.pde6b⁺ female to produce G₂ animals. The female G₂ animals are then crossed back to the G₁ male to produce a G₃ cohort of animals containing animals that are heterozygous, homozygous and wild-type for the mutations in the G₁ animal. This G₃ cohort allows for screening of both recessive and dominant mutations. The sperm of the G₁ founder animal was banked, so that the descendant lines could be re-derived and DNA was also archived for whole genome sequencing, should a phenotype be identified in the G₃ cohort derived from this G₁ founder.

A wide variety of phenotyping tests were undertaken longitudinally typically at an early, mid and late time point, around 4 months, 12 months and 18 months respectively (Figure 1.20).

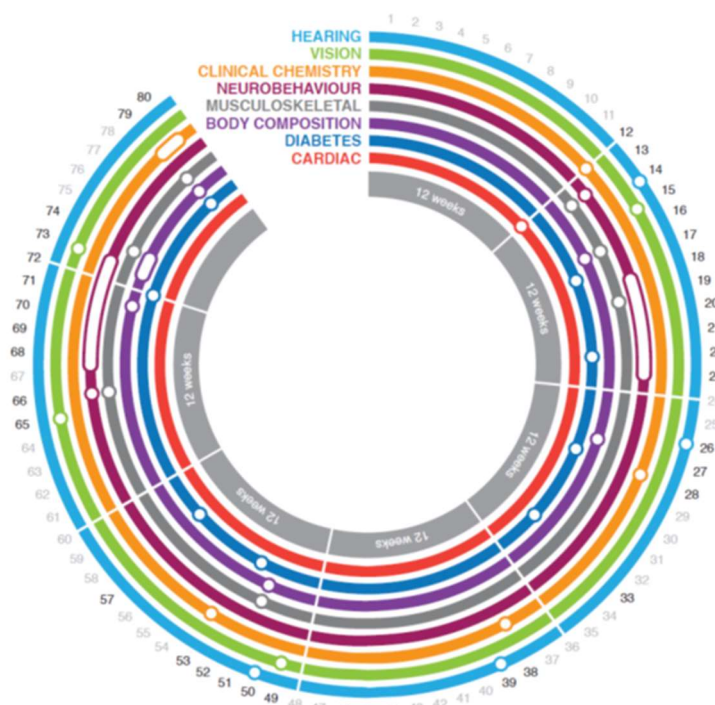


Figure 1. 20. An overview of the time scale and phenotyping that were undertaken as part of the Harwell Ageing Screen. Additional tests or time points were added when required to investigate specific phenotypes. Taken from Blease *et al.*, 2018 [231]

Approximately ¼ of all the mutations identified by the ageing screen resulted in a 'late' phenotype (after 6 months of age), with some phenotyping tests identifying a much larger number of late onset phenotype, for example over 60% of skeletal phenotypes identified by X-ray were late phenotypes [231].

1.5. Thesis Aims and Objectives

The aim of this thesis is to characterise a novel model of late onset OA (MP-107), caused by an ENU induced mutation in the gene *Col1a2*. *Col1a2* is one of the two genes that encode the collagen I alpha chains, which make up the Type I collagen. Mutations in genes coding for the collagen I alpha chains are known to cause diseases such as osteogenesis imperfecta and Ehlers-Danlos syndrome. However, they have not previously been known to play a role in OA.

The objectives include-

- Phenotypic analysis
 - Characterisation of the phenotypes exhibited by the mice in this line by *in vivo* phenotyping.
 - Mechanistic investigation of *ex vivo* tissues.
- Gene identification
 - SNP mapping to identify the region of the genome containing the causative mutation.
 - Whole genome sequencing to identify candidate genes.
 - Sanger sequencing and molecular analysis to confirm effects of the mutation
- Investigation into the effect of abnormal type I collagen
 - Phenotyping of a second line, TM44, which contains an ENU induced mutation in *Col1a1*.
 - Phenotyping of a third line, *Col1a2*-KO, which contains a CRISPR-Cas9 modified *Col1a2* gene, to create a null allele.

- Investigation of the epistasis of mutant genes, and null alleles
 - Phenotype compound crosses of MP-107 and *Col1a2*-KO
 - Phenotype compound crosses of TM44 and *Col1a2*-KO
 - Phenotype compound crosses of MP-107 and TM44

The hypothesis tested in this thesis is that the OA phenotype in MP-107 is caused by the mutation identified in *Col1a2*. The aim of this project beyond this initial hypothesis is through genetic analysis, to establish the mode of action of all of these mutations and through in depth analysis of various tissues, the specific mechanisms by which mutations in these genes can lead to the observed phenotypes. As previously, mentioned COL1A1 and COL1A2 have not been implicated in the pathogenesis of OA in humans. It is therefore of interest animals with mutations in *Col1a1* and *Col1a2*, appear to develop OA. These models could therefore provide valuable insights into the pathogenesis of OA, and how genes not previously associated with the disease could play a role.

Chapter 2: Materials and Method

2.1. Materials Lists

Consumable	Supplier	Product code
20% SDS Solution	National Diagnostics	EC-874
2-Mercaptoethanol (50mM)	Gibco	31350-010
2x Taqman Fast Universal PCR Mastermix	Applied Bioystems	4352042
70µm cell strainer	Greiner bio-one	542070
96F Without lid Microwell plate	Thermo Scientific	269620
96-Well PCR Plate Non-Skirted	4titude	4ti-0750-25
Adhesive Film Covers	Abgene	AB-0558
Adhesive Sealing Sheets	Thermo Scientific	AB-0558
Bovine Serum Albumin	Sigma-Aldrich	A7906-100G
Bovine Serum Albumin, fatty acid free	Sigma-Aldrich	A8806-5G
CELLSTAR 10cm Cell Culture Dishes	Greiner bio-one	664-160
CELLSTAR 6 Well Cell Culture Plate, Sterile, With Lid	Greiner bio-one	657-160
CELLSTAR Cell Culture Flasks 25cm ² , 50ml, Red filter	Greiner bio-one	690-175
CELLSTAR Cell Culture Flasks 75cm ² , 250ml, Red filter	Greiner bio-one	658-175
cOmplete™ Tablets EDTA-free, EASYpack	Roche	04 693 132 001

DMEM (1x) + GlutaMAX™-1 +4.5g/L D-Glucose, -Pyruvate	Gibco	61965-026
DPBS (1x) -CaCl ₂ , -MgCl ₂	Gibco	14190-094
Dried Skimmed Milk		
Ethanol, absolute	Fisher Scientific	E/0650DF/17
Foetal Bovine Serum	Gibco	10500064
High Capacity cDNA Reverse Transcription Kit	Applied Bioystems	4368814
HotShot Mastermix		HS002
Illustra™ DNA Extraction Kit BACC2	GE Healthcare	RPN-8502
LCGreen® Plus+	BioFire	BCHM-ASY- 0005
MEM Non-Essential Amino Acids Solution (100x)	Gibco	11140-050
Methanol	Fisher Scientific	M/4000/PC17
MicroAmp® Fast Optical 96-Well Reaction Plate 0.1mL	Applied Bioystems	4346906
MicroAmp™ Optical Adhesive Film	Applied Bioystems	4311971
Nitrocellulose Membrane (0.45µm)	Invitrogen	LC2001
NP-40	Thermo Fisher	85124
Nucleon BACC2 Genomic DNA Extraction System	GE Healthcare Life Sciences,	RPN8512

NuPAGE™ 4-12% Bis-Tris Gel 1.0mmx12well	Invitrogen	NP0322BOX
NuPAGE™ 4-12% Bis-Tris Gel 1.0mmx15well	Invitrogen	NP0323BOX
NuPAGE™ Antioxidant	Invitrogen	NP0005
NuPAGE™ LDS Sample Buffer	Invitrogen	NP0007
NuPAGE™ MOPS SDS Running Buffer (20x)	Invitrogen	NP0001
NuPAGE™ Sample Reducing Agent (10x)	Invitrogen	NP0004
NuPAGE™ Transfer Buffer (20x)	Invitrogen	NP0006
Penicillin-Streptomycin (10,000U/mL)	Gibco	15140-122
PhosSTOP EASYpack	Roche	04 906 837 001
Pierce® ECL Western Blotting Substrate	Thermo Scientific	32106
Precellys Lysing Kit Tissue Grinding CKmix50_7mL	Bertin Technologies	KT03961-1- 306.7
Precision Plus Protein™ Dual Colour Standard	Bio Rad	1610374
Propan-2-ol	Fisher Scientific	P/7490/21
Proteinase K Solution	QIAGEN	19133
QIAquick Gel Extraction Kit (50)	QIAGEN	28704

QIAquick PCR Purification Kit (50)	QIAGEN	28104
QIAzol Lysis Reagent	QIAGEN	79306
Quick Start™ Bradford 1x Dye Reagent	Bio Rad	500-0205
RNeasy® Maxi Kit (50)	QIAGEN	75144
Syringe filter 0.2µm	Fisherbrand	09-719c
TBS (10x)	Cell Signaling Technology	124985
Triton X-100	Sigma-Aldrich	X100-100ML
Trizma® base	Sigma-Aldrich	T6066-500G
Trizma® hydrochloride	Sigma-Aldrich	T5941-500G
Trypsin (0.25%) phenol red	Gibco	25050-014
Trypsin-EDTA (0.05%) phenol red	Gibco	25300-054
Tween® 20	National Diagnostics	EC-607
Ultrapure Agarose	Invitrogen	16500-500
Vectastain- ABC Rabbit IgG	Vector Laboratories	PK-6101
Whatman filter paper	Whatman	WH1001-929

2.2. Primers

2.2.1. Sequencing Primers for Mutation Validation

Primer	Sequence (5' to 3')
Col1a2_gDNA_Forward	TAGGAGAAATGGTGCCCTGT
Col1a2_gDNA_Reverse	GGCACCAGCATTATCAAGGT
Col1a2_cDNA_Forward	GCGGTGAAGAAGGAAAGAGA
Col1a2_cDNA_Reverse	CAGGAGACCCAGGAAGACCT
Col1a1_gDNA_Forward	CACTTCCGTTACGACATCCCA
Col1a1_gDNA_Reverse	ACACAACCGTCATGACCTTTC
Sectm1a_gDNA_Forward	TCAAAGACACCCAGGACGAC
Sectm1a_gDNA_Reverse	ACAGTGATGACTCCCACAAGG

2.2.2. Primers for Validation of Alternative Splicing by Electrophoresis

Primer	Sequence (5' to 3')
Col1a2_cDNA_Mut_Forward	GACTTGTTGGTGAGCCTGGTC
Col1a2_cDNA_Mut_Reverse	CTCCAGGGCTTAGACAGGGCA
Col1a2_cDNA_WT_Forward	GTGCCAGAGGACTTGTTGGT
Col1a2_cDNA_WT_Reverse	AACCAGGGCTGCCTCTAAGC

2.2.3. Lightscanner Genotyping Primers (Col1a2)

Primer	Sequence (5' to 3')
<i>MP-107</i> Forward	GCCCTGTCTTAGGAAACTCTATC
<i>MP-107</i> Reverse	ATTACACCAGCTCTGCCATCA

<i>MP-107</i> Probe	CATCTCATGCCCTTTCCAGCAGG
---------------------	-------------------------

2.2.4. Allelic Discrimination Genotyping Primers (Col1a1)

Primer	Sequence (5' to 3')
<i>TM-44</i> Forward	CTAGGGCGAGAGAGGTTTCC
<i>TM-44</i> Reverse	CTCACCTGGCACCATCGTT
<i>TM-44</i> WT Probe (FAM)	CGTGGTGTACAAGGTCC
<i>TM-44</i> MUT Probe (TET)	ACGTGGTGTATAAGGTCCC

2.2.5. Copy Number Genotyping Primers (Col1a2-KO)

Primer	Sequence (5' to 3')
Col1a2-DEL2087-MUT Forward	GCTTGCTTGTTCAGCATCAATTAC
Col1a2-DEL2087-MUT Reverse	CGTGGTCCTCTGTCTCCAG
Col1a2-DEL2087-MUT Probe	TAGTCACGTGGCCCTTTGCCAT
Col1a2-DEL2087-LOA-WT Forward	GCTTGCTTGTTCAGCATCAATTAC
Col1a2-DEL2087-LOA-WT Reverse	CGTGGTCCTCTGTCTCCAG
Col1a2-DEL2087-LOA-WT Probe	TAGTCACGTGGCCCTTTGCCAT
Dot1L_Control Forward	GCCCCAGCACGACCATT
Dot1L_Control Reverse	TAGTTGGCATCCTTATGCTTCATC
Dot1L_Control Probe	CCAGCTCTCAAGTCG

2.2.6. Gene Expression Primers

Primer	Sequence (5' to 3')
<i>Col1a2_Mutant_Forward</i>	CAGCGGTGAAGAAGGAAAGAGA
<i>Col1a2_Mutant_Reverse</i>	CATTACACCAGCTCTGCCATCA
<i>Col1a2_Mutant_Probe</i>	AGGGCTTAGACAGGGC
<i>Col1a2_Wild type_Forward</i>	TCCCGGAGAAGCTGGATCT
<i>Col1a2_Wild type_Reverse</i>	CATTACACCAGCTCTGCCATCA
<i>Col1a2_Wild type_Probe</i>	CTTAGAGGCAGCCCTG

2.2.7. sgRNAs for CRISPR/cas9 Deletion

Protospacer sequence	PAM sequence
ATTGATGCAAATTAGACCTT	TGG
GACTTAGCCCTTTCCCCCAA	AGG
CCATTACACGTGTATTGTGC	AGG
CCTGCACAATACACGTGTAA	TGG

2.2.8. Primers for CRISPR Confirmation

Primer	Sequence (5' to 3')
Geno_Col1a2_F1	GGGTAATTGTAGCAAAGAAGTGGG
Geno_Col1a2_R1	TCACAGGTTTCCAGCCGTAG

2.3. Primary Antibodies

Antibody	Species /clonality	Supplier	Code	WB /IHC	Dilution	Size (kDa)
Col1a1	Goat Poly	Santa-Cruz	SC-8784	WB	1:100	139
Col1a1	Goat Poly	Santa-Cruz	SC-8784	IHC	1:200	
Col1a2	Rabbit Poly	Abcam	Ab96723	WB	1:1000	129
Col1a2	Rabbit Poly	Abcam	Ab96723	IHC	1:200	
Col1	Rabbit Poly	Abcam	Ab21286	WB	1:1000	129 /139
BIP	Rabbit mono	Cell signalling	C50B12	WB	1:1000	78
BIP	Rabbit mono	Cell signalling	C50B12	IHC	1:100	
Fibronectin	Rabbit Poly	Proteintech	15613-1-AP	WB	1:1000	250
Actin	Rabbit mono	Abcam	ab176560	WB	1:3000	42

2.4. Secondary Antibodies

Antibody	Supplier	Code	Dilution
IRDye® 680LT Goat anti-Rabbit IgG (H + L)	Li-Cor	926-68021	1:10000
IRDye® 800CW Goat anti-Rabbit IgG (H + L)	Li-Cor	926-32211	1:10000
IRDye® 800CW Goat anti-Mouse IgG (H + L)	Li-Cor	926-32210	1:10000
IRDye® 800CW Donkey anti-Goat IgG (H + L)	Li-Cor	925-32214	1:10000

2.5. Recipes and Buffers

Standard MEF Media:

DMEM + 10 % FBS + 50um mercaptoethanol + 1x non-essential amino acids + Pen/Strep

DMEM	-	439.5 mL
FBS	-	50 mL
MEM amino acids	-	5.0 mL
Penicillin + Streptomycin	-	5.0 mL
Mercaptoethanol	-	0.5 mL

FBS free MEF Media:

DMEM + 50um mercaptoethanol + 1x non-essential amino acids + Pen/Strep

DMEM	-	489.5 mL
MEM amino acids	-	5.0 mL
Penicillin + Streptomycin	-	5.0 mL
Mercaptoethanol	-	0.5 mL

Low FBS MEF Media:

DMEM + 0.5 % FBS + 50um mercaptoethanol + 1x non essential amino acids + Pen/Strep

DMEM	-	487.0 mL
FBS	-	2.5 mL
MEM amino acids	-	5.0 mL
Penicillin + Streptomycin	-	5.0 mL
Mercaptoethanol	-	0.5 mL

Transfer buffer

Transfer Buffer (20X)	-	50 mL
Antioxidant	-	1 mL
Methanol	-	100 mL
Deionized Water	-	849 mL

TBST

TBS (x10) - 100ml

ddH₂O - 899ml

Tween - 1ml

Tendon Digestion solution

Pepsin(3200-4500units/mg) - 750µg

0.5M acetic acid - 30 mL

MOPS running Buffer

MOPs (20X) - 50 mL

Deionized Water - 950 mL

Antioxidant - 2.5 ml

2.6. Animals

2.6.1. Animal husbandry

All animals described herein were housed in the Mary Lyon Centre (MLC), a specific pathogen free (SPF) mouse facility, within the MRC Harwell Institute. The majority of animals were bred and phenotyped on Home office licence 30/3070 “New mouse models of human disease”, when this specific licence came to an end, any further mice were bred on Home office licence 17/0004 (PE40B1D0F) “Breeding genetically altered mice” and then phenotyped on Home office licence 30/3384 “Phenotyping genetically altered mice”, under conditions adhering to the MRC ‘Code of practice for the housing and care of animals bred, supplied or used for scientific purposes’ (December 2014) and subject to review by Animal Welfare and Ethical Review Body (AWERB).

Animals were housed in individually vented cages (IVCs), with food (Irradiated -RM3 (E)-Special Diet Services) and water (mains water purified using reverse osmosis and then chlorinated to 9-13 ppm) provided *ad libitum*. The environment of the IVCs was maintained at a temperature of between 19 and 22°C, a humidity of 45-65% and in a 12:12 light: dark cycle. Welfare checks were performed daily, any welfare issues were escalated to the Named animal care and welfare officer (NACWO) and if necessary the Named veterinary surgeon (NVS) was consulted. Animals were housed separated by sex and with no more than 5 animals to a cage, with the exception of pre-weaning animals, and animals in matings.

2.6.2. MUTA-PED-107 (MP-107)

The animals in this line were derived from the Harwell Ageing screen, an ENU mutagenesis screen designed to identify models of age-related disease. The protocol by which mutagenised mice are generated for a recessive screen has been described previously [231, 238]. Briefly, C57BL/6J males are injected with a total dose of 320mg/kg of ENU, consisting of an initial dose of 120 mg/kg, followed by 2 further doses of 100mg/kg with a week between each dose. After a period of sterility caused by the ENU, these C57BL/6J males (now referred to as G₀) are crossed to C3H.pde6b⁺ female animals to produce G₁ animals. A G₁ male animal is selected, and again crossed with C3H.pde6b⁺ female to produce G₂ animals. The female G₂ animals are then crossed back to the G₁ animal to produce a G₃ cohort of animals containing animals that are heterozygous,

homozygous and wild-type for the mutations in the G₁ animal (Figure 2.1). This G₃ cohort allows for screening of both recessive and dominant mutations [235]. The purpose of crossing the ENU mutagenised animal to a different inbred strain, is to enable mapping of the causative mutation, using the single nucleotide polymorphisms (SNPs) polymorphic between the strains [238].

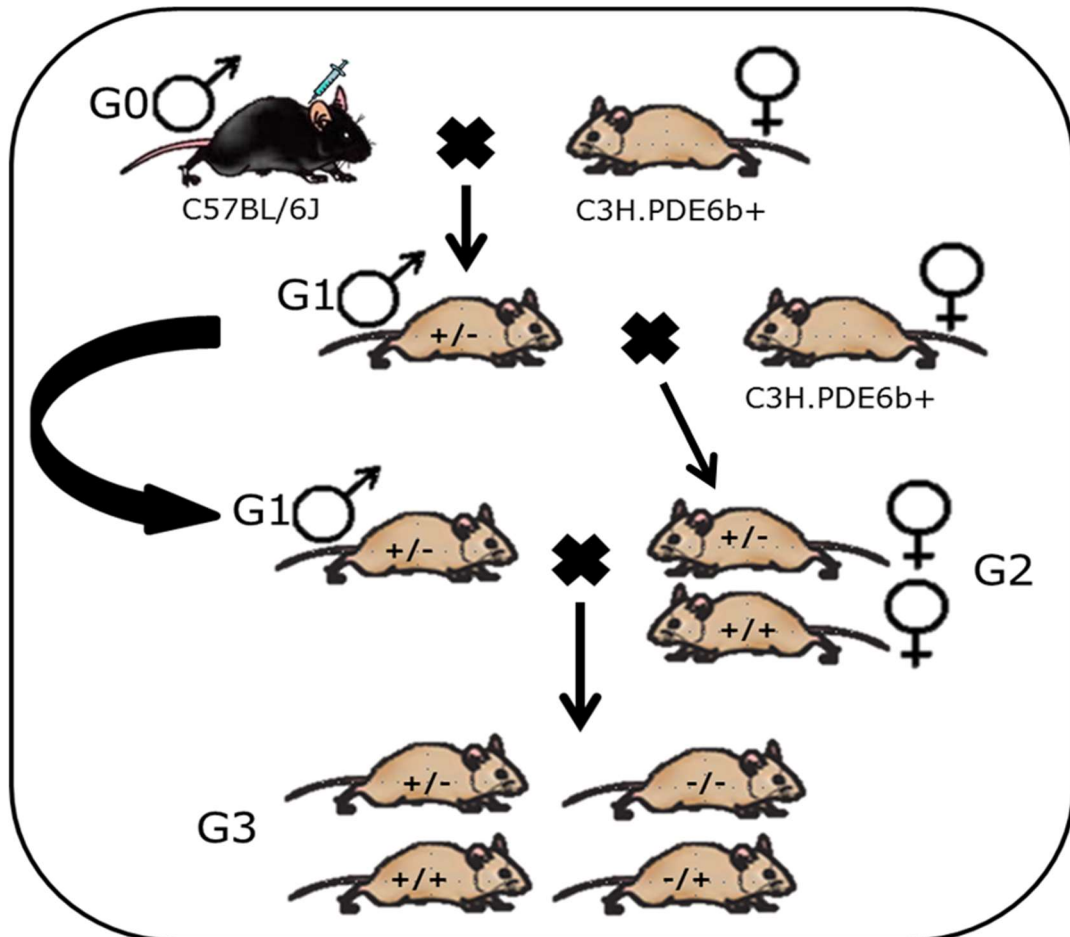


Figure 2.1. A diagram showing the breeding strategy employed in the Harwell Ageing screen. The G₃ cohorts contain animals that are homozygous, heterozygous and wild-type for the ENU mutations.

2.6.3. Bone-TM44 (TM44)

The animals in this line were derived from an ENU mutagenesis screen designed to identify dominant mutations. The method for producing the mutagenised cohorts of animals is the same as detailed in Section 2.6.2, except in this case the G₂ animals underwent phenotyping, rather than the G₃ animals, so only dominant mutations can be identified.

2.6.4. Col1a2-KO

This line was produced using CRISPR Cas9 technology by the Harwell Genome Engineering service. Cas9 mRNA and sgRNAs (detailed in Section 2.2.7) were diluted in microinjection buffer to a working concentration of 100ng/ μ l and 50ng/ μ l respectively. This solution was then delivered by pronuclear injection into 1-cell stage embryos. Injected embryos were re-implanted into CD1 pseudo-pregnant females, which were allowed to litter and rear F₀ progeny. An animal with a 2087 nucleotide deletion was selected as the founder animal for the line Col1a2-KO. The deletion encompassed exons ENSMUSE00001291037, ENSMUSE00001247742 and ENSMUSE00001305705 and induced a premature stop codon and a null allele.

2.7. Identifying the Causative Mutations

2.7.1. DNA Extraction

DNA was extracted from tail samples post mortem using the Nucleon BACC2 Genomic DNA Extraction System (GE Healthcare Life Sciences, USA) according to manufacturer's instructions. Briefly, samples were incubated overnight at 55°C in 200 μ l of 'Reagent B' and 10 μ l of Proteinase K (20mg/ml, Qiagen, Netherlands). 50 μ l of Sodium Perchlorate was added, then inverted 7 times, 200 μ l of Chloroform was added, then inverted 7 times, 30 μ l of Nucleon resin was added before the sample was centrifuged at 200rpm for 2 minutes. The upper phase was transferred to a clean microcentrifuge tube, and 2 volumes of ice cold 100% ethanol were added to precipitate the DNA. The sample was then centrifuged at max speed for 2 minutes to pellet the DNA, which was then washed with 70% ethanol, before being dried and then re-suspended in 50 μ l ddH₂O at 4°C overnight.

2.7.2. Linkage Mapping

200ng of DNA was sent for linkage mapping using the Illumina Golden Gate Mouse MD linkage Panel (Gen-Probe Life Sciences Ltd, UK). This linkage panel contains 1449 SNP loci that are informative across 10 inbred strains. There are approximately 3 SNPs for every 5Mb interval with at least one of these SNPs being informative for each pairwise strain combination in 75% of cases. The ENU mutations are inherited from the C57BL/6J G₀, meaning that regions containing the mutation will either be homozygous for

C57BL/6J for recessive mutations, or heterozygous for dominant mutations. So while not all SNPs are informative for our purposes, this panel allows us to map the causative mutation to a region.

2.7.3. Whole Genome Sequencing

G₁ DNA from the line MP-107 was sent for Whole Genome Sequencing (WGS) utilising the Illumina HiSeq platform (Oxford Genomics Centre, Wellcome Trust Centre for Human Genetics, UK). The reads generated were then aligned to the reference genome (NCBIM38/mm10) by the MRC Harwell Bioinformatics team using Burrows-Wheeler Alignment [239]. Single nucleotide variants (SNVs) were detected using a customised version of the Genome Analysis Toolkit (GATK) [240].

2.8. Mutation Validation

2.8.1. Primer Design

Sequencing primers were designed using the Primer3Plus software (<http://www.bioinformatics.nl/cgi-bin/primer3plus/primer3plus.cgi>) and were tested using an *in silico* PCR program from University of California Santa Cruz (<https://genome.ucsc.edu/cgi-bin/hgPcr>). These oligonucleotides were then synthesised (Eurofins MWG Operon, Germany). The specific primers are detailed in section 2.2.1

2.8.2. PCR Amplification

The relevant DNA was amplified using a 25 µl PCR reaction using the program as follows-

- Step 1 - 95°C for 10 minutes
- Step 2 - 95°C for 30 Seconds
- Step 3 - 60°C for 45 Seconds
- Step 4 - 72°C for 10 minutes
- Step 5 - Cycle to Step 2 40 more times
- Step 6 - 72°C for 15 minutes
- Step 7 - Hold at 4°C

AmpliTaq Gold® 360 DNA Polymerase (Thermo Fisher) was used in the PCR reaction as follows (volumes per 25 µl reaction) -

10X Buffer II	2.5 µl
dNTPs (10mM)	2 µl
Forward Primer (10µM)	1.25 µl
Reverse Primer (10µM)	1.25 µl
MgCl ₂ (25mM)	1.5 µl
DNA (10ng/µl)	1.25 µl
Polymerase	0.125 µl
ddH ₂ O	15.125 µl

5µl of PCR product was then run on a 2% agarose gel to confirm the presence of a product the correct size.

2.8.3. PCR Purification

PCR products were purified using the QIAquick® PCR purification kit (Qiagen, Netherlands) (as per manufacturer's instructions). Briefly, sample is diluted with 'Buffer PB' (a high salt buffer) in a 5:1 ratio, and placed in a QIAquick column and centrifuged at high speed for 1 minute to bind DNA to the silica membrane, flow through is discarded. The membrane is then washed using 'Buffer PE', again by centrifugation at high speed for 1 minute, flow through is discarded. The DNA is then eluted in 'Buffer EB' (10mM Tris Cl. pH 8.5), by adding buffer to the membrane, leaving for 1 minute, before centrifugation at high speed for 1 minute, to elute the DNA into a fresh micocentrifuge tube.

2.8.4. Sanger Sequencing

Purified PCR products were sent for Sanger Sequencing (Source Bioscience, Oxford, UK). PCR Products were supplied at 10ng/μl and sequencing primers (detailed in 2.2.1) were supplied at 3.2ng/μl. Chromatograms were visualised using Lasergene Seqman Pro (DNASTAR, USA)

2.9. Genotyping

2.9.1. Lightscanner

Genotyping for the line MP-107 was performed using the Lightscanner (Idaho technology, USA) high throughput DNA melting analysis system. Asymmetric exhaustive PCR is performed with a 3' blocked oligonucleotide (probe) which binds to the site of the SNP, in addition to the primer pair in the presence of the double stranded DNA binding dye, LCGreen (Biofire). This causes 2 PCR products to be formed, the full PCR product between the normal primer pair and a second between the probe and the opposite strand. Primers were designed using LightScanner Primer Design Software (Idaho technology).

Due to the probe being designed for the mutant allele, the homozygous sample produces the greatest fluorescence, followed by heterozygous samples, and finally the wild-type sample (Figure 2.5).

The PCR reaction using the program as follows-

- Step 1 - 95°C for 2 minutes
- Step 2 - 95°C for 30 Seconds
- Step 3 - 60°C for 30 Seconds
- Step 4 - 72°C for 30 Seconds
- Step 5 - Cycle to Step 2 55 more times
- Step 6 - 95°C for 30 Seconds
- Step 7 -25°C for 30 Seconds
- Step 8 - 15°C for 30 Seconds
- Step 9 - Hold at 4 °C

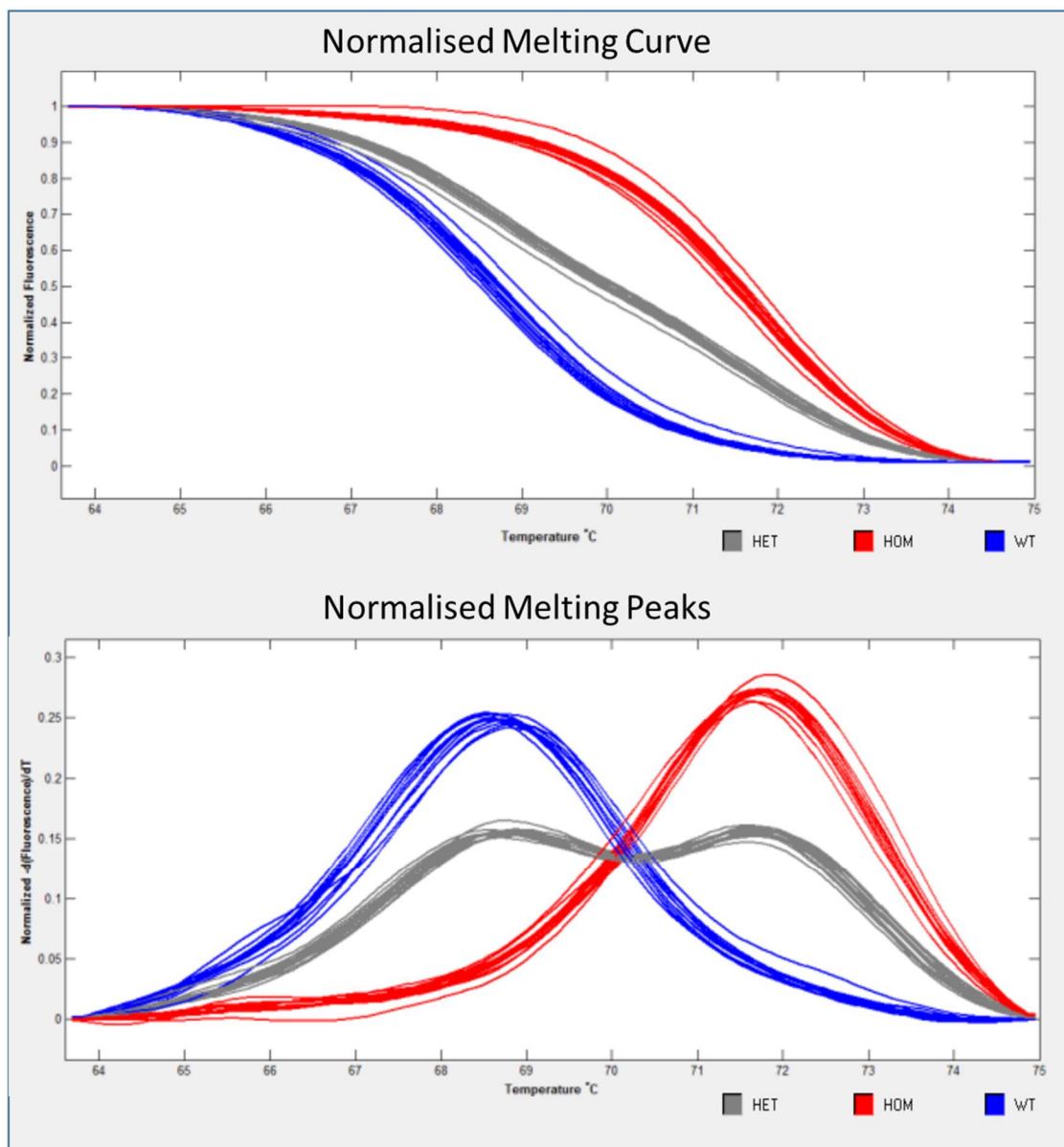


Figure 2.2. Normalized melting curves and peaks, showing how the different genotypes can be identified.

2.9.2. Allelic Discrimination

Genotyping for the line TM44 was performed using the 7500 Fast Real-Time PCR system (Applied Biosystems, ThermoFisher,) and 2 custom Taqman assays with differing labels, one for the wild-type allele (FAM) and one for the mutant allele (TET). The different probes allow for differentiation between the three genotypes. The primer details can be found in Section 2.2.4

ABI GTX Taqman Master Mix (AB bioscience) was used in the qPCR reaction as follows (volumes per 10 μ l reaction) -

ABI GTX Taqman Master Mix	5 μ l
FAM and TET assay (WT probe 5 μ M, MUT probe 5 μ M & primers 15 μ M each)	2 μ l
DNA (10ng/ μ l)	2.5 μ l
ddH ₂ O	0.5 μ l

2.9.3. Copy Number

To genotype the Col1a2-KO line, a genotyping strategy was developed to identify the genotype by copy number. The presence or absence of each allele is identified by recording the number of cycles taken to reach a threshold (CT value), which is inversely correlated to the amount of template DNA.

e.g.

CT 25 = 2 copies of the template DNA

CT 26 = 1 copy of the template DNA

CT >30 = no copies of the template DNA

Using one assay for the wild-type sample and one for the mutant, we are able to accurately identify the genotype; control Dot1L is also included.

WT= 2 copies of the LOA assay template and 0 copies of the mutant assay

HET= 1 copy of the LOA assay template and 1 copy of the mutant assay

HOM= 0 copies of the LOA assay template and 2 copies of the mutant assay

ABI GTX Taqman Master Mix (AB Bioscience) was used in the qPCR reaction as follows with each FAM assay run separately, but in multiplex with the VIC labelled internal control (volumes per 10 µl reaction) -

ABI GTX Taqman Master Mix	5 µl
Primers Dot1L_2F (20µM)	0.225 µl
Primers Dot1L_R (20µM)	0.225 µl
Probe DotL_2M (5µM)	0.2 µl
FAM assay (probe 5µM & primers 15µM each)	0.3 µl
DNA (10ng/µl)	2.5 µl
ddH ₂ O	1.55 µl

2.10. Time course Phenotyping

2.10.1. X-Ray

X-rays images were generated using a Faxitron MX20- specimen radiography system (Faxitron X-ray Corporation, Tucson, AZ). Animals were anaesthetised using a Xylazine (Sedaxylan™, 20mg/mg) / Ketamine (Anesketin™, 100mg/ml) /sterile water solution made up in the ratio 1:2:17, and administered at 10µl/g of bodyweight intraperitoneally.

2.10.2. Dual X-ray Energy Absorption (DEXA)

DEXA images and data were generated using the Lunar PIXImus II Densitometer (GE Medical Systems). Animals were anaesthetised using a Xylazine (Sedaxylan™, 20mg/mg) / Ketamine (Anesketin™, 100mg/ml) /sterile water solution made up in the ratio 1:2:17, and administered at 10µl/g of bodyweight intraperitoneally.

2.10.3. Clinical Chemistry

Two types of blood collection methods were used for clinical chemistry, for early time points blood was collected from the lateral tail vein, and for late, terminal time points, blood was collected via retro-orbital bleed. For blood collection from the lateral tail vein, animals had EMLA, local anaesthetic cream applied to their tails 30 minutes prior to the procedure. The animals were then restrained, and the lateral tail vein cut using a sterile

scalpel blade. Blood was then collected using heparin coated microvette tubes(VWR). The blood flow was then staunched using pressure, before the animal was returned to its home cage. For retro-orbital blood collection, the animal was terminally anaesthetised, with an overdose of pentobarbital, once all pedal and corneal reflexes had ceased a lithium heparin coated capillary tube was inserted into the retro-orbital sinus and blood was collected in a heparin coated microvette tube.

Plasma was separated by centrifugation at 5000xg at 4°C, before being pipetted into a microcentrifuge tube. Plasma samples were analysed using an Olympus U4000 bio analyser.

2.11. Histology

2.11.1. Histological Processing of Knee Joints

Animals were culled, either by cervical dislocation, or by overdose of anaesthetic and retro orbital bleed. The limbs were then fixed in 10% neutral buffered formalin, before being decalcified in 20% formic acid. Knee joints were then embedded in paraffin wax and sections were cut at 5µm using a Finesse ME+ microtome (Thermo Fisher). Sections were transferred to charged slides, and either stained with Haematoxylin and Eosin (H&E), or Fast green and Safranin O, or left unstained for immunohistochemistry (IHC).

2.11.2. Histological Analysis of Embryonic Lungs

Embryos were harvested at 18.5 days post coitum (dpc) from timed intercross matings. Embryos were culled by decapitation before dissection and fixation of the lungs in 10% neutral buffered formalin. Lungs were then embedded in paraffin wax and sections were cut at 5µm using a Finesse ME+ microtome (Thermo Fisher). Sections were transferred to charged slides, and stained with H&E. Analysis was performed using FIJI software.

2.11.3. Immunohistochemistry

Knee sections were obtained as outlined in Section 2.11.2. Slides were dewaxed and antigen retrieval was carried out by incubating sections in 1mg/ml pronase for 30 minutes at 37°C, washing in PBST for 5 minutes and then incubating in 5mg/ml hyaluronidase 30 minutes at 37°C. Endogenous peroxidases were quenched by blocking with 3% hydrogen peroxide in 2-propanol for 15 minutes at room temperature. Immunostaining was then carried out using the ABC Anti-rabbit IgG Kit (AK-5001-NB,

Vectastain). Sections were blocked with goat serum for 30 minutes at room temperature, before incubating with Anti-BiP primary antibody (see section 2.3 for details) for 60 minutes at room temperature. The sections were then washed in PBS before being incubated in the biotinylated secondary included in the kit for 30 minutes at room temperature, before washing again. The sections were then incubated in vectastain reagent for 30 minutes at room temperature before a final wash. DAB is then used as a chromogen for the secondary antibody, and slides were counterstained using haematoxylin.

2.12. Skeletal Staining

2.12.1. Sample Collection

Embryos were harvested at 18.5 dpc from timed intercross matings. The uterus was removed from the pregnant animal and placed in ice cold PBS, and then kept on ice for 20 minutes. The uterus was then transferred into a 10 cm petri dish and covered with fresh ice-cold PBS. The uterus was then opened to allow access to the individual yolk sacs. The yolk sac was then carefully cut open to release the embryo and placenta. A sample of yolk sac was taken for genotyping, and the embryo separated from the placenta at the umbilical cord and placed in a labelled well of a 6 well plate filled with ice cold PBS. This process was repeated until all embryos were in individual wells of PBS. Any blood clots that formed at the navel were removed and the embryos were left on ice for another few minutes before being thoroughly washed to remove any remaining blood, before being placed into fresh wells containing ice cold 95% ethanol.

2.12.2. Sample Preparation

Samples were removed from 95% ethanol, then eyes, skin, adipose tissue and internal organs were removed, before placing the embryo in acetone overnight at room temperature. The acetone further fixes the tissue, permeabilises the tissues and dissolves the remaining adipose tissue. The embryo was then transferred to a glass vial and covered with 0.03% Alcian blue stain diluted in an 80/20 solution of ethanol and glacial acetic acid, and incubated at room temperature overnight. The embryo was then destained by washing twice in 70% ethanol, before incubating overnight in 95% ethanol. The embryo was then transferred into a solution of 1% potassium hydroxide in distilled water for 1 hour at room temperature to pre-clear the tissue. The sample was then

transferred into a solution of 0.005% alizarin red dissolved in 1% potassium hydroxide solution and incubated at 4°C overnight. Finally, the sample is cleared at room temperature in a 50/50 clearing solution of glycerol and 1% potassium hydroxide, until the excess stain is removed, before placing the sample in 100% glycerol until imaging

2.12.3. Sample Imaging

The embryos were initially imaged in glycerol using a Nikon DSLR on a vertical rig, before the limbs were dissected from the embryos and imaged using a Zeiss SterEO V20 discovery microscope with axiocam ERc5s.

2.13. Transmission Electron Microscopy

2.13.1. Sample Collection

18.5 dpc embryos were harvested and decapitated before being fixed in 2% glutaraldehyde prepared in 100 mM phosphate buffer (pH 7.0) at room temperature. After 30 minutes the embryos were removed from the fixative, the tails were dissected from the body of the embryo, and cut into smaller pieces before being placed in fresh fixative. Fixation was continued for 2 hours at 4°C, after which the specimens were washed (twice) in 200mM phosphate buffer, before being placed in PBS (pH 7.0).

2.13.2. Sample Imaging

The fixed samples were then sent to our collaborators in the lab of Prof Karl Kadler at the University of Manchester for imaging. Sections (70-nm thick) were examined for TEM using an FEI Tecnai 12 instrument fitted with a 2k × 2k-cooled CCD camera (F214A, Tietz Video and Image Processing Systems, Gauting, Germany). Analysis was performed using FIJI software

2.14. Differential Scanning Calorimetry (DSC)

2.14.1. Harvesting Tail Tendons

3-month old animals were culled by cervical dislocation and the tail was amputated at the base. The skin was scored along the length and then removed to expose the bundles of tail tendons. The skinned tail was washed in a Petri dish containing PBS to ensure no hairs were attached to the tendon bundles. Using two pairs of robust forceps, the tail was held with one set of forceps at the base and sections of the tail with attached

tendons were removed by pulling with the second set of forceps upwards to the base in sections. The tendons were then dissected from the sections of tail using a sterile scalpel blade and then placed in microcentrifuge tubes, and frozen.

2.14.2. Testing Samples

DSC testing of the samples took place in the lab of our collaborator Prof Helen Birch at the University College of London. The tendon was thawed and weighed in a 40 μ l aluminium crucible with a lid (ME-26763), which was then sealed. The sample was then placed into the DSC1 STARe System (Mettler Toledo, USA) along with an empty reference crucible.

The DSC heating/cooling program is then run as follows-

25°C -> -40°C @ 5°C per minute

-40°C -> 90°C @ 5°C per minute

This produces a thermogram containing peaks as the water content freezes in the 25°C -> -40°C step, and then a peak for the melt, and the denaturation of collagen in the -40°C -> 90°C step.

The lid of the crucible is then perforated and the DSC heating/cooling program is then run as follows-

Perforated crucible-

25°C -> 160°C @ 5°C per minute

This produces a thermogram, containing a peak as the water content evaporates.

2.14.3. Analysis of Samples

The thermograms produced from the samples were analysed using the STARe Evaluation software (Mettler Toledo, USA).

A number of parameters can be calculated from the thermograms produced-

- The percentage free water within the sample can be calculated as the area under the freezing curve.

- The total water can be calculated as the area under the evaporation curve of the perforated crucible.
- The percentage bound water within the sample can be calculated by subtracting the percentage free water from the percentage total water.
- Collagen denaturation temperature is defined by the height of the denaturation peak.
- Collagen enthalpy (or wet enthalpy) is calculated as the area under the curve of the denaturation peak, normalised to weight.
- Dry enthalpy is calculated as wet enthalpy divided by dry mass (calculated from bound water).

2.15. Radiolabelling of Tendons

The radiolabelling of samples was carried out in the lab of our collaborator Dr Liz Canty-Laird at the University of Liverpool.

2.15.1. Harvesting Tail Tendons

21-day old mice were culled by cervical dislocation and the tails were dissected from the body. Each tail was placed in a separate 100mm Petri dish in PBS containing 1% penicillin/streptomycin. The skin was scored along the length and then removed to expose the bundles of tail tendons. Using two pairs of robust forceps, the tail was held with one set of forceps at the base and sections of the tail with attached tendons were removed by pulling with the second set of forceps upwards to the base in sections.

The tail sections with attached tendons were then placed in a fresh Petri dish containing cell culture medium containing 1% (v/v) penicillin/streptomycin

The tendons were then dissected from the sections of tail using a sterile scalpel blade and then placed in a new Petri dish containing cell culture medium containing 1% (v/v) penicillin/streptomycin.

2.15.2. Labelling Samples

The tendons from each mouse was then split between 4 wells of a 24-well plate containing sterile cell culture medium (DMEM) containing 1% (v/v)

penicillin/streptomycin, 2 mM L-glutamine, 200 μ M ascorbate and 400 μ M beta-aminopropionitrile at 37°C and 5% CO₂, and left for 1 hour to equilibrate. The tissues were then transferred from each well to a fresh well containing fresh cell culture medium and 2.5 uCi/ml of [¹⁴C]-proline using fine forceps. Tendons for salt extraction were labelled for 1 hour for an approximately even distribution of (pro) collagen (I) between the intracellular and extracellular extracts. The tendons were then placed briefly in unlabelled supplemented medium to rinse residual [¹⁴C]-proline and chased in unlabelled medium for 3 hours (to allow newly synthesised pro-collagen to be processed and transferred to the extracellular fraction).

2.15.3. Sequential Extractions

Post chase, the tissue was transferred into 100 μ l of salt extraction buffer (1M NaCl, 25mM EDTA, 50 mM Tris-HCl, pH 7.4, containing one Roche mini EDTA-free protease inhibitor cocktail tablet per 10ml), the plate was then place on a shaker with agitation at 4°C. Four sequential extractions was performed, using fresh buffer each time, for varying lengths of time overnight (S1), 6hrs (S2), overnight (S3) and 6hrs (S4) to ensure complete extraction of extracellular labelled collagen before carrying out a final extraction (N) overnight in salt extraction buffer containing 1% NP40. After each extraction, the extract was transferred to a microcentrifuge tube and stored at -20°C.

2.15.4. Analysis of Extracts

The S1, S4 and N extracts were analysed by electrophoresis using 6% Tris-Glycine gels (NuPAGE™, Invitrogen, USA). The S1 extract contains the majority of the extracellular proteins, and the N extract contains the intracellular proteins, the S4 extract is included to confirm the extent of the extraction of extracellular labelled (pro) collagen prior to the lysis of the cells with NP40 extraction buffer.

The gels were then fixed in a solution of 10% methanol and 10% acetic acid for 20 minutes, before repeating with fresh fixative for a second 20 minutes.

The gels were then dried on 3M Whatman paper and exposed to a phosphorimaging plate (BAS-IP MS) for 24 hours and then a second phosphorimaging plate for a further 7 days.

The plates were then imaged using a Typhoon FLA7000 Biomolecular imager (GE healthcare, USA).

2.16. Gene expression analysis

2.16.1. Sample Harvest and RNA Extraction

Embryos were harvested at 18.5 dpc from timed intercross matings. Embryos were culled by decapitation. Tail was taken for genotyping, the embryos were split in half then each half of the embryo (and head) was snap frozen in liquid nitrogen, and stored at -80°C. RNA was produced using the RNeasy Maxi kit (Qiagen) according to manufacturer's instructions. Briefly, half of each embryo was homogenised in QIAzol lysis reagent (Qiagen) using a Precellys 24 tissue homogeniser (Bertin). gDNA eliminator solution was added to the homogenised tissue and shaken vigorously for 15 seconds before chloroform was added and the shaking repeated, before centrifugation for 15 minutes at 5000xg at 4°C. The upper aqueous phase is then mixed in a one to one ratio with 70% ethanol before the RNA is fixed to a membrane using RNeasy spin columns, before eluting the RNA with 200µl RNA-free water. RNA was then stored at -80 °C until required.

2.16.2. CDNA Synthesis

Synthesis of cDNA was performed using a High capacity cDNA reverse transcription kit (Applied Biosystems™ 4368814, Thermo Fisher, USA). Each reaction was composed of the following-

10X RT Buffer	2.0µL
25x dNTP mix (100mM)	0.8µL
10x RT random primers	2.0µL
Multiscribe reverse transcriptase	1.0µL
Nuclease free H ₂ O	4.2µL
RNA (200ng/µL)	µL

The program used was as follows-

Step 1 - 25°C for 10 minutes

Step 2 - 37°C for 120 minutes

Step 3 - 85°C for 5 minutes

Step 4 - Hold at 4 °C

The cDNA was stored at -20°C until required

2.16.3. Real Time qPCR

The Applied Biosystems™ 7500 Fast Real-Time PCR System and software were used for this experiment, with Taqman assays for target and reference genes, and custom Taqman assays (primers detailed in Section 2.2.3) used to differentiate between wild-type and mutant transcript. The reference gene used was Glyceraldehyde 3-phosphate dehydrogenase (GAPDH).

The cDNA was diluted to 2ng/μL cDNA; each cDNA sample was run in triplicate for all assays.

2X Taqman fast universal PCR master mix	10μL
20x Taqman Assay	1μL
ddH ₂ O	4μL
cDNA (2ng/μL)	5μL

2.17. Mechanical Testing of Ex-Vivo Tissues

2.17.1. Mechanical Testing of Tendons

The mechanical testing of tendons was undertaken in the lab of our collaborator Prof Hazel Screen at Queen Mary's University, London, with the assistance of Dr Chavaunne Thorpe.

2.17.1.1. Sample Collection

Animals were culled at 3 months of age by cervical dislocations, and the tail was amputated at the base. The tails were then wrapped in gauze soaked in PBS, before being placed in individually labelled 15 ml falcon tubes and frozen at -20°C until required. It has previously been shown that a single freeze–thaw cycle does not affect tendon mechanical properties [241].

The tails were thawed at room temperature in small batches, the skin was scored along the length and then removed to expose the bundles of tail tendons. The skinned tail was washed in a Petri dish containing PBS to ensure no hairs were attached to the tendon bundles. The tail was held with one set of robust forceps, and with a set of jeweller’s forceps, individual fascicles were pulled to extract them from the bundle of tendons, fascicles shorter than 30 mm were discarded. Once extracted the fascicles were placed in a 10 cm lidded Petri dish, lined with blue roll soaked with PBS, which was then placed at 4°C. Fascicles were regularly moistened with PBS from a spray bottle. The diameter of each fascicle was measured using a laser micrometer (LSM-501, Mitutoyo, Kawasaki, Japan), and cross-sectional area was estimated using the formula πr^2 .

2.17.1.2. Sample Testing

The mechanical properties of the fascicle were determined using an Instron ElectroPuls 1000 (Instron, USA) electrodynamic testing machine equipped with a 250N load cell. The pneumatic grips were modified with a thin layer of rubber and sandpaper, to reduce the likelihood of the fascicle slipping. The distance between the grips was set to 20 mm, and the fascicle was loaded into the top grip first to ensure the fascicle was close to taut and then pre-loaded to 0.2 N, to remove any slack in the sample. Fascicles underwent 10 cycles of loading and unloading as a preconditioning step using a sine wave at frequency of 1 Hz and amplitude of 0.25mm. Immediately after preconditioning, fascicles were pulled to failure at a rate of 1mm/s. Force and extension data were continuously recorded at 100 Hz during preconditioning and the failure test.

2.17.1.3. Analysis

The percentage hysteresis and percentage stress relaxation were calculated between the first and last preconditioning cycles of the pre-conditioning data. The sample failure properties were calculated from the quasi-static test to failure. The start point was the

displacement at which the initial pre-load was reached, prior to preconditioning, and stress and strain were calculated using the estimated cross-sectional area and gauge length for each sample. A continuous modulus was calculated across every 10 data points of each stress strain curve, from which the maximum modulus value was determined [38].

2.17.2. Three Point Bending of the Humerus

2.17.2.1. Sample Collection

3-month old female animals were culled by cervical dislocation, before the skin was removed from both forelimbs. Incisions were made into the muscles at the shoulder and elbow to allow the separation of the humerus at both joints, any remaining ligaments and muscles at the joints were then severed. Each humerus was then wrapped in gauze soaked in PBS, before being placed in individually labelled bags and frozen at -20°C until required.

2.17.2.2. Sample Testing and Analysis

Three point bone bending was performed on both humeri using a Mach-1 Mechanical Tester v500cst (Biomomentum, Canada) equipped with a single-axis load cell of 100N and a 3-point bending attachment. The humeri were loaded via the middle pin at 0.05mm/s until failure. Mach-1 Motion software (Biomomentum, Canada) was used to record the displacement and load, before the data was exported to Excel for analysis.

2.17.3. Tensile Testing of Skin

2.17.3.1. Sample Collection

3-month old female animals were culled by cervical dislocation. A large rectangle of skin was excised by making an incision in the skin in the centre of the abdomen from the pelvis to mid ribcage before cutting laterally around the whole body at top and bottom of the initial incision. The skin was then placed on blotting paper soaked in PBS, wrapped in gauze soaked in PBS, before being placed in individually labelled bags and frozen at -20°C until required.

2.17.3.2. Sample Testing and Analysis

Samples were tested using the Mach-1 Mechanical Tester v500cst (Biomomentum, Canada) with Vertical (Z) stage (ILS100HA), Single-axis load cell of 100N and a tensile grip

attachment. The skin sample was thawed and cut into a dumbbell shaped sample, being careful that the integrity of the sample was not compromised. The wide edges of the sample were fixed in the tensile grip attachment and the sample was subjected to tensile rupture tests at 2mm/s. Mach-1 Motion software (Biomomentum, Canada) was used to record the displacement and load, before the data was exported to Excel for analysis.

2.17.4. Micro-Indentation of the Articular Surface

2.17.4.1. Sample Collection

Animals were culled by cervical dislocation, before the skin was removed from both hind legs. Incisions were made into the muscles at the hip to allow the evulsion of the femoral head from the acetabulum, any remaining ligaments and muscles were then severed. Each leg was then wrapped in gauze soaked in PBS, before being placed in individually labelled bags and frozen at -20°C until required.

2.17.4.2. Sample Testing and Analysis

Samples were tested using the Mach-1 Mechanical Tester v500csst (Biomomentum, Canada) with Vertical (Z) stage(ILS100HA), Horizontal (x) stage (ILS100CC), and Horizontal (y) stage(ILS50BCC), Multi-axis Load cell 17N, spherical indenter and 1.3 MP colour camera.

When required, legs were thawed at room temperature before the femur and tibia were separated and the articular surfaces dissected from the rest of the bone at the growth plate. Tibial plateaus and femoral condyles were attached to a testing chamber filled with PBS. A camera registration system (Biomomentum, Canada) was used to image the tissue and a positional grid was superimposed on the image of the sample. The pixel coordinates were then converted into metric coordinates to allow for automated surface mapping.

At each designated position a perpendicular indentation of 30µm is performed by moving all 3 orthogonal stages simultaneously and at different speeds resulting in a perpendicular indentation speed of 30µm/s. The force is measured using a spherical indenter (D=30 µm) attached to a multi-axial load cell (17N range).

The structural stiffness at each position is calculated by dividing the perpendicular load by the perpendicular displacement. The mean structural stiffness of all indentation sites

within a designated region of the articular surface is calculated, to give an overall structural stiffness for each region.

2.18. Micro Computed Tomography of Bones

2.18.1. Sample Collection and Preparation

Animals were culled at the appropriate time-point via intraperitoneal injection of Euthatal. Death was confirmed by cervical dislocation prior to dissection. Skin was removed from both forelimbs and hind limbs. Incisions were made into the muscles at the shoulder and hip to allow the separation of the limbs from their joints, any remaining ligaments and muscles at the joints were then severed. The spine and tail were amputated above and below the pelvis. Extra tissues were then trimmed from the bone, before placing the pelvis and limbs in 10% neutral buffered formalin for 48 hours before being transferred into 70% ethanol. The femur, tibia and fibula were cut approximately 6mm away from the knee joint using a Dremel tool and a diamond cutting wheel, before being rinsed in PBS to remove bone fragments.

2.18.2. Sample Scanning

Samples were wrapped in non-PVC cling film and then placed snugly inside an appropriately sized container made from polylactic acid (PLA) which was affixed to a brass chuck. The brass chuck was then inserted into the sample holder in the Skyscan 1172 (Bruker, Belgium). The samples were scanned using a 0.5um Aluminium filter at 50kV, 200 μ A, 2x2 camera binning and pixel size 4.34 μ m. Rotational steps were 0.7 degrees with 2 frame averaging.

2.18.3. Sample Analysis

Samples were reconstructed using NRecon (Bruker, Belgium) with a beam hardening correction of 20% and a ring artefact correction 10. The resulting stacks were then re-orientated using Dataviewer (Bruker, Belgium), before analysis and imaging was undertaken using CTAn (Bruker, Belgium). Regions of interest (ROIs) were outline in the epiphyseal bone, metaphyseal bone, or subchondral bone plate. These ROIs were then processed with a higher grayscale index of 66, and custom processing plug-ins of thresholding, despeckling and 3D analysis.

2.19. Optical Projection Tomography of Embryos

Optical Projection Tomography (OPT) is an imaging technique similar to X-ray computed tomography, where visible light is used, instead of X-rays, and passed through an optically cleared sample.

2.19.1. Sample Collection

Embryos were harvested at 12.5 dpc from timed intercross matings. The uterus was removed from the pregnant animal and placed in ice cold PBS, and then kept on ice for 20 minutes. The uterus was then transferred into a 10 cm Petri dish and covered with fresh ice-cold PBS. The uterus was then opened to allow access to the individual yolk sacs. The yolk sac was then carefully cut open to release the embryos and placentas. A sample of yolk sac was taken for genotyping, and the embryos separated from the placenta at the umbilical cord and placed in a labelled well of a 6 well plate filled with ice cold PBS. This process was repeated until all embryos were in individual wells of PBS. Any blood clots that formed at the navel were removed and the embryo were left on ice for another few minutes before being thoroughly washed to remove any remaining blood, before being placed into fresh wells containing ice cold 4% PFA. The samples were then kept at 4°C overnight. The embryos were then embedded in agarose in a cylindrical mould, and mounted to a magnetic chuck. The agarose is then dehydrated using multiple changes of 100% methanol, before clearing with a solution of 1 part benzyl alcohol to 2 parts benzyl benzoate (BABB).

2.19.2. Sample Scanning and Analysis

Scanning of the embryos was undertaken by Dr James Cleak in the MRC Harwell molecular biology group using a custom built OPT system and software (labview) [242]. Images were reconstructed using Nrecon (Bruker).

2.20. Collagen Analysis of Tendons

2.20.1. Harvesting of Tail Tendons

4-month old mice were culled by cervical dislocation and the tails were dissected from the body. Each tail was placed in a separate 100mm Petri dish in PBS containing 1% penicillin/streptomycin. The skin was scored along the length and then removed to

expose the bundles of tail tendons. Using two pairs of robust forceps, the tail was held with one set of forceps at the base and sections of the tail with attached tendons were removed by pulling with the second set of forceps upwards to the base in sections. The tendons were cut away from the bone using dissection scissors, placed in a microcentrifuge tube and stored at -20°C.

2.20.2. Extraction of Collagen

Tail tendon samples were thawed at room temperature before approximately 15mg of each sample was placed in a corresponding 15ml Falcon tube. 3ml Pepsin (25µg/ml) in 0.5M acetic acid was added to each falcon tube and digested at 4°C for 48 hours with shaking.

2.20.3. Analysis of Collagen Content

The tendon extracts were then diluted to 0.25mg/ml, before diluting 1:3 in LDS sample buffer (Nupage). 20µl was then run on 4-12% Tris Bis gel gels at 200V for 100 minutes. The gels were then stained using brilliant Coomassie blue for 30 minutes and then de-stained using a solution of methanol and 0.5M acetic acid in a 50/50 ratio, changing the solution as required. The gel was then imaged using the Biorad Gel Doc XR with a white light conversion screen and Image lab 5.1 software.

2.21. Mouse Embryonic Fibroblasts

2.21.1. Fibroblast Harvest

Embryos were harvested at 12.5 dpc from timed intercross matings. Embryos were culled by decapitation and placed in individual wells of 6 well plates filled with ice cold PBS. The organs, including the heart and liver were then removed from the abdominal cavity and discarded along with the head, tail tips were retained for genotyping purposes. Any blood clots were washed from the embryos, before placing them into individual wells of a 6 well plate with 1.5ml of 0.25% Trypsin. The embryos were then minced using a sterile scalpel blade, before being incubated for 5 minutes at 37°C in a shaking incubator. The embryos were then further homogenised by drawing the minced embryo and trypsin solution through a 21G needle 5 times. 5 ml of standard MEF media (see section 2.6) was then added to inactivate the trypsin. The plate was then placed in

an incubator at 37°C and 5% CO₂ overnight to allow the cells to adhere, before changing the media for fresh media the next day.

2.21.2. Cell Growth and Maintenance

When the cells reached 90% confluence, the cells were transferred to a T25 flask. The old media was removed and the cells were gently washed using 2ml of pre-warmed DPBS. 1 ml of 0.05% Trypsin-EDTA was added to the well after the removal of the DPBS, and the plates were returned to the incubator until the cells had fully dissociated. The trypsin was then deactivated by adding 2ml standard MEF media. The 3 ml containing the dissociated cells were then transferred to a T-25 flask containing 7ml of standard MEF media. The media was then changed for fresh standard MEF media the next day.

While the cells were growing the media was changed every few days. The media was aspirated out of the flask; the cells were then washed gently with pre-warmed DPBS, which was then aspirated and then 10 ml pre-warmed standard MEF media was carefully added to the flask.

When the cells reached 90% confluence, the cells were split 1 in 20 using the same technique as outlined above.

To preserve the cell lines at an early passage, a flask from each MEF line was frozen from the second splitting of passage 2 cells.

2.22. Destabilisation of the Medial Meniscus (DMM)

The surgical method for DMM under aseptic conditions is as described in Blease *et al.* [243]. Briefly, 10-week old animals were anaesthetised using an intraperitoneal injection of Ketamine/Xylazine as well as an analgesic injection of 0.1ml of Torbugesic (0.25mg/ml) and Vetergesic (0.025mg/ml) via subcutaneous injection. Anaesthesia was maintained using isoflurane at 0.5% in oxygen at 2 litres/minute.

The knee was shaved, and swabbed with chlorhexidine, before an initial incision, 8 to 12 mm long, was made medially to the knee with a scalpel exposing the parapatellar ligament. A secondary incision was then made medially to the white parapatellar ligament. The medial meniscotibial ligament (MMTL) was then identified and severed using a microsurgical knife. Any bleeding was staunches with a sterile surgical swab. The joint capsule was then closed with a vicryl suture, and the dermal layer was then closed

using ethilon sutures. The mice were allowed to recover in a warmed recovery box and when weight-bearing returned to their home cage. The animals were culled 6 weeks post-surgery by cervical dislocation, and the hind legs fixed in 10% neutral buffered formalin for 48 hours before being transferred to 70% ethanol.

Histological processing of the knee joints was carried out by the histology department at the Kennedy Centre for Rheumatology. Safranin O stained sections were then evaluated by OARSI scoring by two skilled evaluators.

2.23. Western Blotting

Cells were harvested by dissociating cells by adding 0.05% Trypsin-EDTA, when fully dissociated the trypsin was deactivated by adding 5ml media, before centrifugation at 4°C at 800xg for 5 minutes. The media/trypsin was then siphoned off, before washing in ice cold PBS. The cells were then lysed using a pellet pestle (Kimble) and 250µl Cell Lytic MT with phosphatase and protease inhibitors.

Protein concentration was assessed using a Bradford assay using a uQuant plate reader (Biotek). 20µg of protein was mixed with LDS sample buffer (Nupage) and reducing agent (Nupage) and boiled at 95°C for 10 minutes before being run on a 4-12% Tris-Bis gel at 200V for 60 minutes in MOPs running buffer (see section 2.5). Proteins were then transferred to a nitrocellulose membrane (Invitrogen) with a 0.45µm pore size in transfer buffer (see section 2.5).

The membrane was then blocked using 5% w/v milk powder in TBST (see section 2.5) for 60 minutes with shaking. Primary antibodies were diluted in 5% w/v milk powder in TBST (see section 2.3 for dilutions) and incubated at 4°C overnight with shaking. The membrane was then washed in 3 changes of TBST with shaking for 5 minutes each time before incubating with secondary antibodies diluted in 5% w/v milk powder in TBST (see section 2.3 for dilutions) for an hour at room temperature. Fluorescent antibodies were protected from the light. The membrane was then dried and protected from the light before imaging using the Li-COR Odyssey Cl-X, and image studio lite software (Li-COR).

2.24. Statistical Analysis

Statistical analysis was performed using Prism 7 (Graphpad). Comparisons between 2 groups were performed using unpaired Student's t-test. Where more than two groups were analysed, either a one-way or a two-way ANOVA was used with Bonferoni correction. Chi squared tests were used to assess viability. Mann-Whitney test was used where non-parametric tests were required, for example to analyse osteophyte development. Results were considered significant at $p < 0.05$.

2.25. ARRIVE Guidelines

The ARRIVE guideline (Animal Research: Reporting of In Vivo Experiments) originally published in 2010, and subsequently modified in 2020, are a checklist of information to include when describing animal research [244]. These guidelines are intended to maximise the reliability and quality of research, and to enable better reproducibility and transparency. This includes guidelines covering parameters, such as sample size, inclusion and exclusion criteria, blinding and statistical methods. The reporting of data in this thesis will endeavour to follow these guidelines.

**Chapter 3: Identification and Initial
Characterisation of Phenotypes
Associated with a Point Mutation in
*Col1a2***

3.1. Introduction

This chapter describes the identification and characterisation of a novel mutant mouse line carrying a mutation in *Col1a2*. The mouse line was identified in the Harwell Ageing Screen, which was a large-scale N-ethyl-N-nitrosourea (ENU) mutagenesis screen, whereby a forward genetics approach was utilised to identify novel mutations. The majority of ENU mutagenesis screens age the mice for only a few weeks or months, and therefore only identify mutations relating to early onset disease [235, 236, 245]. The Harwell Ageing Screen addressed this by ageing the animals to 18 months to facilitate identification of mutations causing late onset or chronic phenotypes, in addition to the mutations causing early onset phenotypes. We live in an ageing society with increased populations of older people, which has also increased the burden of late onset disease. Identifying novel models of disease, and their causative mutations, is an important route to therapy, disease prevention and a reduction in this disease burden.

Sperm and DNA from each G₁ founder animal was archived, and two large G₃ cohorts (totalling ~100 mice) were bred from each G₁ founder to ensure, even in lines where the causative mutation was recessive, that there were enough animals to identify the phenotype and map the mutation without further breeding. The G₃ cohorts underwent a recurrent phenotyping regimen until a terminal time point at 18 months of age [238]. Further work to identify the causative mutations and characterise the mutations were undertaken on lines displaying a phenotype. Further details of the ageing screen and breeding schemes are detailed in Sections 1.41 and 2.6.2.

The line Muta-Ped-107 (MP-107), which was initially identified by X-ray imaging as having early onset mild bone abnormalities, including curved olecranon at the elbow, and splayed ischia at the pelvis, subsequently developed late onset OA at the knee joint. The causative mutation was identified as a splice variant in the gene *Col1a2*. In addition to describing the initial identification of the phenotype in the line MP-107 and the determination of the causative mutation; this chapter will also describe a more in-depth phenotyping pipeline involving purpose bred cohorts, tailored to the phenotypes observed in the original G₃ cohort, to further characterise the progression of the phenotypes in this mutant.

3.2. Initial identification of Mutants by X-ray Imaging

As part of the wider Ageing Screen phenotyping pipeline, X-ray imaging was performed at 3, 12 and 18 months of age on all females in the G₃ cohort, providing the animals were sufficiently healthy. At 3 months of age a number of animals were noted to have mild bone abnormalities including a curved olecranon at the elbow, widened or splayed ischia at the pelvis, or both.

The pelvis can be viewed as two halves, known as coxae, with each coxae made up of the ischium, ilium and pubis (plurals- ischia, ilia and pubes), which are fused to form a single unit, and the two coxae are joined together by the sacrum. The ischia and pubes are the posterior part of the pelvis, with the ischia forming the dorsal section and the pubes forming the ventral section. Generally, the ischia of the mice follow the trajectory of the ilia in a symmetrical manner, with the tuberosity of ischium (the most posterior point of the ischium) aligning with the body of the ilium. Where one or both ischia deviate outside of this trajectory, the animals were deemed to have the 'splayed ischia' phenotype (Figure 3.1).

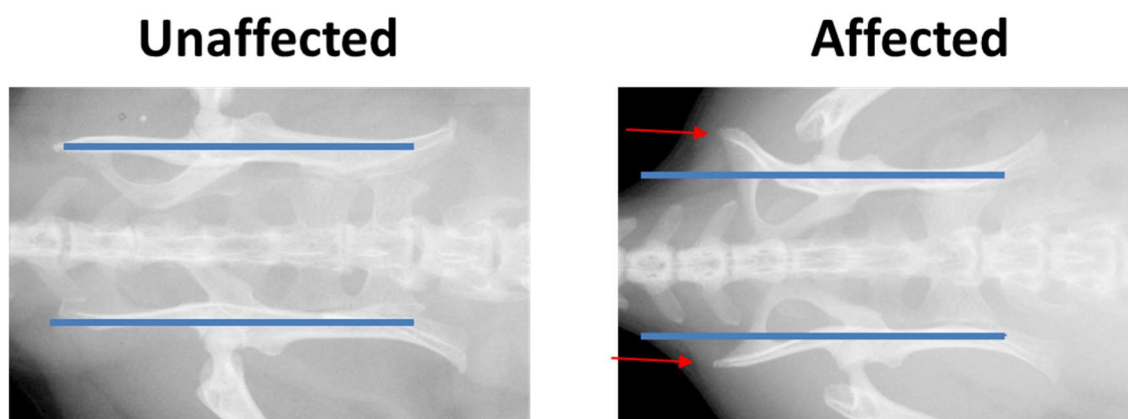


Figure 3.1. Examples of high-resolution radiographs of affected and unaffected pelvises, with annotation to show how the phenotype was defined. The blue lines denote the trajectory of the ilia and pass through the acetabulum, where the tuberosity of ischium deviates outside of these parallel lines, the animal was deemed to have the 'splayed ischia' phenotype (red arrows). These radiographs are to show how the phenotype was defined and are not G₃ animals.

The olecranon is the proximal part of the ulna, and projects beyond the semilunar notch, where the trochlear of the humerus is seated. Generally, the olecranon follows the same trajectory as the ulna, where the olecranon deviates outside of this trajectory, the animals were deemed to have the 'curved olecranon' phenotype (Figure 3.2).

Unaffected



Affected



Figure 3.2. Examples of high-resolution radiographs of affected and unaffected olecranons, with annotation to show how the phenotype was defined. The blue lines denote the trajectory of the ulna and pass through the semilunar notch, where the olecranon deviates from the trajectory, the animal was deemed to have the 'curved olecranon' phenotype (red arrow). These radiographs are to show how the phenotype was defined and are not G₃ animals.

Analysis of the radiographs revealed that at 3 months of age, 11 of 48 animals exhibited the splayed ischia phenotype, and 8 of 48 animals exhibited the curved olecranon phenotype (Table 3.1 and Figure 3.32).

3 months	Ischia	Olecranon	Knee	Total
Affected	11	8	0	15
Unaffected	37	40	48	33
Total	48	48	48	48
Percentage affected	22.92%	16.67%	0%	31.25%

Table 3.1. Table showing numbers of animals with each phenotype at 3 months of age. The phenotypes are recorded in isolation in this table and therefore animals with multiple phenotypes may appear in more than one phenotype column, however total number of animals affected are recorded in the last column

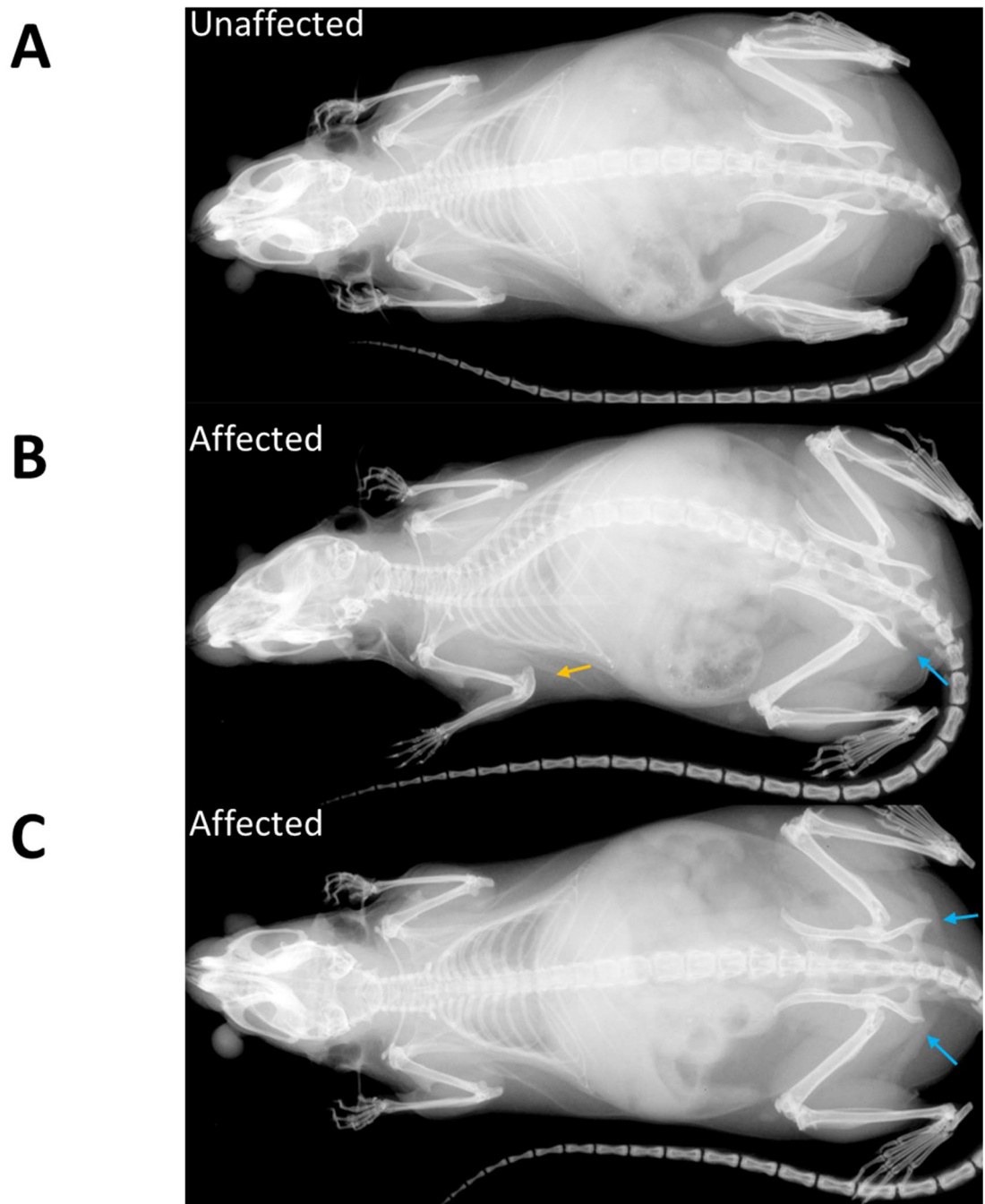


Figure 3.3. Radiographs showing affected and unaffected animals at 3 months of age. (A) The unaffected animals showed no skeletal abnormalities. (B) and (C) The affected animals either showed a curved olecranon at one or both elbows (Orange arrows), or splayed ischia at the pelvis (Blue arrows) or a combination of both phenotypes.

At the 12-month time point, in addition to the abnormalities noted at the ischia and olecranon at 3 months, some animals appeared to show abnormal bone formation at the knee joints. This abnormal bone formation varied in appearance, but the common factor was that bone appeared to form in the vicinity of the knee, but outside of the areas where bone normally forms (Figure 3.4).

Unaffected



Affected



Figure 3.4. Examples of high-resolution radiographs of affected and unaffected knee joints, with annotation to show how the phenotype was defined. The blue arrow on the unaffected knee marks the fabella, a sesamoid bone which is embedded in tendon behind the knee, this is not an example of abnormal bone growth. The red arrow on the affected knee marks the abnormal bone growth at the knee. These radiographs are to show how the phenotype was defined and are not G₃ animals.

Analysis of the radiographs revealed that at 12 months of age, 10 of 39 animals exhibited the splayed ischia phenotype, 6 of 39 animals exhibited the curved olecranon phenotype, and 10 of 39 animals exhibited the abnormal bone growth at the knee phenotype (Table 3.2 and Figure 3.5).

12 months	Ischia	Olecranon	Knee	Total
Affected	10*	6*	10	16
Unaffected	29	33	29	23
Total	39	39	39	39
Percentage Affected	25.64%	15.38%	25.64%	41.03%

Table 3.2. Table showing numbers of animals with each phenotype at 12 months of age. The phenotypes are recorded in isolation in this table and therefore animals with multiple phenotypes may appear in more than one phenotype column, however total number of animals affected are recorded in the last column. The numbers marked with an asterisk (*) are lower than numbers recorded at 3 months, due to some animals being on health checks and therefore unable to undergo anaesthesia or were culled for welfare reasons.

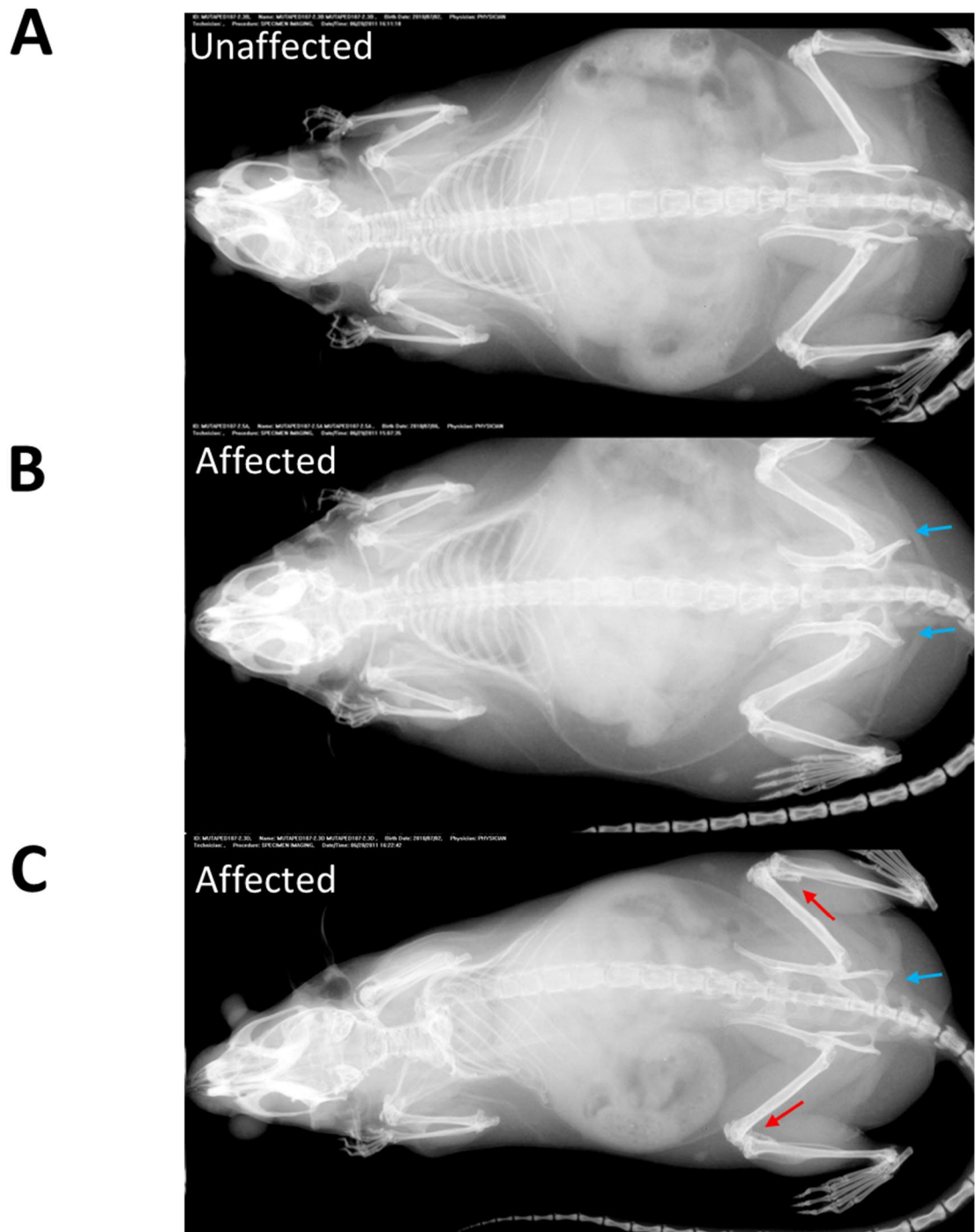


Figure 3.5. Radiographs showing affected and unaffected animals at 12 months of age. The unaffected animals (A) showed no skeletal abnormalities. The affected animals (B & C) either showed a curved olecranon at one or both elbows (not shown in this figure), or splayed ischia at the pelvis (Blue arrows), or abnormal bone growth at the knee joint (Red arrows), or a combination of phenotypes.

At the 18-month time point, in addition to the abnormalities noted at the ischia and olecranon at 3 months, and the abnormal bone formation at the knee joints noted at 12 months, further animals developed abnormal bone formation at the knee joints. The bone formations noted at 12 months had also increased in size (Table 3.3 and Figure 3.6).

18 months	Ischia	Olecranon	Knee	Total
Affected	10*	8	20	21
Unaffected	29	31	19	18
Total	39	39	39	39
Percentage Affected	25.64%	20.51%	51.28%	53.85%

Table 3.3. Table showing numbers of animals with each phenotype at 18 months of age. The phenotypes are recorded in isolation in this table and therefore animals with multiple phenotypes may appear in more than one phenotype column, however the total number of animals affected are recorded in the last column. The number marked with an asterix (*) is lower than the number recorded at 3 months, due to some animals being culled for welfare reasons.

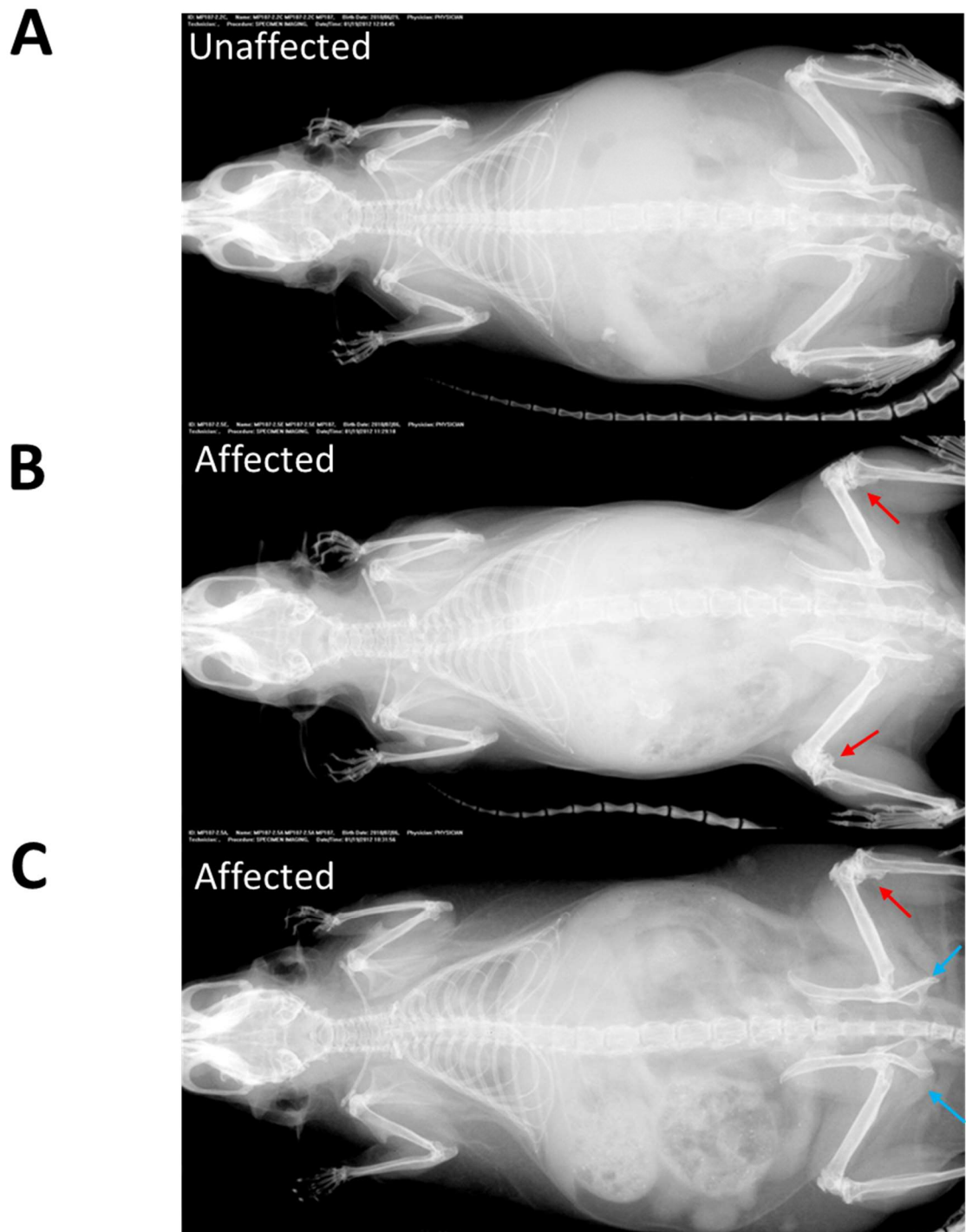


Figure 3.6. Radiographs showing affected and unaffected animals at 18 months of age. The unaffected animals (A) showed no skeletal abnormalities. The affected animals (B & C) either showed a curved olecranon at one or both elbows (not shown in this figure), or splayed ischia at the pelvis (Blue arrows), or abnormal bone growth at the knee joint (Red Arrows), or a combination of phenotypes.

The abnormalities observed at the ischia and olecranon of these animals did not progress in severity, or appear at later time points had they not already manifested by 3 months of age. Addressing each phenotype individually, the splayed ischia phenotype affected between 22 and 26% of animals, the increase in affected animals by percentage was due to a reduction in unaffected animals at the later time points. The curved olecranon phenotype affected between 16 and 21% of animals, again the increase in affected animals by percentage was due to a reduction in unaffected animals at the later time point. The knee phenotype affected between 41 and 54%, this time the increase in affected animals by percentage was due to an increase in affected animals rather than a reduction in unaffected animals at the later time points.

3.3. Mapping and Identification of the Causative Mutation in MP-107

3.3.1. Mapping the Mutation

In order to map the causative mutation(s), DNA was extracted from *post mortem* tail biopsies from 7 affected animals (with all three phenotypes) and an unaffected control animal. 350ng of DNA was sent to Geneseek® to be run on the GigaMUGA panel-143,259-probe Illumina Infinium II array. The GigaMUGA panel identifies Single Nucleotide Polymorphisms (SNPs) which are unique to each particular background strain. As the G₃ animals which underwent phenotyping have a mixed background, it is possible to use the SNPs to identify which portions of the genome were inherited from each ancestral strain. The original mutation was induced in a C57BL/6J mouse, therefore any mutation caused by the ENU will be within the C57BL/6J regions of the genome. A dominant causative mutation would need to be homozygous or heterozygous for C57BL/6J SNPs, whereas if the mutation was recessive the region would need to be homozygous for C57BL/6J SNPs.

A single region was identified on Chromosome 6 from the SNP rs13478719 located at Chr6:38545339 to the proximal end of the chromosome, where all affected animals were either heterozygous or homozygous for C57BL/6J, and an unaffected control animal was homozygous for C3H.Pde6b+. This means all affected animals had at least one C57BL/6J region which could contain the causative mutation whilst the unaffected control animal had no C57BL/6J alleles, and cannot therefore contain the causative

mutation (Figure 3.7). The mouse MP-107-2.11d was heterozygous for C57BL/6J at the SNPs proximal to SNP rs13478719 and homozygous for C3H.Pde6b+ at SNP rs13478719. This indicates the boundary of the region of interest, as any ENU mutation affecting the affected animals listed could only occur on the C57BL/6J genome, and therefore cannot be after Chr6:38545339.

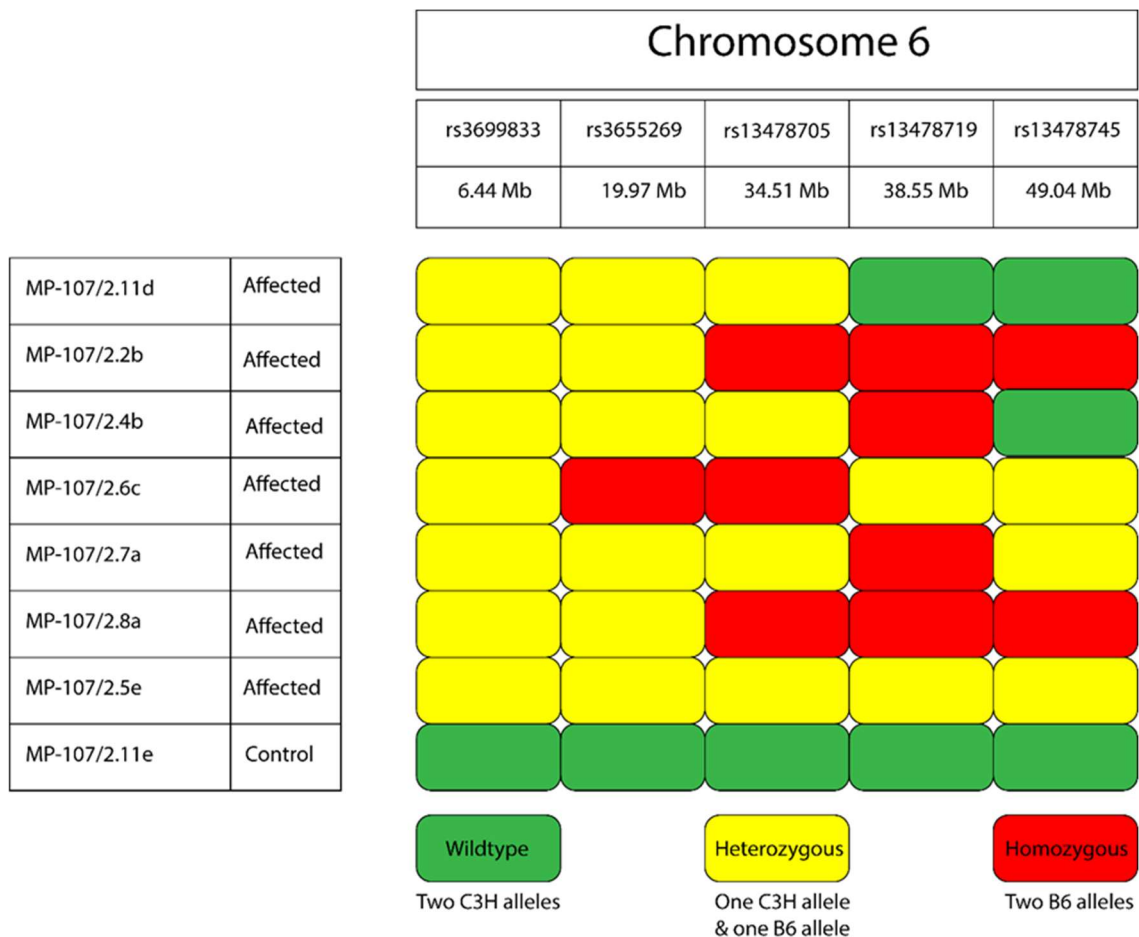


Figure 3.7. SNP mapping panel showing the region of interest on Chromosome 6. All affected animals have at least one C57BL/6J SNP in the ~39Mb region at the proximal end of Chromosome 6, indicating that the causative mutation or mutations are contained within that region.

At this stage it was not possible to say if all phenotypes were caused by a single mutation, however as only one region was identified, if separate mutations are causing these phenotypes, all the causative mutations reside within the same region of the genome.

3.3.2. Whole Genome Sequencing

Whole genome sequencing (WGS) was performed on DNA from the G₁ founder animal, to identify all possible ENU induced mutations in the G₃ cohort, which can subsequently be investigated. WGS was used over exome sequencing as although the 'majority of disease-causing mutations' are located within exons [246] for the purpose of this screen it was important not to be limited to only exonic information.

The mapping data indicates that the causative mutation(s) must reside within the ~39 Mb region at the proximal end of Chromosome 6. The mutations detected within this region were assessed for candidates. A total of 633 mutations were identified in this region, which are summarised in Table 3.4. Mutations are ranked by confidence, where the high confidence mutations have a quality score over 200 and a read depth of over 3, medium confidence have a quality score of between 101 and 200 and a read depth of over 3, and the remaining mutations are classed as low confidence [238, 247]. Reduced read depth or quality scores may reduce confidence that the mutation identified is in fact present, and this is reflected in the confidence groups.

Type of Variant	Confidence			Total
	High	Medium	Low	
3 prime UTR variant	2	0	5	7
5 prime UTR variant	0	1	0	1
Downstream gene variant	2	0	20	22
Intergenic variant	31	31	253	315
Intron variant	18	21	204	243
Missense variant	0	0	0	0
Non coding exon variant	0	0	1	1
Synonymous variant	0	0	0	0
Splice region variant	1	0	0	1
Upstream gene variant	3	1	39	43
Total	57	54	522	633

Table 3.4. Summary of all mutations identified within the ~39Mb region on the proximal end of Chromosome 6, split by confidence (columns) and classification (rows).

The 57 high confidence mutations are listed in Table 3.5.

Position	Reference	Alternate	Functional Class	Gene
3215592	A	G	Intergenic variant	-
3625093	A	G	Intergenic variant	-
3877828	T	G	Intergenic variant	-
4228643	A	G	Intergenic variant	-
4276412	T	G	Intergenic variant	-
4521226	T	A	Splice region variant	<i>Col1a2</i>
4833259	T	C	Downstream gene variant	-
4920383	A	T	Intron variant	<i>Ppp1r9a</i>
6470041	A	T	Intron variant	<i>Gm20617</i>
7113185	A	G	Intergenic variant	-
7403048	A	T	Intergenic variant	-
7717449	A	G	Intergenic variant	-
8506789	C	T	Intron variant	<i>Gm16039</i>
8877658	G	A	Intergenic variant	-
8960717	A	T	Intron variant	<i>Nxph1</i>
9317785	C	T	Intergenic variant	-
9384727	G	A	Intergenic variant	-
9501174	A	C	Intergenic variant	-
9806235	T	A	Intergenic variant	-
10140012	A	C	Intergenic variant	-
10368340	A	G	Intergenic variant	-
10611992	A	T	Intergenic variant	-
11799123	T	A	Intergenic variant	-
12119199	T	A	Intergenic variant	-
13926012	G	A	Intron variant	-
14014424	G	A	Intron variant	-
14226943	G	T	Intergenic variant	-
14755277	A	G	Upstream gene variant	<i>Ppp1r3a</i>
14993940	T	C	Intron variant	<i>Foxp2</i>
16532319	A	G	Intergenic variant	-
19222245	G	T	Intergenic variant	-
20081045	C	T	Intergenic variant	-
20168585	G	T	Intergenic variant	-
20457452	C	T	Intergenic variant	-
23160716	G	C	Upstream gene variant	-
23445271	A	G	Intron variant	<i>Cadps2</i>
24374700	C	G	Intergenic variant	-
24530910	C	A	Intron variant	<i>Asb15</i>
25590535	C	A	Intergenic variant	-
26646401	T	C	Intergenic variant	-
27257089	A	T	Intergenic variant	-
29618661	G	A	Intergenic variant	-
29912296	T	A	3' prime UTR variant	<i>Ahcyl2</i>
31247325	T	C	Intron variant	<i>2210408F21Rik</i>
32653009	C	A	Intergenic variant	-
33093143	T	C	Upstream gene variant	-
34361912	C	T	Intron variant	<i>Akr1b8</i>
34807920	A	T	Intron variant	<i>Agbl3</i>
35978485	A	C	Downstream gene variant	-
36263578	C	G	Intron variant	<i>9330158H04Rik</i>
37062707	T	A	Intron variant	<i>Dgki</i>
37160743	A	G	Intron variant	<i>Dgki</i>
37200104	T	C	Intron variant	<i>Dgki</i>
37283938	T	C	Intron variant	<i>Dgki</i>
37837022	A	G	Intergenic variant	-
38291687	G	A	3' prime UTR variant	<i>Zc3hav1l</i>
38568926	T	C	Intron variant	<i>Luc7l2</i>

Table 3.5. Summary of the 57 high confidence mutations identified within the ~39 Mb region on Chromosome 6. The *Col1a2* mutation highlighted is the most likely candidate, as it is within 3 bases of a splice acceptor site and is therefore the most likely candidate to affect the coding sequence.

Previous publications on ENU mutagenesis screening have found that mutations affecting coding regions are the most common cause for detected phenotypes [235, 236, 238, 245]. In this case, there were no coding mutations at any confidence level, however, there was a high confident splice region variant in *Col1a2*, a thymine (T) to adenine (A) transversion at position 4521226. Splice region variants, can cause coding changes by affecting splicing. In this case the mutation is within 3 bases of the splice acceptor site flanking exon 22 in *Col1a2* and could therefore affect the coding of *Col1a2*.

3.3.3. Confirmation of Mutation

The splice variant in *Col1a2*, was the candidate deemed to be the most likely to be the causative mutation, as there were no coding mutations, and this mutation may have an impact on protein sequence or expression. For this reason, Sanger sequencing was used to confirm the T to A transversion 3 base pairs from the splice acceptor site downstream of Exon 22 in *Col1a2* was present.

Genomic DNA (gDNA) was extracted from tail from the G₁ founder animal, an affected G₃ and unaffected control. This gDNA was sequenced, and both the G₁ and affected G₃ proved to be heterozygous for the mutation, whilst the unaffected control was wild-type for the mutation (Figure 3.8). This demonstrates that the mutation identified in the G₁ WGS is a real mutation and that it has been inherited by at least one animal exhibiting the observed phenotypes.

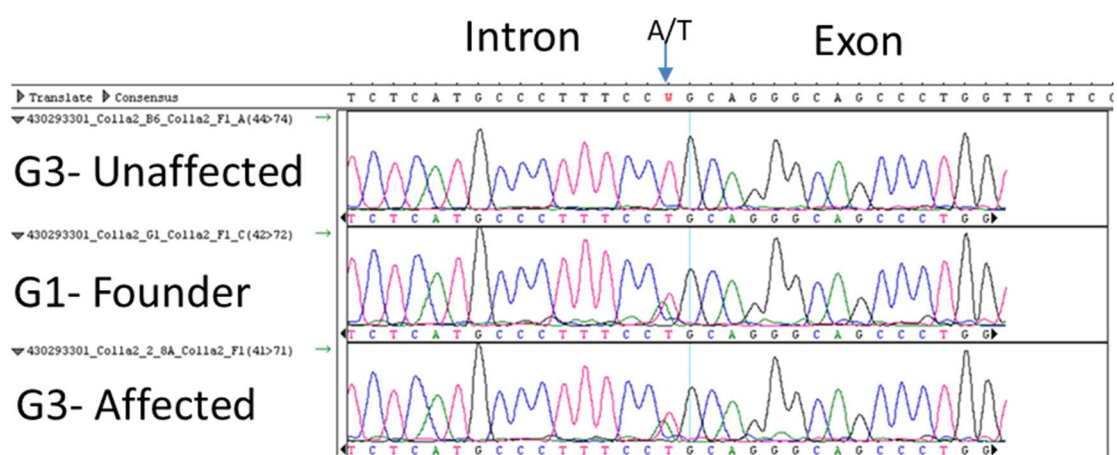


Figure 3.8. Sequencing data for affected and unaffected animals. Both the G₁ and a G₃ affected animal showed the presence of 2 peaks at the mutation site in both, due to being heterozygous for the mutation and therefore having one wild-type allele and one mutant allele. The unaffected G₃ animal shows a single peak at the mutation site as it has two copies of the wild-type allele.

3.4. Analysis of Initial Phenotyping by Genotype

Having confirmed the presence of a *Col1a2* mutation in the G₁ animal and an affected G₃, a Lightscanner assay was developed to enable quick and efficient genotyping. Animals which are homozygous, heterozygous or wild-type for the *Col1a2* mutation will be referred to as *Col1a2*^{107/107}, *Col1a2*^{+/107}, and *Col1a2*^{+/+} respectively. The G₃ animals from the original cohort were then genotyped, and the phenotyping data was then correlated to genotype. The genotyping revealed the absence of *Col1a2*^{107/107} animals in the G₃ cohort indicating that the mutation is likely to be homozygous lethal, and this was supported by the ratio of the remaining genotypes of 2:1 *Col1a2*^{+/107} to *Col1a2*^{+/+}, which is consistent with expected Mendelian ratios [248, 249] (Figure 3.9).

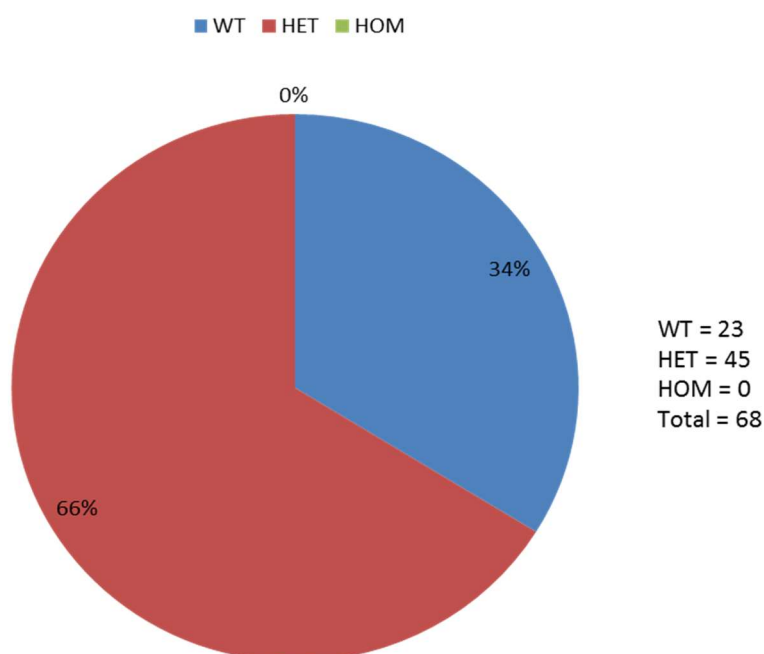


Figure 3.9. Genotyping data from the original G₃ cohort. There were no homozygous (*Col1a2*^{107/107}) animals present and a 2:1 ratio of heterozygous (*Col1a2*^{+/107}) to wild-type (*Col1a2*^{+/+}) animals indicating that the mutation is homozygous lethal.

3.4.1. X-ray Imaging of the MP-107 G₃ cohort

Genotyping of the animals imaged by X-ray revealed that all the animals displaying any phenotype were heterozygous, with the exception of 3 animals, which were of unknown genotype as the animals were culled due to welfare concerns and tissue for genotyping was not available. At 3 months of age, approximately 50% of the unaffected animals

were heterozygous, reducing to approximately 28% at 18 months. This data indicates that while it is likely that all three phenotypes are caused by the observed mutation in *Col1a2*, the mutation either has reduced penetrance, or is causing changes which are not observable using this phenotyping technique. Although 100% of the affected animals with genotyping data are heterozygous for this mutation, it does not exclude the possibility that a separate mutation within this region could be causing any of these phenotypes.

		Individual phenotype			Any phenotype	Genotype		
		Ischia	Olecranon	Knee	Total	Heterozygous	Wildtype	Unknown
3 Months	Affected	11	8	0	15	12	0	3
	Unaffected	37	40	48	33	15	16	1
12 Months	Affected	10	6	10	16	15	0	1
	Unaffected	29	33	29	23	8	15	0
18 Months	Affected	10	8	20	21	21	0	0
	Unaffected	29	31	19	18	5	13	0

Table 3.6. A table showing numbers of affected and unaffected animals at each time point, and the genotypes of those animals. A total of 5 animals included in the table were not genotyped, as they were culled for welfare reasons before the terminal time point, and there was no tissue available for genotyping.

3.4.2. Dual Energy X-ray Analysis (DEXA) of the MP-107 G₃ cohort

DEXA, known as DXA in human studies, uses dual energy x-rays to analyse the body composition including BMC, BMD, fat and lean mass, and percentage fat. As part of the ageing screen pipeline, DEXA scans were performed on female animals at 3, 12 and 18 months. Length of the mouse from the nose tip to the base of the tail was measured and the animals were weighed prior to DEXA scan (10). The majority of the data collected showed no significant difference between the genotypes with the exception of BMD at the 12-month time point (WT-Mean-0.06441, StDev-0.0027, n-10; HET-Mean-0.05786, StDev-0.004865, n-11; P=0.002, Student t-test), and length at 18-month time point (WT-Mean-10.85, StDev-0.32, n-11; HET-Mean-11.16, StDev-0.28, n-16; P=0.02, Student t-test). Length was measured from nose to the base of tail using a ruler to the nearest millimetre, as such the measurement is not exact and subject to variability, and it is unlikely that this parameter is of any biological relevance.

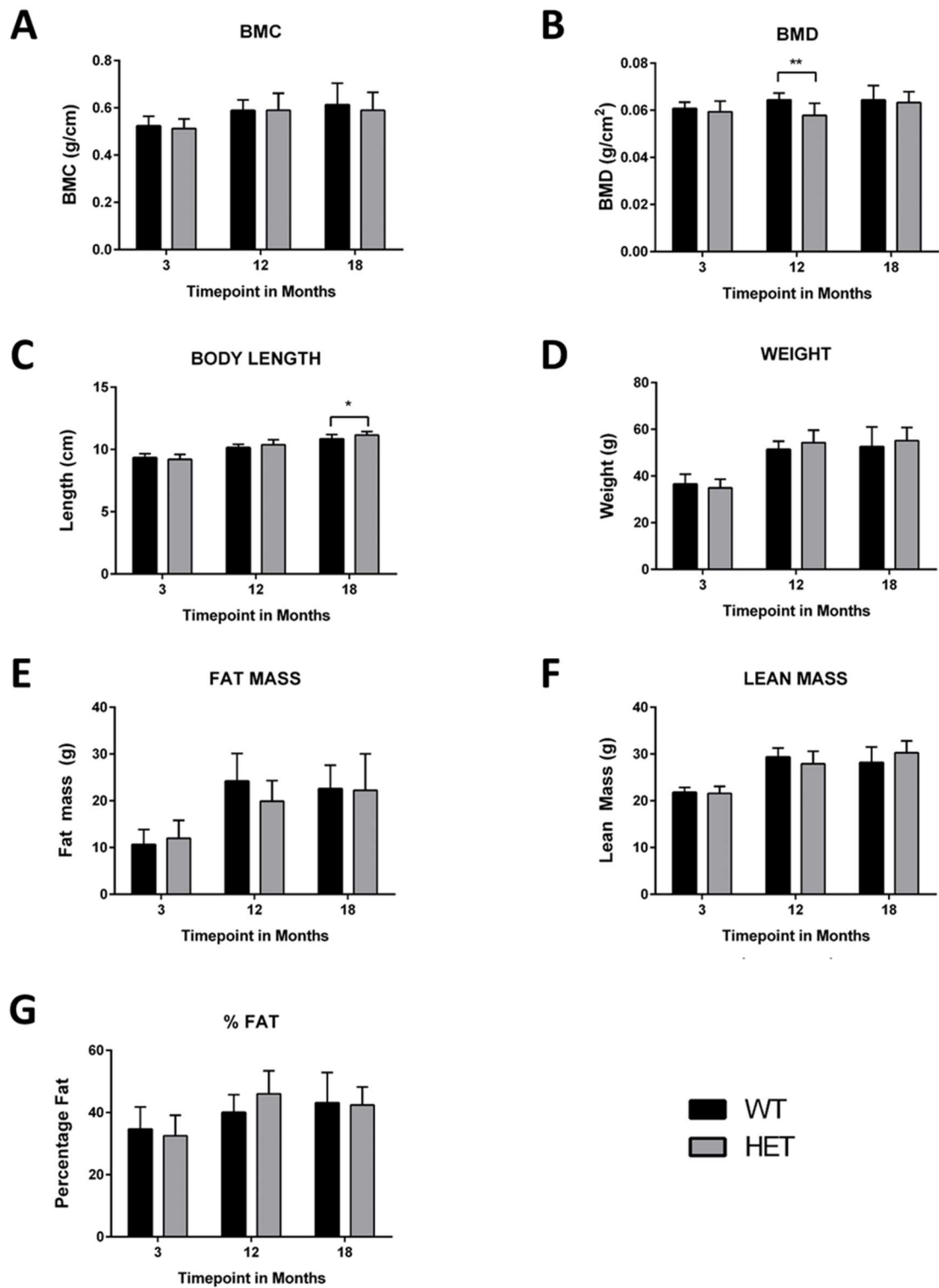


Figure 3.10. Graphs showing the DEXA data from female wild types and heterozygotes at 3-, 12- and 18-month time points. (A) No significant difference in bone mineral content between genotypes at any time point. (B) Heterozygotes (HET, *Col1a2*⁺¹⁰⁷) have a significantly reduced bone mineral density at the 12-month time point compared to wild type (WT, *Col1a2*^{+/+}). (C) Heterozygotes (HET, *Col1a2*⁺¹⁰⁷) have a significantly higher length at the 18-month time point compared to wild type (WT, *Col1a2*^{+/+}). No significant difference between genotypes at any time point in (D) Weight, (E) Fat mass, (F) Lean Mass or (G) Percentage Fat. *P<0.05, **P<0.01.

At 12 months, the heterozygous animals exhibited a reduced BMD compared with the wild-type animals, however at 18 months there was no significant difference between genotypes. Comparing the means across the time points indicate that the heterozygous BMD increased between the 12-month and 18-month time points, meaning there was no difference at 18 months (Table 3.7).

	Wild types			Heterozygotes			P Value
	Mean	SD	N	Mean	SD	N	
3 Months	0.060733	0.002531	9	0.05938	0.004296	10	0.446
12 Months	0.06441	0.002715	10	0.057864	0.004865	11	0.002
18 Months	0.064391	0.005814	11	0.062692	0.004787	12	0.605

Table 3.7. A table showing mean BMD for female animals of both genotypes across the three time points. SD= standard deviation and N = numbers of heterozygotes (*Col1a2^{+/-}*) and wild types (*Col1a2^{+/+}*) across the three time points. Student T-test Significant P<0.05.

It is possible that this was the result of 2 separate phenotypes, the mutation could be causing a reduction in BMD which is statistically significant at 12 months, this reduction is then mitigated due to the extra ossified tissue observed at 18 months by X-ray (Figure 3.3.), which could increase the BMD.

Although the male animals were not part of the X-ray/DEXA pipeline it was decided, after noting the extra bone growth at the knee in 12-month female animals, to scan male animals at 18-months. As there are no other time points to compare the data to, the data is displayed with the 18-month female data, previously shown in Figure 3.10 (Figure 3.11).

It appears the only parameters with significant differences between genotypes in the male animals are to do with adiposity, as both % Fat (WT-Mean-18.61, StDev-3.498, n-3; HET-Mean-26.33, StDev-4.360, n-9; T-Test-P=0.029) and Fat mass (WT-Mean-7.94, StDev-1.34, n-3; HET-Mean-12.58, StDev-2.84, n-9; T-Test-P=0.032) were significantly different between genotypes. The low n number of the wild types (3) coupled with one animal being considerably leaner (13.7% Fat) than the other animals sharing its genotype (20.4-21.7% Fat), mean that these results must be interpreted with caution.

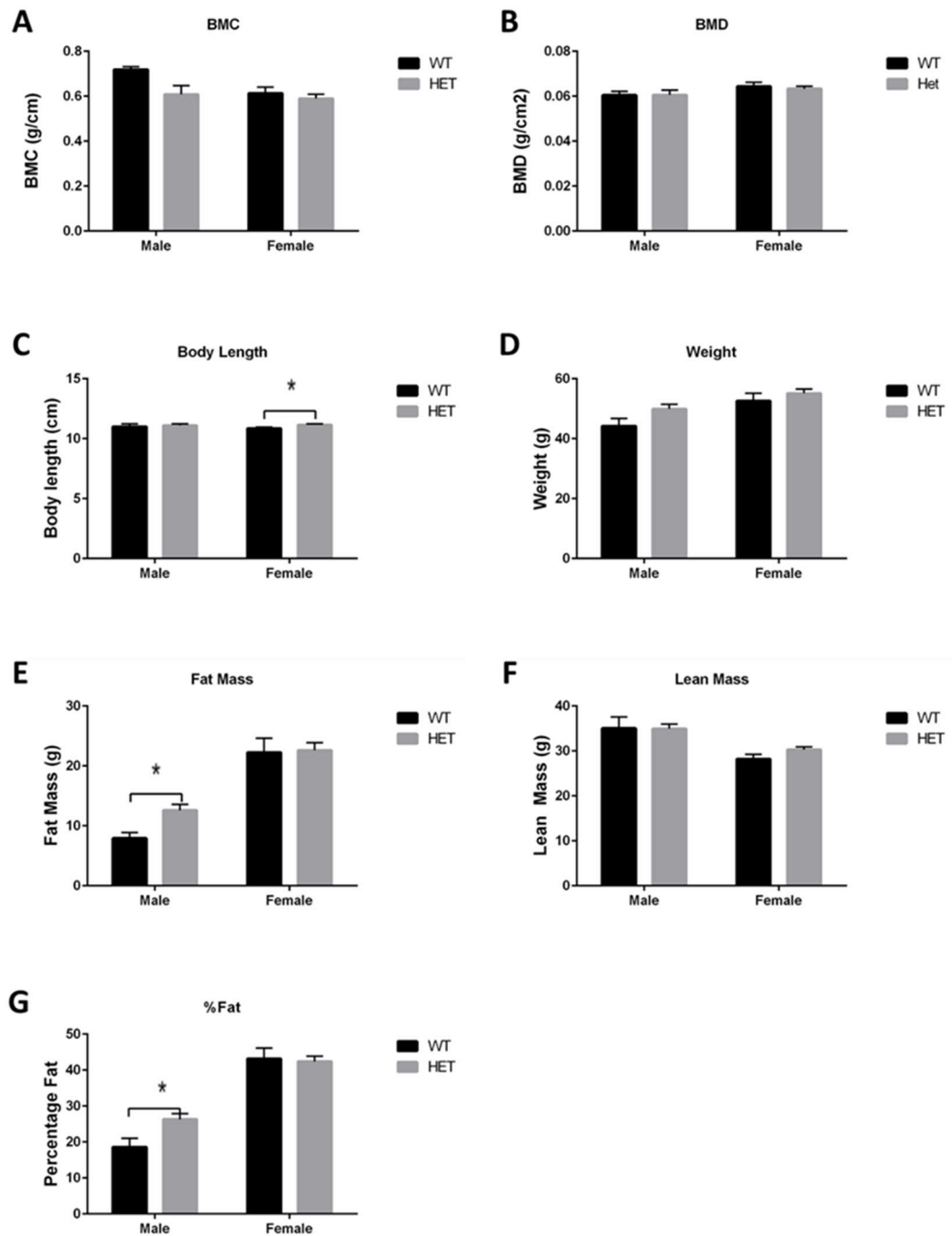


Figure 3.11. Graphs showing the DEXA data from wild types and heterozygotes of both sexes at the 18-month time point. No significant difference in (A) Bone mineral content or (B) Bone mineral density between genotypes in either sex (C) Female heterozygotes (HET, *Col1a2*^{+/¹⁰⁷) have a significantly higher length compared to female wild types (WT, *Col1a2*^{+/⁺). (D) No significant difference in weight between genotypes in either sex. Male heterozygotes showed a significant increase in (E) Fat mass, and (G) Percentage Fat compared to male wild types, no significant differences were identified in females. (F) No significant difference in lean mass between genotypes in either sex. *P<0.05.}}

3.4.3. Clinical Chemistry of the MP-107 G₃ cohort

Blood was collected for a limited clinical chemistry panel at 6 and 12 months from female animals, from the lateral tail vein, and for a larger panel at the 18-month terminal time point, from the retro-orbital sinus. The reason for only performing a limited panel at the earlier time points, is that this was part of a longitudinal study and therefore the amount of blood that could be collected was limited due to welfare regulations at 6 and 12 months. There were no restrictions on the amount of blood that could be collected at the terminal time point, which enabled a larger panel of tests. Male animals in these pipelines were used for metabolic testing, and therefore not available for clinical chemistry.

The plasma from these blood samples were separated via centrifugation and analysed by the clinical chemistry department at MRC Harwell using an Olympus AU400 Bioanalyser (Table 3.8).

To summarise the data presented below in Table 3.8- No significant differences between genotypes were detected in the following assays at any time point: urea, creatinine, calcium, inorganic phosphates, alkaline phosphatase (ALP), alanine aminotransferase (ALT), aspartate aminotransferase (AST), lactate dehydrogenase (LDH), amylase, creatine kinase (CK), sodium, potassium, total cholesterol, low-density lipoproteins (LDL), glucose, triglycerides, glycerol, free fatty acids, iron, uric acid, fructose.

Significant differences were detected in 5 assays, but no assays showed significant differences at more than one time point. Details of these assays are listed below-

- **Total protein** - The heterozygous animals displayed a significantly elevated level when compared with the wild-type animals in the 12-month cohort. No difference was identified in either the 6- or 18-month panel.
- **Albumin** - The heterozygous animals displayed a significantly elevated level when compared with the wild-type animals in the 12-month cohort. No difference was identified in either the 6- or 18-month panel.
- **Bilirubin** - The heterozygous animals displayed a significantly reduced level when compared with the wild-type animals in the 18-month cohort. No difference was

identified in the 12-month panel and this parameter was not included in the 6-month panel.

- **Chloride** - The heterozygous animals displayed a significantly elevated level when compared with the wild-type animals in the 18-month male cohort. This parameter was not included in either the 6- or 12-month panel.
- **High-density lipoproteins (HDL)** - The heterozygous animals displayed a significantly reduced level when compared with the wild-type animals in the 18-month cohort. This parameter was not included in either the 6- or 12-month panel.

The significant differences that were identified in the 12-month samples, total protein and albumin, were not replicated in the 18-month samples, indicating that the differences noted between genotypes are either transient or false positives. The chloride and HDL assays were only measured at 18 months and therefore it is not possible to know if these results are a late onset phenotype, or if these changes occurred in heterozygous animals from an earlier age. The significant difference in bilirubin only occurred at 18 months and there was no significant difference at 12 months indicating this may be a late onset phenotype.

Test	6 Months						12 Months						18 Months								
	Wildtype			Heterozygous			Wildtype			Heterozygous			Wildtype			Heterozygous					
	Mean	SD	n	Mean	SD	n	P-Value	Mean	SD	n	Mean	SD	n	Mean	SD	n	Mean	SD	n	P-Value	
Urea	8.8200	0.9009	10	8.3692	1.2449	13	0.3468	7.9311	1.2748	9	7.6431	0.5432	13	0.4796	8.8717	1.3893	6	9.3858	1.3961	12	0.4714
Creatinine	13.5800	1.6382	10	13.6000	1.7963	12	0.9795	13.1429	2.9985	7	11.9333	1.5348	9	0.2271	12.4333	1.0919	6	13.4333	2.1472	12	0.3037
Calcium	2.4720	0.1040	10	2.4650	0.0766	12	0.8687	2.4622	0.0702	9	2.4646	0.0902	13	0.9475	2.7267	0.1285	6	2.6867	0.1482	12	0.5819
Inorganic Phosphates	9.5580	0.2819	10	9.6846	0.5723	13	0.5135	10.0978	0.2360	9	9.9985	0.2217	13	0.3261	2.4167	0.4637	6	2.5450	0.7122	12	0.6959
ALP	84.2000	16.2099	10	109.6667	36.4859	12	0.0544	100.3556	31.4118	9	99.3231	29.4723	13	0.9381	146.3833	61.3705	6	135.5917	89.4379	12	0.7950
ALT	53.9200	16.8981	10	48.2333	17.9120	12	0.4748	56.5556	20.3432	9	67.8769	28.7902	13	0.3227	166.7167	127.3648	6	105.2500	78.3710	12	0.2208
AST	60.3200	19.7717	10	67.2000	19.8327	13	0.4402	73.1778	17.8369	9	90.8923	35.7670	13	0.1872	217.1167	142.4696	6	154.2417	100.6451	12	0.2918
Total Protein	61.8600	1.9678	10	62.5167	2.0174	12	0.4717	61.3333	1.0176	6	64.1273	3.0299	11	0.0154	62.1500	6.4966	6	55.6083	7.6227	12	0.0916
Albumin	33.3600	0.9992	10	34.4667	1.3888	12	0.0520	32.5333	1.4877	9	34.7231	1.9667	13	0.0106	32.6833	3.5644	6	29.5583	3.8724	12	0.1176
Bilirubin	-	-	-	-	-	-	-	2.5111	0.3665	9	2.8154	0.6150	13	0.2003	3.1000	0.8266	6	2.2000	0.7246	12	0.0304
LDH	333.6000	90.6501	10	385.5000	143.1832	12	0.3371	481.4571	139.2005	7	397.9556	132.1299	9	0.1692	1100.2167	514.7349	6	758.8667	356.3316	12	0.1173
Amylase	753.8000	76.9075	10	772.3333	56.0288	12	0.5545	619.8000	62.0018	7	591.9455	186.1756	11	0.6719	706.9333	168.5311	6	633.4583	122.1330	12	0.3038
CK	45.8000	14.7905	10	46.1667	22.6783	12	0.9658	38.8444	13.2198	9	37.5385	12.4328	13	0.8103	210.3250	106.8676	4	267.5222	185.5283	9	0.5819
Sodium	-	-	-	-	-	-	-	-	-	-	-	-	-	-	148.0000	1.0954	6	148.7500	2.5207	12	0.4362
Potassium	-	-	-	-	-	-	-	-	-	-	-	-	-	-	6.8583	1.3676	6	6.7500	1.3662	12	0.8862
Chloride	-	-	-	-	-	-	-	-	-	-	-	-	-	-	104.8333	1.9508	6	108.0833	3.1214	12	0.0234
Total Cholesterol	-	-	-	-	-	-	-	-	-	-	-	-	-	-	5.0017	1.2692	6	3.8208	1.1520	12	0.1102
HDL	-	-	-	-	-	-	-	-	-	-	-	-	-	-	3.2850	0.8050	6	2.3067	0.7902	12	0.0482
LDL	-	-	-	-	-	-	-	-	-	-	-	-	-	-	0.9900	0.3638	6	0.8050	0.3793	12	0.3741
Glucose	-	-	-	-	-	-	-	-	-	-	-	-	-	-	16.3583	7.3224	6	14.5592	5.3646	12	0.6363
Triglycerides	-	-	-	-	-	-	-	-	-	-	-	-	-	-	2.3100	0.9550	6	3.7000	4.3822	12	0.3349
Glycerol	-	-	-	-	-	-	-	-	-	-	-	-	-	-	470.9500	231.6479	6	553.2333	244.8138	12	0.5320
Free Fatty Acids	-	-	-	-	-	-	-	-	-	-	-	-	-	-	0.6617	0.1702	6	0.9283	0.4122	12	0.0861
Iron	-	-	-	-	-	-	-	-	-	-	-	-	-	-	32.7667	2.6979	6	33.9583	3.8400	12	0.4884
Uric Acid	-	-	-	-	-	-	-	-	-	-	-	-	-	-	268.6400	145.6017	5	294.1333	137.6583	9	0.7787
Fructose	-	-	-	-	-	-	-	-	-	-	-	-	-	-	195.2500	18.7046	6	177.2333	32.1168	12	0.1794

Table 3.8. A table showing the means, standard deviation and n numbers for each clinical chemistry parameter for both wildtype and heterozygous female animals at each time point. The p values for the difference between genotypes is also shown (Student t-test). Tests showing a significant difference between genotypes are highlighted in Yellow.

3.4.4. Histology of the MP-107 G₃ cohort

To investigate the changes observed by X-ray, knee joints from heterozygous and wild-type animals from the G₃ cohort were fixed in 10% neutral buffered formalin before being processed for histology. Initial histology of heterozygote sagittal sections showed the observed bone growth appeared to be severe osteophyte formation, and that there was an absence of cartilage at the load bearing region of the tibial plateau and the femoral condyle (Figure 3.12).

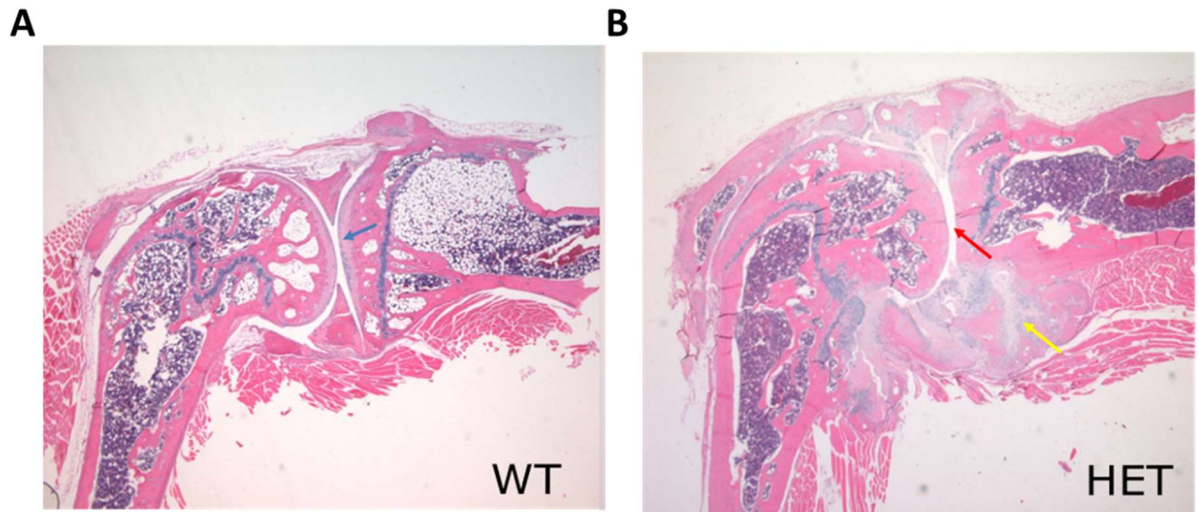


Figure 3.12. H&E stained sections of knee joints from wild types and heterozygotes at 18 months. (A) The wild-type (WT, *Col1a2*^{+/+}) knee joint shows normal healthy cartilage at the articular surface (Blue arrow). (B) The heterozygote (HET, *Col1a2*^{+/¹⁰⁷}) knee joint shows severe osteophyte formation (Yellow arrow) and an absence of articular cartilage on the femoral condyle and tibial plateau (Red arrow).

Due to the two-dimensional nature of histological sections, further sections on a different plane (coronal) were taken from knee joints from heterozygous and wild-type animals (Figure 3.13).

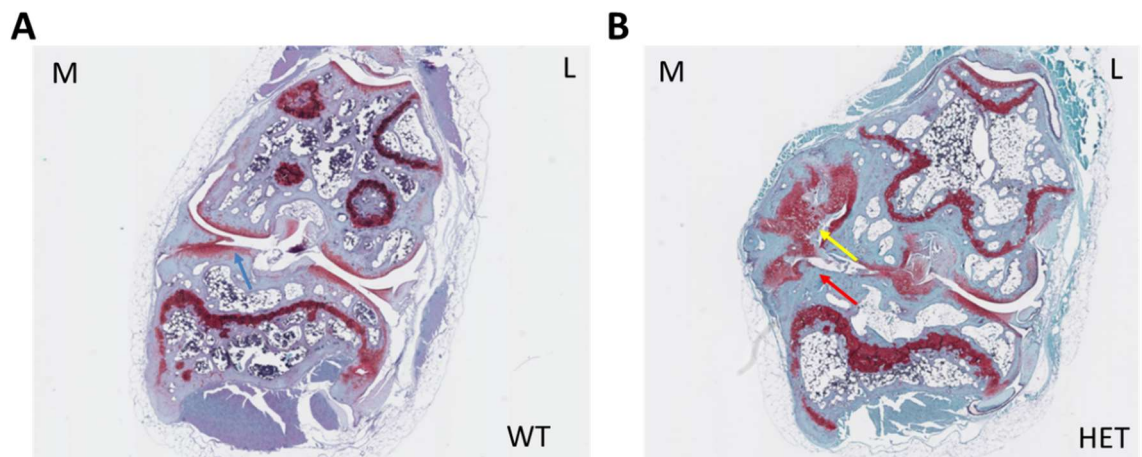


Figure 3.13. Safranin O stained sections of knee joints from wild types and heterozygotes at 18 months. (A) The wild-type joint (WT, *Col1a2*^{+/+}) shows normal healthy cartilage at the articular surface (Blue arrow). (B) The heterozygote knee (HET, *Col1a2*^{+/¹⁰⁷}) shows severe osteophyte formation (Yellow arrow) and an absence of articular cartilage on the femoral condyle and tibial plateau (Red arrow). (Medial side indicated by M, Lateral side indicated by L).

These coronal sections also showed the cartilage loss and severe osteophyte formation in heterozygotes. However, it showed that the cartilage loss was not uniform across both tibial plateaus and femoral condyles, as appeared in the initial sections. This histology indicates a late onset OA phenotype develops in the heterozygotes. *Col1a2* mutations have previously been associated with osteogenesis imperfecta and Ehlers-Danlos syndrome, but not with OA.

3.5. Investigating the Effect of the *Col1a2* Mutation on Coding DNA

Having established the phenotypes present in this line, and that the *Col1a2* mutation is present in all affected animals with genotyping data available, it is important to investigate what specific effect this mutation in the genomic DNA is having downstream.

3.5.1. Sequencing of Embryo DNA Confirms the Homozygous Lethal Phenotype

Genotyping of the original G₃ cohort revealed that no homozygotes were present in the animals that were genotyped, and the ratios of heterozygotes to wild types indicated a homozygous lethal phenotype. To investigate if this was the case, timed intercross matings between male heterozygotes (HET, *Col1a2*^{+/¹⁰⁷}) and female heterozygotes (HET, *Col1a2*^{+/¹⁰⁷}) were established to harvest embryos for genotyping. Genotyping of 18.5

dpc embryos indicated that homozygotes (HOM, *Col1a2*^{107/107}) were present. Sanger sequencing of genomic DNA (gDNA) was used to confirm the presence of the mutation, that was indicated by the genotyping by Lightscanner (Figure 3.14). The Sanger sequencing showed that in addition to the previously noted double peak for adenosine and thymine in the heterozygote and the single peak for thymine in the wild type, the homozygote displayed a single peak for adenosine, confirming that two copies of the mutation are present in these animals, and no wild-type allele is present.

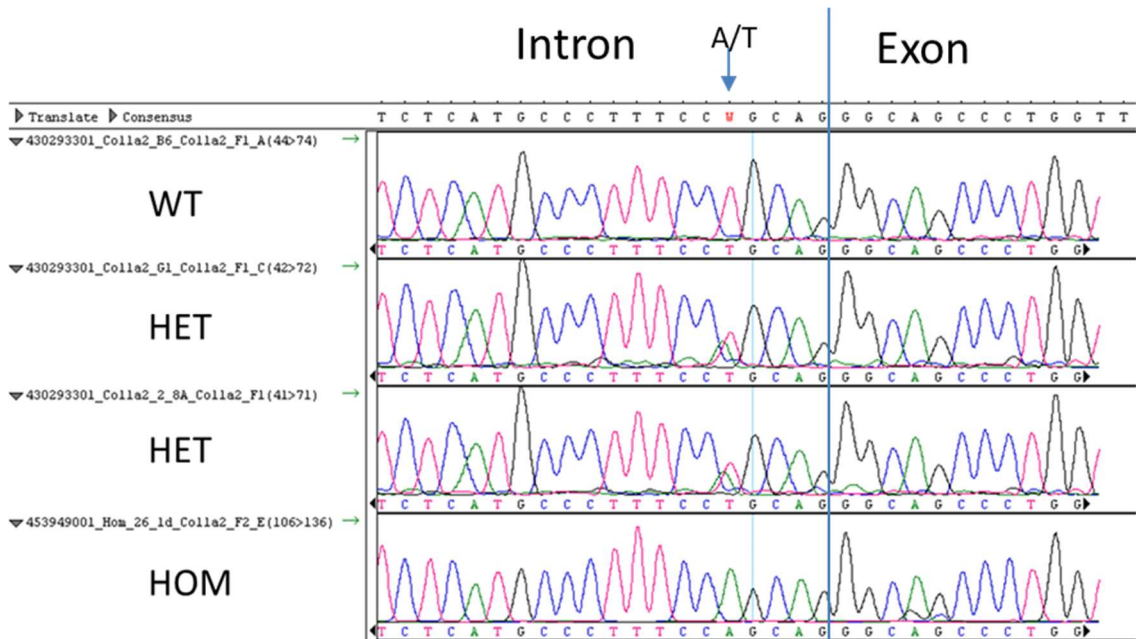


Figure 3.14. Chromatographs showing the nucleotides present at position 4521226 for wild types, heterozygotes and homozygotes. The wild type (WT, *Col1a2*^{+/+}) shows a single 'T' peak indicating the presence of thymine on both alleles, the heterozygotes (HET, *Col1a2*^{+/107}) show a 'T' and an 'A' peaks indicating the presence of a thymine on one allele and adenosine on the other, the homozygote (HOM, *Col1a2*^{107/107}) shows a single 'A' peak indicating the presence of adenosine on both alleles.

3.5.2. Predicting the Impact of the Mutation on the Transcription of the *Col1a2* Gene

Splicing plays an essential role in the transcription of genomic sequence to coding sequence. Mutations in the splice region, either within or close to, the splice donor or acceptor site can have a profound effect on the splicing, leading to issues such as frame shifts and premature stop codons. Splice site prediction software was utilised to predict how this T to an A transversion might affect the coding DNA (cDNA) (Table 3.9).

Using the reference sequence, the three software packages; Fruitfly, Netgene and ASSP, predicted 2 splice acceptor sites. One of which (AG²) was located immediately adjacent to the exon and was predicted by all three software packages, the other (AG¹) was over 80 bases away from the exon and was only predicted by one software package (Fruitfly).

Using the mutant sequence, containing the T to an A transversion, 3 possible splice acceptor sites were predicted. The two mentioned in the paragraph above, which were identified in the reference sequence, and a third splice acceptor site (AG³) which was created by the T to an A transversion. It should be noted that while Netgene and ASSP both predicted the novel splice acceptor site (AG³), they also predicted the splice acceptor site adjacent to the Exon (AG²) that was predicted using a reference transcript.

Reference Transcript						
CATATCTTTCCTCTT AG ¹ GAGAAATGGTGCCTGTCTTAGGAACTCTATCTGATGAGATCTAAAGATTCTCTA ATCTCCTGCCATCTCATGCCCTTCC TGCAG ² GGCAGCCCTGGTTCTCGAGGTCTTCTGGAGCTGATGGCAGA GCTGGTGAATGGTGAGTCACTCATCACTTACTTTCCAGGAAGGACCTTGATAA						
Intron	Exon	Predicted splice acceptor site		Site of T to A transversion		
Software	Type	Score	Confidence	Cut off reached	Predicted splice site	Splice site
FruitFly ^a	Acceptor	-	0.67 [#]	Yes	cctgtctt AG ¹ gaaactc	AG ¹
	Acceptor	-	0.94 [#]	Yes	tttcc TGCAG ² ggcagcc	AG ²
NetGene ^b	Acceptor	-	1*	Yes	tttcc TGCAG ² ggcagcc	AG ²
ASSP ^c	Acceptor	11.11	0.658	Yes	tttcc TGCAG ² ggcagcc	AG ²
<i>AG- Splice acceptor site</i>				<i>^ Intron/Exon boundary</i>		
Mutant Transcript						
CATATCTTTCCTCTT AG ¹ GAGAAATGGTGCCTGTCTTAGGAACTCTATCTGATGAGATCTAAAGATTCTCTA ATCTCCTGCCATCTCATGCCCTTCC AG ³ CAG ² GGCAGCCCTGGTTCTCGAGGTCTTCTGGAGCTGATGGCAG AGCTGGTGAATGGTGAGTCACTCATCACTTACTTTCCAGGAAGGACCTTGATAA						
Intron	Exon	Predicted splice acceptor site		Site of T to A transversion		
Software	Type	Score	Confidence	Cut off reached	Predicted splice site	Splice site
FruitFly ^a	Acceptor	-	0.67 [#]	Yes	cctgtctt AG ¹ gaaactc	AG ¹
	Acceptor	-	0.8 [#]	Yes	tttcc AG ³ cagggcagcc	AG ³
NetGene ^b	Acceptor	-	0.34*	Yes	tttcc AG ³ cagggcagcc	AG ³
	Acceptor	-	0.97*	Yes	tttcc AG ² ggcagcc	AG ²
ASSP ^c	Acceptor	7.867 ⁺	0.468	Yes	tttcc AG ³ cagggcagcc	AG ³
	Acceptor	8.5 ⁺	0.359	Yes	tttcc AG ² ggcagcc	AG ²
<i>AG- Splice acceptor site</i>				<i>^ Intron/Exon boundary</i>		
Splice site predictor software						
a http://www.fruitfly.org/cgi-bin/seq_tools/splice.pl ([#] Acceptor site cut off : 0.4)						
b http://www.cbs.dtu.dk/services/NetGene2 (*Acceptor site cut off: 0.2)						
c http://wangcomputing.com/assp/evaluation.html (⁺ Acceptor site cut off : 2.2)						

Table 3.9. A table showing the predicted splice acceptor sites from three different predictor tools. All three splice site prediction tools predicts an additional splice acceptor site in the mutant transcript, created by the T to an A transversion 5 bases upstream of the intron-exon boundary.

This alternative splice acceptor site, occurring in the mutant sequence, is located 3 bases upstream of the original splice site, if this splice acceptor site is used three bases of intronic sequence would be incorporated into the exon as an extra codon. This is demonstrated in Figure 3.15

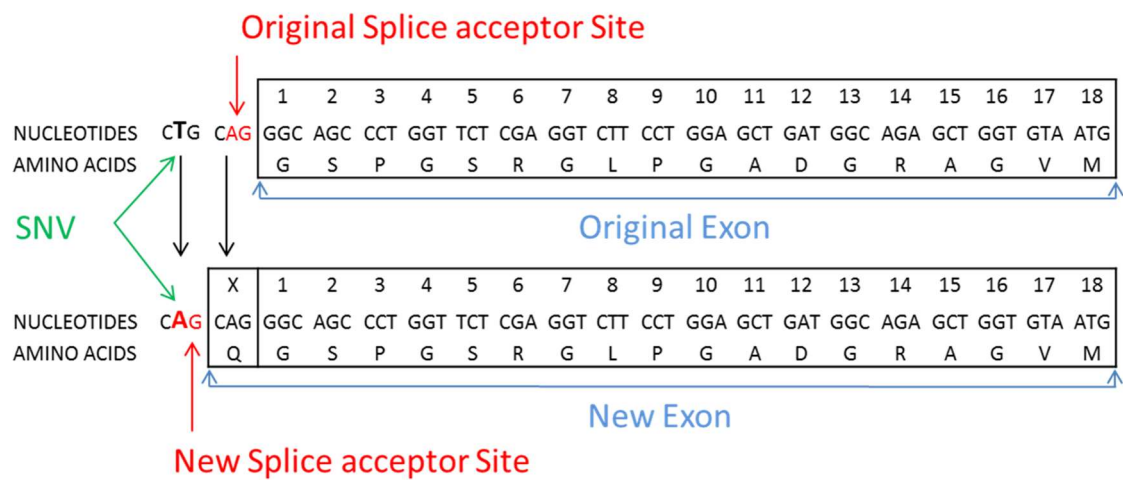


Figure 3.15. A diagram showing how the *Col1a2* mutation affects the exon. The T to an A transversion creates a new splice acceptor site, leading to the incorporation of 3 bases of intronic sequence into the exon as an extra amino acid glutamine (Q).

Collagen I alpha chains contain a repeating glycine motif, whereby every third amino acid is a glycine. This is very important for the formation of the tight triple helix of the heterotrimer. Disruption of this repeating motif is very often deleterious and causes a range of conditions including osteogenesis imperfecta (OI), Ehlers-Danlos Syndrome (EDS), and an overlap condition with elements of both diseases (OI/EDS). The incorporation of 3 intronic bases into Exon 22 will disrupt the repeating glycine motif, as the intronic bases 'CAG' codes for the amino acid Glutamine (Q), when incorporated into the exon. This is demonstrated in Figure 3.16.

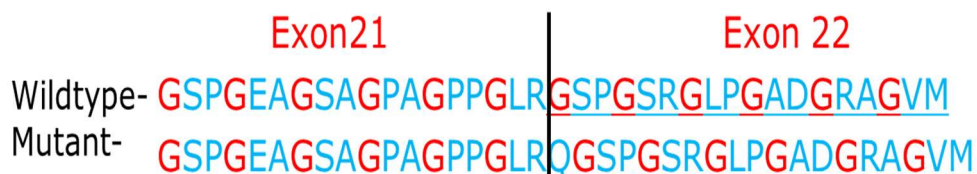


Figure 3.16. A diagram showing the disruption of the repeating glycine motif. The alternative splice acceptor site disrupts the repeating glycine motif in the middle of the helical domain of *Col1a2* by the insertion of the amino acid glutamine (Q). The glycines are represented by the red Gs and amino acids in the X-Y positions are shown in blue.

3.5.3. Confirmation of Effect of the *Col1a2* Mutation on Coding DNA

All splice site prediction tools used, predicted the creation of a novel splice acceptor site, which would be likely to cause the inclusion of intronic sequence as an extra amino acid. To validate this prediction Sanger sequencing of cDNA was used (Figure 3.17)

The forward sequence using a 5' primer (Figure 3.17A) shows the presence of two traces in both the heterozygous sample and in the homozygous sample, from the Exon 21/22 boundary. The reverse sequence using a 3' primer (Figure 3.17B) showed differences in the traces when compared with the forward sequence using a 5' primer. This is due to the 5' primer starting to align the sequence in Exon 21 and then showing 2 traces from the splice site into Exon 22 and the 3' primer starting to align the sequence in Exon 22 and then showing 2 traces from the splice site into Exon 21. In both cases the presence of the second trace is triggered at the Exon 21/22 boundary.

The presence of a double trace in the heterozygous sample was expected as there is one wild-type allele and one mutant allele. However, in the homozygous sample, where both alleles are mutant it was expected there would only be the single trace including the intronic sequence. The presence of a second trace indicates that, even in the presence of two copies of the mutant gDNA transcript, both splice sites located close to Exon 22 (AG² and AG³ in Table 3.9), are being used. It is likely that this is because although a second splice site was created, the original splice site was not destroyed and the spliceosome is using both to some degree. It was predicted by 2 of the splice site prediction softwares (Netgene and ASSP) that the mutation would still allow for splicing at the original splice site.

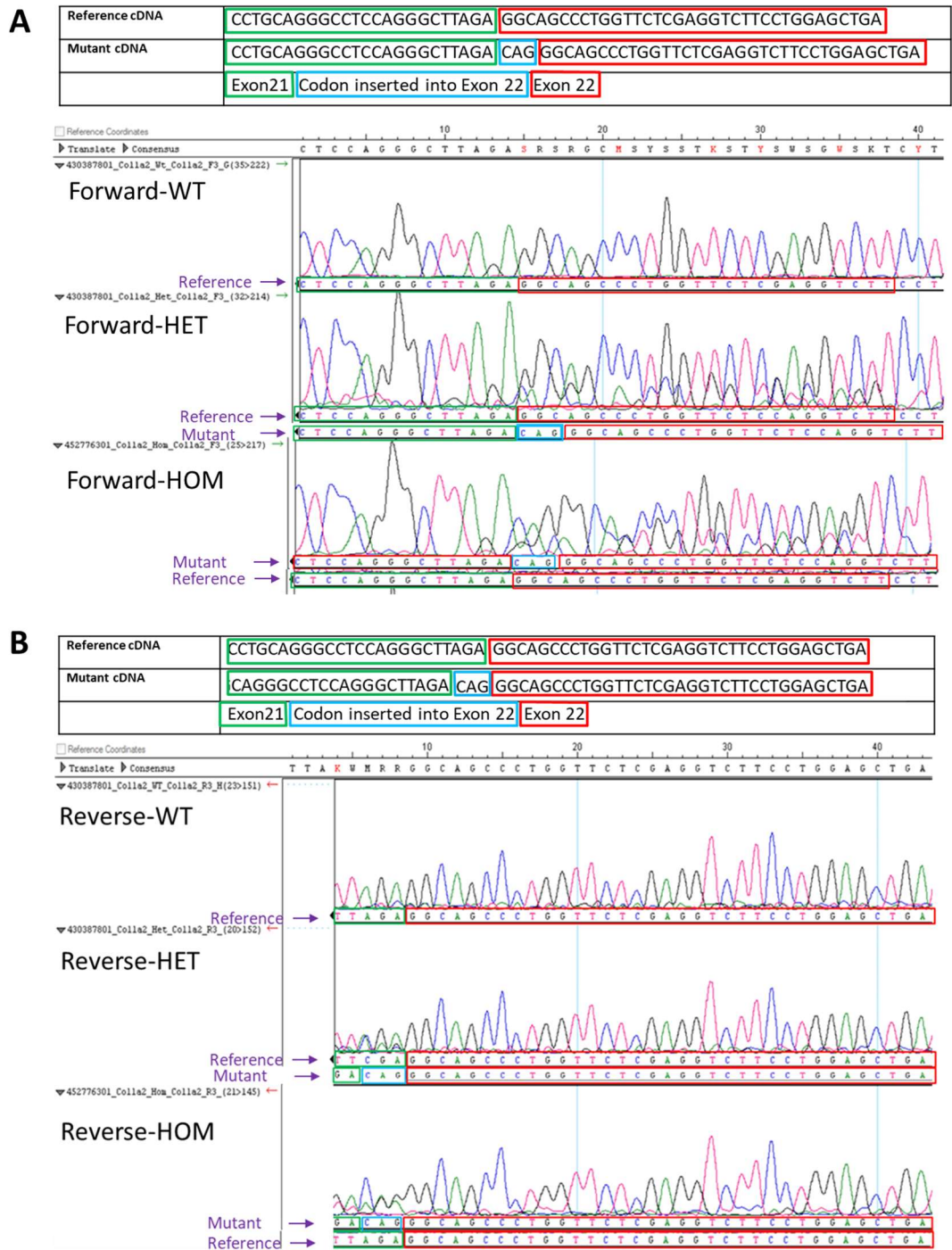


Figure 3.17. Sanger sequencing chromatograms from all three genotypes using both forward (5'→3' primer) and reverse (3'→5' primer). (A) Traces from wild type (WT, *Col1a2*^{+/+}), heterozygotes (HET, *Col1a2*^{+/107}) and homozygotes (HOM, *Col1a2*^{107/107}) cDNA in the 5'→3' direction. The wild type displays the reference sequence only, and the heterozygote and homozygote display both the reference sequence and the mutant sequence (including the additional 'CAG' incorporated from the alternative splicing), with multiple traces visible in the region coding for Exon 22. (B) Traces from wild type (WT, *Col1a2*^{+/+}), heterozygotes (HET, *Col1a2*^{+/107}) and homozygotes (HOM, *Col1a2*^{107/107}) cDNA in the 3'→5' direction. The wild type displays the reference sequence only, and the heterozygote and homozygote display both the reference sequence and the mutant sequence (including the additional 'CAG' incorporated from the alternative splicing), with multiple traces visible in the region coding for Exon 21 and the insertion.

3.5.3.1. Confirmation of Alternative Splicing Using PCR

Sanger sequencing confirmed the hypothesis that the mutation in *Col1a2* would lead to alternative splicing and three bases of intronic sequence being incorporated into the cDNA, resulting in the insertion of an extra amino acid at the beginning of Exon 22. However, the sequencing chromatograms containing two separate traces are difficult to visualise, and could be interpreted incorrectly. To confirm that the presence of multiple traces in the sequencing was due to the presence of multiple transcripts produced by the use of alternative splice acceptor sites, primers were designed across the Exon 21-22 boundary to identify and confirm the alternative transcripts. One of the primers for the mutant primer set incorporated the inserted CAG, meaning that it would only amplify the mutant transcript with the insertion in the cDNA, the primers for the wild-type primer set did not incorporate the inserted CAG, meaning that it would only amplify the wild-type transcript. The PCR products were then imaged on a gel (Figure 3.18). The results indicated that the homozygous and heterozygous animals contain both wild-type and mutant transcript, as previously seen in the sequencing chromatograms, and the wild type animal contains only the wild-type transcript.

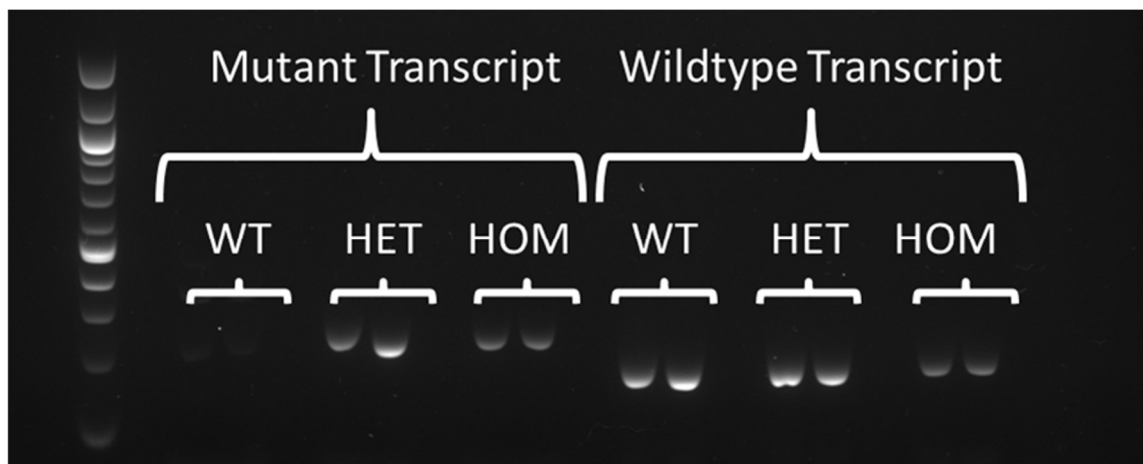


Figure 3.18. PCR products showing the wild-type and mutant transcripts across all three genotypes. Mutant transcript was detected in heterozygous (HET, *Col1a2*^{+/¹⁰⁷}), and homozygous (HOM, *Col1a2*^{107/107}) cDNA. Wild-type transcript was detected in wild-type (WT, *Col1a2*^{+/+}), heterozygous (HET, *Col1a2*^{+/¹⁰⁷}), and homozygous (HOM, *Col1a2*^{107/107}) cDNA, despite the lack of wild-type alleles in the homozygous gDNA. For the primers used, see Section 2.2.2.

3.5.3.2. Confirmation of Alternative Splicing Using qPCR

The PCR of cDNA demonstrated that there was still wild-type transcript being produced in the mice that were homozygous for the mutation, despite not having a wild-type

allele. In order to examine if the alternative use of the splice acceptor sites were uniform or random, relative expression of the 2 alternative transcripts were measured using custom Taqman probes (Figure 3.19). The expression data again showed that wild-type transcript was present in the homozygous mutant samples, however the wild-type transcript was present in much lower levels than in the heterozygous sample, indicating that the splicing occurs at the novel splice site preferentially. The reason why splicing still occurs at the original splice site is unclear.

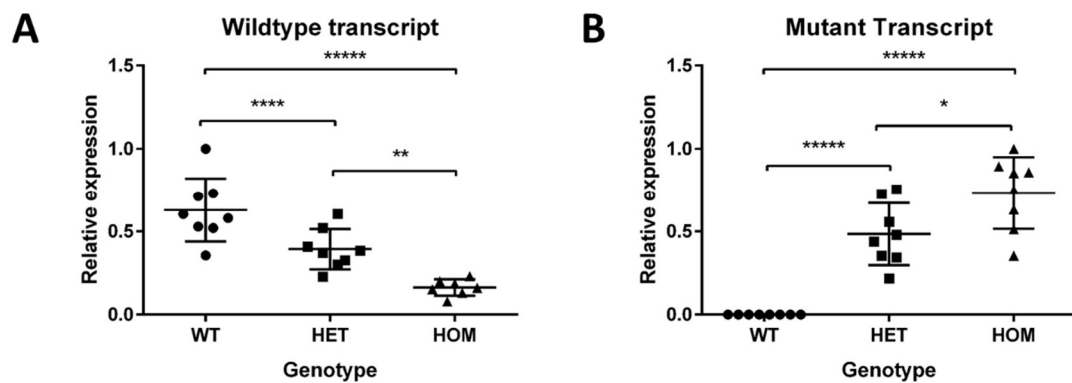


Figure 3.19. Graphs showing relative expression of wild-type and mutant transcript using custom Taqman probes across all three genotypes. (A) The relative expression of the wild-type transcript was shown to be significantly higher in wild types (WT, *Col1a2*^{+/+}), than heterozygotes (HET, *Col1a2*^{+/¹⁰⁷) and homozygotes (HOM, *Col1a2*^{107/107}), and significantly higher in heterozygotes (HET, *Col1a2*^{+/¹⁰⁷) than homozygotes (HOM, *Col1a2*^{107/107}). Note that homozygotes are producing wild-type transcript. (B) The relative expression of the wild-type transcript was shown to be significantly lower in wild types (WT, *Col1a2*^{+/+}), than heterozygotes (HET, *Col1a2*^{+/¹⁰⁷) and homozygotes (HOM, *Col1a2*^{107/107}), and significantly lower in heterozygotes (HET, *Col1a2*^{+/¹⁰⁷) than homozygotes (HOM, *Col1a2*^{107/107}). Note that wild types are not producing mutant transcript. (For all genotypes n=8, One-way Anova- *P<0.05, **P<0.01, *** P<0.001, **** P<0.0001, ***** P<0.00001. For Taqman probe details see section 2.2.5).}}}}

As previously stated, the disruption of the glycine repeating motif can have a severe effect on the collagen I heterotrimer. To investigate if the expression of *Col1a1* was altered due to the mutation in *Col1a2*, relative expression of *Col1a1* and *Col1a2* was measured using Taqman probes (Figure 3.20). There is no significant difference between genotypes in the relative expression of *Col1a2*. The relative expression of *Col1a1* is significantly reduced in the homozygotes, when compared to the heterozygotes and wild types. This data likely means that in the homozygous *Col1a2*^{107/107} animals *Col1a1* is downregulated. The reason for this downregulation is unclear, however it may be related to impaired trimerisation of the pro-collagen I molecule, as this is where the pro

$\alpha 1$ and pro $\alpha 2$ chains interact. *Col1a1* expression has been found to be downregulated in chondrocytes of a mouse model of OI with a mutation in *Col1a2* (*G610C*) [250].

This reduction in relative expression may be dose dependant, as there is no difference between wild type and heterozygotes in *Col1a1* expression, even with the increased levels of mutant transcript and decreased levels of wild-type transcript in the heterozygotes when compared with wild type.

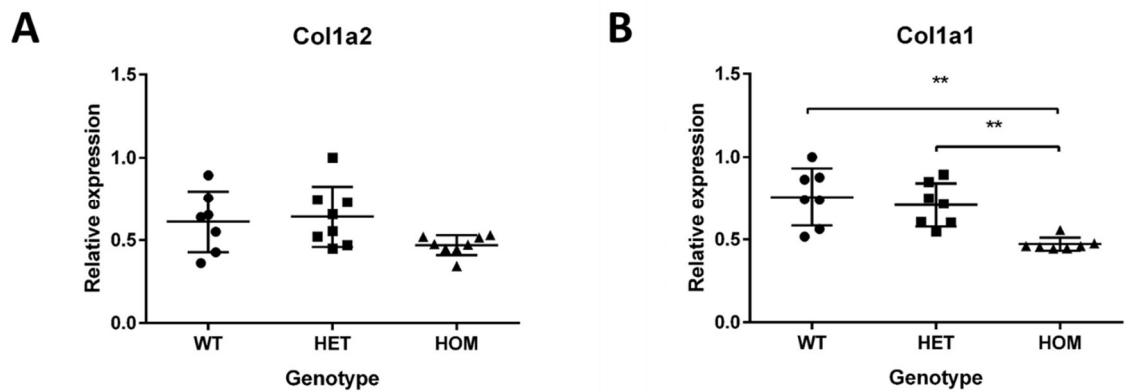


Figure 3.20. Graphs showing relative expression of *Col1a2* and *Col1a1* across all three genotypes. (A) There was no significant difference in relative expression of *Col1a2* between any of the genotypes. (B) The relative expression of *Col1a1* was shown to be significantly reduced in homozygotes (HOM, *Col1a2*^{107/107}), when compared to heterozygotes (HET, *Col1a2*^{+ /107}) and wild types (WT, *Col1a2*^{+ /+}), there was no significant difference between to heterozygotes (HET, *Col1a2*^{+ /107}) and wild types (WT, *Col1a2*^{+ /+}). (For all genotypes n=8, One-way ANOVA **P<0.01. Taqman probe used were *Col1a1*-Mn00801666_g1, *Col1a2*-Mm00483888_m1).

3.6. *Col1a2*^{107/107} Phenotypes

3.6.1. Identification of Perinatal Lethality in MP-107 Homozygotes

We observed that there were no adult homozygous *Col1a2*^{107/107} animals in the G₃ cohort, or in subsequent cohorts produced. However, viable homozygous *Col1a2*^{107/107} embryos were present at 18.5 dpc, indicating a perinatal lethal phenotype. In order to investigate the lethality and the phenotypes present in the homozygous *Col1a2*^{107/107} embryos, intercross mating between heterozygous *Col1a2*^{+ /107} male and heterozygous *Col1a2*^{+ /107} female MP-107 animals were established. Initially the number of offspring

were recorded, and then genotyped 21 days postnatally (P21), and a subsequent cohort was harvested and genotyped at 18.5 dpc (Figure 3.21).

The numbers of each genotype observed at 18.5 dpc do not differ significantly from Mendelian ratios ($\chi^2= 5.13$, 2df, $P<0.05$) and indicate that the homozygous animals are viable throughout gestation.

By comparison, the analysis of P21 mice arising from the intercross mating between heterozygous *Col1a2*^{+/¹⁰⁷} male and heterozygous *Col1a2*^{+/¹⁰⁷} female MP-107 animals demonstrated a complete lack of homozygous *Col1a2*^{107/¹⁰⁷} animals. The numbers of surviving mice, heterozygotes and wild-type, conform to a 2:1 mendelian ratio that would be expected if homozygotes are embryonic lethal ($\chi^2= 1.04$, 1df, $P<0.3$). In these intercross cohorts, the number of animals that were recorded at birth, but subsequently went missing prior to weaning were significant (11/50 animals born) suggesting that the *Col1a2*^{107/¹⁰⁷} animals die shortly after birth. If these missing animals were assumed to be homozygotes then the numbers conform to the expected mendelian ratio ($\chi^2= 1.32$, 2df, $P<0.5$).

In one subsequent litter, two animals were observed gasping and were culled for welfare reasons on the day of birth. Genotyping of these animals indicated that these animals were homozygote *Col1a2*^{107/¹⁰⁷}.

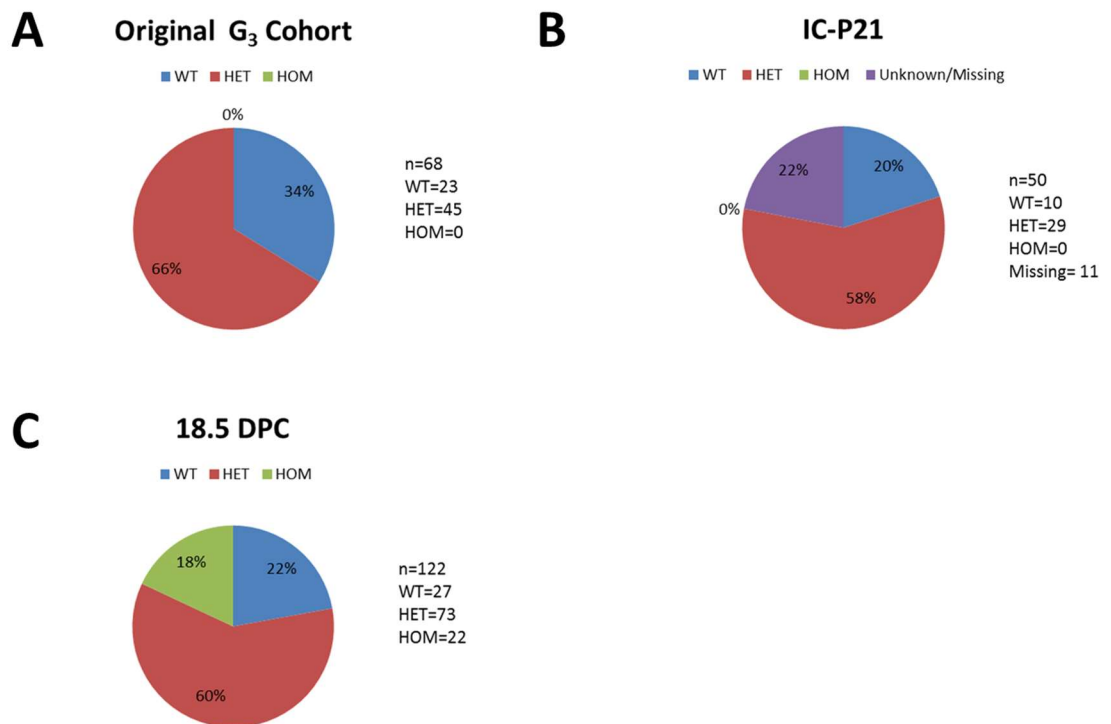


Figure 3.21. Genotyping data of embryonic and weaned animals indicate a perinatal lethal phenotype. (A) Genotyping data from the original G₃ cohort show that there were no homozygous (HOM, *Col1a2*^{107/107}) animals present and a 2:1 ratio of heterozygous (HET, *Col1a2*^{+ /107}) to wild-type (WT, *Col1a2*^{+ /+}) animals indicating that the mutation is homozygous lethal. (B) Genotyping data for P21 animals produced from intercross matings between heterozygous *Col1a2*^{+ /107} male and heterozygous *Col1a2*^{+ /107} female MP-107 animals showed that there were no homozygous (*Col1a2*^{107/107}) animals present. However, 22% of animals recorded at birth were found to be missing by weaning and were therefore not genotyped at P21. At P21 the heterozygous (*Col1a2*^{+ /107}) to wild-type (*Col1a2*^{+ /+}) animals were not significantly different from the expected 2:1 Mendelian ratios that would be expected if homozygotes are embryonic lethal ($\chi^2 = 1.04$, 1df, $P > 0.3$). (C) Genotyping data of the 18.5 dpc embryos collected from intercross mating between heterozygous *Col1a2*^{+ /107} male and heterozygous *Col1a2*^{+ /107} female MP-107 animals showed that homozygous (*Col1a2*^{107/107}) animals were viable at 18.5 dpc. The number of genotypes did not differ significantly from Mendelian ratios ($\chi^2 = 5.13$, 2df, $P > 0.05$).

3.6.2. Embryonic Lung Phenotype in MP-107 Homozygotes

The perinatal lethal phenotype of the *Col1a2*^{107/107} animals could have a variety of causes. However, the observation of *Col1a2*^{107/107} pups gasping indicated that the respiratory system could be the cause. To investigate this, 18.5 dpc embryos were harvested and the lungs fixed for histological processing. Initial evaluation of H&E stained sections of the lungs showed a thickened interstitial mesenchyme with decreased space within the airways (Figure 3.22).

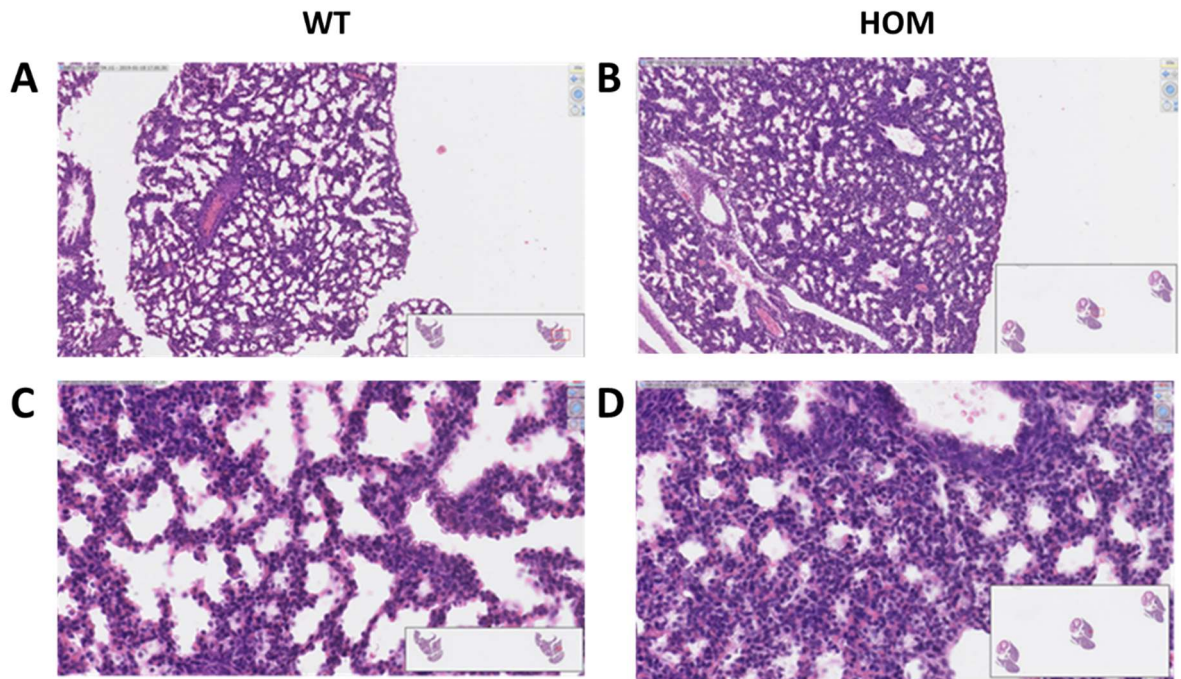


Figure 3.22. Histological sections of 18.5 dpc embryonic lung tissue of wild-type and homozygous embryos. Homozygous animals (HOM, *Col1a2*^{107/107}) (B&D) show a thickened interstitial mesenchyme, and narrowed airways, compared to the wild-type animals (WT, *Col1a2*^{+/+}) (A&C). Sections stained with haematoxylin and eosin (H&E), magnification of 10x (A&B) and 40X (C&D).

To quantify these apparent differences, the diameters of the airways and the number of airways were measured at X40 magnification [251] (Figure 3.23).

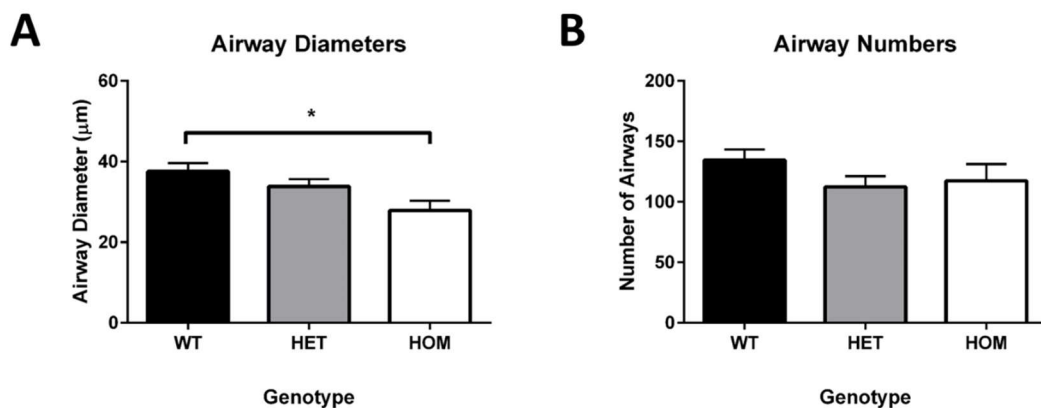


Figure 3.23. Analysis of airway size and airway number in the lungs of the three genotypes. (A) Homozygotes (HOM, *Col1a2*^{107/107}) had significantly reduced airway diameters, when compared with wild types (WT, *Col1a2*^{+/+}), no difference was detected between the heterozygotes (HET, *Col1a2*⁺¹⁰⁷ and the other two genotypes. (B) No significant difference was detected between genotypes in airway number. (ANOVA, * P<0.05, N- WT=8, Het=15, Hom=12).

It was observed that the number of airways did not significantly vary between genotypes, however the *Col1a2*^{107/107} animals had significantly smaller airways, when

compared with the *Col1a2*^{+/+} animals. There was no significant difference between the *Col1a2*^{+/¹⁰⁷} animals, and either *Col1a2*^{+/+} or *Col1a2*^{107/107} animals. This reduction in the size of the airways was likely due to the thickened interstitial mesenchyme expanding into the airways in the *Col1a2*^{107/107} animals.

3.6.3. Whole Mount Embryonic Skeletal Staining of MP-107 Embryos

Due to the lethal phenotype, it was not possible to observe any bone phenotype in the adult *Col1a2*^{107/107} animals. To investigate if there were any bone phenotypes in the *Col1a2*^{107/107} embryos, 18.5 dpc embryos were harvested and fixed, before undergoing skeletal staining using Alizarin red and Alcian blue. This staining allows the skeletal structure of the embryo to be visualised. Alizarin red binds to calcium, causing bones to be stained red, and Alcian blue binds to sulphated glycosaminoglycans present in cartilage, causing cartilaginous tissue to be stained blue [252] (Figure 3.24).

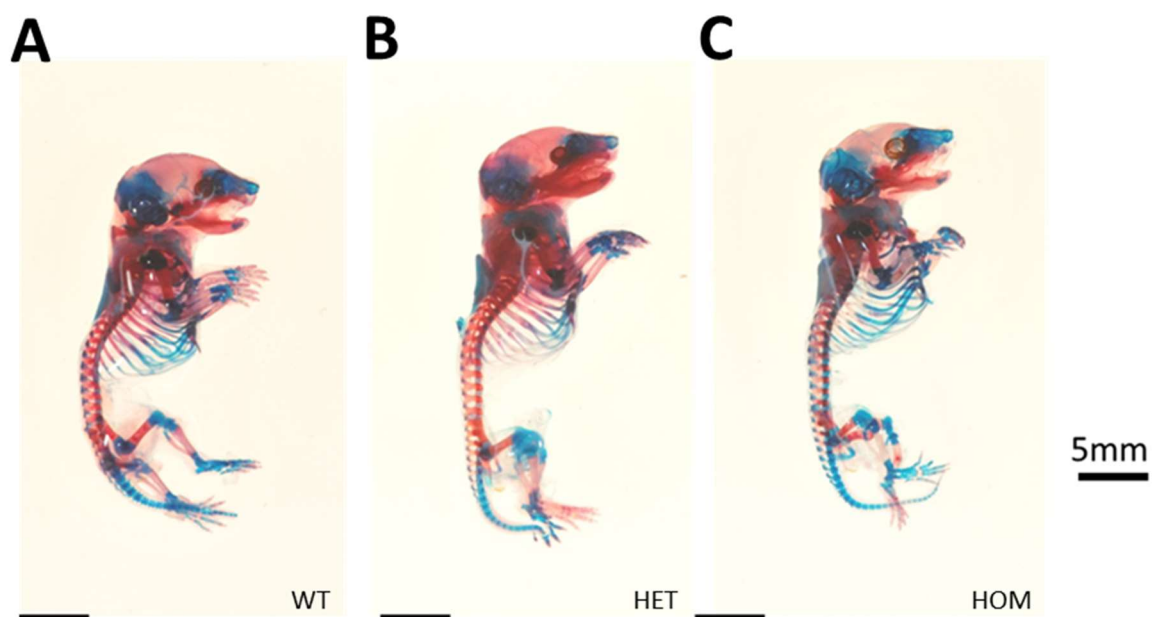


Figure 3.24. Whole-mount embryonic skeletal staining, of 18.5 dpc embryos of all three genotypes using Alizarin red and Alcian blue. All three genotypes, (A) wild type (WT, *Col1a2*^{+/+}), (B) heterozygote (HET, *Col1a2*^{+/¹⁰⁷}) and (C) homozygote (HOM, *Col1a2*^{107/107}) show similar gross morphology at 18.5 dpc.

There were no overt differences in size, including crown to rump length, however it was noted that the homozygous (*Col1a2*^{107/107}) animals had some evidence of deformation in the long bones, including bones being angled rather than straight (Figure 3.25). The defects observed in the humeri and femurs are likely caused by breakage of the bones in utero, due to the angled rather than straight bone and deeper red staining indicating

presence of extra bone. The presence of breaks in these bones indicate that the homozygous *Col1a2*^{107/107} mutation is leading to an OI phenotype.

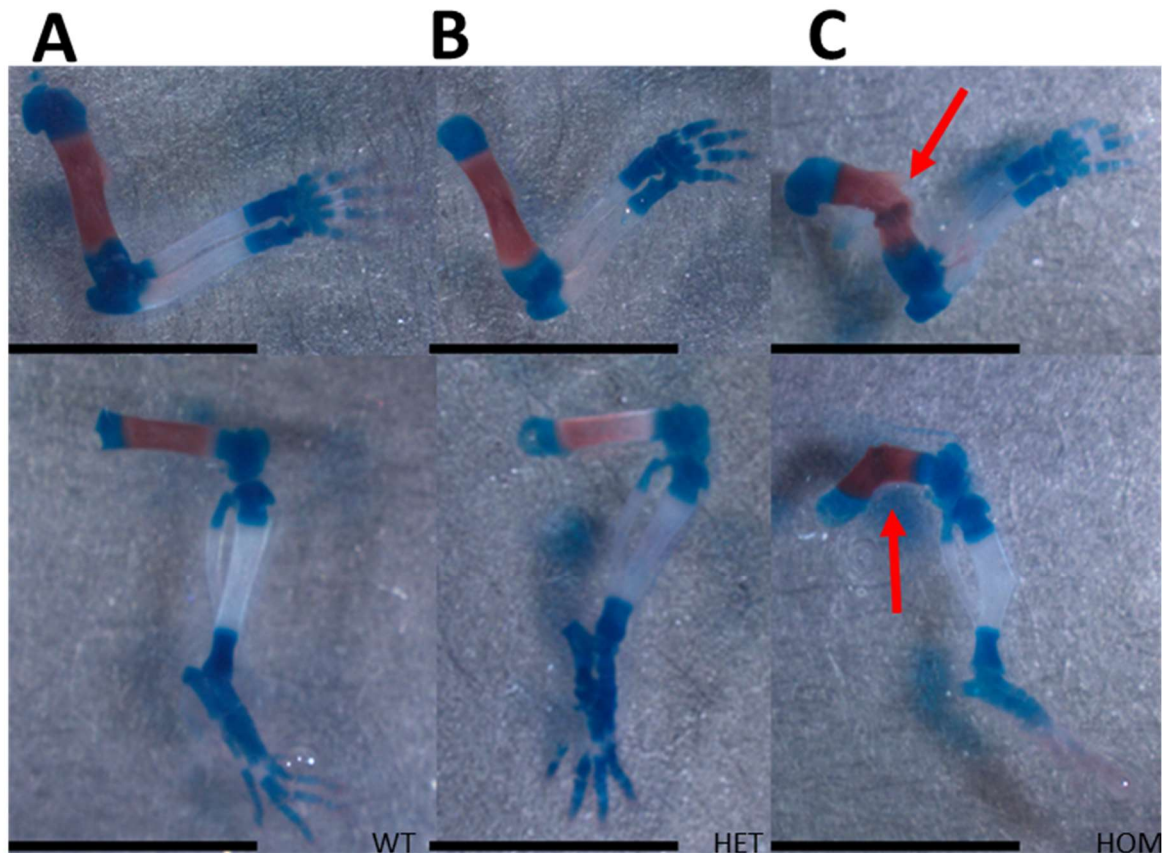


Figure 3.25. Dissected limbs of 18.5 dpc embryos of all three genotypes stained using Alizarin red and Alcian blue. (A) Wild type (WT, *Col1a2*^{+/+}) and (B) heterozygotes (HET, *Col1a2*^{+/107}) show no deformity of the long bones. (C) The humerus and femur of the homozygotes (HOM, *Col1a2*^{107/107}) shows apparent breakage, indicated by deeper red staining and a deviation in angle (red arrows) compared with the straight bones seen in wild types (WT, *Col1a2*^{+/+}), and heterozygotes (HET, *Col1a2*^{+/107}). Scale bar=5mm

3.7. Deep Phenotyping of MP-107 Over a 2-18 Month Time Course

3.7.1. Overview of Animals and Time Points

The initial phenotyping cohort showed early mild bone abnormalities, and a late onset OA phenotype. The main focus of this phenotyping was to investigate the OA phenotype, due to the progressive nature of the phenotype, and its clinical relevance. The ischia and olecranon phenotypes were also investigated, but to a lesser degree.

The presence of osteophytes was detectable by X-ray in a number of animals at 12 months of age; however, the earliest point of detection is likely at some point between 3 and 12 months. As part of an ageing pipeline, it was not possible to do histology on the joints until the terminal time point at 18 months, meaning there was no data on the early progression of the disease, only of late-stage OA. In order to overcome this, a time course was established with 7 cohorts, consisting of 10 wild type animals (5 of each sex) and 10 heterozygous animals (5 of each sex), totalling 140 animals. These animals were aged to specific time points before undergoing a phenotyping pipeline, culminating in a terminal bleed, and harvesting of tissues to enable *ex vivo* analysis such as μ CT and histology (Figure 3.26). The time points chosen were 2, 4, 6, 9, 12, 15 and 18 months old.

The fact that each cohort was bred only for a specific time point, not as part of a longitudinal study, has the benefit of allowing in-depth histology and μ CT analysis at each time point, however it is not without its drawbacks. As previously mentioned, the splicing, and therefore effect of the mutation, varies and therefore there will be some variation between individual animals in each phenotype. The cohort size was designed to allow sufficient numbers for analysis, and to balance the logistics of ageing multiple cohorts before phenotyping.

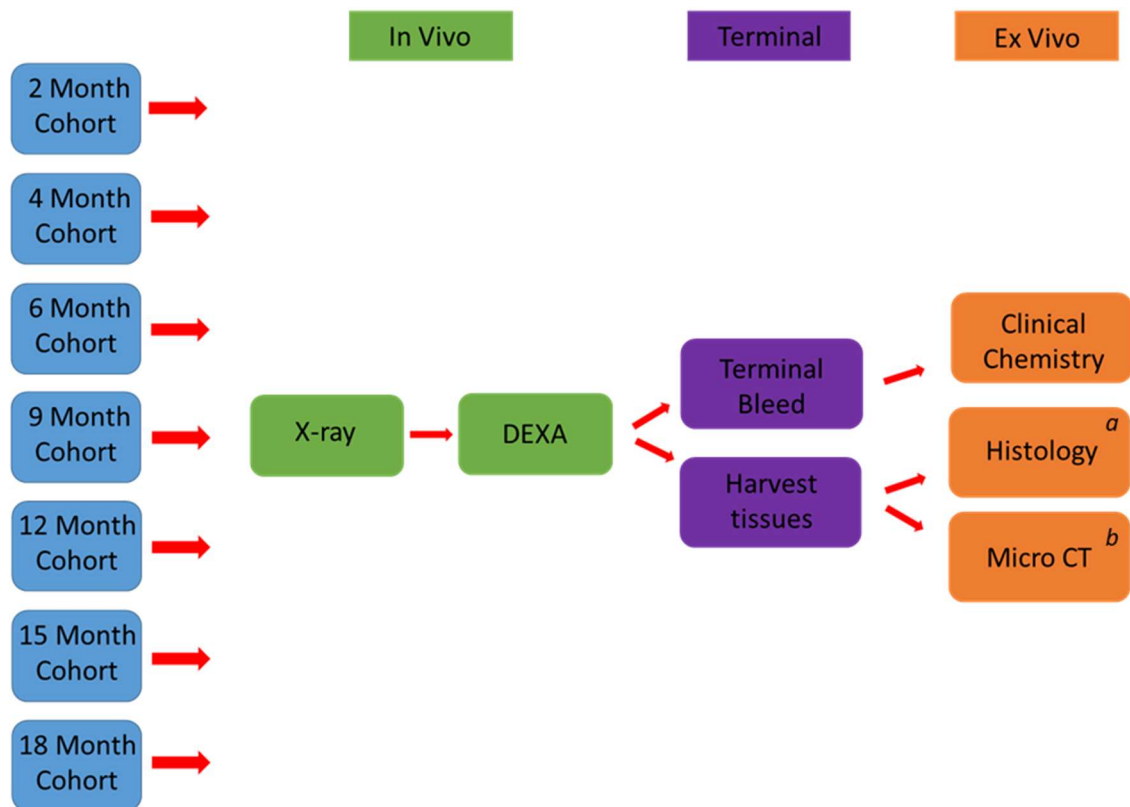


Figure 3.26. A diagram showing the seven different cohorts and the phenotyping pipeline which each underwent. Each cohort was made up of 5 animals of each sex/genotype- (Male Het n=5, Male WT n=5, Female Het n=5, Female WT n=5), all animals underwent all procedures, except ^a-only 4-, 9-,12- and 18-month cohorts, ^b-only 4-, 9- and 18-month cohorts.

3.7.2. X-ray Imaging of MP-107 Animals

Each cohort underwent X-ray imaging to examine the bone phenotypes at the assigned time point. The main purpose of this imaging was to assess when the abnormal bone growth at the knee first presented, as the G₃ cohort indicated the early phenotypes do not change in severity. Radiographs were taken under terminal anaesthesia, so that the resolution, and number, of images were not limited due to Home Office licence restrictions, and were evaluated for any abnormalities, blind to the genotype.

High-resolution radiographs of examples of wild type and heterozygote pelvises at each of the time points, show evidence of splayed ischia in some heterozygotes at every time point (Figure 3.27), emphasising the variability in these phenotypes.

High-resolution radiographs of examples of wild type and heterozygotes elbow joints at each of the time points, show evidence of curved olecranons in some heterozygotes at

every time point, with the exception of the 9-month time point where no animals exhibited the curved olecranon phenotype (Figure 3.28). Additionally, radiographs of two heterozygous animals, one in each of the 4- and 6-month cohorts, which exhibited the curved olecranon, also exhibited evidence of a fracture in the ulna (shown in Figure 3.28). While a break was only visible by X-ray in two of the animals exhibiting the curved olecranon phenotype, the phenotype may be the result of a fracture in the ulna, while the bone was growing. This could explain the variability in the phenotype, as only heterozygotes that sustained a fracture would develop this phenotype.

High-resolution radiographs of examples of wild type and heterozygotes knee joints at each of the time points show evidence of abnormal bone growth at the knee in heterozygotes at the 9-, 12-, 15- and 18-month time points (Figure 3.29).

Lower resolution full body radiographs of heterozygotes and wild types at each time point are included in Appendix 3.

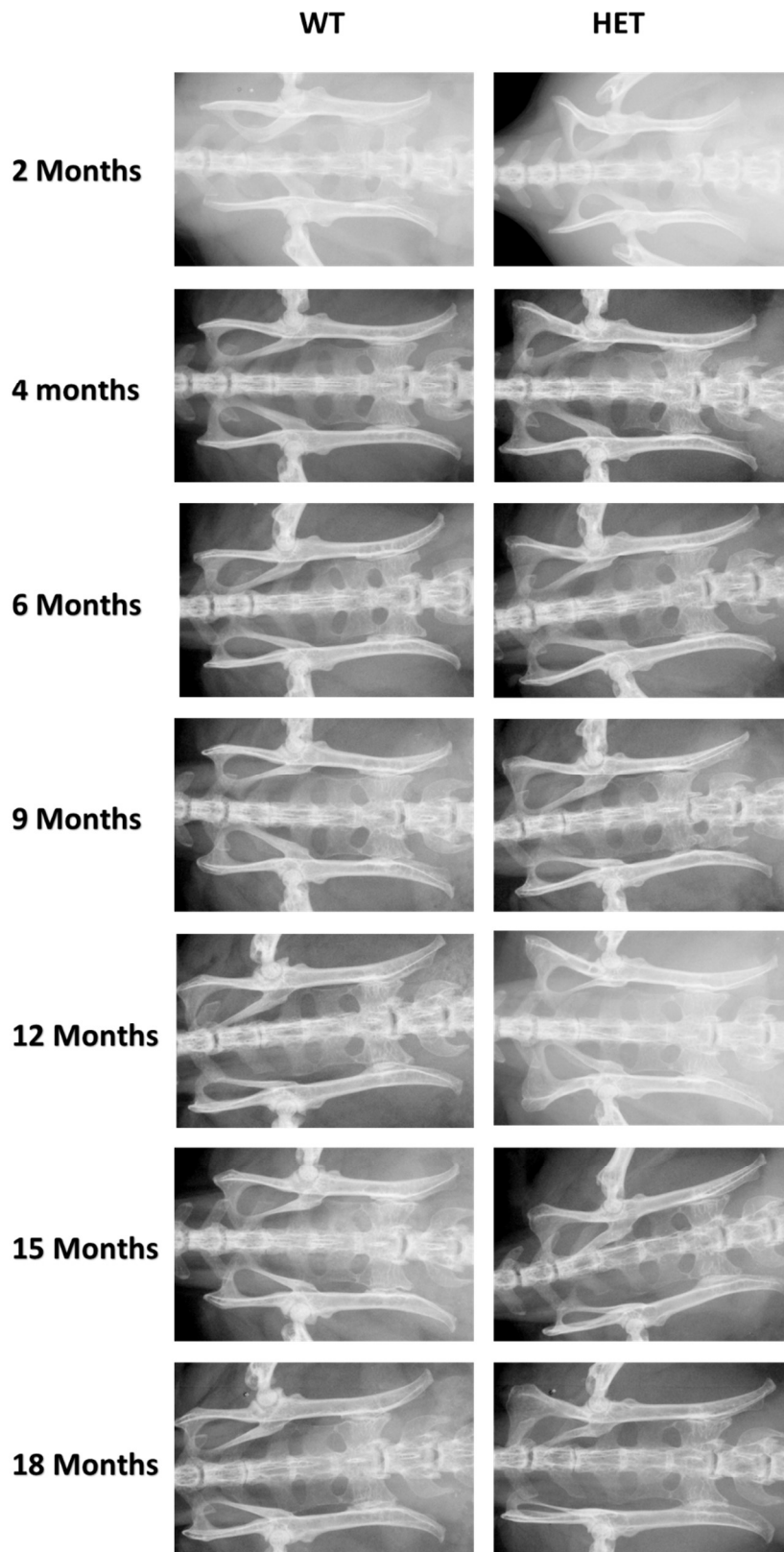


Figure 3.27. Examples of high-resolution radiographs of wild-type (WT, *Col1a2*^{+/+}) and heterozygous (HET, *Col1a2*^{+/¹⁰⁷}) pelvises at each of the time points. At every time point, at least 40% of heterozygotes exhibited the splayed ischia phenotype.

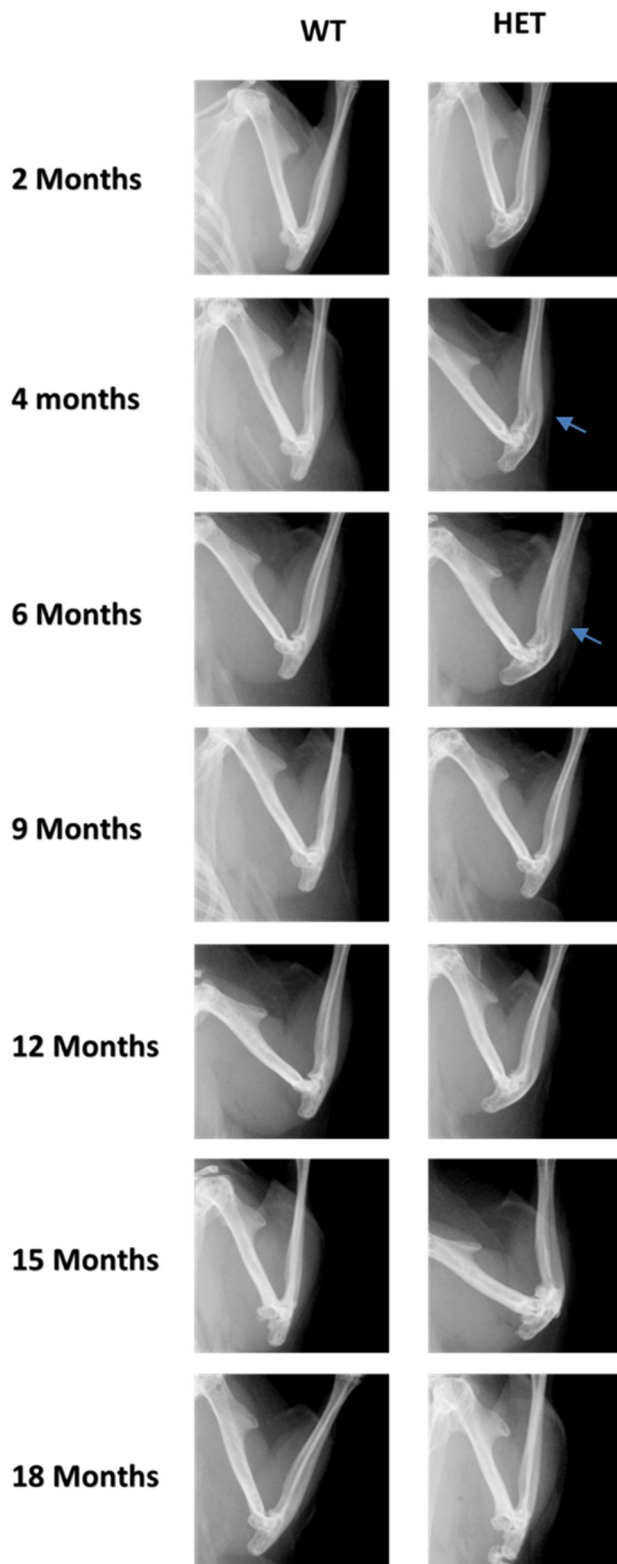


Figure 3.28. Examples of high-resolution radiographs of wild-type (WT, Col1a2+/+) and heterozygous (HET, Col1a2+/107) elbow joints at each of the time points. At every time point, with the exception of the 9-month time point, at least one heterozygote exhibited the phenotype. Two heterozygotes exhibiting the curved olecranon at 4- and 6-months showed evidence of a fracture in the ulna (Blue arrows).



Figure 3.29. Examples of high-resolution radiographs of wild-type (WT, *Col1a2*^{+/+}) and heterozygous (HET, *Col1a2*^{+/¹⁰⁷) knee joints at each of the time points. At every time point after the 9-month time point, at least 50% of heterozygotes exhibited the abnormal bone growth phenotype (Blue arrows). At the 2-, 4- and 6-month time points no evidence of abnormal bone growth at the knee was detected.}

Incidences of the three phenotypes observed by X-ray often coincided with each other. Figure 3.30 shows the number of animals in each cohort with each phenotype or collection of phenotypes.

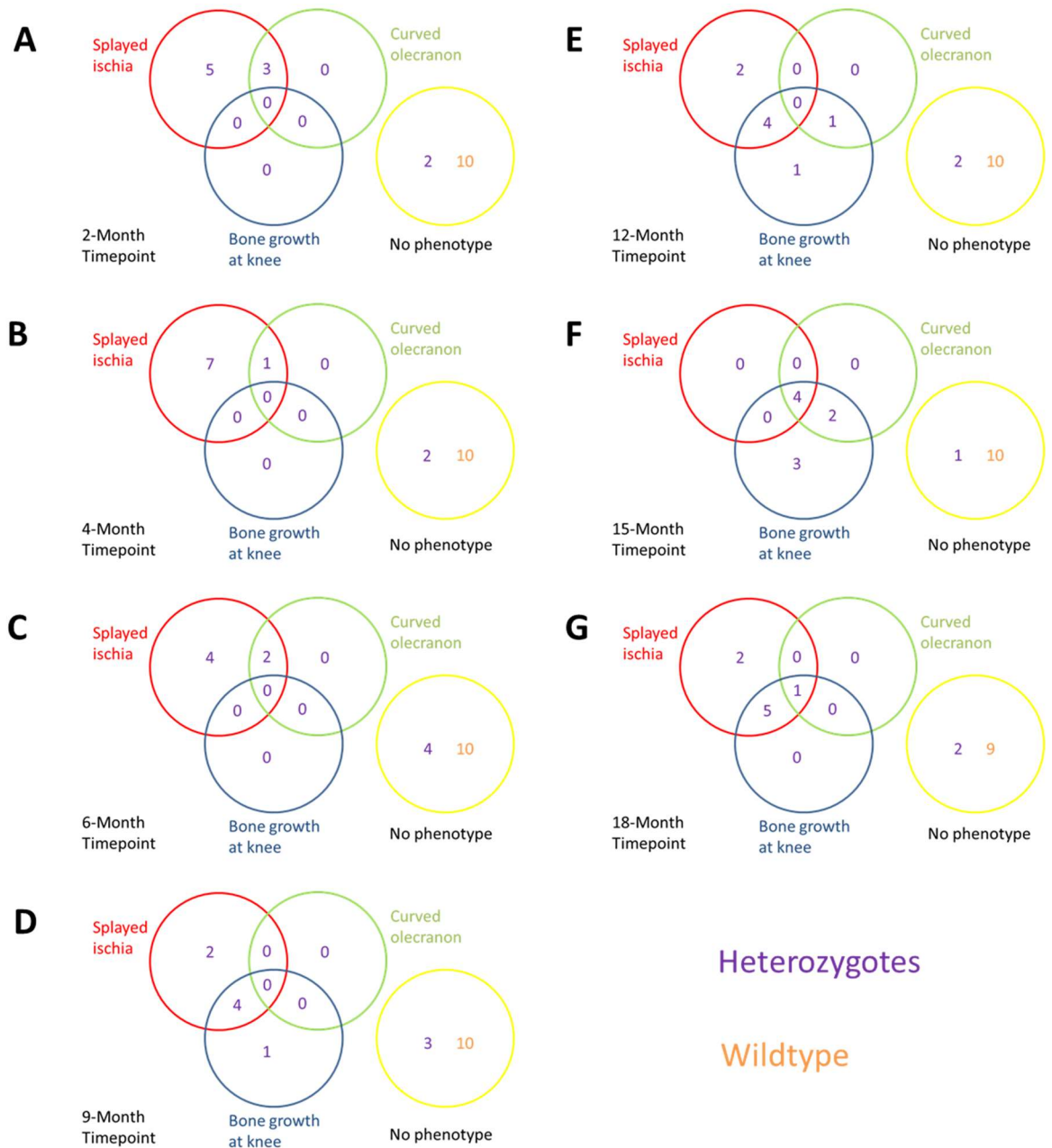


Figure 3.30. A diagram displaying how many animals of each genotype displayed each phenotype, or combination of phenotypes at each of the time points: (A)2 Months, (B)4 Months, (C)6 Months, (D)9 Months, (E)12 Months, (F)15 Months, (G)18 Months. Heterozygote animals (*Col1a2*^{+/¹⁰⁷}) are displayed in purple and wild-type animals (*Col1a2*^{+/⁺}) are displayed in orange.

The variable nature of the splice mutation, coupled with the resulting mixture of early and late phenotypes makes it difficult to assess what percentage of heterozygotes show

a phenotype. Collating the X-ray data across all time points enables an estimation of the percentage of animals that display a phenotype.

Approximately 78% of heterozygotes develop some form of phenotype identifiable by X-ray imaging. 65% of heterozygotes exhibit the splayed ischia, 22 % exhibit the curved olecranon, and 37% exhibit the abnormal bone growth at the knee (Table 3.10). The olecranon and ischia phenotypes are early onset phenotypes and therefore will be evident in heterozygotes of all ages, however the knee phenotype, which was originally identified as a late onset phenotype, is first identified in this time course experiment at 9 months and becomes increasingly prevalent as the animals age. The incidence in all heterozygotes was 37%, and rises to 65% in heterozygotes above 9 months of age

All time points	Ischia (%)	Olecranon (%)	Knee (%)	Any phenotype (%)
Male - Heterozygotes	65	17	34	80 %
Male - Wild types	0	0	0	0%
Female - Heterozygotes	65	25	40	77%
Female - Wild types	0	0	0	0%
Combined - Heterozygotes	65	22	37	78%
Combined - Wild types	0	0	0	0%

Table 3.10. A table showing the percentage of affected animals across all genotypes and time points.

The position of the abnormal bone growth raises the possibility that the abnormal bone growth could be due to ossification of ligaments and/or joint capsule, this will be discussed further in a later section.

3.7.3. DEXA Analysis of MP-107 Animals

DEXA scans were used to evaluate the body composition in each of the seven cohorts previously described and listed in Table 3.9. DEXA analysis allowed BMD and BMC to be calculated giving information about the skeleton of the animals and to compare genotypes. In addition to these skeletal parameters, the DEXA analysis also allows calculation of lean and fat mass. The weight and length, from base of tail to tip of nose, were determined immediately prior to DEXA scan.

The results of all of these parameters are detailed in Table 3.11. The significant results are summarised below.

- **Weight** - In two cohorts, 4-month male animals and 12-month female animals, the heterozygous animals were significantly lighter than the wild-type animals. In one cohort, 15-month male heterozygous animals were significantly heavier than the wild-type animals.
- **Length** - In one cohort, 4-month female animals, the heterozygous animals were significantly shorter in length than the wild-type animals
- **Lean Mass** - In one cohort, 12-month female animals, the heterozygous animals had significantly lower lean mass than the wild-type animals.
- **BMC** - In two cohorts, 4-month male animals and 6-month female animals, the heterozygous animals had significantly lower BMC than the wild-type animals.
- **BMD** - In three cohorts, 4-month male animals, and 15- and 18-month female animals, the heterozygous animals had significantly lower BMD than the wild-type animals.

There was only one parameter where a significant difference was found in 2 consecutive time points of the same sex. Heterozygous female mice in the 15- and 18-months had significantly lower BMD than the wild-type mice at the same time points.

It should be noted that this was not a longitudinal study and each cohort was only used for that specific time point. As seen in other phenotyping data, the mutation does not necessarily always result in a phenotype, and this coupled with the limited cohort size means that it is difficult to draw conclusions from this data, in isolation.

	BMD			BMC			% Fat			Fat Mass			Lean Mass			Length			Weight							
	Mean	SD	N	P-Value	Mean	SD	N	P-Value	Mean	SD	N	P-Value	Mean	SD	N	P-Value	Mean	SD	N	Mean	SD	N	P-Value			
2 months Females	0.06208	0.001852	5	0.107291	0.53614	0.039821	5	0.741874	19.196	1.12622	5	0.980568	4.866296	0.967057	5	0.665072	20.4357	1.322909	5	0.320059	5	0.291617	25.302	1.432961	5	0.333147
2 months Male	0.06244	0.000561	5	0.117116	0.53302	0.028608	5	0.0665308	12.372	0.39957	5	0.180162	3.695334	0.930078	5	0.748078	26.00067	0.497028	5	0.474235	5	0.442338	29.696	0.972226	5	0.454807
4 months Females	0.07056	0.00087	5	0.384245	0.76204	0.206352	5	0.284622	35.924	1.591485	5	0.256236	14.67771	1.96197	5	0.280418	26.51429	3.900947	5	0.525938	5	0.0188935	41.192	2.887181	5	0.145687
4 months Male	0.07222	0.002197	5	0.001779	0.70104	0.024848	5	0.033941	25.928	0.615194	5	0.855837	11.78533	0.892244	5	0.158611	33.77647	2.264942	5	0.125924	5	0.269154	45.56	1.839163	5	0.014547
6 months Females	0.06994	0.004086	5	0.115834	0.7025	0.016516	5	0.019174	38.286	0.526445	5	0.05302	17.78287	1.830503	5	0.430367	28.69113	2.540196	5	0.659034	5	0.880144	46.474	3.07734	5	0.360104
6 months Male	0.06628	0.003682	5	0.744566	0.63574	0.040689	5	0.943287	26.114	0.584623	5	0.811635	10.789	1.806875	5	0.171203	30.169	2.127996	5	0.304553	5	0.112277	40.958	3.867575	5	0.21455
9 months Females	0.07246	0.003276	5	0.452369	0.69418	0.029912	5	0.084592	37.242	1.386977	5	0.126278	12.30212	0.379861	5	0.07159	29.85313	3.274071	5	0.946631	5	0.773719	47.476	2.428327	5	0.226275
9 months Male	0.06586	0.002767	5	0.272102	0.62134	0.04059	5	0.641706	27.534	0.531285	5	0.180128	12.06996	1.187214	5	0.593476	31.95004	3.224038	5	0.142533	5	0.170083	44.02	3.201144	5	0.245513
12 months Females	0.07246	0.003276	5	0.158223	0.69418	0.029912	5	0.305383	29.818	0.760736	5	0.945669	16.71754	1.543267	5	0.193213	29.99417	4.232225	5	0.020761	5	0.144068	51.836	1.49137	5	0.041174
12 months Male	0.06876	0.005941	5	0.852397	0.71614	0.065128	5	0.546945	20.526	0.69402	5	0.673053	8.995415	1.099545	5	0.582485	34.72098	2.485555	5	0.363974	5	1	45.656	1.464986	5	0.337659
15 months Females	0.07076	0.003378	5	0.016295	0.73946	0.075018	5	0.054366	28.278	0.722235	5	0.449725	13.44322	4.135134	5	0.275442	33.63078	3.469616	5	0.075994	5	0.249443	47.074	3.742548	5	0.924967
15 months Male	0.06628	0.002869	5	0.936077	0.68222	0.052543	5	0.767059	25.912	0.748107	5	0.771767	9.514824	2.565984	5	0.464094	32.18718	4.562321	5	0.075994	5	0.249443	48.83	3.344482	5	0.049502
18 months Females	0.067384	0.001655	5	0.017742	0.72348	0.071614	5	0.191632	31.006	0.849131	5	0.776932	10.59729	0.948206	5	0.669032	32.5319	3.08944	5	0.056336	5	0.065628	47.242	5.120941	5	0.127411
18 months Male	0.06534	0.002957	5	0.082146	0.68686	0.064502	5	0.690912	22.852	0.716363	5	0.720193	14.12515	1.208008	5	0.556082	28.16885	3.20605	5	0.391026	5	0.834021	43.6475	4.989982	4	0.647047

Table 3.11. DEXA data for all tested cohorts presented in the form of means, standard deviations and n numbers for all DEXA parameters. Statistical testing between wildtype (WT, Col1a2^{+/+}) and heterozygous (HET, Col1a2^{+/-}) animals from each cohort employed the student t test- P values < 0.1 highlighted in green, P values < 0.05 highlighted in yellow.

3.7.4. Clinical Chemistry of MP-107 Animals

Clinical chemistry data from the G₃ cohort was limited due to the nature of a longitudinal study, and the quantity of blood that can be taken, for both the health of the animals and to comply with Home Office Licence regulation. As this study was cross sectional and each cohort was culled at a different time point, it was possible to extract a much higher volume of blood via a retro-orbital bleed performed under terminal anaesthetic, than was possible in the initial screen. The higher volume of blood collected enabled a large panel of assays to be run at each time point. The plasma from these blood samples were then separated via centrifugation and the plasma analysed by the clinical chemistry department at MRC Harwell using an Olympus AU400 Bioanalyser. It should be noted that due to a freezer failure the samples from the 18-month cohort were unusable, and are therefore not included here.

The means, standard deviation and n numbers for each cohort and parameters are presented in the Tables 3.12a and 3.12b. In addition to this data the P values from student t tests comparing genotypes in each cohort are also displayed.

To summarise the data- No significant difference between genotypes in any of the cohorts was detected in the following assays– sodium, chloride, alanine aminotransferase (ALT), aspartate aminotransferase (AST), total protein, albumin, total cholesterol, high-density lipoproteins (HDL), low-density lipoproteins (LDL), free fatty acids, glycerol, total bilirubin, lactate dehydrogenase (LDH), amylase, creatine kinase (CK), fructose and uric acid.

Significant differences were detected in 9 assays, however only 2 assay showed significant differences in more than one cohort, creatinine and calcium, and in the case of creatine, in one cohort the level was elevated and in the other reduced. Details of these assays are listed below:

- **Potassium** - The heterozygous animals displayed a significantly reduced level when compared with the wild-type animals in the 6-month male cohort.
- **Urea** - The heterozygous animals displayed a significantly elevated level when compared with the wild-type animals in the 6-month female cohort.
- **Creatinine** - The heterozygous animals displayed a significantly reduced level when compared with the wild-type animals in the 4-month female cohort, and

in the 9-month male cohort, the heterozygous animals displayed a significantly elevated level when compared with the wild-type animals.

- **Calcium** - The heterozygous animals displayed a significantly reduced level when compared with the wild-type animals, in the 2-month and 6-month male cohorts.
- **Inorganic Phosphate** - The heterozygous animals displayed a significantly elevated level when compared with the wild-type animals in the 15-month male cohort.
- **Alkaline phosphatase (ALP)** - The heterozygous animals displayed a significantly elevated level when compared with the wild-type animals in the 6-month male cohort.
- **Glucose** - The heterozygous animals displayed a significantly reduced level when compared with the wild-type animals in the 2-month male cohort.
- **Triglycerides** - The heterozygous animals displayed a significantly elevated level when compared with the wild-type animal in the 6-month female cohort.
- **Iron** - The heterozygous animals displayed a significantly elevated level when compared with the wild-type animals in the 2-month female cohort.

One of the disadvantages of this study is that as each cohort is independent, the result of each assay is only statistically analysed within each cohort, rather than across the time course. Despite this, as each cohort contains the same number of animals of each genotype, it is reasonable to expect authentic results to be somewhat replicated across time points. The vast majority of significant results occur at only one time point/sex, and are therefore not indicative of a clinical chemistry phenotype, especially when the clinical chemistry analysis from the original ageing cohort is taken into account. This indicates that the study may have been underpowered due to the variability in phenotypes.

3.8. Micro Computed Tomography of MP-107 Animals

Ex vivo 3D imaging, such as micro computed tomography (μ CT) is a far better tool for understanding the excess bone growth around the knee joint than the X-ray imaging used *in vivo*. μ CT allows not only 3D imaging of bone at higher resolution, but also allows analysis of the trabecular bone, subchondral bone and subchondral bone plate. This analysis of the bone structure can inform about the changes the *Col1a2*⁺¹⁰⁷ mutation is causing prior to the overt phenotype observed.

At the terminal time point, the limbs and pelvis were removed and fixed in 10% neutral buffered formalin for 48 hours before being transferred into 70% ethanol for storage. μ CT was used to image examples of the elbow joint and pelvis of a wild-type and heterozygous animals. The early onset phenotypes including the splayed ischia and curved olecranon do not appear to progress in severity and for this reason only an early time point (2-months) was used. The knee phenotype consisting of abnormal bone growth and culminating in OA develops over time, so μ CT was used to image the knee joints from both male and female animals in the 4-, 9- and 18-month cohorts, to investigate the progression of the OA phenotype and the formation of excess bone around the joint. The three time points were chosen for the following reasons: the 4-month cohort, as this was prior to any observed bone changes at the knee by X-ray; the 9-month cohort, as this was the first time point where changes at the knee were observed; and the 18-month cohort as changes to the knee were most severe at this time point.

++

3.8.1. 3D Imaging of Bone Phenotypes in of MP-107 Animals

Curved olecranon were noted in radiographs of some heterozygotes, however, as the images are two-dimensional, it is not possible to know from the X-ray imaging the full extent of the bone abnormality. μ CT imaging of elbow joints from an affected heterozygote and an unaffected wild type were used to better understand the abnormal bone structure in three dimensions (Figure 3.31). 3D imaging revealed that in the heterozygote elbow, the 'curved olecranon' phenotype observed in the radiograph, was the result of the olecranon deviating from the trajectory of the ulna, in the direction of the humerus.

In both the 4- and 6-month cohorts, evidence of a fracture in the ulna was identified in two individual heterozygotes exhibiting the curved olecranon phenotype. There was no evidence of fracture in the radiographs of any of the 2-month old heterozygote animals exhibiting the curved olecranon phenotype. However, in the 3D rendering of the elbow joint of the randomly selected heterozygote from the 2-month cohort (MP-107-C3H\58.1i), there is evidence of a fracture in the ulna that was not visible by X-ray imaging (Figure. 3.26).

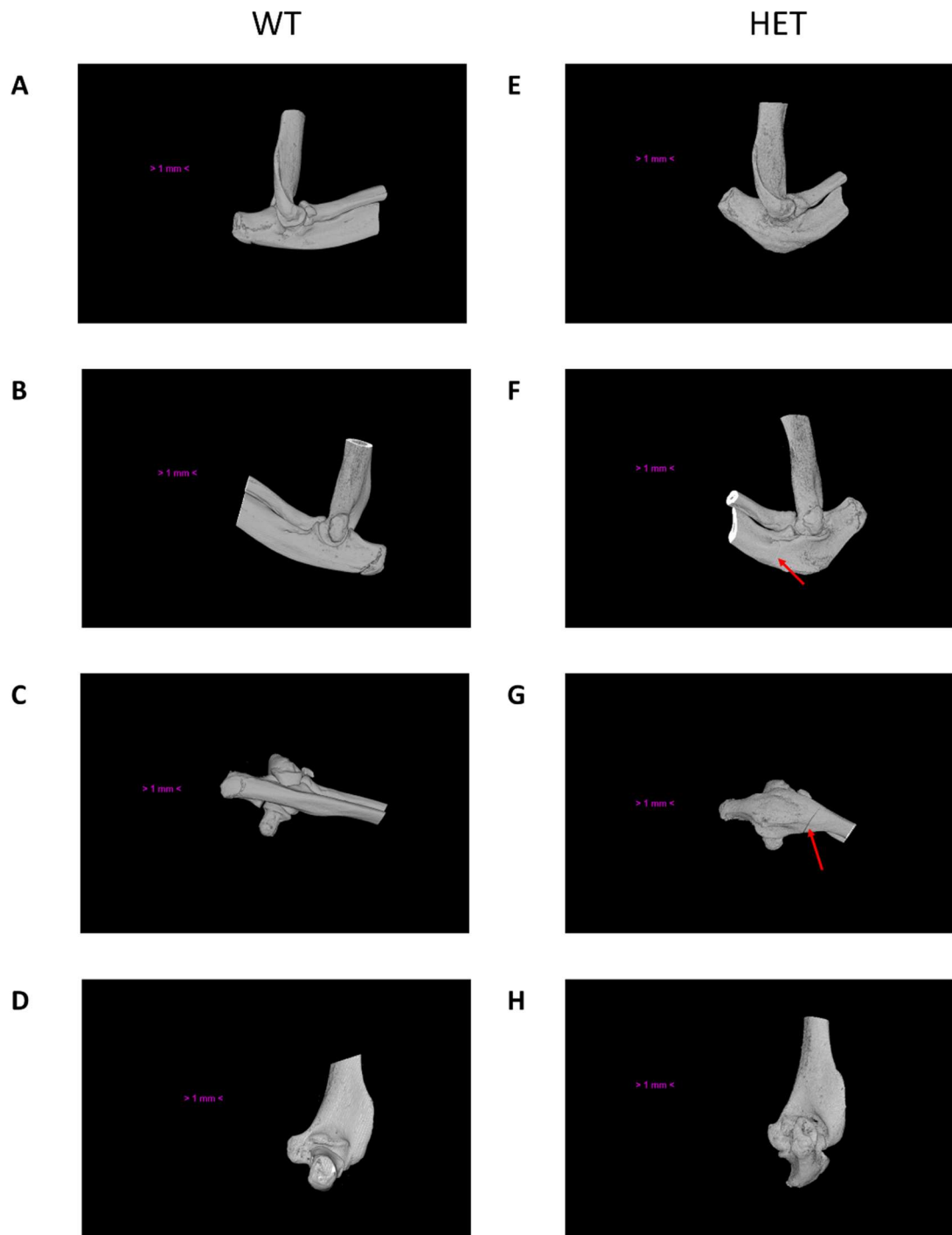


Figure 3.31. 3D reconstructions of the elbow joints of a wild type (WT, *Col1a2*^{+/+}) (A-D) and a heterozygote (HET, *Col1a2*^{+/¹⁰⁷}) (F-H) from the 2-month cohort. (E&F) show the clear curvature of the olecranon in the heterozygote, which is not present in the wild type (A&B). (F&G) show evidence of fracture in the ulna of the heterozygote (red arrows).

A cut through of the 3D reconstruction indicates that the evidence seen on the surface of the reconstruction is not an artefact, and that the fracture penetrates the whole way through the cortical bone (Figure 3.32).

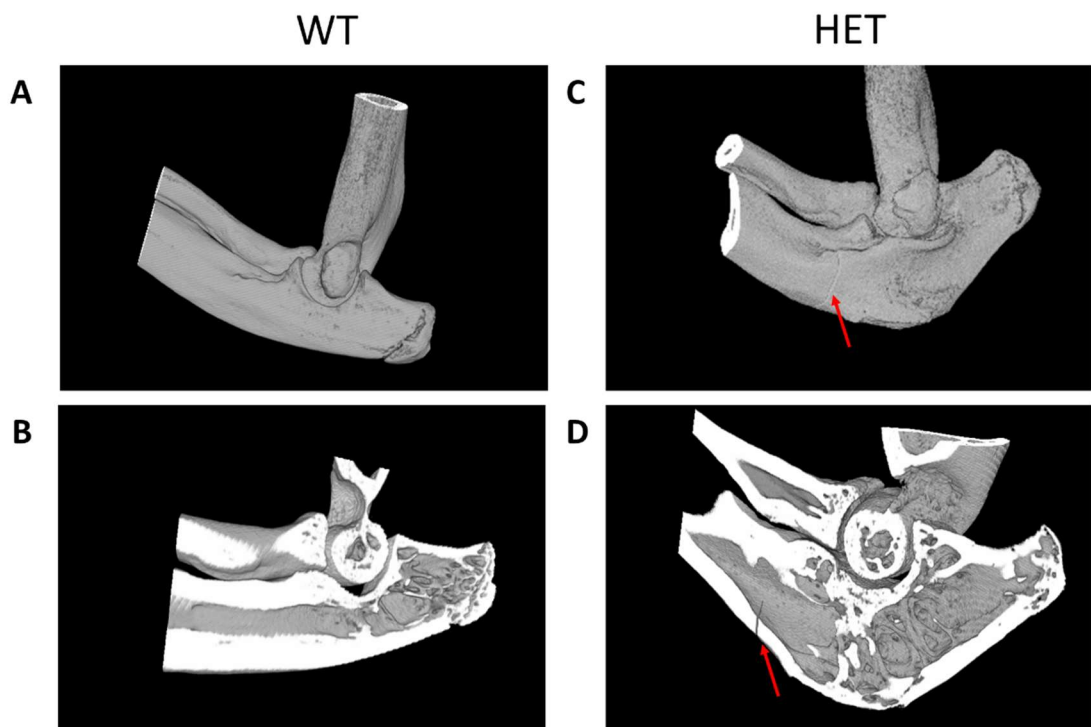


Figure 3.32. 3D reconstructions of the elbow joints of a wild type (WT, *Col1a2*^{+/+}) (A&B) and a heterozygote (HET, *Col1a2*^{+/107}) (C&D) from the 2-month cohort with cutaway. Wild type shows no evidence of fracture either in the whole 3D reconstruction (A) or the sectioned reconstruction (B). Heterozygote shows evidence of fracture in both the whole 3D reconstruction (C) or the sectioned reconstruction (D)(red arrows)

Radiographs in Section 3.7.2 (Figure 3.28), show the presence of fractures in some heterozygotes presenting the curved olecranon phenotype. Figure 3.31 and Figure 3.32 show evidence of fracture in a heterozygote, presenting with the curved olecranon phenotype, which was not detectable by X-ray.

While no conclusion can be drawn from presence of a fracture in these 3 heterozygote animals presenting with the curved olecranon phenotype, it does raise the possibility that fractures, even if undetectable by X-ray, could be the root cause of the curved olecranon phenotype and warrants further study.

Splayed ischia were noted in radiographs, however, as the images are 2D and the ischia are just the dorsal section of the posterior part of the pelvis, it is not known exactly how the observed 'splayed ischia' relate to other parts of the pelvis. μ CT imaging of the pelvis from an affected heterozygote and an unaffected wild type were used to better understand the abnormal bone structure in three dimensions. 3D rendering showed the ischia in this heterozygote diverge from the trajectory of the ilia, as was expected from

the radiographs (Section 3.7.2, Figure 3.27), the ischia in the wild type appear to follow the trajectory of the ilia (Figure 3.33).

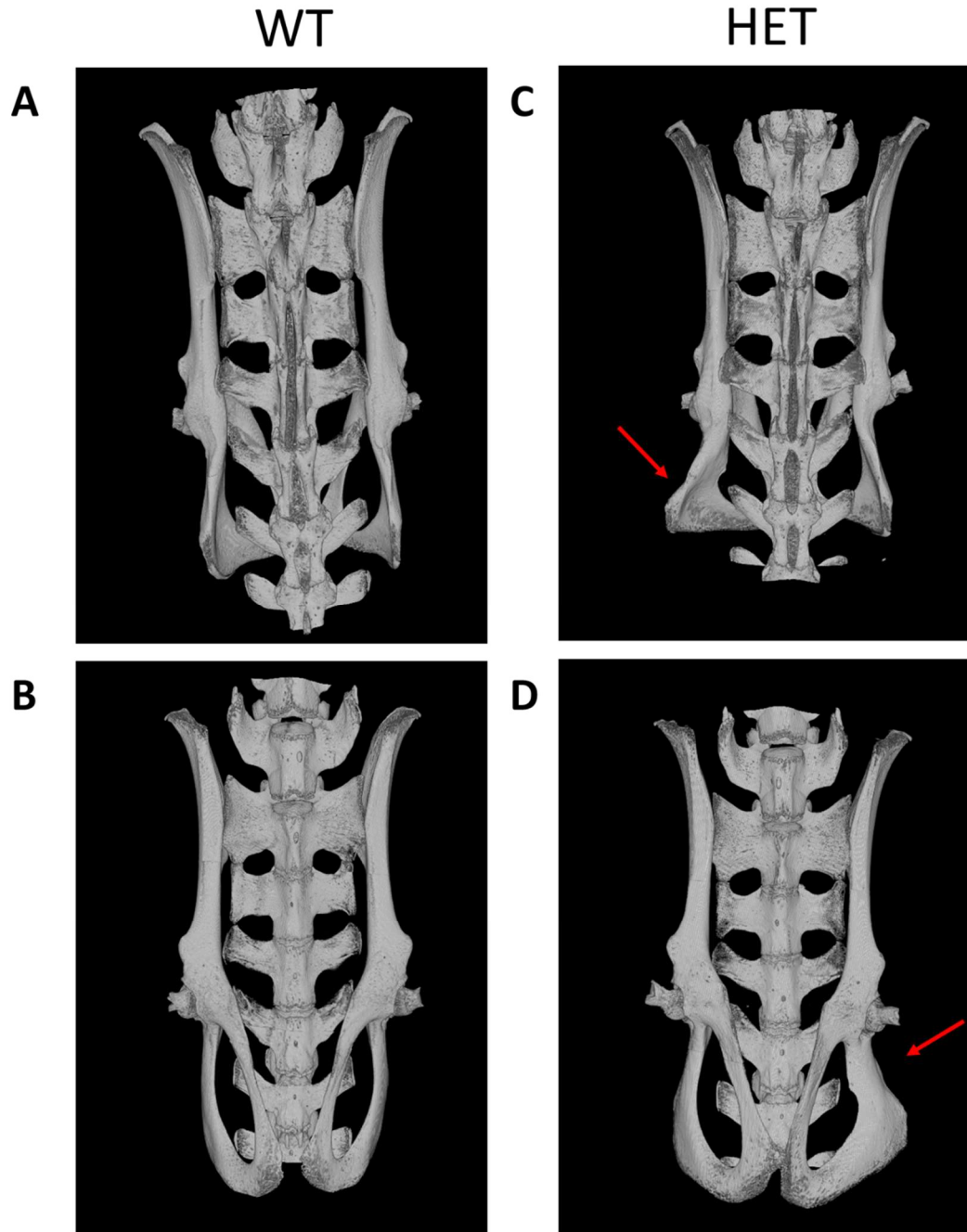


Figure 3.33. 3D reconstructions of the pelvis of a wild type (WT, *Col1a2*^{+/+}) (A&B) and a heterozygote (HET, *Col1a2*^{+/107}) (C&D) from the 2-month cohort in the dorsal and ventral views. Wild type shows no evidence of splayed ischia in either the dorsal (A), or the ventral (B) position. Heterozygote shows evidence of splayed ischia in both the dorsal (A), and the ventral (B) position (red arrows).

Viewing the 3D rendering from both anterior and posterior aspects revealed that in addition to splayed ischia, the pubis was also deformed in the heterozygote (Figure 3.34).

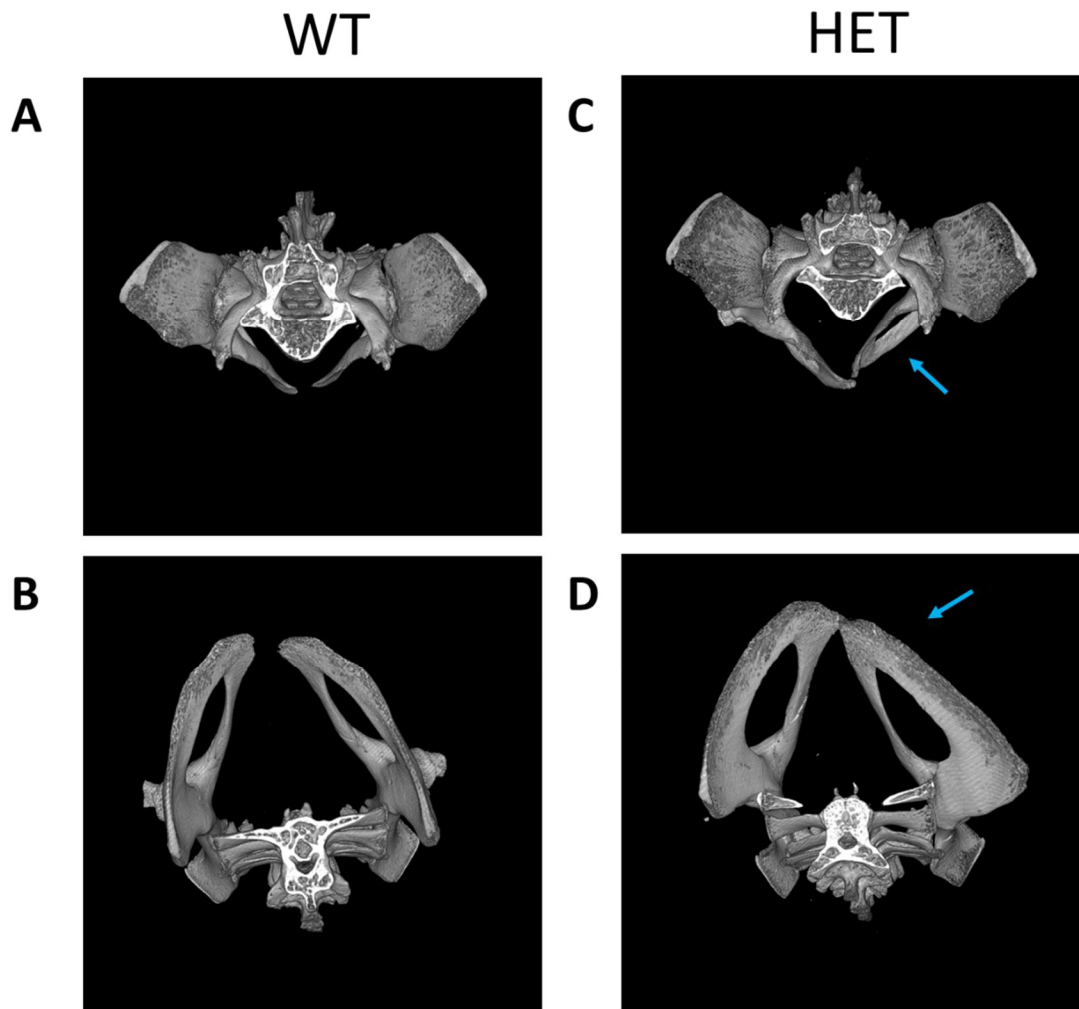


Figure 3.34. 3D reconstructions of the pelvis of a wild type (WT, *Col1a2^{+/+}*) (A&B) and a heterozygote (HET, *Col1a2^{+ /107}*) (C&D) from the 2-month cohort in the anterior and posterior views. Wild type shows no evidence of an abnormal pubis in either the anterior (A), or the posterior (B) position. Heterozygote shows evidence of a deformed pubis in both the anterior (A), and the posterior (B) position (blue arrows).

Cross sections of the 3D rendering in the transverse plane showed evidence of marked asymmetry in the heterozygous pelvis, where the wild-type pelvis showed no evidence of asymmetry. The cross sections indicate that the divergences of the trajectories of the two coxae are anterior to the acetabulum, indicating that changes in the ilia are also present, in addition to the changes in the pubis and ischia (Figure 3.35).

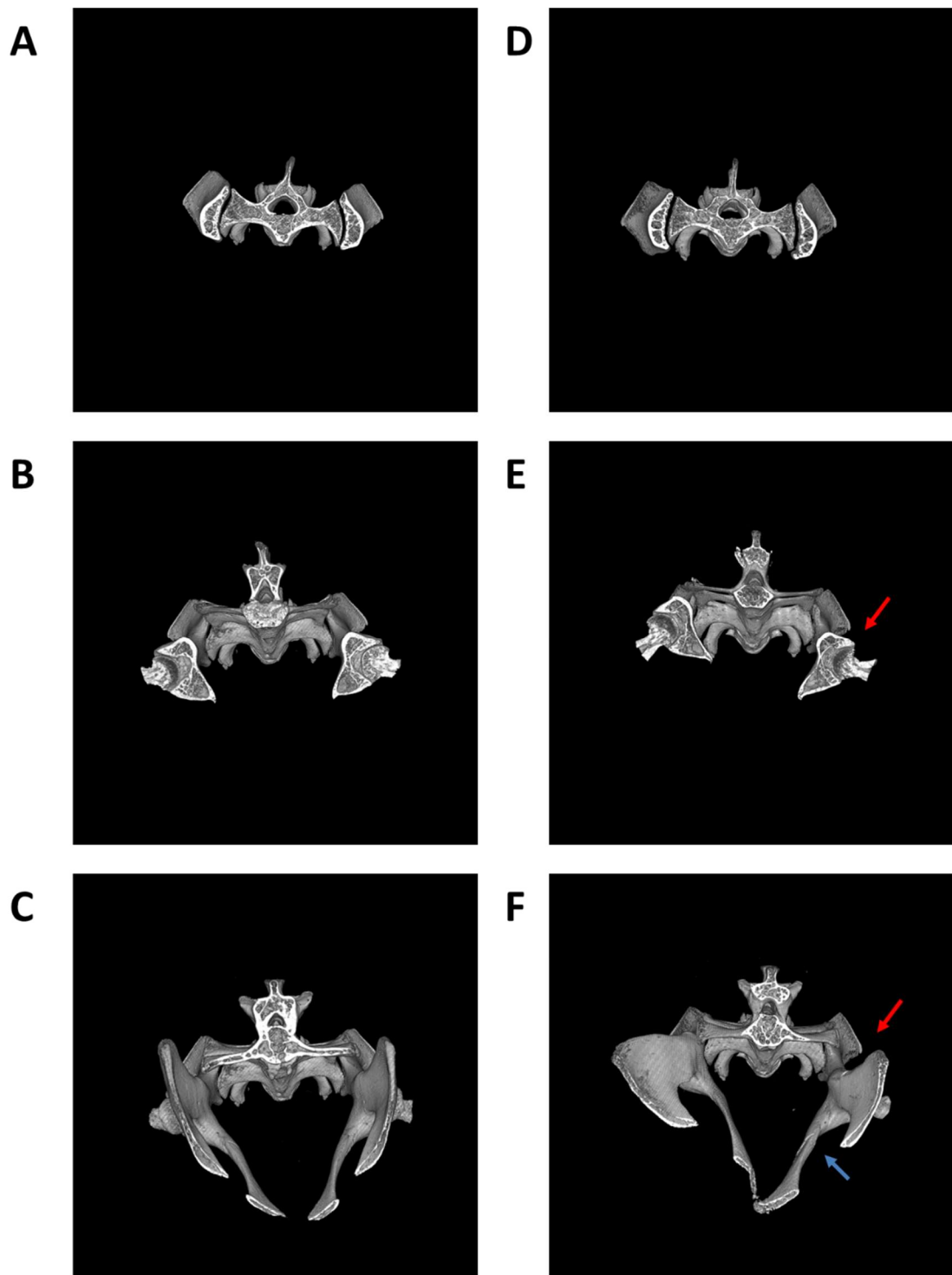


Figure 3.35. Cutaways on the transverse plane of 3D reconstructions of the pelvis of a wild type (WT, *Col1a2*^{+/+}) (A-C) and a heterozygote (HET, *Col1a2*^{+/107}) (D-F) from the 2-month cohort. Wild type shows no evidence of asymmetry in the transverse plane at the sacrum (A), the acetabulum (B), or the pubes (C). Heterozygote shows no evidence of asymmetry in the transverse plane at the sacrum (A), however there is evidence of marked asymmetry at both the acetabulum (B), and the pubes (C)(red arrows). This indicates the changes in the pelvis are also present in the ilia. An artefact from the reconstruction is present in the image F (blue arrow); 3D imaging confirms this is an artefact, not a fracture.

No evidence of fractures was found, however micro-fractures leading to deformation of the bone cannot be ruled out.

The X-ray images initially used to identify the abnormal bone growth at the knee only allowed a two-dimensional view of the joint, meaning that due to positioning it was possible to miss abnormal bone growth. This proved to be the case in one of the 4-month heterozygous animals, which was scored as unaffected by X-ray, but reconstructed 3D scans of the knee showed calcification of the medial collateral ligament (MCL), with possible involvement of the joint capsule (Figure 3.36). The earliest any abnormal bone growth or calcification had been observed by X-ray imaging was 9 months of age (see Section 3.7.2, Figure 3.29).

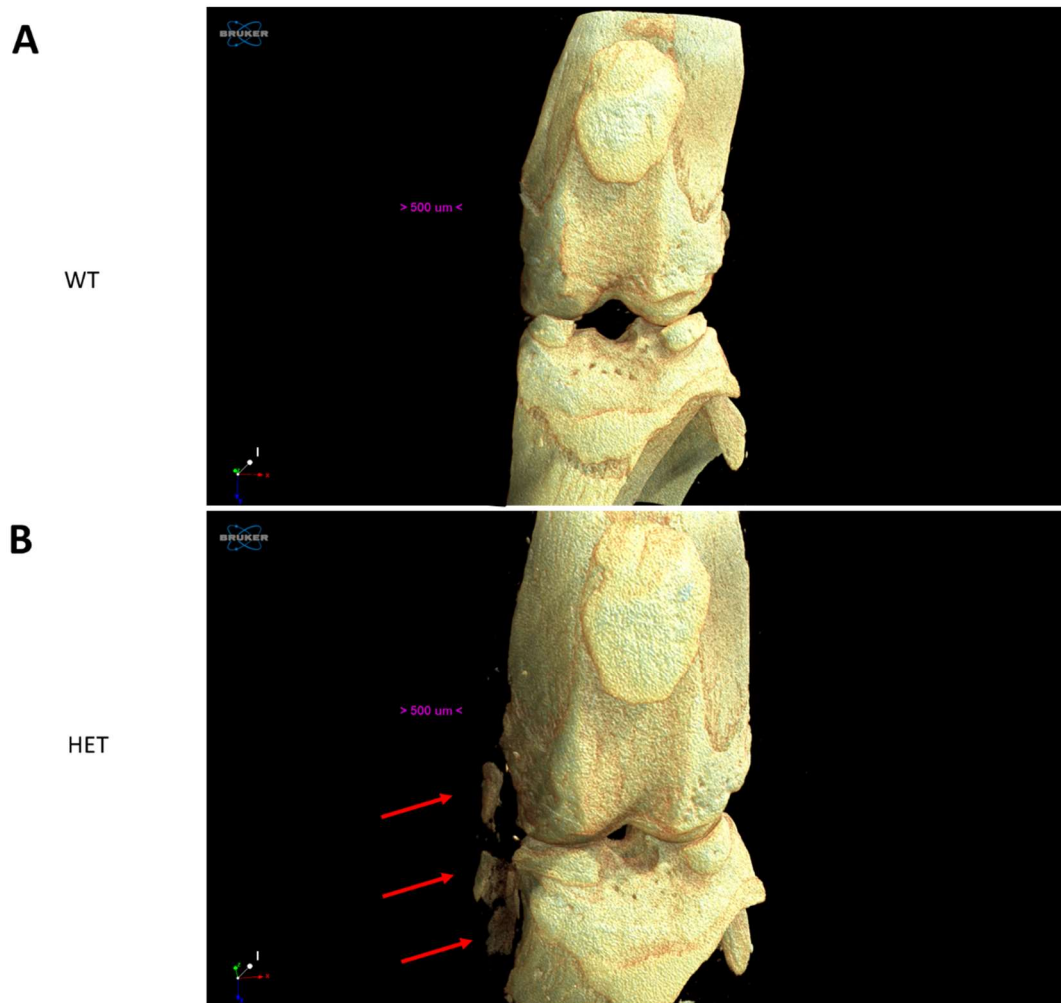


Figure 3.36. 3D reconstructions of the left knees of wild-type and heterozygous animals from the 4-month cohort. (A) Wild-type (WT, *Col1a2*^{+/+}) knee joint with no obvious abnormal bone growth or calcification. (B) Heterozygous (HET, *Col1a2*^{+/¹⁰⁷}) knee exhibiting evidence of calcification of the medial collateral ligament (red arrows).

In the 9-month cohort, abnormal bone growth was observed in 50% (5) of the heterozygous animals by X-ray imaging, and the 3D reconstructed scans confirmed these observations as calcification of the MCL, with involvement of the synovium and/or capsule. The calcification seen in the 9-month heterozygous animals were, where present, more severe than seen in the 4-month cohort. No calcification was observed in the wild-type scans (Figure 3.37).

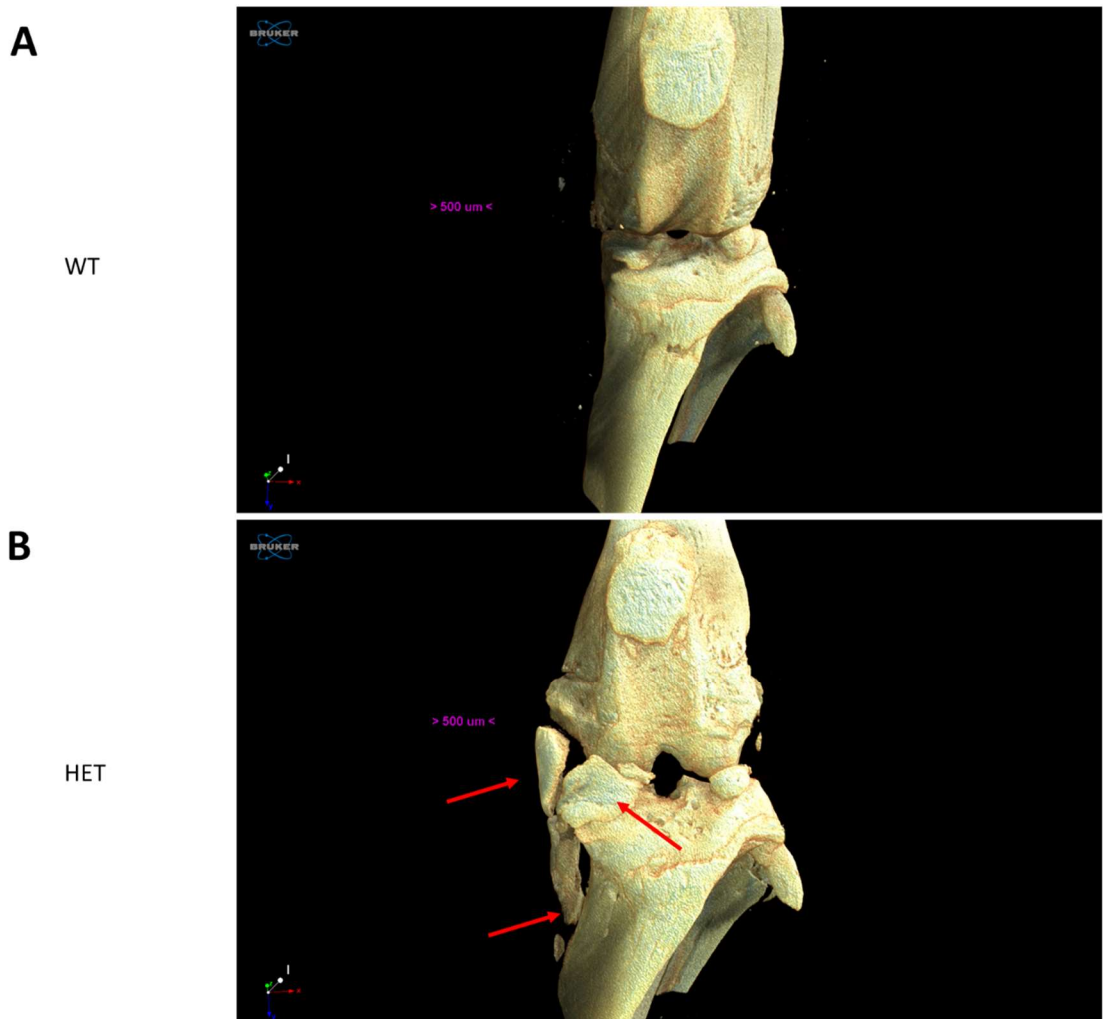


Figure 3.37. 3D reconstructions of the left knees of wild-type and heterozygous animals from the 9-month cohort. (A) Wild-type (WT, *Col1a2*^{+/+}) knee joint with no obvious abnormal bone growth or calcification. (B) Heterozygous (HET, *Col1a2*^{+/¹⁰⁷}) knee exhibiting evidence of major calcification of the medial collateral ligament and synovium/capsule, as well as osteophytes originating in the bone (red arrows).

In the 18-month cohort, abnormal bone growth was observed in 60% (6) of the heterozygous animals by X-ray imaging, and the 3D reconstructed scans confirmed these observations as large osteophytes as well as ossification of the ligaments, capsule or

possibly synovium, and meniscus. Some calcification of the ligaments was observed in the wild-type scans, albeit very mild and similar in appearance to the calcification observed in the 4-month heterozygous scan (Figure 3.38).

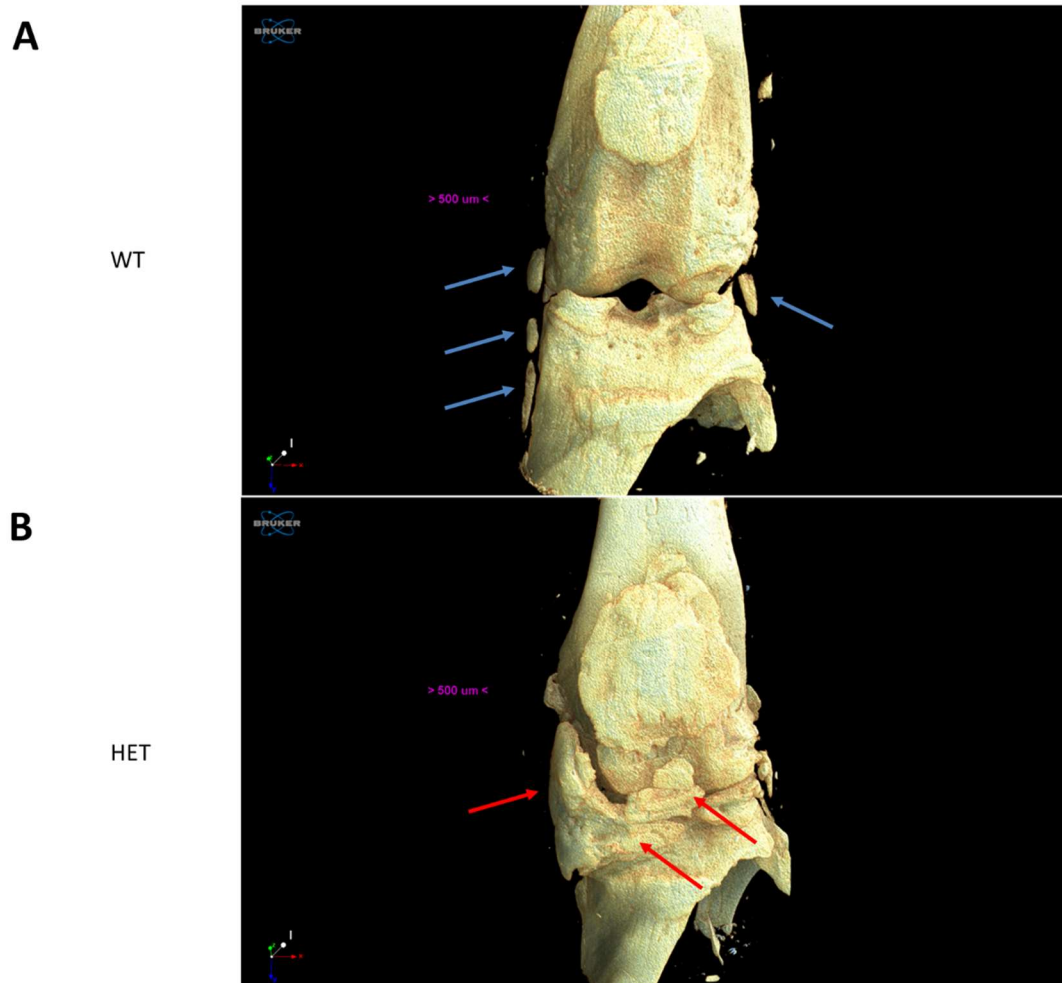


Figure 3.38. 3D reconstructions of the left knees of wild-type and heterozygous animals from the 18-month cohort. (A) Wild-type (WT, *Col1a2*^{+/+}) knee joint appears normal and exhibits some minor calcification of the ligaments (blue arrows). (B) Heterozygous (HET, *Col1a2*^{+/¹⁰⁷}) showed evidence of major calcification of the medial collateral ligament, synovium, capsule and menisci as well as large osteophytes originating in the bone (red arrows).

The μ CT imaging of the knee joints has shown that there is evidence of calcification at an earlier time point than detected by X-ray imaging, and that animals without the early onset splayed ischia phenotype develop the abnormal calcification, indicating that the knee phenotype is independent of the ischia phenotype (Table 3.13).

			N number	X-Ray Ischia	X-Ray Knee	μCT Knee
4 months	Female	WT	5	0	0	0
		HET	5	3	0	5
	Male	WT	5	0	0	0
		HET	5	5	0	2
9 months	Female	WT	5	0	0	0
		HET	5	3	4	5
	Male	WT	5	0	0	0
		HET	5	3	1	4
18 months	Female	WT	5	0	0	1*
		HET	5	4	2	4
	Male	WT	4	0	0	2*
		HET	5	4	4	5

Table 3.13. A table displaying the number of animals phenotyped at each time point and the number of animals presenting with each phenotype. The μCT imaging showed that some heterozygotes (HET, *Col1a2*^{+/¹⁰⁷}), which did not appear to show the abnormal bone growth at the knee by X-ray, actually did have abnormal bone growth at the knee. Some heterozygotes developed abnormal bone growth in the knee in the absence of the ischia phenotype. *At 18 months 3 wild types (WT, *Col1a2*^{+/⁺}) showed some very minor calcification of the MCL as see in Figure 3.34A.

A comparison of the incidence of abnormal bone formation between genotypes of each sex, at each time point was carried out using the Mann-Whitney U test (Table 3.14) Statistical analysis revealed a significant difference between genotypes at 4 and 9 months in female animals and at 9 months in male animals. At 18 months the minor calcification identified in 3 wild type animals (1 female and 2 males), meant that despite high incidence and severity of calcification, no significant difference was detected at 18 months.

			N number	Abnormal bone identified	U	P Value
4 months	Female	WT	5	0	25	0.004
		HET	5	5	0	
	Male	WT	5	0	17.5	0.177
		HET	5	2	7.5	
9 months	Female	WT	5	0	25	0.004
		HET	5	5	0	
	Male	WT	5	0	22.5	0.020
		HET	5	4	2.5	
18 months	Female	WT	5	1*	20	0.093
		HET	5	4	5	
	Male	WT	4	2*	15	0.128
		HET	5	5	5	

Table 3.14. A table comparing the number of animals identified with the abnormal bone phenotype at the knee, by μ CT at each time point. Statistical analysis revealed a significant difference between genotypes at 4 and 9 months in female animals and at 9 months in Male animals. *At 18 months 3 wild types (WT, *Col1a2^{+/+}*) showed some very minor calcification of the MCL as see in Figure 3.34A.

The μ CT imaging of the elbow joint has shown additional evidence of ulna fractures in heterozygotes exhibiting the curved olecranon phenotype, and it is possible that the fractures lead to the curved olecranon phenotype. The μ CT imaging of the pelvis has shown that there is evidence of asymmetry between the 2 sides of the pelvis in the ilia, ischia and pubes, and that the phenotype was more severe than the radiographs indicated. No evidence of fractures was detected in the heterozygotes; however, fractures cannot be ruled out as a cause.

3.8.2. Metaphyseal Trabecular Analysis of MP-107 Animals

Analysis of the trabecular bone can help elucidate what changes the mutation may be having on the bone structure, and whether any changes could be leading to the phenotypes observed in the line MP-107. To explore whether there were changes to the underlying bone structure of the knee, a region of interest was identified in the trabecular bone below the growth plate of the tibia. Automated analysis of this region allowed comparison between genotypes at all three time points. The drawing of the region of interest was performed blind to genotype, and the genotypes were only synched with the data for comparison between genotypes.

Analysis of the trabecular bone in the tibia revealed a number of trends in males across time points (Figure 3.39). All results for μ CT analysis available in Appendix 2.

Heterozygotes consistently appeared to have lower bone volume fraction (Bone volume/trabecular volume- BV/TV) than wild-type animals, with a significant difference at both 9 months (WT Mean-10.75, SD-1.83, N-5, HET Mean-7.07, SD-2.03, N-5, P=0.028) and 18 months (WT Mean-9.28, SD-2.72, N-4, HET Mean-5.15, SD-2.42, N-7, P=0.043) and difference just short of significance at 4-months (WT Mean-15.11, SD-1.44, N-5, HET Mean-12.54, SD-1.80, N-5, P=0.056).

Heterozygotes consistently had a higher trabecular separation than wild-type animals, with a significant difference at both 4 months (WT Mean-0.161, SD-0.010, N-5, HET Mean-0.187, SD-0.015, N-5, P=0.028) and 9 months (WT Mean-0.205, SD-0.016, N-5, HET Mean-0.253, SD-0.032, N-5, P=0.0257).

Heterozygotes had a significantly higher trabecular thickness than the wild types at 4 months (WT Mean-0.039, SD-0.0006, N-5, HET Mean-0.045, SD-0.0025, N-5, P=0.0028) with no significant difference at either 9 or 18 months, and there was no clear trend in trabecular thickness.

Heterozygotes consistently had a significantly lower trabecular number than wild type animals at 4 months (WT Mean-3.84, SD-0.34, N-5, HET Mean-2.82, SD-0.47, N-5, P=0.008), 9 months (WT Mean-2.58, SD-0.40, N-5, HET Mean-1.67, SD-0.48, N-5, P=0.020), and 18 months (WT Mean-2.04, SD-0.59, N-4, HET Mean-1.03, SD-0.56, N-7, P=0.030).

Bone volume fraction (BV/TV) and trabecular number appeared to decline with age in both genotypes and trabecular separation appeared to increase with age in both genotypes, however as each cohort was independent no statistical analysis was performed. No particular trend was observed in the trabecular thickness of either genotype.

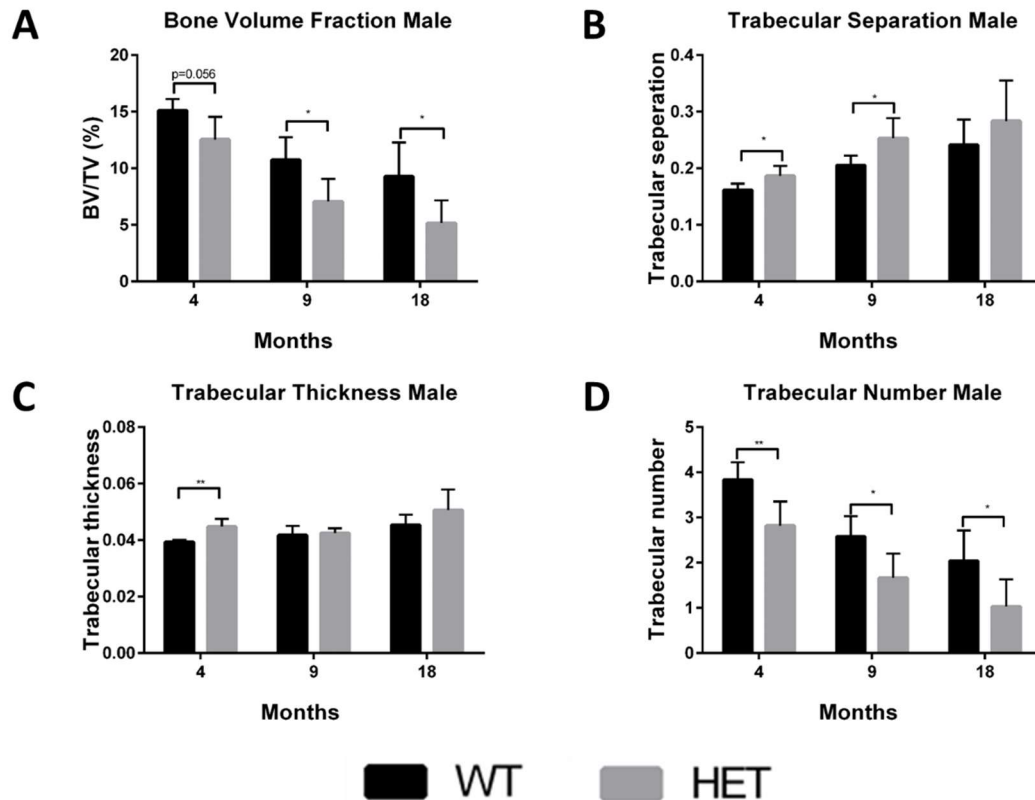


Figure 3.39. μ CT analysis of trabecular bone in male animals. (A) Heterozygotes (HET, *Col1a2*^{+/¹⁰⁷) show a reduction in the bone volume fraction when compared with wild types (WT, *Col1a2*^{+/⁺) at 9- and 18-months. (B) Heterozygotes (HET, *Col1a2*^{+/¹⁰⁷) show an increase in the trabecular separation when compared with wild types (WT, *Col1a2*^{+/⁺) at 4- and 9-months. (C) Heterozygotes (HET, *Col1a2*^{+/¹⁰⁷) show an increase in the trabecular thickness when compared with wild type (WT, *Col1a2*^{+/⁺) at 4-months. (D) Heterozygotes (HET, *Col1a2*^{+/¹⁰⁷) show a reduction in the trabecula number when compared with wild types (WT, *Col1a2*^{+/⁺) at 4-, 9- and 18-months. Student T-test *P<0.05, **P<0.01}}}}}}}}

Analysis of the trabecular bone in the tibia revealed similar trends in females across time points, however the number of significantly different features was reduced compared to the males (Figure 3.40).

The bone volume fraction (BV/TV) followed a similar pattern to that seen in the males with heterozygotes' bone volume fractions appearing lower than wild-type animals, however there were no statistically different results.

The trabecular separation followed a similar pattern to that seen in the males with heterozygotes' bone volume fractions being higher than wild-type animals, however there was only one statistically significant difference at 9 months (WT Mean-0.151, SD-0.024, N-5, HET Mean-0.203, SD-0.036, N-5, P=0.043).

Heterozygotes had a significantly higher trabecular thickness than the wild types at 9 months (WT Mean-0.054, SD-0.005, N-5, HET Mean-0.063, SD-0.005, N-5, P=0.029), with no significant difference at either 4 or 18 months, there was no clear trend in trabecular thickness.

The trabecular number followed a similar pattern to that seen in the males with heterozygotes' trabecular number being lower than wild-type animals, however only the difference at 9 months was significant (WT Mean-3.56, SD-0.63, N-5, HET Mean-2.17, SD-0.78, N-5, P=0.024).

Bone volume fraction (BV/TV) and trabecular number appeared to decline with age in both genotypes and trabecular separation appeared to increase with age in both genotypes, however as each cohort was independent no statistical analysis was performed. No particular trend was observed in the trabecular thickness of either genotype.

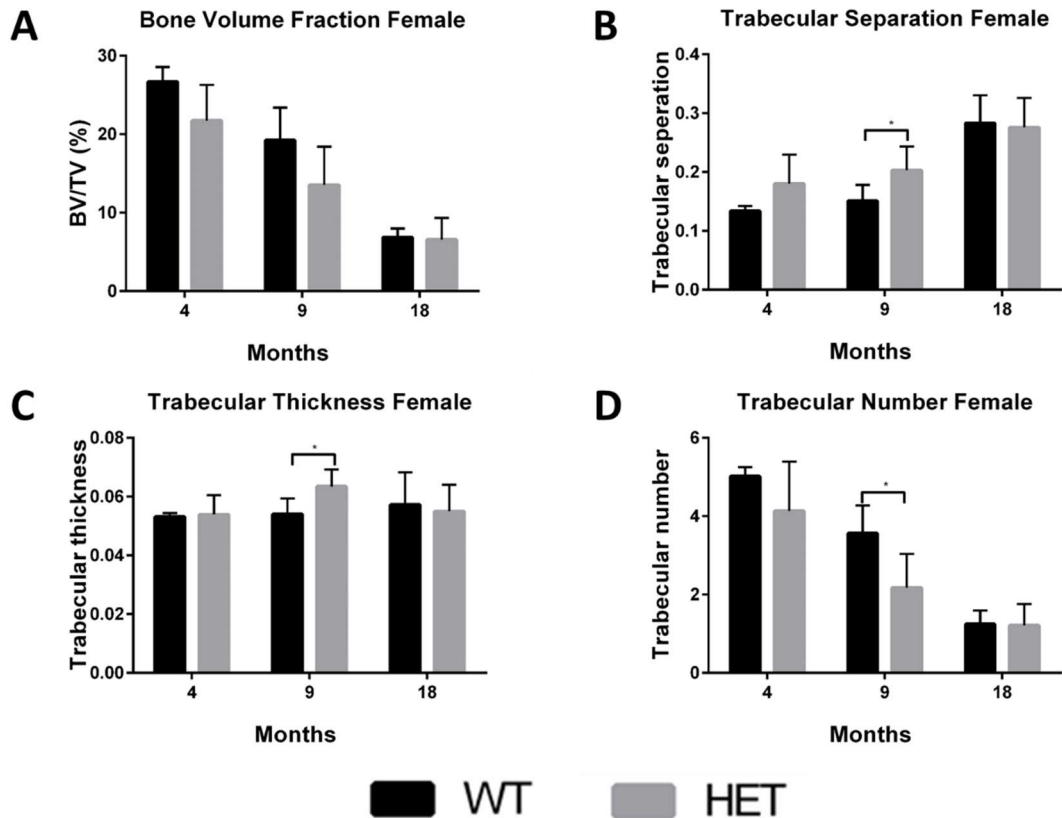


Figure 3.40. μ CT analysis of trabecular bone in female animals. (A) No significant difference in the bone volume fraction of heterozygotes (HET, *Col1a2*^{+/¹⁰⁷) was detected when compared with wild types (WT, *Col1a2*^{+/⁺) at any time point. (B) Heterozygotes (HET, *Col1a2*^{+/¹⁰⁷) show an increase in the trabecular separation when compared with wild types (WT, *Col1a2*^{+/⁺) at 9-months. (C) Heterozygotes (HET, *Col1a2*^{+/¹⁰⁷) show an increase in the trabecular thickness when compared with wild type (WT, *Col1a2*^{+/⁺) at 9-months. (D) Heterozygotes (HET, *Col1a2*^{+/¹⁰⁷) show a reduction in the trabecula number when compared with wild types (WT, *Col1a2*^{+/⁺) at 9- months. Student T-test *P<0.05.}}}}}}}}

The analysis of the trabecular bone indicates that in the male heterozygote mice at various time points the bone volume fraction and trabecular number is reduced and the trabecular separation and trabecular thickness is increased. The female results were less consistent than the males; however, there were some time points that also showed these trends. Reduced bone volume fraction is seen in osteoporotic bones [253] and in a study of osteoporotic men, increased trabecular separation and decreased trabecular number were associated with an increased fracture risk [254]. This indicates that the trabecular bone is osteopenic and at increased risk of fracture.

3.8.3. Epiphyseal Trabecular Analysis of MP-107 Animals

Analysis of the epiphyseal bone can help elucidate what changes the mutation may be having on the subchondral trabecular bone structure. The subchondral trabecular bone is directly below the subchondral bone plate. Changes to this trabecular bone may have an impact on both the subchondral cortical bone and the articular cartilage

To explore whether there were changes to the structure of the subchondral trabecular bone, a region of interest was identified between the subchondral bone plate and the growth plate for analysis. Automated analysis of this region allowed comparison between genotypes at all three time points. The drawing of the region of interest was performed blind to genotype and the genotypes were only synched with the data for comparison between genotypes.

Analysis of the subchondral bone in the tibia revealed a number of trends in males across time points (Figure 3.41).

Heterozygotes had a significantly lower bone volume fraction (BV/TV) than wild-type animals at 9 months (WT Mean-27.71, SD-1.53, N-5, HET Mean-23.44, SD-1.27, N-5, P=0.0026), there were no differences at 4 or 18 months.

Heterozygotes had a significantly higher trabecular separation than wild-type animals at both 4 months (WT Mean-0.141, SD-0.009, N-5, HET Mean-0.159, SD-0.006, N-5, P=0.0091), and 9 months (WT Mean-0.146, SD-0.008, N-5, HET Mean-0.174, SD-0.006, N-5, P=0.0005).

Heterozygotes had a significantly higher trabecular thickness than wild-type animals at both 4 months (WT Mean-0.023, SD-0.0003, N-5, HET Mean-0.026, SD-0.0008, N-5, P=0.0006) and 9 months (WT Mean-0.025, SD-0.0009, N-5, HET Mean-0.027, SD-0.0007, N-5, P=0.0425).

Heterozygotes had significantly lower trabecular number than wild-type animals, at both 4 months (WT Mean-11.45, SD-0.51, N-5, HET Mean-9.91, SD-0.36, N-5, P=0.0011) and 9 months (WT Mean-10.92, SD-0.59, N-5, HET Mean-8.75, SD-0.43, N-5, P=0.0004).

There did not appear to be any obvious trends with age as seen in the metaphyseal trabecular bone.

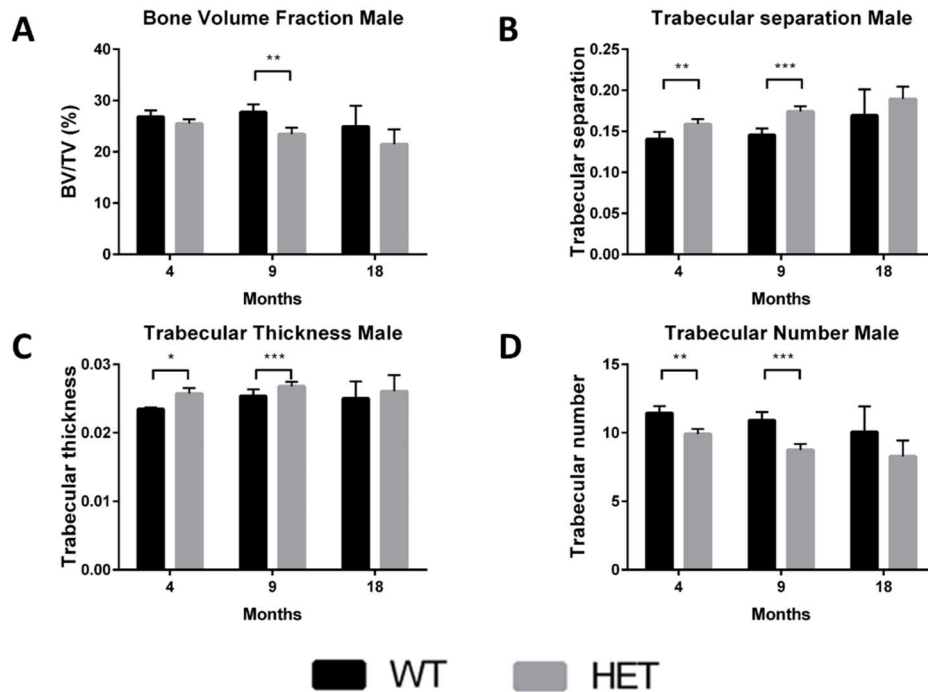


Figure 3.41. μ CT analysis of the subchondral trabecular bone in male animals. (A) Heterozygotes (HET, *Col1a2*^{+/-107}) show a reduction in the bone volume fraction when compared with wild types (WT, *Col1a2*^{+/+}) at 9-months. (B) Heterozygotes (HET, *Col1a2*^{+/-107}) show an increase in the trabecular separation when compared with wild types (WT, *Col1a2*^{+/+}) at 4- and 9-months. (C) Heterozygotes (HET, *Col1a2*^{+/-107}) show an increase in the trabecular thickness when compared with wild type (WT, *Col1a2*^{+/+}) at 4- and 9-months. (D) Heterozygotes (HET, *Col1a2*^{+/-107}) show a reduction in the trabecula number when compared with wild types (WT, *Col1a2*^{+/+}) at 4- and 9-months. Student T-test *P<0.05, **P<0.01, ***p<0.001.

Analysis of the subchondral bone in the tibia revealed a number of trends in females across time points (Figure 3.42).

Heterozygotes had a significantly lower bone volume fraction (BV/TV) than wild-type animals at 4 months (WT Mean-27.13, SD-0.78, N-5, HET Mean-24.04, SD-0.65, N-5, P=0.00028), there were no differences at 9 or 18 months.

Heterozygotes had a significantly higher trabecular separation than wild-type animals at 4 months (WT Mean-0.171, SD-0.008, N-5, HET Mean-0.200, SD-0.006, N-5, P=0.00045), at 9 months the difference was trending towards significance (WT Mean-0.177 SD-0.013, N-5, HET Mean-0.193, SD-0.005, N-5, P=0.054).

Heterozygotes had a significantly higher trabecular thickness than the wild types at 9 months (WT Mean-0.026 SD-0.0017, N-5, HET Mean-0.029, SD-0.0013, N-5, P=0.0071),

with no significant difference at either 4 or 18 months, there was no clear trend in trabecular thickness.

Heterozygotes showed a significantly lower trabecular number than wild-type animals at 4 months (WT Mean-10.18 SD-0.41, N-5, HET Mean-8.71, SD-0.63, N-5, P=0.0045), and 9 months (WT Mean-10.01 SD-1.00, N-5, HET Mean-7.79, SD-0.36, N-5, P=0.0031), the 18-month cohort showed no difference.

There did not appear to be any obvious trends with age as seen in the metaphyseal trabecular bone.

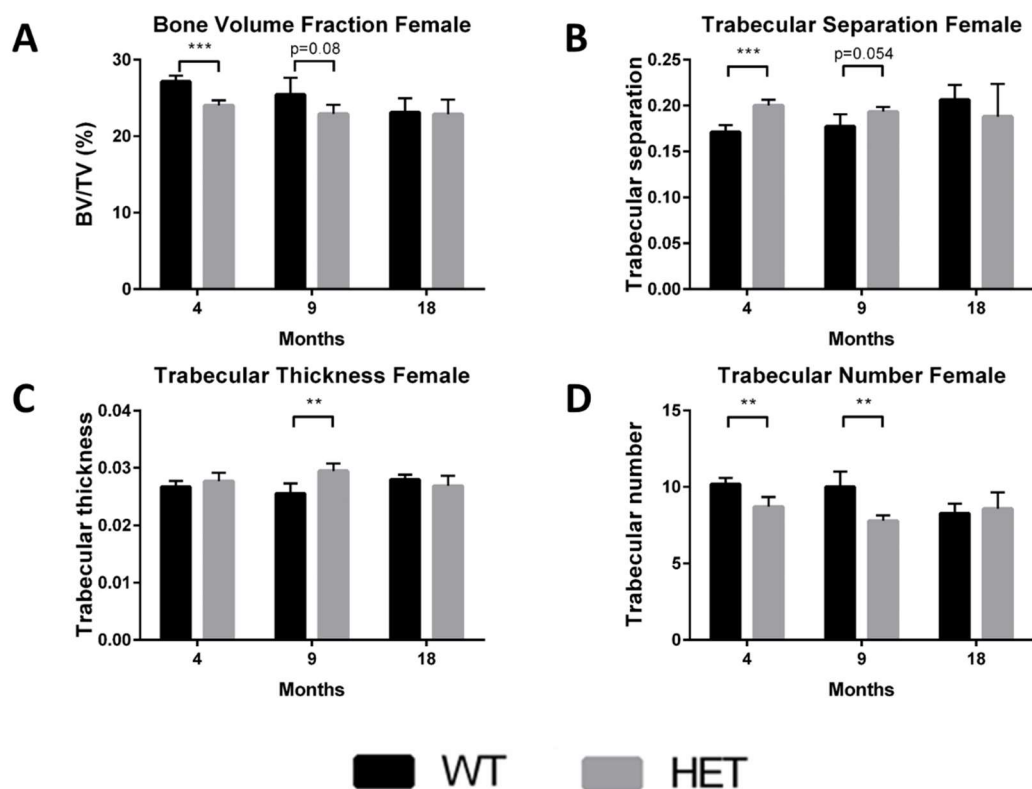


Figure 3.42. μ CT analysis of the subchondral trabecular bone in female animals. (A) Heterozygotes (HET, *Col1a2*^{+/¹⁰⁷}) show a reduction in the bone volume fraction when compared with wild types (WT, *Col1a2*^{+/⁺}) at 4-months. (B) Heterozygotes (HET, *Col1a2*^{+/¹⁰⁷}) show an increase in the trabecular separation when compared with wild types (WT, *Col1a2*^{+/⁺}) at 4-months. (C) Heterozygotes (HET, *Col1a2*^{+/¹⁰⁷}) show an increase in the trabecular thickness when compared with wild types (WT, *Col1a2*^{+/⁺}) at 9-months. (D) Heterozygotes (HET, *Col1a2*^{+/¹⁰⁷}) show a reduction in the trabecula number when compared with wild types (WT, *Col1a2*^{+/⁺}) at 4- and 9-months. Student T-test *P<0.05, **P<0.01, ***p<0.001.

The analysis of the subchondral trabecular bone is very similar to the metaphyseal trabecular bone indicating that the subchondral bone is osteopenic and at increased risk of fracture. Interestingly there were no significant differences between genotypes in

the 18-month cohort, where you would perhaps expect more differences due to sclerosis.

3.8.4. Subchondral Bone Plate Analysis of MP-107 Animals

The subchondral bone plate (SBP) was assessed for average thickness for both the medial and lateral condyle of the tibial plateau. This measurement actually consists of the SBP and the zone of calcified cartilage (ZCC). An increase in thickness could be indicative of increased mineralisation of the un-mineralised cartilage by the ZCC or sclerosis of the SBP [180]. To explore whether there were changes to the SBP of the lateral and medial tibial plateaux, regions of interest were identified and outlined. Automated analysis of these regions allowed thickness be measured, and a comparison between genotypes made at all three time points (Figure 3.43). The drawing of the region of interest was performed blind to genotype, and the genotypes were only synched with the data for comparison between genotypes.

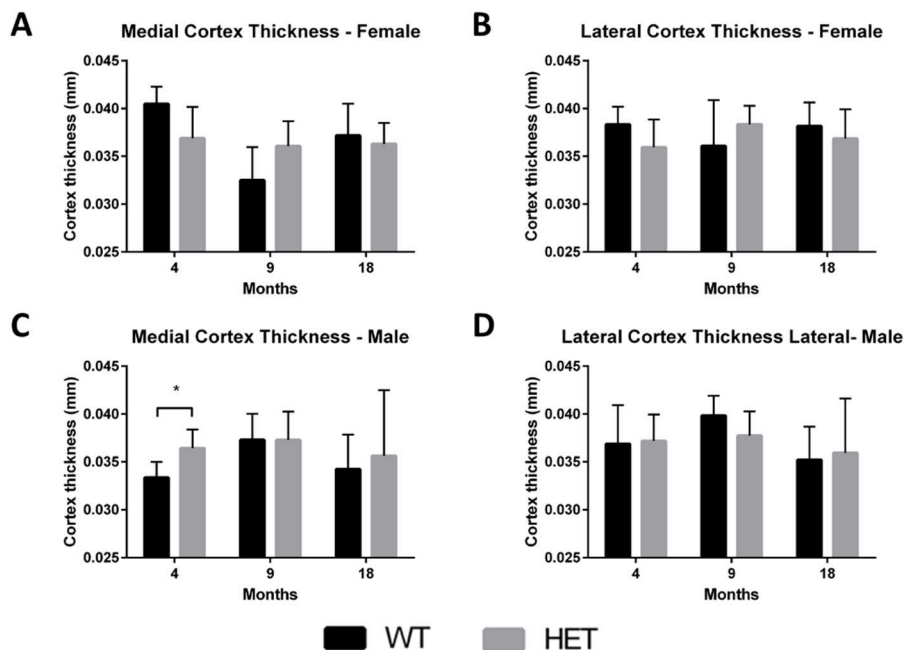


Figure 3.43. μ CT analysis of the thickness of the subchondral bone plate (SBP) of the lateral and medial tibial plateaux. (A) No significant difference was detected in the thickness of the medial SBP between heterozygotes (HET, *Col1a2*^{+/-107}) and wild types (WT, *Col1a2*^{+/+}) females at any time point. (B) No significant difference was detected in the thickness of the lateral SBP between heterozygotes (HET, *Col1a2*^{+/-107}) and wild types (WT, *Col1a2*^{+/+}) females at any time point. (C) A significant increase in the thickness of the medial SBP was detected in the male heterozygotes (HET, *Col1a2*^{+/-107}) when compared with the male wild types (WT, *Col1a2*^{+/+}) at 4-months, no significant difference was detected at any other time point. (D) No significant difference was detected in the thickness of the lateral SBP between heterozygotes (HET, *Col1a2*^{+/-107}) and wild types (WT, *Col1a2*^{+/+}) males at any time point. Student T-test *P<0.05.

No significant difference in thickness of the subchondral bone was detected in any cohort with the exception of the 4-month male cohort, where the medial condyle of male heterozygotes was increased compared to the wild types. The absence of any differences at later time points indicates that the heterozygotes are not developing thickened sclerotic subchondral bone plates.

The differences detected between heterozygotes and wild types in the metaphyseal and epiphyseal trabecular bone indicates that the bone is osteopenic, and structurally weaker in the heterozygotes.

3.9. Time Course Histology of MP-107 Animals

The μ CT imaging indicated that there were changes occurring in the tissues surrounding the knee joint of heterozygote mice much earlier than was visible in radiographs. Histology was performed on the knee joints from animals in the 4-, 9-, 12- and 18-month cohorts, to investigate whether the changes seen in the μ CT imaging led to changes within the joints, and whether the OA observed in the G₃ cohort, occurred earlier than 18 months.

3.9.1. Histological analysis of MP-107 knee joints at 4 Months

Histological analysis of Safranin O stained coronal section of knee joints from wild-type (WT, *Col1a2^{+/+}*) and heterozygous (HET, *Col1a2^{+/107}*) animals at 4 months of age show no differences in the articular cartilage, or signs of osteophytes (Figure 3.44).

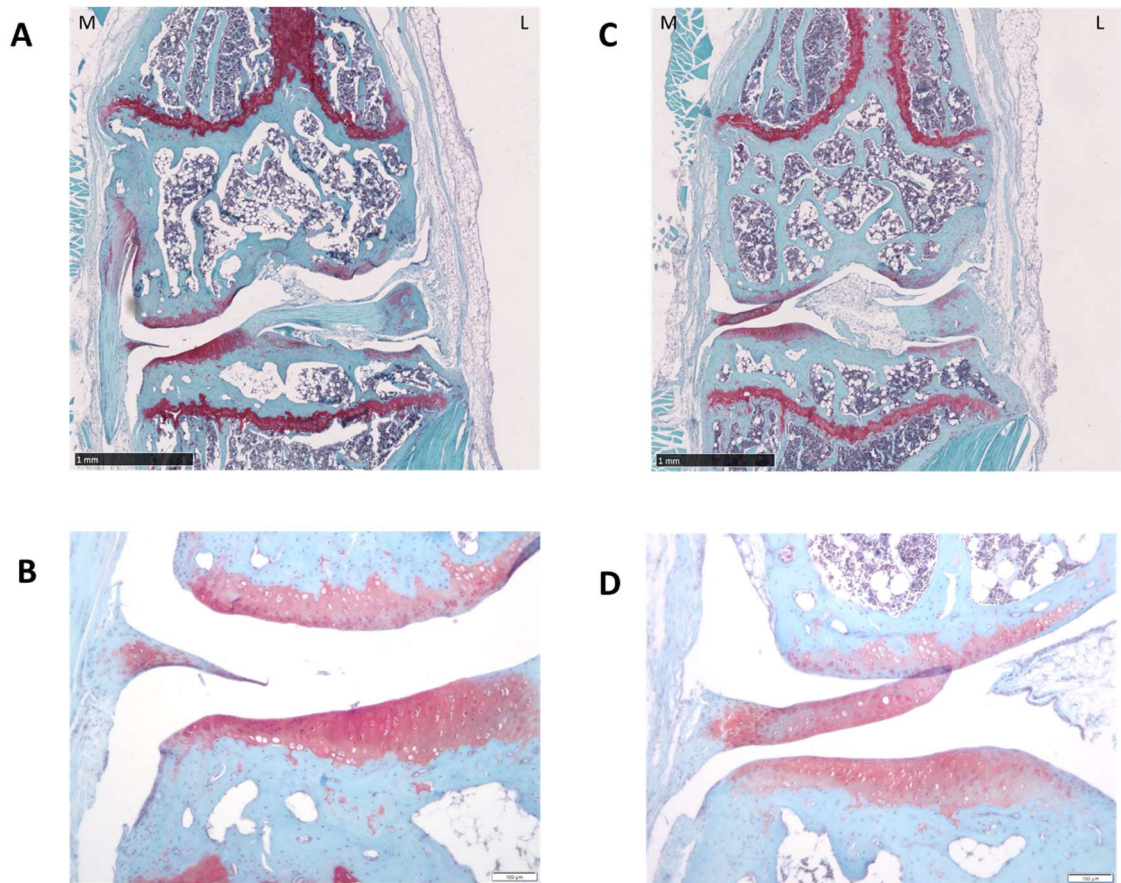


Figure 3.44. Safranin O stained histological section of knee joints from wild-type and heterozygous animals at 4 months of age. (A+B) Wild-type (WT, *Col1a2*^{+/+}) and (C-D) heterozygous (HET, *Col1a2*^{+/107}) animals at 4 months of age show no differences in the articular cartilage, or signs of osteophytes. (Scale bar A+C-1mm, B+D 100μm, Medial and Lateral sides labelled with M and L respectively).

3.9.2. Histological analysis of MP-107 knee joints at 9 Months

Histological analysis of Safranin O stained coronal section of knee joints from wild-type (WT, *Col1a2*^{+/+}) and heterozygous (HET, *Col1a2*^{+/107}) animals at 9 months of age show that the heterozygotes have regular healthy articular cartilage; however there is evidence of osteophyte formation and hypertrophy of the soft tissues. The wild types have regular healthy articular cartilage and no evidence of osteophyte formation (Figure 3.45).

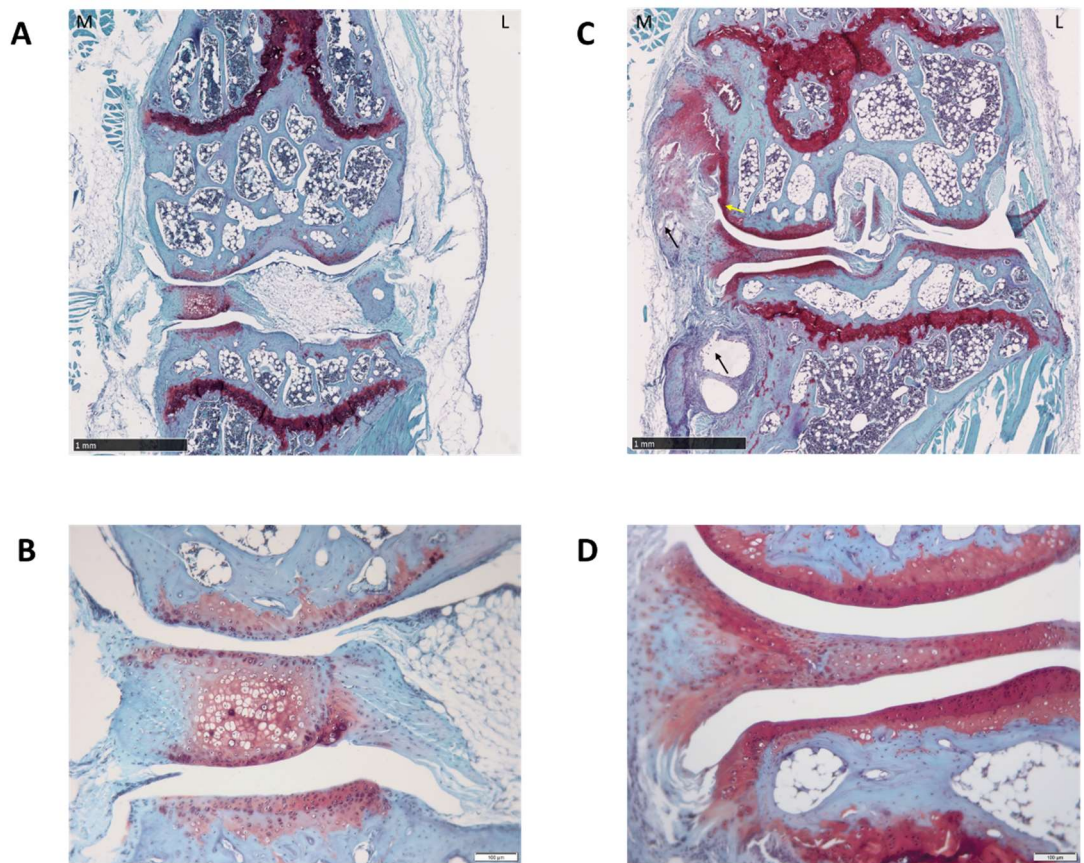


Figure 3.45. Safranin O stained histological section of knee joints from wild-type and heterozygous animals at 9 months of age. (A+B) Wild types (WT, *Col1a2*^{+/+}) have smooth healthy articular cartilage and no evidence of osteophyte formation, Safranin O staining appears weaker, however there is no evidence of damage to cartilage. (C-D) Heterozygous (HET, *Col1a2*^{+/107}) sections have smooth healthy articular cartilage, but also show evidence of hypertrophy of soft tissue (Black arrows) and some evidence of osteophyte formation (Yellow arrow). (Scale bar A+C-1mm, B+D 100μm, Medial and Lateral sides labelled with M and L respectively).

3.9.3. Histological analysis of MP-107 knee joints at 12 Months

Histological analysis of Safranin O stained coronal section of knee joints from wild-type (WT, *Col1a2*^{+/+}) and heterozygous (HET, *Col1a2*^{+/107}) animals at 12 months of age show that the heterozygotes have regular healthy articular cartilage however there is evidence of osteophyte and chondrophyte formation, and soft tissue ossification. The wild types have regular healthy articular cartilage and no evidence of osteophyte formation. The osteophytes in the heterozygous joints appear to be affecting the alignment of the joint and are having an effect on the quality of some of the heterozygous sections (Figure 3.46).

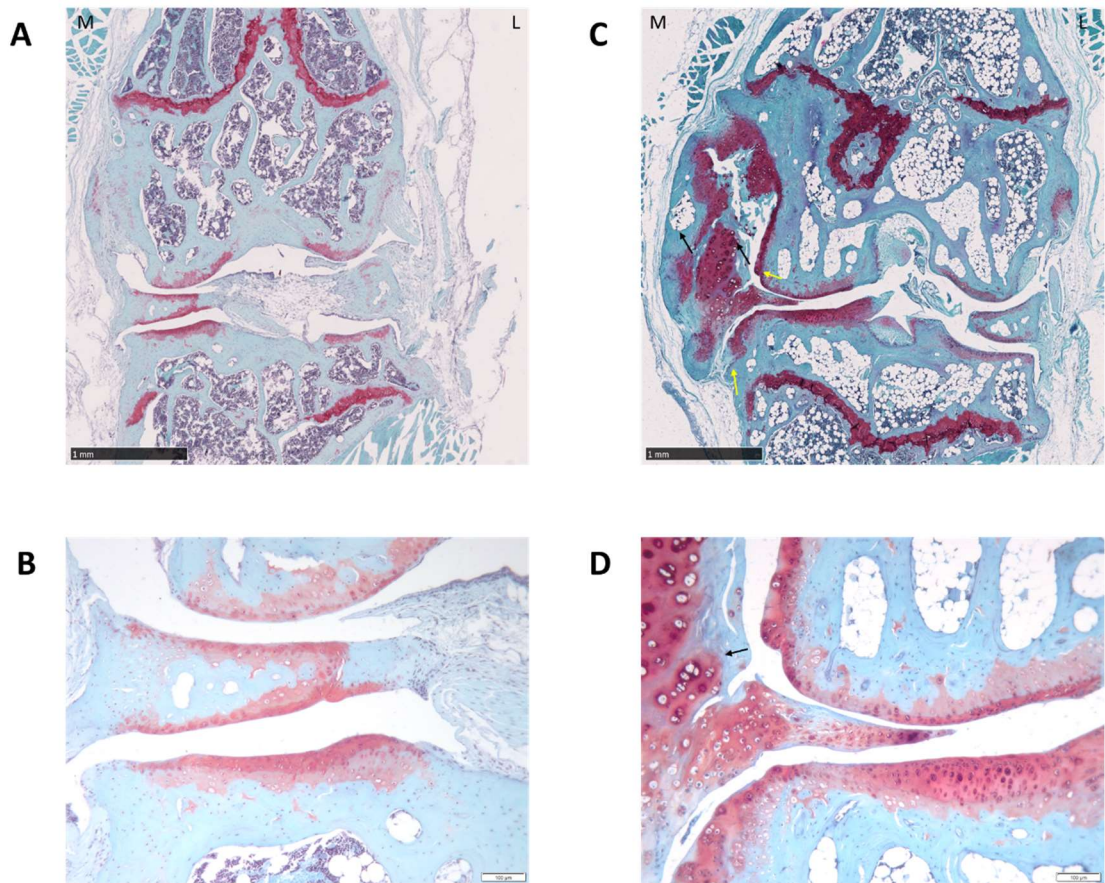


Figure 3.46. Safranin O stained histological section of knee joints from wild-type and heterozygous animals at 12 months of age. (A+B) Wild types (WT, *Col1a2*^{+/+}) have smooth healthy articular cartilage and no evidence of osteophyte formation. (C-D) Heterozygotes (HET, *Col1a2*^{+/¹⁰⁷}) have smooth healthy articular cartilage, evidence of chondrophyte formation (Black arrows) and some evidence of osteophyte formation (Yellow arrows). (Scale bar A+C-1mm, B+D 100μm, Medial and Lateral sides labelled with M and L respectively).

3.9.4. Histological analysis of MP-107 knee joints at 18 Months

Histological analysis of Safranin O stained coronal section of knee joints from wild-type (WT, *Col1a2*^{+/+}) and heterozygous (HET, *Col1a2*^{+/¹⁰⁷}) animals at 18 months of age show that the heterozygotes have irregular and damaged articular cartilage, large osteophytes, hypertrophy of the soft tissues and a damaged meniscus. The wild types have regular healthy articular cartilage and no evidence of osteophyte formation. Previous μ CT imaging did appear to show some calcification of ligaments, but this was not obvious using histology (Figure 3.47).

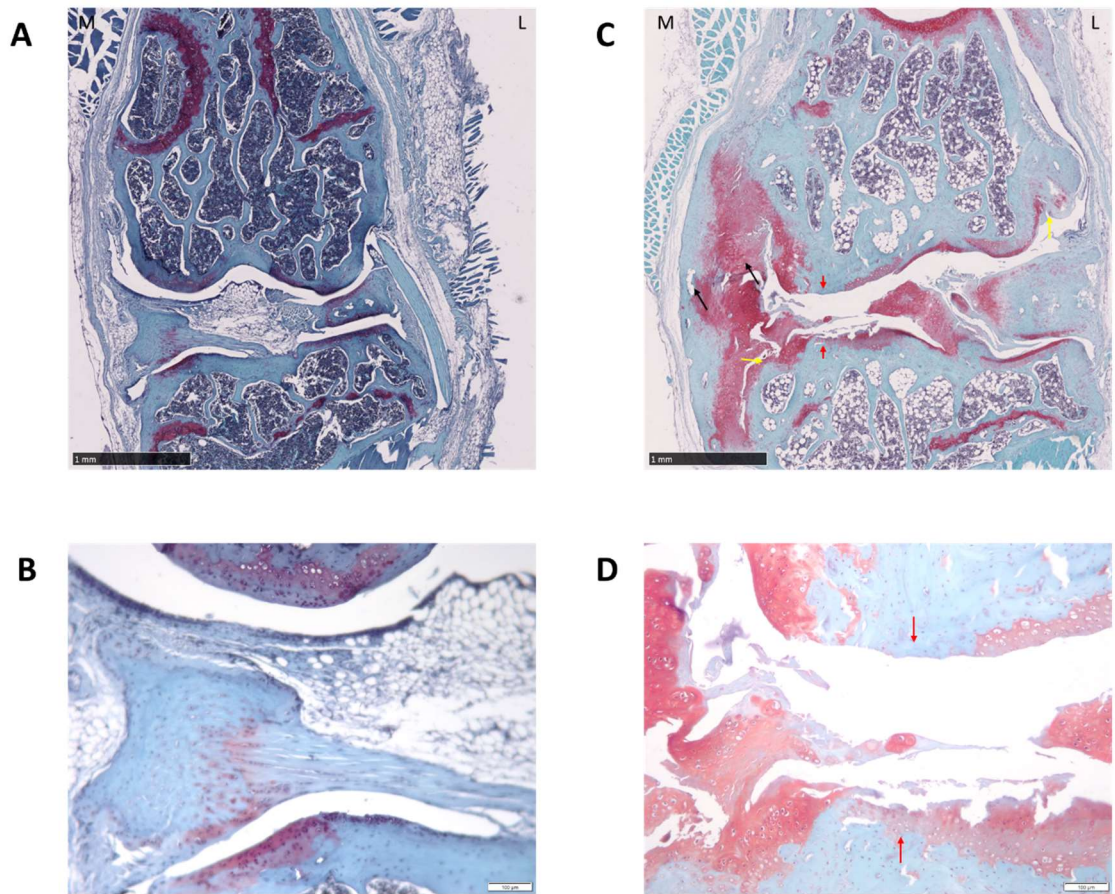


Figure 3.47. Safranin O stained histological section of knee joints from wild-type and heterozygous animals at 18 months of age. (A+B) Wild types (WT, *Col1a2*^{+/+}) have some minor signs of fissuring and no evidence of osteophyte formation. (C-D) Heterozygotes (HET, *Col1a2*^{+/¹⁰⁷}) have irregular severely damaged articular cartilage (red arrows), evidence of hypertrophy of the soft tissues (Black arrows) and evidence of osteophyte formation (Yellow arrows). The meniscus is severely damaged. (Scale bar A+C-1mm, B+D 100μm, Medial and Lateral sides labelled with M and L respectively).

Histological sections of heterozygous knees show evidence of abnormal bone formation, typically involving the ligament and joint capsule, and synovial fibrosis. This is similar to the effects observed by μ CT. Despite this, OARSI scoring of histological sections [255] reveals that there is only a difference in the cartilage between heterozygotes and wild types at 18 months (Figure 3.48). The observed changes in the MCL and osteophyte development were visible as early as 9 months, both on histological sections and μ CT, indicating that these changes precede the observed cartilage changes.

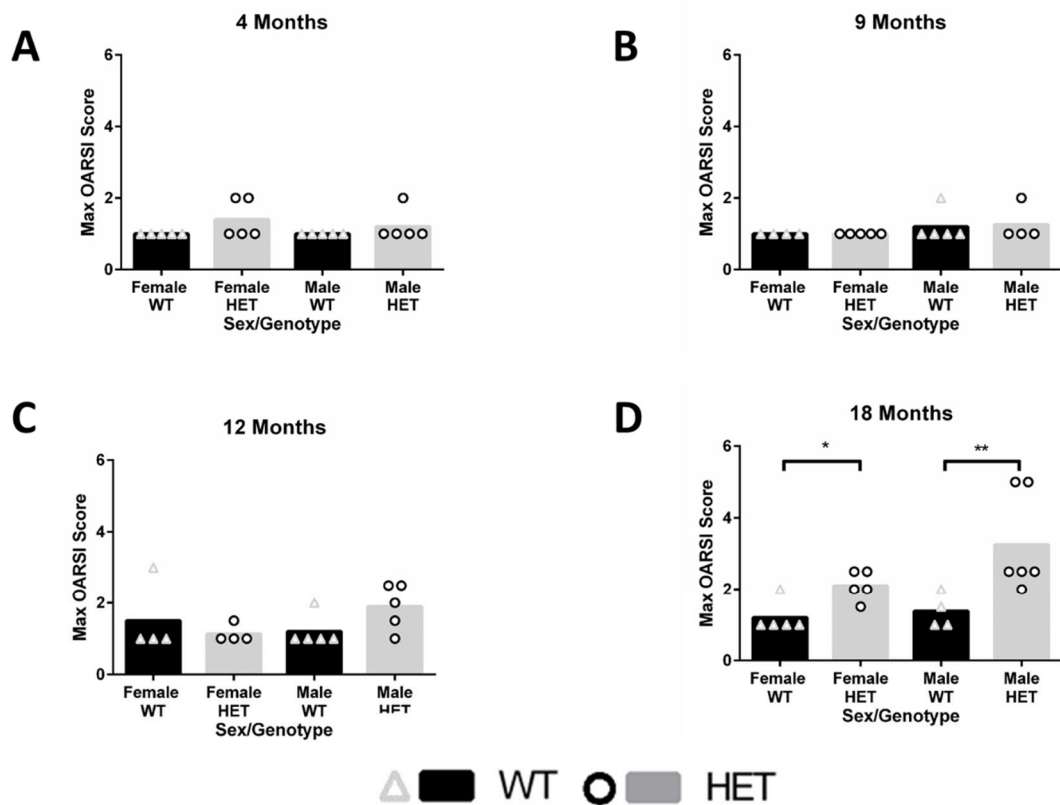


Figure 3.48. Maximum OARSI scores of Safranin O stained histological section of knee joints across the four time points. (A-C) No significant differences were observed between genotypes of either sex at the 4-, 9- and 12-month time points. (D) In both sexes heterozygotes (HET, *Col1a2*^{+/¹⁰⁷) had significantly higher max OARSI scores than their wild type (WT, *Col1a2*^{+/⁺) counterparts. (All group n=5, with the exception of 18M male WT n=4, 9M male HET n=4, 9M male WT n=4, scoring included medial and tibial sides of the femur and tibia. Statistical test used was Mann-Whitney * P<0.05, ** P<0.01- 18M males P=0.0095, 18M females P= 0.0317)}}

3.10. Discussion

The mutant line MP-107 was identified from the Harwell Ageing screen, with mild, early onset bone abnormalities, including splayed ischia and a curved olecranon. As the line was aged, a number of animals developed abnormal bone growth at the knee joint and histological analysis of the knee joint showed damaged articular cartilage, in addition to the abnormal bone growth.

SNP mapping revealed a region on Chromosome 6 likely to contain the causative mutation, and WGS identified a splice region variant in *Col1a2*. Subsequent Sanger sequencing confirmed that the affected animals, where DNA was available, were all heterozygous for this mutation. No homozygotes were identified in the G₃ cohort, and homozygotes produced from intercross matings were found to be lethal at P0.

The observed perinatal lethality of the *Col1a2*^{107/107} animals appears to be attributable to respiratory insufficiency. This conclusion was reached due to the observation of a number of new-born *Col1a2*^{107/107} pups gasping and needing to be culled for welfare purposes, coupled with the reduction in airway size in the *Col1a2*^{107/107} animals. Histological analysis of embryonic lungs revealed that the airways of homozygous lungs were smaller than those of wild-type and heterozygous lungs, due to thickened interstitial mesenchyme. The alveolar walls and interstitium are primarily comprised of type I and III collagen, which provide a structural framework and contribute to the lung mechanics. Type I collagen provides mechanical stability and structure, and therefore abnormal collagen I may impair the ability of the alveoli to expand and contract properly, and fulfil their function [256]. The whole mount skeletal staining of 18.5 dpc embryos clearly show breaks in the long bones of *Col1a2*^{107/107} embryos, which indicate an osteogenesis imperfecta (OI) phenotype. The perinatal lethality due to the lung phenotype and the *in utero* breakage of the long bones is very similar to the Brittle IV mouse model of OI [80].

The mutation was predicted to be a splice region variant, creating a new splice acceptor site affecting the splicing between Exon 21 and Exon 22. PCR and Sanger sequencing of cDNA showed that the mutation did cause a new splice acceptor site to be formed, causing 3 bases from the intron to be incorporated as a new amino acid within Exon 22, in effect causing an insertion of Glutamine into the protein disrupting the repeating glycine motif. Where normally there are two amino acids between each glycine (G-X-Y_n), in this case there were three. A large proportion of osteogenesis imperfecta cases are caused by glycine substitutions, which also cause the repeating glycine motif to be disrupted[46-48]. Glycine substitutions result in 5 amino acids between two glycines rather than the normal two [73]. This could explain the apparent mildness of the bone phenotypes in this line compared to those often seen in humans.

A complicating factor was found to be that as the original splice site is not destroyed, the spliceosome produces both mutant and wild-type transcripts even when both alleles are mutant. It appears that the amount of wild-type and mutant transcript varies between mice of the same genotype, which could account for the variability of the phenotype. Almost 300 unique splice variants in *COL1A1* and *COL1A2* have been shown

to cause OI phenotypes in human, 210 splice variants in *COL1A1*, and 84 in *COL1A2* [46-48].

An experiment was designed to allow more in-depth investigation of the phenotypes seen in the heterozygotes across a number of time points. X-ray imaging confirmed that the incidence of the splayed ischia and curved olecranon did not increase at later time points, and that the incidences of the knee phenotype did. The phenotypes observed at the pelvis and the elbow are similar to those seen in some mouse model of OI, including the *Brtl* model, the phenotype observed in these lines were also variable [80, 81].

The experiment also showed the variability in phenotype: in the 15-month male cohort 80 % of animals showed a phenotype including 4 animals with the knee phenotype, one of which also displayed the curved olecranon, but no animals displayed the splayed ischia phenotype. The X-ray imaging also indicated that some heterozygotes showed detectable bone growth at the knee as early as 9 months.

Neither the DEXA analysis nor the clinical chemistry analysis produced any parameters that were consistently significantly different between genotypes.

μ CT imaging at 4, 9 and 18 months confirmed the presence of abnormal bone growth as early as 4 months, and that this phenotype develops over time. The mouse model of OA, *Str/ort*, exhibits similar abnormal bone growth, although this line exhibits a more severe phenotype at early timepoints[257]. A similar phenotype has also been identified in the experimental line known as *Ubr5^{mt}*, *UBR5* was shown to play a role in maintaining cartilage homeostasis and suppressing metaplasia [258]. Analysis of the 3D imaging of trabecular bone revealed that male heterozygous animals had a significantly reduced bone volume fraction and trabecular number, and a significant increase in trabecular separation at multiple time points, in addition to a significant increase in trabecular thickness at a single time point. This trend was replicated in the female heterozygotes, albeit with fewer significant results and both male and female heterozygotes showed similar trends in the subchondral bone. There was only a single time point where there was any significant difference in the cortex thickness of the tibial plateau. The variability in the statistical difference is likely due to the small cohort size and the variability of the phenotype within heterozygotes. However, the μ CT results do indicate that the heterozygotes generally have weaker bones and may a mild form of osteogenesis

imperfecta. The *Brtl* mouse model of OI has been shown to exhibit similar phenotypes including reduced bone volume fraction and trabecular thickness in 6 month old animals, when compared to wild-types, although this analysis was performed on femoral trabecular bone, rather than tibial [259, 260].

Histology indicated that OA does develop in heterozygotes in the later cohorts, indicated by the damaged articular cartilage. However, the osteophytes, ossification of ligament and synovial inflammation seen in earlier cohorts without cartilage damage indicates that in this mutant line, these changes precede the articular cartilage damage. It is therefore possible that the cartilage lesions could be a result of ossification of ligaments and meniscus, or the synovial inflammation that preceded them [261, 262].

The evidence in this chapter indicates that an ENU induced A to T transversion in the gene *Col1a2* leads to a disruption of the repeating glycine motif in *Col1a2*. The homozygotes are lethal and the heterozygotes develop different bone structure leading to mild bone abnormalities and evidence of fracture. Although, heterozygotes develop OA, from the data in this chapter it is not possible to discern the specific mechanisms causing the OA.

Chapter 4: Tissue Specific Effects of the *Col1a2*^{107/+} Mutation

4.1. Introduction

The previous results chapter established that the MP-107 mutant, carrying a splice mutation in *Col1a2*, developed mild bone abnormalities and OA. Collagen I is a major constituent of bone, and therefore bone phenotypes arising from a mutation in *Col1a2* is not surprising. One of the major diseases associated with mutations in *Col1a1* and *Col1a2* in humans is Osteogenesis Imperfecta (OI), a disease characterised by brittle, fragile bones. In addition to OI, some types of Ehlers Danlos Syndrome (EDS) can also be caused by mutations in *Col1a1* and *Col1a2*. EDS are a group of connective tissue disorders, primarily caused by abnormalities in the structure, production or processing of Collagens (including I, III, V). A common feature in many types of EDS is hypermobile joints and elastic skin.

Col1a1 and *Col1a2* mutations are not normally associated with OA. However, as OA is an arthropathy involving all the various tissues of the joint, it is surprising that genes causing defects in bone and connective tissue are not always associated with the disease.

In this chapter, I focus on investigating the phenotypes and behaviour of collagen I and collagen I rich tissues, such as bones, tendons and skin. I hypothesise that the mutation in *Col1a2* is causing the phenotypes described in Chapter 3 as a result of an OI/EDS phenotype. If such phenotypes are observed it will be important to establish the relationship, if any, between the phenotypes observed in the *Col1a2*^{+/¹⁰⁷ and reported in Chapter 3 and the spectrum of OI/EDS-like phenotypes.}

4.2. Mechanical Testing

Collagen I is a very important protein in a wide range of tissues, especially those with mechanical function. Collagen I forms the organic matrix, which is then mineralised to give bones their strength, stores elastic energy in tendons and ligaments, and transmits force between tissues. As such, observing how collagen I rich tissues behave in the MP-107 mutant could elucidate the mechanisms by which a mutation in *Col1a2* leads to the observed phenotypes. It is known that some mutations in collagen I genes lead to bone brittleness and breakage in OI, or joint laxity in EDS, it is therefore possible that the heterozygous mutation in MP-107, could be leading to such phenotypes. The tissues

tested in this section include skin, tendon fascicles, bone and the articular surface of the tibial plateau and femoral condyles (subchondral bone and cartilage). Due to the lethality observed in the homozygous *Col1a2*^{107/107} animals, mechanical testing was only performed on heterozygous *Col1a2*^{+/107} and wild-type *Col1a2*^{+/+} animals.

4.2.1. Mechanical Testing of Tail Tendon Fascicles of MP-107 Animals

Mechanical testing of tendon fascicles enables measurements of tensile strength and elasticity in the fascicles of the tendon. As around 70-80% of the dry weight of tendons is collagen I, changes to the collagen I trimer are likely to have an impact in how this tissue behaves [28].

Fascicles were dissected from tail tendons of heterozygous *Col1a2*^{+/107} and wild-type *Col1a2*^{+/+} mice at 3 months of age and subjected to mechanical testing consisting of 10 cycles of loading and unloading, followed by a pull to failure [38]. Before testing, the diameter of each fascicle was measured, and the cross-sectional area (CSA) calculated to facilitate the calculation of various mechanical parameters post-testing. Heterozygous fascicles had a significantly larger CSA than the wild-type fascicles (P=0.045, Figure 4.1). The larger CSA of the heterozygous fascicles could be due to the disrupted glycine repeating motif causing micro-unfolding or a kink in trimers containing the mutant protein, increasing the diameter of the molecules, and in turn the collagen fibres. Another explanation could be that the abnormal protein causes an increase of water within the tissue, leading to a larger CSA. It is not possible at this point to determine which of these scenarios is more likely.

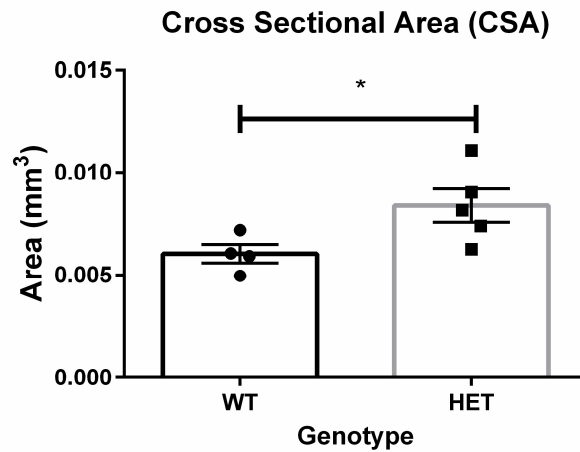


Figure 4.1. Calculated cross sectional area (CSA) of both heterozygous (HET, *Col1a2*^{+/¹⁰⁷}) and wild-type (WT, *Col1a2*^{+/⁺}) fascicles. The CSA from heterozygous (HET, *Col1a2*^{+/¹⁰⁷}) fascicles were significantly larger than wild-type (WT, *Col1a2*^{+/⁺}) fascicles (WT n=4 animals, HET n=5 animals, replicates min 12 fascicles per animal). T-test *= P<0.05

The data from the mechanical testing was analysed in two parts, the ‘cyclic loading’ phase and the ‘pull to failure’ phase. Parameters derived from cyclic loading included: 1) maximum force at cycle 1, 2) stress relaxation and 3) hysteresis. Parameters derived from the pull to failure included: 1) failure stress, 2) failure strain, 3) failure load, 4) maximum modulus and 5) strain at maximum modulus.

To view how the fascicles behave initially, force/extension data from the cyclic loading and unloading is plotted (Figure 4.2). The heterozygous fascicles appear to allow an initial extension under very little load (shown by the ‘toe’ near the origin), indicating a difference in the initial elastic behaviour.

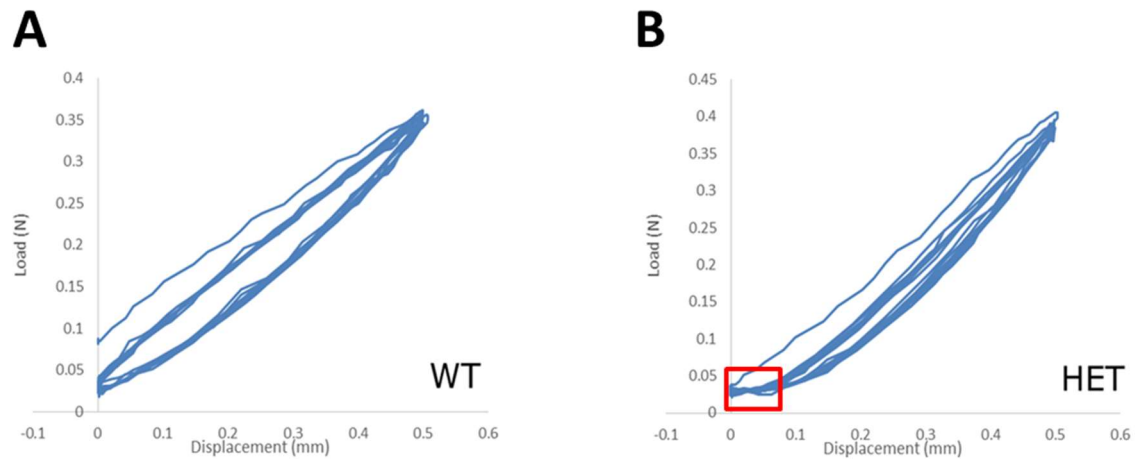


Figure 4.2. Representative force-extension graphs from wild-type (*WT, Col1a2^{+/+}*) (A) and heterozygous (HET, *Col1a2^{+/-}*) (B) fascicles. The heterozygous fascicle (B) shows an altered ‘toe’ of the graph (red box) indicating an extension for very little force after the first loading, suggesting altered viscoelastic properties of the heterozygous fascicle when compared with the wild-type fascicle (A).

In addition to this change in the force/extension behaviour, the area between the loading and unloading curves is reduced in the heterozygous animals, indicating a change in viscoelasticity. This change can be calculated as percentage hysteresis, which is a measure of energy dissipation (Figure 4.3).

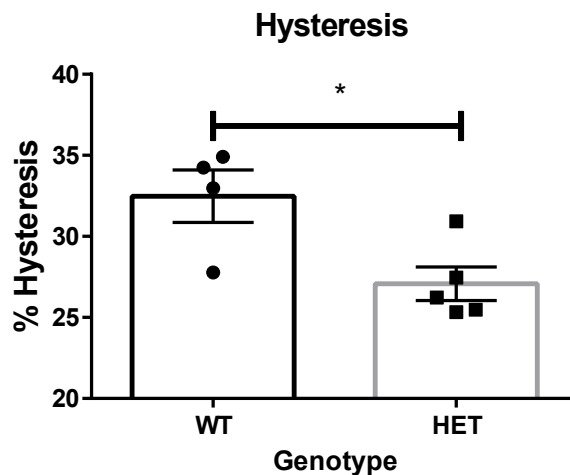


Figure 4.3. Percentage hysteresis of wild-type (*WT, Col1a2^{+/+}*) and heterozygous (HET, *Col1a2^{+/-}*) fascicles. The heterozygous (HET, *Col1a2^{+/-}*) fascicles exhibit a significant reduction in percentage hysteresis, when compared with wild-type (*WT, Col1a2^{+/+}*) fascicles (WT n=4 animals, HET n=5 animals, replicates min 12 fascicles per animal). Student T-test *= P<0.05

At least 12 fascicles from each animal were tested, and the mean value for each animal calculated, and it was observed that there was a significant reduction in the percentage

hysteresis in the fascicles of heterozygous *Col1a2*^{+/¹⁰⁷ animals when compared with fascicles from wild-type *Col1a2*^{+/⁺ animals (P=0.219).}}

The stress relaxation was also calculated as another measure of viscoelastic behaviour; however, the stress relaxation data were not analysable. In all samples regardless of genotype, some fascicles produced negative stress relaxation values. This was caused by excessive noise in the load channel due to the small scale of mouse tail tendon fascicles.

The maximum force exerted in the primary cycle of the cyclic loading was measured, as a constituent of the stress relaxation calculation, and there was no significant difference between genotypes (Figure 4.4)

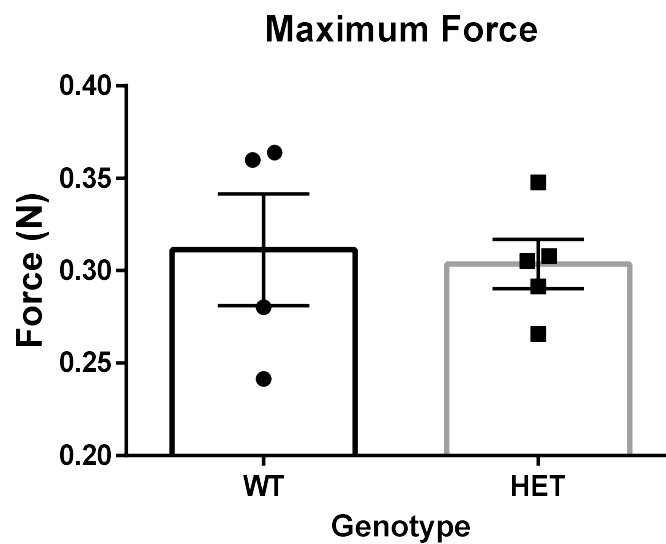


Figure 4.4. Maximum force of wild-type (WT, *Col1a2*^{+/⁺) and heterozygous (HET, *Col1a2*^{+/¹⁰⁷) fascicles. No significant difference was detected in the maximum force between genotypes (WT n=4 animals, HET n=5 animals, replicates min 12 fascicles per animal). T-test*= P<0.05}}

There were no significant differences between genotypes in any of the parameters derived from the pull to failure including: 1) failure stress, 2) failure strain, 3) failure load, 4) maximum modulus and 5) strain at maximum modulus. (Figure 4.5).

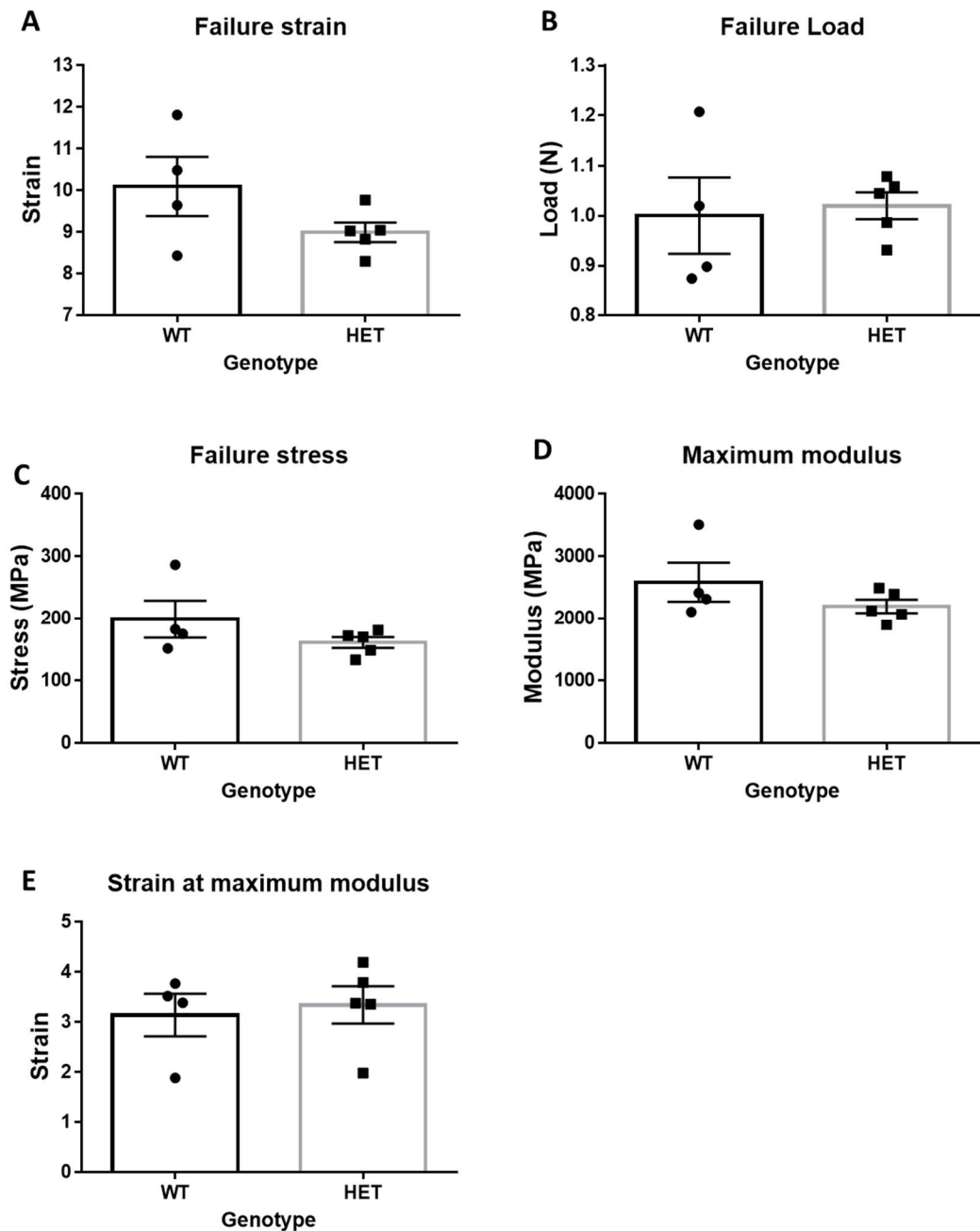


Figure 4.5. Graphs showing parameters from the ‘pull to failure’ phase of wild-type and heterozygous fascicles. (A) failure Strain, (B) failure Load, (C) failure Stress, (D) maximum modulus and (E) strain at maximum modulus showed no significant difference between heterozygous (HET, *Col1a2*^{+/-107}) and wild-type (WT, *Col1a2*^{+/+}) samples, (WT n=4 animals, HET n=5 animals, replicates min 12 fascicles per animal). T-test* = P<0.05

The lack of significant differences in the ‘pull to failure’ parameters indicate that the heterozygous fascicles are not inherently weaker or stronger than the wild-type fascicles. The significant difference in hysteresis between genotypes suggests a difference in the viscoelastic mechanical properties of collagen I in these mice. Hysteresis in tendons is generally thought of as a re-ordering of the multilevel fibre structure, and water movement leading to energy loss in the loading-unloading cycle

[263]. A reduced percentage hysteresis enables higher elastic energy return [264]. In behaviours where mechanical energy is absorbed, rather than stored and returned, such as absorbing impacts, a higher hysteresis is beneficial [265]. This means that the heterozygous tendons are likely to be less effective at absorbing impacts than the wild-type tendons.

It should be noted that the mice analysed were a mixture of males and females, however the literature suggests that there is no significant difference in the mechanical properties of tendons between sexes [266].

4.2.2. Three-point Bone Bending of MP-107 Animals

The three-point bending test is a mechanical test of flexural strength, in bones a reduction of flexural strength could indicate brittle bones [267]. Due to limited resources, it was not possible to perform all mechanical tests on both sexes; female animals were selected over male animals, as previous studies indicate that the BMD is lower in females than males, and therefore any effect present would be more likely to be identified in females [268]. Humeri were harvested from 5 female heterozygotes *Col1a2^{+/-107}* and 5 female wild types *Col1a2^{+/+}* at 3 months old.

Three-point bending of these humeri using the Mach-1 multi-axial mechanical tester revealed a decrease in maximum flexural load ($P=0.0136$) and work to fracture ($P=0.325$) in the heterozygous animals, when compared to the wild-type animals (Figure 4.6). This indicates that the bones of the heterozygotes are more brittle and fragile than the wildtypes. Coupled with the evidence of fracture in some of the heterozygous mice phenotyped indicates a mild OI phenotype in the heterozygotes, in addition to the OI phenotype observed in the homozygotes.

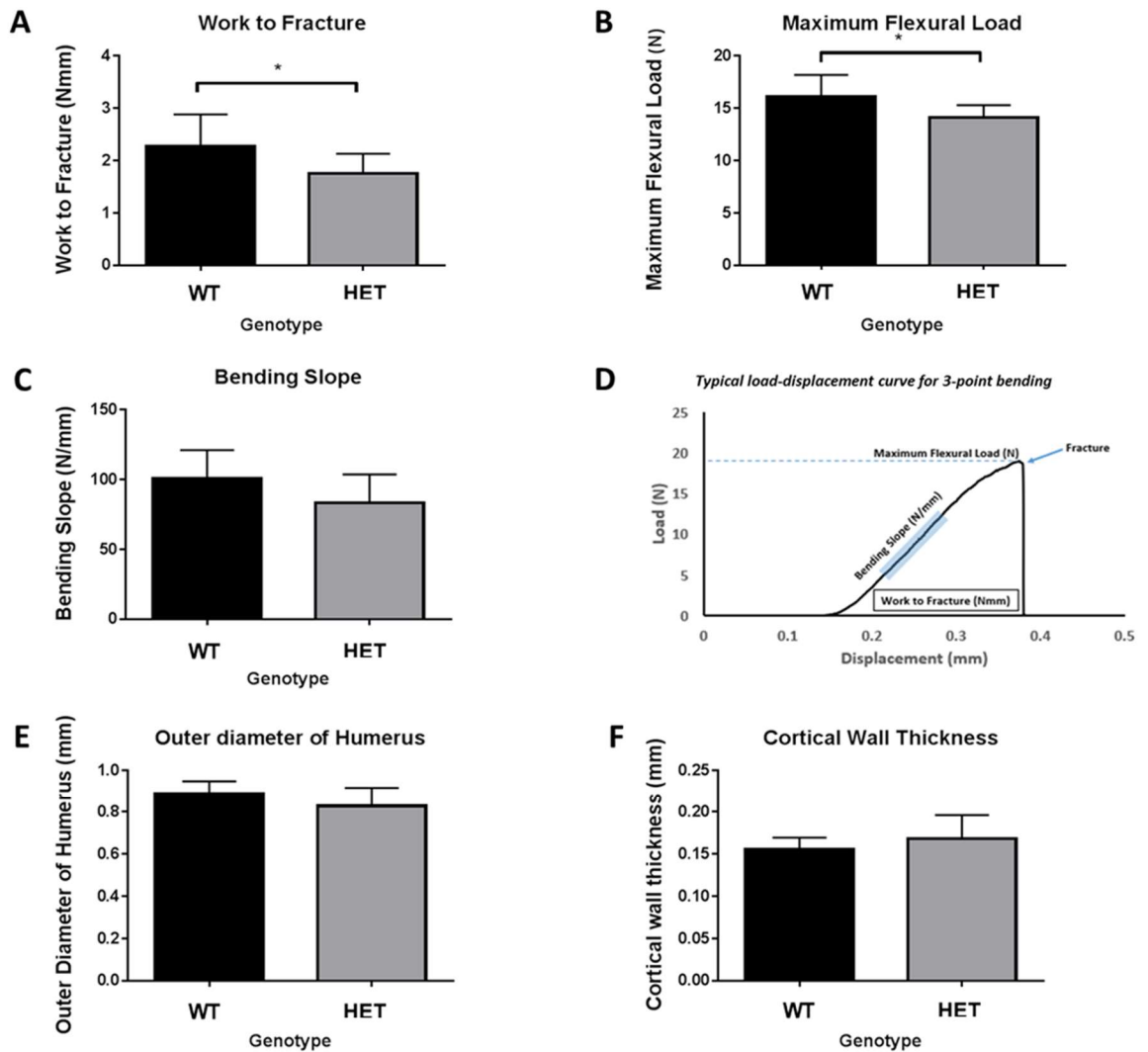


Figure 4.6. Three-point bending analysis of wild-type and heterozygous humeri. In heterozygotes (HET, *Col1a2*^{+/¹⁰⁷) work to fracture (A), and maximum flexural load (B) were significantly reduced when compared to wild types (WT, *Col1a2*^{+/⁺). No significant difference was detected between genotypes in bending slope (C), outer diameter (E) and cortical wall thickness (F). (D) Shows a typical load-displacement graph showing the parameters in (A-C). T-test *P<0.05 (For all genotypes n=5).}}

4.2.3. Tensile Skin Testing of MP-107 Animals

Tensile skin testing is a mechanical test of tensile strength and elasticity [269]. Changes in elasticity or strength could be indicative of an EDS phenotype. Abdominal skin was harvested from the same animals described in three-point bone bending (Section 4.2.2.), 5 female heterozygotes *Col1a2*^{+/¹⁰⁷ and 5 female wild types *Col1a2*^{+/⁺.}}

Tensile rupture testing of this abdominal skin using the Mach-1 multi-axial mechanical tester showed no significant difference in load at rupture or elastic slope. However, there was a significant reduction in the initial elastic slope (P=0.0317) of heterozygous

animals when compared with wild type animals (Figure 4.7). This is very similar to the behaviour seen in the mechanical testing of fascicles, where there is an initial displacement for very little force (See section 4.2.1).

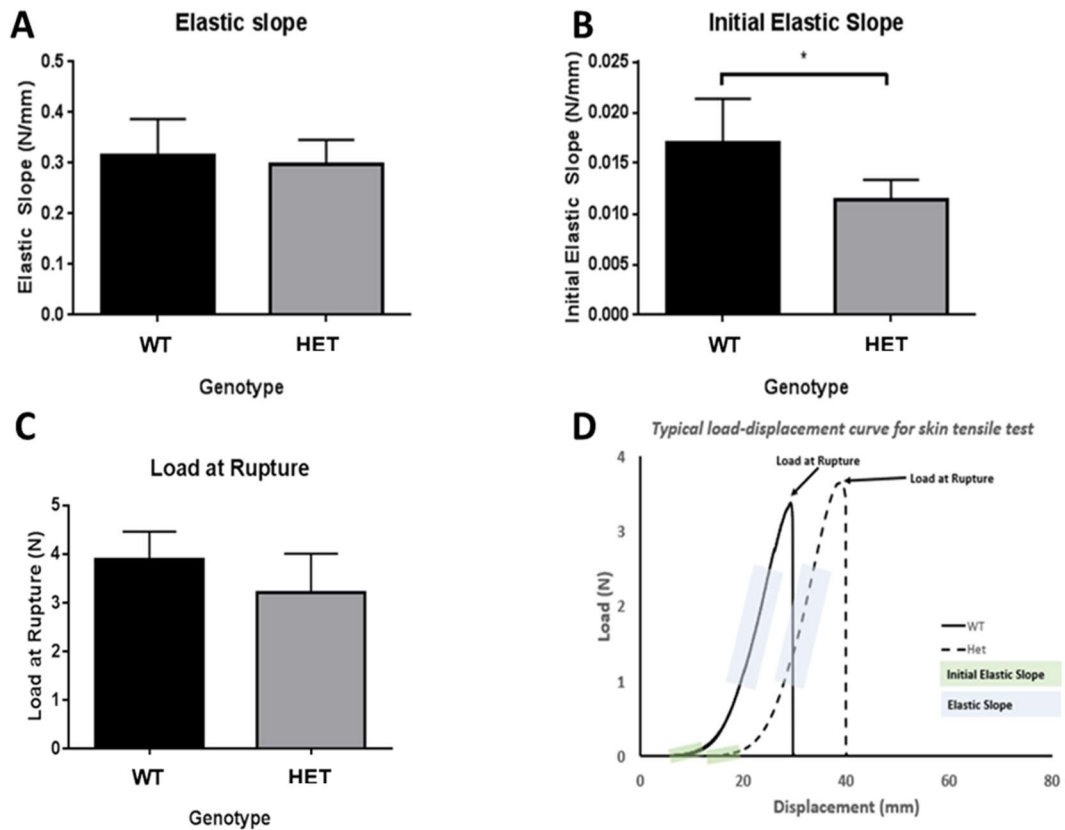


Figure 4.7. Tensile testing analysis of wild-type and heterozygous skin. No significant difference was detected between genotypes in elastic slope (A) or load at rupture (C). In heterozygotes (HET, *Col1a2*^{+/¹⁰⁷) initial elastic slope (B) was significantly reduced when compared to wild types (WT, *Col1a2*^{+/⁺). (D) Shows a typical load-displacement graph showing the parameters in (A-C). T-test *P<0.05 (For all genotypes n=5).}}

4.2.4. Micro-Indentation of the Articular Surface of MP-107 Animals

Micro indentation can be used to investigate the structural stiffness of a material [270]. The articular cartilage of the femoral condyles and tibial plateau are often damaged in OA, and information about the structural stiffness of the tissues that make up these surfaces could inform about any underlying phenotypes that could be contributing to the MP-107 heterozygous animals developing OA.

Whole hind legs were harvested from the same animals described in three-point bone bending (Section 4.3.3.), 5 female heterozygotes *Col1a2^{+/-107}* and 5 female wild types *Col1a2^{+/+}*. The tibial plateaux and femoral condyles from these whole legs underwent automated indentation analysis using the Mach-1 Mechanical Tester (Figure 4.8).

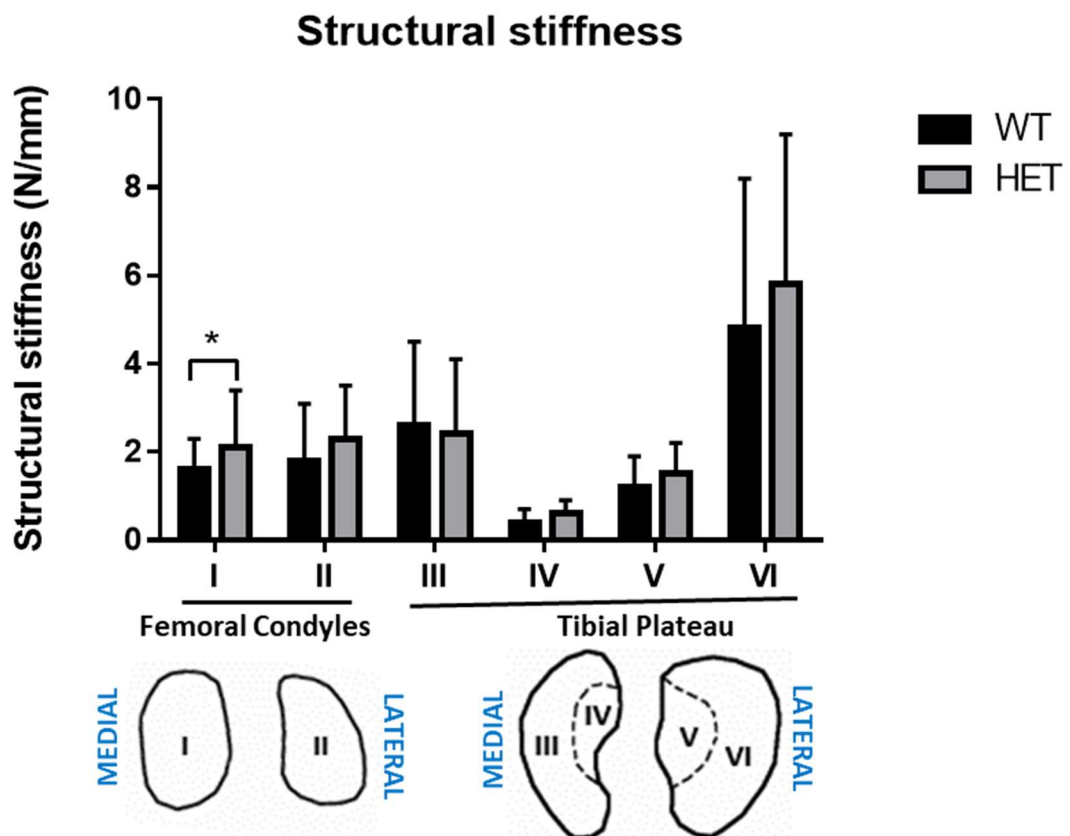


Figure 4.8. Structural stiffness analysis of the femoral condyles and tibial plateaux of heterozygotes and wild types. The medial femoral condyle of heterozygotes (HET, *Col1a2^{+/-107}*) exhibited increased structural stiffness compared to wild types (WT, *Col1a2^{+/+}*). No other region exhibited significant differences between genotypes. T-test $*=P<0.05$ (For all genotypes $n=5$).

The indentation analysis reveals that the medial femoral condyles of heterozygous animals exhibit higher structural stiffness than those of wild-type animals. No other region exhibited significant differences between genotypes.

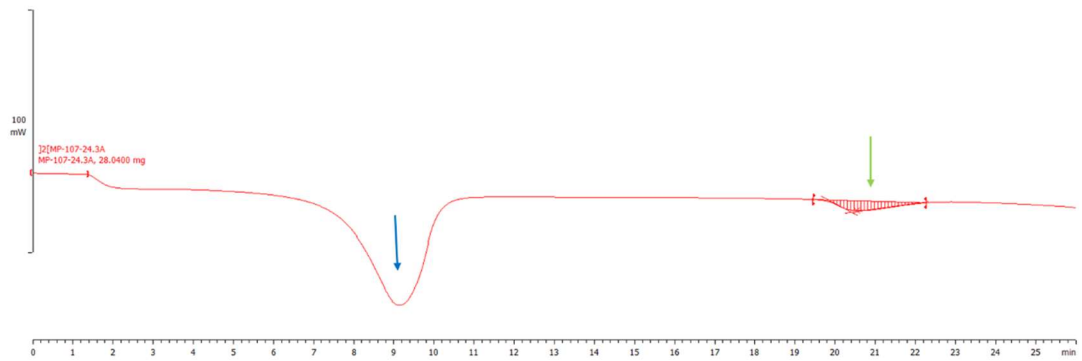
While the medial femoral condyle of heterozygotes exhibits a higher structural stiffness than the wild types, it should be noted that as the tissue tested included both articular cartilage and subchondral bone, it is not possible to attribute the change in the structural stiffness to either cartilage or bone specifically.

4.3. Differential Scanning Calorimetry of MP-107 Tail Tendons

Differential scanning calorimetry (DSC) is a method of thermal analysis. Heat flow is measured as the temperature in the crucible is varied, which can then be used to calculate a range of parameters which can inform the material analysed. Mechanical testing of fascicles extracted from tail tendons showed that the heterozygous fascicle behaved differently than wild type fascicles. DSC can provide information about the collagen heterotrimer within the tendon, and whether there is altered collagen heterotrimer in the heterozygotes [271].

Tail tendons were harvested from female heterozygous *Col1a2*^{+/¹⁰⁷ and wild-type *Col1a2*^{+/⁺ animals at 3 months of age and frozen at -80°C. Samples were later thawed and thermograms were produced using DSC (Figure 4.9).}}

A



B

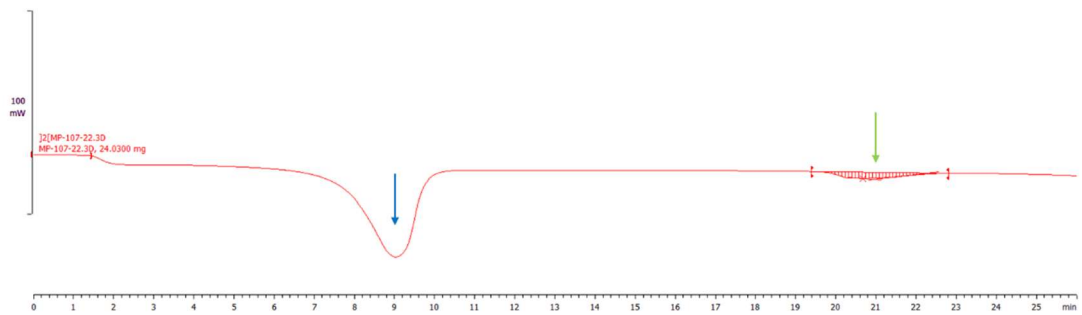


Figure 4.9. Representative differential scanning calorimetry thermograms from wild type and heterozygote tendons. The wild type (A) and heterozygotes (B) thermograms show similar peaks for the melt curve (Blue arrows) and the denaturation of collagen (Green arrows).

The thermograms were then used to calculate a number of parameters including dry and wet enthalpy, collagen denaturation temperature and percentage bound water (Figure 4.10).

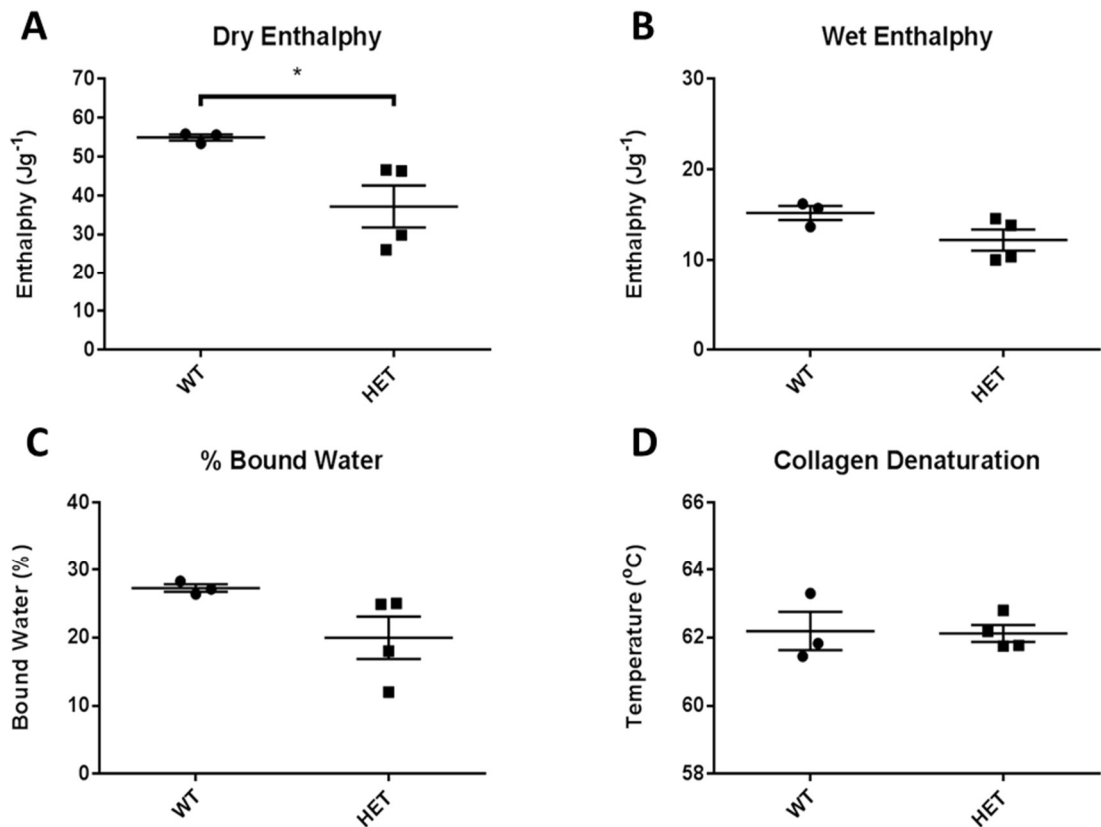


Figure 4.10. Differential scanning calorimetry analysis of heterozygous and wild-type tail tendons. (A) A significant reduction in dry enthalpy of heterozygous (HET, *Col1a2*^{+/¹⁰⁷}) tendons was detected when compared with wild-type (WT, *Col1a2*^{+/+}) tendons. No significant difference was detected between genotypes in (B) wet enthalpy, (C) percentage bound water, or (D) collagen denaturation temperature. T-test*=P<0.05 (Wt n=3, Het n=4).

The tendons showed no significant difference in collagen denaturation temperature, percentage bound water, or the wet enthalpy. However, there was a significant reduction in the dry enthalpy (P=0.398) of heterozygous samples compared to wild-type samples. This difference indicates that less energy is required to break apart the heterozygous trimer, due the trimer being less stable. It is unknown at this time what is causing the increased instability in the heterozygous sample. It is likely for one of two reasons, either that there is homotrimer, consisting of three α 1 chains, present due to the mutant α 2 chain not being incorporated into the collagen I trimer, or the disrupted repeating glycine motif of the mutant α 2 chain is impairing the structural integrity of the heterotrimer.

4.4. Collagen Secretion Analysis of MP-107 Tendons

Radiolabelling using ^{14}C - Proline can be used to investigate the composition of collagen I in tail tendons, and if there is impaired secretion [272]. This technique can answer the question raised by the DSC of what is causing the destabilisation of the Collagen trimer.

The radiolabelled bands of the Pro α 1 (ProCol1a1), Pro α 2 (ProCol1a2), pC α 1 (ProCol1a1 with N terminal propeptide cleaved), pC α 2(ProCol1a2 with N terminal propeptide cleaved), show no difference between genotypes in either intracellular or extracellular extracts. This indicates that the mutant α 2 chain is not being retained intracellularly, as if this was the case the extracellular band in the heterozygous samples would be lighter and the intracellular bands would be darker.



Figure 4.11. Images of radio labelled collagen extracted from wild-type and heterozygous tendons. Similar levels of pro α 1, pro α 2 pC α 1, pC α 2 in the N (final detergent extract) and S1(first salt extract) extracts in wild-type (WT1, WT2, WT3, *Col1a2*^{+/+}) samples and heterozygous (HET1, HET2, HET3, *Col1a2*^{+/¹⁰⁷}) samples, indicate that the Collagens are being secreted normally. The S4 extract (fourth salt extract) is included to show that the majority of the extracellular collagens had been extracted prior to the N extraction indicating that the collagens found in the N extraction were intracellular collagens. (pro α 1 indicates an alpha I procollagen with both n and c propeptides attached, pC α 1 indicates an alpha I procollagen with only the C propeptide attached.) The lanes of the gels were re-ordered for ease of viewing, the unmodified images of the gels are included in Appendix 1.

SYPRO Ruby total protein staining of S1 (first salt extract) and N extracts (final detergent extract) show a similar amount of protein was extracted in samples of each genotype, in both the intracellular and extracellular extracts (Figure 4.12). This confirms that any difference or similarity seen in the radiolabelling is not due to differences in protein levels between samples.

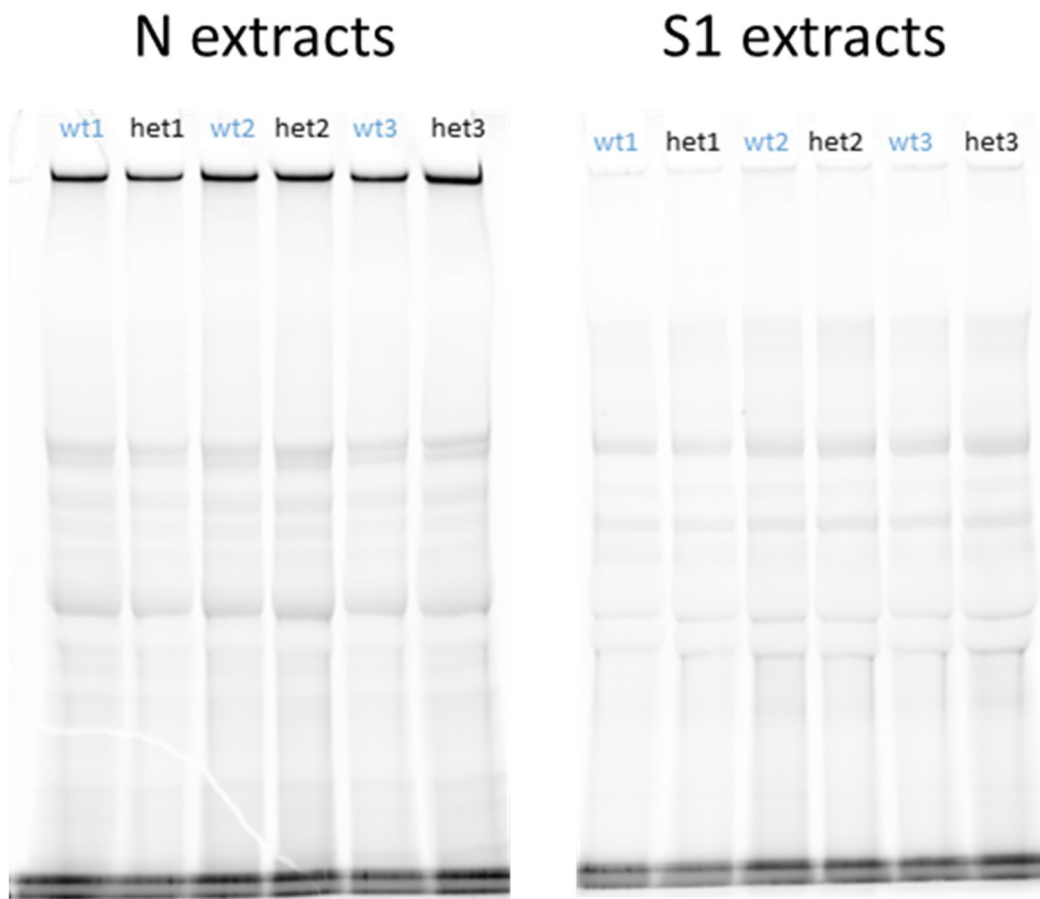


Figure 4.12. Sypro Ruby total protein stained gels of tendon extracts. S1 (first Salt extract) and N extracts (final detergent extract) run on Tris-Glycine gels and stained with Sypro Ruby total protein stain, show that there are similar levels of proteins extracted from both wild-type (WT1, WT3, WT3, *Col1a2*^{+/+}) samples and heterozygous (HET1, HET2, HET3, *Col1a2*^{+/¹⁰⁷}) samples.

The radiolabelling reveals that the mutant collagen is not being retained intracellularly and that the collagen I molecule produced is heterotrimeric rather than homotrimeric.

4.5. Transmission Electron Microscopy of MP-107 Embryonic Tail Tendon

The mutant $\alpha 2$ chain appears, from previous experimental data (Section 4.6), to be incorporated into the collagen I molecule, and that this is having an effect on the stability of the heterotrimer (Section 4.5) and on the mechanical behaviour of tendon fascicles (Section 4.3.1). Transmission electron microscopy (TEM) enables highly magnified viewing of the tendons, including the arrangement of the collagen I fibrils and the tenocytes. This imaging allows differences between the tenocytes and collagen fibrils to be identified [273]. Embryonic tail was harvested at 18.5 dpc and used for TEM, to enable the comparison between all three genotypes (Figure 4.13). TEM images show that the Endoplasmic Reticulum (ER) in the tenocytes is swollen and distended in the homozygotes and heterozygotes, when compared to the wild types. It should be noted that the degree of swelling in the ER was more variable in the heterozygotes. The swollen and distended ER is likely an indication of ER stress [274, 275].

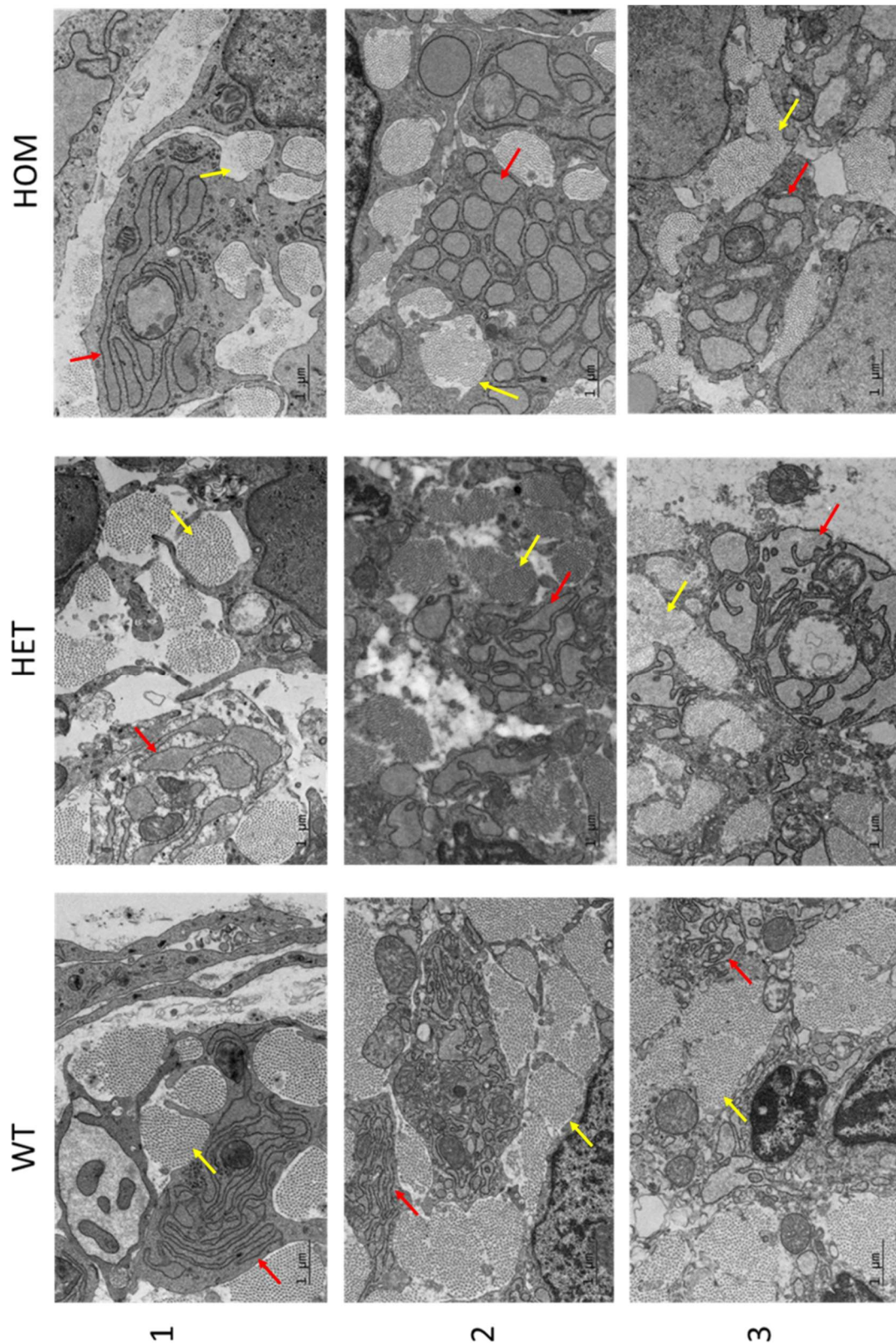


Figure 4.13. TEM images of embryonic tail tendon from homozygous, heterozygous and wild-type embryos. Homozygous (HOM, $Col1a2^{107/107}$) and heterozygous (HET, $Col1a2^{+/107}$) samples show bloated Endoplasmic Reticulum (ER) when compared with wild-type (WT, $Col1a2^{+/+}$), indicating ER stress within the cells. The homozygotes appears to be more affected by this ER stress than the heterozygotes (red arrows). The bundles of collagen I fibres in the homozygous $Col1a2^{107/107}$ also appear to be less densely packed than those in either the heterozygous $Col1a2^{+/107}$ or the wildtype $Col1a2^{+/+}$ samples (yellow arrows). For higher magnification TEM images see Appendix 4 (For all genotypes $n=3$, denoted by 1,2,3).

The bundles of collagen fibrils appeared to be smaller and more disorganised in the heterozygous and homozygous samples, when compared to the wild-type samples. To quantify this observation, the number of fibrils per bundle were counted blind to genotype, and subsequently assigned a genotype. (Figure 4.14).

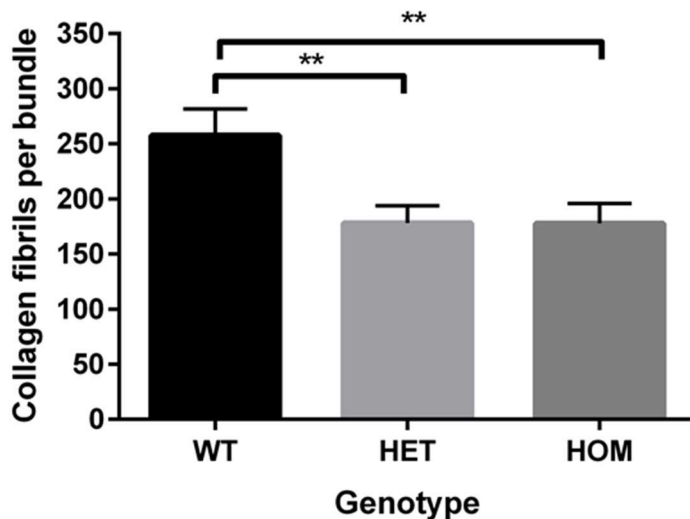


Figure 4.14. Quantitative analysis of collagen fibrils in TEM images of embryonic tail tendons from homozygous, heterozygous and wild-type embryos. Collagen fibrils per bundle were counted in TEM images of embryonic tail tendons from animals of each genotype homozygote, heterozygote and wild type. Homozygous (HOM, *Col1a2*^{107/107}) and heterozygous (HET, *Col1a2*^{+ /107}) samples exhibit reduced number of fibrils per fibril bundle when compared with wild-type (WT, *Col1a2*^{+ /+}) samples. One-way ANOVA: ** P<0.01 (n=3 for all genotypes).

Statistical analysis revealed that the heterozygote and homozygote had significantly fewer collagen fibrils per bundle than the wild type (P=0.0053). There was no difference between heterozygote and homozygote. It should be noted that no determination was made on the sex of the embryos used for TEM.

4.6. Analysis of ER Stress in MP-107 Mouse Embryonic Fibroblasts (MEFs)

TEM imaging revealed evidence of ER stress in heterozygous (HET, *Col1a2*^{+ /107}) and homozygous (HOM, *Col1a2*^{107/107}) tenocytes. To further investigate the ER stress, that the bloated ER implied was present, MEFs were harvested 2 days post confluence and homogenised in Cell lytic™ with the addition of phosphate inhibitors and protease inhibitors using a Pellet Pestle. A positive control was created by treating wild-type MEFs with Thapsigargin to induce ER stress, prior to harvesting.

A western blot was run using cell lysate from each genotype and the positive control sample (Figure 4.15).

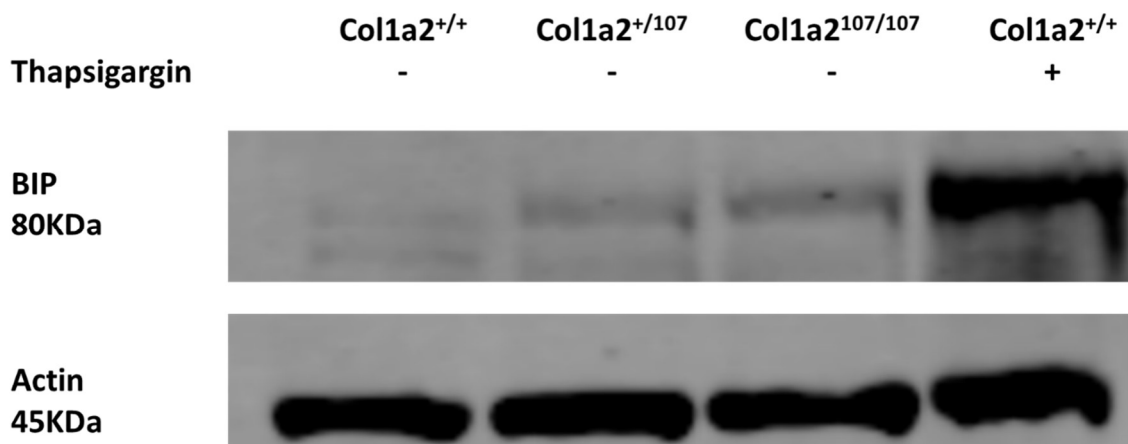


Figure 4.15. Western blot showing levels of BIP in MP-107 MEF cell lysates. Untreated wild-type (*Col1a2^{+/+}*), heterozygous (*Col1a2^{+ / 107}*) and homozygous (*Col1a2^{107 / 107}*) cell lysates run along with Thapsigargin treated wild type cell lysates labelled with BIP and Actin (See section 2.3 for antibody details). Heterozygous (*Col1a2^{+ / 107}*) and homozygous (*Col1a2^{107 / 107}*) cell lysates appear to show elevated levels of BIP protein when compared to wild-type (*Col1a2^{+/+}*) lysates. The uncropped gel is shown in Appendix 5.

The western blot suggests that there BIP is present at higher levels in the heterozygous and homozygous samples, although not in as high levels as the thapsigargin treated sample. BIP (Binding immunoglobulin protein) is a chaperone protein located in the endoplasmic reticulum, and is commonly used as a marker of ER stress. The increased levels of BIP is another indication of ER stress in the heterozygous and homozygous MP-107 cells.

4.7. Immunohistochemistry Analysis of ER Stress in MP-107 Articular Cartilage

Previous studies have shown that OA induction by destabilisation of the medial meniscus increases ER stress in chondrocytes [276]. Additionally, markers of ER stress such as BIP and Bag-1 have been shown to be upregulated in articular cartilage from OA patients with advanced disease [277]. It is therefore possible that any increase in markers of ER stress noted in the chondrocytes of animals with OA, could be as result of the cartilage degradation rather than the cause of it. It was therefore more appropriate to investigate if there was evidence of ER stress in the absence of cartilage degradation

in heterozygotes. As previously discussed, not all heterozygotes develop the ossification observed by X-ray and μ CT.

Histological sections from MP-107 wild-type (WT, *Col1a2*^{+/+}) and heterozygous (HET, *Col1a2*^{+/¹⁰⁷}) knee joints which showed no sign of OA by histology at 18 months were assessed, by immunohistochemistry, using an Anti-BIP Antibody as a marker of ER stress (for details see Section 2.3), before secondary antibodies and DAB staining were used to visualise the distributions of the protein.

A negative control for this experiment was created by incubating a wild-type section with serum without the primary antibody. Neither wild-type section, either incubated with the primary antibody or without, showed any DAB staining in the chondrocytes. Some chondrocytes in the heterozygous section, which was incubated with the primary antibody, appeared to be stained with the DAB (Figure 4.16).

The enhanced staining in the MP-107 heterozygotes suggests that the chondrocytes may have elevated levels of ER stress.

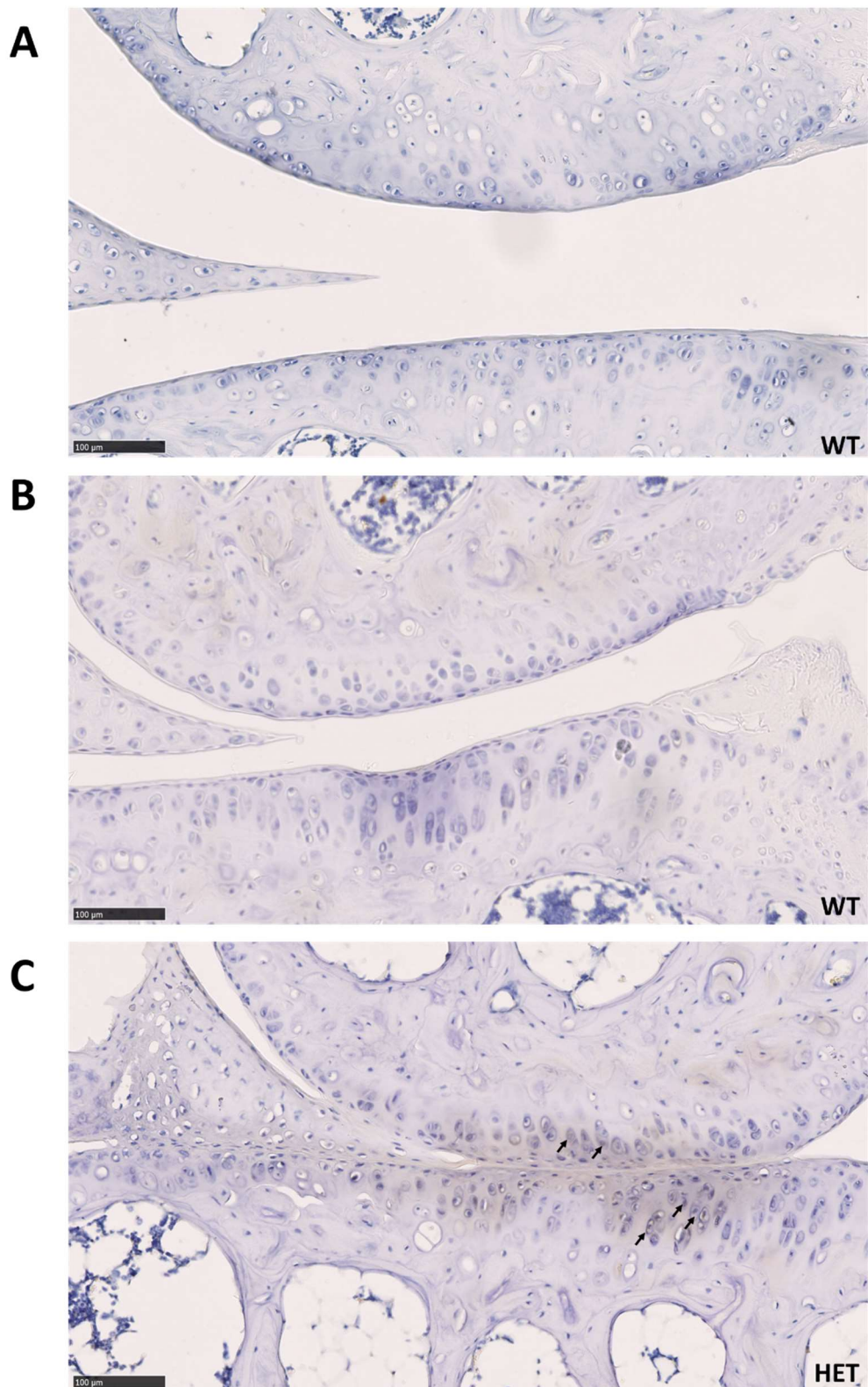


Figure 4.16. Immunohistochemical staining of wild-type and heterozygous knee sections using BIP antibody. (A) Negative control wild-type (WT, Col1a2^{+/+}) section without primary antibody, (B) Wild-type (WT, Col1a2^{+/+}) section with primary antibody, (C) Heterozygous (HET, Col1a2^{+/107}) section with primary antibody. Dark brown staining is only visible in the chondrocytes of the heterozygous section (black arrows), indicating increased levels of ER stress in the heterozygote chondrocytes. It should be noted that only one 18-month heterozygous animal showed no evidence of joint damage, and was therefore used for IHC, and therefore no statistical testing was carried out. For higher magnification images see Appendix 6.

4.8. Destabilisation of the Medial Meniscus (DMM) in MP-107 Knees

DMM surgery is a method of surgically inducing OA, by severing the medial menisco-tibial ligament to destabilise the medial meniscus [278]. This technique induces OA as a result of destabilising the joint, leading to accelerated damage. In this case we are using DMM surgery as a challenge to investigate if the MP-107 heterozygotes (*Col1a2^{+/-107}*) are predisposed to developing OA as a result of joint instability.

Cohorts of heterozygous and wild-type animals underwent DMM surgery to investigate if the mutation in *Col1a2* increased the susceptibility to surgically induced OA. Surgery was performed at 8 weeks of age, and animals were culled 6 weeks post-operatively, to take joints for histology.

Histological analysis of Safranin O sections of DMM treated animals show damage to the articular cartilage in both heterozygotes (HET, *Col1a2^{+/-107}*) and wild types (WT, *Col1a2^{+/+}*), in addition the heterozygotes displayed osteophytes. Histological analysis of H&E sections of sham treated animals show no increase in damage to the articular cartilage or increase in the presence of osteophytes in heterozygotes (HET, *Col1a2^{+/-107}*) compared to wild types (WT, *Col1a2^{+/+}*) (Figure 4.17).

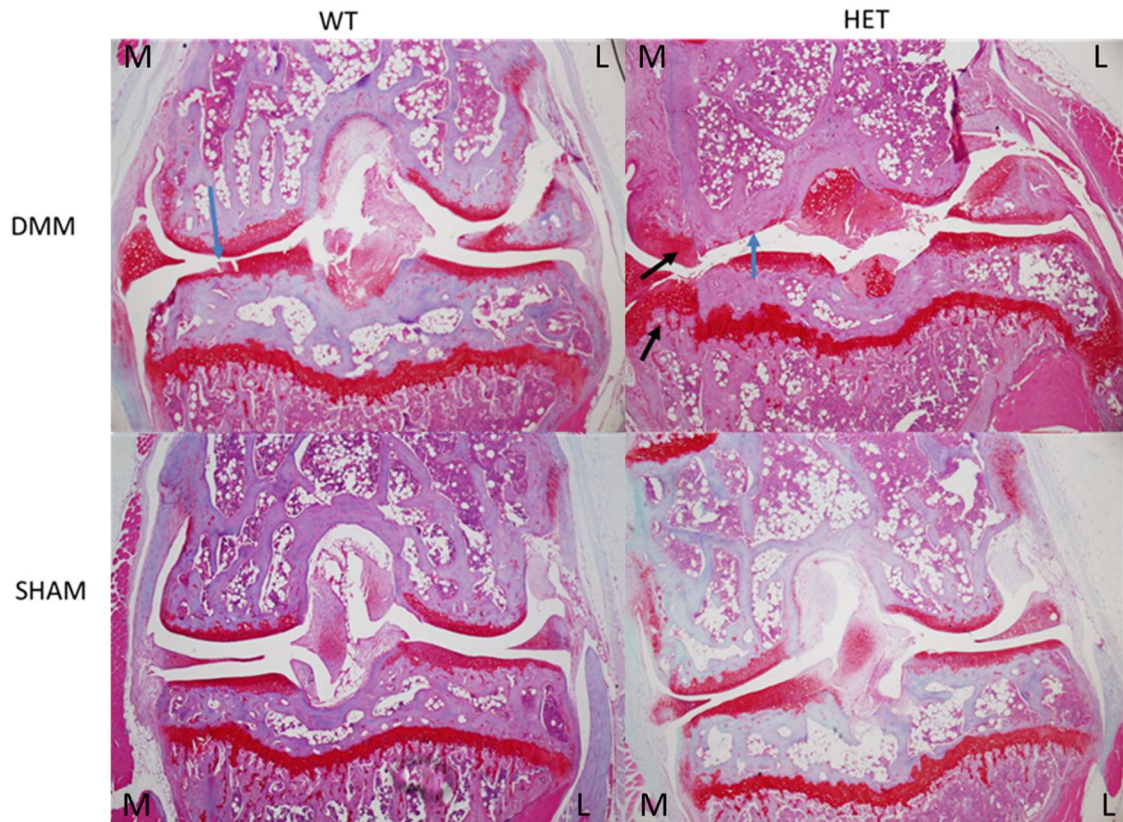


Figure 4.17. Safranin O stained histological section of knee joints from DMM operated and sham operated wild-type and heterozygous animals. DMM-treated animals show damage to the articular cartilage (Blue arrows) in both heterozygotes (HET, *Col1a2*^{+/¹⁰⁷) and wild types (WT, *Col1a2*^{+/⁺), in addition the heterozygotes displayed severe osteophytes (black Arrows). Sham-treated animals show no damage to the articular cartilage or osteophytes in either heterozygotes (HET, *Col1a2*^{+/¹⁰⁷) or wild types (WT, *Col1a2*^{+/⁺). Medial and tibial orientation indicated by M and T respectively.}}}}

As with other phenotypes observed in MP-107, the histology of the DMM treated heterozygotes was variable, with some animals having severe cartilage loss and others comparable cartilage loss to wild types. An F test between genotypes, reveals that there is a significant variance in the females, but not the males (Female- F-74.76, DFn-4, DFd-3, P=0.0049, Males- F-1.316, DFn-2, DFd-4, P=0.3496). The histology from the operated and sham operated samples were scored using the OARSI scoring system [279], unfortunately no OARSI scoring data is available for the female sham operated animals. There was no significant difference detected between the DMM operated heterozygotes (HET, *Col1a2*^{+/¹⁰⁷) and wild types (WT, *Col1a2*^{+/⁺) in either sex. In males, where sham operated OARSI scoring data was available there was a significant increase in OARSI score in the DMM operated wild types (WT, *Col1a2*^{+/⁺) compared with the sham operated wild types (WT, *Col1a2*^{+/⁺), but no significant difference with the DMM operated heterozygotes (HET, *Col1a2*^{+/¹⁰⁷) (Figure 4.18).}}}}}

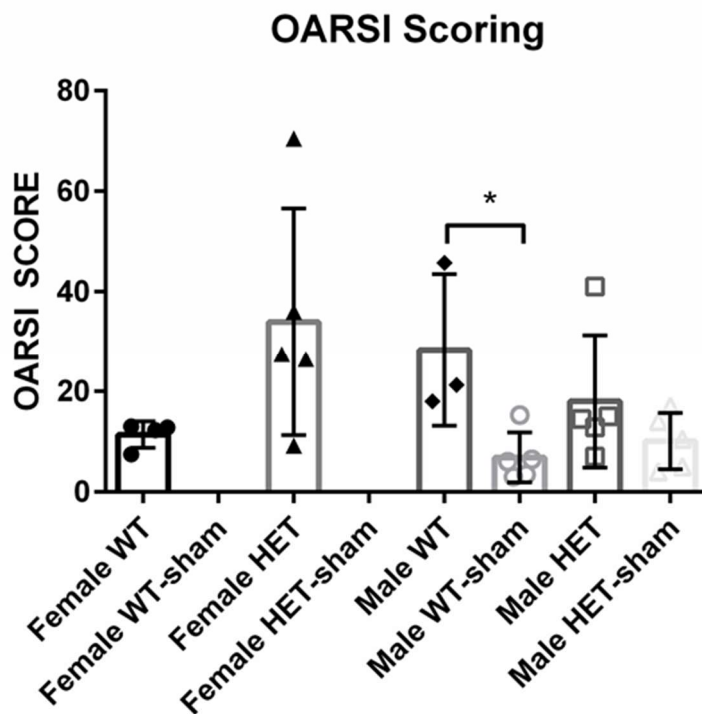


Figure 4.18. Histological analysis of Safranin O stained histological section of knee joints from wild-type and heterozygous animals including from DMM operated and sham operated. No significant difference in cartilage damage was detected between the heterozygotes (HET, Col1a2^{+/-107}) and the wild types (WT, Col1a2^{+/+}) in either sex. Where the OARSI data for Sham surgery was available, there was a significant increase in OARSI scores in the DMM operated wild types (WT, Col1a2^{+/+}) compared to the sham operated wild types (WT, Col1a2^{+/+}).

It should be noted that although the OARSI scoring did not reveal a significant difference in the cartilage, all heterozygotes of both sexes that were DMM operated showed osteophytes in the histology. Incidence of osteophytes in the wild-type DMM operated animals varied between 33% (1/3 males) and 50% (2/4 female). Statistical testing using the Mann-Whitney U test found that there was no statistical difference between genotype, this is likely due to the small cohort sizes making this experiment underpowered (Males-WT- n=3, U=12.5, HET- n=5, U=2.5, P=0.076; Females-WT- n=4, U=15, HET- n=5, U=5, P=0.128). The relatively early end-point for this experiment of 6 weeks post-surgery may have led to less severe cartilage degradation than would have been seen at 8 or 10 weeks, and therefore no significant difference was detected between genotypes.

4.9. Discussion

The mechanical testing of bones indicated that the humeri of heterozygous *Col1a2*^{+/107} animals were significantly more brittle than the humeri of wild-type *Col1a2*^{+/+} animals, indicating a mild OI phenotype [80]. Bone fractures were only observed by X-ray in the humeri of two heterozygotes, which also exhibited the curved olecranon phenotype, however μ CT imaging revealed further evidence of fracture in the humerus of another heterozygote exhibiting the curved olecranon phenotype. These examples of fractures occurring in tandem with the olecranon phenotype, coupled with the observation of *in utero* fractures leading to bone deformation in homozygous embryos *Col1a2*^{107/107} (See Section 3.5.3), raise the possibility that minor fractures *in utero*, while not visible by X-ray, could be leading to the mild bone abnormalities observed, including the curved olecranon and splayed ischia seen in the heterozygotes [280]. It is also conceivable that the OI phenotype could be related to microfractures in the subchondral bone, although these have not been observed at this time.

Mechanical testing of tendon fascicles and skin indicate that both tissues have altered viscoelastic properties. Both tissue types have an altered initial elastic slope and the tendon fascicles also had a reduction in hysteresis, meaning that there is less energy loss on each cycle. While this can be viewed as advantageous in terms of higher elastic energy return [264], it reduces the ability of the tendon to absorb energy [265]. These changes to the visco-elastic properties could be indicative of an EDS phenotype, where skin is often hyperextensible, and joints are hypermobile [281, 282]. The model proposed by Frantzl et al. indicates that initial extension is a result of the removal of the macroscopic crimp followed by straightening of molecular kinks in the gaps between Collagen molecules [36]. It is likely that the altered mechanical properties are a result of micro-unfolding at the site of the repeating glycine motif disruption. This could explain why the initial elastic slope differs between genotypes, but the elastic slope does not (see section 4.2.3). This demonstrates that the MP-107 heterozygotes exhibit an EDS-like phenotype in addition to the OI phenotype. Some models of osteogenesis imperfecta, such as *oim* exhibit changes in the tendon mechanical strength, which while not replicated here, does demonstrate the connected phenotypes [283, 284]. It should be noted that due fascicles, extracted from mouse tail tendon, being very small and

delicate, they can dry out quickly which can affect mechanical properties, and can increase noise on the load channels [285].

The differential scanning calorimetry (DSC) data showing a reduced dry enthalpy in the heterozygotes *Col1a2^{+/-107}* when compared with the wild types *Col1a2^{+/+}*, could explain why these tissues exhibit these behaviours. The reduced stability indicated by the reduced dry enthalpy could be due to micro unfolding of the collagen I heterotrimer, or the presence of homotrimers [271]. The radiolabelling of tendons indicated that there was no issue with $\alpha 2$ chains being retained intracellularly, and that the levels of $\alpha 1$ and $\alpha 2$ in the extracellular extract were similar in both genotypes [272]. This demonstrates that the $\alpha 2$ is being incorporated into the trimer, and micro-unfolding is likely impairing the formation of the collagen fibres and fibrils, leading to altered visco-elastic properties. The DSC data also showed that there was no significant difference between bound water content in the tendons between genotypes. This indicates that the increased CSA of fascicles observed in Section 4.2.11, is unlikely to be due to increased water content.

TEM imaging shows enlarged, bloated endoplasmic reticulum (ER), a marker of ER stress, in the heterozygotes and homozygotes, which can be indicative of physiologic or pathological stress [286]. Protein analysis of cell lysates from MEFs indicated that there was increased ER stress in homozygous and heterozygous MEFs. MEFs are a useful tool to enable investigation of the homozygotes despite a lethal phenotype, however there are limitations in using MEFs including phenotypically heterogeneous subtypes of MEFs, and the potential for other cell types to be present in the culture [287]. Immunostaining indicated an increase BIP staining in chondrocytes in the heterozygous articular cartilage, compared to the wild-type articular cartilage, however due to a lack of suitable samples, only sections from one heterozygous animal were used, and therefore while this information appears to support other evidence of ER stress, no conclusions should be drawn from the IHC alone. TEM imaging of dermis of EDS patients has shown evidence of ER stress, including dilated ER in fibroblasts of dermis of patients with EDS [288] and reduced number of fibrils [289, 290].

The radiolabelling and DSC results indicate that mutant protein is being secreted; however, it is possible that a fraction of the mutant protein is being retained intracellularly, and this could be causing an unfolded protein response, leading to ER stress. Boot-Handford *et al.* have stated that it is rare ERAD causes upregulation of BIP, indicating that this is probably not what is causing the ER-stress [70]. The biosynthesis, folding and secretion of collagens is a very complicated process, and delays in the processing can also lead to ER stress, and therefore further investigation into what is causing the ER stress is warranted. Quantification of the collagen fibrils in the tendons demonstrated that both heterozygote and homozygote tendons contain significantly fewer collagen fibrils per bundle. Micro-unfolding due to the disrupted glycine motif could explain this phenotype, in addition to the mechanical behaviours and reduced stability of the heterozygotes, as the micro-unfolding will cause the collagen heterotrimer, and in turn the collagen fibres and fibrils to require more space.

Indentation analysis indicates that there are some regions of the articular surface which have increased structural stiffness in the heterozygous *Col1a2*^{+/¹⁰⁷ animals when compared with the wild-type *Col1a2*^{+/+} animals. The articular cartilage is primarily made up of collagen II, with only small amounts of collagen I, it is therefore unlikely that the changes are directly due to changes in the collagen I protein in the articular cartilage. It is more likely we are either observing a difference in the subchondral bone, or a secondary change in the articular cartilage perhaps caused as a by-product of ER Stress. [291]. The μ CT data (Section 3.6.5.3) does indicate the subchondral bone of the heterozygotes is structurally altered, however this does not rule out ER stress as a cause, and this warrants further investigation.}

The DMM experiment was likely underpowered, and the results were inconclusive. The severe OA and osteophytes observed in some heterozygotes were not replicated in all heterozygotes, and there was no significant difference between genotypes.

There are four types of EDS caused by mutations in *COL1A1* and *COL1A2*. A specific arginine to cysteine mutation (Arg134Cys) in *COL1A1* has been observed to cause a classical EDS phenotype [96]. Mutations in *COL1A2*, leading to a complete deficiency of pro α 2 (I) collagen, including splice mutations and nonsense mutations have been shown to lead to cardiac-valvular EDS [98]. Arginine to cysteine mutations including the

previously mentioned example(Arg134Cys) as well as others (including Arg312Cys, Arg574Cys, Arg1093Cys) in *COL1A1* have been observed to cause a vascular EDS phenotype, possibly due to the extra cysteine residue causing additional intermolecular bonding [96, 101]. Mutations in *COL1A1* and *COL1A2* preventing the cleavage of the N-propeptide (most commonly skipping exon 6) leads to arthrochalasia EDS. Due to the mutation in MP-107 being in *Col1a2*, only cardiac-valvular EDS and arthrochalasia EDS subtypes would fit with this mutation. However, the mutation in MP-107 does not cause a deficiency in pro $\alpha 2$ (I) collagen and is unlikely to impair the cleavage of N-propeptide due to the location of the mutation being in the middle of the helical domain. It is therefore unlikely that MP-107 is modelling one of these EDS subtypes.

In addition to EDS caused by mutations in *COL1A1* or *COL1A2*, there is also an OI/EDS overlap disorder, where symptoms of both disorders were observed. Until recently OI/EDS overlap disorder was associated only with mutations preventing or delaying the cleavage of the procollagen N-propeptide. However, a different type of OI/EDS overlap syndrome was identified where the mutations did not affect the cleavage of the N-propeptide [115]. Over 20 patients were identified from 13 families, with this novel type of EDS, with mutations identified right across both *COL1A1* and *COL1A2*, including in the c-terminal half of the helical domain, and subsequently named COL1-related overlap disorder. Interestingly, even in families where all individuals carried identical mutations in *COL1A1* or *COL1A2*, the phenotypes presented varied. The presence of phenotypes associated with both OI and EDS in MP-107 heterozygotes indicates that rather than modelling OI or EDS, the line MP-107 likely models Col-1 related overlap disorder as described in Morlino *et al.*, 2019 [115].

A mouse model of OI/EDS (published prior to the term Col-1 related disorder) called Jrt published by Chen *et al.* [117] showed similar phenotypes at the ischia and olecranon to those seen in MP-107, which were again attributed to fractures. The presence of the phenotypes was variable across animals of the same phenotype (*Col1a1^{Jrt/+}*), and the affected animals showed altered mechanical and material properties of skin, indicating skin fragility. This adds further weight to the hypothesis that MP-107 heterozygotes have an overlap disorder.

These results show a novel association of an osteoarthritis phenotype with a Col-1 related disorder caused by a mutation in *Col1a2*. In addition to providing knowledge about the genotype/phenotype relationship in Col-1 related disorder, this model could be used to further understand how changes in Collagen I can lead to osteoarthritis.

**Chapter 5: Identification and Initial
Characterisation of Phenotypes
Associated with a Point Mutation in
*Col1a1***

5.1. Introduction

Prior to the start of the Harwell Ageing Screen, several ENU mutagenesis screens were undertaken at MRC Harwell [235, 245, 292]. One of these was a G₁ dominant screen, whereby cohorts of G₁ animals underwent phenotyping to identify any early onset phenotypes caused by dominant mutations. To produce the G₁ mice, C57BL/6J male animals (G₀) were injected with ENU, and mated with C3H females to produce cohorts of mice (G₁) heterozygous for the mutations induced in the spermatogonia of the G₀ animal. Once a phenotype had been identified, the G₁ animal was crossed with C3H, to produce a cohort of G₂ animals to confirm the phenotype and identify the causative mutation, see Section 2.6.2, Figure 2.1 for the breeding scheme.

Among the phenotyping procedures was X-ray imaging, and a G₁ animal was identified as having mild bone abnormalities. The subsequent G₂ line was named Bone-TM\44. The initial phenotyping, mapping and exome sequencing of this line was performed prior to the start of this project by Dr Chris Esapa. The line was then banked and no further work was undertaken. Where work was previously carried out by Dr Esapa, it will be noted. Due to the similarities between early phenotypes in this line, and the early phenotypes in the line MP-107, this line was re-derived to allow further phenotyping and analysis of the mutations. For ease, the line was renamed TM44 upon re-derivation. The aim of this chapter is to establish if the phenotypes in this line mirror those observed in MP-107 and if the causative mutation affects the Collagen I heterotrimer.

5.2. Identification of Early Phenotype in the line TM44

X-ray imaging at 4 months of age revealed that a female G₁ animal displayed mild bone abnormalities, including curved olecranon and splayed ischia (C.Esapa) (Figure 5.1).



Figure 5.1. An X-ray image of the G₁ founder animal of the line TM44. The animal displays curved olecranon at both elbows (orange arrows) and splayed ischia at the pelvis (blue arrows).

A G₂ cohort was established by crossing the G₁ founder female animal with a male C3H animal to produce 4 litters of progeny, comprising 19 females and 19 males. This cohort was phenotyped by X-ray imaging at 3 months of age. Of these 38 animals, 12 animals, 8 males and 4 females showed skeletal abnormalities, including curved olecranon and splayed ischia, in isolation or in combination (C.Esapa) (Figure 5.2).

No further phenotyping was performed on the G₂ cohort at this time. DNA was extracted from tissue harvested from affected animals, and sperm from the affected male animals was banked.



Figure 5.2. Representative X-ray images showing affected and unaffected animals. (A) An unaffected animal with a normal olecranon and ischia. (B&C) Affected animals showing curved olecranon (orange arrows) and splayed ischia at the pelvis (blue arrows), in combination or isolation.

5.3. Mapping and Identification of the mutation in the line TM44

5.3.1. Mapping the Mutation in TM44

DNA from 8 affected animals underwent SNP mapping to identify a region which would contain the causative mutation (C.Esapa). As the G_2 animals which underwent phenotyping have a mixed background, it is possible to use the SNPs to identify which portions of the genome were inherited from each ancestral strain. The original mutation

was created in a C57BL/6J mouse, therefore any mutation caused by the ENU will be on the C57BL/6J regions of the genome. The original phenotype was identified in a G₁ animal, which must be heterozygous for any ENU induced mutation; therefore, the mutation must be dominant. The G₂ cohort, being an outcross cohort, will only contain animals that are wild-type or heterozygous for the mutation and a dominant causative mutation would need to be heterozygous for C57BL/6J SNPs. A region was identified on Chromosome 11, from 82.70 Mb to the distal end of the chromosome, where all affected animals were heterozygous, indicating that the causative mutation was within this region at the distal end of Chromosome 11 (Figure 5.3).

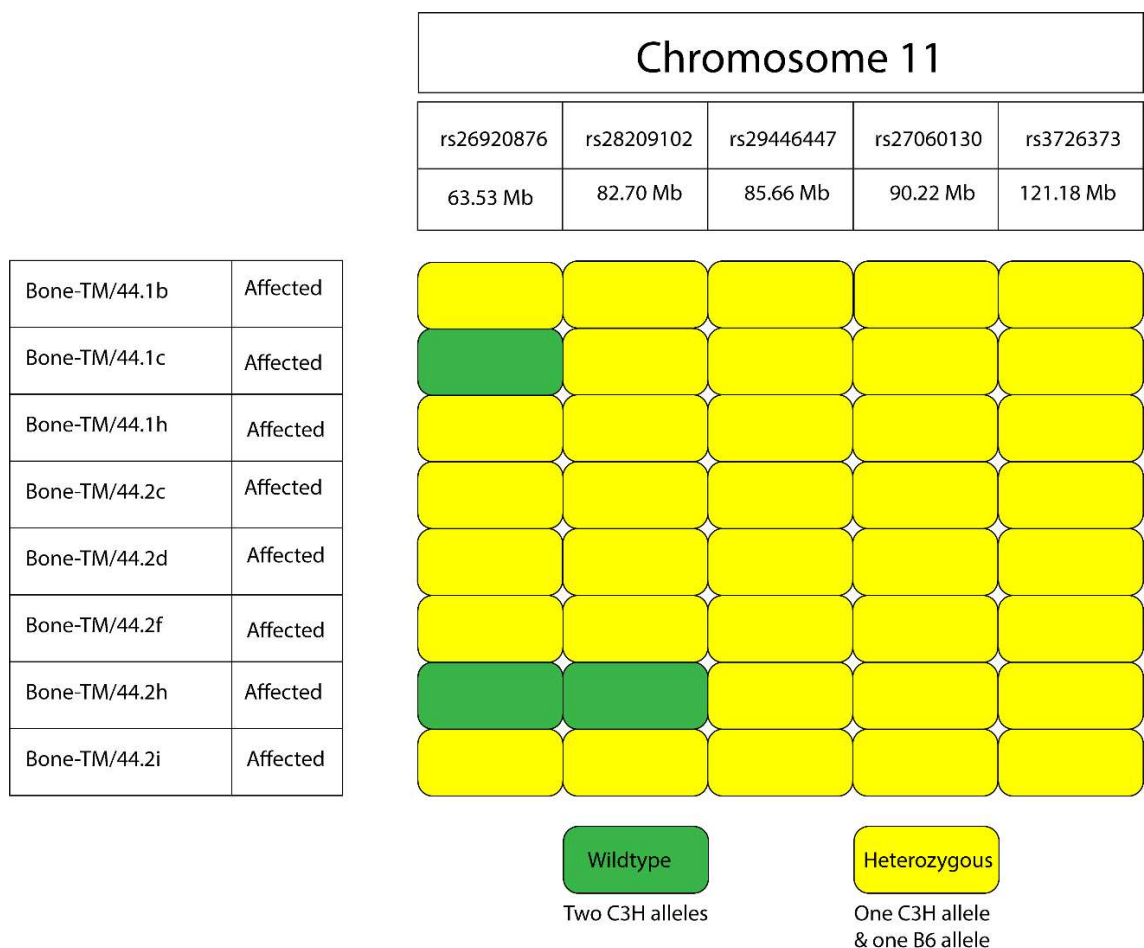


Figure 5.3. SNP mapping panel showing the region of interest on Chromosome 11. All affected animals have one C57BL/6J allele and one C3H allele in the ~40Mb region at the distal end of Chromosome 11, indicating that the causative mutation is dominant and contained within that region.

5.3.2. Exome Sequencing of TM44

Exome sequencing performed by C.Esapa identified two high confidence mutations within the region on Chromosome 11. The first was a cytosine to thymine transition at base 2029 (C2029T), causing a premature stop in place of a glutamine (Gln677Stop) in Exon 31 of the gene *Col1a1*. The second was an adenine to a guanine transition at base 413 (A413G), causing an amino acid change, a glutamic acid in place of a glycine (Glu138Gly) in Exon 4 of the gene *Sectm1a*.

5.3.3. Confirmation of Mutations in the line TM44

The two mutations identified by exome sequencing were subsequently confirmed using Sanger sequencing in affected animals, showing the animals to be heterozygous for both mutations (C.Esapa). Unfortunately, at the time, unaffected animals were not sequenced so the reference trace included in Figure 5.4 and Figure 5.5 is from an unaffected animal from the re-derived TM44 line at a later date. This confirms that these mutations were only present in affected animals and that one of these mutations is likely causative.

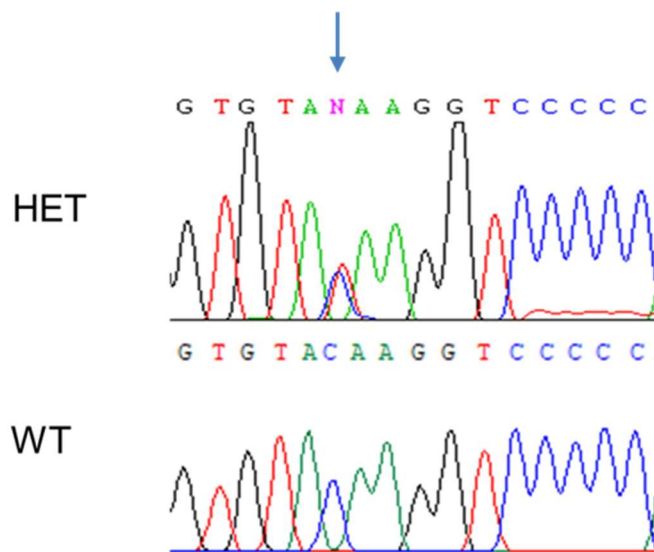


Figure 5.4. Sanger sequencing traces confirming the presence of a heterozygous mutation in *Col1a1* in affected animals. An affected animal from the G2 cohort shows two peaks indicating a heterozygous mutation and an unaffected animal from the re-derived line showing no mutation in *Col1a1* (indicated by a blue arrow).

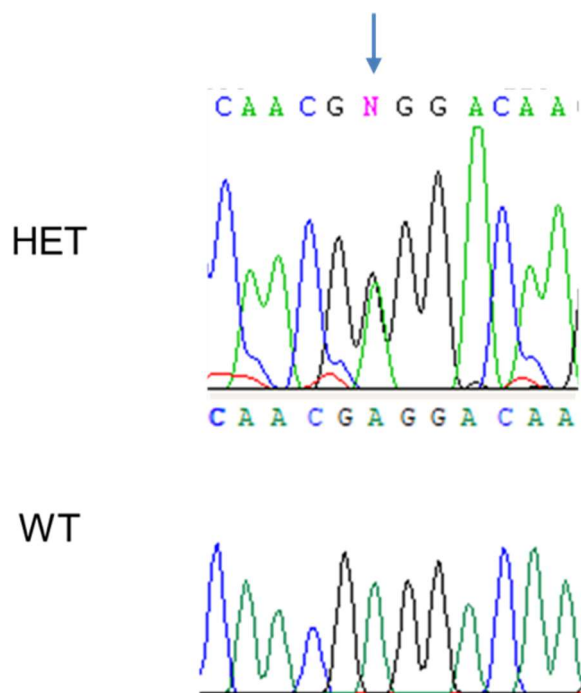


Figure 5.5. Sanger sequencing traces confirming the presence of a heterozygous mutation in *Sectm1a* in affected animals. An affected animal from the G2 cohort shows two peaks indicating a heterozygous mutation and an unaffected animal from the re-derived line showing no mutation in *Sectm1a* (indicated by a blue arrow).

5.3.4. Segregation of Mutations in the line TM44

Due to the nature of the ENU mutagenesis screen, the line TM44 was on a mixed C3H/HeH and C57BL6/J background. To reduce the amount of C57BL6/J and segregate the different mutations, the line was backcrossed to C3H/HeH for multiple generations. Sequencing of the two identified mutations at backcross 6 (BC6) showed segregation of the mutations eliminating *Sectm1a* as a candidate gene (Figure 5.6). Much of the work in this chapter was carried out prior to the successful segregation of mutations. To indicate where animals with the segregated mutation are used, the designation of both genes will be used i.e., the affected animal TM44\14.1d from Figure 5.6 would be described as heterozygous (HET, *Col1a1*^{+/*TM44*}, *Sectm1a*^{+/*+*}).

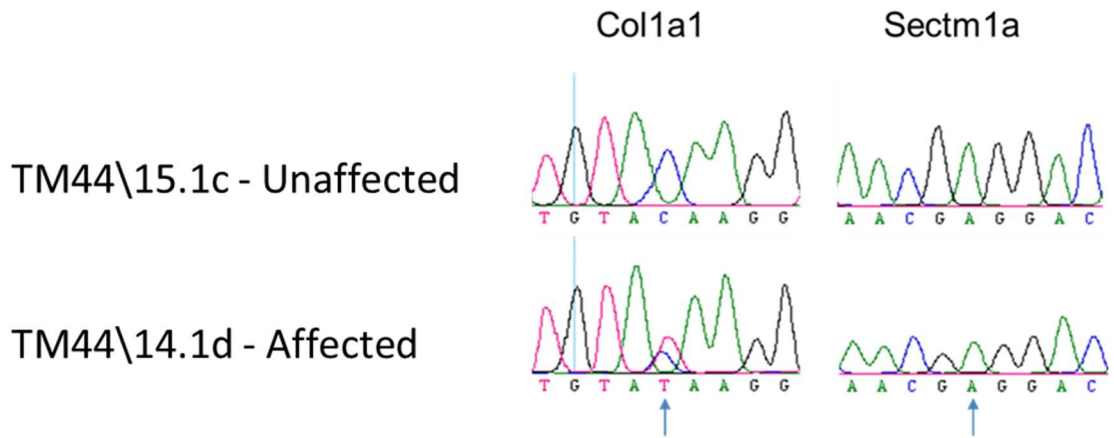


Figure 5.6. Sanger sequencing traces showing the segregation of mutations in affected animals. Affected animals from backcross 6 were heterozygous for the *Col1a1* mutation (C/T), but wild-type for the *Sectm1a* mutation (A/A); and unaffected animals were wild-type for both the *Col1a1* mutation (C/C), and wild-type for the *Sectm1a* mutation (A/A). The sites of the mutations in both genes are marked by blue arrows.

5.4. Identification of a Lethal Phenotype in TM44 Homozygotes

The G₂ cohort only contained heterozygotes and wild types, due to being the product of matings between the heterozygote G₁ founder female animal with a male wild-type C3H/HeH animal. It was therefore unknown what phenotypes the homozygote would display. The line was re-derived using banked G₂ sperm and C3H/HeH oocytes, to produce wild-type and heterozygous offspring. After genotyping to confirm genotype, intercross matings between male heterozygotes (*Col1a1*^{+/^{TM44}) and female heterozygotes (*Col1a1*^{+/^{TM44}) were set up to produce to an intercross (IC) cohort containing homozygotes (*Col1a1*^{TM44/^{TM44}), heterozygotes (*Col1a1*^{+/^{TM44}) and wild types (*Col1a1*^{+/⁺). Genotyping of the IC cohort at P21 revealed that there were no homozygotes present (Figure 5.7). The proportion of heterozygous animals to wild-type animals was 2:1, indicating a homozygous lethal phenotype; a Chi squared test shows that the numbers are statistically different from the expected ($\chi^2= 9.91$, 2df, P<0.01). This experiment was carried out prior to the segregation of the mutations.}}}}}

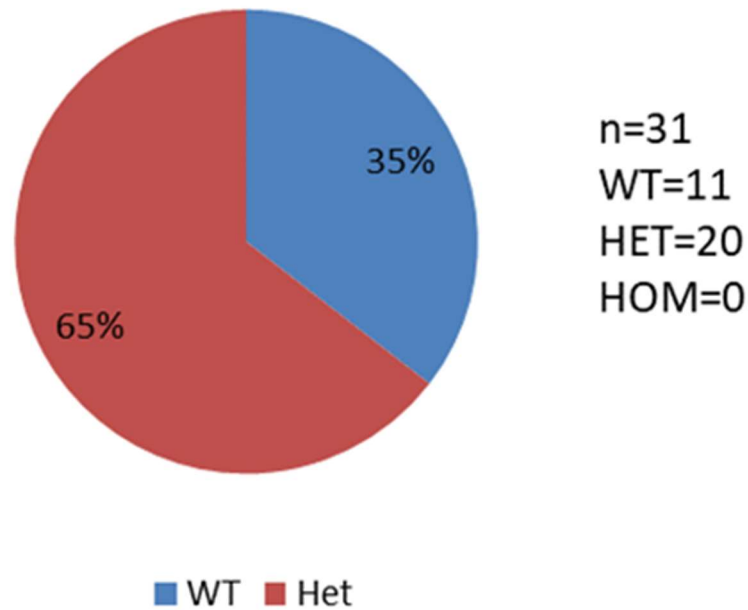


Figure 5.7 Proportions of animals of each genotype at weaning (stage P21). Heterozygotes (HET, $Col1a1^{+/TM44}$) making up 65% percent of the offspring and wild types (WT, $Col1a1^{+/+}$) making up 35% is indicative of a homozygous lethal phenotype.

To investigate the time point of the embryonic lethality, analysis of 14.5 dpc embryos from intercross matings between male heterozygotes ($Col1a1^{+/TM44}$) and female heterozygotes ($Col1a1^{+/TM44}$) was undertaken. At 14.5 dpc homozygous embryos were present at the expected ratios ($\chi^2 = 0.67$, 2df, $P > 0.5$), however none of the homozygous embryos were alive and there was evidence of reabsorption (Figure 5.8). The animals that were alive replicated the ratios observed at weaning.

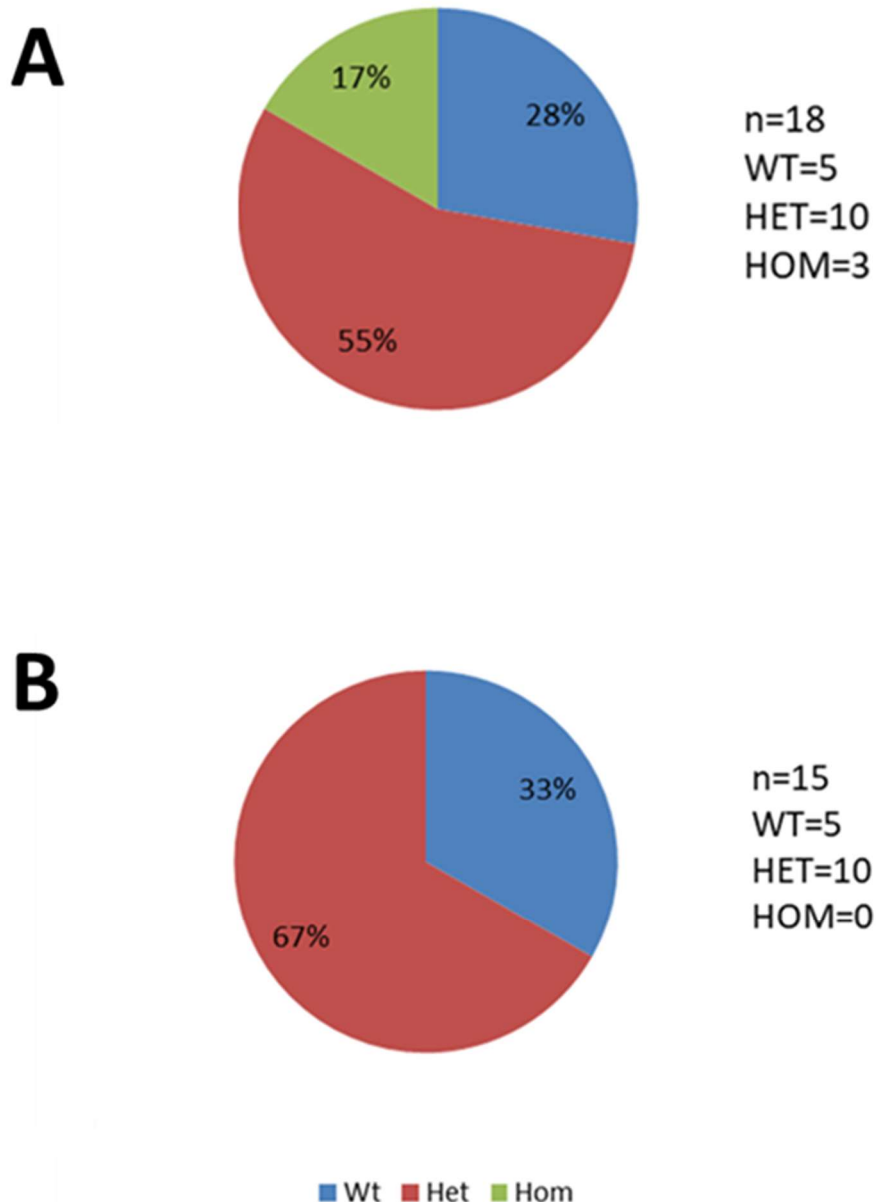


Figure 5.8. Proportions of embryos of each genotype at 14.5 days post-coitum. (A) The ratios of the total number of homozygote (HOM, $Col1a1^{TM44/TM44}$), heterozygote (HET, $Col1a1^{+/TM44}$) and wild type (WT, $Col1a1^{+/+}$) embryos does not differ from expected values from an intercross mating ($\chi^2 = 0.67$, 2df, $P > 0.5$). (B) When dead animals were excluded, the ratios of the living embryos mirrored that of the IC P21 cohort, with no homozygotes (HOM, $Col1a1^{TM44/TM44}$) present, and heterozygotes (HET, $Col1a1^{+/TM44}$) accounting for 67% and wild types (WT, $Col1a1^{+/+}$) 33%.

Having established that homozygous embryos were not viable at 14.5 dpc, further embryos were analysed at 12.5 dpc. Homozygous embryos were found to be alive and present in the expected ratios at this embryonic stage ($\chi^2 = 0.73$, 2df, $P > 0.5$) (Figure 5.9), indicating that lethality occurs between 12.5 dpc and 14.5 dpc.

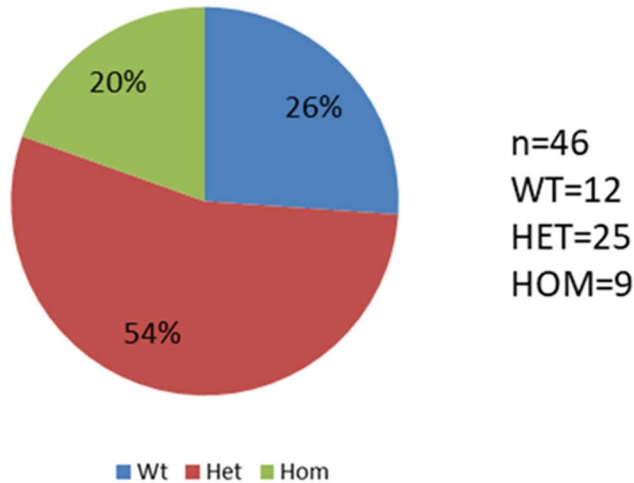


Figure 5.9. Proportions of embryos of each genotype at 12.5 days post coitum. The ratios of the total number of homozygote (HOM, Col1a1^{TM44/TM44}), heterozygote (HET, Col1a1^{+ /TM44}) and wild type (WT, Col1a1^{+ /+}) embryos does not differ from expected values from an intercross mating ($\chi^2= 0.73$, 2df, $P>0.5$). This indicates that the point of lethality is between 12.5dpc and 14dpc.

5.5. Optical Projection Tomography of TM44 Embryos

We employed optical projection tomography (OPT) imaging to analyse the phenotypes of the homozygous embryos. OPT is a useful technique as it allows 3D imaging without the laborious preparation involved in μ CT imaging of whole embryos. The resulting images can be reconstructed to allow 3D modelling and segmentation to allow for examination of specific planes throughout the embryo [293]. Initial measurements such as crown to rump length showed no significant difference between genotypes (Figure 5.10).

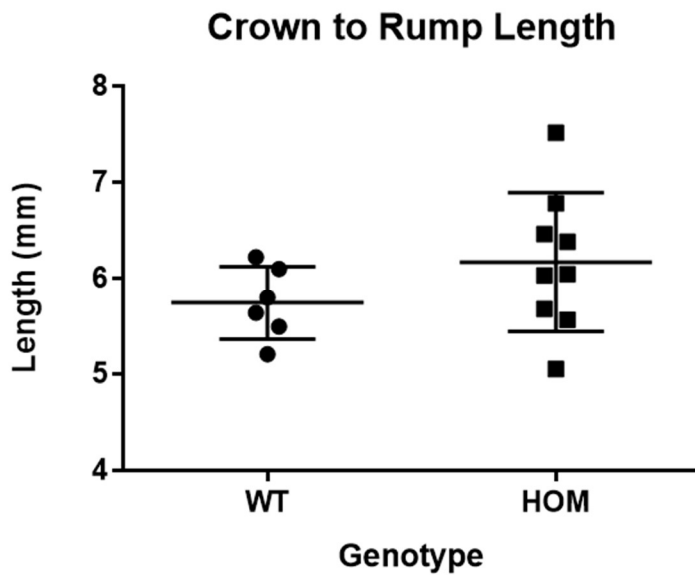


Figure 5.10. A graph showing the measured crown to rump length of wild-type (WT, *Col1a1*^{+/+}) and homozygous (HOM, *Col1a1*^{TM44/TM44}) embryos. Statistical analysis showed no significant difference in length between the two genotypes. (T-test)

Further analysis demonstrated that a number of homozygous animals had enlarged conical skulls, and in some cases evidence that a build-up of pressure had forced a large hole to appear in the skull. Segmentation revealed that in a number of cases this pressure, likely caused by a build-up of cerebrospinal fluid (CSF) in the skull, was leading to hydrocephaly and deformation of the ventricles (Figure 5.11).

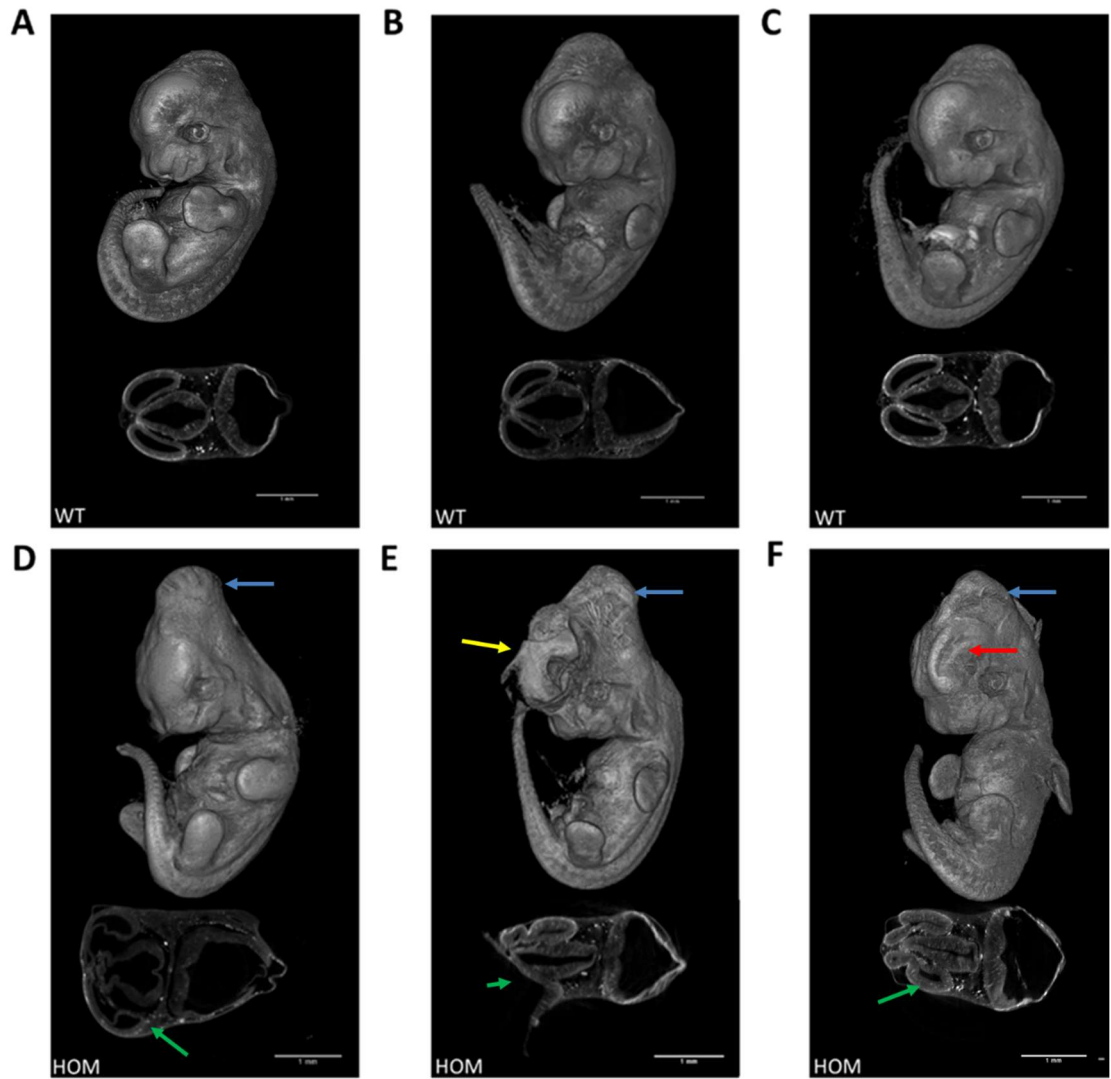


Figure 5.11. Representative OPT imaging of wild-type and homozygous embryos. (A-C) The wild-type (WT, *Col1a1*^{+/+}) embryos display a normal gross morphology for embryos at this stage when viewed in 3D, and a 2D section through the brain shows normal ventricles. (D-F) The homozygous (HOM, *Col1a1*^{TM44/TM44}) embryos display abnormal gross morphology when viewed in 3D, including elongated, conical skulls (blue arrows) in (D-F), in addition one homozygote (E) showed evidence of damage to the skull in what appears to be a release of pressure from within the skull (yellow arrow) and one homozygote (F) shows evidence of deformation inwards (red arrow). 2D section through the brains of the homozygotes shows abnormal brain and ventricles in (D-F).

5.6. Phenotyping of the TM44 line

X-ray imaging from the original G₂ Cohort identified early onset mild bone abnormalities, including curved olecranon and splayed ischia. To investigate whether the line TM44 also displayed a late onset OA phenotype, similar to that seen in MP-107, a cohort of re-derived animals was aged to 18 months and underwent X-ray imaging and DEXA analysis and histology at 18 months, with addition X-ray imaging at 12 months of age. Following

the successful segregation of the *Col1a1* and *Sectm1a* mutations in the TM44 line, a small cohort uniquely carrying the *Col1a1* mutation was bred for phenotyping at 2 months of age in order to confirm that the *Sectm1a* mutation was not causative, and to allow a direct comparison of early phenotypes with MP-107. Unfortunately, due to the segregation of mutations occurring late in the project, it was not possible to age animals with solely the *Col1a1* mutation.

5.6.1. X-ray Imaging of TM44 Animals

X-ray imaging of animals with the segregated mutations at 2 months of age revealed that animals that were heterozygous for the *Col1a1* mutation in the absence of the *Sectm1a* mutation (HET, *Col1a1*^{+/^{TM44}, *Sectm1a*^{+/⁺) exhibited the early bone phenotypes of curved olecranon and splayed ischia. This indicates that *Col1a1* is the causative mutation for these phenotypes. The combination of phenotypes is shown in Figure 5.12, and examples of the radiographs are shown in Figure 5.13.}}

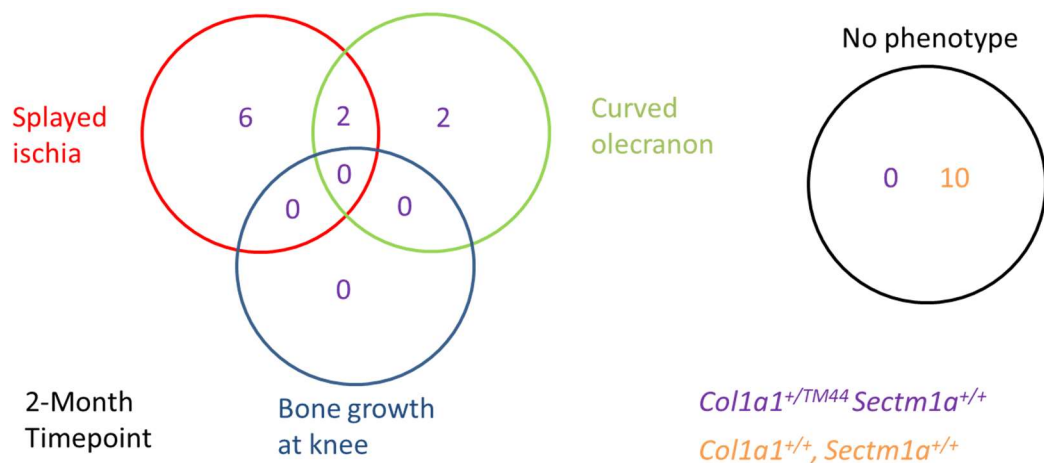


Figure 5.12. Diagram showing the number of animals that exhibited each phenotype, or combination of phenotypes for wild-type and heterozygous animals at 2 months of age. All heterozygous (HET, *Col1a1*^{+/^{TM44}, *Sectm1a*^{+/⁺) animals exhibited at least one phenotype, no wild-type (WT, *Col1a1*^{+/⁺, *Sectm1a*^{+/⁺) animals exhibited a phenotype.}}}}

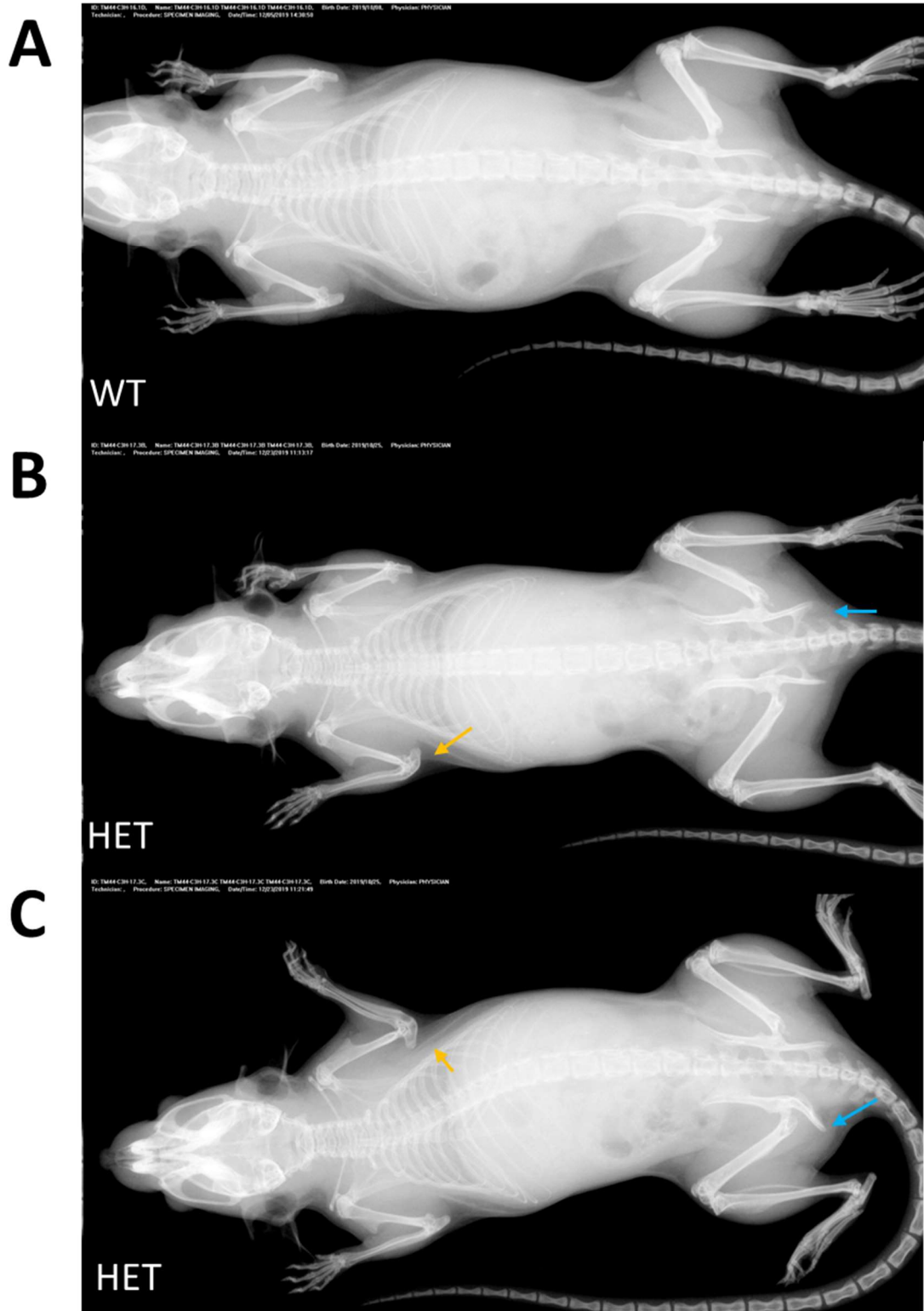


Figure 5.13. Representative X-ray images of wild-type and heterozygous animals at 2 months. (A) Wild type (WT, *Col1a1*^{+/+}, *Sectm1a*^{+/+}) animals exhibited no evidence of the curved olecranon or splayed ischia (B&C) heterozygous (HET, *Col1a1*^{+/TM44}, *Sectm1a*^{+/+}) animals either exhibited the curved olecranon (orange arrow), or the splayed ischia (Blue arrow), or a combination, confirming *Col1a1* as the causative mutation.

All animals which were heterozygous for the *Col1a1* mutation showed some phenotype regardless of sex (Table 5.1).

2 months	N	Ischia	Olecranon	Knee	Total Affected	Percentage Affected
Male - <i>Col1a1</i> ^{+/<i>TM44</i>} , <i>Sectm1a</i> ^{+/<i>+</i>}	5	3	2	0	5	100 %
Male - <i>Col1a1</i> ^{+/<i>+</i>} , <i>Sectm1a</i> ^{+/<i>+</i>}	5	0	0	0	0	0%
Female - <i>Col1a1</i> ^{+/<i>TM44</i>} , <i>Sectm1a</i> ^{+/<i>+</i>}	5	5	2	0	5	100%
Female - <i>Col1a1</i> ^{+/<i>+</i>} , <i>Sectm1a</i> ^{+/<i>+</i>}	5	0	0	0	0	0%

Table 5.1. A table displaying the number of animals phenotyped in the 2-month cohort and the number of animals presenting with each phenotype. 100 % of heterozygotes (*Col1a1*^{+/*TM44*}, *Sectm1a*^{+/*+*}) exhibited either the curved olecranon, the splayed ischia, or a combination of phenotypes. No phenotype was observed in the wild types (*Col1a1*^{+/*+*}, *Sectm1a*^{+/*+*}).

In addition to the previously noted phenotypes of curved olecranon at the elbow and splayed ischia at the pelvis, in the heterozygotes (HET, *Col1a1*^{+/*TM44*}, *Sectm1a*^{+/*+*}), one heterozygote (HET, *Col1a1*^{+/*TM44*}, *Sectm1a*^{+/*+*}) appeared to have extra bone formation at the elbow rather than the curved olecranon seen in other heterozygous animals (Figure 5.14). It should be noted that this animal was included, in Figure 5.12 and Table 5.1 as having an olecranon phenotype, however as this was not the only phenotype in this animal, it would not affect the percentage affected if excluded.

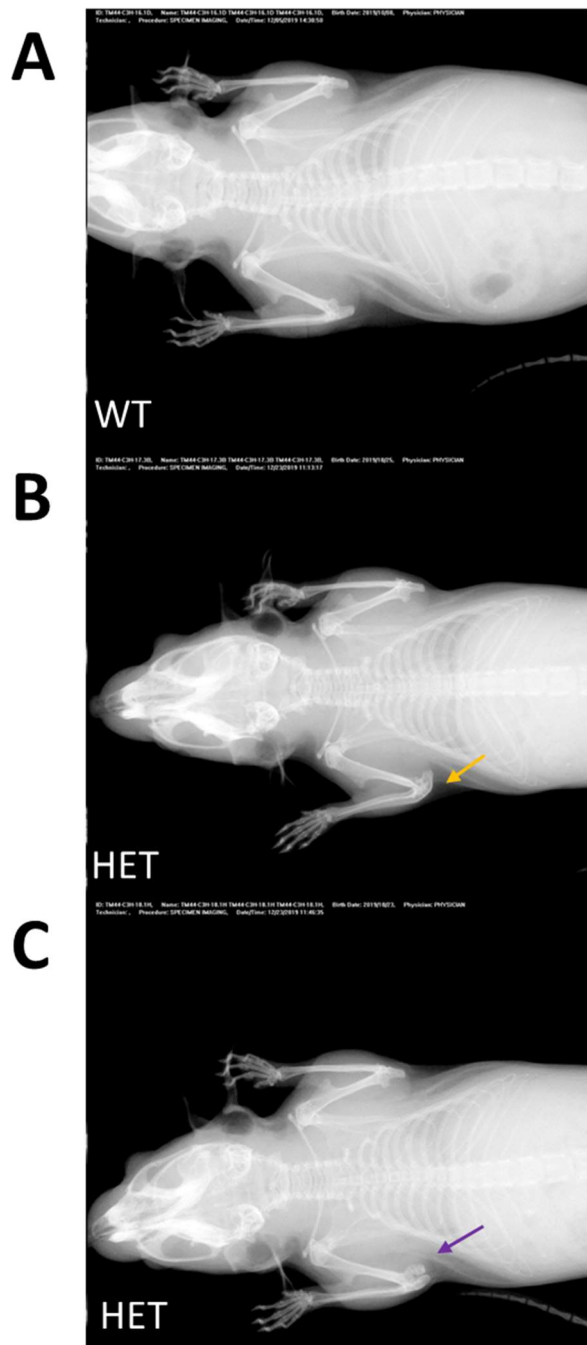


Figure 5.14. X-ray images of wild-type and heterozygous animals at 2 months showing the olecranon phenotypes. (A) Wild type (WT, $Col1a1^{+/+}$, $Sectm1a^{+/+}$) exhibits no evidence of the curved olecranon, (B) a heterozygote (HET, $Col1a1^{+/TM44}$, $Sectm1a^{+/+}$) exhibits the curved olecranon (orange arrow), (C) a heterozygote (HET, $Col1a1^{+/TM44}$, $Sectm1a^{+/+}$) exhibits apparent abnormal bone growth at the olecranon (Purple arrow) (only seen in one animal).

A small cohort of TM44 animals were aged to 18 months to investigate whether the TM44 animals exhibited late onset phenotypes. These animals were bred prior to the segregation of mutations, and therefore carry the *Sectm1a* mutation in addition to the *Col1a2* mutation. Animals were X-rayed at 12 and 18 months. At 12 months, in addition

to the early phenotype previously noted, a number of heterozygotes (HET, *Col1a1*^{+/^{TM44}) were starting to show abnormal bone growth at the knee (5/8, 62.5% male heterozygotes and 5/6, 83.3% female heterozygotes), similar in appearance to the phenotype seen in MP-107. Four heterozygotes were also observed to have a mild bone abnormality at the heel. No phenotype was observed in the wild types (*Col1a1*^{+/+}) (Figure 5.15).}

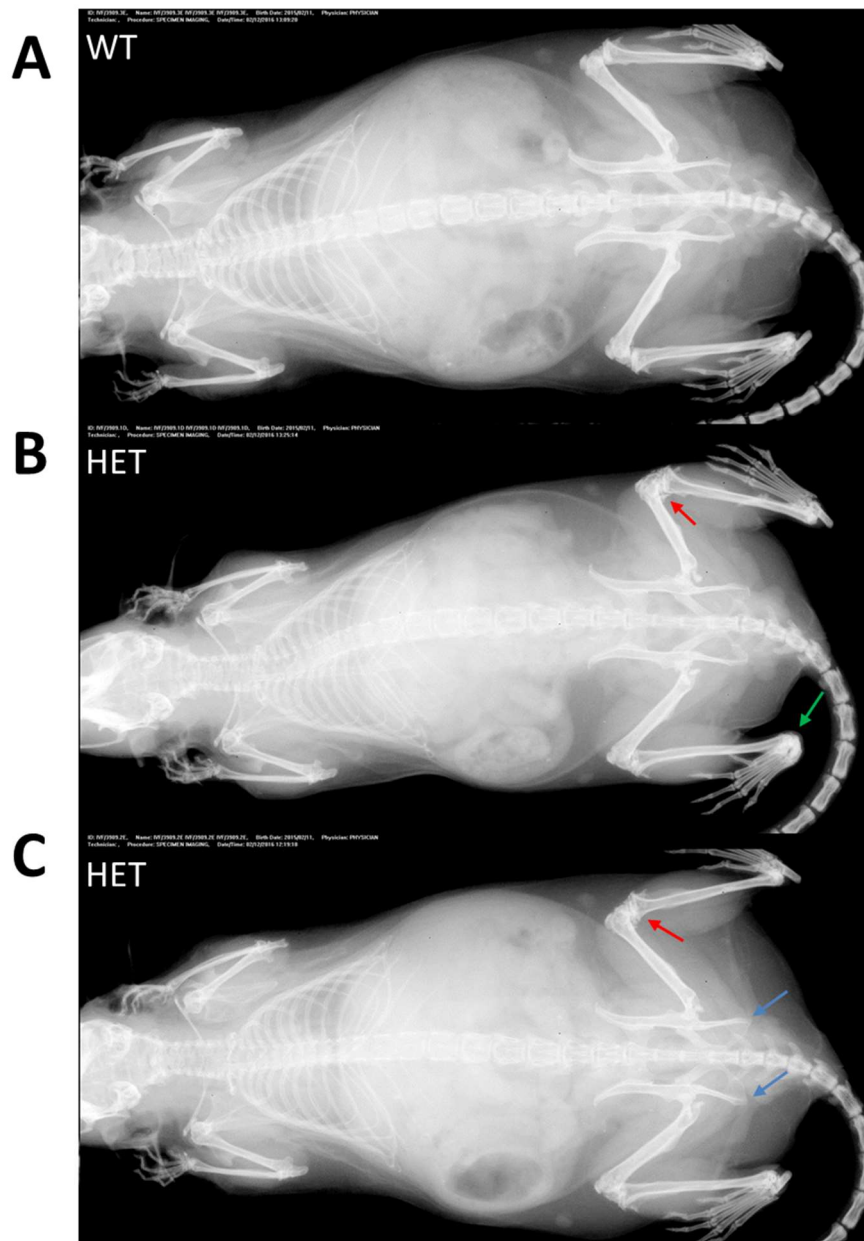


Figure 5.15. Representative X-ray images of wild-type and heterozygous animals at 12 months. (A) Wild-type (WT, *Col1a1*^{+/+}) and (B&C) heterozygous (HET, *Col1a1*^{+/^{TM44}) animals at 12 months of age. (A) Wild types (WT, *Col1a1*^{+/+}) display no evidence of the curved olecranon splayed ischia or abnormal bone growth at the knee. (B-C) Heterozygotes (HET, *Col1a1*^{+/^{TM44}) displays curved olecranon (not shown in this figure), abnormal bone growth at the knee (red arrow), splayed ischia (blue arrow), abnormal calcaneus (green arrow) or a combination of phenotypes.}}

At the 18-month time point, two animals that did not display the abnormal bone growth at the knee had developed the phenotype. At 12-months, 100% of heterozygotes exhibited some form of phenotype, and at 18-months 100% of heterozygotes exhibited the knee phenotype. No phenotype was observed in the wild types (Figure 5.16).

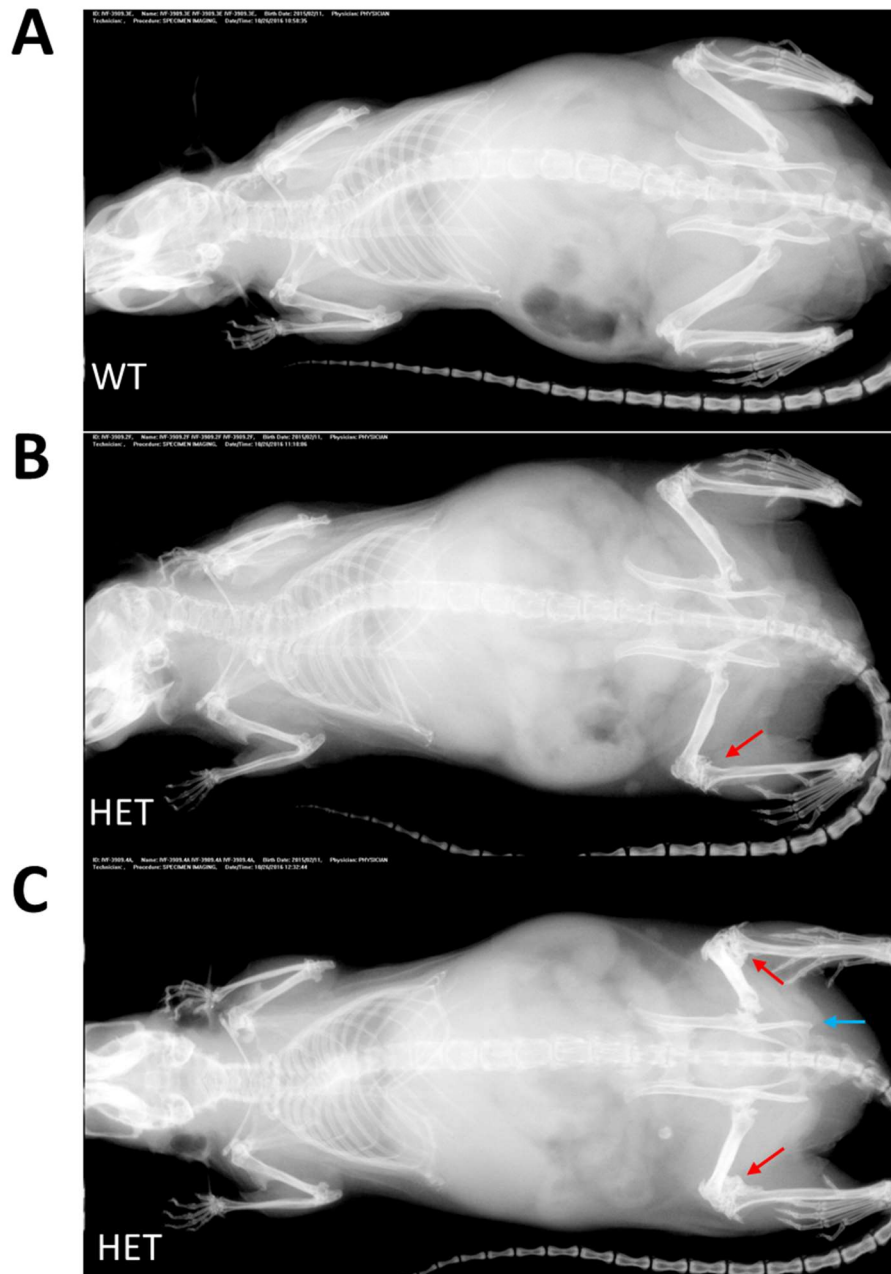


Figure 5.16. Representative X-ray images of wild-type and heterozygous animals at 18 months. (A) Wild-type (WT, *Col1a1*^{+/+}) and (B&C) heterozygous (HET, *Col1a1*^{+/TM44}) animals at 12 months of age. (A) Wild types (WT, *Col1a1*^{+/+}) display no evidence of the curved olecranon splayed ischia or abnormal bone growth at the knee. (B-C) Heterozygotes (HET, *Col1a1*^{+/TM44}) displays curved olecranon (not shown in this figure), abnormal bone growth at the knee (red arrow), splayed ischia (blue arrow) or a combination of phenotypes. No heterozygous (HET, *Col1a1*^{+/TM44}) animals exhibited the abnormal calcaneus at 18 months as affected animals were culled due to welfare reasons.

Table 5.2 shows the number of animals displaying each phenotype in each cohort, and Figure 5.17 shows the actual combination of phenotypes that were observed.

Cohort	Genotype	N	Ischia	Olecranon	Knee	Heel	Total Affected	Percentage Affected
12-month Male	<i>Col1a1^{+ / TM44}</i>	8	2	3	5	3	8	100 %
	<i>Col1a1^{+ / +}</i>	6	0	0	0	0	0	0%
12 month Female	<i>Col1a1^{+ / TM44}</i>	6	5	0	5	0	6	100%
	<i>Col1a1^{+ / +}</i>	4	0	0	0	0	0	0%
18-month Male	<i>Col1a1^{+ / TM44}</i>	3	1*	1*	3*	0*	3	100 %
	<i>Col1a1^{+ / +}</i>	4	0	0	0	0	0	0%
18-month Female	<i>Col1a1^{+ / TM44}</i>	5	4*	0	5	0	5	100%
	<i>Col1a1^{+ / +}</i>	4	0	0	0	0	0	0%

Table 5.2. A table displaying the number of animals phenotyped in the 12- and 18-month cohorts and the number of animals presenting with each phenotype. 100% of heterozygotes (*Col1a1^{+ / TM44}*) exhibited either the curved olecranon, the splayed ischia, abnormal bone growth at the knee, the abnormal calcaneus, or a combination of phenotypes. No phenotype was observed in the wild types (*Col1a1^{+ / +}*) *numbers reduced from 12 months due to 6 animals being culled for welfare purposes.

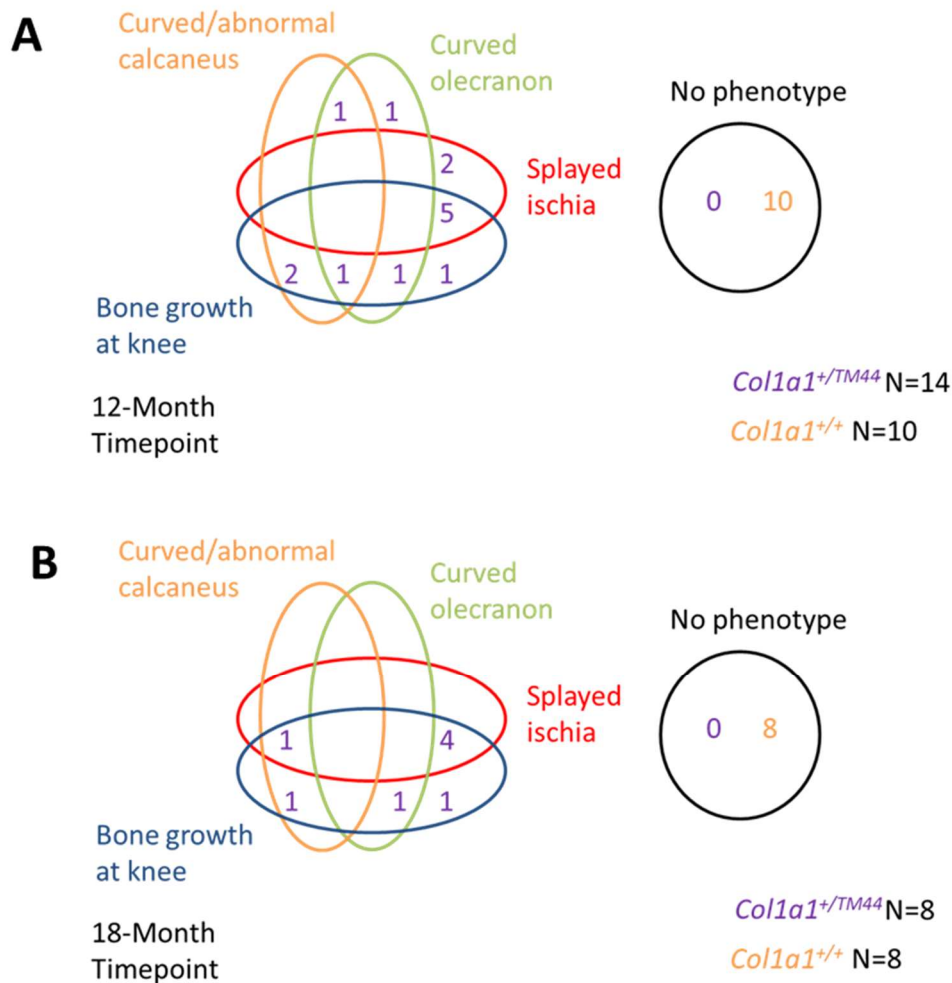


Figure 5.17. Diagram showing the number of animals that exhibited each phenotype, or combination of phenotypes for wild-type and heterozygous animals at 12- and 18-months. (A) At 12-months all heterozygous (HET, *Col1a1^{+TM44}*) exhibit at least one of the following three phenotypes, curved olecranon, splayed ischia or abnormal bone growth at the knee, either in isolation or in combination. Additionally, four heterozygotes also exhibited an abnormal calcaneus; this phenotype was only ever observed in combination with another phenotype. No wild-type (WT, *Col1a1^{+/+}*) animals exhibited any phenotype. (B) At 18-months all heterozygous (HET, *Col1a1^{+TM44}*) exhibit at least one of the following three phenotypes, curved olecranon, splayed ischia or abnormal bone growth at the knee, either in isolation or in combination. No heterozygotes exhibited the abnormal calcaneus phenotype, as those animals were all culled for welfare reasons. No wild-type (WT, *Col1a1^{+/+}*) animals exhibited any phenotype. Reduced N numbers at 18 months were due to animals being culled for welfare reasons.

The X-ray data shows that the TM44 heterozygotes exhibit similar phenotypes to MP-107, with the addition of a phenotype affecting the calcaneus. These three cohorts show higher incidence of the observed phenotypes in TM44 than in MP-107.

5.6.2. DEXA Analysis of TM44 Animals

DEXA allows accurate analysis of bone composition. DEXA analysis was undertaken for the 2-month cohort of TM44 animals with segregated mutations and the 18-month cohort of TM44 animals bred at a previous backcross, before the segregation of mutations, and therefore contains both the *Sectm1a* and the *Col1a1* mutation.

The 2-month cohort showed that heterozygotes (HET, *Col1a1*^{+/^{TM44}, *Sectm1a*^{+/⁺) had a significantly decreased BMC and BMD when compared to wild types (WT, *Col1a1*^{+/⁺, *Sectm1a*^{+/⁺). This significant difference was observed in both sexes (Figure 5.18) (BMC- Male P=0.000009, Female P=0.00285, BMD- Male P=0.0240, Female P=0.00074). No significant differences were observed in any other parameter. The phenotypes observed are an indication that the line TM44 may be osteoporotic, and at a higher risk of bone fracture, indicating a mild osteogenesis imperfecta phenotype.}}}}

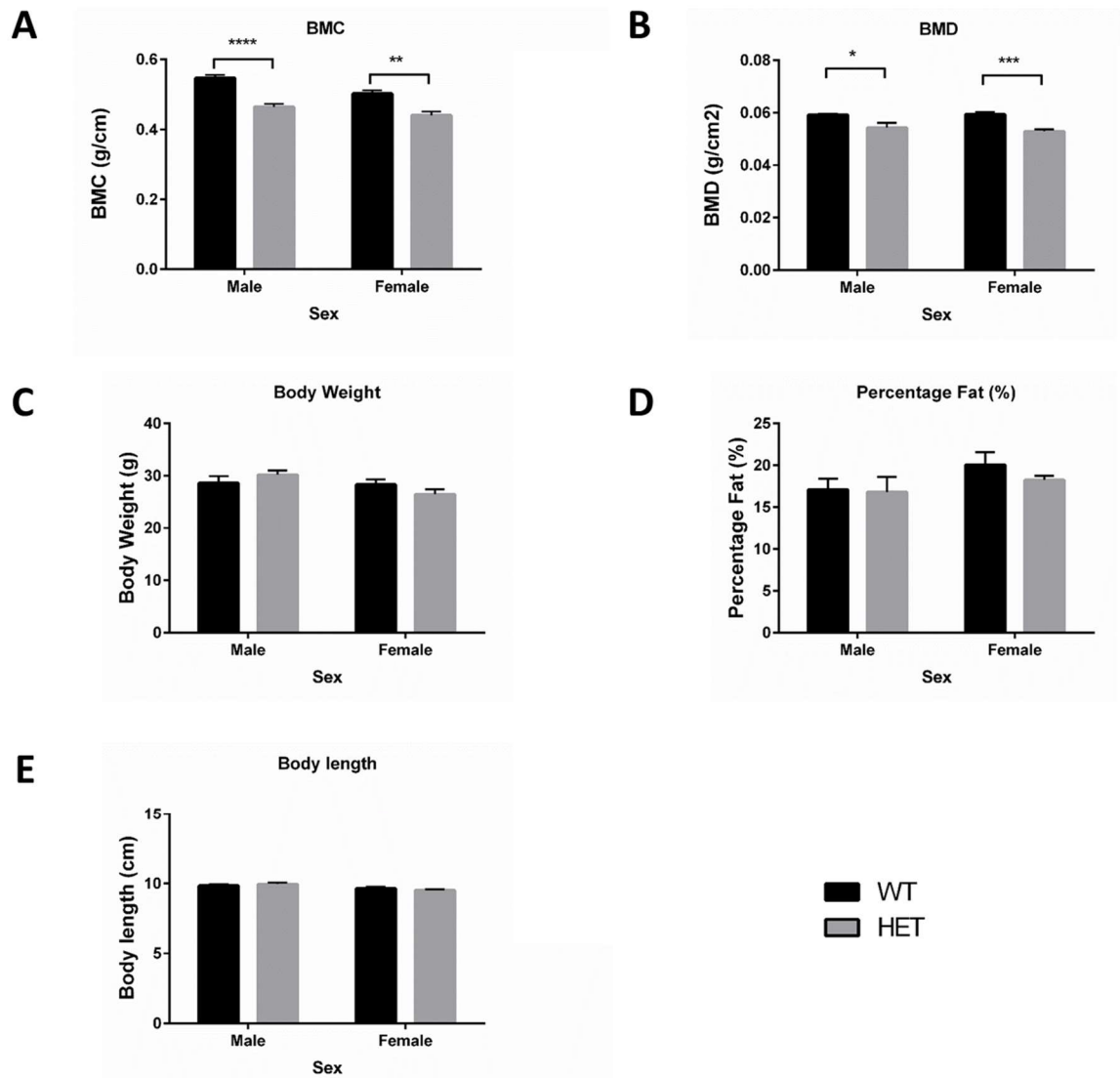


Figure 5.18. DEXA analysis of wild types and heterozygotes of both sexes at 2-months. (A) A significant reduction in bone mineral content was observed in the heterozygotes (HET, *Col1a1*^{+/*TM44*}, *Sectm1a*^{+/*+*}) compared to wild types (WT, *Col1a1*^{+/*+*}, *Sectm1a*^{+/*+*}) in both sexes. (B) A significant reduction in bone mineral density was observed in the heterozygotes (HET, *Col1a1*^{+/*TM44*}, *Sectm1a*^{+/*+*}) compared to wild types (WT, *Col1a1*^{+/*+*}, *Sectm1a*^{+/*+*}) in both sexes. No significant difference between genotypes was observed in (C) Weight, (D) Percentage Fat or (E) Length. (N = 5 Female HET, 5 Female WT, 5 Male HET, 5 Male WT, *P<0.05, **P<0.01, *** P<0.001, **** P<0.0001)

DEXA analysis of the 18-month cohort showed that heterozygotes (HET, *Col1a1*^{+/*TM44*}) had a significantly reduced percentage fat when compared to wild types (WT, *Col1a1*^{+/*+*}) in females (P=0.025). No significant difference was observed in the BMD, BMC, body weight or body length between genotypes of either sex, and no significant difference between genotypes in percentage fat in males (Figure 5.19).

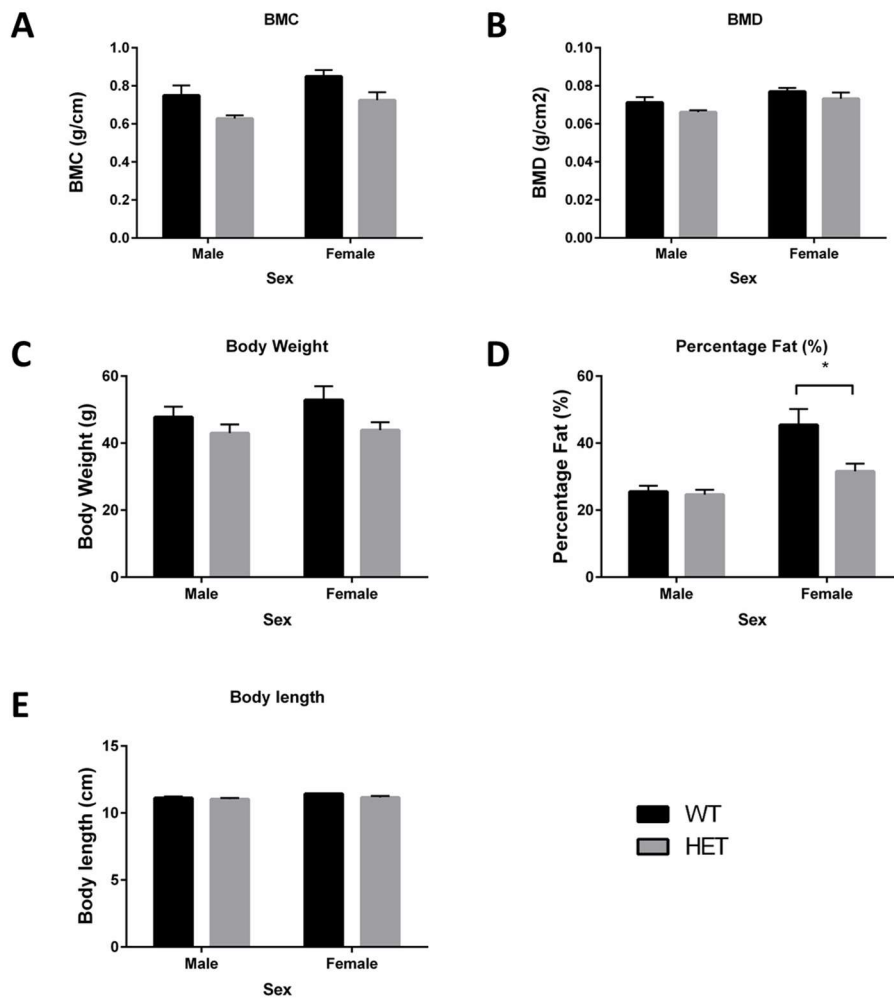


Figure 5.19. DEXA analysis of wild types and heterozygotes of both sexes at 18-months. No significant difference was observed between genotypes in either sex in (A) bone mineral content, (B) bone mineral density, (C) body weight or (E) body length. (D) No significant difference was observed in percentage fat between genotypes in males, however, females heterozygotes (HET, *Col1a1*^{+/*TM44*}) exhibited a reduced percentage fat when compared with wild types (WT, *Col1a1*^{+/*+*}) (N = 5 Female HET, 4 Female WT, 3 Male HET, 4 Male WT T-Test *P<0.05).

It is not known why the female heterozygotes show a reduction in percentage fat; however, this could be a result of the knee abnormalities making it more difficult for the female heterozygotes to over-eat, as food is stored in a hopper. The reduction in both BMC and BMD seen in the 2-month cohort is not replicated here. This could be due to the 2-month cohort being a much later backcross, as this was required to segregate mutations, and therefore has a reduced proportion of the C57BL/6J genome, or it could be that the effect diminishes with age.

5.6.3. Histological analysis of TM44 Knee Joints

Histological analysis of 18-month old knee joints reveal that in addition to the abnormal bone formation observed by X-ray imaging, the heterozygotes (HET, *Col1a1*^{+/*TM44*}) also show a profound loss of articular cartilage indicating an OA phenotype (Figure 5.20).

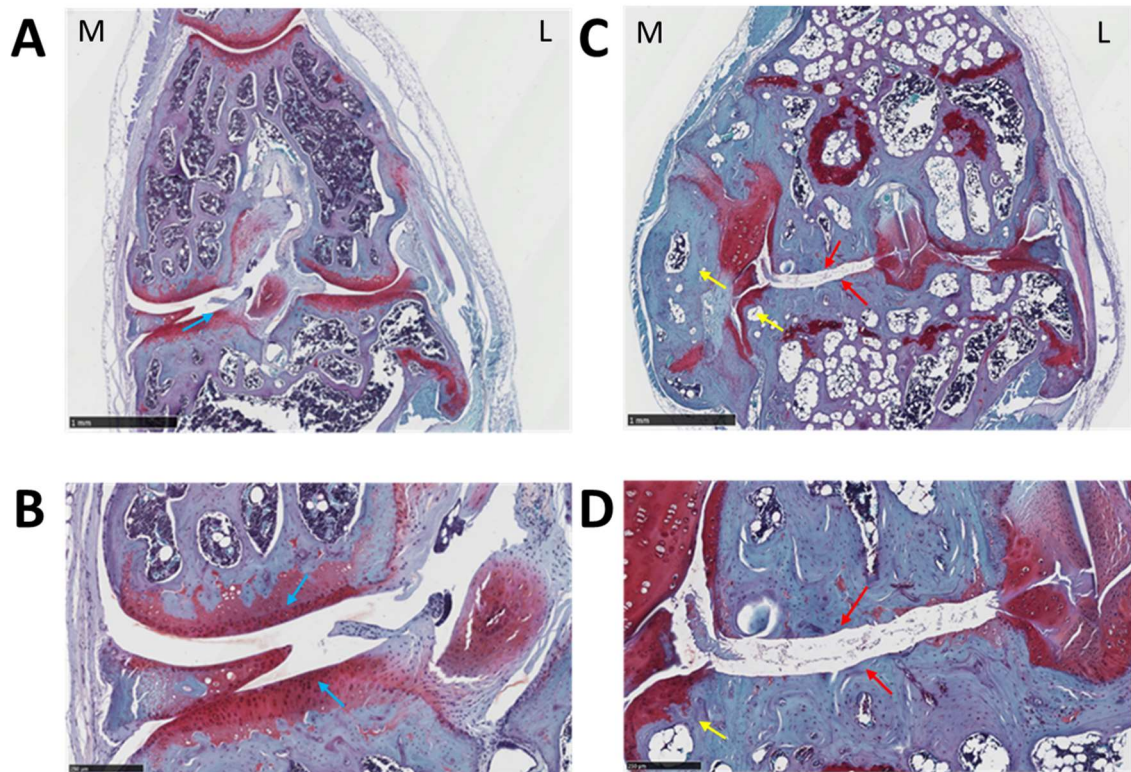


Figure 5.20. Safranin O stained sections of knee joints from a wildtype and a heterozygote at 18 months. (A-B) The wild-type (WT, *Col1a1*^{+/*+*}) joint shows normal healthy cartilage at the articular surface (Blue arrow) and no evidence of osteophytes. (C-D) The heterozygous (HET, *Col1a1*^{+/*TM44*}) knee shows severe osteophyte formation (Yellow arrows), synovial inflammation and an absence of articular cartilage on the medial femoral condyle and medial tibial plateau (Red arrow). Medial and lateral side denoted by M and L respectively.

OARSI scoring of histological sections from heterozygous and wild-type knees indicates that there is a significantly elevated maximum OARSI score in the heterozygotes when compared with wild types ($P=0.0357$). This comparison was only carried out in male mice, as there were too few tissue samples taken from the female cohort to do statistical analyses.

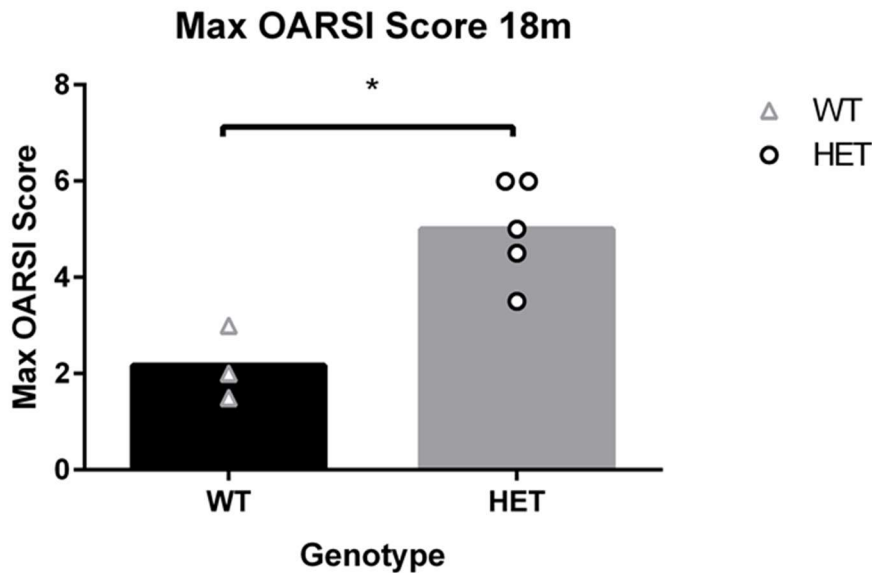


Figure 5.21. Maximum OARSI scores of Safranin O stained histological section of knee joints from wild-type and heterozygous male animals at 18-months of age. Heterozygote (HET, *Col1a2*^{+/¹⁰⁷) max OARSI scores were significantly higher than their wild type (WT, *Col1a2*^{+/⁺) counterparts (Het- N=5, WT- N=3, Mann Whitney test *p<0.05).}}

5.7. Collagen Content of TM44 Tendons

Mutations in the collagen I genes could reasonably be assumed to cause changes in the folding and make-up of the collagen I heterotrimer. It is known that collagen I can exist as a homotrimer made up solely of $\alpha 1$ chains. Analysis of radiolabelled collagen in MP-107 tail tendons in Chapter 4 (Section 4.5) revealed that there was no difference in either the extracellular, or the intracellular collagen I between wild-type and heterozygous samples, indicating that the mutant COL1A2 was being produced and incorporated into the collagen fibrils.

The radiolabelling assay was not available for the analysis of TM44 lines. For this reason, to analyse the secretion of collagen I, Collagen was extracted from 4-month old tail tendons using a pepsin/acetic acid extraction, before being analysed using gel electrophoresis. Separating out the $\alpha 1$ and $\alpha 2$ bands on a gel before staining allows a comparison of the ratio of $\alpha 1$ and $\alpha 2$. The theory behind this is that as normal collagen I is a heterotrimer of two $\alpha 1$ chains and one $\alpha 2$ chain, the expected ratio would be approximately 2:1 (provided the bands are solely $\alpha 1$ and $\alpha 2$). If a mutation impairs the production of the heterotrimer, homotrimer may be produced instead, which would modify the ratio in the heterozygote. The collagen extracts from wild-type and heterozygous tendons from both MP-107 and TM44, were diluted to 0.25mg/ml and

samples were run on a 4-12% Tris-Bis gel, before staining with Brilliant Coomassie blue stain. (Figure 5.22).

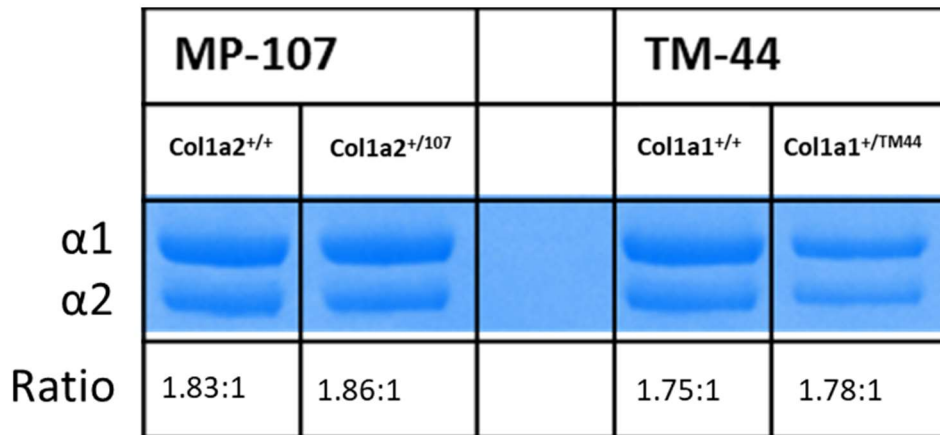


Figure 5.22. Coomassie stained collagen extracts from wild-type and heterozygous tendons for the lines MP-107 and TM44. The ratio of $\alpha 1$: $\alpha 2$ is displayed beneath each lane. The analysis shows no visible difference in ratio of $\alpha 1$ to $\alpha 2$ between genotypes in either MP-107 or TM44, indicating the TM44 heterozygote is not producing homotrimer.

Comparison of the ratio of $\alpha 1$ to $\alpha 2$ between wild type (WT, *Col1a2^{+/+}*) and heterozygotes (HET, *Col1a2^{+/107}*) are similar in MP-107. Indicating that this assay is a suitable alternative to the unavailable radiolabelling assay. No obvious difference was identified between ratio of $\alpha 1$ to $\alpha 2$ in wild types (WT, *Col1a1^{+/+}*) and heterozygotes (HET, *Col1a1^{+/TM44}*) in TM44, indicating that the heterozygote is not producing homotrimer. It should be noted that as the extract from the tendon will contain other proteins, these bands may contain similar sized proteins, which could account for the ratios not being exactly 2:1.

5.8. Discussion

The line TM44 was originally incorporated into this project due to the similarities in the early onset phenotypes, consisting of splayed ischia and curved olecranon, between this line and MP-107. The subsequent identification of a late onset knee phenotype consisting of abnormal bone growth, and cartilage loss at the articular surface mirrored the late phenotype seen in MP-107.

The initial work of Dr Esapa in mapping the causative mutation to a region on Chromosome 6, and the identification of *Col1a1* and *Sectm1a* as possible candidate genes, laid the groundwork for the eventual segregation of these mutations. The segregation of the *Sectm1a* and *Col1a1* mutations occurred after many rounds of backcrossing, and therefore happened towards the end of the project. As a result, it was not possible to age the animals heterozygous for the *Col1a2* mutation and wild-type for the *Sectm1a* mutation (*Col1a1*^{+/^{TM44}, *Sectm1a*^{+/⁺) in order to confirm that the late phenotype occurred in the absence of the *Sectm1a* mutation. However, early phenotyping did confirm that the splayed ischia and curved olecranon do occur in the presence of the *Col1a1* mutation alone. The segregation of the mutations and the presence of the early bone phenotypes indicate that the premature stop in *Col1a1* is the causative mutation.}}

Like the MP-107 line, the TM44 is found to be homozygous lethal, although the TM44 is lethal far earlier in development than MP-107. The homozygous embryos were found to be lethal between 12.5 and 14.5 dpc and showed evidence of hydrocephalus. Interestingly, parallels can be drawn between this lethal phenotype and the *Mov-13*^{-/-} model of Type II OI, which is recorded as having arrested development between day 11 and day 12 of gestation, and being lethal between days 13 and 14. The first observation of type I collagen in the embryo is around day 9, however day 11-12 is when high transcription of *Col1a1* occurs [294].

The three phenotypes observed by X-ray in heterozygotes of both lines, appear with greater frequency in the TM44 line, with 100% of heterozygotes (*Col1a1^{+ / TM44}*) exhibiting at least one of the phenotypes, while in the MP-107 line 20-40% of heterozygotes (*Col1a2^{+ / 107}*) exhibited no phenotype. The histology of the knee joints of heterozygotes from the line TM44 (*Col1a1^{+ / TM44}*) is very similar to the histology of the knee joints of heterozygotes from the line MP-107 (*Col1a2^{+ / 107}*), including the presence of large osteophytes and articular cartilage erosion. In addition to the phenotypes noted in the MP-107 line, X-ray imaging revealed that three male TM44 heterozygotes (*Col1a1^{+ / TM44}*) also displayed an abnormal calcaneus at 12 months. These animals were culled for welfare reasons due to impaired mobility.

DEXA analysis indicates that the heterozygotes (*Col1a1^{+ / TM44}*) have osteopenia. The osteopenic phenotype shown by DEXA analysis in the TM44 heterozygotes (*Col1a1^{+ / TM44}*), was not replicated in the MP-107 heterozygotes (*Col1a2^{+ / 107}*). However the μ CT analysis did indicate evidence of osteopenia in the heterozygotes (*Col1a2^{+ / 107}*) [295]. That both lines show evidence of osteopenia is not surprising given the similarities in the bone phenotype. The fact that osteopenia was not detected by DEXA in MP-107, and only by μ CT analysis indicates again that the phenotype in TM44 is more severe than in MP-107.

The similarities in phenotypes between heterozygous (*Col1a1^{+ / TM44}*) TM44 animals and heterozygous (*Col1a2^{+ / 107}*) MP-107 animals are numerous and are summarised in Figure 5.23 along with images from wild-type (*Col1a2^{+ / +}*) MP-107 animals for reference. Both lines display the same early phenotypes of curved olecranon, splayed ischia, the same late phenotypes including abnormal bone growth at the knee and loss of articular cartilage with osteophyte formation.

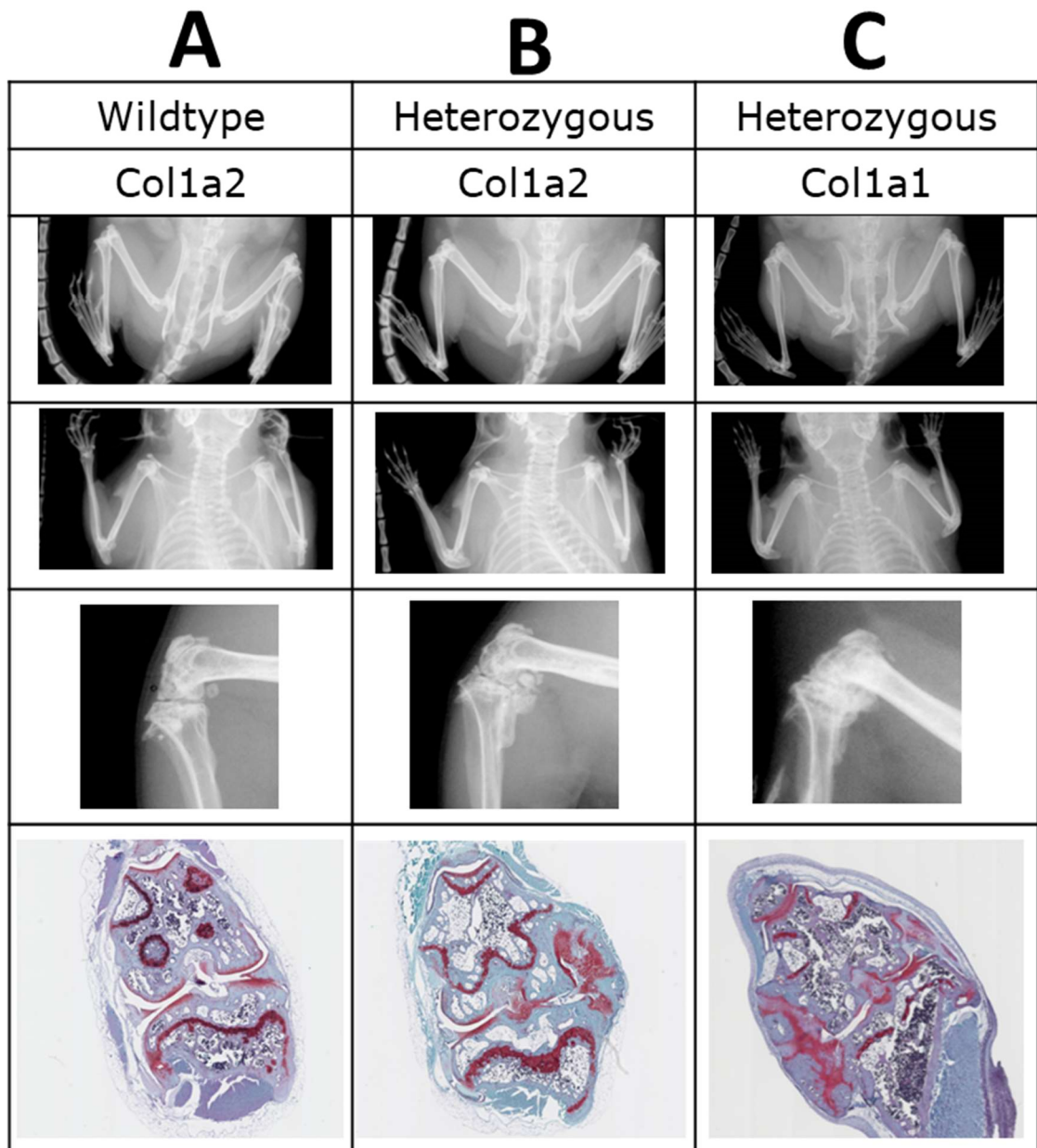


Figure 5.23. A figure comparing the observed phenotypes between the lines MP-107 and TM44. (A) MP-107 wild types (*Col1a2*^{+/+}) show no abnormalities at the pelvis or olecranon at 3 months of age, and no evidence of abnormal bone growth or osteoarthritis at the knee at 18 months. (B) MP-107 heterozygotes (*Col1a2*^{+/107}) and (C) TM44 heterozygotes (*Col1a1*^{+/TM44}) exhibit the splayed ischia at the pelvis and the curved olecranon at the elbow at 3 months of age, in addition to the abnormal bone growth at the knee, and osteoarthritis at 18 months of age.

Both lines contain mutations in collagen I alpha chains, the mutation in MP-107 is a splice variant in *Col1a2* leading to the inclusion of an extra amino acid in the protein coding sequence, while the mutation in TM44 is a premature stop in *Col1a1* which may be far more deleterious. This is borne out in the phenotype data, with homozygous lethality at an earlier developmental time point in TM44 accompanied by a more severe adult phenotype in the heterozygote reflected in the number of affected animals and a

more severe osteoporosis phenotype. Moreover, in MP-107, wild-type transcript is produced even in the homozygote (*Col1a2*^{107/107}). This may be mediating the damaging effects of the mutation, leading to lethality at a later time point and a less severe phenotype. We will return to a more detailed discussion of the genetic mechanisms of each mutation in Chapter 7.

Chapter 6: Initial Characterisation of Phenotypes Exhibited by *Col1a2* Null Mice

6.1. Introduction

The ENU mutation in MP-107 is within the gene *Col1a2*, and leads to early onset phenotypes such as a curved olecranon and splayed ischia, and late phenotypes such as OA. The mechanism by which the mutation leads to the phenotypes is not yet clear. To help elucidate the mechanism, it is important to understand what happens in the absence of the gene that contains the mutation. For this reason, the knockout of the *Col1a2* gene (*Col1a2*-KO) was generated. Viability testing and phenotyping, such as X-ray imaging and DEXA analysis, were carried out to investigate the phenotype of a null *Col1a2* allele, and to determine if similar phenotypes were observed in the *Col1a2*-KO line and MP-107. The aim of this chapter is to investigate if knocking out *Col1a2* results in similar phenotypes to those observed in MP-107 and TM44, and to provide further information about the mechanisms by which the phenotypes occur.

6.2. Creation of the *Col1a2*-KO Line

A knockout of the *Col1a2* gene (*Col1a2*-KO) was created by the gene editing team at MRC Harwell using CRISPR-Cas9 technology to delete critical exons in the gene *Col1a2*. A large region of 2087 nucleotides encompassing EXON 2 (ENSMUSE00001291037), Exon 3 (ENSMUSE00001247742) and Exon 4 (ENSMUSE00001305705) was deleted to induce a premature stop codon and a null allele.

Briefly, Cas9 mRNA and sgRNAs (detailed in section 2.2.6) were diluted and mixed in a microinjection buffer to the working concentrations of 100 ng/μl and 50 ng/μl each respectively. The sgRNAs in the buffer were then delivered by pronuclear injection into 1-cell stage C57BL/6N embryos. Injected embryos were re-implanted in CD1 pseudo-pregnant females. Host females were allowed to litter and rear F₀ progeny.

An F₀ animal was identified with the desired deletion, and an F₁ cohort was then produced by crossing to C57BL/6N, producing 7 offspring, 5 heterozygotes (*Col1a2*^{+/-}) and 2 wild types (*Col1a2*^{+/+}). The heterozygotes were then backcrossed to C57BL/6N to bulk up the colony before heterozygous animals were intercrossed to produce the cohorts containing *Col1a2*^{-/-} mice.

6.3. Viability analysis of the *Col1a2*-KO Line

Intercross matings between male heterozygotes (HET, *Col1a2*^{+/-}) and female heterozygotes (HET, *Col1a2*^{+/-}) were established to investigate the viability of the *Col1a2*-KO line. Genotyping of the offspring of these intercross revealed that animals of all three genotypes wild types (WT, *Col1a2*^{+/+}), heterozygotes (HET, *Col1a2*^{+/-}) and homozygotes (HOM, *Col1a2*^{-/-}) were present. Statistical analysis indicates that there is no reduced viability and that all genotypes are represented in the expected ratios ($\chi^2=0.51, 2df, P>0.7$) (Figure 6. 1).

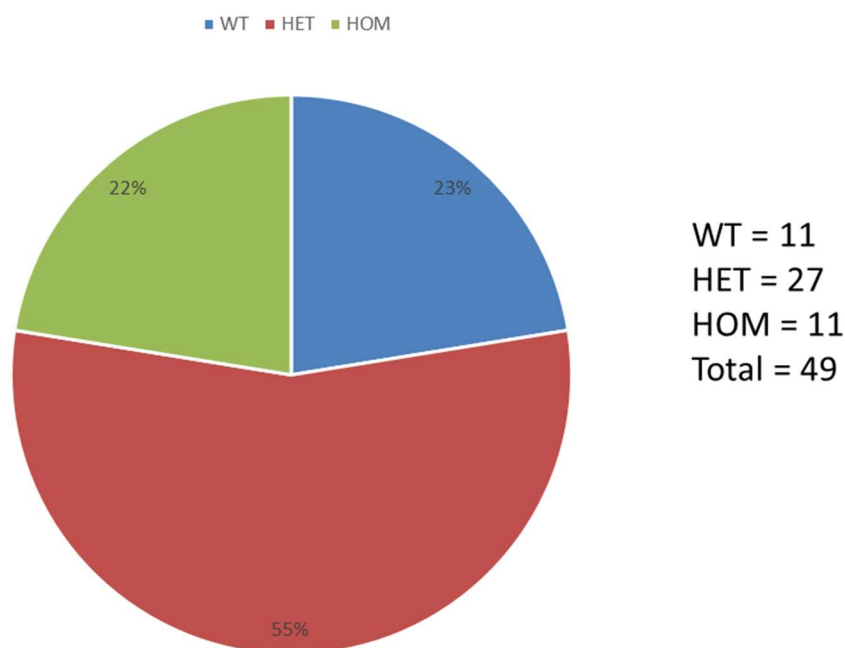


Figure 6.1. Proportions of animals of each genotype at weaning from intercross matings. Homozygotes (HOM, *Col1a2*^{-/-}) accounted for 22% of animals, heterozygotes (HET, *Col1a2*^{+/-}) accounted for 55% of animals and wild types (WT, *Col1a2*^{+/+}) accounted for the remaining 23%. The number of animals of each genotype does not significantly differ from the expected, indicating all genotypes are viable ($\chi^2=0.51, 2df, P>0.7$).

6.4. Phenotyping of the *Col1a2*-KO Line

The *Col1a2*-KO line is the first of the three lines investigated where the homozygous animals are viable into adulthood. As such, intercross cohorts of animals including all three genotypes were bred for phenotyping. Due to an unusually high number of male animals that were culled for welfare purposes only female animals were included in this analysis, the reasons for these welfare concerns will be addressed later in this chapter. The phenotyping included X-ray imaging and DEXA analysis at an early time point (2 months) and a late time point (12 months).

6.4.1. X-ray Imaging of the *Col1a2*-KO line

X-ray imaging at 2 months of age indicated the presence of mild bone abnormalities in heterozygotes (HET, *Col1a2*^{+/-}) and homozygotes (HOM, *Col1a2*^{-/-}). The heterozygotes (HET, *Col1a2*^{+/-}) exhibited only a mild splayed ischia phenotype, and homozygotes (HOM, *Col1a2*^{-/-}) exhibited mild splayed ischia and a curved olecranon phenotype. As seen previously in MP-107 and TM44, these phenotypes are variable. Not all heterozygotes or homozygotes exhibited phenotypes. There was no evidence of abnormal bone growth at the knee at either time point (Figure 6.2).

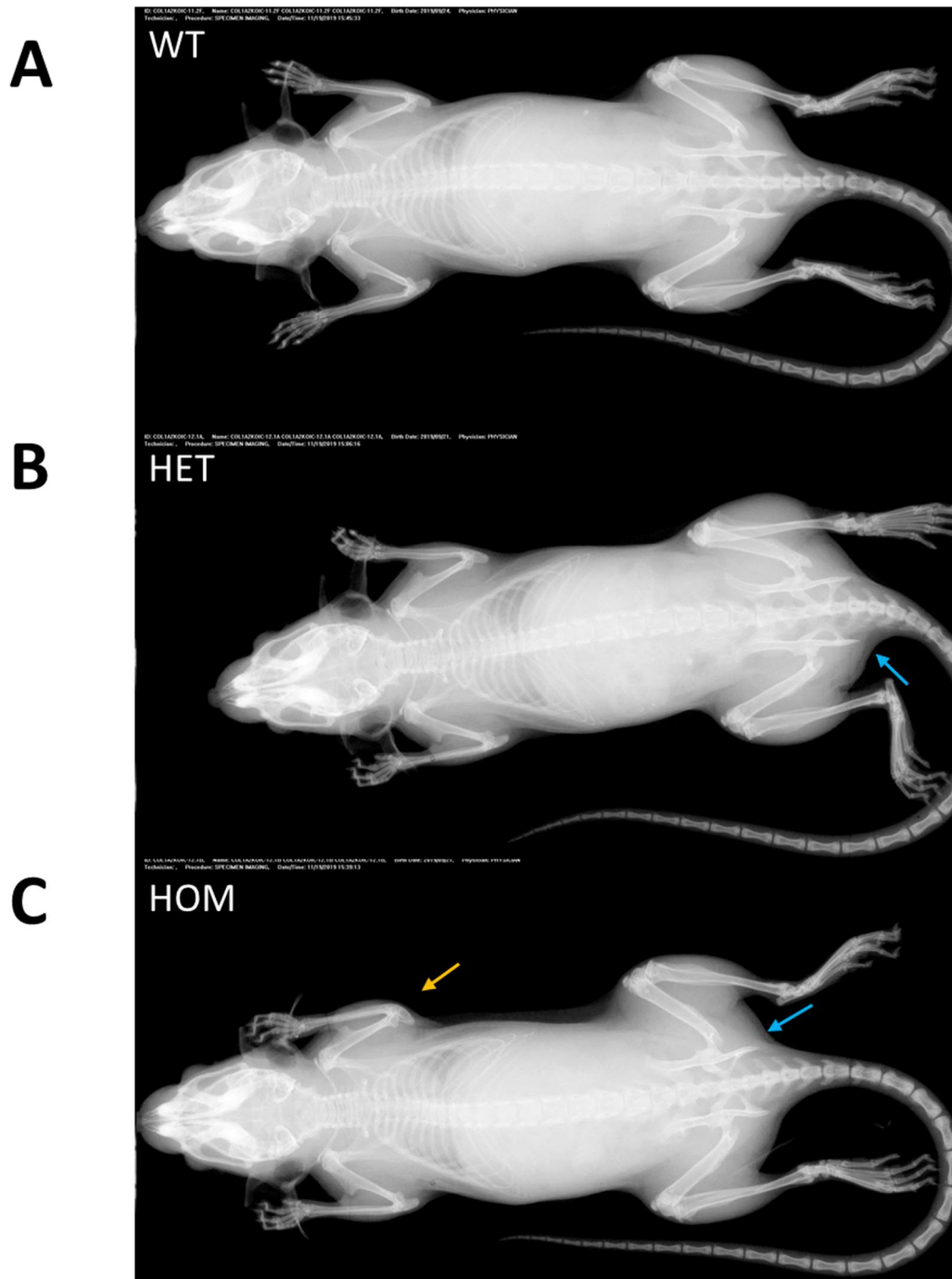


Figure 6.2. Representative X-ray images of female animals of all three genotypes at 2-months of age. (A) Wild types (WT, *Col1a2*^{+/+}) exhibited no evidence of the curved olecranon or splayed ischia (B) 40% of heterozygotes (HET, *Col1a2*^{+/-}) exhibited a splayed ischia phenotype (Blue arrow), and (C) 60% of homozygotes (HOM, *Col1a2*^{-/-}) exhibited a splayed ischia phenotype (Blue arrow) with some animals also exhibiting a curved olecranon phenotype (Orange arrow). No evidence of abnormal bone growth at the knee was detected in any genotype.

X-ray imaging at 12 months of age indicated the presence of mild bone abnormalities in heterozygotes (HET, *Col1a2*^{+/-}) and homozygotes (HOM, *Col1a2*^{-/-}). The heterozygotes (HET, *Col1a2*^{+/-}) exhibited only splayed ischia phenotype, and homozygotes (HOM,

Col1a2^{-/-}) exhibited splayed ischia and a curved olecranon phenotype. As seen previously in MP-107 and TM44, these phenotypes are variable. Not all heterozygote and homozygotes exhibited phenotypes. There was no evidence of abnormal bone growth at the knee (Figure 6.3).

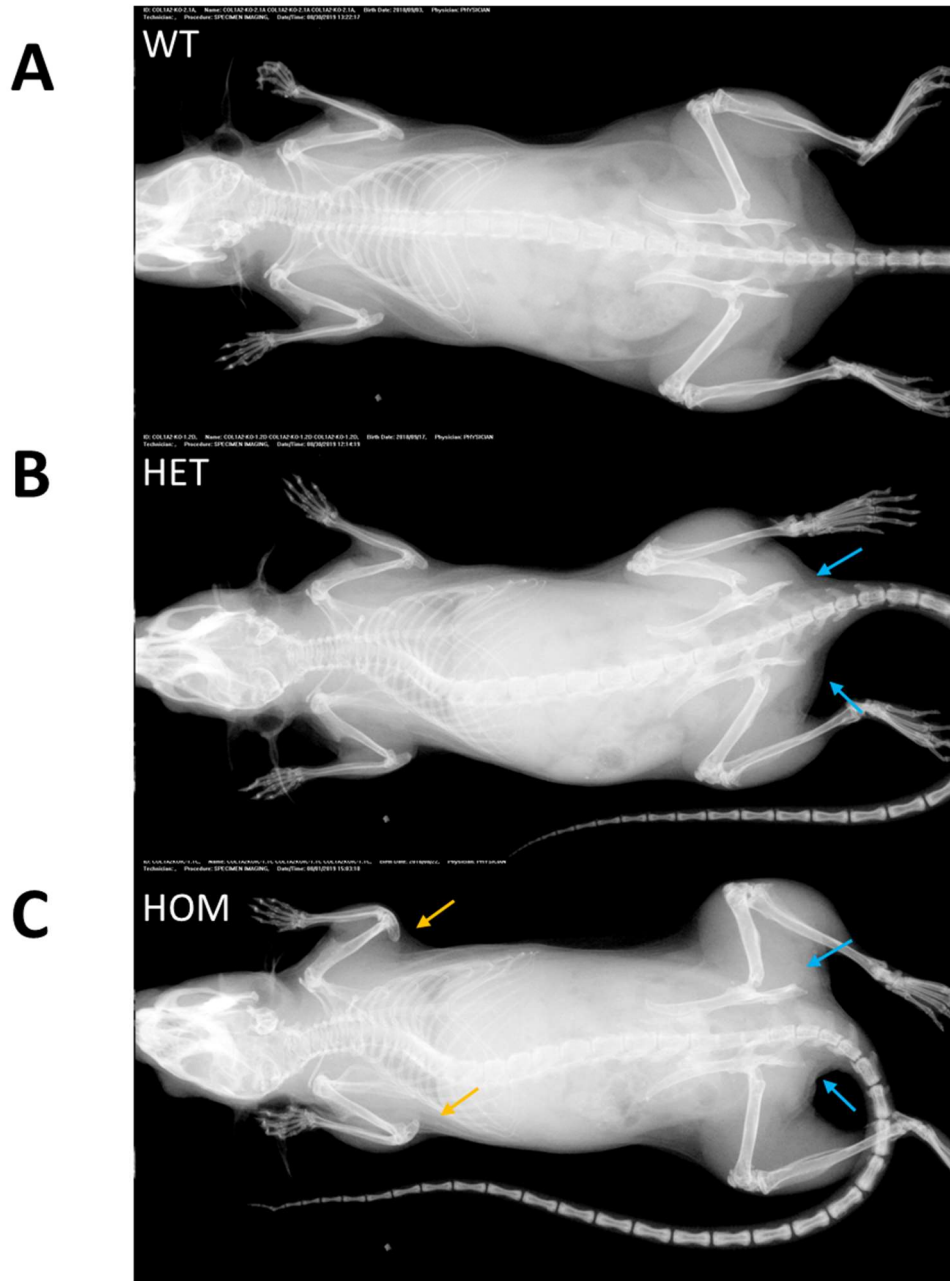


Figure 6.3. Representative X-ray images of female animals of all three genotypes at 12-months of age. (A) Wild types (WT, *Col1a2*^{+/+}) exhibited no evidence of the curved olecranon or splayed ischia, (B) 60% of heterozygotes (HET, *Col1a2*^{+/-}) exhibited a splayed ischia phenotype (Blue arrow), and (C) 70% of homozygotes (HOM, *Col1a2*^{-/-}) exhibited a splayed ischia phenotype (Blue arrow) with some animals also exhibiting a curved olecranon phenotype (Orange arrow). No evidence of abnormal bone growth at the knee was detected in any genotype.

No heterozygotes (HET, *Col1a2*^{+/-}) exhibited the curved olecranon at all, and no homozygotes (HOM, *Col1a2*^{-/-}) exhibited the curved olecranon in isolation, it only occurred in tandem with the splayed ischia phenotype (Table 6.1). This indicates that the heterozygotes exhibit a less severe phenotype than the homozygotes.

Cohort	Genotype	N	Ischia	Olecranon	Knee	Total Affected	Percentage Affected
2-month	<i>Col1a2</i> ^{+/+}	7	0	0	0	0	0%
	<i>Col1a2</i> ^{+/-}	5	2	0	0	2	40%
	<i>Col1a2</i> ^{-/-}	6	4	1	0	4	67%
12-month	<i>Col1a2</i> ^{+/+}	3	0	0	0	0	0%
	<i>Col1a2</i> ^{+/-}	5	3	0	0	3	60%
	<i>Col1a2</i> ^{-/-}	7	5	3	0	5	71%

Table 6.1. A table displaying the number of animals presenting with each phenotype in the 2- and 12-month female cohorts.

6.4.2. DEXA Analysis of the *Col1a2*-KO line

DEXA analysis was carried out on the same cohorts that were used for X-ray imaging, at 2 and 12 months of age, to investigate whether the loss of one or more *Col1a2* alleles caused changes in parameters such as BMC and BMD. Statistical analysis showed that there was no significant difference in either BMD or BMC between the genotypes (Figure 6.4).

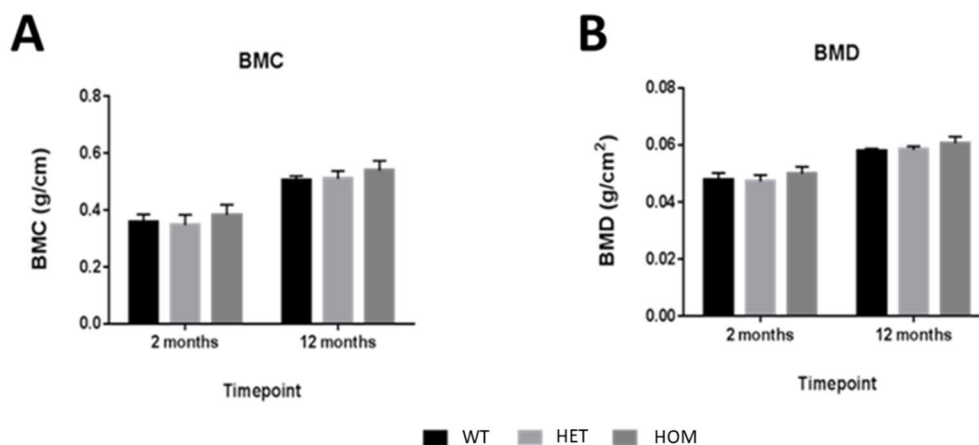


Figure 6.4 DEXA analysis of all three genotypes in the 2- and 12-month female cohorts. No significant differences were detected in either (A) bone mineral content (BMC) or (B) bone mineral density (BMD) between wild types (WT, *Col1a2*^{+/+}), heterozygotes (HET, *Col1a2*^{+/-}) and homozygotes (HOM, *Col1a2*^{-/-}) at 2- and 12-months of age. (2 month cohort- WT-N=7, HET-N=5, Hom-N=6, 12 month cohort- WT-N=3, HET-N=5, Hom-N=7- Statistical test- one way ANOVA).

6.5. Welfare Observations of the *Col1a2*-KO line

It was noted that a number of male animals, older than 6 months of age, had swollen ankles and were culled for welfare reasons. In male homozygotes swollen ankles occurred with an incidence of 31% (5/16), in heterozygotes 13% (7/53) and in wild types 3% (1/27). Initially, the occurrence of swollen ankles was attributed to fighting. However due to the genotypes of the affected animals, two affected homozygotes and an unaffected wild types were X-ray imaged to try to identify a possible cause for the swollen ankles. Both affected homozygotes imaged exhibited calcification of the Achilles tendon, while the unaffected wild types did not (Figure 6.5). In 2020, a preprint paper [296] found similar swollen ankles in their *Col1a2* null male animals, although they did not attribute a cause.

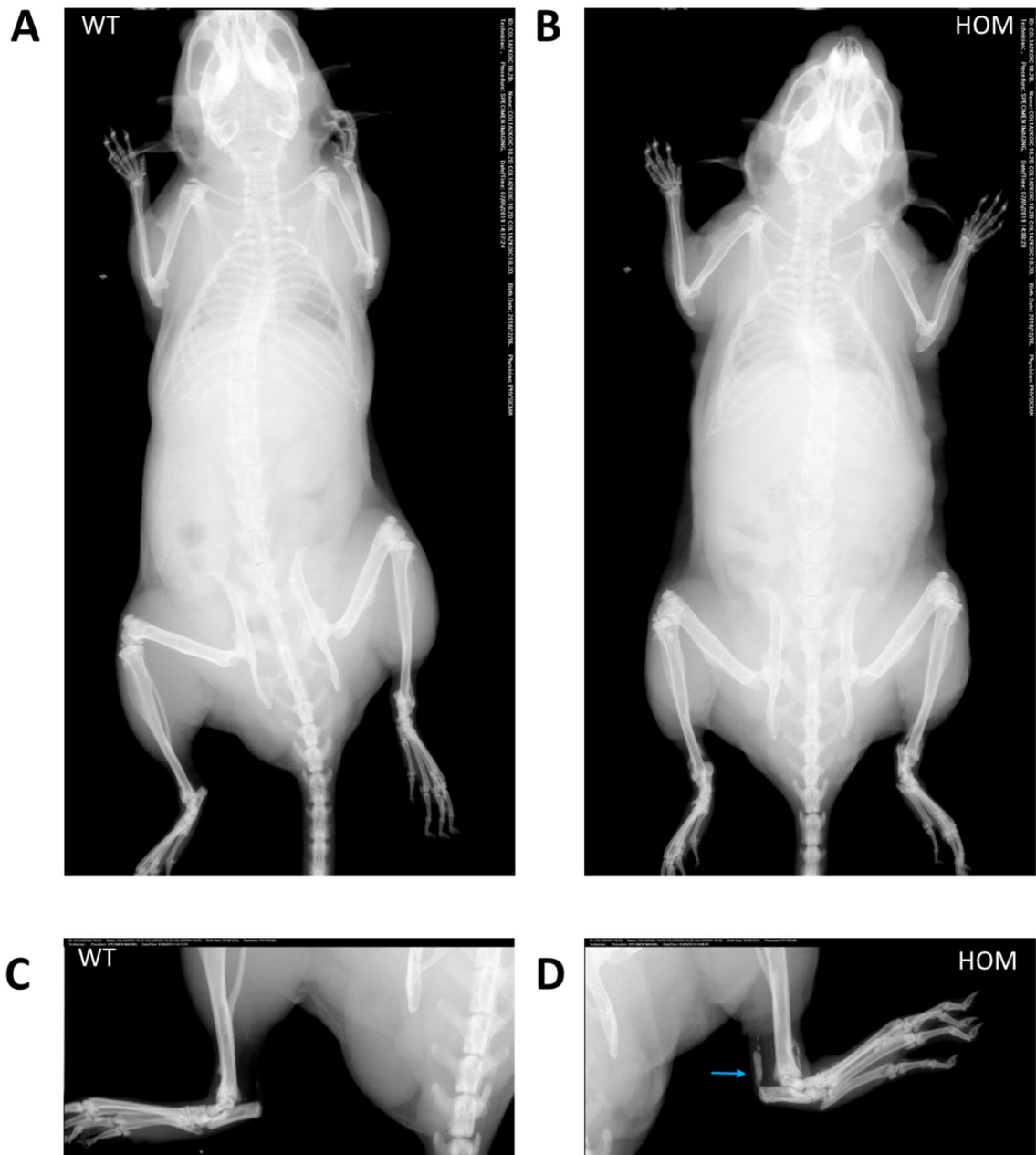


Figure 6.5. X-ray images from a male wild type and a male homozygote, showing the calcified Achilles tendon in the homozygote. Neither the (A) wild type (WT, *Col1a2*^{+/+}), or the (B) homozygote (HOM, *Col1a2*^{-/-}) animals exhibited any overt phenotypes. High-resolution X-ray imaging of the ankles of (C) a wild type (WT, *Col1a2*^{+/+}), and (D) a homozygote (HOM, *Col1a2*^{-/-}) reveals that the homozygote with swollen ankles exhibited a calcified Achilles tendon (blue arrow).

6.6. Collagen Content of *Col1a2*-KO Tendons

As discussed in section 5.11, the radiolabelling assay was not available for the analysis of TM44 lines and this was the case for this line too. To confirm that this line produced homotrimer $\alpha 1$ (I), the collagens were extracted from tail tendon from all three genotypes in this line, as previously explained.

The collagen extracts from wild-type and heterozygous tendons from both MP-107 and TM44, and all three genotypes in the line *Col1a2*-KO were diluted to 0.25mg/ml and samples were run on a 4-12% Bis-Tris gel, before staining with Brilliant Coomassie blue stain. (Figure 6.6).

	MP-107			TM-44			Col1a2-KO		
	Col1a2 ^{+/+}	Col1a2 ^{+/107}		Col1a1 ^{+/+}	Col1a1 ^{+/TM44}		Col1a2 ^{+/+}	Col1a2 ^{+/-}	Col1a2 ^{-/-}
$\alpha 1$									
$\alpha 2$									
Ratio	1.83:1	1.86:1		1.75:1	1.78:1		2.08:1	2.84:1	409:1

Figure 6.6. Coomassie stained collagen extracts from all available genotypes for each of the lines, MP-107, TM44 and *Col1a2*-KO. The ratio of $\alpha 1$: $\alpha 2$ is displayed beneath each lane. The analysis shows no visible difference in ratio of $\alpha 1$ to $\alpha 2$ between genotypes in either MP-107 or TM44. In the case of the *Col1a2*-KO differences were detectable between all three genotypes.

The ratios of $\alpha 1$ to $\alpha 2$ in the MP-107 and TM44 have been discussed previously (Section 5.7), and are included here to validate the Coomassie staining as an alternative for the unavailable radiolabelling assay. In both MP-107 and TM44, the wild-type and heterozygous ratios are comparable. The ratios varied between the three genotypes in the *Col1a2*-KO line, as expected with a *Col1a2* null allele. The heterozygote (HET, *Col1a2*^{+/-}) exhibits a 37% increase in the ratio between the $\alpha 1$ to $\alpha 2$ band compared to the wild type (WT, *Col1a2*^{+/+}). The homozygous (HOM, *Col1a2*^{-/-}) collagen sample exhibited a 200-fold increase in the ratio between $\alpha 1$ and $\alpha 2$. These results in the *Col1a2*-KO line, are due to the null alleles of *Col1a2*, causing an increase in $\alpha 1$ production and homotrimer. It should be noted that as the extract from the tendon will contain other proteins, these bands may contain similar sized proteins, which could account for the ratios being lower than the expected 2:1 for heterotrimers, and why a very subtle band is detected in the homozygous *Col1a2*-KO extract (HOM, *Col1a2*^{-/-}) allowing for a ratio to be calculated.

6.7. Discussion

The viability testing analysis outlined in this chapter shows that the Col1a2-KO homozygotes are viable, and that all genotypes are represented at the expected ratios. While the homozygotes Col1a2-KO (*Col1a2*^{-/-}) are viable, homozygote MP-107 (*Col1a2*^{107/107}) and homozygote TM44 (*Col1a1*^{TM44/TM44}) both have lethal phenotypes. The *Mov-13* model is effectively a null *Col1a1* allele, while the *oim* model is effectively a null *Col1a2* allele. The *Mov-13* homozygote is lethal, and the *oim* homozygote is viable [66, 76]. It is therefore not surprising that the *Col1a2*-KO homozygote is also viable as the null *Col1a2* allele appears to have a less severe effect, presumably as homotrimers can be formed. The reduced severity of the *Col1a2* null compared with the *Col1a2* mutant is very informative and we will return to a more detailed discussion of the genetic mechanisms of the respective mutations in Chapter 7.

The early phenotypes observed by X-ray in heterozygous MP-107 (*Col1a2*^{+/¹⁰⁷) and TM44 (*Col1a1*^{+/^{TM44}) animals, were also observed in the heterozygous Col1a2-KO (*Col1a2*^{+/-}) animals at slightly lower frequency than either MP-107 or TM44. Homozygous Col1a2-KO (*Col1a2*^{-/-}) also exhibited the early bone phenotypes, with the frequency being higher than heterozygous MP-107 (*Col1a2*^{+/¹⁰⁷), but still lower than the TM44 (*Col1a1*^{+/^{TM44}) animals. No evidence of any abnormal bone growth at the knee was detected in either the heterozygous (*Col1a2*^{+/-}) or homozygous (*Col1a2*^{-/-}) Col1a2-KO animals at the later time point, although it should be noted that animals were only aged to 12 months due to time constraints. These results indicate that the bone phenotypes are less severe in the Col1a2-KO animals than in the MP-107 and TM44 lines. As is also seen in human patients, null COL1A2 alleles tend to result in less severe OI phenotypes, than mutations affecting the glycine repeating motif [46-48].}}}}

DEXA analysis of Col1a2-KO animals showed there were no significant differences between genotypes in BMD and bone mineral content at either, the early, or the late time point. This indicates that if any osteoporosis phenotype is present, it is less severe than the TM-44 heterozygotes (*Col1a1*^{+/^{TM44}). No direct comparison can be drawn with the MP-107 heterozygotes (*Col1a2*^{+/¹⁰⁷), as they showed no phenotype using DEXA, but a phenotype was detected using μ CT, a technique which was not used for these mice.}}

The calcification of the Achilles tendons in some of the *Col1a2*-KO mice, appears to be another variable phenotype that is not present in all mice, and appears to be limited to male mice over the age of 2 months. This may be due to the increased likelihood of fighting in adult male mice housed together. The preprint paper by Lee *et al.* observed a similar 'swollen ankle' phenotype in their male *Col1a2* null animals, however no cause was attributed to the swollen ankles [296]. No 'ankle phenotype' phenotype was observed in MP-107 mice, however 3 male heterozygous TM44 animals were found to have abnormalities at the calcaneus at 12 months of age by X-ray imaging (See section 5.6.1, Figure 5.15 and Table 5.3). These animals were kept under observation and were culled before the 18-month time point due to impaired movement.

The collagen analysis of tendons confirmed that in the homozygote, the collagen I in tendon was homotrimer, and both heterotrimer and homotrimer were present in the heterozygote tendons.

The data presented in this chapter indicates that a single or double null *Col1a2* allele results in a less severe OI phenotype than either a mutation affecting the glycine repeating motif in *Col1a2* or a non-sense mutation in *Col1a*.

**Chapter 7: Investigating the Genetics
and Effects of Mutations in *Col1a1* and
Col1a2 Using Compound Crosses**

7.1. Introduction

The similarities and differences between the two ENU lines and the knockout line raises a number of mechanistic questions about the severity of the mutations in *Col1a1* and *Col1a2* alleles. Both MP-107 and TM44 heterozygous animals display very similar overt phenotypes such as the skeletal abnormalities and the late onset severe OA at the knee joint (See Chapter 5, Figure 5.19). Homozygotes of both lines were lethal embryonically or perinatally (See Chapter 3, Figure 3.21 and Chapter 5, Figure 5.8). In contrast, the *Col1a2* null homozygote was viable (See Chapter 6, Figure 6.1). The homozygotes exhibited a similar early phenotype including the splayed ischia and curved olecranon, but showed no evidence of abnormal bone growth at the knee at 12-months. The heterozygotes exhibited a milder early phenotype displaying the splayed ischia phenotype only (See Chapter 6, Figure 6.3).

In addition, TM44 heterozygotes (*Col1a1*^{+/*TM44*}) exhibit low BMD and low bone mineral content phenotypes at 2 months of age when compared to the wild-type animals, while MP-107 heterozygotes (*Col1a2*^{+/*107*}) and *Col1a2*-KO heterozygotes (*Col1a2*^{+/-}) and homozygotes (*Col1a2*^{-/-}) do not (See Chapter 3, Table 3.11; Chapter 5, Figure 5.19, and Chapter 6, Figure 6.4).

Whilst all of these lines have mutations in genes coding for collagen I alpha chains, the nature of the mutations are very different, and the roles each of the alpha chains play are different, leading to questions about the mechanisms by which these mutations lead to the phenotypes we see.

To observe how these genes interact and to throw light on the genetic mechanisms involved, the two ENU mutant lines, TM44 and MP-107, and the *Col1a2* knockout line, were intercrossed in a compound cross experiment. After an initial viability assessment involving all animals at weaning (P21), a small cohort of male animals were X-ray imaged and DEXA scanned at 4 months of age.

It should be noted that there is some variation in the backgrounds of these animals, and this should be taken into account when interpreting results. The MP-107 animals used in these crosses are congenic C3H/HeH. The TM44 animals are incipient congenic C3H/HeH, and therefore still have a small amount of C57BL/6J in their genome (<1%).

The *Col1a2*-KO line was created on the C57BL/6N genome. Ideally these crosses would be carried out with all lines on the same congenic background, however due to time constraints this was not possible.

The crosses included in this chapter are

- TM44 (*Col1a1*^{+/*TM44*}) x MP-107 (*Col1a2*^{+/*107*}) – Section 7.2
- *Col1a2*-KO (*Col1a2*^{+/-}) x MP-107 (*Col1a2*^{+/*107*}) – Section 7.3
- TM44 (*Col1a1*^{+/*TM44*}) x *Col1a2*-KO (*Col1a2*^{+/-}) – Section 7.4

7.2. TM44 x MP-107 Compound Cross

7.2.1. Viability Assessment of the TM44/MP-107 Compound Cross

Intercross matings between heterozygous TM44 (*Col1a1*^{+/*TM44*}) and heterozygous MP-107 (*Col1a2*^{+/*107*}) animals were used to produce a cohort of compound genotypes, which would in theory contain animals of the following genotypes-

Wild type MP-107 / Wild type TM44 - *Col1a2*^{+/*+*}, *Col1a1*^{+/*+*}

Wild type MP-107 / Heterozygous TM44 - *Col1a2*^{+/*+*}, *Col1a1*^{+/*TM44*}

Heterozygous MP-107 / Wild type TM44- *Col1a2*^{+/*107*}, *Col1a1*^{+/*+*}

Heterozygous MP-107 / Heterozygous TM44 - *Col1a2*^{+/*107*}, *Col1a1*^{+/*TM44*}

The total number of pups was recorded at birth, and animals were genotyped at weaning, at approximately P21. Of 88 pups born, 9 pups went missing between birth and weaning, and the remaining 79 pups were genotyped (Table 7.1). It is likely that the 9 missing animals had a lethal phenotype, and were ingested by the mother.

Statistical analysis indicates that the ratios of genotypes differ from the expected Mendelian ratios ($\chi^2= 7.86$, 3df, $P<0.05$). The genotyping data revealed that the pups were present in the expected ratios for all the genotypes except for the *Col1a2*^{+/*107*}, *Col1a2*^{+/*TM44*}, which were present at around half the expected numbers (using total number of animals born). Although it is not possible to confirm whether the missing

pups were $Col1a2^{+/107}$, $Col1a2^{+/TM44}$, as they went missing prior to genotyping, the ratios do indicate that approximately half of the $Col1a2^{+/107}$, $Col1a2^{+/TM44}$ pups died postnatally (Figure 7.1).

Genotype	Number
$Col1a2^{+/107}$, $Col1a1^{+/TM44}$	10
$Col1a2^{+/+}$, $Col1a1^{+/TM44}$	20
$Col1a2^{+/107}$, $Col1a1^{+/+}$	27
$Col1a2^{+/+}$, $Col1a1^{+/+}$	22
Unknown	9

Table 7.1. A table displaying the number of animals of each genotype from intercross matings between TM44 heterozygotes and MP-107 heterozygotes. Nine animals went missing without genotyping and are therefore included in their own category.

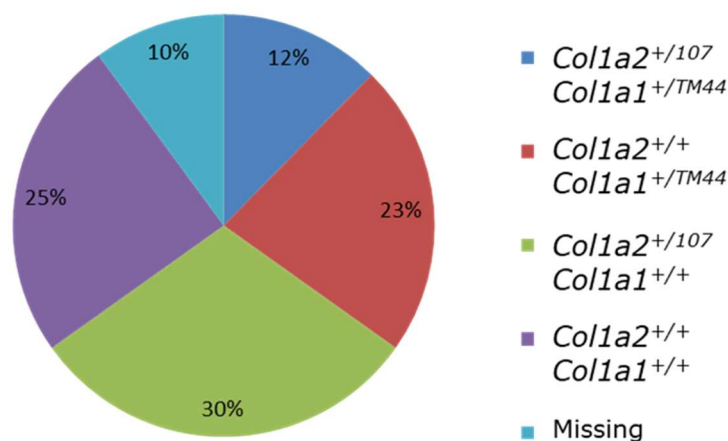


Figure 7.1. Proportions of animals of each genotype produced from intercross matings between TM44 heterozygotes and MP-107 heterozygotes. Ten percent of animals born subsequently went missing, presumed dead and ingested by the mother.

As noted in previous chapters, *Col1a1*^{+/*TM44*} and *Col1a2*^{+/*107*} animals are viable, so the reduced viability of the *Col1a2*^{+/*107*}, *Col1a1*^{+/*TM44*} animals indicates that there is some interaction between the mutant genes.

7.2.2. X-ray Imaging of the TM44/MP-107 Compound Cross at 4-months

X-ray imaging of animals in the MP-107xTM44 male cohort at 4 months of age revealed that the majority of animals with at least one mutant allele, *Col1a2*^{+/*107*} or *Col1a1*^{+/*TM44*}, exhibited a similar early phenotype to the heterozygote MP-107 (*Col1a2*^{+/*107*}) and heterozygote TM44 (*Col1a1*^{+/*TM44*}), including splayed ischia at the pelvis, a curved olecranon or a combination of both phenotypes. The animals with both mutant alleles also exhibit a similar phenotype (*Col1a2*^{+/*107*}, *Col1a1*^{+/*TM44*}), however the incidence is increased with all double heterozygotes exhibiting a phenotype (Table 7.2 and Figure 7.2). A single *Col1a2*^{+/*107*}, *Col1a1*^{+/*TM44*} animal also exhibited the abnormal calcaneus phenotype (Figure 7.3), similar to the phenotype observed in some TM44 heterozygotes (See Chapter 5, Figure 5.15).

Genotype	N	Ischia	Olecranon	Calcaneus	Total Affected	Percentage Affected
<i>Col1a2</i> ^{+/<i>107</i>} , <i>Col1a1</i> ^{+/<i>TM44</i>}	4	4	1	1	4	100%
<i>Col1a2</i> ^{+/<i>+</i>} , <i>Col1a1</i> ^{+/<i>TM44</i>}	4	3	0	0	3	75%
<i>Col1a2</i> ^{+/<i>107</i>} , <i>Col1a1</i> ^{+/<i>+</i>}	4	3	1	0	3	75%
<i>Col1a2</i> ^{+/<i>+</i>} , <i>Col1a1</i> ^{+/<i>+</i>}	4	0	0	0	0	0%

Table 7.2. A table showing the number of animals exhibiting each phenotype, for each genotype in the phenotyping cohort resulting from the TM44 and MP-107 intercross.

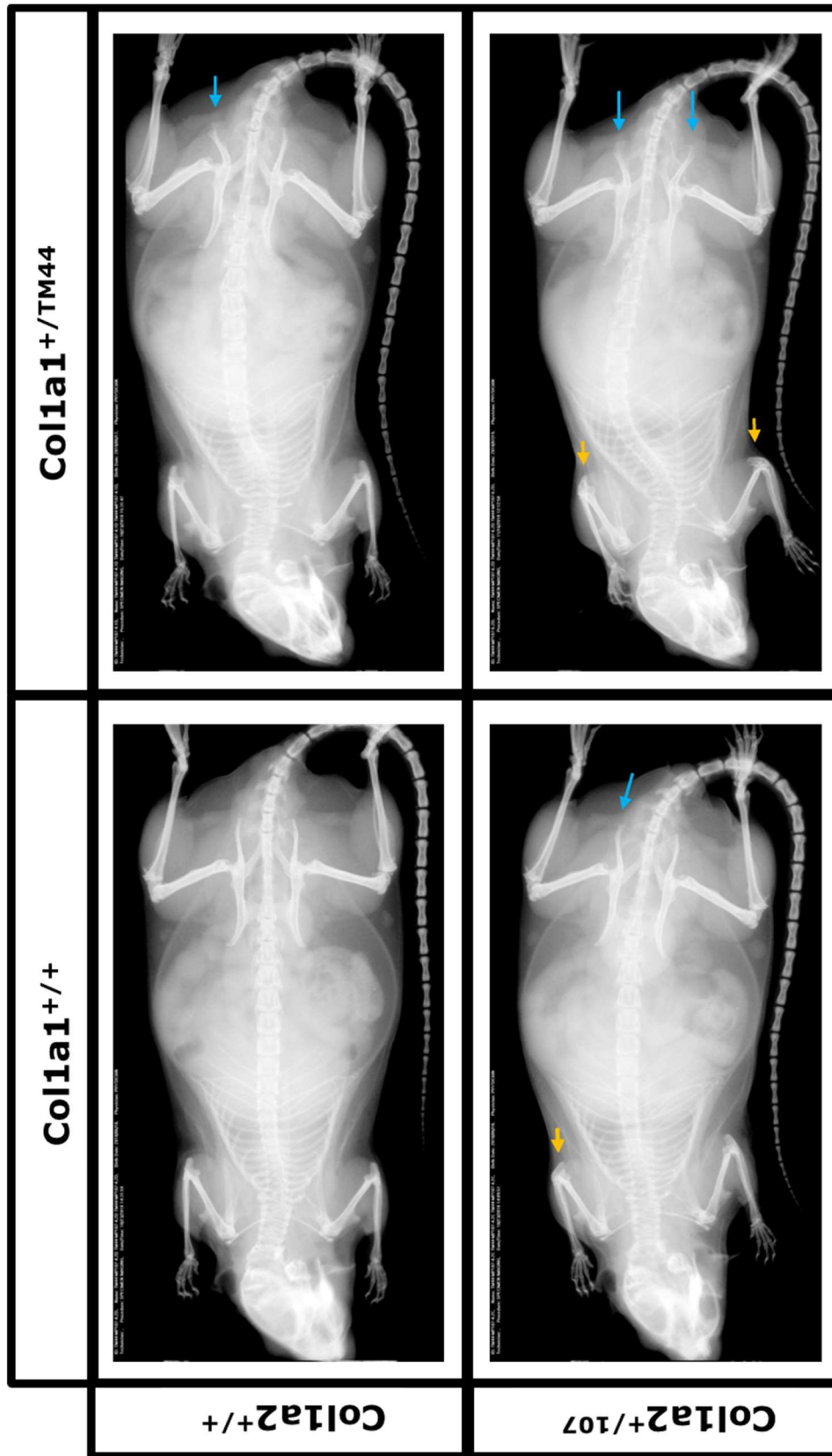


Figure 7.2. Radiographs showing the phenotypes exhibited by each of the compound genotypes resulting from intercross matings between TM44 heterozygotes and MP-107 heterozygotes at 4-months. The *Col1a2^{+/107}*, *Col1a1^{+/TM44}* and *Col1a1^{+/+}* exhibit curved olecranon processes (orange arrow) in combination with a splayed ischium (blue arrow), *Col1a2^{+/+}*, *Col1a1^{+/TM44}* exhibits a splayed ischium (blue arrow).

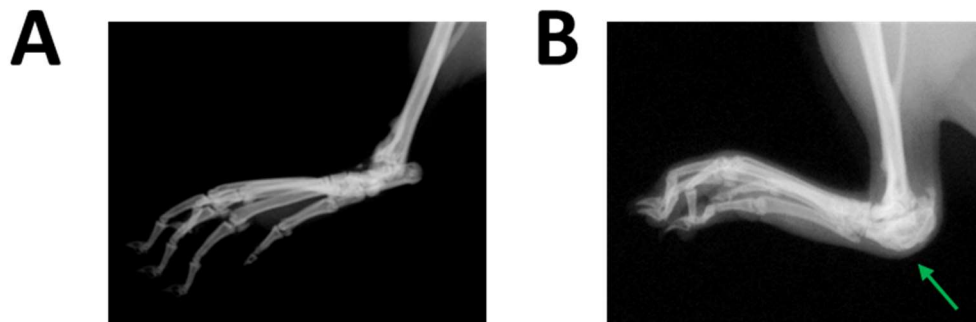


Figure 7.3. Radiographs comparing the calcaneus of a compound wild type and a compound heterozygote resulting from intercross matings between TM44 heterozygotes and MP-107 heterozygotes at 4-months. (A) The calcaneus of the *Col1a2*^{+/+}, *Col1a1*^{+/+} animals appears normal, (B) the calcaneus of the *Col1a2*^{+/¹⁰⁷}, *Col1a1*^{+/^{TM44}} animal appears curved, and to have abnormal bone growth, only one of the four *Col1a2*^{+/¹⁰⁷}, *Col1a1*^{+/^{TM44}} animals exhibited this phenotype.

7.2.3. DEXA Analysis of the TM44/MP-107 Compound Cross at 4-months

DEXA analysis of animals in the MP-107xTM44 male cohort revealed that there were no differences between genotypes in either BMD or BMC (Figure 7.4). The phenotyping on each individual lines showed that the *Col1a1*^{+/^{TM44}} animals exhibited a significantly reduced BMD and BMC when compared with *Col1a1*^{+/+} animals at the 2-month early time point, while the *Col1a2*^{+/¹⁰⁷} animals showed no difference in reduced BMD and BMC when compared with to the *Col1a2*^{+/+} animals (See Chapter 3, Table 3.11 and Chapter 5, Figure 5.16).

The *Col1a1*^{+/^{TM44}}, *Col1a2*^{+/+} animals would logically behave similarly to the *Col1a1*^{+/^{TM44}} from the individual TM44 line, as there should be no effect of the *Col1a2* allele, however no significant difference was found. It is likely that this loss of effect is due to the experiment being underpowered, as the individual original TM44 line only contained two genotypes, *Col1a1*^{+/^{TM44}} and *Col1a1*^{+/+}, and this compound cohort contains 4 genotypes and therefore an ANOVA was used. While there is a slight variation in background, it is unlikely this would play a role, as both lines were over 99% C3H.

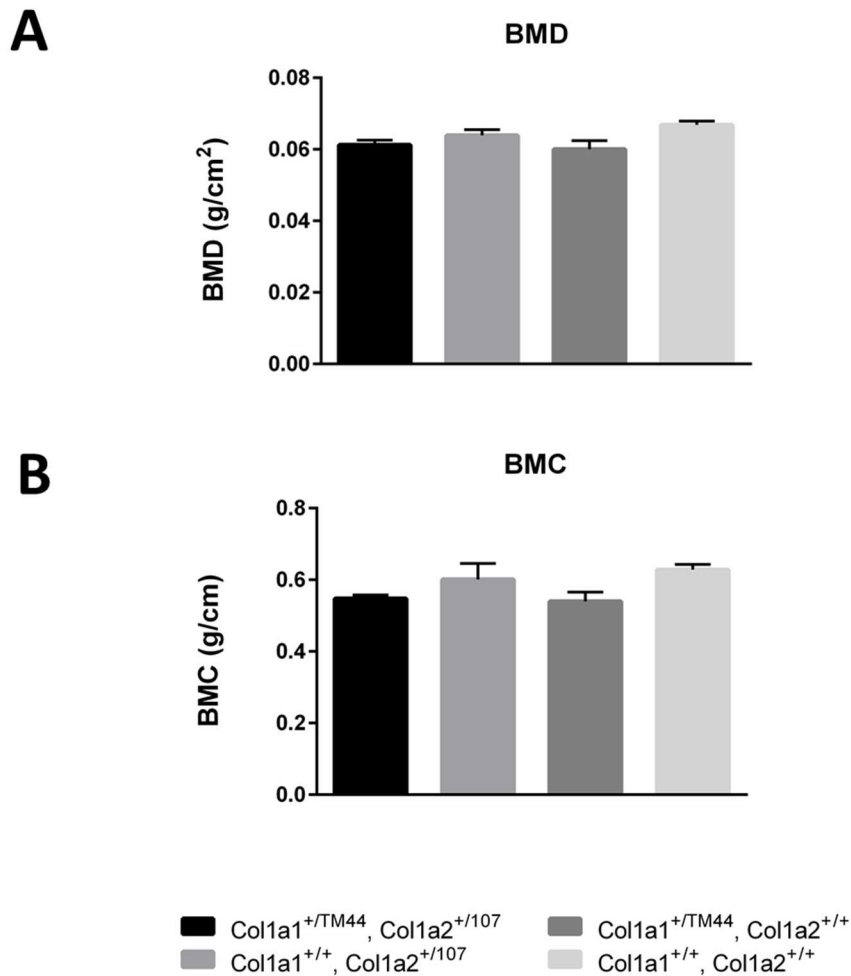


Figure 7.4. DEXA analysis of all four compound genotypes resulting from intercross matings between TM44 heterozygotes and MP-107 heterozygotes at 4-month. Neither (A) Bone mineral density (BMD) nor (B) Bone mineral content (BMC) differed between genotypes (one-way ANOVA, N=4 for all genotypes).

7.2.4. X-ray Imaging of the TM44/MP-107 Compound Cross at 12-months

A limited number of animals (only 1 of each genotype) were aged to 12 months of age and X-ray imaged. While no conclusions can be drawn due to the limited numbers, the *Col1a2*⁺¹⁰⁷, *Col1a1*^{+TM44} and *Col1a2*^{+/+}, *Col1a1*^{+TM44} animals both displayed a knee phenotype observable by X-ray imaging, while the *Col1a2*⁺¹⁰⁷, *Col1a1*^{+/+} and *Col1a2*^{+/+}, *Col1a1*^{+/+} animals did not (Figure 7.7).

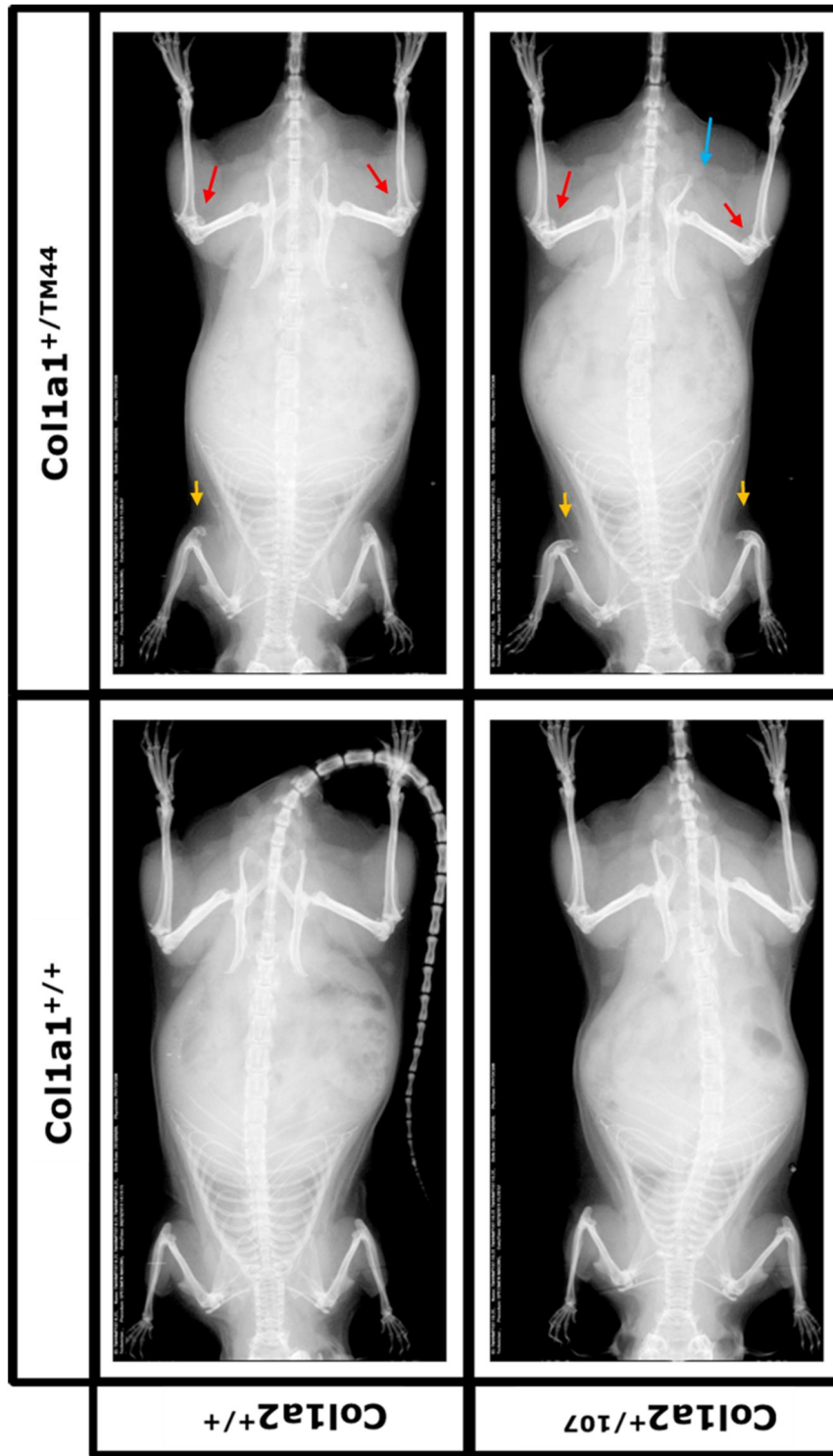


Figure 7.5 Radiographs showing the phenotypes exhibited by each of the compound genotypes resulting from intercross matings between TM44 heterozygotes and MP-107 heterozygotes at 12-months. The *Col1a2^{+/107}*, *Col1a1^{+/TM44}* and *Col1a2^{+/+}*, *Col1a1^{+/TM44}* exhibit abnormal bone growth at the knee (red arrow), in addition to curved olecranon processes (orange arrow) and in the case of *Col1a2^{+/107}*, *Col1a1^{+/TM44}* a splayed ischium (blue arrow). No phenotype was identified in either *Col1a2^{+/+}* or *Col1a1^{+/+}*.

As seen in the individual MP-107 line phenotyping (Chapter 3, Section 6), upwards of 20% of heterozygotes ($Col1a2^{+/107}$) show no phenotype by X-ray, so the lack of phenotype in the single $Col1a2^{+/107}$, $Col1a1^{+/+}$ animal is not surprising.

7.3. MP-107 x Col1a2 KO Compound Cross

7.3.1. Viability Assessment of the Col1a2-KO/MP-107 Compound Cross

Intercross matings between heterozygous Col1a2-KO ($Col1a2^{+/-}$) and heterozygous MP-107 ($Col1a2^{+/107}$) animals were used to produce a compound cohort, which would in theory contain animals of the following genotypes-

Wild type MP-107 / Wild type Col1a2-KO - $Col1a2^{+/+}$

Wild type MP-107 / Heterozygous Col1a2-KO - $Col1a2^{+/-}$

Heterozygous MP-107 / Wild type Col1a2-KO - $Col1a2^{+/107}$

Heterozygous MP-107 / Heterozygous Col1a2-KO - $Col1a2^{-/107}$

The total number of pups was recorded at birth, and animals were genotyped at weaning, at approximately P21 (Table 7.3 and Figure 7.6).

Genotype	Number
$Col1a2^{-/107}$	10
$Col1a2^{+/-}$	7
$Col1a2^{+/107}$	11
$Col1a2^{+/+}$	13

Table 7.3. A table displaying the number of animals of each genotype from intercross matings between MP-107 heterozygotes and Col1a2-KO heterozygotes.

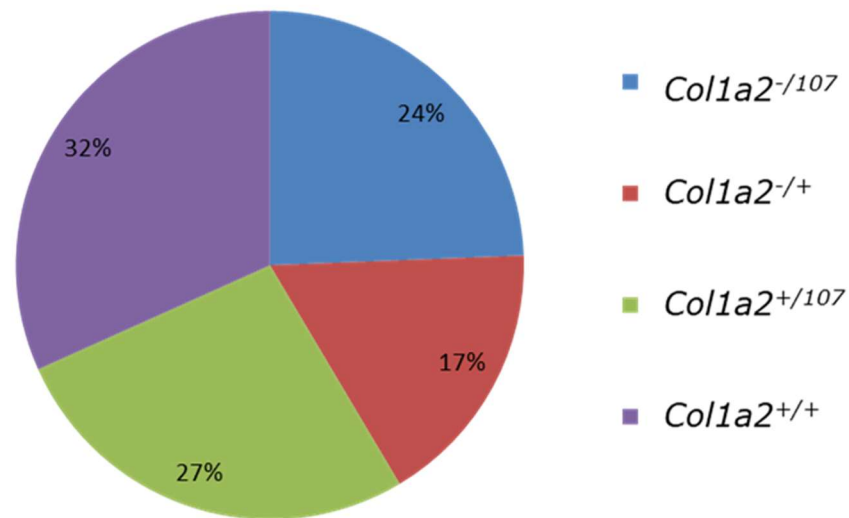


Figure 7.6. Proportions of animals of each genotype produced from intercross matings between *Col1a2*-KO heterozygotes and MP-107 heterozygotes.

Statistical analysis indicates that the ratios of genotypes do not differ from the expected Mendelian ratios ($\chi^2 = 1.83$, 3df, $P > 0.5$), and that there are no lethal phenotypes observed in this cross.

The homozygote MP-107 (*Col1a2*^{107/107}) was non-viable, so the fact that the double heterozygote (*Col1a2*^{-/¹⁰⁷}) is viable is intriguing. It suggests that the MP-107 mutation is a dominant negative mutation and indicates that the mode of action of the mutation is via the presence of the mutant protein, not the lack of wild-type protein.

7.3.2. X-Ray Imaging of the *Col1a2*-KO/MP-107 Compound Cross at 4-Months

X-ray imaging of animals in the MP-107/*Col1a2*-KO male cohort at 4 months of age revealed that only animals containing a mutant MP-107 allele (*Col1a2*^{+/¹⁰⁷} or *Col1a2*^{-/¹⁰⁷}) exhibited any phenotype and then the incidence was only 25%. No evidence of splayed ischia at the pelvis was observed, and a curved olecranon was observed in each of the *Col1a2*^{+/¹⁰⁷} and *Col1a2*^{-/¹⁰⁷} animals (Table 7.4 and Figure 7.7). It should be noted that this cohort only contained two *Col1a2*^{+/⁺} animals. No animals displayed the abnormal calcaneus. However, as this phenotype has only been observed in heterozygote TM44 animals (*Col1a1*^{+/^{TM44}}) or animals with a compound genotype containing *Col1a1*^{+/^{TM44}}, it would not be expected to appear in this compound cross.

Genotype	N	Ischia	Olecranon	Calcaneus	Total Affected	Percentage Affected
<i>Col1a2</i> ^{-/¹⁰⁷}	4	0	1	0	1	25%
<i>Col1a2</i> ^{+/⁻}	4	0	0	0	0	0%
<i>Col1a2</i> ^{+/¹⁰⁷}	4	0	1	0	1	25%
<i>Col1a2</i> ^{+/⁺}	2	0	0	0	0	0%

Table 7.4. A table showing the number of animals exhibiting each phenotype, for each genotype in the phenotyping cohort resulting from the *Col1a2*-KO and MP-107 intercross.

Both the heterozygote MP-107 (*Col1a2*^{+/¹⁰⁷}) and heterozygote *Col1a2*-KO (*Col1a2*^{+/⁻}) animals from the individual lines showed a degree of variability in the phenotype. However, in this cross in both genotypes, where there should be no impact from the other allele: *Col1a2*^{+/¹⁰⁷} and *Col1a2*^{+/⁻} the incidences are much lower than seen in the individual line. *Col1a2*^{+/¹⁰⁷} in the MP-107 line was 80% affected at early time points, but in this compound cross only 25% affected. *Col1a2*^{+/⁻} in the *Col1a2*-KO line was 40% affected at early time points, but in this compound cross 0% affected. It is unlikely that this is due to the different genetic backgrounds of the progenitor lines, as both were congenic on their respective background and therefore a reduction in both compound heterozygotes (*Col1a2*^{+/¹⁰⁷} and *Col1a2*^{+/⁻}) would not be expected if the backgrounds were the cause. It is possible that the reduced percentage of affected animals is due to the small cohort size, with only 4 animals of each of these compound heterozygote genotypes (*Col1a2*^{+/¹⁰⁷} and *Col1a2*^{+/⁻}).

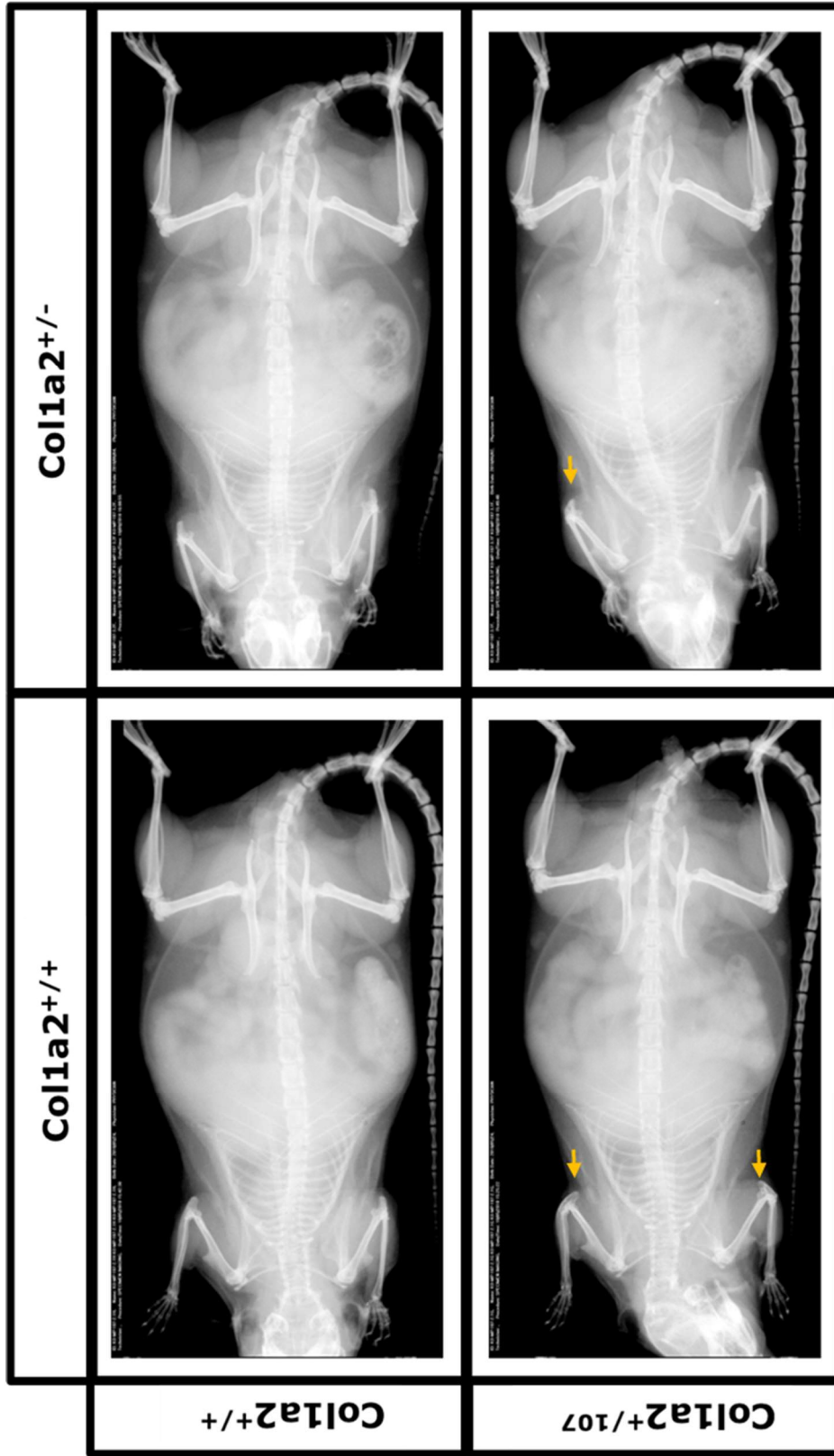


Figure 7.7. Radiographs showing the phenotypes exhibited by each of the compound genotypes resulting from intercross matings between *Col1a2*-KO heterozygotes and MP-107 heterozygotes at 4-months. The *Col1a2*⁺¹⁰⁷ and *Col1a2*⁻¹⁰⁷ exhibit curved olecranon processes (orange arrow) *Col1a2*^{+/-} and *Col1a2*^{+/-} exhibits no overt skeletal phenotype.

7.3.3. DEXA of the *Col1a2*-KO/MP-107 Compound Cross at 4-Months

DEXA analysis of animals in the MP-107/*Col1a2*-KO male cohort at 4 months of age revealed that there were no significant differences in BMD or bone mineral content in any of the genotypes. (Figure 7.8). It should be noted that this cohort only contained two *Col1a2*^{+/+} animals, and therefore the statistical testing should be interpreted with caution. The one-way ANOVA was repeated both with and without this genotype and in neither case were any differences detected. As there was no DEXA phenotype detected in either of the individual lines, it is not surprising that a phenotype is not detected here. However, as the cohort size here was similar to that used in (Section 7.2.3) and would therefore have the same limitation of power, a larger cohort would be required to rule out any additive effects of the two mutant alleles.

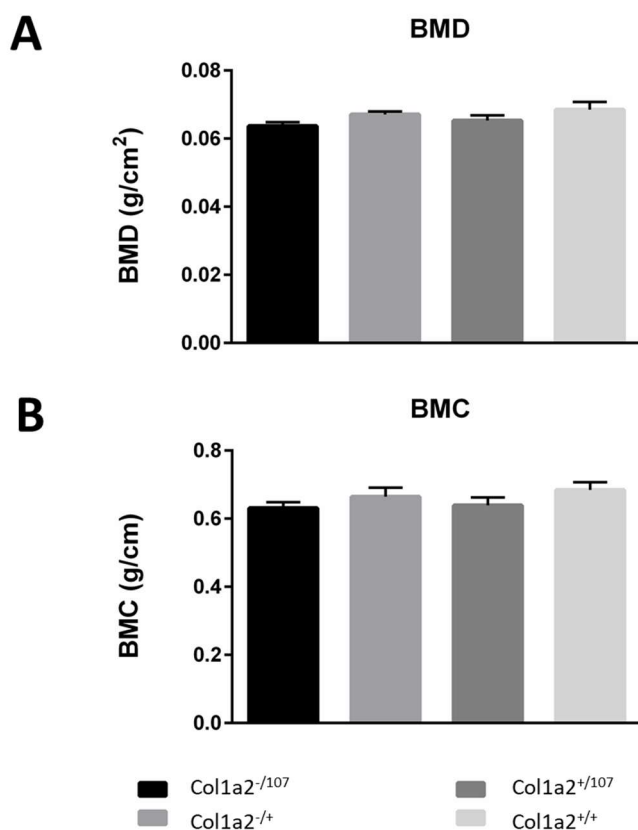


Figure 7.8. DEXA analysis of all four compound genotypes resulting from intercross matings between TM44 heterozygotes and MP-107 heterozygotes at 4-month. Neither (A) Bone mineral density (BMD) nor (B) Bone mineral content (BMC) differed between genotypes. (One-way ANOVA N=4 for all genotypes, except for *Col1a2*^{+/+} where N=2)

7.4. TM44 x Col1a2 KO Compound Cross

7.4.1. Viability Assessment of the TM44/Col1a2-KO Compound Cross

Intercross matings between heterozygous TM44 ($Col1a1^{+/TM44}$) and heterozygous Col1a2-KO ($Col1a2^{+/-}$) animals were used to produce a compound cohort, which would in theory contain animals of the following genotypes-

Wild type Col1a2-KO / Wild type TM44 - $Col1a2^{+/+}$, $Col1a1^{+/+}$

Heterozygous Col1a2-KO / Wild type TM44 - $Col1a2^{+/-}$, $Col1a1^{+/+}$

Wild type Col1a2-KO / Heterozygous TM44 - $Col1a2^{+/+}$, $Col1a1^{+/TM44}$

Heterozygous Col1a2-KO / Heterozygous TM44 - $Col1a2^{+/-}$, $Col1a1^{+/TM44}$

The total number of pups was recorded at birth, and animals were genotyped at weaning, at approximately P21 (Table 7.5 and Figure 7.9).

Genotype	Number
$Col1a2^{-/+}$, $Col1a1^{+/TM44}$	11
$Col1a2^{+/+}$, $Col1a1^{+/TM44}$	12
$Col1a2^{-/+}$, $Col1a1^{+/+}$	9
$Col1a2^{+/+}$, $Col1a1^{+/+}$	15

Table 7.5. A table displaying the number of animals of each genotype from intercross matings between TM44 heterozygotes and Col1a2-KO heterozygotes.

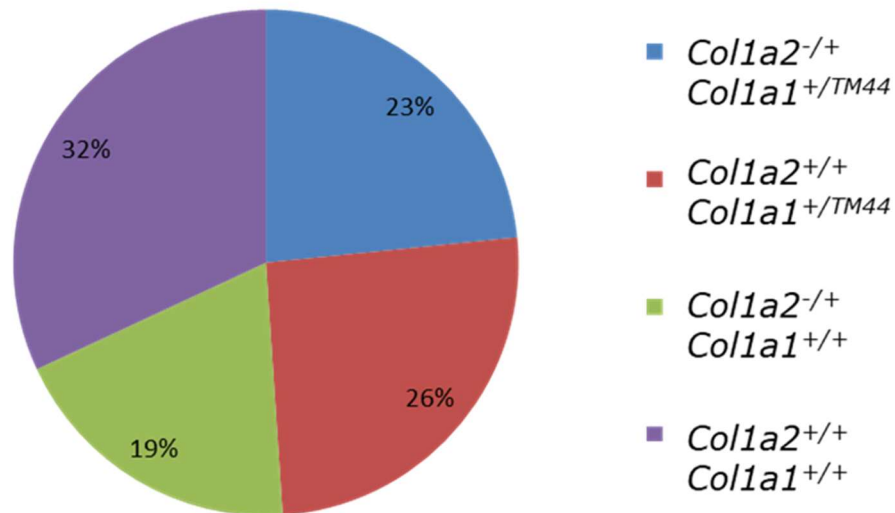


Figure 7.9. Proportions of animals of each genotype produced from intercross matings between *Col1a2*-KO heterozygotes and TM44 heterozygotes.

Statistical analysis indicates that the ratios of genotypes do not differ from the expected Mendelian ratios ($\chi^2 = 1.60$, 3df, $P > 0.5$), and that there is no lethal phenotype in this line.

As noted earlier in this chapter the *Col1a2*^{+/¹⁰⁷}, *Col1a1*^{+/TM44} animals arising from the intercross between heterozygous TM44 (*Col1a1*^{+/TM44}) and heterozygous MP-107 (*Col1a2*^{+/¹⁰⁷}) animals exhibited some level of lethality. In this line, the mutant *Col1a2*^{+/¹⁰⁷} allele is replaced by a null *Col1a2*^{+/-} and this prevents the lethal phenotype. Again, it suggests that the MP-107 mutation is a dominant negative mutation and indicates that the mode of action of the MP-107 mutation is via the presence of the mutant protein, not the lack of wild-type protein.

7.4.2. X-ray Imaging of the TM44/*Col1a2*-KO Compound Cross at 4-Months

X-ray imaging of animals in the *Col1a2*-KO/TM44 male cohort at 4 months of age revealed that all animals with a mutant TM44 *Col1a1* allele (*Col1a1*^{+/TM44}) exhibited a similar early phenotype to the heterozygote TM44 (*Col1a1*^{+/TM44}), including splayed ischia at the pelvis, a curved olecranon, or a combination of both phenotypes, whether or not a null *Col1a2* allele (*Col1a2*^{+/-}) was present (Table 7.6 and Figure 7.10).

Additionally, one animal of each of these genotypes ($Col1a2^{+/-}$, $Col1a1^{+/TM44}$) and $Col1a2^{+/+}$, $Col1a1^{+/TM44}$) exhibited the abnormal calcaneus phenotype observed in the original TM44 line (See Chapter 5, Figure 5.15) and in the TM44/MP-107 compound cross (Figure 7.3)

The animals with a null $Col1a2$ allele ($Col1a2^{-/-}$), without the presence of a mutant $Col1a1$ allele ($Col1a1^{+/TM44}$) exhibit no phenotype, a lower incidence to what was previously seen in the individual line (40%) and similar to the effect seen in the MP107/ $Col1a2$ -KO compound cross (See Section 7.3.2).

As with the MP107/ $Col1a2$ -KO compound cross, the lines crossed here were on different genetic backgrounds, with TM44 being incipient congenic on C3H, and $Col1a2$ -KO being congenic C57BL/6N. The addition of C57BL/6N genome to the animals with the TM44 mutant allele ($Col1a2^{-/+}$, $Col1a1^{+/TM44}$ and $Col1a2^{+/+}$, $Col1a1^{+/TM44}$) has not reduced the percentage of affected animals.

The animals with added C3H to their C57BL/6J genome ($Col1a2^{+/-}$, $Col1a1^{+/+}$ and $Col1a2^{+/+}$, $Col1a1^{+/+}$) showed no phenotypes although only the $Col1a2^{+/-}$, $Col1a1^{+/+}$ animals would be expected to display a phenotype, and only 40%. While it is possible that the addition of C3H is responsible for the reduction in affected animals, it is equally possible that this is due to the small cohort size.

Genotype	N	Ischia	Olecranon	Calcaneus	Total Affected	Percentage Affected
$Col1a2^{+/-}$, $Col1a1^{+/TM44}$	4	3	0	1	4	100 %
$Col1a2^{+/+}$, $Col1a1^{+/TM44}$	4	3	0	1	4	100%
$Col1a2^{+/-}$, $Col1a1^{+/+}$	4	0	0	0	0	0%
$Col1a2^{+/+}$, $Col1a1^{+/+}$	4	0	0	0	0	0%

Table 7.6. A table showing the number of animals exhibiting each phenotype, for each genotype in the phenotyping cohort resulting from the $Col1a2$ -KO and TM44 intercross.

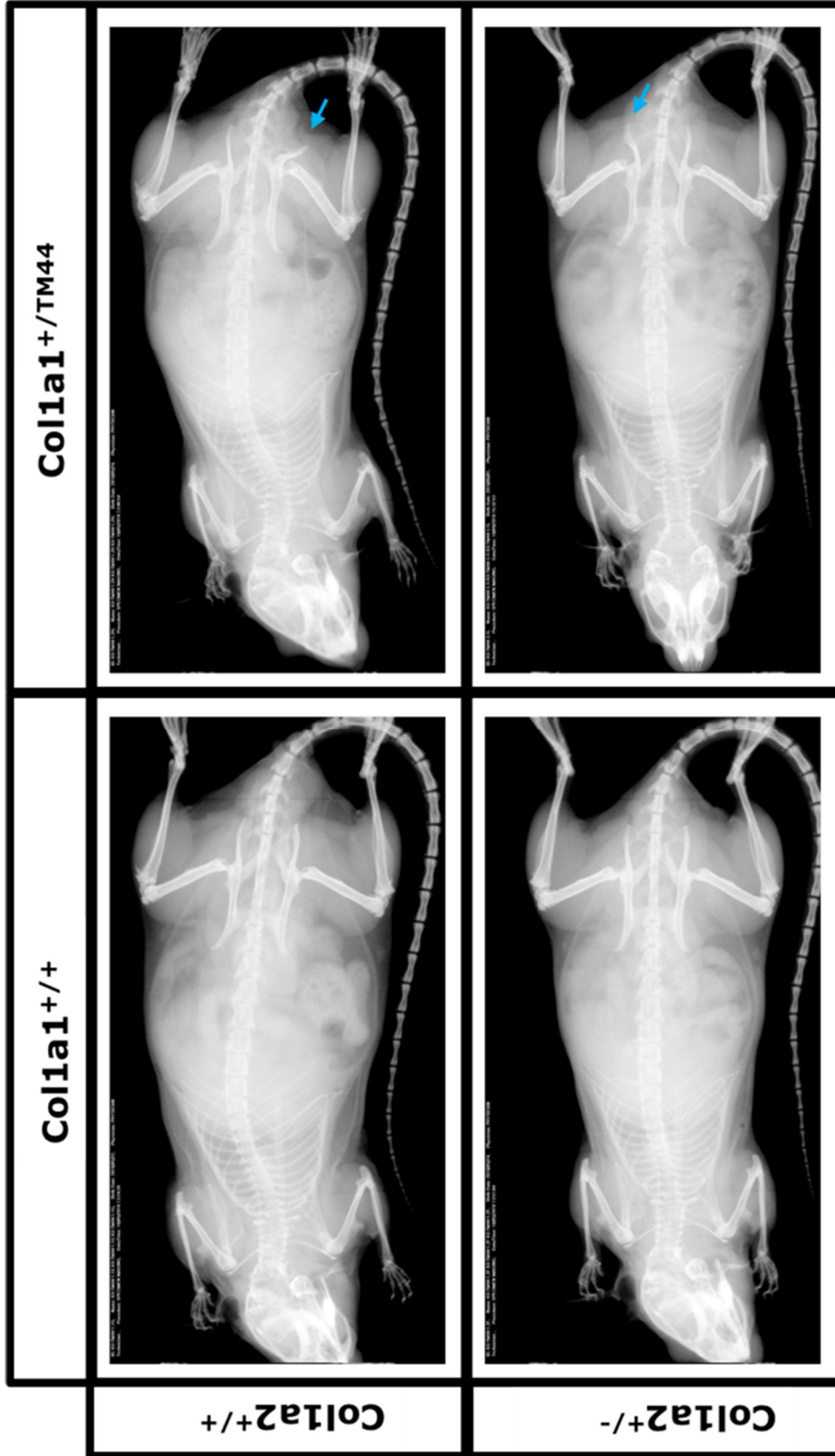


Figure 7.10. Radiographs showing the phenotypes exhibited by each of the compound genotypes resulting from intercross matings between Col1a2-KO heterozygotes and MP-107 heterozygotes at 4-months. The Col1a2^{+/-}, Col1a1^{+/TM44} and Col1a2^{+/-}, Col1a1^{+/TM44} exhibit splayed ischia (blue arrow). The Col1a2^{+/-}, Col1a1^{+/+} and Col1a2^{+/+}, Col1a1^{+/+} exhibit no overt skeletal phenotype.

7.4.3. DEXA Analysis of the TM44/Col1a2-KO Compound Cross at 4-Months

DEXA analysis of animals in the TM-44/Col1a2-KO male cohort at 4 months of age revealed that there were no significant differences in BMD or bone mineral content in any of the genotypes. (Figure 7.11).

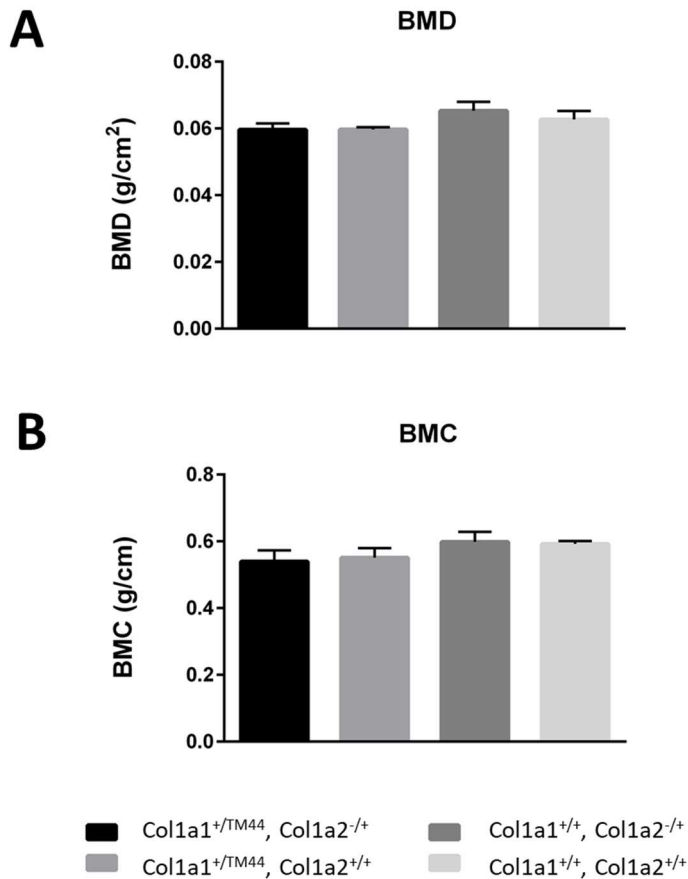


Figure 7.11. DEXA analysis of all four compound genotypes resulting from intercross matings between TM44 heterozygotes and Col1a2-KO heterozygotes at 4-month. Neither (A) Bone mineral density (BMD) nor (B) Bone mineral content (BMC) differed between genotypes (One-way ANOVA N=4 for all genotypes).

As mentioned previously (See Section 7.2.3), it is possible that the statistical testing here may be underpowered to observe if there is a difference in this cohort.

7.5. Discussion

The compound cross experiment revealed interesting insights into the mutations and their modes of action. As noted in previous chapters, *Col1a1*^{+TM44} and *Col1a2*⁺¹⁰⁷ animals are viable, so the reduced viability of the double heterozygotes from the

compound cross between the MP-107 and TM44 ($Col1a2^{+/107}$, $Col1a1^{+/TM44}$) indicates that there is some interaction between the mutant genes. It also provides additional confirmation that the mutations are causative.

The double heterozygotes from the compound cross between the Col1a2-KO and TM44 ($Col1a2^{+/-}$, $Col1a1^{+/TM44}$) were viable. Thus, comparing the 2 double heterozygotes, ($Col1a2^{+/107}$, $Col1a1^{+/TM44}$ and $Col1a2^{+/-}$, $Col1a1^{+/TM44}$), the mutant $Col1a2^{+/107}$ allele in ($Col1a2^{+/107}$, $Col1a1^{+/TM44}$), is replaced by a null $Col1a2^{+/-}$ in ($Col1a2^{+/-}$, $Col1a1^{+/TM44}$), and this restores the viable phenotype. This reflects the nature of the mutation in MP-107, as its presence in tandem with the TM44 mutation is more deleterious than the presence of the TM44 mutant allele and a null Col1a2 allele.

The compound cross experiment revealed that the $Col1a2^{+/107}$, $Col1a1^{+/TM44}$ animals were less viable than either $Col1a2^{+/107}$ animals or $Col1a1^{+/TM44}$ animals confirming epistasis between mutant genes. This experiment also revealed that the $Col1a2^{-/107}$ was less deleterious than $Col1a2^{107/107}$, which indicates that the MP-107 mutation is likely a gain of function mutation, possibly acting as a dominant negative. The presence of a single mutant $Col1a2$ allele and a null allele was less deleterious than two copies of the mutant $Col1a2$ allele, which indicates that the severity of phenotype is related to the quantity of mutant protein, rather than the absence of wildtype protein.

Due to the variable nature of the phenotypes, the small cohort sizes and the limitations of X-ray imaging, drawing conclusions from the X-ray imaging data of the compound crosses is difficult. Table 7.7 shows collated incidence of early phenotype across the three individual lines and the compound crosses at the early time points.

		TM44		MP-107		Col1a2-KO	
		Col1a1 ^{+/+}	Col1a1 ^{+/TM44}	Col1a2 ^{+/+}	Col1a2 ^{+/107}	Col1a2 ^{+/+}	Col1a2 ^{+/-}
TM44	Col1a1 ^{+/+}	0%	100% ^c	0%	75%	0%	0%
	Col1a1 ^{+/TM44}	100% ^c	N/A	75%	100% ^a	100%	100%
MP-107	Col1a2 ^{+/+}	0%	75%	0%	80%	0% ^b	0%
	Col1a2 ^{+/107}	75%	100% ^a	80%	N/A	25%	25%
Col1a2-KO	Col1a2 ^{+/+}	0%	100%	0% ^b	25%	0%	40%
	Col1a2 ^{+/-}	0%	100%	0%	25%	40%	67%

Table 7.7. A table displaying the incidence of early phenotype in the lines TM44, MP-107 and Col1a2-KO, and the compound lines. The unshaded boxes indicate the data from the individual lines (with grey shading where the animals were non-viable). Green shading indicates the data from the MP-107 x TM44 cross, blue shading indicates the data from the Col1a2-KO x TM44 cross, and yellow shading indicates the data from the Col1a2-KO x TMP-107 cross. ^a indicates that the genotype had reduced viability, ^b indicates only 2 animals were X-rayed. ^c It should be noted that in the case of heterozygous TM44 (*Col1a1^{+/TM44}*) animals from original cohort, although 100% of the early cohort exhibited an early phenotype, some of the 12-month old cohort did not exhibit any of the early phenotypes (ischia/olecranon/calcaneus) and therefore this 100% incidence is a snapshot and is not a true representation of all *Col1a1^{+/TM44}* animals.

It is clear that the TM44 line has the highest incidence of phenotypes detectable by X-ray in the individual lines, followed by MP-107 and then by Col1a2-KO, where even the homozygous animals had a lower incidence than the heterozygotes of the other two lines (Table 7.7, white boxes). Any compound cross genotype which contained a single *Col1a1* allele (*Col1a1^{+/TM44}*) in any of the genotypes in the compound crosses causes the highest incidence within each compound cross, with a lower incidence of 75%. The compound cross of MP-107 and Col1a2-KO contains the lowest incidence of X-ray phenotypes, with animals containing an MP-107 mutant allele (*Col1a2^{+/107}*) having an incidence of only 25%, much lower than the 80% seen in the individual line MP-107 (80%). The animals with the Col1a2-KO allele in the absence of any other mutant allele (*Col1a2^{-/+}* and *Col1a2^{-/-}*, *Col1a1^{+/+}*) show incidence of 0%, compared with 40% for heterozygotes from the Col1a2-KO line (*Col1a2^{-/+}*). It is possible to explain this variance due the inherent variances in the phenotypes in all three lines, and the limitations of small cohort sizes and X-ray imaging. Larger cohorts would reveal if this were the case.

Chapter 8: General Discussion

8.1. Summary of Results

To summarise these results, each line will be addressed individually before discussing how each of these lines provides information about the other and leads to general synthesis and conclusions.

8.1.1. MP-107

The majority of this thesis has focused on the line MP-107. The direction of the project changed over time, from identifying the causative gene behind the observed phenotype in the original cohort, to identifying a range of other phenotypes in a wide range of tissues and the mechanisms underlying the observed phenotypes. There were a number of complicating factors in this investigation including alternative splicing, resulting in variable levels of mutant transcript, and in the case of homozygous mutant, wild-type transcript in the absence of the wild-type genomic sequence; variable phenotypes between animals of the same genotype; and the possibility that some phenotypes could be secondary to one or more other phenotypes.

Initial phenotyping of MP-107 revealed the presence of two early phenotypes, a curved olecranon at the elbow, and splayed ischia at the pelvis and a third late onset phenotype at the knee involving abnormal bone growth and cartilage erosion.

8.1.1.1 Causative mutation in MP-107

A T to A transversion was identified at position 4521226 of Chromosome 6. The effect of this splice region variant was the incorporation of three intronic bases into the exon as an extra amino acid, which disrupted the repeating glycine motif. A large proportion of osteogenesis imperfecta cases are caused by glycine substitutions, which also cause the repeating glycine motif to be disrupted [46-48].

Further analysis of the cDNA using both PCR and qPCR revealed that even in the absence of wild-type genomic sequence, wild-type cDNA was produced indicating that the original splice acceptor site was used, in addition to the novel splice acceptor site, albeit at a far lower rate. From the data obtained, it appeared that the levels of mutant and wild-type transcript varied. Genotyping of affected and unaffected animals revealed that there was a degree of variability in the phenotypes, including heterozygotes, which did not show any of the phenotypes. It is therefore possible that the variability in

phenotype could be linked with the level of mutant, or wild-type transcript, but this has not been shown here. However, expression of *Col1a1* was shown to be downregulated in the homozygotes compared with both the wild types and heterozygotes. *Col1a1* expression has previously been found to be downregulated in chondrocytes of a mouse model of OI with a mutation in *Col1a2 (G610C)* [250].

8.1.1.2 Homozygous Lethal Phenotype of MP-107

Homozygous animals were found to have a perinatal lethal phenotype. Homozygous embryos were viable at 18.5 dpc, however some homozygous pups were identified in 'respiratory distress' at P0. Approximately a quarter of pups from intercross matings went missing shortly after birth. It is likely that this was causing the gasping phenotype observed in some homozygotes, which in turn caused the death of the homozygotes. The disappearance is likely due to the mothers consuming the cadavers soon after death. An OI mouse model (*Brtl*), with a mutation in *Col1a1*, has previously been reported to die shortly after birth from respiratory distress [250].

8.1.1.3 OI phenotypes of MP-107

In addition to the mild bone abnormalities including curved olecranons and splayed ischia in the heterozygous animals, other bone phenotypes were detected, including a reduced BMD in female heterozygotes at 12 months of age. Due to the possible confounding effect of the mixed background, further phenotyping was carried out on incipient congenic cohorts, with a cleaner C3H/HeH background, particularly as C57BL/6J animals have been shown to have lower BMD than C3H/HeH or F1 hybrids [271]. The BMD phenotype was replicated in some cohorts, but not others and a lowered BMC phenotype was noted in two cohorts.

Three-point bending of humeri showed a decrease in maximum flexural load and work to fracture in the heterozygous animals. Analysis of the trabecular bone of the epiphysis and metaphysis showed a number of differences between genotypes including in the bone volume fraction, trabecular number, trabecular separation and trabecular thickness. Taking all of these bone phenotypes together, in addition to the bone breakages identified in some heterozygous animals, by X-ray and μ CT imaging, it appears that a mild type IV OI phenotype is present in the heterozygotes. Additionally, the mild bone phenotypes of splayed ischia and curved olecranons look similar to phenotypes

seen in an OI model, *Brtl*, which have been attributed to fractures [80]. The *Brtl* model has a glycine substitution in *Col1a1* and exhibits variable phenotypes including similar ischia and olecranon phenotypes and some lethality. The lethal phenotype of the MP-107 homozygotes, coupled with the evidence of bone breakage in utero, indicates a more severe OI phenotype than the type I/IV seen in heterozygotes, similar to type II OI in humans. The presence of an OI phenotype is perhaps not surprising given that approximately 90% of cases of OI in humans are due to mutations in either *COL1A1* or *COL1A2* [53], the vast majority of which affect the repeating glycine motif.

8.1.1.4 EDS phenotypes of MP-107

Mechanical testing of skin and tendons revealed that both tissues have altered visco-elastic properties. There was no difference in the load at rupture in either tissue, however the skin appeared to be hyperextensible, likely due to the removal of the macroscopic crimp followed by straightening of molecular kinks in the gaps between Collagen molecules [36]. The radio labelling experiment indicated that there was no observable difference between the genotypes either intracellularly or extracellularly, indicating that the mutant protein is being secreted. Pepsin digestion and Coomassie staining of tendon fascicles also indicated that there was no difference in $\alpha 1/\alpha 2$ ratio, indicating that the collagen I in the heterozygous tendons is heterotrimer. Tendon fascicles underwent DSC analysis, which revealed a difference in the dry entropy of the samples suggesting that the collagen molecules are less confined within the fibril structure [271, 297]. Together these results indicate that mutant $\alpha 2$ chains are being incorporated into the collagen fibrils. The DSC data suggests that the mutation may be causing micro-unfolded regions within the molecule, making them less stable, and therefore requiring less energy to break apart the collagen I molecule [73]. It is therefore likely that the altered mechanical properties are a result of this micro-unfolding at the site of the repeating glycine motif disruption. This could explain why the initial elastic slope differs between genotypes, but the elastic slope does not (see section 4.2.3).

Additionally, the TEM imaging of tendon revealed that the homozygous and heterozygous tendons had a reduced number of fibrils compared to wild-type tendons, which could also alter the mechanical properties. A reduction in the number of fibrils may lead to a reduction in the amount of ground substance in the ECM, and therefore

the amount of water that can be retained. This implies an EDS, or EDS like phenotype, as two common phenotypes shown by patients with EDS are hyperextensible skin, and ligament laxity leading to joint hypermobility [298].

8.1.1.5 OA phenotypes of MP-107

The heterozygous MP-107 (*Col1a2*⁺¹⁰⁷) animals showed ossification of the collateral ligaments and synovium, from as early as 4 months in the female animals and 9 months in the males by μ CT, although it should be noted that no tissue from animals between these time points underwent μ CT analysis. Significant differences were detected between the genotypes at the early time points due to the lack of any ossification in the wild types, however at 18 months there was evidence of some minor ossification in the wild types, which is not surprising as the incidence of ossified ligaments in human increase with age [299, 300]. Between 80% (female) and 100% (male) of heterozygotes exhibited severe ossification, and between 20% (female) and 50% (male) of wild types exhibited some mild ossification (see Chapter 3, Figure 3.38 for a comparison). As this analysis was based on the presence or absence of the ossification, rather than severity, no significant difference was detected at 18 months. A volumetric analysis of this ossified tissue, would likely remedy this [257]. Ossification and inflammation of the synovium was noted in histological sections of heterozygotes in the 12- and 18-month cohorts.

OARSI scoring of histological sections of the knee revealed that in both males and female, the heterozygotes had significantly higher scores at 18 months than their wild type counterparts, confirming the OA phenotype. It is worth noting that the ligament and synovium changes in heterozygotes precede the cartilage damage. Ramos-Mucci *et al.*, reported increased volume of mineralised tissue in joint space, and increased ossification of the meniscus and collateral ligaments in animals with spontaneous and induced OA [257].

The ossification of ligaments occurring before the cartilage damage in MP-107, does not necessarily indicate causation, but this would be worthy of further investigation. It has been suggested that pathological calcification of joint tissues is likely a disease initiator, for example there is a strong association between the presence of calcium crystals in synovial fluid and disease severity in OA patients [301]. The calcification of the soft

tissues could disrupt normal mechanoadaptive joint responses and lead to increased levels of potentially pro-inflammatory crystals in the synovial fluid [301, 302].

OA was surgically induced using DMM surgery on a small cohort of animals. There was a large degree of variability in the levels of OA that were produced, meaning that no significant difference was detected. Due to the variability in phenotype observed in the heterozygotes, it is extremely likely that this experiment was underpowered. Animals were culled 6 weeks post-surgery; it is likely that a stronger effect would have been seen if there had been a longer period between the surgery and culling of the animals[278].

Analysis of μ CT data in Chapter 3 demonstrated an increased incidence of abnormal bone growth in heterozygotes when compared to wild types at multiple time points, and this is similar to what is seen in the DMM surgical model of OA. The histological analysis in Chapter 3 also indicated that the osteophyte formation in heterozygotes preceded cartilage changes, and that may also be the case with this DMM experiment. However, to further investigate this, a longer period of time between surgery and harvesting tissue should be used.

Micro-indentation analysis of the femoral condyles revealed a significant increase in structural stiffness in the medial femoral condyle of the heterozygotes compared with the wild types. No difference was detected in the lateral femoral condyles or the tibial plateaux. It should be noted that while the indenter was applied to the cartilage, the subchondral bone will have an effect, and therefore this difference cannot be attributed to a single tissue.

8.1.1.6 ER stress phenotypes in MP-107

TEM imaging revealed the presence of dilated ER in homozygous and heterozygous tenocytes. Cell lysates of MEFs harvested from 12.5 dpc embryos of all genotypes, were probed with BIP, a marker of ER stress, which indicated that homozygotes and heterozygotes had increased levels of ER stress compared to wild types. IHC was undertaken on 18-month knee sections, again using an Anti-BIP antibody, and DAB staining revealed evidence of ER stress in the chondrocytes of the heterozygous articular cartilage. Combined with the evidence that the mutant protein is secreted rather than retained intracellularly, it appears that the ER stress is likely linked to a delay in the

collagen folding process. The G610C mouse of OI, which has a glycine substitution in *Col1a2*, exhibits ER stress in the chondrocytes and osteoblasts [250].

Chondrocytes are particularly sensitive to ER stress, due to their secretory role, and ER stress has been associated with OA [70]. BIP has also been reported to be upregulated in osteoarthritic tissue in both humans and mice [276, 303]. For this reason, the sections used for the IHC experiment were from a heterozygote that did not show signs of OA, to reduce the risk of ER stress being secondary to the OA itself. However, further experiments with additional samples are required to be able to draw conclusions.

8.1.2. TM44

6.1.1.1. Causative mutation in TM44

Mapping of affected animals and unaffected controls identified a region on Chromosome 11; exome sequencing revealed two mutations, which were confirmed by Sanger sequencing. Subsequent segregation of mutations revealed the causative mutation as a nonsense mutation causing a premature stop codon in Exon 31 of the gene *Col1a1*.

8.1.2.1 Bone Phenotypes of TM44

Phenotyping of the line TM44 was not as extensive as MP-107. Nevertheless, initial phenotyping of TM44 revealed the presence of similar early phenotypes to those observed in MP-107, including a curved olecranon at the elbow, and splayed ischia at the pelvis, abnormal bone growth and cartilage erosion in the knee. Three animals also exhibited abnormal calcaneus. The phenotypes observed were variable, as seen in MP-107, however every heterozygote TM44 animals in the studied cohort displayed at least one of the bone phenotypes.

DEXA analysis indicates that the heterozygotes (*Col1a1*^{+/*TM44*}) have significantly lower BMD and BMC in both sexes at 2 months of age, indicating that the animals are osteopenic. The presence of similar phenotypes at the olecranon and pelvis, to those seen in models of OI (*BrtI*), OI/EDS overlap (*Jrt*) and MP-107, which have been attributed to bone breakage, coupled with this observed osteopenic phenotype indicates an OI phenotype [80, 117]. Additionally, in another model of OI with a mutation in *Col1a1*

(*seal*), 50% of homozygous animals exhibited swollen heels and footpads due to pathological fractures, which could explain the phenotype at the calcaneus of this line [304].

8.1.2.2 OA Phenotype of TM44

100% of animals exhibited abnormal bone growth at the knee by 12 months, indicating an earlier onset disease, although OARSI scoring was only performed at 18 months, so it is not possible to confirm the large deposits of abnormal bone were coinciding with cartilage degradation at the earlier time point. At 18 months 100% of the heterozygotes displayed evidence of OA, a higher proportion than observed in MP-107.

8.1.2.3 Homozygous Lethal Phenotype of TM44

The homozygous embryos were found to be lethal between 12.5 and 14.5 dpc and showed evidence of hydrocephalus, similar to the *Mov-13*^{-/-} model of Type II OI, which is recorded as having arrested development between day 11 and day 12 of gestation around the time when high transcription of *Col1a1* occurs, and death shortly [294].

8.1.2.4 EDS or Col1 Related Overlap Phenotype of TM44

Analysis of tendon collagen extracts reveals that the $\alpha 1 / \alpha 1$ ratio is similar between genotypes (and to MP-107) indicating that homotrimer is not formed, and the molecular weight of the $\alpha 1$ band is also similar, indicating that a truncated protein is not present. This indicated that the mutant protein is unlikely to be able to trimerise, and is likely removed by ERAD. Likely leading to a reduction of collagen I produced. Further work is required to establish if this is in fact the nature of the TM-44 mutation.

There are examples of similar nonsense mutations in Exon 31 leading to OI (Type I/IV) in humans [305, 306] and to Col1-related overlap disorder [80, 115]. Due to the phenotyping analysis on TM44 being limited in scope, it is not possible to discern what specific disorder TM44 models.

8.1.3. *Col1a2*-KO

8.1.3.1 Bone Phenotypes of *Col1a2*-KO

As with TM44, phenotyping of the line *Col1a2*-KO was not as extensive as MP-107. However, initial phenotyping of *Col1a2*-KO revealed the presence of similar early phenotypes to those observed in MP-107 and TM44, including a curved olecranon at the elbow, and splayed ischia at the pelvis. These phenotypes were present in both homozygous and heterozygous animals. No difference in BMC or BMD was detected. Nevertheless, as shown for MP-107, this does not mean that the bones are not osteopenic, just that any difference is not detectable by whole body DEXA analysis.

8.1.3.2 OA Phenotype of *Col1a2*-KO

No heterozygotes or homozygotes were identified as having abnormal growth at the knee at 12 months. Animals were not aged further so it is not possible to say whether *Col1a2*-KO animals, either heterozygotes or homozygotes would have gone on to develop abnormal bone formation at the knee or an OA phenotype.

8.1.3.3 EDS or Col1 Related Overlap Phenotype of *Col1a2*-KO

The collagen analysis of tendons, confirmed that in the homozygote, the collagen I in tendon was homotrimer, and both heterotrimer and homotrimer were present in the heterozygote tendons.

8.1.4. Genetics

The viability of the *Col1a2*-KO homozygotes (*Col1a2*^{-/-}) indicates that the absence of COL1A2 protein is less deleterious than the mutation seen in MP-107, where *Col1a2*^{107/107} animals were not viable. Moreover, the presence of a single mutant MP-107 *Col1a2* allele and a null allele in the double mutant (*Col1a2*^{-/107}) was less deleterious than two copies of the mutant *Col1a2* allele, which indicates that the severity of phenotype is related to the quantity of mutant protein, rather than the absence of wild-type protein.

In addition the compound cross experiment revealed that the *Col1a2*^{+/107}, *Col1a1*^{+/TM44} animals were less viable than either *Col1a2*^{+/107} animals or *Col1a1*^{+/TM44} animals confirming epistasis between mutant genes. Overall, we can conclude from the extensive genetic analysis that the MP-107 mutation is likely a gain of function mutation.

8.2. Overall Conclusions

All three lines show evidence of an OI phenotype. The more thorough phenotyping of MP-107 allows a more in-depth analysis of this model. The *Col1a2*-KO appears to have a mild type I/IV OI phenotype in both heterozygotes and homozygotes. The TM44 heterozygotes also appear to have a type IV OI phenotype, with late onset OA, and the homozygotes appear to have a type II OI phenotype, it is important to note that this line did not undergo phenotyping which would reveal the presence of an EDS phenotype so this cannot be ruled out. The MP-107 homozygotes, have an OI type II phenotype, and the heterozygotes have an OI, EDS and OA phenotype. Due to the presence of both OI and EDS phenotypes, it is likely that this line is a model for Col1-related overlap disorder.

The cause of the OA phenotype in the MP-107 line and TM44 line is not entirely clear. There is more evidence for possible mechanisms in the MP-107 line, due to the variety of phenotyping procedures undertaken.

As previously stated, OA is a disorder involving the whole joint, and many of the tissues that make up the joint are made up of collagen I. It is therefore highly likely that abnormal collagen I could alter the behaviour, and interactions of these tissues.

A large proportion of ligament, tendon, joint capsule and meniscus are composed of collagen I fibres. Mechanical testing of tendons provided evidence that in MP-107 heterozygous fascicles, the hysteresis is reduced, making tissues less effective at absorbing energy. The collagen I tissues within the joint all play a stabilising role in the knee joint, to varying degrees. Ossification of soft tissues is often a response to trauma, micro trauma or repetitive mechanical stress [307]. Therefore the ossification of the ligaments, which precedes the cartilage erosion, could be a sign that the joint is not behaving normally. Ossification in tendons and meniscus is known to occur in animals with OA, however it is not known which process precedes the other [257]. It is also known that modifying the heterotypic nature of tendons, such as targeted deletion of Collagen V, can result in EDS and early onset OA [104].

The EDS phenotypes seen in the skin and tendon may indicate that there is a level of joint hypermobility in heterozygotes. It is well established that joint injury is a major

predictor of developing OA [308-310]. Patients with EDS are at a far higher risk of complications of hypermobility which include symptomatic subluxation, dislocation, and tendon ruptures [298]. It is therefore possible the OA observed in the MP-107 line could be secondary to joint injury. Although there is little published evidence that inherited hypermobility predisposes to OA in humans, Sun *et al.* have shown that a mouse model of classic EDS, does exhibit OA [104].

The μ CT of MP-107 heterozygotes revealed altered subchondral trabecular bone. The relationship between articular cartilage and subchondral bone is well established. Additionally, it has been shown in multiple cases that abnormal *COL1A1* and *COL1A2* can lead to altered mineralisation and affect osteoblast differentiation, which could modify the remodelling process that occurs in the subchondral bone

The presence of markers for ER stress in the chondrocytes of heterozygotes, could indicate that the mutation may be having an effect on the chondrocytes which could then lead to apoptosis, or impede the ability of the chondrocytes to modulate homeostasis. Chondrocytes produce collagen I as a minor ECM collagen and it is therefore not surprising that a collagen processing delay may cause knock on effects in this tissue. The A α model of OI leads to osteoblast ER-stress mediated apoptosis [71].

A simple mechanical explanation for the development of OA could be that the breakage in the pelvis, could be leading to an abnormal gait, which in turn causes abnormal loading, and OA. This is unlikely to be the cause due to the OA phenotype occurring in animals, which did not exhibit the splayed ischia phenotype, however gait analysis could be used to investigate if this is the case.

The possible mechanisms listed above are all direct results of the collagen I mutations, however there are instances where mutations in collagen I lead to dysregulation of other genes, which could lead to altered cartilage or bone homeostasis; these possibilities will be discussed in the next section.

8.3. Implications for the Study of Osteoarthritis

One of the aims of this project was to elucidate the mechanism by which the mutations in either of the collagen I genes resulted in OA. The experiments have shown lots of potential causes of OA, without showing that any one phenotype directly causes the OA

phenotype observed in our mice. Some of these mechanisms have been discussed in the previous chapter. However, the interaction of the tissues within the joint has been shown to play a role in OA [161], and it is therefore possible the changes observed could be leading indirectly to OA. For example, cross-talk of bone and cartilage at the osteochondral junction is known to occur, and therefore the OI phenotype and changes to the subchondral trabecular bone may influence the biomechanical response to joint loading indirectly [311].

Figure 8.1. shows many of the interactions between the joint tissues that can have an effect on the progression of OA.

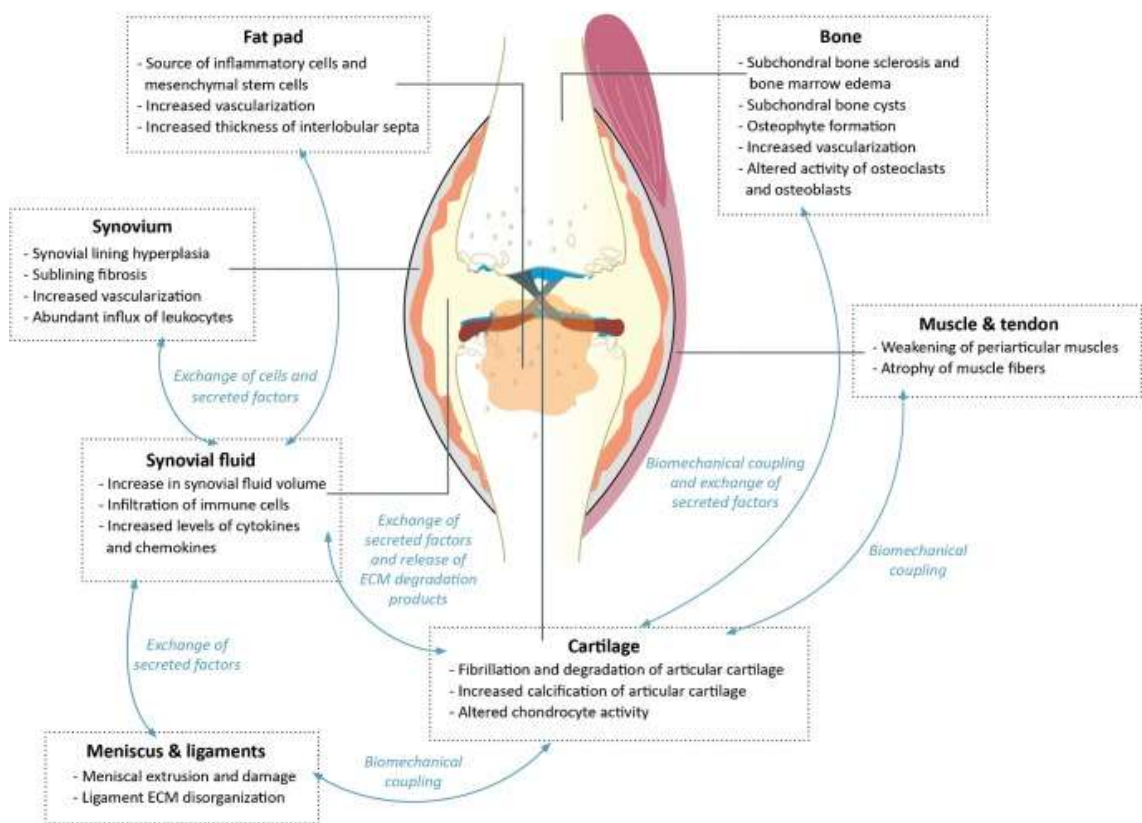


Figure 8.1. A representation of an osteoarthritic knee, including the main contributing tissue and their interactions. Articular cartilage loss typifies OA but the exact balance of tissue involvement and interaction is dependent on both joint site and OA subtypes. Taken from Mimpen and Snelling, 2019 [312].

OA is a disease of the joints, and involves all the tissues of the joint. Given so many of the components of a joint are tissues which contain collagen I, it is perhaps surprising that the genes *COL1A1* and *COL1A2* have not been found to be associated with OA, with the exception of a study of a small founder population in Canada, where an association

was found between *COL1A2* and hip OA [313]. This study is likely underpowered, however, due to the nature of a founder population, mutations are more likely to be replicated within the population. Loughlin *et al.*, found a weak association between *COL1A1* and OA, however upon correcting for multiple testing the result was not significant [314]. It is therefore possible that mutations in collagen I genes may be having an effect on a small subset of patients, making them more difficult to identify.

It is feasible that the mutation in *Col1a1* or *Col1a2* is impairing a cartilage repair process within the osteoarthritic cartilage. Several different studies have shown that chondrocytes in OA cartilage express matrix genes that are expressed at very low levels, or not at all, in normal cartilage, including collagen I genes [315-318]. Styczynska-Soczka *et al.* suggest that the increased production of collagen type I during cartilage degeneration implies that there may be a change in the differentiation status of some chondrocytes towards a fibroblastic phenotype. They also suggest that a mechanically weak fibro-cartilaginous repair tissue is present in otherwise macroscopically non-degenerate human cartilage, which then degenerates [319]. Miosge *et al.* found that the levels of collagen type I mRNA were increased as the degeneration worsened, supporting the conclusion that collagen type I gradually becomes one of the factors involved in the pathogenesis of OA [315]. Impairment of a repair process could certainly explain the severity of the late onset OA phenotype that the MP-107 animals develop.

The line MP-107 was noted to exhibit signs of ER stress in tenocytes, fibroblasts and chondrocytes. This ER stress may lead to ER stress mediated apoptosis of these cells, which could result in altered cartilage homeostasis and degeneration [71]. Apoptosis is observed in OA, but it is not clear if it is the cause of irreversible cartilage degeneration or if it is initiated by it [320, 321]. Nevertheless, Uehara *et al.* demonstrated that ER stress induced apoptosis contributes to articular cartilage degradation using a *Chop* knockout [322].

The surgical induction of OA in the line MP-107 was inconclusive and would need to be repeated in an appropriately powered study.

It appears that in the line MP-107 the ossification of the soft tissues including the synovium, ligaments and capsule precedes the destruction of the cartilage, however as the degradation of cartilage occurs at the molecular level long before it is observable by

histology it is not possible to say with certainty that it precedes the degradation of cartilage. While it may not be the case that the bone changes precede cartilage destruction in other models or in OA patients, it could prove a useful tool for investigating the downstream effects of this ossification including alterations to the synovial fluid, both from the release of crystallites, and the impairment of the type A and B cells in the synovium.

Finally, Bianchi *et al.*, showed that modification of *Col1a1* can affect cytoskeletal organization, affecting osteoblast proliferation, collagen deposition, integrin and TGF- β signalling [81]. It would therefore be prudent to investigate if this is having an effect on the pathogenesis of OA as TGF- β levels have been found to be elevated in the synovial fluid of OA patients and TGF- β is thought to play a role in synovitis [323-326]. While the elevated TGF- β levels may be part of a pro-repair mechanism, other downstream effects of altering *Col1a1* expression should be investigated.

There are many ways in which a mouse model that develops late onset OA could be used to help elucidate the mechanisms that lead to OA, either due to the genetic component, or the mechanical or chemical pathways identified. For example, studies have shown that genetic predisposition to hip OA is often due to altered shape of the joint, leading to altered mechanical load [327, 328]. It is possible that a similar mechanism is happening here, and modelling the joint to investigate change associated with the genetic changes could elucidate mechanisms leading to OA.

8.4. Implications for the Study of OI/ EDS

Generally the mechanisms causing OI as a result of mutations in Collagen I genes are fairly well understood, and it is unlikely that the work discussed here will have much of an impact in the field of OI as a single disorder, additionally there are many mouse model of OI caused by mutations in Collagen I genes.

Classical EDS and vascular EDS are very rarely caused by mutations in Collagen I genes, the more common types of EDS caused by mutations in Collagen I genes are arthrochalasia EDS and cardiac-valvular EDS. There are no mouse models of EDS caused by mutations in Collagen I genes, and therefore these models could be used to improve

the understanding of how mutant collagen I affects the material and mechanical properties of collagen rich tissues, such as skin, tendons and ligaments.

OI/EDS overlap, or Col-1 overlap disorder, appear to be almost exclusively caused by mutations in Collagen I genes, and therefore these mouse lines would be a useful resource to help understand the development of this disorder and why it appears to be distinct from the both OI and EDS.

8.5. Future Work

The work detailed here has not been able to elucidate the specific mechanism by which mutations in *Col1a1* and *Col1a2* lead to OA, only possible mechanisms. Were time not limited, several avenues of investigation could have been undertaken.

8.5.1 Further Study of Bone Phenotypes

The bone phenotyping undertaken in this study was limited to mechanical testing and μ CT imaging and analysis. However, the μ CT work undertaken in this study did not investigate the structure of cortical bone. However, the mechanical testing of humeri indicated that there were differences in the mechanical properties in the cortical bone. Further μ CT analysis of cortical bone provides information about why the MP-107 heterozygote bones are weaker than the wild types.

OI phenotypes can arise from abnormal osteoblast function. A wide variety of phenotyping tests were carried out by Jeong *et al.* on the G610C model of OI, including dynamic and static histomorphometry, which could indicate if the mutations had an effect on the bone remodelling, as well as the effect on all the cell types involved in the remodelling process [329]. Additionally, the effect of the mutation on steady state bone resorption *in vivo* could be determined by analysis of the serum level of the type I collagen α 1 chain C-terminal telopeptide (CTX), a biomarker for osteoclast activity [304].

To investigate the quality of the osteoid which is subsequently mineralised, the hydroxyproline content could be measured in demineralised bone hydrolysate, to indicate the collagen content [304].

8.5.2 Further Study of Collagen Phenotypes

DSC analysis revealed that the collagen molecules had a lower dry enthalpy, indicating the collagen molecules are less confined within the fibril structure. Atomic force

microscopy could be used to investigate what the structural changes to the collagen molecules are, and how these impact the formation of the fibrils.

The mechanical testing of tendons indicated that there was an increased initial extension for little force in the so-called 'toe' of the graph. It is believed that the toe of the extension is the straightening of the crimped fibres. Polarised light microscopy could be used to investigate if the abnormal collagen fibrils in MP-107 heterozygotes have an impact on the crimp waveform of fascicles, which might help explain the mechanical differences in these animals.

TEM showed that the collagen fibrils in MP-107 heterozygous and homozygous tail tendons were less densely packed than in wild types. 3D TEM would allow imaging of the fibrils to understand how the less densely packed fibril bundles interact with each other.

8.5.3 Further Study of OA Phenotype

The calcification of ligaments in heterozygous mice was visible in μ CT imaging from as early as 4 months of age. Ramos-Mucci *et al.* investigated the calcification of the ligaments and meniscus of STR/ort animals with OA, using a volumetric analysis of ossified tissue. This technique could provide clear evidence as to the development of the phenotype observed in the MP-107 heterozygotes over time [257].

The presence of crystals in the synovial fluid as a result of the ossification of the soft tissues of the joint could be increasing the severity of disease and therefore assessing the crystals in synovial fluid prior to articular cartilage degradation could be informative. Recovering synovial fluid from the murine joint is difficult, however, Seifer *et al.* have published a method [330]. It should be noted that the presence of crystals in the synovial fluid of OA patients does not necessarily indicate that they are pathogenic [331]. A compound cross with the Toll like receptor 4 (TLR4) knock out could be informative in this regard.

Although the OA phenotype was present in animals that did not show an abnormal pelvis, it is still possible that there was a mild pelvis abnormality that wasn't identified, but that still had an impact on gait. Gait analysis could therefore be used to investigate

whether heterozygotes had a gait abnormality that might cause abnormal loading, leading to OA.

Phenotyping of skin and tendons of MP-107 indicated that there were altered mechanical properties of these tissues, and indicated that the heterozygous animals may have some degree of joint laxity. *Ex vivo* joint laxity experimentation may indicate if this is the case, and using an *in vivo* non-invasive murine joint loading model such as described by Poulet *et al.*, may indicate if this instability is leading to OA [225].

Analysis of the subchondral bone of MP-107 via μ CT imaging and analysis did not show any difference between genotypes, due to the effect the *Col1a2* mutation had on bones including trabecular bone alteration, mechanically weaker bone and increased fracture risk, it is surprising no difference was detected here. It is possible that the resolution of the imaging undertaken was insufficient, and therefore imaging using advanced higher resolution techniques such as synchrotron X-ray tomography may enable a better understanding of the bone changes within the joint [332].

To investigate if the OA phenotype is a result of alterations in the joint shape during development as a result of the mutations in *Col1a1* or *Col1a2*, an inducible knock in of the mutations could be used to ensure the joint forms normally. Should the OA phenotype still appear, then it is likely that the phenotype is as a result of one of the mechanism discussed here, where as if no phenotype occurred this would indicate that the OA phenotype is caused due to changes during development, such as altered joint morphology.

With the exception of the micro-indentation assay and histological analysis, changes to the articular cartilage were not investigated in these lines. Further μ CT imaging using phosphotungstic acid as a contrast agent will allow visualisation and comparison of the cartilage in 3 dimensions [243, 333].

8.5.4 Further Study of Genetics

The MP-107 mutation leads to the production of both wild-type and alternatively spliced mutant transcripts. It is unknown what effect variation in the levels of these transcripts between cells, or between animals might have on phenotype. It would be of considerable interest to investigate the levels of the two possible transcripts in

heterozygous animals with varying phenotypes and to establish if there is a link between levels of mutant transcript expression and phenotype severity.

While GWAS studies have not identified either *COL1A1* or *COL1A2* as being associated with OA, the knowledge that a mutation in either of these genes can lead to an OA phenotype, regardless of the mode of action, could make these genes a possible target for further study. OA clinics often have DNA biobanks for patients with OA, and a possible research angle could be screening these DNA samples for mutations in either of these genes.

Bibliography

1. Ricard-Blum, S., *The collagen family*. Cold Spring Harb Perspect Biol, 2011. **3**(1): p. a004978.
2. Brodsky, B. and Persikov, A.V., *Molecular structure of the collagen triple helix*. Adv Protein Chem, 2005. **70**: p. 301-39.
3. Malhotra, V. and Erlmann, P., *The pathway of collagen secretion*. Annu Rev Cell Dev Biol, 2015. **31**: p. 109-24.
4. Abreu-Velez, A.M. and Howard, M.S., *Collagen IV in Normal Skin and in Pathological Processes*. N Am J Med Sci, 2012. **4**(1): p. 1-8.
5. Kadler, K.E., Baldock, C., Bella, J., and Boot-Handford, R.P., *Collagens at a glance*. J Cell Sci, 2007. **120**(Pt 12): p. 1955-8.
6. Han, S., Makareeva, E., Kuznetsova, N.V., DeRidder, A.M., Sutter, M.B., Losert, W., . . . Leikin, S., *Molecular mechanism of type I collagen homotrimer resistance to mammalian collagenases*. J Biol Chem, 2010. **285**(29): p. 22276-81.
7. Canelon, S.P. and Wallace, J.M., *beta-Aminopropionitrile-Induced Reduction in Enzymatic Crosslinking Causes In Vitro Changes in Collagen Morphology and Molecular Composition*. PLoS One, 2016. **11**(11): p. e0166392.
8. Rossert, J. and de Crombrughe, B., *Type I Collagen: Structure, Synthesis, and Regulation*, in *Principles of Bone Biology (Second Edition)*, J.P. Bilezikian, L.G. Raisz, and G.A. Rodan, Editors. 2002,, Academic Press. p. 189-210.
9. Marcus, M., Vrkic, N., and Getaldic-Svarc, B., *Analytical evaluation of P1NP assay, a biochemical marker of bone turnover*. Biochemia Medica, 2006. **16**(2): p. 178 - 190.
10. Myllyharju, J., *Intracellular Post-Translational Modifications of Collagens*, in *Collagen: Primer in Structure, Processing and Assembly*, J. Brinckmann, H. Notbohm, and P.K. Müller, Editors. 2005, Springer Berlin Heidelberg: Berlin, Heidelberg. p. 115-147.
11. Cole, C.N. and Scarcelli, J.J., *Transport of messenger RNA from the nucleus to the cytoplasm*. Curr Opin Cell Biol, 2006. **18**(3): p. 299-306.
12. Zhang, Y. and Stefanovic, B., *LARP6 Meets Collagen mRNA: Specific Regulation of Type I Collagen Expression*. Int J Mol Sci, 2016. **17**(3): p. 419.
13. Makareeva, E. and Leikin, S., *Collagen Structure, Folding and Function*, in *Osteogenesis Imperfecta: A Translational Approach to Brittle Bone Disease*, J.R. Shapiro, et al., Editors. 2014, Academic Press. p. 71-84.
14. Berg, R.A. and Prockop, D.J., *The thermal transition of a non-hydroxylated form of collagen. Evidence for a role for hydroxyproline in stabilizing the triple-helix of collagen*. Biochem Biophys Res Commun, 1973. **52**(1): p. 115-20.
15. Yamauchi, M. and Shiiba, M., *Lysine hydroxylation and cross-linking of collagen*. Methods Mol Biol, 2008. **446**: p. 95-108.

16. Cali, T., Vanoni, O., and Molinari, M., *The endoplasmic reticulum crossroads for newly synthesized polypeptide chains*. *Prog Mol Biol Transl Sci*, 2008. **83**: p. 135-79.
17. Jin, L., Pahuja, K.B., Wickliffe, K.E., Gorur, A., Baumgartel, C., Schekman, R., and Rape, M., *Ubiquitin-dependent regulation of COPII coat size and function*. *Nature*, 2012. **482**(7386): p. 495-500.
18. Stephens, D.J., *Cell biology: Collagen secretion explained*. *Nature*, 2012. **482**(7386): p. 474-5.
19. Canty, E.G. and Kadler, K.E., *Procollagen trafficking, processing and fibrillogenesis*. *J Cell Sci*, 2005. **118**(Pt 7): p. 1341-53.
20. Greenspan, D.S., *Biosynthetic Processing of Collagen Molecules*, in *Collagen: Primer in Structure, Processing and Assembly*, J. Brinckmann, H. Notbohm, and P.K. Müller, Editors. 2005, Springer Berlin Heidelberg: Berlin, Heidelberg. p. 149-183.
21. Prockop, D.J. and Fertala, A., *Inhibition of the Self-assembly of Collagen I into Fibrils with Synthetic Peptides: Demonstration that assembly is driven by specific binding sites on the monomers**. *Journal of Biological Chemistry*, 1998. **273**(25): p. 15598-15604.
22. Thorpe, C.T. and Screen, H.R.C., *Tendon Structure and Composition*, in *Metabolic Influences on Risk for Tendon Disorders*, P.W. Ackermann and D.A. Hart, Editors. 2016, Springer International Publishing: Cham. p. 3-10.
23. Depalle, B., Qin, Z., Shefelbine, S.J., and Buehler, M.J., *Influence of cross-link structure, density and mechanical properties in the mesoscale deformation mechanisms of collagen fibrils*. *Journal of the Mechanical Behavior of Biomedical Materials*, 2015. **52**: p. 1-13.
24. Myllyharju, J. and Kivirikko, K.I., *Collagens, modifying enzymes and their mutations in humans, flies and worms*. *Trends Genet*, 2004. **20**(1): p. 33-43.
25. Fratzl, P., *Collagen: Structure and Mechanics, an Introduction*, in *Collagen: Structure and Mechanics*, P. Fratzl, Editor. 2008, Springer US: Boston, MA. p. 1-13.
26. Canty, E.G. and Kadler, K.E., *Collagen fibril biosynthesis in tendon: a review and recent insights*. *Comparative Biochemistry and Physiology Part A: Molecular & Integrative Physiology*, 2002. **133**(4): p. 979-985.
27. Hulmes, D.J.S., *Building Collagen Molecules, Fibrils, and Suprafibrillar Structures*. *Journal of Structural Biology*, 2002. **137**(1-2): p. 2-10.
28. Rumian, A.P., Wallace, A.L., and Birch, H.L., *Tendons and ligaments are anatomically distinct but overlap in molecular and morphological features—a comparative study in an ovine model*. *Journal of Orthopaedic Research*, 2007. **25**(4): p. 458–464.
29. Wenger, M.P.E., Bozec, L., Horton, M.A., and Mesquida, P., *Mechanical Properties of Collagen Fibrils*. *Biophysical Journal*, 2007. **93**(4): p. 1255–1263.
30. Kjaer, M., *Role of Extracellular Matrix in Adaptation of Tendon and Skeletal Muscle to Mechanical Loading*. *Physiological Reviews*, 2004. **84**(2): p. 649-698.
31. Riley, G., *The pathogenesis of tendinopathy. A molecular perspective*. *Rheumatology (Oxford)*, 2004. **43**(2): p. 131-42.
32. Parmar, K., *Tendon and ligament: basic science, injury and repair*. *Orthopaedics and Trauma*, 2018. **32**(4): p. 241-244.
33. Thorpe, C.T., Birch, H.L., Clegg, P.D., and Screen, H.R.C., *Tendon Physiology and Mechanical Behavior*, in *Tendon Regeneration*. 2015, Elsevier. p. 3–39.
34. Shearer, T., Thorpe, C.T., and Screen, H.R.C., *The relative compliance of energy-storing tendons may be due to the helical fibril arrangement of their fascicles*. *J R Soc Interface*, 2017. **14**(133).
35. Quigley, A.S., Bancelin, S., Deska-Gauthier, D., Legare, F., Kreplak, L., and Veres, S.P., *In tendons, differing physiological requirements lead to functionally distinct nanostructures*. *Sci Rep*, 2018. **8**(1): p. 4409.
36. Fratzl, P., Misof, K., Zizak, I., Rapp, G., Amenitsch, H., and Bernstorff, S., *Fibrillar structure and mechanical properties of collagen*. *J Struct Biol*, 1998. **122**(1-2): p. 119-22.
37. Gupta, H.S., Seto, J., Krauss, S., Boesecke, P., and Screen, H.R., *In situ multi-level analysis of viscoelastic deformation mechanisms in tendon collagen*. *J Struct Biol*, 2010. **169**(2): p. 183-91.
38. Thorpe, C.T., Godinho, M.S.C., Riley, G.P., Birch, H.L., Clegg, P.D., and Screen, H.R.C., *The interfascicular matrix enables fascicle sliding and recovery in tendon, and behaves more elastically in energy storing tendons*. *J Mech Behav Biomed Mater*, 2015. **52**: p. 85-94.
39. Launey, M.E., Buehler, M.J., and Ritchie, R.O., *On the Mechanistic Origins of Toughness in Bone*. *Annual Review of Materials Research*, 2010. **40**(1): p. 25-53.
40. Ott, S.M., *Cortical or Trabecular Bone: What's the Difference?* *American Journal of Nephrology*, 2018. **47**(6): p. 373–375.

41. Orimo, H., *The mechanism of mineralization and the role of alkaline phosphatase in health and disease*. J Nippon Med Sch, 2010. **77**(1): p. 4-12.
42. Stock, S.R., *The Mineral-Collagen Interface in Bone*. Calcif Tissue Int, 2015. **97**(3): p. 262-80.
43. Schwarcz, H.P., Abueidda, D., and Jasiuk, I., *The Ultrastructure of Bone and Its Relevance to Mechanical Properties*. Frontiers in Physics, 2017. **5**(39).
44. Clarke, B., *Normal bone anatomy and physiology*. Clin J Am Soc Nephrol, 2008. **3 Suppl 3**: p. S131-9.
45. Nair, A.K., Gautieri, A., Chang, S.W., and Buehler, M.J., *Molecular mechanics of mineralized collagen fibrils in bone*. Nat Commun, 2013. **4**: p. 1724.
46. Dalgleish, R., *The human type I collagen mutation database*. Nucleic Acids Res, 1997. **25**(1): p. 181-7.
47. Dalgleish, R., *The Human Collagen Mutation Database 1998*. Nucleic Acids Res, 1998. **26**(1): p. 253-5.
48. Dalgleish, R., Teh, W.K., and Osredok, I. *Osteogenesis Imperfecta Variant Database*. 2008 November 18, 2020 May 5, 2021].
49. van Dijk, F.S., Cobben, J.M., Kariminejad, A., Maugeri, A., Nikkels, P.G., van Rijn, R.R., and Pals, G., *Osteogenesis Imperfecta: A Review with Clinical Examples*. Mol Syndromol, 2011. **2**(1): p. 1-20.
50. Baljet, B., *Aspects of the history of Osteogenesis imperfecta (Vrolik's syndrome)*. Annals of Anatomy - Anatomischer Anzeiger, 2002. **184**(1): p. 1-7.
51. Sillence, D.O., Senn, A., and Danks, D.M., *Genetic heterogeneity in osteogenesis imperfecta*. J Med Genet, 1979. **16**(2): p. 101-16.
52. Rauch, F. and Glorieux, F.H., *Osteogenesis imperfecta*. . The Lancet, 2004. **363**(9418): p. 1377-1385.
53. Sykes, B., Ogilvie, D., Wordsworth, P., Wallis, G., Mathew, C., Beighton, P., . . . et al., *Consistent linkage of dominantly inherited osteogenesis imperfecta to the type I collagen loci: COL1A1 and COL1A2*. Am J Hum Genet, 1990. **46**(2): p. 293-307.
54. Makitie, R.E., Costantini, A., Kampe, A., Alm, J.J., and Makitie, O., *New Insights Into Monogenic Causes of Osteoporosis*. Front Endocrinol (Lausanne), 2019. **10**: p. 70.
55. Chetty, M., Roomaney, I.A., and Beighton, P., *The evolution of the nosology of osteogenesis imperfecta*. Clin Genet, 2021. **99**(1): p. 42-52.
56. Barnes, A.M., Chang, W., Morello, R., Cabral, W.A., Weis, M., Eyre, D.R., . . . Marini, J.C., *Deficiency of cartilage-associated protein in recessive lethal osteogenesis imperfecta*. N Engl J Med, 2006. **355**(26): p. 2757-64.
57. Morello, R., Bertin, T.K., Chen, Y., Hicks, J., Tonachini, L., Monticone, M., . . . Lee, B., *CRTAP is required for prolyl 3-hydroxylation and mutations cause recessive osteogenesis imperfecta*. Cell, 2006. **127**(2): p. 291-304.
58. Cabral, W.A., Chang, W., Barnes, A.M., Weis, M., Scott, M.A., Leikin, S., . . . Marini, J.C., *Prolyl 3-hydroxylase 1 deficiency causes a recessive metabolic bone disorder resembling lethal/severe osteogenesis imperfecta*. Nat Genet, 2007. **39**(3): p. 359-65.
59. van Dijk, F.S., Nesbitt, I.M., Zwikstra, E.H., Nikkels, P.G., Piersma, S.R., Fratantoni, S.A., . . . Pals, G., *PP1B mutations cause severe osteogenesis imperfecta*. Am J Hum Genet, 2009. **85**(4): p. 521-7.
60. Vranka, J.A., Sakai, L.Y., and Bachinger, H.P., *Prolyl 3-hydroxylase 1, enzyme characterization and identification of a novel family of enzymes*. J Biol Chem, 2004. **279**(22): p. 23615-21.
61. Qi, Y. and Xu, R., *Roles of PLODs in Collagen Synthesis and Cancer Progression*. Front Cell Dev Biol, 2018. **6**: p. 66.
62. Christiansen, H.E., Schwarze, U., Pyott, S.M., AlSwaid, A., Al Balwi, M., Alrasheed, S., . . . Byers, P.H., *Homozygosity for a missense mutation in SERPINH1, which encodes the collagen chaperone protein HSP47, results in severe recessive osteogenesis imperfecta*. Am J Hum Genet, 2010. **86**(3): p. 389-98.
63. Alanay, Y., Avaygan, H., Camacho, N., Utine, G.E., Boduroglu, K., Aktas, D., . . . Krakow, D., *Mutations in the gene encoding the RER protein FKBP65 cause autosomal-recessive osteogenesis imperfecta*. Am J Hum Genet, 2010. **86**(4): p. 551-9.
64. Valencia, M., Caparros-Martin, J.A., Sirerol-Piquer, M.S., Garcia-Verdugo, J.M., Martinez-Glez, V., Lapunzina, P., . . . Ostergaard, E., *Report of a newly indentified patient with mutations in BMP1 and underlying pathogenetic aspects*. Am J Med Genet A, 2014. **164A**(5): p. 1143-50.

65. Van Dijk, F.S. and Silencio, D.O., *Osteogenesis imperfecta: clinical diagnosis, nomenclature and severity assessment*. Am J Med Genet A, 2014. **164A**(6): p. 1470-81.
66. Forlino, A., Cabral, W.A., Barnes, A.M., and Marini, J.C., *New perspectives on osteogenesis imperfecta*. Nature Reviews Endocrinology, 2011. **7**(9): p. 540-557.
67. Zhuang, J., Tromp, G., Kuivaniemi, H., Nakayasu, K., and Prockop, D.J., *Deletion of 19 base pairs in intron 13 of the gene for the pro alpha 2(I) chain of type-I procollagen (COL1A2) causes exon skipping in a proband with type-I osteogenesis imperfecta*. Hum Genet, 1993. **91**(3): p. 210-6.
68. Prockop, D.J. and Kivirikko, K.I., *Heritable diseases of collagen*. N Engl J Med, 1984. **311**(6): p. 376-86.
69. Brodsky, J.L., *Cleaning up: ER-associated degradation to the rescue*. Cell, 2012. **151**(6): p. 1163-7.
70. Boot-Handford, R.P. and Briggs, M.D., *The unfolded protein response and its relevance to connective tissue diseases*. Cell Tissue Res, 2010. **339**(1): p. 197-211.
71. Lisse, T.S., Thiele, F., Fuchs, H., Hans, W., Przemec, G.K.H., Abe, K., . . . de Angelis, M.H., *ER Stress-Mediated Apoptosis in a New Mouse Model of Osteogenesis imperfecta*. PLOS Genetics, 2008. **4**(2): p. e7.
72. Marini, J.C., Forlino, A., Cabral, W.A., Barnes, A.M., San Antonio, J.D., Milgrom, S., . . . Byers, P.H., *Consortium for osteogenesis imperfecta mutations in the helical domain of type I collagen: regions rich in lethal mutations align with collagen binding sites for integrins and proteoglycans*. Hum Mutat, 2007. **28**(3): p. 209-21.
73. Pack, M., Constantinou, C.D., Kalia, K., Nielsen, K.B., and Prockop, D.J., *Substitution of serine for alpha 1(I)-glycine 844 in a severe variant of osteogenesis imperfecta minimally destabilizes the triple helix of type I procollagen. The effects of glycine substitutions on thermal stability are either position of amino acid specific*. J Biol Chem, 1989. **264**(33): p. 19694-9.
74. Li, H., Jiang, X., Delaney, J., Franceschetti, T., Bilic-Curcic, I., Kalinovsky, J., . . . Kalajzic, I., *Immature osteoblast lineage cells increase osteoclastogenesis in osteogenesis imperfecta murine*. The American journal of pathology, 2010. **176**(5): p. 2405-2413.
75. Barker, D.D., Wu, H., Hartung, S., Breindl, M., and Jaenisch, R., *Retrovirus-induced insertional mutagenesis: mechanism of collagen mutation in Mov13 mice*. Molecular and Cellular Biology, 1991. **11**(10): p. 5154-5163.
76. Jaenisch, R., Harbers, K., Schnieke, A., Löhler, J., Chumakov, I., Jähner, D., . . . Hoffmann, E., *Germline integration of moloney murine leukemia virus at the Mov13 locus leads to recessive lethal mutation and early embryonic death*. Cell, 1983. **32**(1): p. 209-16.
77. Bonadio, J., Saunders, T.L., Tsai, E., Goldstein, S.A., Morris-Wiman, J., Brinkley, L., . . . et al., *Transgenic mouse model of the mild dominant form of osteogenesis imperfecta*. Proc Natl Acad Sci U S A, 1990. **87**(18): p. 7145-9.
78. Jepsen, K.J., Schaffler, M.B., Kuhn, J.L., Goulet, R.W., Bonadio, J., and Goldstein, S.A., *Type I collagen mutation alters the strength and fatigue behavior of Mov13 cortical tissue*. Journal of Biomechanics, 1997. **30**(11): p. 1141-1147.
79. Enderli, T.A., Burtch, S.R., Templet, J.N., and Carriero, A., *Animal models of osteogenesis imperfecta: applications in clinical research*. Orthop Res Rev, 2016. **8**: p. 41-55.
80. Forlino, A., Porter, F.D., Lee, E.J., Westphal, H., and Marini, J.C., *Use of the Cre/lox recombination system to develop a non-lethal knock-in murine model for osteogenesis imperfecta with an alpha1(I) G349C substitution. Variability in phenotype in BrtlIV mice*. J Biol Chem, 1999. **274**(53): p. 37923-31.
81. Bianchi, L., Gagliardi, A., Maruelli, S., Besio, R., Landi, C., Gioia, R., . . . Forlino, A., *Altered cytoskeletal organization characterized lethal but not surviving Brtl+/- mice: insight on phenotypic variability in osteogenesis imperfecta*. Hum Mol Genet, 2015. **24**(21): p. 6118-33.
82. Chipman, S.D., Sweet, H.O., McBride, D.J., Davison, M.T., Marks, S.C., Shuldiner, A.R., . . . Shapiro, J.R., *Defective pro alpha 2(I) collagen synthesis in a recessive mutation in mice: a model of human osteogenesis imperfecta*. Proceedings of the National Academy of Sciences, 1993. **90**(5): p. 1701-1705.
83. Saban, J., Zussman, M.A., Havey, R., Patwardhan, A.G., Schneider, G.B., and King, D., *Heterozygous oim mice exhibit a mild form of osteogenesis imperfecta*. Bone, 1996. **19**(6): p. 575-9.
84. Daley, E., Streeten, E.A., Sorkin, J.D., Kuznetsova, N., Shapses, S.A., Carleton, S.M., . . . McBride, D.J., Jr., *Variable bone fragility associated with an Amish COL1A2 variant and a knock-in mouse model*. J Bone Miner Res, 2010. **25**(2): p. 247-61.

85. Byers, P.H., *Ehlers-Danlos syndrome: recent advances and current understanding of the clinical and genetic heterogeneity*. J Invest Dermatol, 1994. **103**(5 Suppl): p. 47s-52s.
86. Ehlers, E., *Cutis laxa: Neigung zu Haemorrhagien in der Haut, Lockerung mehrerer Artikulationen*. Dermatologische Zeitung, 1901. **8**: p. 173-174.
87. Danlos, H., *Un cas de cutis laxa avec tumeurs par contusion chronique des coudes et des genoux*. Bull Soc Derm Syph Bulletin de la Societe francaise de dermatologie et de syphiligraphie, 1908. **19**: p. 70-72.
88. Miget, A., *Le Syndrome d'Ehlers-Danlos*. Thèses, Université de Paris Faculté de médecine. 1933: L.Arnette.
89. Barabas, A.P., *Heterogeneity of the Ehlers-Danlos syndrome: description of three clinical types and a hypothesis to explain the basic defect(s)*. British Medical Journal, 1967. **2**(5552): p. 612-613.
90. Beighton, P. and Wells, R.S., *Ehlers-Danlos Syndrome (Two Cases)*. Proceedings of the Royal Society of Medicine, 1968. **61**(10): p. 987-988.
91. McKusick, V.A., *Heritable disorders of connective tissue*. 4th ed. 1972, St Louis: Mosby.
92. Malfait, F., Francomano, C., Byers, P., Belmont, J., Berglund, B., Black, J., . . . Tinkle, B., *The 2017 international classification of the Ehlers-Danlos syndromes*. Am J Med Genet C Semin Med Genet, 2017. **175**(1): p. 8-26.
93. Syx, D., De Wandele, I., Symoens, S., De Rycke, R., Hougrand, O., Voermans, N., . . . Malfait, F., *Bi-allelic AEBP1 mutations in two patients with Ehlers-Danlos syndrome*. Human Molecular Genetics, 2019. **28**(11): p. 1853-1864.
94. Blackburn, P.R., Xu, Z., Tumelty, K.E., Zhao, R.W., Monis, W.J., Harris, K.G., . . . Atwal, P.S., *Bi-allelic Alterations in AEBP1 Lead to Defective Collagen Assembly and Connective Tissue Structure Resulting in a Variant of Ehlers-Danlos Syndrome*. The American Journal of Human Genetics, 2018. **102**(4): p. 696-705.
95. Symoens, S., Syx, D., Malfait, F., Callewaert, B., De Backer, J., Vanakker, O., . . . De Paepe, A., *Comprehensive molecular analysis demonstrates type V collagen mutations in over 90% of patients with classic EDS and allows to refine diagnostic criteria*. Hum Mutat, 2012. **33**(10): p. 1485-93.
96. Nuytinck, L., Freund, M., Lagae, L., Pierard, G.E., Hermanns-Le, T., and De Paepe, A., *Classical Ehlers-Danlos syndrome caused by a mutation in type I collagen*. Am J Hum Genet, 2000. **66**(4): p. 1398-402.
97. Beighton, P., Solomon, L., and Soskolne, C.L., *Articular mobility in an African population*. Ann Rheum Dis, 1973. **32**(5): p. 413-8.
98. Schwarze, U., Hata, R., McKusick, V.A., Shinkai, H., Hoyme, H.E., Pyeritz, R.E., and Byers, P.H., *Rare autosomal recessive cardiac valvular form of Ehlers-Danlos syndrome results from mutations in the COL1A2 gene that activate the nonsense-mediated RNA decay pathway*. Am J Hum Genet, 2004. **74**(5): p. 917-30.
99. Guarneri, V., Morlino, S., Di Stolfo, G., Mastroianno, S., Mazza, T., and Castori, M., *Cardiac valvular Ehlers-Danlos syndrome is a well-defined condition due to recessive null variants in COL1A2*. Am J Med Genet A, 2019. **179**(5): p. 846-851.
100. Pepin, M.G., Schwarze, U., Rice, K.M., Liu, M., Leistriz, D., and Byers, P.H., *Survival is affected by mutation type and molecular mechanism in vascular Ehlers-Danlos syndrome (EDS type IV)*. Genet Med, 2014. **16**(12): p. 881-8.
101. Malfait, F., Symoens, S., De Backer, J., Hermanns-Lê, T., Sakalihasan, N., Lapière, C.M., . . . De Paepe, A., *Three arginine to cysteine substitutions in the pro-alpha (I)-collagen chain cause Ehlers-Danlos syndrome with a propensity to arterial rupture in early adulthood*. Human Mutation, 2007. **28**(4): p. 387-395.
102. Byers, P.H., Duvic, M., Atkinson, M., Robinow, M., Smith, L.T., Krane, S.M., . . . Schwarze, U., *Ehlers-Danlos syndrome type VIIA and VIIB result from splice-junction mutations or genomic deletions that involve exon 6 in the COL1A1 and COL1A2 genes of type I collagen*. American Journal of Medical Genetics, 1997. **72**(1): p. 94-105.
103. Giunta, C., Chambaz, C., Pedemonte, M., Scapolan, S., and Steinmann, B., *The arthrochalasia type of Ehlers-Danlos syndrome (EDS VIIA and VIIB): the diagnostic value of collagen fibril ultrastructure*. Am J Med Genet A, 2008. **146A**(10): p. 1341-6.
104. Sun, M., Connizzo, B.K., Adams, S.M., Freedman, B.R., Wenstrup, R.J., Soslowsky, L.J., and Birk, D.E., *Targeted deletion of collagen V in tendons and ligaments results in a classic Ehlers-Danlos syndrome joint phenotype*. Am J Pathol, 2015. **185**(5): p. 1436-47.

105. Wenstrup, R.J., Florer, J.B., Brunskill, E.W., Bell, S.M., Chervoneva, I., and Birk, D.E., *Type V collagen controls the initiation of collagen fibril assembly*. J Biol Chem, 2004. **279**(51): p. 53331-7.
106. Cooper, T.K., Zhong, Q., Krawczyk, M., Tae, H.J., Muller, G.A., Schubert, R., . . . Briest, W., *The haploinsufficient Col3a1 mouse as a model for vascular Ehlers-Danlos syndrome*. Vet Pathol, 2010. **47**(6): p. 1028-39.
107. Smith, L.B., Hadoke, P.W., Dyer, E., Denvir, M.A., Brownstein, D., Miller, E., . . . Greenfield, A., *Haploinsufficiency of the murine Col3a1 locus causes aortic dissection: a novel model of the vascular type of Ehlers-Danlos syndrome*. Cardiovasc Res, 2011. **90**(1): p. 182-90.
108. Bowen, C.J., Calderon Gjadrosic, J.F., Burger, Z., Rykiel, G., Davis, E.C., Helmers, M.R., . . . Dietz, H.C., *Targetable cellular signaling events mediate vascular pathology in vascular Ehlers-Danlos syndrome*. J Clin Invest, 2020. **130**(2): p. 686-698.
109. Raff, M.L., Craigen, W.J., Smith, L.T., Keene, D.R., and Byers, P.H., *Partial COL1A2 gene duplication produces features of osteogenesis imperfecta and Ehlers-Danlos syndrome type VII*. Human Genetics, 2000. **106**(1): p. 19-28.
110. Nicholls, A.C., Valler, D., Wallis, S., and Pope, F.M., *Homozygosity for a splice site mutation of the COL1A2 gene yields a non-functional pro(alpha)2(I) chain and an EDS/OI clinical phenotype*. J Med Genet, 2001. **38**(2): p. 132-6.
111. Makareeva, E., Cabral, W.A., Marini, J.C., and Leikin, S., *Molecular mechanism of alpha 1(I)-osteogenesis imperfecta/Ehlers-Danlos syndrome: unfolding of an N-anchor domain at the N-terminal end of the type I collagen triple helix*. J Biol Chem, 2006. **281**(10): p. 6463-70.
112. Lund, A., Joensen, F., Christensen, E., Duno, M., Skovby, F., and Schwartz, M., *A novel arginine-to-cysteine substitution in the triple helical region of the alpha1(I) collagen chain in a family with an osteogenesis imperfecta/Ehlers-Danlos phenotype*. Clin Genet, 2008. **73**(1): p. 97-101.
113. Cabral, W.A., Makareeva, E., Colige, A., Letocha, A.D., Ty, J.M., Yeowell, H.N., . . . Marini, J.C., *Mutations near amino end of alpha1(I) collagen cause combined osteogenesis imperfecta/Ehlers-Danlos syndrome by interference with N-propeptide processing*. J Biol Chem, 2005. **280**(19): p. 19259-69.
114. Malfait, F., Symoens, S., Goemans, N., Gyftodimou, Y., Holmberg, E., Lopez-Gonzalez, V., . . . De Paepe, A., *Helical mutations in type I collagen that affect the processing of the amino-propeptide result in an Osteogenesis Imperfecta/Ehlers-Danlos Syndrome overlap syndrome*. Orphanet J Rare Dis, 2013. **8**: p. 78.
115. Morlino, S., Micale, L., Ritelli, M., Rohrbach, M., Zoppi, N., Vandersteen, A., . . . Castori, M., *COL1-related overlap disorder: A novel connective tissue disorder incorporating the osteogenesis imperfecta/Ehlers-Danlos syndrome overlap*. Clin Genet, 2020. **97**(3): p. 396-406.
116. Nadiarnykh, O., Plotnikov, S., Mohler, W.A., Kalajzic, I., Redford-Badwal, D., and Campagnola, P.J., *Second harmonic generation imaging microscopy studies of osteogenesis imperfecta*. J Biomed Opt, 2007. **12**(5): p. 051805.
117. Chen, F., Guo, R., Itoh, S., Moreno, L., Rosenthal, E., Zappitelli, T., . . . Aubin, J.E., *First mouse model for combined osteogenesis imperfecta and Ehlers-Danlos syndrome*. J Bone Miner Res, 2014. **29**(6): p. 1412-23.
118. *Consensus development conference: diagnosis, prophylaxis, and treatment of osteoporosis*. Am J Med, 1993. **94**(6): p. 646-50.
119. Marshall, D., Johnell, O., and Wedel, H., *Meta-analysis of how well measures of bone mineral density predict occurrence of osteoporotic fractures*. BMJ, 1996. **312**(7041): p. 1254-9.
120. *Assessment of fracture risk and its application to screening for postmenopausal osteoporosis. Report of a WHO Study Group*. World Health Organ Tech Rep Ser, 1994. **843**: p. 1-129.
121. Hernlund, E., Svedbom, A., Ivergard, M., Compston, J., Cooper, C., Stenmark, J., . . . Kanis, J.A., *Osteoporosis in the European Union: medical management, epidemiology and economic burden. A report prepared in collaboration with the International Osteoporosis Foundation (IOF) and the European Federation of Pharmaceutical Industry Associations (EFPIA)*. Arch Osteoporos, 2013. **8**: p. 136.
122. Gueguen, R., Jouanny, P., Guillemin, F., Kuntz, C., Pourel, J., and Siest, G., *Segregation analysis and variance components analysis of bone mineral density in healthy families*. J Bone Miner Res, 1995. **10**(12): p. 2017-22.
123. Pocock, N.A., Eisman, J.A., Hopper, J.L., Yeates, M.G., Sambrook, P.N., and Eberl, S., *Genetic determinants of bone mass in adults. A twin study*. J Clin Invest, 1987. **80**(3): p. 706-10.

124. Flicker, L., Hopper, J.L., Rodgers, L., Kaymakci, B., Green, R.M., and Wark, J.D., *Bone density determinants in elderly women: a twin study*. J Bone Miner Res, 1995. **10**(11): p. 1607-13.
125. Stewart, T.L. and Ralston, S.H., *Role of genetic factors in the pathogenesis of osteoporosis*. J Endocrinol, 2000. **166**(2): p. 235-45.
126. Laine, C.M., Joeng, K.S., Campeau, P.M., Kiviranta, R., Tarkkonen, K., Grover, M., . . . Makitie, O., *WNT1 mutations in early-onset osteoporosis and osteogenesis imperfecta*. N Engl J Med, 2013. **368**(19): p. 1809-16.
127. Laine, C.M., Wessman, M., Toiviainen-Salo, S., Kaunisto, M.A., Mayranpaa, M.K., Laine, T., . . . Makitie, O., *A novel splice mutation in PLS3 causes X-linked early onset low-turnover osteoporosis*. J Bone Miner Res, 2015. **30**(3): p. 510-8.
128. van Dijk, F.S., Zillikens, M.C., Micha, D., Riessland, M., Marcelis, C.L., de Die-Smulders, C.E., . . . Pals, G., *PLS3 mutations in X-linked osteoporosis with fractures*. N Engl J Med, 2013. **369**(16): p. 1529-36.
129. Spotila, L.D., Constantinou, C.D., Sereda, L., Ganguly, A., Riggs, B.L., and Prockop, D.J., *Mutation in a gene for type I procollagen (COL1A2) in a woman with postmenopausal osteoporosis: evidence for phenotypic and genotypic overlap with mild osteogenesis imperfecta*. Proc Natl Acad Sci U S A, 1991. **88**(12): p. 5423-7.
130. Spotila, L.D., Colige, A., Sereda, L., Constantinou-Deltas, C.D., Whyte, M.P., Riggs, B.L., . . . et al., *Mutation analysis of coding sequences for type I procollagen in individuals with low bone density*. J Bone Miner Res, 1994. **9**(6): p. 923-32.
131. Grant, S.F., Reid, D.M., Blake, G., Herd, R., Fogelman, I., and Ralston, S.H., *Reduced bone density and osteoporosis associated with a polymorphic Sp1 binding site in the collagen type I alpha 1 gene*. Nat Genet, 1996. **14**(2): p. 203-5.
132. Uitterlinden, A.G., Burger, H., Huang, Q., Yue, F., McGuigan, F.E., Grant, S.F., . . . Ralston, S.H., *Relation of alleles of the collagen type I alpha1 gene to bone density and the risk of osteoporotic fractures in postmenopausal women*. N Engl J Med, 1998. **338**(15): p. 1016-21.
133. Mann, V., Hobson, E.E., Li, B., Stewart, T.L., Grant, S.F., Robins, S.P., . . . Ralston, S.H., *A COL1A1 Sp1 binding site polymorphism predisposes to osteoporotic fracture by affecting bone density and quality*. J Clin Invest, 2001. **107**(7): p. 899-907.
134. Pyeritz, R.E. and McKusick, V.A., *The Marfan syndrome: diagnosis and management*. N Engl J Med, 1979. **300**(14): p. 772-7.
135. Joseph, K.N., Kane, H.A., Milner, R.S., Steg, N.L., Williamson, M.B., Jr., and Bowen, J.R., *Orthopedic aspects of the Marfan phenotype*. Clin Orthop Relat Res, 1992(277): p. 251-61.
136. Maumenee, I.H., *The eye in the Marfan syndrome*. Trans Am Ophthalmol Soc, 1981. **79**: p. 684-733.
137. McKusick, V.A., *The cardiovascular aspects of Marfan's syndrome: a heritable disorder of connective tissue*. Circulation, 1955. **11**(3): p. 321-42.
138. Judge, D.P. and Dietz, H.C., *Marfan's syndrome*. Lancet (London, England), 2005. **366**(9501): p. 1965-1976.
139. Matt, P., Schoenhoff, F., Habashi, J., Holm, T., Van Erp, C., Loch, D., . . . Gen, T.A.C.C., *Circulating transforming growth factor-beta in Marfan syndrome*. Circulation, 2009. **120**(6): p. 526-32.
140. Benke, K., Agg, B., Szilveszter, B., Tarr, F., Nagy, Z.B., Polos, M., . . . Szabolcs, Z., *The role of transforming growth factor-beta in Marfan syndrome*. Cardiol J, 2013. **20**(3): p. 227-34.
141. Phillips, C.L., Shrago-Howe, A.W., Pinnell, S.R., and Wenstrup, R.J., *A substitution at a non-glycine position in the triple-helical domain of pro alpha 2(I) collagen chains present in an individual with a variant of the Marfan syndrome*. J Clin Invest, 1990. **86**(5): p. 1723-8.
142. Caffrey, J. and Silverman, W.A., *Infantile Cortical Hyperostosis: Preliminary Report On a New Syndrome* American Journal of Roentgenology and Radium Therapy, 1945. **54**: p. 1-16.
143. Roske, G., *Eine eigenartige Knochenerkrankung im Säuglingsalter*. Monatsschrift für Kinderheilkunde, 1930. **47**: p. 385-393.
144. Emmery, L., Timmermans, J., Christens, J., and Fryns, J.P., *Familial infantile cortical hyperostosis*. Eur J Pediatr, 1983. **141**(1): p. 56-8.
145. Maclachlan, A.K., Gerrard, J.W., Houston, C.S., and Ives, E.J., *Familial infantile cortical hyperostosis in a large Canadian family*. Can Med Assoc J, 1984. **130**(9): p. 1172-4.
146. Gensure, R.C., Makitie, O., Barclay, C., Chan, C., Depalma, S.R., Bastepe, M., . . . Juppner, H., *A novel COL1A1 mutation in infantile cortical hyperostosis (Caffey disease) expands the spectrum of collagen-related disorders*. J Clin Invest, 2005. **115**(5): p. 1250-7.

147. Kamoun-Goldrat, A., Martinovic, J., Saada, J., Sonigo-Cohen, P., Razavi, F., Munnich, A., and Le Merrer, M., *Prenatal cortical hyperostosis with COL1A1 gene mutation*. Am J Med Genet A, 2008. **146A**(14): p. 1820-4.
148. Cucchiari, M., de Girolamo, L., Filardo, G., Oliveira, J.M., Orth, P., Pape, D., and Reboul, P., *Basic science of osteoarthritis*. J Exp Orthop, 2016. **3**(1): p. 22.
149. Devez, L.A. and Loeser, R.F., *Is osteoarthritis one disease or a collection of many?* Rheumatology (Oxford), 2018. **57**(suppl_4): p. iv34-iv42.
150. Martel-Pelletier, J., Barr, A.J., Cicuttini, F.M., Conaghan, P.G., Cooper, C., Goldring, M.B., . . . Pelletier, J.P., *Osteoarthritis*. Nat Rev Dis Primers, 2016. **2**: p. 16072.
151. Poole, A.R., *Osteoarthritis as a whole joint disease*. HSS J, 2012. **8**(1): p. 4-6.
152. Zhang, Y. and Jordan, J.M., *Epidemiology of osteoarthritis*. Clin Geriatr Med, 2010. **26**(3): p. 355-69.
153. Buckwalter, J.A. and Martin, J.A., *Osteoarthritis*. Adv Drug Deliv Rev, 2006. **58**(2): p. 150-67.
154. Kellgren, J. and Lawrence, J., *Atlas of standard radiographs. The epidemiology of chronic rheumatism*. Vol. 2. 1963, Oxford: Blackwell Scientific Publications.
155. Kellgren, J.H. and Lawrence, J.S., *Radiological assessment of osteo-arthrosis*. Ann Rheum Dis, 1957. **16**(4): p. 494-502.
156. Bijlsma, J.W., Berenbaum, F., and Lafeber, F.P., *Osteoarthritis: an update with relevance for clinical practice*. Lancet, 2011. **377**(9783): p. 2115-26.
157. Bedson, J. and Croft, P.R., *The discordance between clinical and radiographic knee osteoarthritis: a systematic search and summary of the literature*. BMC Musculoskelet Disord, 2008. **9**: p. 116.
158. Gunn, C., *Bones and Joints* 7th ed. 2017: Elsevier
159. Petersson, I.F., *Occurrence of osteoarthritis of the peripheral joints in European populations*. Ann Rheum Dis, 1996. **55**(9): p. 659-61.
160. Hunter, D.J. and Eckstein, F., *Exercise and osteoarthritis*. J Anat, 2009. **214**(2): p. 197-207.
161. Loeser, R.F., Goldring, S.R., Scanzello, C.R., and Goldring, M.B., *Osteoarthritis: a disease of the joint as an organ*. Arthritis Rheum, 2012. **64**(6): p. 1697-707.
162. Wieland, H.A., Michaelis, M., Kirschbaum, B.J., and Rudolph, K.A., *Osteoarthritis - an untreatable disease?* Nat Rev Drug Discov, 2005. **4**(4): p. 331-44.
163. Pearle, A.D., Warren, R.F., and Rodeo, S.A., *Basic science of articular cartilage and osteoarthritis*. Clin Sports Med, 2005. **24**(1): p. 1-12.
164. Sophia Fox, A.J., Bedi, A., and Rodeo, S.A., *The basic science of articular cartilage: structure, composition, and function*. Sports Health, 2009. **1**(6): p. 461-8.
165. Buckwalter, J.A. and Mankin, H.J., *Articular cartilage: tissue design and chondrocyte-matrix interactions*. Instr Course Lect, 1998. **47**: p. 477-86.
166. Goldring, M.B., *Osteoarthritis and cartilage: the role of cytokines*. Curr Rheumatol Rep, 2000. **2**(6): p. 459-65.
167. Akkiraju, H. and Nohe, A., *Role of Chondrocytes in Cartilage Formation, Progression of Osteoarthritis and Cartilage Regeneration*. Journal of developmental biology, 2015. **3**(4): p. 177-192.
168. Soltz, M.A. and Ateshian, G.A., *Interstitial fluid pressurization during confined compression cyclical loading of articular cartilage*. Ann Biomed Eng, 2000. **28**(2): p. 150-9.
169. Sancho-Tello, M., Milián, L., Mata Roig, M., Martín de Llano, J.J., and Carda, C., *Chapter 18 - Cartilage Regeneration and Tissue Engineering*, in *Advances in Biomechanics and Tissue Regeneration*, M.H. Doweidar, Editor. 2019, Academic Press. p. 361-378.
170. Chen, F.H., Rousche, K.T., and Tuan, R.S., *Technology Insight: adult stem cells in cartilage regeneration and tissue engineering*. Nat Clin Pract Rheumatol, 2006. **2**(7): p. 373-82.
171. Buckwalter, J.A., Mow, V.C., and Ratcliffe, A., *Restoration of Injured or Degenerated Articular Cartilage*. J Am Acad Orthop Surg, 1994. **2**(4): p. 192-201.
172. Poole, C.A., *Articular cartilage chondrons: form, function and failure*. J Anat, 1997. **191 (Pt 1)**: p. 1-13.
173. Vincent, T.L., *Targeting mechanotransduction pathways in osteoarthritis: a focus on the pericellular matrix*. Curr Opin Pharmacol, 2013. **13**(3): p. 449-54.
174. Alexopoulos, L.G., Setton, L.A., and Guilak, F., *The biomechanical role of the chondrocyte pericellular matrix in articular cartilage*. Acta Biomaterialia, 2005. **1**(3): p. 317-325.
175. Muir, H., *The chondrocyte, architect of cartilage. Biomechanics, structure, function and molecular biology of cartilage matrix macromolecules*. Bioessays, 1995. **17**(12): p. 1039-48.

176. Knudson, W., Ishizuka, S., Terabe, K., Askew, E.B., and Knudson, C.B., *The pericellular hyaluronan of articular chondrocytes*. Matrix Biol, 2019. **78-79**: p. 32-46.
177. Mueller, M.B. and Tuan, R.S., *Anabolic/Catabolic balance in pathogenesis of osteoarthritis: identifying molecular targets*. PM R, 2011. **3**(6 Suppl 1): p. S3-11.
178. Kokebie, R., Aggarwal, R., Lidder, S., Hakimiyan, A.A., Rueger, D.C., Block, J.A., and Chubinskaya, S., *The role of synovial fluid markers of catabolism and anabolism in osteoarthritis, rheumatoid arthritis and asymptomatic organ donors*. Arthritis Research & Therapy, 2011. **13**(2): p. R50.
179. Mueller, M.B. and Tuan, R.S., *Anabolic/Catabolic Balance in Pathogenesis of Osteoarthritis: Identifying Molecular Targets*. PM&R, 2011. **3**(6S): p. S3-S11.
180. Oegema, T.R., Carpenter, R.J., Hofmeister, F., and Thompson, R.C., *The interaction of the zone of calcified cartilage and subchondral bone in osteoarthritis*. Microscopy Research and Technique, 1997. **37**(4): p. 324-332.
181. Madry, H., van Dijk, C.N., and Mueller-Gerbl, M., *The basic science of the subchondral bone*. Knee Surg Sports Traumatol Arthrosc, 2010. **18**(4): p. 419-33.
182. Goldring, M.B. and Goldring, S.R., *Articular cartilage and subchondral bone in the pathogenesis of osteoarthritis*. Ann N Y Acad Sci, 2010. **1192**: p. 230-7.
183. Li, G., Yin, J., Gao, J., Cheng, T.S., Pavlos, N.J., Zhang, C., and Zheng, M.H., *Subchondral bone in osteoarthritis: insight into risk factors and microstructural changes*. Arthritis Res Ther, 2013. **15**(6): p. 223.
184. Castaneda, S., Roman-Blas, J.A., Largo, R., and Herrero-Beaumont, G., *Subchondral bone as a key target for osteoarthritis treatment*. Biochem Pharmacol, 2012. **83**(3): p. 315-23.
185. Goldring, S.R., *Role of bone in osteoarthritis pathogenesis*. Med Clin North Am, 2009. **93**(1): p. 25-35, xv.
186. Li, F., Tang, Y., Song, B., Yu, M., Li, Q., Zhang, C., . . . Yang, R., *Nomenclature clarification: synovial fibroblasts and synovial mesenchymal stem cells*. Stem Cell Res Ther, 2019. **10**(1): p. 260.
187. Johnston, S.A., *Osteoarthritis: Joint Anatomy, Physiology, and Pathobiology*. Veterinary Clinics of North America: Small Animal Practice, 1997. **27**(4): p. 699-723.
188. Iwanaga, T., Shikichi, M., Kitamura, H., Yanase, H., and Nozawa-Inoue, K., *Morphology and functional roles of synoviocytes in the joint*. Arch Histol Cytol, 2000. **63**(1): p. 17-31.
189. Tamer, T.M., *Hyaluronan and synovial joint: function, distribution and healing*. Interdiscip Toxicol, 2013. **6**(3): p. 111-25.
190. Fox, A.J., Bedi, A., and Rodeo, S.A., *The basic science of human knee menisci: structure, composition, and function*. Sports Health, 2012. **4**(4): p. 340-51.
191. Makris, E.A., Hadidi, P., and Athanasiou, K.A., *The knee meniscus: structure-function, pathophysiology, current repair techniques, and prospects for regeneration*. Biomaterials, 2011. **32**(30): p. 7411-31.
192. Hunter, D.J. and Bierma-Zeinstra, S., *Osteoarthritis*. Lancet, 2019. **393**(10182): p. 1745-1759.
193. Glyn-Jones, S., Palmer, A.J., Agricola, R., Price, A.J., Vincent, T.L., Weinans, H., and Carr, A.J., *Osteoarthritis*. Lancet, 2015. **386**(9991): p. 376-87.
194. Heijink, A., Gomoll, A.H., Madry, H., Drobnic, M., Filardo, G., Espregueira-Mendes, J., and Van Dijk, C.N., *Biomechanical considerations in the pathogenesis of osteoarthritis of the knee*. Knee Surg Sports Traumatol Arthrosc, 2012. **20**(3): p. 423-35.
195. Man, G.S. and Mologhianu, G., *Osteoarthritis pathogenesis - a complex process that involves the entire joint*. J Med Life, 2014. **7**(1): p. 37-41.
196. Felson, D.T. and Neogi, T., *Osteoarthritis: is it a disease of cartilage or of bone?* Arthritis Rheum, 2004. **50**(2): p. 341-4.
197. Cox, L.G., van Donkelaar, C.C., van Rietbergen, B., Emans, P.J., and Ito, K., *Alterations to the subchondral bone architecture during osteoarthritis: bone adaptation vs endochondral bone formation*. Osteoarthritis Cartilage, 2013. **21**(2): p. 331-8.
198. Uchino, M., Izumi, T., Tominaga, T., Wakita, R., Minehara, H., Sekiguchi, M., and Itoman, M., *Growth factor expression in the osteophytes of the human femoral head in osteoarthritis*. Clin Orthop Relat Res, 2000(377): p. 119-25.
199. Blaney Davidson, E.N., Vitters, E.L., van Beuningen, H.M., van de Loo, F.A., van den Berg, W.B., and van der Kraan, P.M., *Resemblance of osteophytes in experimental osteoarthritis to transforming growth factor beta-induced osteophytes: limited role of bone morphogenetic protein in early osteoarthritic osteophyte formation*. Arthritis Rheum, 2007. **56**(12): p. 4065-73.
200. van der Kraan, P.M. and van den Berg, W.B., *Osteophytes: relevance and biology*. Osteoarthritis Cartilage, 2007. **15**(3): p. 237-44.

201. Brandt, K.D., *Osteophytes in osteoarthritis. Clinical aspects*. Osteoarthritis Cartilage, 1999. **7**(3): p. 334-5.
202. Abramson, S.B., *Inflammation in osteoarthritis*. J Rheumatol Suppl, 2004. **70**: p. 70-6.
203. Bondeson, J., Wainwright, S.D., Lauder, S., Amos, N., and Hughes, C.E., *The role of synovial macrophages and macrophage-produced cytokines in driving aggrecanases, matrix metalloproteinases, and other destructive and inflammatory responses in osteoarthritis*. Arthritis Res Ther, 2006. **8**(6): p. R187.
204. Mapp, P.I., *Innervation of the synovium*. Ann Rheum Dis, 1995. **54**(5): p. 398-403.
205. Stecher, R.M. and Hersh, A.H., *Heberden's Nodes: The Mechanism of Inheritance in Hypertrophic Arthritis of the Fingers*. J Clin Invest, 1944. **23**(5): p. 699-704.
206. Spector, T.D., Cicuttini, F., Baker, J., Loughlin, J., and Hart, D., *Genetic influences on osteoarthritis in women: a twin study*. BMJ, 1996. **312**(7036): p. 940-3.
207. Valdes, A.M. and Spector, T.D., *The contribution of genes to osteoarthritis*. Rheum Dis Clin North Am, 2008. **34**(3): p. 581-603.
208. Cornelis, F.M., Luyten, F.P., and Lories, R.J., *Functional effects of susceptibility genes in osteoarthritis*. Discov Med, 2011. **12**(63): p. 129-39.
209. Spector, T.D. and MacGregor, A.J., *Risk factors for osteoarthritis: genetics*. Osteoarthritis Cartilage, 2004. **12 Suppl A**: p. S39-44.
210. Fernandez-Moreno, M., Rego, I., Carreira-Garcia, V., and Blanco, F.J., *Genetics in osteoarthritis*. Curr Genomics, 2008. **9**(8): p. 542-7.
211. Yucesoy, B., Charles, L.E., Baker, B., and Burchfiel, C.M., *Occupational and genetic risk factors for osteoarthritis: a review*. Work, 2015. **50**(2): p. 261-73.
212. Evangelou, E., Valdes, A.M., Kerkhof, H.J., Styrkarsdottir, U., Zhu, Y., Meulenbelt, I., . . . Translation Research in Europe Applied Technologies for, O., *Meta-analysis of genome-wide association studies confirms a susceptibility locus for knee osteoarthritis on chromosome 7q22*. Ann Rheum Dis, 2011. **70**(2): p. 349-55.
213. Kerkhof, H.J., Lories, R.J., Meulenbelt, I., Jonsdottir, I., Valdes, A.M., Arp, P., . . . van Meurs, J.B., *A genome-wide association study identifies an osteoarthritis susceptibility locus on chromosome 7q22*. Arthritis Rheum, 2010. **62**(2): p. 499-510.
214. Reynard, L.N. and Barter, M.J., *Osteoarthritis year in review 2019: genetics, genomics and epigenetics*. Osteoarthritis Cartilage, 2020. **28**(3): p. 275-284.
215. Ratneswaran, A. and Kapoor, M., *Osteoarthritis year in review: genetics, genomics, epigenetics*. Osteoarthritis Cartilage, 2021. **29**(2): p. 151-160.
216. Shane Anderson, A. and Loeser, R.F., *Why is osteoarthritis an age-related disease? Best practice & research*. Clinical rheumatology, 2010. **24**(1): p. 15-26.
217. Jin, W.S., Choi, E.J., Lee, S.Y., Bae, E.J., Lee, T.-H., and Park, J., *Relationships among Obesity, Sarcopenia, and Osteoarthritis in the Elderly*. Journal of obesity & metabolic syndrome, 2017. **26**(1): p. 36-44.
218. Wu, W., Billinghamurst, R.C., Pidoux, I., Antoniou, J., Zukor, D., Tanzer, M., and Poole, A.R., *Sites of collagenase cleavage and denaturation of type II collagen in aging and osteoarthritic articular cartilage and their relationship to the distribution of matrix metalloproteinase 1 and matrix metalloproteinase 13*. Arthritis Rheum, 2002. **46**(8): p. 2087-94.
219. Campisi, J. and d'Adda di Fagagna, F., *Cellular senescence: when bad things happen to good cells*. Nature Reviews Molecular Cell Biology, 2007. **8**(9): p. 729-740.
220. Cope, P.J., Ourradi, K., Li, Y., and Sharif, M., *Models of osteoarthritis: the good, the bad and the promising*. Osteoarthritis Cartilage, 2019. **27**(2): p. 230-239.
221. Samvelyan, H.J., Hughes, D., Stevens, C., and Staines, K.A., *Models of Osteoarthritis: Relevance and New Insights*. Calcif Tissue Int, 2020.
222. Vincent, T.L., Williams, R.O., Maciewicz, R., Silman, A., Garside, P., and Arthritis Research, U.K.a.m.w.g., *Mapping pathogenesis of arthritis through small animal models*. Rheumatology (Oxford), 2012. **51**(11): p. 1931-41.
223. Jaeger, K., Selent, C., Jaehme, W., Mahr, S., Goebel, U., Ibrahim, S., . . . Mueller-Hilke, B., *The genetics of osteoarthritis in STR/ort mice*. Osteoarthritis Cartilage, 2008. **16**(5): p. 607-14.
224. Staines, K.A., Poulet, B., Wentworth, D.N., and Pitsillides, A.A., *The STR/ort mouse model of spontaneous osteoarthritis - an update*. Osteoarthritis Cartilage, 2017. **25**(6): p. 802-808.
225. Poulet, B., Westerhof, T.A., Hamilton, R.W., Shefelbine, S.J., and Pitsillides, A.A., *Spontaneous osteoarthritis in Str/ort mice is unlikely due to greater vulnerability to mechanical trauma*. Osteoarthritis Cartilage, 2013. **21**(5): p. 756-63.

226. Russell, W.L., Kelly, E.M., Hunsicker, P.R., Bangham, J.W., Maddux, S.C., and Phipps, E.L., *Specific-locus test shows ethylnitrosourea to be the most potent mutagen in the mouse*. Proc Natl Acad Sci U S A, 1979. **76**(11): p. 5818-9.
227. Hitotsumachi, S., Carpenter, D.A., and Russell, W.L., *Dose-repetition increases the mutagenic effectiveness of N-ethyl-N-nitrosourea in mouse spermatogonia*. Proc Natl Acad Sci U S A, 1985. **82**(19): p. 6619-21.
228. Justice, M.J., Noveroske, J.K., Weber, J.S., Zheng, B., and Bradley, A., *Mouse ENU mutagenesis*. Hum Mol Genet, 1999. **8**(10): p. 1955-63.
229. Bielas, J.H. and Heddle, J.A., *Proliferation is necessary for both repair and mutation in transgenic mouse cells*. Proc Natl Acad Sci U S A, 2000. **97**(21): p. 11391-6.
230. Favor, J., *The mutagenic activity of ethylnitrosourea at low doses in spermatogonia of the mouse as assessed by the specific-locus test*. Mutat Res, 1998. **405**(2): p. 221-6.
231. Blease, A., Nicol, T., Falcone, S., Starbuck, B., Greenaway, S., Hutchinson, M., and Potter, P.K., *Generation and Identification of Mutations Resulting in Chronic and Age-Related Phenotypes in Mice*. Curr Protoc Mouse Biol, 2018. **8**(2): p. e42.
232. Coghill, E.L., Hugill, A., Parkinson, N., Davison, C., Glenister, P., Clements, S., . . . Brown, S.D., *A gene-driven approach to the identification of ENU mutants in the mouse*. Nat Genet, 2002. **30**(3): p. 255-6.
233. Concepcion, D., Seburn, K.L., Wen, G., Frankel, W.N., and Hamilton, B.A., *Mutation rate and predicted phenotypic target sizes in ethylnitrosourea-treated mice*. Genetics, 2004. **168**(2): p. 953-9.
234. Takahasi, K.R., Sakuraba, Y., and Gondo, Y., *Mutational pattern and frequency of induced nucleotide changes in mouse ENU mutagenesis*. BMC Mol Biol, 2007. **8**: p. 52.
235. Nolan, P.M., Peters, J., Strivens, M., Rogers, D., Hagan, J., Spurr, N., . . . Hunter, J., *A systematic, genome-wide, phenotype-driven mutagenesis programme for gene function studies in the mouse*. Nat Genet, 2000. **25**(4): p. 440-3.
236. Hrabe de Angelis, M.H., Flaswinkel, H., Fuchs, H., Rathkolb, B., Soewarto, D., Marschall, S., . . . Balling, R., *Genome-wide, large-scale production of mutant mice by ENU mutagenesis*. Nat Genet, 2000. **25**(4): p. 444-7.
237. Brown, S.D.M., *Advances in mouse genetics for the study of human disease*. Hum Mol Genet, 2021.
238. Potter, P.K., Bowl, M.R., Jeyarajan, P., Wisby, L., Blease, A., Goldsworthy, M.E., . . . Brown, S.D., *Novel gene function revealed by mouse mutagenesis screens for models of age-related disease*. Nat Commun, 2016. **7**: p. 12444.
239. Li, H. and Durbin, R., *Fast and accurate short read alignment with Burrows-Wheeler transform*. Bioinformatics, 2009. **25**(14): p. 1754-60.
240. McKenna, A., Hanna, M., Banks, E., Sivachenko, A., Cibulskis, K., Kernytsky, A., . . . DePristo, M.A., *The Genome Analysis Toolkit: a MapReduce framework for analyzing next-generation DNA sequencing data*. Genome Res, 2010. **20**(9): p. 1297-303.
241. Huang, H., Zhang, J., Sun, K., Zhang, X., and Tian, S., *Effects of repetitive multiple freeze-thaw cycles on the biomechanical properties of human flexor digitorum superficialis and flexor pollicis longus tendons*. Clin Biomech (Bristol, Avon), 2011. **26**(4): p. 419-23.
242. Wong, M.D., Dazai, J., Walls, J.R., Gale, N.W., and Henkelman, R.M., *Design and implementation of a custom built optical projection tomography system*. PLoS One, 2013. **8**(9): p. e73491.
243. Blease, A., Das Neves Borges, P., Curtinha, M., Javaheri, B., von Loga, I.S., Parisi, I., . . . Potter, P.K., *Studying Osteoarthritis Pathogenesis in Mice*. Curr Protoc Mouse Biol, 2018. **8**(4): p. e50.
244. Percie du Sert, N., Hurst, V., Ahluwalia, A., Alam, S., Avey, M.T., Baker, M., . . . Würbel, H., *The ARRIVE guidelines 2.0: Updated guidelines for reporting animal research*. PLOS Biology, 2020. **18**(7): p. e3000410.
245. Brown, S.D. and Nolan, P.M., *Mouse mutagenesis-systematic studies of mammalian gene function*. Hum Mol Genet, 1998. **7**(10): p. 1627-33.
246. Meynert, A.M., Ansari, M., FitzPatrick, D.R., and Taylor, M.S., *Variant detection sensitivity and biases in whole genome and exome sequencing*. BMC Bioinformatics, 2014. **15**: p. 247.
247. Simon, M.M., Mallon, A.-M., Howell, G.R., and Reinholdt, L.G., *High throughput sequencing approaches to mutation discovery in the mouse*. Mammalian genome : official journal of the International Mammalian Genome Society, 2012. **23**(9-10): p. 499-513.
248. Miko, I., *Gregor Mendel and the Principles of Inheritance*. Nature Education, 2008. **1**(1).

249. Strachan, T. and Read, A., *Mendelian pedigree patterns*, in *Human molecular genetics*. 2004, Garland Science: New York.
250. Scheiber, A.L., Guess, A.J., Kaito, T., Abzug, J.M., Enomoto-Iwamoto, M., Leikin, S., . . . Otsuru, S., *Endoplasmic reticulum stress is induced in growth plate hypertrophic chondrocytes in G610C mouse model of osteogenesis imperfecta*. *Biochem Biophys Res Commun*, 2019. **509**(1): p. 235-240.
251. Tateossian, H., Morse, S., Simon, M.M., Dean, C.H., and Brown, S.D., *Interactions between the otitis media gene, Fbxo11, and p53 in the mouse embryonic lung*. *Dis Model Mech*, 2015. **8**(12): p. 1531-42.
252. Rigueur, D. and Lyons, K.M., *Whole-mount skeletal staining*. *Methods Mol Biol*, 2014. **1130**: p. 113-121.
253. Boskey, A.L. and Imbert, L., *Bone quality changes associated with aging and disease: a review*. *Ann N Y Acad Sci*, 2017. **1410**(1): p. 93-106.
254. Legrand, E., Chappard, D., Pascaretti, C., Duquenne, M., Krebs, S., Rohmer, V., . . . Audran, M., *Trabecular bone microarchitecture, bone mineral density, and vertebral fractures in male osteoporosis*. *J Bone Miner Res*, 2000. **15**(1): p. 13-9.
255. Pritzker, K.P., Gay, S., Jimenez, S.A., Ostergaard, K., Pelletier, J.P., Revell, P.A., . . . van den Berg, W.B., *Osteoarthritis cartilage histopathology: grading and staging*. *Osteoarthritis Cartilage*, 2006. **14**(1): p. 13-29.
256. Liu, L., Stephens, B., Bergman, M., May, A., and Chiang, T., *Role of Collagen in Airway Mechanics*. *Bioengineering (Basel)*, 2021. **8**(1).
257. Ramos-Mucci, L., Javaheri, B., van 't Hof, R., Bou-Gharios, G., Pitsillides, A.A., Comerford, E., and Poulet, B., *Meniscal and ligament modifications in spontaneous and post-traumatic mouse models of osteoarthritis*. *Arthritis Research & Therapy*, 2020. **22**(1): p. 171.
258. Mellis, D., Staines, K.A., Peluso, S., Georgiou, I.C., Dora, N., Kubiak, M., . . . Ditzel, M., *Ubiquitin-protein ligase Ubr5 cooperates with hedgehog signalling to promote skeletal tissue homeostasis*. *PLoS Genet*, 2021. **17**(4): p. e1009275.
259. Sinder, B.P., White, L.E., Salemi, J.D., Ominsky, M.S., Caird, M.S., Marini, J.C., and Kozloff, K.M., *Adult Brtl/+ mouse model of osteogenesis imperfecta demonstrates anabolic response to sclerostin antibody treatment with increased bone mass and strength*. *Osteoporos Int*, 2014. **25**(8): p. 2097-107.
260. Sinder, B.P., Salemi, J.D., Ominsky, M.S., Caird, M.S., Marini, J.C., and Kozloff, K.M., *Rapidly growing Brtl/+ mouse model of osteogenesis imperfecta improves bone mass and strength with sclerostin antibody treatment*. *Bone*, 2015. **71**: p. 115-23.
261. Sun, Y., Mauerhan, D.R., Honeycutt, P.R., Kneisl, J.S., Norton, H.J., Zinchenko, N., . . . Gruber, H.E., *Calcium deposition in osteoarthritic meniscus and meniscal cell culture*. *Arthritis research & therapy*, 2010. **12**(2): p. R56-R56.
262. MacMullan, P.A. and McCarthy, G.M., *The meniscus, calcification and osteoarthritis: a pathologic team*. *Arthritis Research & Therapy*, 2010. **12**(3): p. 116.
263. Thorpe, C.T., Birch, H.L., Clegg, P.D., and Screen, H.R.C., *The role of the non-collagenous matrix in tendon function*. *International Journal of Experimental Pathology*, 2013. **94**(4): p. 248-259.
264. Alexander, R.M., *Tendon elasticity and muscle function*. *Comp Biochem Physiol A Mol Integr Physiol*, 2002. **133**(4): p. 1001-11.
265. Peltonen, J., Cronin, N.J., Stenroth, L., Finni, T., and Avela, J., *Viscoelastic properties of the Achilles tendon in vivo*. *Springerplus*, 2013. **2**(1): p. 212.
266. Sarver, D.C., Kharaz, Y.A., Sugg, K.B., Gumucio, J.P., Comerford, E., and Mendias, C.L., *Sex differences in tendon structure and function*. *Journal of Orthopaedic Research*, 2017. **35**(10): p. 2117-2126.
267. Deckard, C., Walker, A., and Hill, B.J., *Using three-point bending to evaluate tibia bone strength in ovariectomized young mice*. *J Biol Phys*, 2017. **43**(1): p. 139-148.
268. Orwoll, E.S., Belknap, J.K., and Klein, R.F., *Gender specificity in the genetic determinants of peak bone mass*. *J Bone Miner Res*, 2001. **16**(11): p. 1962-71.
269. Ghorbel-Feki, H., Masood, A., Caliez, M., Gratton, M., Pittet, J.C., Lints, M., and Dos Santos, S., *Acousto-mechanical behaviour of ex-vivo skin: Nonlinear and viscoelastic properties*. *Comptes Rendus Mécanique*, 2019. **347**(3): p. 218-227.
270. Lu, X.L., Mow, V.C., and Guo, X.E., *Proteoglycans and mechanical behavior of condylar cartilage*. *J Dent Res*, 2009. **88**(3): p. 244-8.

271. Nash, A., Notou, M., Lopez-Clavijo, A.F., Bozec, L., de Leeuw, N.H., and Birch, H.L., *Glucosepane is associated with changes to structural and physical properties of collagen fibrils*. Matrix Biol Plus, 2019. **4**: p. 100013.
272. Canty-Laird, E.G., Lu, Y., and Kadler, K.E., *Stepwise proteolytic activation of type I procollagen to collagen within the secretory pathway of tendon fibroblasts in situ*. Biochem J, 2012. **441**(2): p. 707-17.
273. Starborg, T., Kalson, N.S., Lu, Y., Mironov, A., Cootes, T.F., Holmes, D.F., and Kadler, K.E., *Using transmission electron microscopy and 3View to determine collagen fibril size and three-dimensional organization*. Nat Protoc, 2013. **8**(7): p. 1433-48.
274. Chavez-Valdez, R., Flock, D.L., Martin, L.J., and Northington, F.J., *Endoplasmic reticulum pathology and stress response in neurons precede programmed necrosis after neonatal hypoxia-ischemia*. Int J Dev Neurosci, 2016. **48**: p. 58-70.
275. Wang, Y., Osakue, D., Yang, E., Zhou, Y., Gong, H., Xia, X., and Du, Y., *Endoplasmic Reticulum Stress Response of Trabecular Meshwork Stem Cells and Trabecular Meshwork Cells and Protective Effects of Activated PERK Pathway*. Invest Ophthalmol Vis Sci, 2019. **60**(1): p. 265-273.
276. Kung, L.H.W., Mullan, L., Soul, J., Wang, P., Mori, K., Bateman, J.F., . . . Boot-Handford, R.P., *Cartilage endoplasmic reticulum stress may influence the onset but not the progression of experimental osteoarthritis*. Arthritis Research & Therapy, 2019. **21**(1): p. 206.
277. Nugent, A.E., Speicher, D.M., Gradisar, I., McBurney, D.L., Baraga, A., Doane, K.J., and Horton, W.E., Jr., *Advanced osteoarthritis in humans is associated with altered collagen VI expression and upregulation of ER-stress markers Grp78 and bag-1*. J Histochem Cytochem, 2009. **57**(10): p. 923-31.
278. Glasson, S.S., Blanchet, T.J., and Morris, E.A., *The surgical destabilization of the medial meniscus (DMM) model of osteoarthritis in the 129/SvEv mouse*. Osteoarthritis Cartilage, 2007. **15**(9): p. 1061-9.
279. Glasson, S.S., Chambers, M.G., Van Den Berg, W.B., and Little, C.B., *The OARSI histopathology initiative - recommendations for histological assessments of osteoarthritis in the mouse*. Osteoarthritis Cartilage, 2010. **18 Suppl 3**: p. S17-23.
280. Bogan, R., Riddle, R.C., Li, Z., Kumar, S., Nandal, A., Faugere, M.C., . . . Clemens, T.L., *A mouse model for human osteogenesis imperfecta type VI*. J Bone Miner Res, 2013. **28**(7): p. 1531-6.
281. Pierard, G.E., Pierard, S., Delvenne, P., and Pierard-Franchimont, C., *In vivo evaluation of the skin tensile strength by the suction method: pilot study coping with hysteresis and creep extension*. ISRN Dermatol, 2013. **2013**: p. 841217.
282. Nielsen, R.H., Coupe, C., Jensen, J.K., Olsen, M.R., Heinemeier, K.M., Malfait, F., . . . Kjaer, M., *Low tendon stiffness and abnormal ultrastructure distinguish classic Ehlers-Danlos syndrome from benign joint hypermobility syndrome in patients*. FASEB J, 2014. **28**(11): p. 4668-76.
283. Misof, K., Landis, W.J., Klaushofer, K., and Fratzl, P., *Collagen from the osteogenesis imperfecta mouse model (oim) shows reduced resistance against tensile stress*. The Journal of clinical investigation, 1997. **100**(1): p. 40-45.
284. McBride, D.J., Jr., Choe, V., Shapiro, J.R., and Brodsky, B., *Altered collagen structure in mouse tail tendon lacking the alpha 2(I) chain*. J Mol Biol, 1997. **270**(2): p. 275-84.
285. Reuvers, J., Thoreson, A.R., Zhao, C., Zhang, L., Jay, G.D., An, K.-N., . . . Amadio, P.C., *The mechanical properties of tail tendon fascicles from lubricin knockout, wild type and heterozygous mice*. Journal of structural biology, 2011. **176**(1): p. 41-45.
286. Lin, J.H., Walter, P., and Yen, T.S.B., *Endoplasmic reticulum stress in disease pathogenesis*. Annual review of pathology, 2008. **3**: p. 399-425.
287. Singhal, P.K., Sassi, S., Lan, L., Au, P., Halvorsen, S.C., Fukumura, D., . . . Seed, B., *Mouse embryonic fibroblasts exhibit extensive developmental and phenotypic diversity*. Proceedings of the National Academy of Sciences, 2016. **113**(1): p. 122.
288. Angwin, C., Ghali, N., Baker, D., Brady, A.F., Pope, F.M., Vandersteen, A., . . . van Dijk, F.S., *Electron microscopy in the diagnosis of Ehlers-Danlos syndromes: correlation with clinical and genetic investigations*. Br J Dermatol, 2020. **182**(3): p. 698-707.
289. Wechsler, H.L. and Fisher, E.R., *EHLERS-DANLOS SYNDROME. PATHOLOGIC, HISTOCHEMICAL AND ELECTRON MICROSCOPIC OBSERVATIONS*. Arch Pathol, 1964. **77**: p. 613-9.
290. Cole, W.G. and Mäkitie, O., *Primary Disorders of Connective Tissue*, in *Textbook of Pediatric Rheumatology*. 2016, Elsevier. p. 706-719.

291. Hughes, A., Oxford, A.E., Tawara, K., Jorczyk, C.L., and Oxford, J.T., *Endoplasmic Reticulum Stress and Unfolded Protein Response in Cartilage Pathophysiology; Contributing Factors to Apoptosis and Osteoarthritis*. Int J Mol Sci, 2017. **18**(3).
292. Acevedo-Arozena, A., Wells, S., Potter, P., Kelly, M., Cox, R.D., and Brown, S.D., *ENU mutagenesis, a way forward to understand gene function*. Annu Rev Genomics Hum Genet, 2008. **9**: p. 49-69.
293. Quintana, L. and Sharpe, J., *Optical projection tomography of vertebrate embryo development*. Cold Spring Harb Protoc, 2011. **2011**(6): p. 586-94.
294. Schnieke, A., Harbers, K., and Jaenisch, R., *Embryonic lethal mutation in mice induced by retrovirus insertion into the alpha 1(I) collagen gene*. Nature, 1983. **304**(5924): p. 315-20.
295. Cesar, R., Boffa, R.S., Fachine, L.T., Leivas, T.P., Silva, A.M.H., Pereira, C.A.M., . . . Rollo, J.M.D.A., *Evaluation of Trabecular Microarchitecture of Normal Osteoporotic and Osteopenic Human Vertebrae*. Procedia Engineering, 2013. **59**: p. 6-15.
296. Lee, K.J., Rambault, L., Bou-Gharios, G., Clegg, P.D., Akhtar, R., Czanner, G., . . . Canty-Laird, E.G., *Collagen (I) homotrimer potentiates the osteogenesis imperfecta (oim) mutant allele and reduces survival in male mice*. bioRxiv 2020.
297. Miles, C.A. and Ghelashvili, M., *Polymer-in-a-Box Mechanism for the Thermal Stabilization of Collagen Molecules in Fibers*. Biophysical Journal, 1999. **76**(6): p. 3243-3252.
298. Shirley, E.D., Demaio, M., and Bodurtha, J., *Ehlers-danlos syndrome in orthopaedics: etiology, diagnosis, and treatment implications*. Sports Health, 2012. **4**(5): p. 394-403.
299. Murakami, Y., Morino, T., Hino, M., Misaki, H., and Miura, H., *Progression of Ossification of the Anterior Longitudinal Ligament Associated With Diffuse Idiopathic Skeletal Hyperostosis by Age: A Study of Computed Tomography Findings Over 5 Years*. Global Spine J, 2021. **11**(5): p. 656-661.
300. Uchida, K., Yayama, T., Cai, H.-X., Nakajima, H., Sugita, D., Guerrero, A.R., . . . Baba, H., *Ossification process involving the human thoracic ligamentum flavum: role of transcription factors*. Arthritis research & therapy, 2011. **13**(5): p. R144-R144.
301. Nalbant, S., Martinez, J.A., Kitumnuaypong, T., Clayburne, G., Sieck, M., and Schumacher, H.R., Jr., *Synovial fluid features and their relations to osteoarthritis severity: new findings from sequential studies*. Osteoarthritis Cartilage, 2003. **11**(1): p. 50-4.
302. Yan, J.-f., Qin, W.-p., Xiao, B.-c., Wan, Q.-q., Tay, F.R., Niu, L.-n., and Jiao, K., *Pathological calcification in osteoarthritis: an outcome or a disease initiator?* Biological Reviews, 2020. **95**(4): p. 960-985.
303. de Seny, D., Bianchi, E., Baiwir, D., Cobraiville, G., Collin, C., Delière, M., . . . Malaise, M.G., *Proteins involved in the endoplasmic reticulum stress are modulated in synovitis of osteoarthritis, chronic pyrophosphate arthropathy and rheumatoid arthritis, and correlate with the histological inflammatory score*. Scientific Reports, 2020. **10**(1): p. 14159.
304. Tabeta, K., Du, X., Arimatsu, K., Yokoji, M., Takahashi, N., Amizuka, N., . . . Beutler, B., *An ENU-induced splice site mutation of mouse Col1a1 causing recessive osteogenesis imperfecta and revealing a novel splicing rescue*. Scientific Reports, 2017. **7**(1): p. 11717.
305. Korkko, J., Ala-Kokko, L., De Paepe, A., Nuytinck, L., Earley, J., and Prockop, D.J., *Analysis of the COL1A1 and COL1A2 genes by PCR amplification and scanning by conformation-sensitive gel electrophoresis identifies only COL1A1 mutations in 15 patients with osteogenesis imperfecta type I: identification of common sequences of null-allele mutations*. Am J Hum Genet, 1998. **62**(1): p. 98-110.
306. Lindahl, K., Astrom, E., Rubin, C.J., Grigelioniene, G., Malmgren, B., Ljunggren, O., and Kindmark, A., *Genetic epidemiology, prevalence, and genotype-phenotype correlations in the Swedish population with osteogenesis imperfecta*. Eur J Hum Genet, 2015. **23**(8): p. 1042-50.
307. Meyers, C., Lisiecki, J., Miller, S., Levin, A., Fayad, L., Ding, C., . . . James, A.W., *Heterotopic Ossification: A Comprehensive Review*. JBMR Plus, 2019. **3**(4): p. e10172.
308. Garriga, C., Goff, M., Paterson, E., Hrusecka, R., Hamid, B., Alderson, J., . . . Watt, F.E., *Clinical and molecular associations with outcomes at 2 years after acute knee injury: a longitudinal study in the Knee Injury Cohort at the Kennedy (KICK)*. The Lancet Rheumatology, 2021.
309. McWilliams, D.F., Leeb, B.F., Muthuri, S.G., Doherty, M., and Zhang, W., *Occupational risk factors for osteoarthritis of the knee: a meta-analysis*. Osteoarthritis Cartilage, 2011. **19**(7): p. 829-39.
310. Gardiner, B.S., Woodhouse, F.G., Besier, T.F., Grodzinsky, A.J., Lloyd, D.G., Zhang, L., and Smith, D.W., *Predicting Knee Osteoarthritis*. Ann Biomed Eng, 2016. **44**(1): p. 222-33.
311. Zhou, X., Cao, H., Yuan, Y., and Wu, W., *Biochemical Signals Mediate the Crosstalk between Cartilage and Bone in Osteoarthritis*. BioMed Research International, 2020. **2020**: p. 5720360.

312. Mimpfen, J.Y. and Snelling, S.J.B., *Chondroprotective Factors in Osteoarthritis: a Joint Affair*. *Curr Rheumatol Rep*, 2019. **21**(8): p. 41.
313. Snelgrove, T.A., Peddle, L.J., Stone, C., Nofball, F., Peddle, D., Squire, D., . . . Rahman, P., *Association of COL1A2, COL2A1 and COL9A1 and primary osteoarthritis in a founder population*. *Clin Genet*, 2005. **67**(4): p. 359-60.
314. Loughlin, J., Sinsheimer, J.S., Mustafa, Z., Carr, A.J., Clipsham, K., Bloomfield, V.A., . . . Chapman, K., *Association analysis of the vitamin D receptor gene, the type I collagen gene COL1A1, and the estrogen receptor gene in idiopathic osteoarthritis*. *J Rheumatol*, 2000. **27**(3): p. 779-84.
315. Miosge, N., Hartmann, M., Maelicke, C., and Herken, R., *Expression of collagen type I and type II in consecutive stages of human osteoarthritis*. *Histochemistry and Cell Biology*, 2004. **122**(3): p. 229-236.
316. Fukui, N., Ikeda, Y., Ohnuki, T., Tanaka, N., Hikita, A., Mitomi, H., . . . Ochi, T., *Regional differences in chondrocyte metabolism in osteoarthritis: A detailed analysis by laser capture microdissection*. *Arthritis & Rheumatism*, 2008. **58**(1): p. 154-163.
317. Brew, C.J., Clegg, P.D., Boot-Handford, R.P., Andrew, J.G., and Hardingham, T., *Gene expression in human chondrocytes in late osteoarthritis is changed in both fibrillated and intact cartilage without evidence of generalised chondrocyte hypertrophy*. *Annals of the Rheumatic Diseases*, 2010. **69**(01): p. 234-240.
318. Aigner, T., Bertling, W., Stöss, H., Weseloh, G., and von der Mark, K., *Independent expression of fibril-forming collagens I, II, and III in chondrocytes of human osteoarthritic cartilage*. *The Journal of Clinical Investigation*, 1993. **91**(3): p. 829-837.
319. Styczynska-Soczka, K., Amin, A.K., and Hall, A.C., *Cell-associated type I collagen in nondegenerate and degenerate human articular cartilage*. *J Cell Physiol*, 2021.
320. Hwang, H.S. and Kim, H.A., *Chondrocyte Apoptosis in the Pathogenesis of Osteoarthritis*. *Int J Mol Sci*, 2015. **16**(11): p. 26035-54.
321. Takada, K., Hirose, J., Senba, K., Yamabe, S., Oike, Y., Gotoh, T., and Mizuta, H., *Enhanced apoptotic and reduced protective response in chondrocytes following endoplasmic reticulum stress in osteoarthritic cartilage*. *Int J Exp Pathol*, 2011. **92**(4): p. 232-42.
322. Uehara, Y., Hirose, J., Yamabe, S., Okamoto, N., Okada, T., Oyadomari, S., and Mizuta, H., *Endoplasmic reticulum stress-induced apoptosis contributes to articular cartilage degeneration via C/EBP homologous protein*. *Osteoarthritis Cartilage*, 2014. **22**(7): p. 1007-17.
323. Remst, D.F., Blom, A.B., Vitters, E.L., Bank, R.A., van den Berg, W.B., Blaney Davidson, E.N., and van der Kraan, P.M., *Gene expression analysis of murine and human osteoarthritis synovium reveals elevation of transforming growth factor beta-responsive genes in osteoarthritis-related fibrosis*. *Arthritis Rheumatol*, 2014. **66**(3): p. 647-56.
324. Schlaak, J.F., Pfers, I., Meyer Zum Büschenfelde, K.H., and Märker-Hermann, E., *Different cytokine profiles in the synovial fluid of patients with osteoarthritis, rheumatoid arthritis and seronegative spondylarthropathies*. *Clin Exp Rheumatol*, 1996. **14**(2): p. 155-62.
325. Shen, J., Li, S., and Chen, D., *TGF-beta signaling and the development of osteoarthritis*. *Bone Res*, 2014. **2**.
326. Blom, A.B., van Lent, P.L., Holthuysen, A.E., van der Kraan, P.M., Roth, J., van Rooijen, N., and van den Berg, W.B., *Synovial lining macrophages mediate osteophyte formation during experimental osteoarthritis*. *Osteoarthritis Cartilage*, 2004. **12**(8): p. 627-35.
327. Baker-LePain, J.C. and Lane, N.E., *Relationship between joint shape and the development of osteoarthritis*. *Current opinion in rheumatology*, 2010. **22**(5): p. 538-543.
328. Murphy, N.J., Eyles, J.P., and Hunter, D.J., *Hip Osteoarthritis: Etiopathogenesis and Implications for Management*. *Advances in therapy*, 2016. **33**(11): p. 1921-1946.
329. Jeong, Y., Daghlas, S.A., Xie, Y., Hulbert, M.A., Pfeiffer, F.M., Dallas, M.R., . . . Phillips, C.L., *Skeletal Response to Soluble Activin Receptor Type IIB in Mouse Models of Osteogenesis Imperfecta*. *J Bone Miner Res*, 2018. **33**(10): p. 1760-1772.
330. Seifer, D.R., Furman, B.D., Guilak, F., Olson, S.A., Brooks, S.C., 3rd, and Kraus, V.B., *Novel synovial fluid recovery method allows for quantification of a marker of arthritis in mice*. *Osteoarthritis Cartilage*, 2008. **16**(12): p. 1532-8.
331. Rosenthal, A.K., *Crystals, inflammation, and osteoarthritis*. *Current opinion in rheumatology*, 2011. **23**(2): p. 170-173.
332. Madi, K., Staines, K.A., Bay, B.K., Javaheri, B., Geng, H., Bodey, A.J., . . . Lee, P.D., *In situ characterization of nanoscale strains in loaded whole joints via synchrotron X-ray tomography*. *Nat Biomed Eng*, 2020. **4**(3): p. 343-354.

333. Das Neves Borges, P., Forte, A.E., Vincent, T.L., Dini, D., and Marenzana, M., *Rapid, automated imaging of mouse articular cartilage by microCT for early detection of osteoarthritis and finite element modelling of joint mechanics*. *Osteoarthritis Cartilage*, 2014. **22**(10): p. 1419-28.

Appendices

Appendix 1 - Radiolabelling Gels

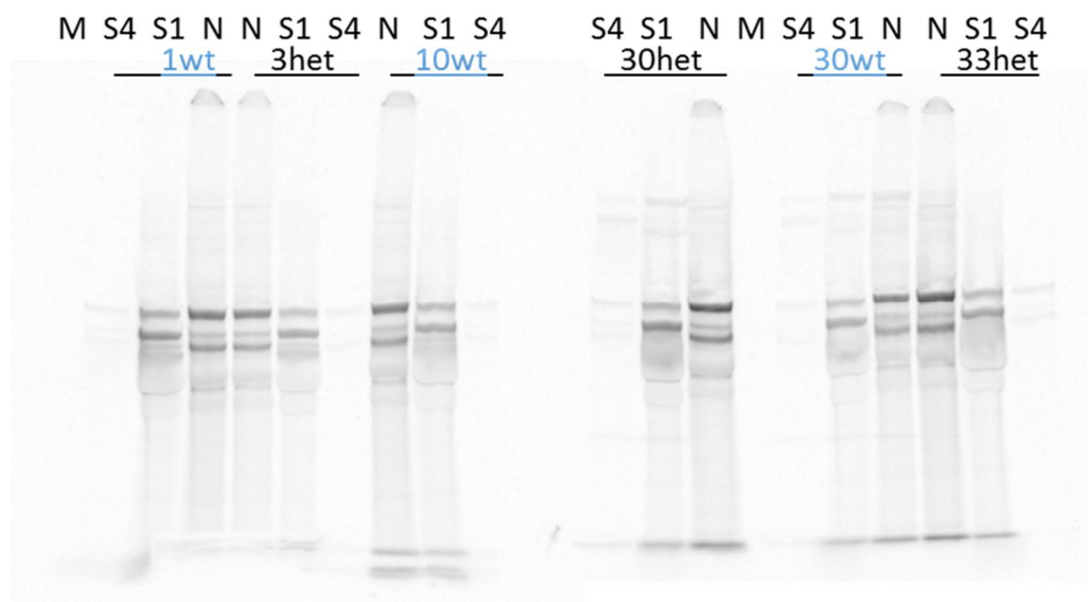


Figure 9.1. S1 (first Salt extract), S4 (fourth Salt extract) and N extracts (final detergent extract) run on Tris-Glycine gels and then exposed to a phosphor plate, show that there are similar levels of pro α 1, pro α 2 p α 1, p α 2 in the N and S1 extracts of the *wild type* (WT, *Col1a2*^{+/+}) samples when compared to the *heterozygous Col1a2*^{+/¹⁰⁷ samples, indicating that the Collagens are being secreted normally. The S4 extract is included to show that the majority of the extracellular collagens had been extracted prior to the N extraction indicating that the Collagens found in then extraction were intracellular.}

Milestone	Activity	Frequency	Pre-Test (Mean ± SD)			Post-Test (Mean ± SD)			t	P	Effect Size	Cohen's d	N
			Mean	SD	Min	Mean	SD	Min					
4 Months	Fine Motor Skills	Reach for objects	10.00	2.00	7.00	11.50	2.50	8.00	1.50	0.0001	0.75	0.75	20
		Transfer objects	10.00	2.00	7.00	11.50	2.50	8.00	1.50	0.0001	0.75	0.75	20
		Stack blocks	10.00	2.00	7.00	11.50	2.50	8.00	1.50	0.0001	0.75	0.75	20
		Put objects in container	10.00	2.00	7.00	11.50	2.50	8.00	1.50	0.0001	0.75	0.75	20
		Push objects	10.00	2.00	7.00	11.50	2.50	8.00	1.50	0.0001	0.75	0.75	20
		Pull objects	10.00	2.00	7.00	11.50	2.50	8.00	1.50	0.0001	0.75	0.75	20
	Gross Motor Skills	Walk independently	10.00	2.00	7.00	11.50	2.50	8.00	1.50	0.0001	0.75	0.75	20
		Crawl independently	10.00	2.00	7.00	11.50	2.50	8.00	1.50	0.0001	0.75	0.75	20
		Stand with support	10.00	2.00	7.00	11.50	2.50	8.00	1.50	0.0001	0.75	0.75	20
		Stand without support	10.00	2.00	7.00	11.50	2.50	8.00	1.50	0.0001	0.75	0.75	20
		Walk with support	10.00	2.00	7.00	11.50	2.50	8.00	1.50	0.0001	0.75	0.75	20
		Walk without support	10.00	2.00	7.00	11.50	2.50	8.00	1.50	0.0001	0.75	0.75	20
8 Months	Fine Motor Skills	Transfer objects	10.00	2.00	7.00	11.50	2.50	8.00	1.50	0.0001	0.75	0.75	20
		Stack blocks	10.00	2.00	7.00	11.50	2.50	8.00	1.50	0.0001	0.75	0.75	20
		Put objects in container	10.00	2.00	7.00	11.50	2.50	8.00	1.50	0.0001	0.75	0.75	20
		Push objects	10.00	2.00	7.00	11.50	2.50	8.00	1.50	0.0001	0.75	0.75	20
		Pull objects	10.00	2.00	7.00	11.50	2.50	8.00	1.50	0.0001	0.75	0.75	20
		Use simple tools	10.00	2.00	7.00	11.50	2.50	8.00	1.50	0.0001	0.75	0.75	20
	Gross Motor Skills	Walk independently	10.00	2.00	7.00	11.50	2.50	8.00	1.50	0.0001	0.75	0.75	20
		Crawl independently	10.00	2.00	7.00	11.50	2.50	8.00	1.50	0.0001	0.75	0.75	20
		Stand with support	10.00	2.00	7.00	11.50	2.50	8.00	1.50	0.0001	0.75	0.75	20
		Stand without support	10.00	2.00	7.00	11.50	2.50	8.00	1.50	0.0001	0.75	0.75	20
		Walk with support	10.00	2.00	7.00	11.50	2.50	8.00	1.50	0.0001	0.75	0.75	20
		Walk without support	10.00	2.00	7.00	11.50	2.50	8.00	1.50	0.0001	0.75	0.75	20
18 Months	Fine Motor Skills	Transfer objects	10.00	2.00	7.00	11.50	2.50	8.00	1.50	0.0001	0.75	0.75	20
		Stack blocks	10.00	2.00	7.00	11.50	2.50	8.00	1.50	0.0001	0.75	0.75	20
		Put objects in container	10.00	2.00	7.00	11.50	2.50	8.00	1.50	0.0001	0.75	0.75	20
		Push objects	10.00	2.00	7.00	11.50	2.50	8.00	1.50	0.0001	0.75	0.75	20
		Pull objects	10.00	2.00	7.00	11.50	2.50	8.00	1.50	0.0001	0.75	0.75	20
		Use simple tools	10.00	2.00	7.00	11.50	2.50	8.00	1.50	0.0001	0.75	0.75	20
	Gross Motor Skills	Walk independently	10.00	2.00	7.00	11.50	2.50	8.00	1.50	0.0001	0.75	0.75	20
		Crawl independently	10.00	2.00	7.00	11.50	2.50	8.00	1.50	0.0001	0.75	0.75	20
		Stand with support	10.00	2.00	7.00	11.50	2.50	8.00	1.50	0.0001	0.75	0.75	20
		Stand without support	10.00	2.00	7.00	11.50	2.50	8.00	1.50	0.0001	0.75	0.75	20
		Walk with support	10.00	2.00	7.00	11.50	2.50	8.00	1.50	0.0001	0.75	0.75	20
		Walk without support	10.00	2.00	7.00	11.50	2.50	8.00	1.50	0.0001	0.75	0.75	20

Table 9.2. A table showing the results of the full analysis of the subchondral bone across all three time points and a statistical comparison (student t-test) between genotypes. P values highlighted in green indicate P<0.1, P values highlighted in yellow indicate P<0.05.

Appendix 3- Time Course Full Body X-rays

2 Months X-ray

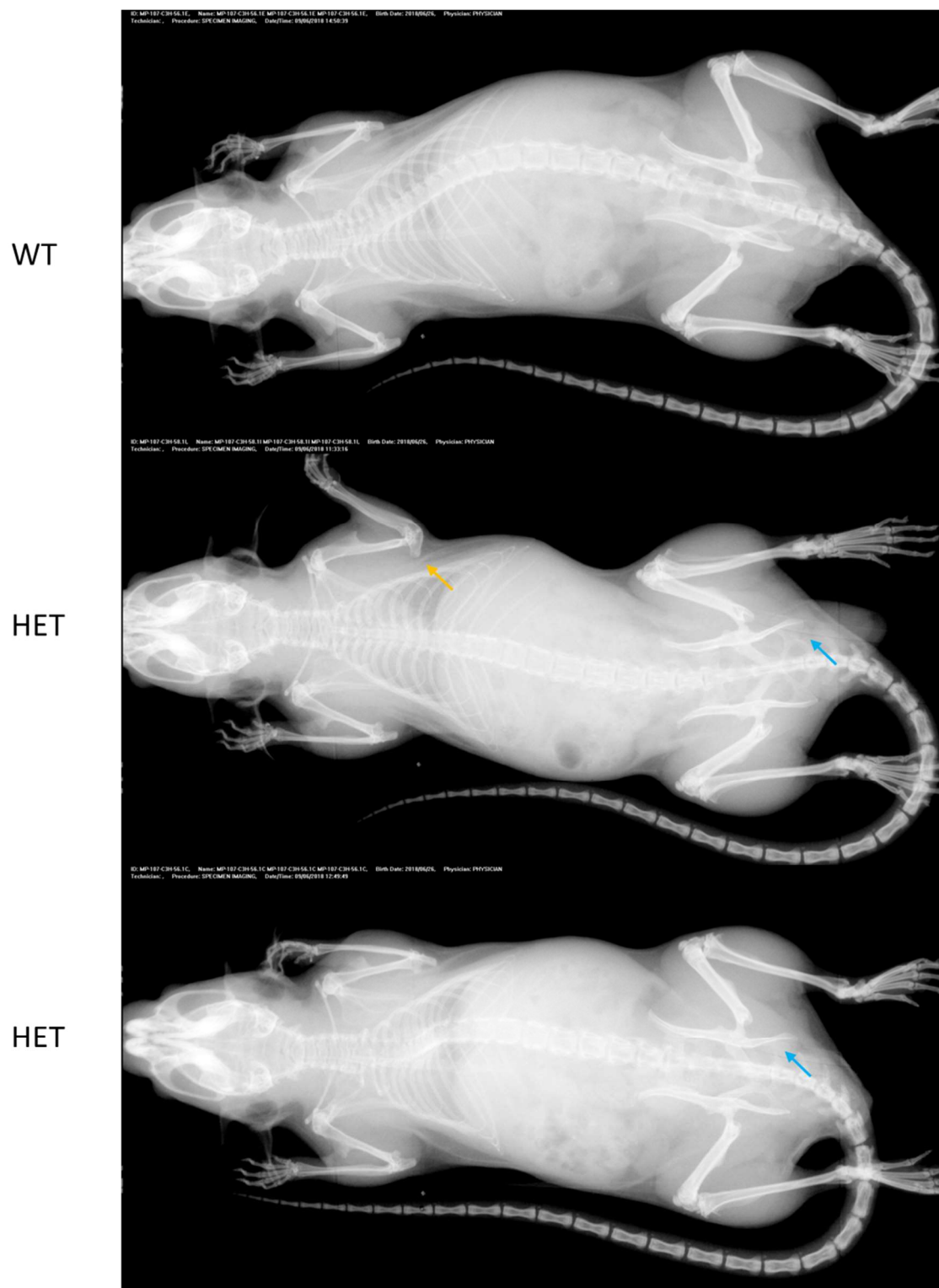


Figure 9.2. Representative X-ray images of wild type (WT, *Col1a2*^{+/+}) and heterozygous (HET, *Col1a2*^{+/¹⁰⁷}) animals at 2 months of age. At this time point the majority of heterozygous animals either showed a curved olecranon at one or both elbows (orange arrows), or splayed ischia at the pelvis (blue arrows) or a combination of both phenotypes.

4 Months X-ray

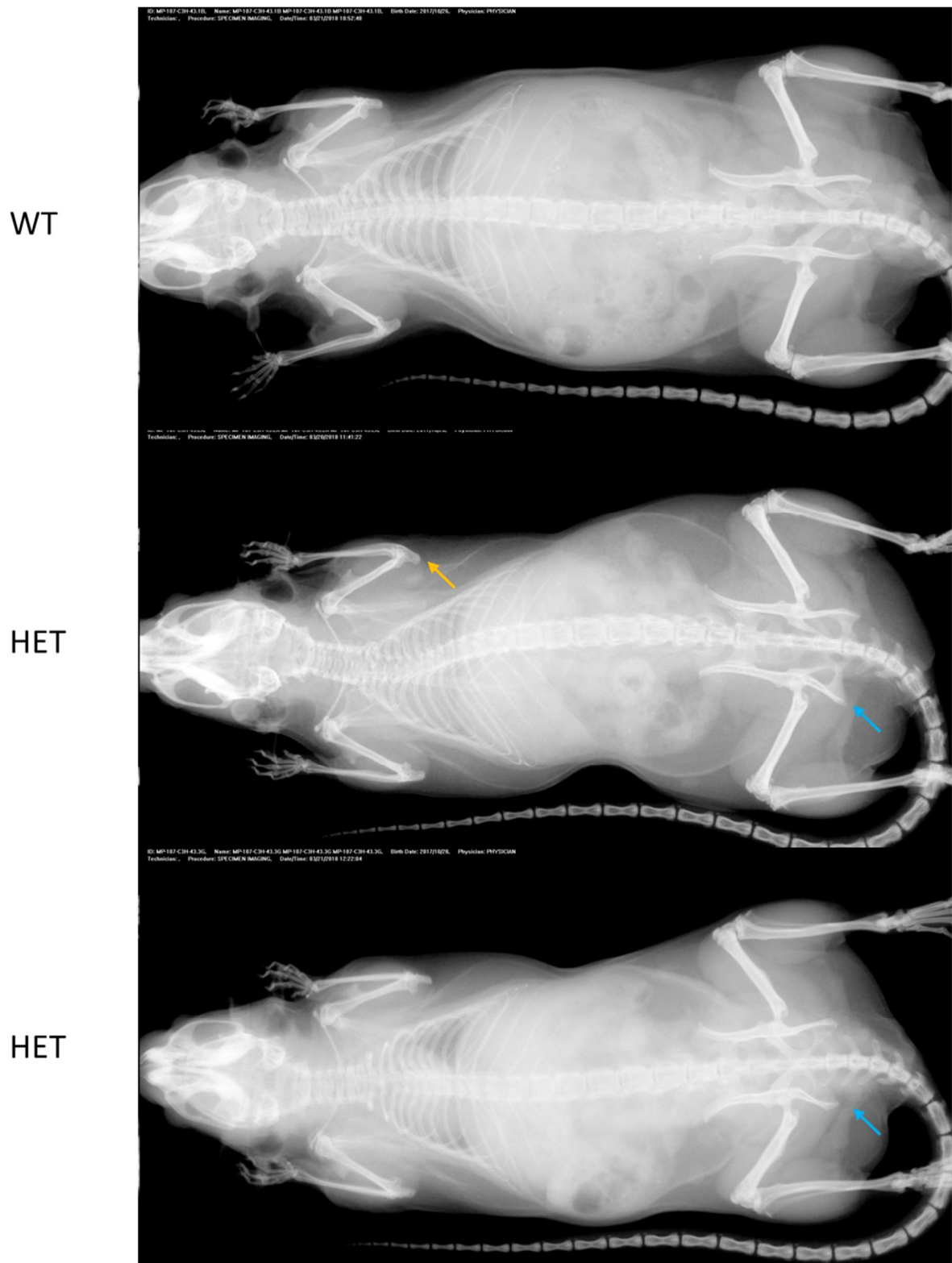


Figure 9.3. Representative X-ray images of wild type (WT, *Col1a2*^{+/+}) and heterozygous (HET, *Col1a2*^{+/107}) animals at 4 months of age. At this time point the majority of heterozygous animals either showed a curved olecranon at one or both elbows (orange arrows), or splayed ischia at the pelvis (blue arrows) or a combination of both phenotypes.

6 Months X-ray

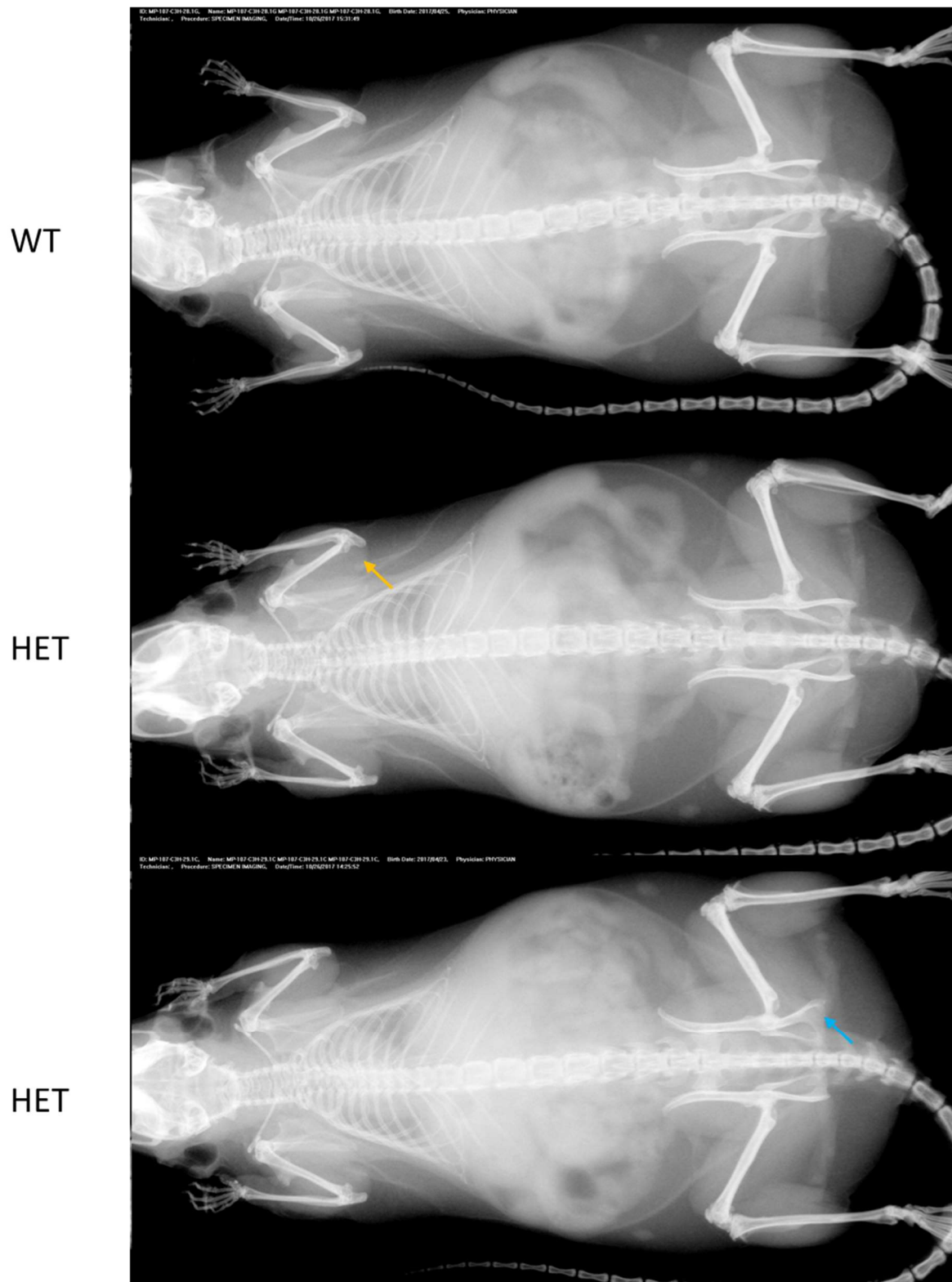


Figure 9.4. Representative X-ray images of wild type (WT, *Col1a2*^{+/+}) and heterozygous (HET, *Col1a2*^{+/107}) animals at 6 months of age. At this time point the majority of heterozygous animals either showed a curved olecranon at one or both elbows (orange arrows), or splayed ischia at the pelvis (blue arrows) or a combination of both phenotype

9 Months X-ray

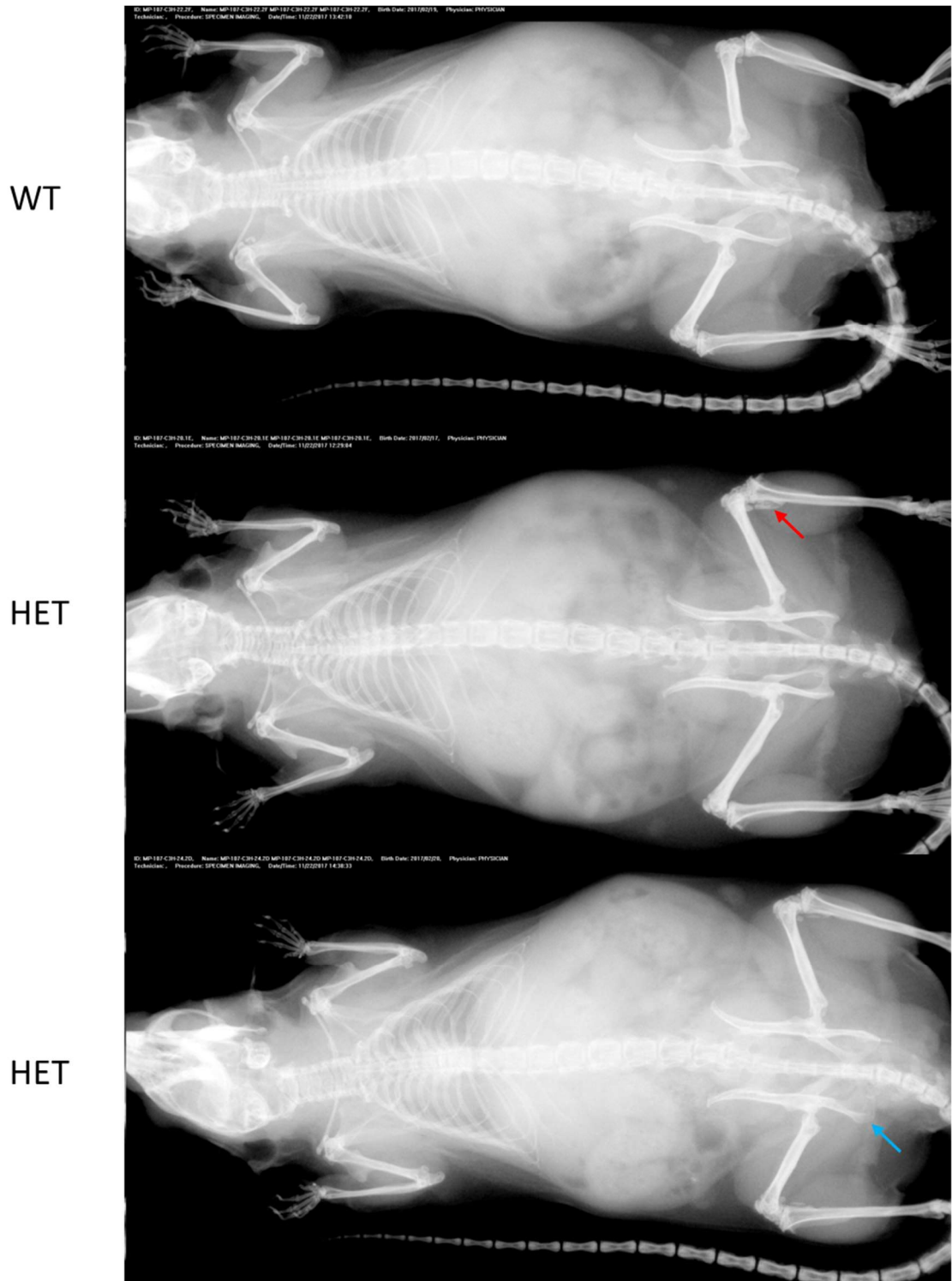
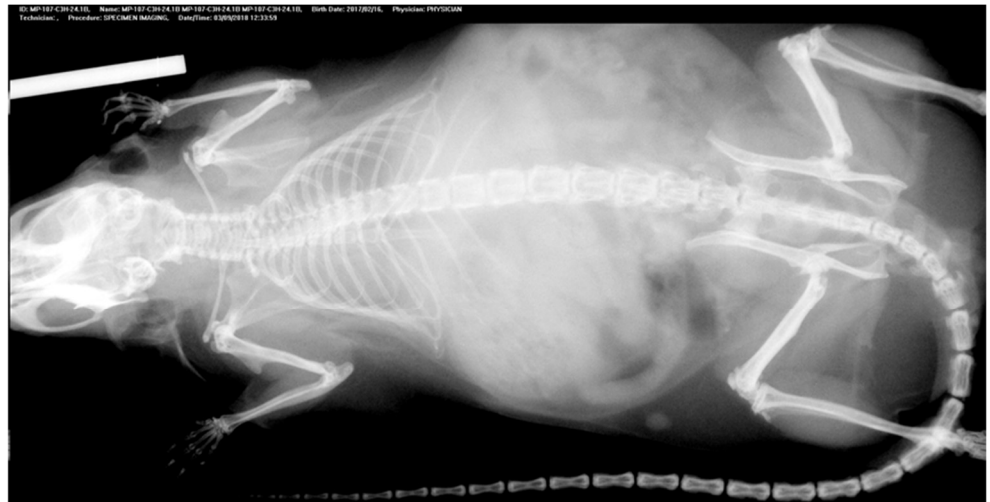


Figure 9.5. Representative X-ray images of wild type (WT, *Col1a2*^{+/+}) and heterozygous (HET, *Col1a2*^{+/¹⁰⁷}) animals at 9 months of age. At this time point the majority of heterozygous animals either showed splayed ischia at the pelvis (blue arrows), abnormal bone growth at the knee (red arrows), or a combination of both phenotypes, no animals were observed to have the curved olecranon phenotype.

12 Months X-ray

WT



HET



HET

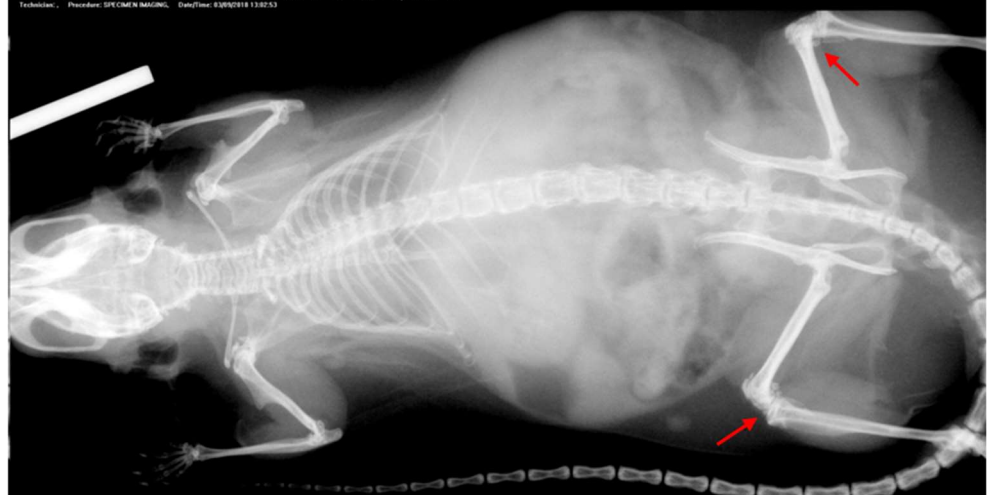


Figure 9.6. Representative X-ray images of wild type (WT, *Col1a2*^{+/+}) and heterozygous (HET, *Col1a2*^{+/¹⁰⁷) animals at 12 months of age. At this time point the majority of heterozygous animals either showed a curved olecranon at one or both elbows (orange arrows), splayed ischia at the pelvis, abnormal bone growth at the knee (red arrows), or a combination of phenotype.}

15 Months X-ray

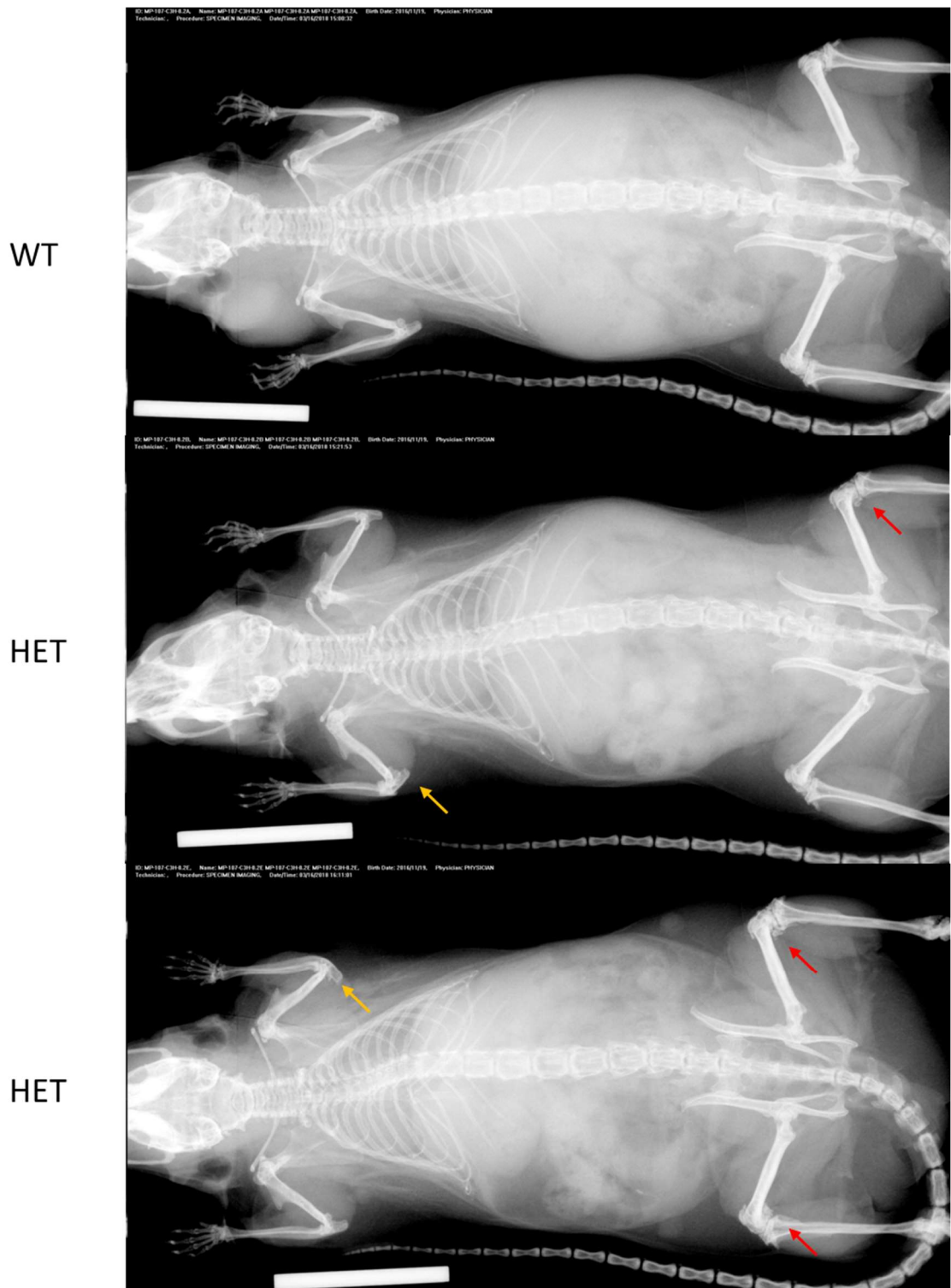


Figure 9.7. Representative X-ray images of wild type (WT, *Col1a2*^{+/+}) and heterozygous (HET, *Col1a2*^{+/¹⁰⁷}) animals at 15 months of age. At this time point the majority of heterozygous animals either showed a curved olecranon at one or both elbows (orange arrows), splayed ischia at the pelvis, abnormal bone growth at the knee (red arrows), or a combination of phenotypes.

18 Months X-ray

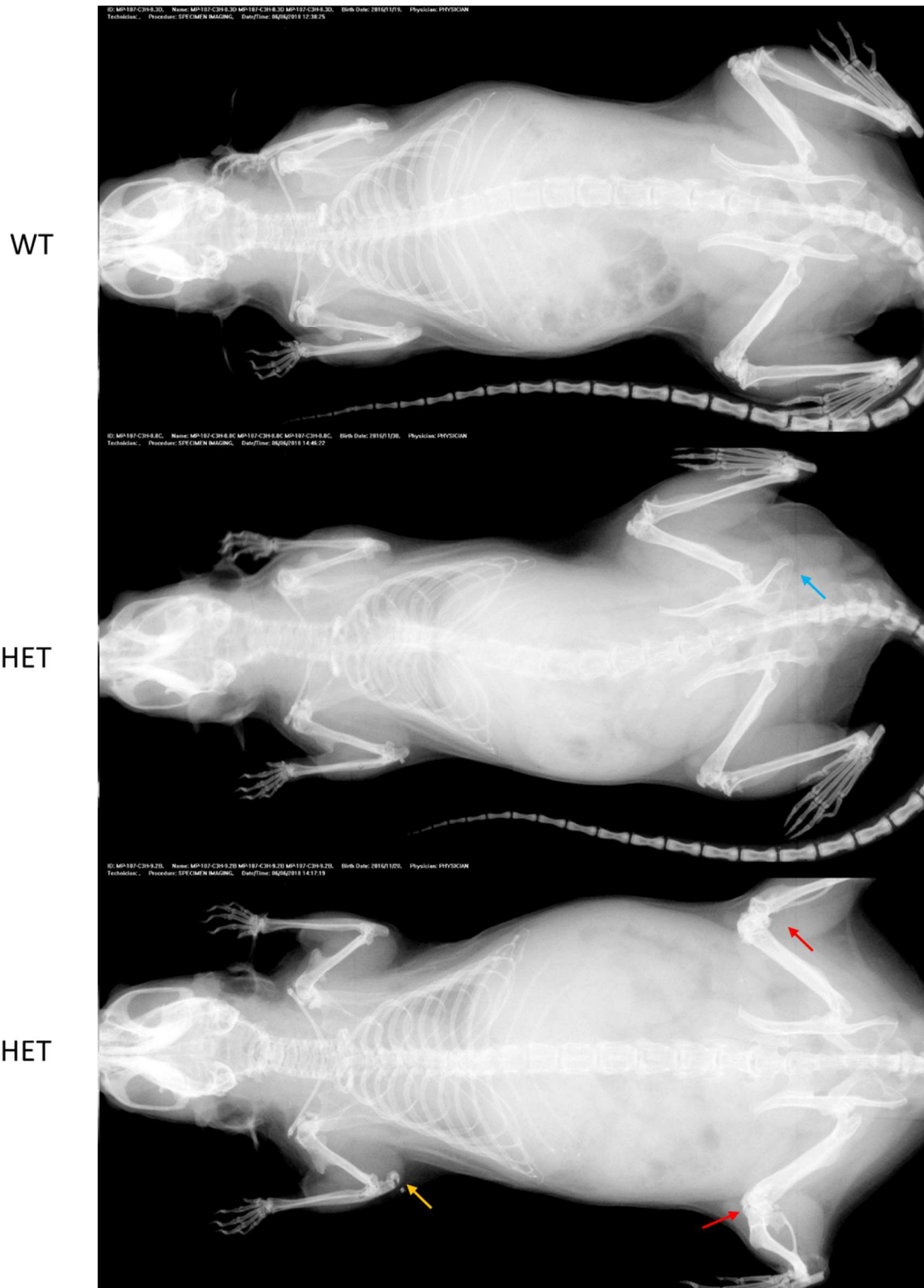


Figure 9.8. Representative X-ray images of wild type (WT, *Col1a2*^{+/+}) and heterozygous (HET, *Col1a2*^{+/¹⁰⁷}) animals at 18 months of age. At this time point the majority of heterozygous animals either showed a curved olecranon at one or both elbows (orange arrows), splayed ischia at the pelvis (blue arrows), abnormal bone growth at the knee (red arrows), or a combination of phenotypes.

WT



HET



Figure 9.9. Higher resolution X-ray images of the knees of a wild type (WT, *Col1a2*^{+/+}) and a heterozygous (HET, *Col1a2*^{+/¹⁰⁷) animal at 18 months of age. The heterozygous animals show abnormal excess bone growth at the knee (Red arrows).}

Appendix 4- High Magnification TEM Images

WT

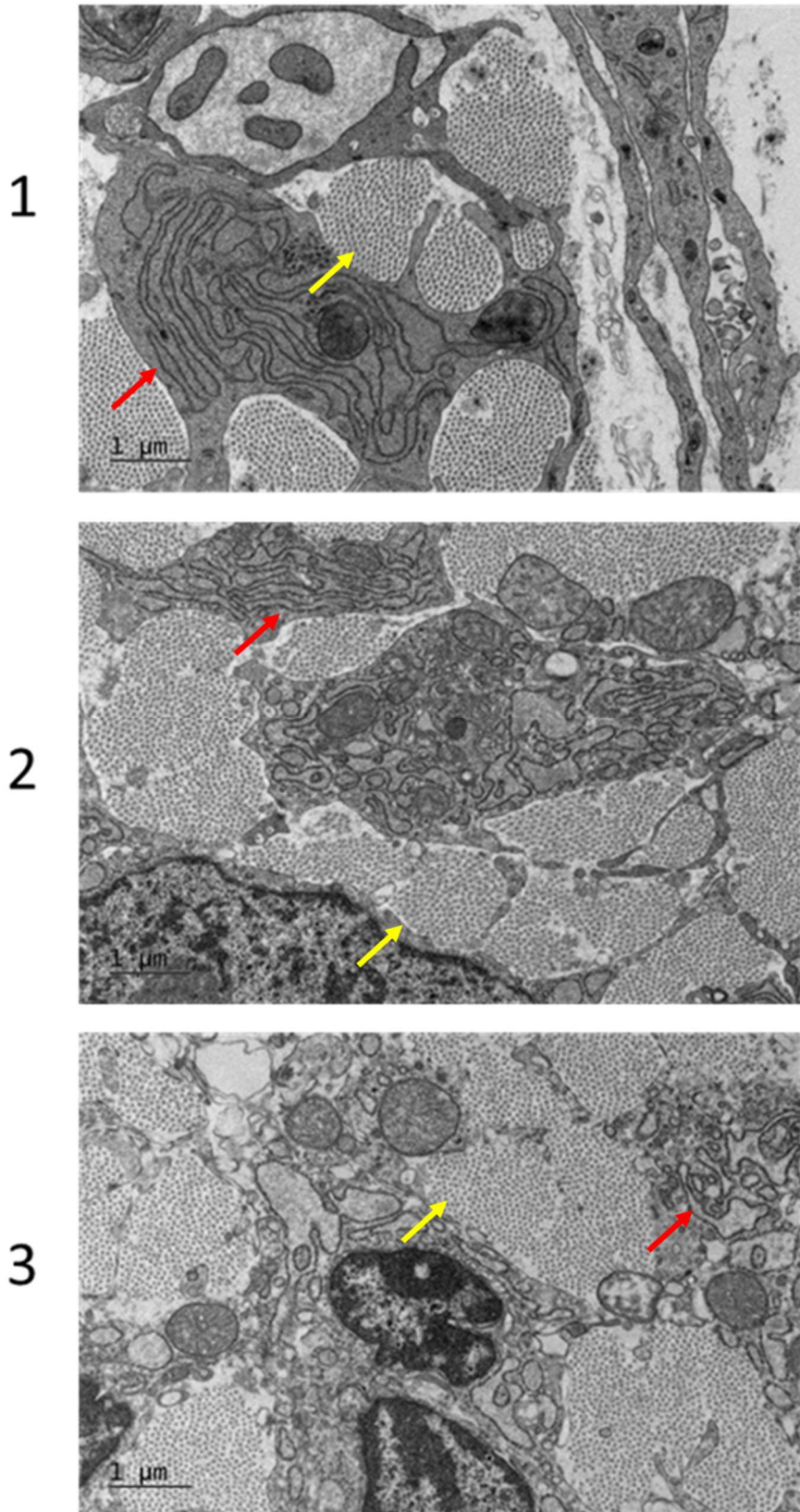


Figure 9.10. TEM images of embryonic tail tendon from wild-type embryos. Red arrows indicate the ER and yellow arrows the collagen fibrils.

HET

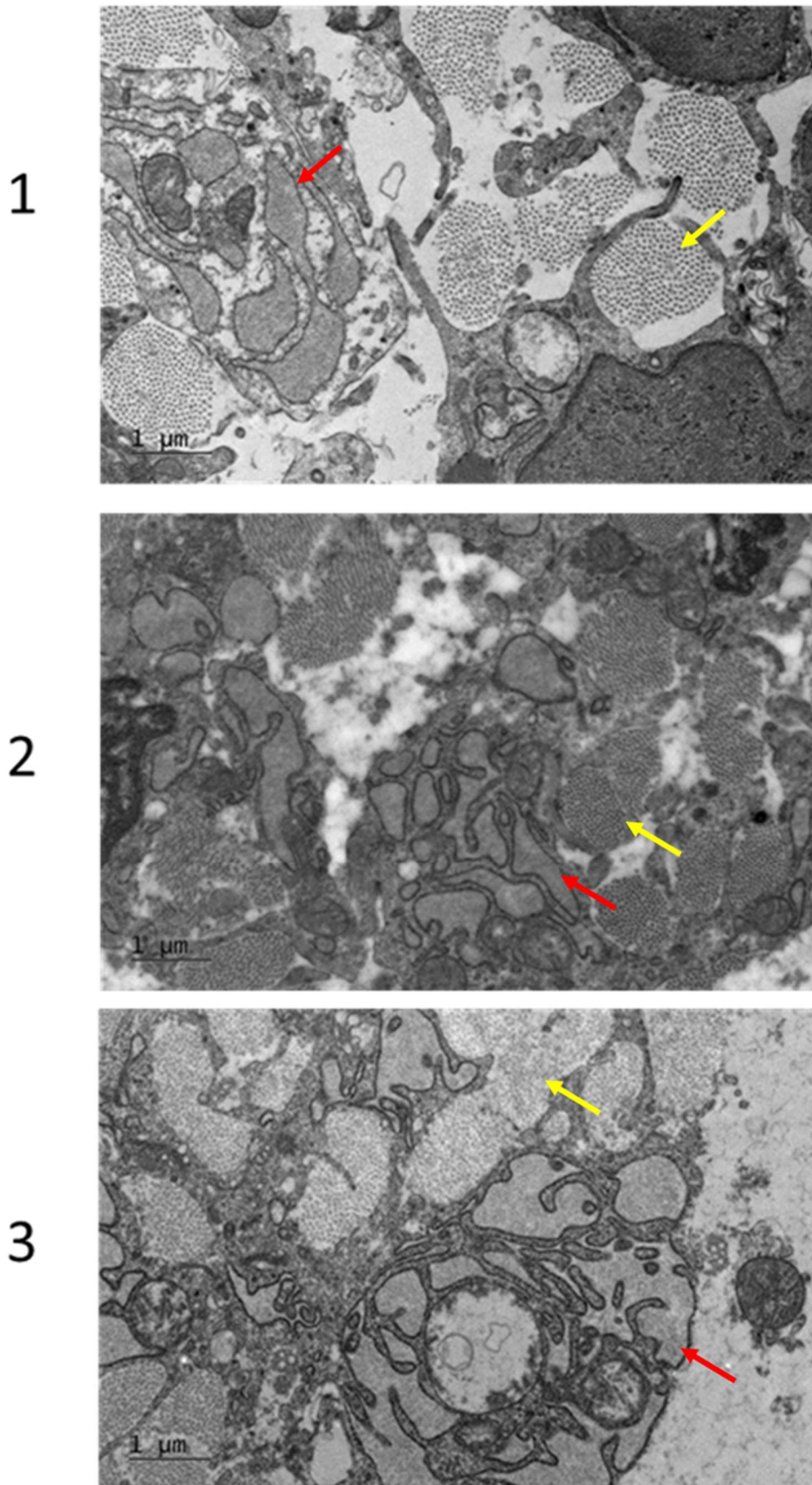


Figure 9.11. TEM images of embryonic tail tendon from heterozygous embryos. Red arrows indicate the ER and yellow arrows the collagen fibrils.

HOM

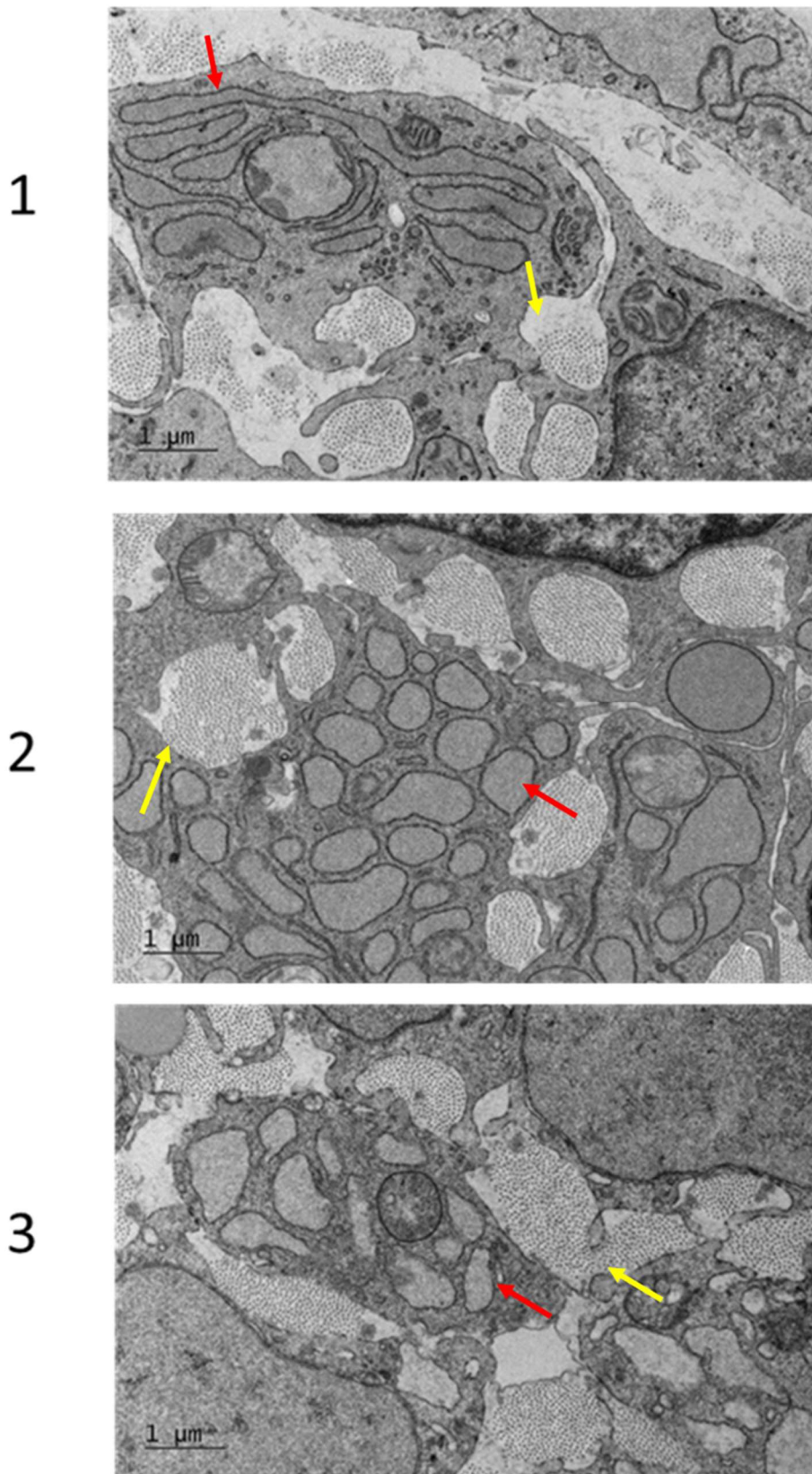


Figure 9.12. TEM images of embryonic tail tendon from homozygous embryos. Red arrows indicate the ER and yellow arrows the collagen fibrils.

Appendix 5- Full Gels for ER Stress of MEFs

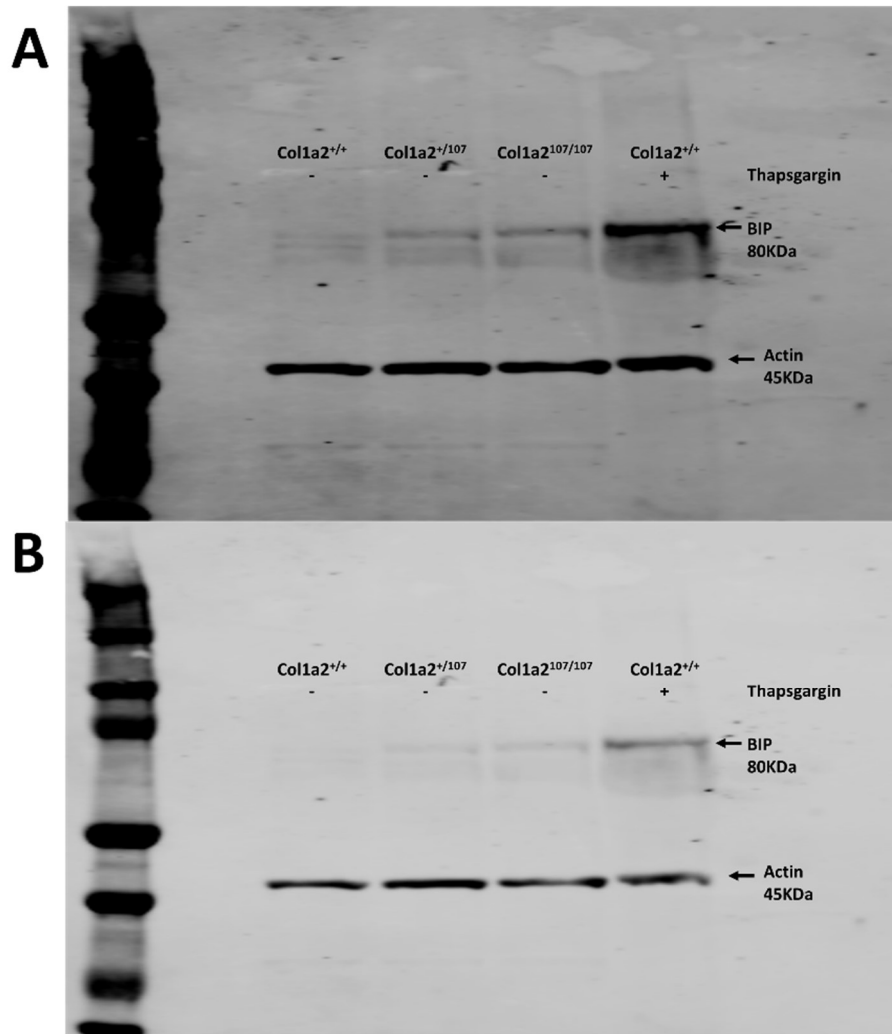


Figure 9.13. Western blot showing levels of BIP in cell lysates from MP-107 MEFs. A and B both show the same blot, with brightness adjusted. Samples are as described in Figure 8.2.

Appendix 6- Immunohistochemistry Analysis of ER Stress in Articular Cartilage

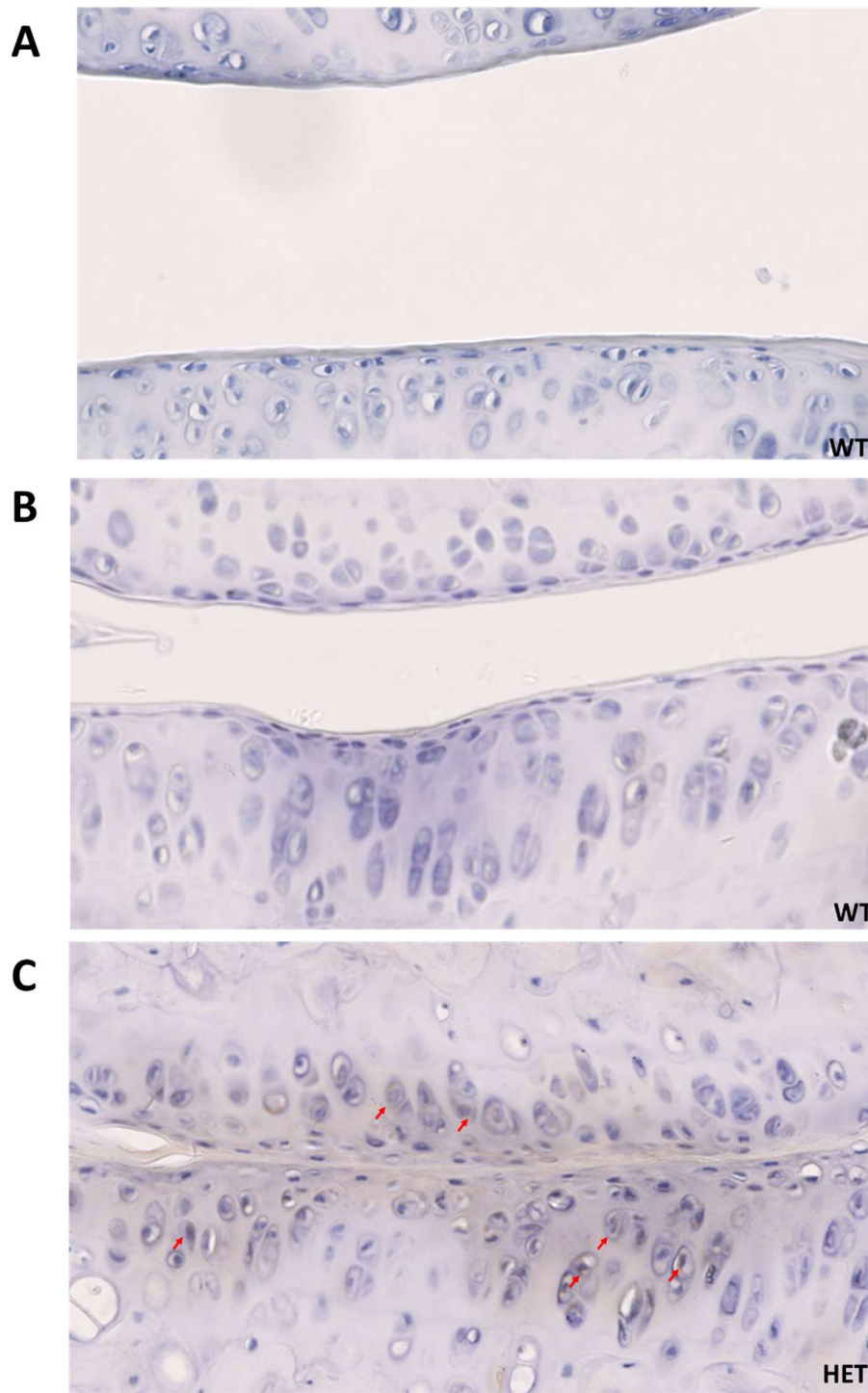


Figure 9.14. Immunohistochemical staining of wild-type and heterozygous knee sections using BIP antibody. (A) Negative control wild-type (WT, Col1a2+/+) section without primary antibody, (B) Wild-type (WT, Col1a2+/+) section with primary antibody, (C) Heterozygous (HET, Col1a2+/107) section with primary antibody. Dark brown staining is only visible in the chondrocytes of the heterozygous section (black arrows), indicating increased levels of ER stress in the heterozygote chondrocytes. It should be noted that only one 18-month heterozygous animal showed no evidence of joint damage, and was therefore used for IHC, and therefore no statistical testing was carried out.